THE 19th METALLOGRAPHY & FRACTOGRAPHY (METALLO & FRACTO)

SELECTED PEER-REVIEWED EXTENDED ARTICLES BASED ON ABSTRACTS PRESENTED AT THE 19th METALLOGRAPHY & FRACTOGRAPHY (METALLO & FRACTO 2025)

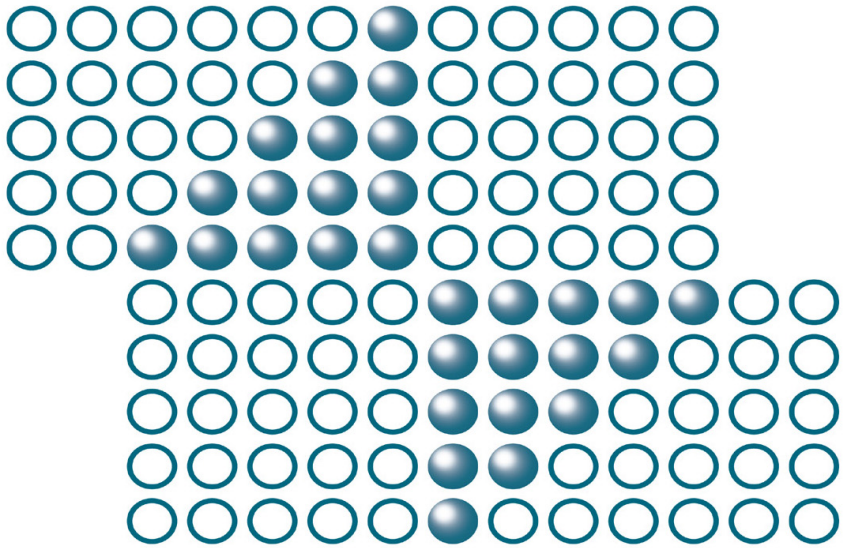

EDITED BY
DR. PETER HORŇAK
DR. MILOŠ MATVIJA

TRANS TECH PUBLICATIONS

The 19th Metallography & Fractography (Metallo & Fracto)

Selected peer-reviewed extended articles based on abstracts presented at the 19th Metallography & Fractography (Metallo & Fracto 2025)

Edited by
Dr. Peter Horňak
Dr. Miloš Matvija

The 19th Metallography & Fractography (Metallo & Fracto)

Selected peer-reviewed extended articles based on abstracts presented at the 19th Metallography & Fractography (Metallo & Fracto 2025)

Aggregated Book

Edited by

Dr. Peter Horňak and Dr. Miloš Matvija

Scientific.Net

Trans Tech Publications Ltd
Seestrasse 24c
CH-8806 Baech
Switzerland
https://www.scientific.net

Volume 250 of
Scientific Books Collection
ISBN 978-3-0364-0793-7

Full text available online at *https://www.scientific.net*

***Distributed** worldwide by*

Trans Tech Publications Ltd
Seestrasse 24c
CH-8806 Baech
Switzerland

Phone: +41 (44) 922 10 22
e-mail: sales@scientific.net

Preface

Regular traditional conference on Metallography, Fractography, and Materials Science "Metallography & Fractography 2025" took place between 23rd – 25th April 2025 in the High Tatra Mountains in the Slovak Republic. The tradition of this conference was established by Professor Ivan Hrivňák, the founder of physical metallurgy in Slovakia. The conference was established in 1969 and is organized in the three-year interval. The actual edition was the 19th already.

The conference has been featured as an important event for the presentation of results achieved in materials science and engineering. The conference focus widened long ago to cover not only the field of metal materials but also numerous modern materials and technologies as well. The conference participants come from universities, academic research institutions, and different branches of industry not only from all corners of Europe but from overseas as well with an interest in materials science and engineering. The conference has also strong support from companies which are experts in the unique experimental equipment. Exhibitions of instruments and equipment make it possible for the participants to acquaint themselves with recent achievements in research and investigation technology. The conference's ambition is regularly to expand the program to cover new approaches, new advanced materials, and technologies, new findings in fundamental research and practical production as well as to intensify international contacts.

We are very grateful to all authors who presented their actual research in the form of invited papers, lectures, and posters. The papers presented at the conference reflect the actual state of knowledge and the most important subjects that materials science deals with. Our special thanks are going to the Chairmen of the International Scientific Committee and to all members of this Committee for their help and advice in preparing the conference. One big thank is also due to all the session chairs, who directed the program. We also would like to acknowledge the work of all reviewers for their skilled and responsible judgment of all manuscripts to improve the scientific quality of submitted papers. We would like particularly obliged to the members of the Organizing Committee for their practical help in preparing the conference and the Proceedings. We also appreciate the publishers of this journal for their support in the preparation of the Proceedings.

We are also very grateful to Peter Mésároš, Rector of the Technical University of Košice, Pavol Hvizdoš, Director of the Institute of Materials Research of Slovak Academy of Sciences, Karel Saksl, Dean of the Faculty of Materials, Metallurgy and Recycling of the Technical University of Košice, and Alica Mašlejová, Head of the Institute of Materials, Faculty of Materials, Metallurgy and Recycling at the Technical University of Košice, for their help during the conference preparation.

We would like to acknowledge the assistance and support that we received from all co-organizers, several individuals, and organizations in the preparation of this symposium.

The success of this conference first depended on the quality of the research of all participants and their enthusiasm for topics of metallography, fractography, and materials science. Therefore, we would like to thank all the participants for contributing to the fruitful and convivial atmosphere of the conference which also implies the stimulating and fascinating surroundings of the conference locality in Nový Smokovec, the heart of the High Tatras Mountains.

Košice, December 2025

Peter Horňak and Miloš Matvija

Committees

Chair of the Symposium

Peter Horňak	Institute of Materials, Faculty of Materials, Metallurgy and Recycling of the Technical University of Košice, Košice, Slovakia
Pavol Hvizdoš	Institute of Materials Research, Slovak Academy of Sciences, Košice, Slovakia

International Scientific Committee

Joint Chairmen

Ján Dusza	Institute of Materials Research, Slovak Academy of Sciences, Košice, Slovakia
Akio Nishimoto	Kansai University, Osaka, Japan
Margita Longauerová	Metal Science Society at the Slovak Academy of Sciences, Slovakia
Panyawat Wangyao	Faculty of Engineering, Chulalongkorn University, Bangkok, Thailand
Katalin Balázsi	Institute of Technical Physics and Materials Science, Hungarian Academy of Sciences, Budapest, Hungary
Pavol Beraxa	ŽP Research & Development Center s.r.o., Podbrezová, Slovakia
Janette Brezinová	Institute of Technology and Materials Engineering, Faculty of Mechanical Engineering, Technical University of Košice, Košice, Slovakia
Pavel Diko	Institute of Experimental Physics of Slovak Academy of Sciences, Košice, Slovakia
Martin Fujda	Institute of Materials, Faculty of Materials, Metallurgy and Recycling, Technical University of Košice, Košice, Slovakia
Roland Haubner	Institute of Chemical Technologies and Analytics, University of Technology Vienna, Vienna, Austria
Peter Horňak	Institute of Materials, Faculty of Materials, Metallurgy and Recycling, Technical University of Košice, Košice, Slovakia
Christian Chimani	AIT Austrian Institute of Technology GmbH, TU Wien, Vienna, Austria
Jozef Janovec	Institute of Materials, Faculty of Materials, Metallurgy and Recycling, Technical University of Košice, Košice, Slovakia
Kamila Janovská	Department of Industrial Systems Management, Faculty of Materials Science and Technology, VSB - Technical University of Ostrava, Ostrava, Czech Republic
Lucyna Jaworska	Faculty of Metals Engineering and Industrial Computer Science, AGH University of Science and Technology, Krakow, Poland
Josef Kasl	Research and Testing Institute Pilsen s.r.o., Pilsen, Czech Republic
Viera Kohuteková	Research and Development, U. S. Steel Košice, s.r.o., Košice, Slovakia
Radomila Konečná	Department of Materials Engineering, Faculty of Mechanical Engineering, University of Žilina, Žilina, Slovakia
Alexandra Kovalčíková	Institute of Materials Research, Slovak Academy of Sciences, Košice, Slovakia
Ludvík Kunz	Institute of Physics of Materials, Czech Academy of Sciences, Brno, Czech Republic
Pavel Lejček	Institute of Physics, Czech Academy of Sciences, Prague, Czech Republic
Petr Louda	Department of Material Science, Faculty of Mechanical Engineering, Technical University of Liberec, Liberec, Czech Republic

Eva Mazancová	Faculty of Materials Science and Technology, VSB - Technical University of Ostrava, Ostrava, Czech Republic
Roman Moravčík	Faculty of Materials Science and Technology in Trnava, Slovak University of Technology in Bratislava, Trnava, Slovakia
Martin Nosko	Institute of Materials and Machine Mechanics, Slovak Academy of Sciences, Bratislava, Slovakia
Peter Palček	Department of Materials Engineering, Faculty of Mechanical Engineering, University of Žilina, Žilina, Slovakia
Jaroslav Pokluda	Department of Micromechanics of Materials and Engineering Acoustics, Faculty of Mechanical Engineering, Brno University of Technology, Brno, Czech Republic
Ladislav Rožek	GM for Testing Laboratories, U. S. Steel Košice, s.r.o., Košice, Slovakia
Karel Saksl	Institute of Materials, Faculty of Materials, Metallurgy and Recycling, Technical University of Košice, Košice, Slovakia
František Simančík	Institute of Materials and Machine Mechanics of Slovak Academy of Sciences, Bratislava, Slovakia
Pavol Šajgalík	President, Slovak Academy of Sciences, Bratislava, Slovakia
Jiří Švejcar	Institute of Materials Science and Engineering, Faculty of Mechanical Engineering, Brno University of Technology, Brno, Czech Republic
Eva Tillová	Department of Materials Engineering, Faculty of Mechanical Engineering, University of Žilina, Žilina, Slovakia
Ján Viňáš	Institute of Technology and Materials Engineering, Faculty of Mechanical Engineering, Technical University of Košice, Košice, Slovakia
Vlastimil Vodárek	Department of Materials Engineering and Recycling, Faculty of Materials Science and Technology, VSB - Technical University of Ostrava, Ostrava, Czech Republic
Dalibor Vojtěch	Faculty of Chemical Technology, University of Chemistry and Technology Prague, Prague, Czech Republic

Honorary Committee

Peter Horňak	Chairman of the Symposium, Institute of Materials, Faculty of Materials, Metallurgy and Recycling, Technical University of Košice, Košice, Slovakia
Pavol Hvizdoš	Co-Chairman of the Symposium, Director, Institute of Materials Research, Slovak Academy of Sciences, Košice, Slovakia
Ján Dusza	Joint Chairman, Institute of Materials Research, Slovak Academy of Sciences, Košice, Slovakia
Ivan Hrivňák	Founder of the Metallography Symposium, Bratislava, Slovakia
Kenji Ikeuchi	Long-term Co-Chairman of the Metallography Symposium, Osaka, Japan
Margita Longauerová	Long-term Chairman of the Metallography Symposium, Košice, Slovakia
Svätoboj Longauer	Long-term Specialist in the Field of Material Science, Košice, Slovakia
Pavol Beraxa	Director, ŽP VVC s.r.o., Podbrezová, Slovakia
Zuzana Gažová	Director, Institute of Experimental Physics of Slovak Academy of Sciences, Košice, Slovakia
Peter Horňak	President, Metal Science Society at the Slovak Academy of Sciences, Slovakia
Kamila Janovská	Dean, Faculty of Materials Science and Technology, VSB - Technical University of Ostrava, Ostrava, Czech Republic
Alica Mašlejová	Director, Institute of Materials, Faculty of Materials, Metallurgy and Recycling, Technical University of Košice, Košice, Slovakia

Peter Mésároš	Rector, Technical University of Košice, Košice, Slovakia
Viera Kohuteková	General Manager, Research and Development, U. S. Steel Košice, s.r.o., Košice, Slovakia
Ludvík Kunz	Director, Institute of Physics of Materials, Czech Academy of Sciences, Brno, Czech Republic
Erik Navara	Long-term Specialist in the Field of Material Science, Jihlava, Czech Republic
Ľudovít Parilák	Founder of ŽP Research & Development Center s.r.o., Podbrezová, Slovakia
Karel Saksl	Dean, Faculty of Materials, Metallurgy and Recycling, Technical University of Košice, Košice, Slovakia
Vladimír Soták	President, Železiarne Podbrezová a. s., Podbrezová, Slovakia
Pavol Šajgalík	Long-term President, Slovak Academy of Sciences, Bratislava, Slovakia
Esa Vuorinen	Senior Professor, Luleå University of Technology, Luleå, Sweden
Bogdan G. Wendler	Professor, Technical University of Lodz, Lodz, Poland
Petr Zuna	Professor, Faculty of Mechanical Engineering, Czech Technical University in Prague, Prague, Czech Republic

Organizing Committee

Peter Horňak	Chairman, Institute of Materials, Faculty of Materials, Metallurgy and Recycling, Technical University of Košice, Košice, Slovakia
Pavol Hvizdoš	Co-Chairman, Institute of Materials Research, Slovak Academy of Sciences, Košice, Slovakia
Miloš Matvija	Secretary of the Symposium, Institute of Materials, Faculty of Materials, Metallurgy and Recycling, Technical University of Košice, Košice, Slovakia
Tomáš Lukáč	Economic Department of the Symposium, Lumakon, s. r. o., Košice, Slovakia
Martin Fujda	Institute of Materials, Faculty of Materials, Metallurgy and Recycling, Technical University of Košice, Košice, Slovakia
Katarína Gáborová	Institute of Materials, Faculty of Materials, Metallurgy and Recycling, Technical University of Košice, Košice, Slovakia
Mária Hagarová	Institute of Materials, Faculty of Materials, Metallurgy and Recycling, Technical University of Košice, Košice, Slovakia
Beáta Ballóková	Institute of Materials Research, Slovak Academy of Sciences, Košice, Slovakia
Radovan Bureš	Institute of Materials Research, Slovak Academy of Sciences, Košice, Slovakia
Mária Fáberová	Institute of Materials Research, Slovak Academy of Sciences, Košice, Slovakia
Dávid Medveď	Institute of Materials Research, Slovak Academy of Sciences, Košice, Slovakia
Erika Múdra	Institute of Materials Research, Slovak Academy of Sciences, Košice, Slovakia
Marek Vojtko	Institute of Materials Research, Slovak Academy of Sciences, Košice, Slovakia
Pavel Bekeč	ŽP VVC s.r.o., ŽP Podbrezová, Podbrezová, Slovakia
Mária Demčáková	GM for Testing Laboratories, U. S. Steel Košice, s.r.o., Košice, Slovakia
Peter Kalmár	GM for Testing Laboratories, U. S. Steel Košice, s.r.o., Košice, Slovakia

Acknowledgement

The Conference Committee wishes to acknowledge the assistance and encouragement that we have received from several individuals and organizations in the preparation of this event, from companies taking part in the exhibition, and which also sponsor this symposium, are as follows:

General Advertising Partners:
Anton Paar Slovakia s.r.o.
JEOL (Europe) SAS – organizační složka
KVANT spol. s r. o.
RMS Košice s.r.o.
ŽP VVC s.r.o.

Advertising Partners:
Metalco Testing s.r.o.
Nadácia SPP
NAT Holding s.r.o.
VUJE, a.s.
ZENA-R Slovakia, s.r.o.
ZwickRoell s.r.o

Exhibitors:
Anton Paar Slovakia s.r.o.
Carl Zeiss Slovakia, s.r.o.
JEOL (Europe) SAS – organizační složka
KVANT spol. s r. o.
Metalco Testing s.r.o.
SPECION, s.r.o.
ZENA-R Slovakia, s.r.o.
ZwickRoell s.r.o

Organizers

Institute of Materials
Faculty of Materials, Metallurgy and Recycling
Technical University of Košice
Košice, Slovak Republic
Letná 1/9, 042 00 Košice-Sever, Slovak Republic
phone: +421 55 602 2543, +421 55 602 2539
e-mails: peter.hornak@tuke.sk, milos.matvija@tuke.sk
website: konferencie.net/metalo

Institute of Materials Research of the
Slovak Academy of Sciences
Košice, Slovak Republic
Watsonova 47, 040 01 Košice, Slovak Republic
phone: +421 55 792 2402
e-mail: imrsas@saske.sk
website: wwwnew.saske.sk/imr/

Lumakon, s.r.o,
Košice, Slovak Republic
Na Šajbe 1A, 040 01 Košice, Slovak Republic
phone: +421 903 249 123
e-mail: metalo@konferencie.net
website: konferencie.net/metalo

Co-organizers

Slovak Metal Science Society of the
Slovak Academy of Sciences, Slovak Republic

Institute of Experimental Physics of the
Slovak Academy Of Sciences, Košice, Slovak Republic

Research and Development Usse,
U.S. Steel Košice, S.R.O., Košice, Slovak Republic

ŽP VVC S.R.O., Podbrezová,
Slovak Republic

Conference Participants

Photo of Conference Participants (April 24, 2025, Conference Dinner)

Table of Contents

Chapter 4: Welding

Chapter 5: Tribology

Chapter 6: Applied Materials and Engineering Applications

Chapter 7: Metallographic Studies of Archaeological Metals

Chapter 8: Fatigue, Fractography and Failure Analysis

CHAPTER 1:

Plasma Nitriding of Stainless Steels

Published in: Key Engineering Materials
ISSN: 1662-9795, Vol. 1044, pp 51-58
doi:10.4028/p-lU7XPA

Submitted: 2025-05-27
Revised: 2025-12-04
Accepted: 2025-12-19
Online: 2026-03-03

Effects of Gas Composition and Gas Pressure on Plasma Nitriding of Ferritic Stainless Steel Using 304 Stainless Steel Screen

Akio Nishimoto[1,a*], Ojiro Kishimoto[2,b] and Daichi Tanaka[1,c]

[1]Department of Chemistry and Materials Engineering, Faculty of Chemistry, Materials and Bioengineering, Kansai University, 3-3-35 Yamate-cho, Suita, Osaka 564-8680, Japan

[2]Graduate School of Science and Engineering, Kansai University, Osaka 564-8680, Japan

[a*]akionisi@kansai-u.ac.jp, [b]k479920@kansai-u.ac.jp, [c]d.tanaka141010.d@gmail.com

Keywords: plasma nitriding, stainless steel, screen-assisted direct current plasma nitriding, gas pressure, ferritic stainless steel, surface engineering.

Abstract. Conventional plasma nitriding can induce defects due to direct plasma formation on the surface of the treated material. To address this issue, the screen-assisted direct current plasma nitriding (S-DCPN) method was developed, which generates plasma on both the sample and a surrounding screen, thereby reducing such defects. In this study, S-DCPN was applied to ferritic stainless steel (SUS430) using austenitic stainless steel (SUS304) as the screen material. Treatments were performed at 633 K for 15 hours under gas pressures of 200 and 600 Pa, with varying gas compositions of 75 % N_2 – 25 % H_2, 50 % N_2 – 50 % H_2, and 25 % N_2 – 75 % H_2. To evaluate the effects of gas composition and pressure, a range of analyses was conducted, including X-ray diffraction (XRD), cross-sectional microstructural observations, glow discharge optical emission spectrometry (GD-OES), hardness testing, and corrosion testing. The results revealed the formation of the α_N phase, a supersaturated solid solution of nitrogen in ferrite, under all conditions. Nitrogen diffusion and surface hardness increased with higher hydrogen content, and corrosion resistance was notably enhanced under the 25 % N_2 – 75 % H_2 condition. These findings demonstrate the effectiveness of S-DCPN in improving the surface properties of ferritic stainless steel while maintaining or enhancing corrosion resistance.

Introduction

In recent years, low-temperature nitriding has attracted global attention as an effective surface modification technique for stainless steel. Nitriding improves the surface hardness of metallic materials by enabling nitrogen to diffuse into the surface, forming nitrides or a supersaturated solid solution of nitrogen into the metal matrix [1–3]. This process enhances hardness, corrosion resistance, wear resistance, and fatigue strength. Common nitriding methods include gas nitriding using ammonia, salt-bath nitriding using cyanide-based salts, and plasma nitriding, which employs glow discharge in a low vacuum with nitrogen-containing gas. Among these, plasma nitriding is considered energy-efficient and time-saving due to the active nitrogen species involved [1, 2, 4–10].

In conventional DC plasma nitriding (DCPN), plasma forms directly on the material surface by applying a high cathode voltage. However, this can lead to non-uniform nitriding, melting, or localized defects due to abnormal discharges and edge effects [11–17]. To address these issues, screen-assisted DCPN (S-DCPN) was developed. In this method, a metal mesh screen surrounds the sample, and plasma is generated on both the screen and the sample surfaces. The plasma near the screen contains nitrogen molecules, radicals, ions, hydrogen-related radicals (e.g., NiHj), and electrons. According to the sputtering and deposition mechanism [14, 18–20], metal atoms ejected from the screen by nitrogen ion bombardment combine with nitrogen radicals to form metal nitrides (MNs), which are then deposited onto the sample surface. These MNs decompose into lower-nitrogen-content nitrides (M_XN), releasing nitrogen that diffuses into the sample and contributes to nitriding. For instance, in iron nitrides, nitrogen is released during the sequential decomposition of FeN → ε-$Fe_{2\text{-}3}N$ → γ'-Fe_4N → Fe, allowing further diffusion. However, excessive MN deposition over time may hinder nitrogen diffusion [21–24].

To counter this, voltage is also applied to the sample in the S-DCPN process to remove surface deposits. The screen additionally serves as a radiant heat source and reduces the cathode voltage applied to the sample, thereby mitigating edge effects typical in conventional DCPN [25].

Stainless steels are widely used due to their excellent corrosion resistance. They are classified as austenitic, ferritic, martensitic, duplex, and precipitation-hardening types, each with distinct mechanical and corrosion properties. While many studies have investigated low-temperature nitriding of austenitic stainless steels, research on ferritic and duplex types remains limited. In ferritic stainless steels, low-temperature nitriding typically results in the formation of an expanded ferrite (α_N or Sα) phase, where nitrogen is supersaturated in the α-Fe matrix [26, 27].

In a previous study, ferritic stainless steel SUS430 was treated by DCPN and active screen plasma nitriding (ASPN) using an austenitic stainless steel SUS304 screen. XRD analysis revealed α_N phase peaks at 623 K and 673 K on the DCPN-treated sample edges, and at 673 K and 723 K for ASPN-treated samples. CrN precipitation was observed at temperatures above 723 K at the DCPN center, above 623 K at the DCPN edges, and above 723 K in ASPN-treated specimens. As a result, the DCPN-treated samples exhibited lower pitting corrosion resistance due to CrN formation at all temperatures. In contrast, ASPN-treated samples generally showed improved corrosion resistance compared to untreated material, except at 623 K. The highest corrosion resistance was observed at 673 K due to α_N phase formation, while CrN precipitation above 723 K reduced it [28].

Extended low-temperature nitriding (633–653 K for 15 hours) has been shown to increase hardness and improve corrosion resistance. However, treatment temperature and time significantly influence the nitrided layer, and further investigation is needed due to the limited number of studies. Notably, previous reports suggest that gas composition and pressure strongly affect nitriding behavior and the resulting layer properties [29, 30]. Therefore, this study investigates the effects of gas composition and pressure on the S-DCPN treatment of SUS430 at 633 K for 15 hours to identify optimal nitriding conditions for ferritic stainless steel.

Experimental Procedure

Experimental Samples.

Ferritic stainless steel SUS430 was used as the test material in this study. The SUS430 samples were cut from 25 mm-diameter bars into 5 mm-thick disks. The top surface of each sample was wet-polished using #220 to #2000 grit abrasive paper, followed by buffing to a mirror finish with alumina powder having a particle diameter of 1 μm.

Plasma Nitriding.

Plasma nitriding was carried out using a DC plasma nitriding unit (JIN-1S, NDK Inc.). The screen was made of expanded metal mesh using austenitic stainless steel SUS304, with a diameter of 150 mm and a height of 60 mm. The following procedure was used for S-DCPN treatment. After aligning a radiation thermometer with the sample, the furnace was evacuated to a pressure below 10 Pa using a vacuum pump. A gas mixture, 75 % N_2 – 25 % H_2 (N_2:H_2 = 3:1), 50 % N_2 – 50 % H_2 (N_2:H_2 = 1:1), or 25 % N_2 – 75 % H_2 (N_2:H_2 = 1:3), was introduced into the ballast tank and exhausted simultaneously to maintain the desired furnace pressure (200 Pa or 600 Pa). A glow discharge was then generated between the sample stage, the metal screen, and the furnace wall to raise the processing temperature. Once the sample temperature reached the target value of 633 K, S-DCPN treatment was carried out for 15 hours. After nitriding, the gas supply was maintained until the sample cooled to room temperature, at which point air was introduced into the furnace for sample removal.

Evaluation Method.

To evaluate the effects of low-temperature nitriding on ferritic stainless steel, the following analyses were performed: X-ray diffraction (XRD), cross-sectional microstructure observation, glow discharge optical emission spectrometry (GD-OES), hardness testing, and corrosion testing. XRD analysis was conducted using a fully automated horizontal multipurpose diffractometer, with Cu-Kα

radiation (λ = 0.15405 nm) at 40 kV and 200 mA. For cross-sectional observation, the nitrided samples were cut perpendicular to the surface, etched with 0.67 % $CuCl_2$ hydrochloric acid solution, and examined using an optical microscope once the microstructure became visible.

GD-OES analysis was carried out using a Marcus-type high-frequency glow-discharge optical emission spectrometer to evaluate the depth profiles of elemental distribution. Hardness testing was conducted with a micro-Vickers tester to compare surface and cross-sectional hardness values. For corrosion testing, the nitrided sample was spot-welded to SUS304 lead wires and masked with Teflon tape, leaving a 6 mm-diameter exposed area. A 3.5 mass% NaCl solution was used as the electrolyte, with Ag/AgCl as the reference electrode and Pt as the counter electrode. The potential was swept from −1.0 V to +1.5 V using a potentiostat, and the resulting current was recorded using a data logger.

Results and Discussion

Figure 1 shows the XRD results of the S-DCPN-treated specimens. Diffraction lines corresponding to the α_N phase, a supersaturated solid solution of nitrogen in the ferrite phase, were observed under all treatment conditions. In each case, the diffraction peaks were shifted to lower angles compared to those of the untreated samples, indicating lattice expansion [31]. Furthermore, the formation of ε-Fe_2N and Cr_2N phases was confirmed in the 25 % N_2 – 75 % H_2 samples. Figure 2 further demonstrates that the lattice expansion ratio of the α_N phase at the surface increased with a higher hydrogen ratio in the process gas. The variation in lattice expansion observed at different process gas pressures is likely attributed to differences in nitrogen solubility near the sample surface, as well as the size and quantity of surface deposits formed during treatment.

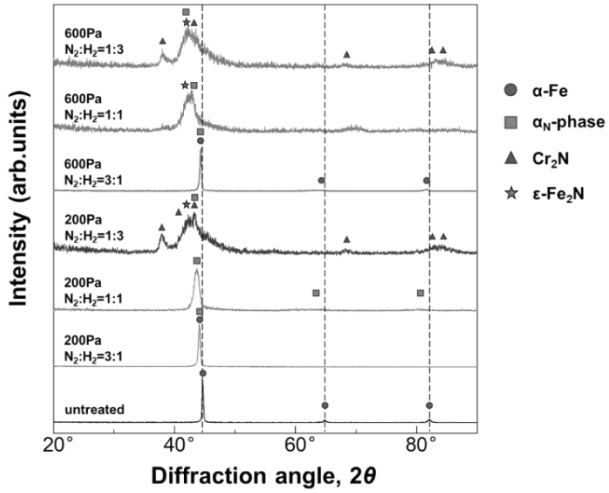

Fig. 1. XRD pattern of SUS430 sample treated by S-DCPN.

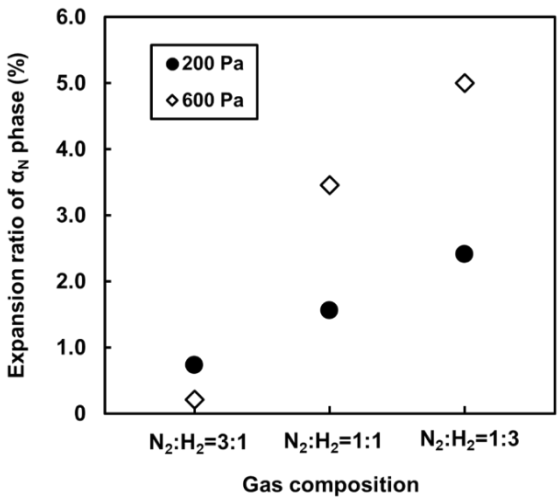

Fig. 2. Expansion ratio of α_N phase of SUS430 sample treated by S-DCPN.

Figure 3 shows the results of GD-OES measurements of the nitrogen diffusion zone of SUS430 treated with S-DCPN. The data indicate that the nitrogen concentration near the surface, the depth of nitrogen diffusion, the nitrogen content at a given depth, and the overall nitrogen-enriched region increased with higher hydrogen content in the process gas. The near-surface nitrogen concentrations were 10.3 at% for the 200 Pa, 75 % N_2 – 25 % H_2 sample, 15.7 at% for the 200 Pa, 50 % N_2 – 50 % H_2 sample, and 33.4 at% for the 200 Pa, 25 % N_2 – 75 % H_2 sample. Similarly, the values were 11.9 at% for the 600 Pa, 75 % N_2 – 25 % H_2 sample, 17.6 at% for the 600 Pa, 50 % N_2 – 50 % H_2 sample, and 30.2 at% for the 600 Pa, 25 % N_2 – 75 % H_2 sample. The corresponding nitrogen diffusion depths were 50.25 μm, 6.93 μm, and 12.11 μm for the 200 Pa samples with 75 % N_2 – 25 % H_2, 50 % N_2 – 50 % H_2, and 25 % N_2 – 75 % H_2, respectively, and 5.1 μm, 6.7 μm, and 11.9 μm for the 600 Pa samples with the same respective gas compositions. These results suggest that the increased hydrogen content enhances the contribution of hydrogen ions in the plasma, which improves surface cleaning and activation via reduction effects, thereby facilitating nitrogen absorption and diffusion.

Furthermore, the higher hydrogen ratio is likely to promote the formation of NH radicals such as NiHj, which may further enhance the nitriding effect.

Figure 4 presents the results of the hardness tests. The surface hardness of all S-DCPN-treated samples increased compared to that of the untreated sample. This increase can be attributed to lattice distortions caused by the substitution of different elements in the solid solution. Such distortions make it more difficult for dislocations to move, as more energy is required to shift distorted lattice planes than uniform atomic planes [32]. Both the surface hardness and the depth of the hardened layer increased with higher hydrogen content in the process gas. In general, it is reported that hardness increases due to the formation of Fe nitrides and Cr nitrides [28, 33]. In the present results as well, as shown by the XRD result in Fig. 1, ε-Fe_2N and Cr_2N were formed in the 25 % N_2 – 75 % H_2 sample, leading to a higher nitrogen concentration in the interior and an improvement in the hardness inside the specimen. As shown in the GD-OES results in Fig. 3, increasing the hydrogen ratio led to higher nitrogen concentrations and deeper nitrogen-enriched regions, which likely contributed to the enhanced hardness through greater nitrogen diffusion into the substrate.

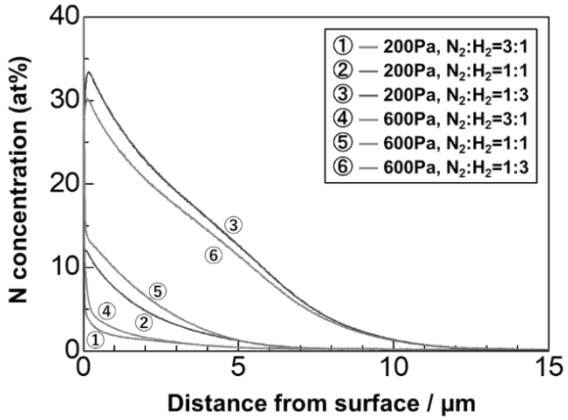

Fig. 3. GD-OES nitrogen profile of SUS430 sample treated by S-DCPN.

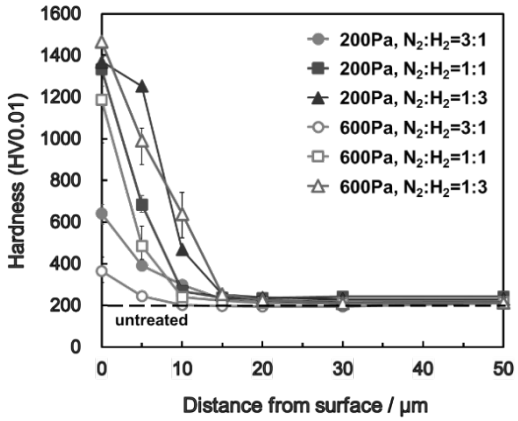

Fig. 4. Cross-sectional hardness profile of SUS430 sample treated by S-DCPN.

Figure 5 shows the cross-sectional microstructures observed by optical microscopy. A white layer, indicative of excellent corrosion resistance, was observed in the cross sections of samples treated with S-DCPN at 200 Pa and 600 Pa under gas compositions of 50 % N_2 – 50 % H_2 and 25 % N_2 – 75 % H_2. The thicknesses of this surface layer were approximately 6.1 μm for the 200 Pa, 50% N_2 – 50 % H_2 sample, 12.0 μm for the 200 Pa, 25 % N_2 – 75 % H_2 sample, 7.2 μm for the 600 Pa, 50 % N_2 – 50 % H_2 sample, and 10.4 μm for the 600 Pa, 25 % N_2 – 75 % H_2 sample. These results indicate that the thickness of the nitrided layer increased with a higher hydrogen ratio in the process gas. This trend is consistent with the results shown in Fig. 3, where the nitrogen concentration and diffusion depth also increased with increasing hydrogen content. In contrast, no distinct white layer was observed in the sample treated with 75 % N_2 – 25 % H_2 at either pressure, indicating that a sufficient nitrided layer did not form. In this case, the α_N phase, a supersaturated solid solution of nitrogen in the ferrite phase, is believed to have formed only in a very shallow region near the surface. Moreover, iron nitride precipitates were observed within the α_N phase in the 75 % N_2 – 25 % H_2 sample, suggesting insufficient nitrogen diffusion and incorporation.

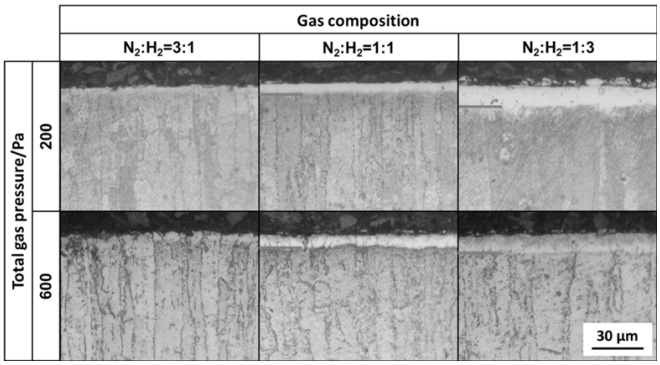

Fig. 5. Cross-sectional microstructure of SUS430 sample treated by S-DCPN.

Figure 6 shows the results of polarization tests conducted on S-DCPN-treated samples in a 3.5 mass% NaCl solution, and Fig. 7 presents the corresponding pitting corrosion potentials derived from the polarization curves. As shown in Fig. 6, the increase in current density with increasing voltage was suppressed in all S-DCPN-treated samples compared to the untreated sample, indicating improved pitting corrosion resistance. Based on the XRD results presented in Fig. 1, this improvement can be attributed to the formation of a supersaturated solid solution of nitrogen in the ferrite phase under all treatment conditions. This nitrogen species, present in the nitrided layer, participates in the following reaction (Equation 1), which suppresses the formation of a localized low pH and chloride-rich (Cl^-) environment at the steel surface [34, 35]:

$$N + 4\,H^+ + 3e^- \rightarrow NH_4^+ \quad (1)$$

Moreover, it was observed that the rate of current density increase with voltage gradually decreased as the hydrogen content in the process gas increased. This trend is consistent with the GD-OES results shown in Fig. 3, where increased hydrogen content promoted greater nitrogen diffusion into the substrate. The pitting potentials extracted from the polarization curves are shown in Fig. 7. Samples treated at 200 Pa and 600 Pa with gas compositions of 75 % N_2 – 25 % H_2 and 50 % N_2 – 50 % H_2 exhibited little difference in pitting potential compared to the untreated sample, with the 75 % N_2 – 25 % H_2 samples showing slightly lower corrosion resistance. This may be due to non-uniform nitrided layer formation under this gas composition. In contrast, the sample treated with 25 % N_2 – 75 % H_2 exhibited a significantly higher pitting corrosion potential than the untreated sample, indicating a marked improvement in corrosion resistance. The enhancement is likely due to increased nitrided layer thickness and the formation of ε-Fe_2N and Cr_2N compounds, both of which were promoted by the higher hydrogen content in the process gas.

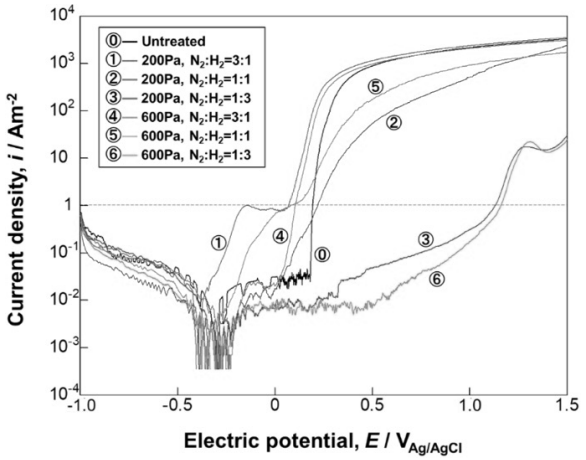

Fig. 6. Polarization curve in the 3.5 mass% NaCl of SUS430 sample treated by S-DCPN.

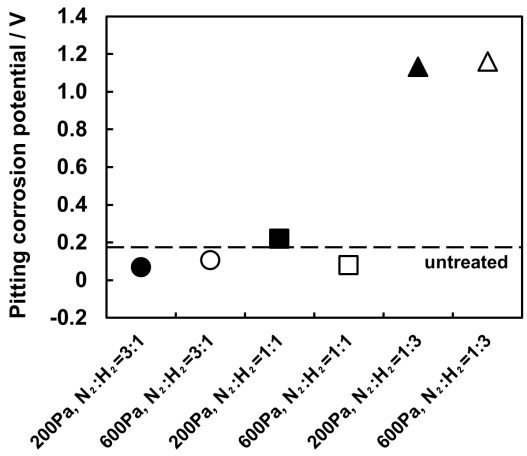

Fig. 7. Pitting corrosion potential of SUS430 of treated by S-DCPN.

Conclusion

To clarify the optimal nitriding conditions for ferritic stainless steel SUS430, S-DCPN treatments were conducted at gas pressures of 200 and 600 Pa, treatment temperature of 633 K, treatment time of 15 hours, and under three gas compositions: 75 % N_2 – 25 % H_2, 50 % N_2 – 50 % H_2, and 25 % N_2 – 75 % H_2. An austenitic stainless steel screen was used to assist plasma generation during the treatments. The following conclusions were drawn from the study:

(1) X-ray diffraction analysis confirmed the presence of the α_N phase, a supersaturated solid solution of nitrogen in the ferrite phase, under all treatment conditions. In the 25 % N_2 – 75 % H_2 sample, diffraction lines of iron nitride and chromium nitride precipitates were also observed.

(2) Cross-sectional microstructural observations revealed α_N phase layers with excellent corrosion resistance in the samples treated with 75 % N_2 – 25 % H_2 and 50 % N_2 – 50 % H_2 gas compositions.

(3) GD-OES measurements showed that increasing the hydrogen content in the process gas led to higher nitrogen concentration near the sample surface, deeper nitrogen diffusion, increased nitrogen content at equivalent depths, and broader nitrogen-enriched zones.

(4) Hardness testing demonstrated that all S-DCPN-treated samples exhibited increased surface hardness compared to the untreated sample. Moreover, both the hardness value and the depth of the hardened layer increased with higher hydrogen content in the process gas.

(5) Corrosion testing revealed improved pitting corrosion resistance in all treated samples, evidenced by a reduced rate of current density increase with rising voltage compared to the untreated material. This improvement became more pronounced with higher hydrogen content. Notably, the pitting corrosion potential was significantly enhanced in the sample treated with 25 % N_2 – 75 % H_2.

References

[1] A. Fossati, F. Borgioli, E. Galvanetto, T. Bacci, Corrosion resistance properties of glow-discharge nitrided AISI 316L austenitic stainless steel in NaCl solutions, Corros. Sci., 48 (2006) 1513-1527.

[2] F. Borgioli, A. Fossati, E. Galvanettol, T. Bacci, G. Pradelli, Glow discharge nitriding of AISI 316L austenitic stainless steel: Influence of treatment pressure, Surf. Coat. Technol., 200 (2006) 5503-5513.

[3] L.C. Gontijo, R. Machado, L.C. Casteletti, S.E. Kuri, P.A.P. Nascente, X-ray diffraction characterisation of expanded austenite and ferrite in plasma nitrided stainless steels, Surf. Eng., 26 (2010) 265-270.

[4] F. Borgioli, E. Galvanetto, T. Bacci, Surface modification of austenitic stainless steel by means of low pressure glow-discharge treatments with nitrogen, Coatings, 9 (2019) 604.

[5] B. Larisch, U. Brusky, H.J. Spies, Plasma nitriding of stainless steels at low temperatures, Surf. Coat. Technol., 116-119 (1999) 205-211.

[6] L.D. Tadepalli, A.M. Gosala, L. Kondamuru, A review on effects of nitriding of AISI409 ferritic stainless steel, Mater. Today, 26 (2020) 1014-1020.

[7] J. Alphonsa, S. Mukherjee, Study of plasma nitriding and nitrocarburising of AISI 430F stainless steel for high hardness and corrosion resistance, Corros. Eng. Sci. Technol., 53 (2018) 16-33.

[8] L. Li, R. Liu, Q. Liu, Z. Wu, X. Meng, Y. Fang, Effects of initial microstructure on the low-temperature plasma nitriding of ferritic stainless steel, Coatings, 12 (2022) 1404.

[9] M.T. Umemura, L.B. Varela, C.E. Pinedo, R.C. Cozza, Assessment of tribological properties of plasma nitrided 410S ferritic-martensitic stainless steels, Wear, 426-427 (2019) 49-58.

[10] E. Menthe, A. Bulak and J. Olfe, A Zimmermann, Improvement of the mechanical properties of austenitic stainless steel after plasma nitriding, Surf. Coat. Technol., 133-134 (2000) 259-263.

[11] C. Alves, Jr., E.F. da Silva, A.E. Martinelli, Effect of workpiece geometry on the uniformity of nitrided layers, Surf. Coat. Technol., 139 (2001) 1-5.

[12] C.X. Li, J. Georges, X.Y. Li, Active screen plasma nitriding of austenitic stainless steel, Surf. Eng., 18 (2002) 453-457.

[13] K.J.B. Ribeiro, R.R.M. de Sousa, Industrial application of AISI 4340 steels treated in cathodic cage plasma nitriding technique, 479 (2008) 142-147.

[14] S.C. Gallo, H. Dong, On the fundamental mechanisms of active screen plasma nitriding, Vacuum, 84 (2009) 321-325.

[15] M. Olzon-Dionysio, M. Campos, M. Kapp, S. de Souza, S.D. de Souza, Influences of plasma nitriding edge effect on properties of 316 L stainless Steel, Surf. Coat. Technol., 204 (2010) 3623-3628.

[16] Z.L. Zhang, T. Bell, Structure and corrosion resistance of plasma nitrided stainless steel, Surf. Eng., 1 (1985) 131-136.

[17] K. Szymkiewicz, J. Morgiel, Ł. Maj, M. Pomorska, M. Tarnowski, T. Wierzchoń, TEM investigations of active screen plasma nitrided Ti6Al4V and Ti6Al7Nb alloys, Surf. Coat. Technol., 383 (2020) 125268.

[18] C. Zhao, C.X. Li, H. Dong, T. Bell, Study on the active screen plasma nitriding and its nitriding mechanism, Surf. Coat. Technol., 201 (2006) 2320-2325.

[19] A. Saeed, A.W. Khan, F. Jan, M. Abrar, M. Khalid, M. Zakaullah, Validity of "sputtering and re-condensation" model in active screen cage plasma nitriding process, Appl. Surf. Sci., 273 (2013) 173-178.

[20] A. Nishimoto, T. Matsukawa, H. Nii, Effect of screen open area on active screen plasma nitriding of austenitic stainless steel, ISIJ Int., 54 (2014) 916-919.

[21] P. Hubbard, D. G. McCulloch, E.D. Doyle, S.J. Dowey, J.N. George, A fundamental contribution to a study of the active screen plasma nitriding process, BHM, 151 (2006) 441-445.

[22] A. Nishimoto, K. Nakazawa, Active screen plasma nitriding of titanium alloy using titanium double screen, Mater. Sci., 891 (2017) 11-17.

[23] P. Hubbard, S.J. Dowey, J.G. Partridge, E. D. Doyle, D. G. McCulloch, Investigation of nitrogen mass transfer within an industrial plasma nitriding system II: application of a biased screen, Surf. Coat. Technol., 204 (2010) 1151-1157.

[24] A. Nishimoto, T. Tanaka, T. Matsukawa, Effect of surface deposited layer on active screen plasma nitriding, Mater. Perform. Charact., 5 (2016) 386-395.

[25] A. Nishimoto, T. Fukube, T. Tanaka, Effect of surface deposits on nitriding layer formation of active screen plasma nitriding, Mater. Trans., 57 (2016) 1811-1815.

[26] E. de Araújo Junior, R.M. Bandeira, M.D. Manfrinato, J.A. Moreto, R. Borges, S. dos Santos Vales, P.A. Suzuki, L.S. Rossino, Effect of ionic plasma nitriding process on the corrosion and micro-abrasive wear behavior of AISI 316L austenitic and AISI 470 super-ferritic stainless steels, J. Mater. Res. Technol., 8 (2019) 2180-2191.

[27] B.C.E. Schibicheski Kurelo, G.B. de Souza, F.C. Serbena, C.M. Lepienski, P.C. Borges, Mechanical properties and corrosion resistance of α_N-rich layers produced by PIII on a super ferritic stainless steel, Surf. Coat. Technol., 403 (2020) 126388.

[28] H. Nii, A. Nishimoto, Surface modification of ferritic stainless steel by active screen plasma nitriding, J. Phys. Conf. Ser., 379 (2012) 012052.

[29] A. Nishimoto, K. Nagatsuka, R. Narita, H. Nii, K. Akamatsu, Effect of gas pressure on active screen plasma nitriding response, J. ASTM Int., 8 (2011) JAI103286.

[30] O. Kishimoto, A. Nishimoto, Low temperature direct current plasma nitriding of ferritic stainless steel with metal screen, Heat Treating Conf. Proc., 84901 (2024) 114-121.

[31] L.C. Gontijo, R. Machado, L.C. Casteletti, S.E. Kuri, P.A.P. Nascente, X-ray diffraction characterisation of expanded austenite and ferrite in plasma nitrided stainless steels, Surf. Eng., 26 (2010) 265-270.

[32] S. Setsuo, “Strengthening mechanism and critical strength of iron, Materia Jpn., 36 (1997) 675-679.

[33] S. Hamashima, A. Nishimoto, Thickening of S-phase and Sα-phase of various stainless steels treated by low temperature plasma nitriding using screen, Mater. Trans., 63 (2022) 1170-1178.

[34] L.A. Luiz, B.C.E.S. Kurelo, G.B. de Souza, J. de Andrade, C.E.B. Marino, Effect of nitrogen plasma immersion ion implantation on the corrosion protection mechanisms of different stainless steels, Mater. Today, 28 (2021) 102655.

[35] E. De Las Heras, G. Ybarra, D. Lamas, A. Cabo, E. Laura Dalibon, S. P. Bruhl, Plasma nitriding of 316L stainless steel in two different N_2-H_2 atmospheres-influence on microstructure and corrosion resistance, Surf. Coat. Technol., 313 (2017) 47-54.

Published in: Key Engineering Materials
ISSN: 1662-9795, Vol. 1044, pp 59-65
doi:10.4028/p-j81aN2

Submitted: 2025-11-18
Revised: 2025-12-04
Accepted: 2025-12-19
Online: 2026-03-03

Active-Screen Plasma Nitriding of Small Thin Rolled Stainless Steel Plates

Kenzo Sumiya[1,a*], Shinkichi Tokuyama[1,b], Tatsuyuki Aoki[1,c], Junichi Fukui[1,d], Atsushi Nishiyama[2,e] and Akio Nishimoto[3,f]

[1]Hatta Kogyo Co. Ltd., Sakai, Osaka 599-8265, Japan

[2]Mikitec Co., Ltd., Amagasaki, Hyogo 660-0083, Japan

[3]Department of Chemistry and Materials Engineering, Faculty of Chemistry, Materials and Bioengineering, Kansai University, Osaka 564-8680, Japan

[a*]kenzo@hatta.co.jp, [b]tokuyama@hatta.co.jp, [c]aoki@hatta.co.jp, [d]junichifukui@icloud.com, [e]atsushi@mikitec.co.jp, [f]akionisi@kansai-u.ac.jp

Keywords: Austenitic Stainless Steel, Active Screen Plasma Nitriding, Expanded Austenite, Small Thin Rolled Plate.

Abstract. The purpose of this study is to clarify the mechanical properties of the expanded austenite (S phase) formed in austenitic stainless steel (ASS). A small thin rolled plate of SUS304 with 0.5 mm thickness was used as test sample. The test sample was nitrided by active screen plasma nitriding (ASPN) at low processing temperature of 400 °C and 450 °C during 4 hrs. processing time. S phase was formed on the surface of the test sample. The surface hardness of ASPN sample was higher than that of untreated sample. Furthermore, tensile tests and fracture surface observations revealed that the tensile strength was also improved compared to untreated samples.

Introduction

Austenitic stainless steel (ASS) takes advantage of its high functionality, excellent corrosion resistance, ductility, and durability, and is used in a wide range of fields such as power generation, chemical and food industries, household goods, building materials, and automobile parts. However, ASS has limitations such as low hardness, low bending rigidity, and low wear resistance. Surface hardening treatments such as nitriding improve mechanical properties, expanding the range of applications for fine and precision machining.

Plasma nitriding and carburizing treatments are considered suitable for surface modification of ASS, which has a strong passive film, since they can remove the oxide film on the surface of the treated object using sputtering effects. However, corrosion resistance can be significantly reduced at high temperatures. Decreasing corrosion resistance can be prevented by lowering the processing temperature to 698 K or less. The nitrided and carburized layer with hardness and corrosion resistance produced by low-temperature treatment is called "expanded austenite, γ_N" or "S phase" [1, 2].

Although many research has been investigated the formation of the S phase and its properties, there are still some aspects that are not clear regarding the mechanical properties of the S phase [1–4]. Active screen plasma nitriding (ASPN) and carburizing (ASPC) is an excellent method for generating active species and producing a uniform heated area [5–6].

In this study, low-temperature ASPN are applied to small thin ASS rolled plate with 0.5 mm thickness to investigate formation and mechanical property of S phase. This study focuses on the effect of S phase on tensile strength. The test sample was nitrided during 4 hrs. processing time at 400 °C and 450 °C processing temperature conditions at 500 Pa gas pressure. The generated nitrided layer was evaluated by observing cross-sectional microstructures and X-ray diffraction (XRD) measurements. The mechanical properties of surface hardness and tensile strength of untreated and ASPN samples were compared. The effect of S phase generation on the tensile strength was investigated by the tensile test and fracture surface observation.

Materials and Methods

Materials. A small thin rolled plate composed of SUS 304 stainless steel was used as a test sample. Figure 1 shows the shape of the test sample. This test sample was designed as a tensile test specimen. A SUS 304 plate with a thickness of 0.78 mm was solution heat treated, then rolled to a thickness of 0.5 mm, and processed into the shape in Fig. 1 by wire cutting. The width and length of parallel part are 3 mm and 30 mm, respectively. The clamping area width is 10 mm. There is a small hole with a diameter of ϕ2 mm near the end, which allows the test sample to be suspended during ASPN processing. After wire cutting, the test sample was polished with abrasive paper and finally cleaned by ultrasonic cleaning.

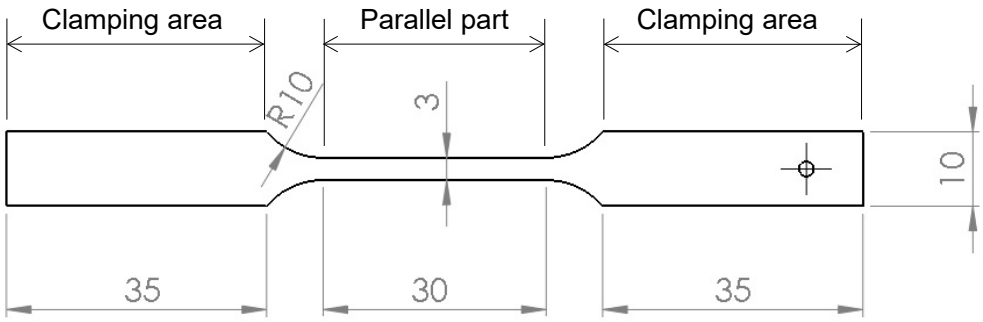

Fig. 1 Shape and size of a test sample of small thin rolled plate (mm).

Active-Screen Plasma Nitriding. Figure 2 shows a schematic diagram of an apparatus for ASPN of thin rolled plate test sample. The test sample was suspended from the screen. Consequently, plasma was formed on both the screen and test sample. The screen material was an expanded mesh composed of SUS 304 stainless steel with outer diameter of ϕ360 mm and height of 180 mm. The distance between the test sample and the screen was 50 mm. Table 1 shows the experimental conditions. The plasma nitriding was conducted for 4 h at 400 and 450 °C processing temperature under a 50 % N_2 – 50 % H_2 atmosphere with a pressure of 500 Pa. During the ASPN processing, the temperature of test sample was measured with a radiation thermometer (IR-CZ1X, CHINO CORPORATION, Tokyo, Japan).

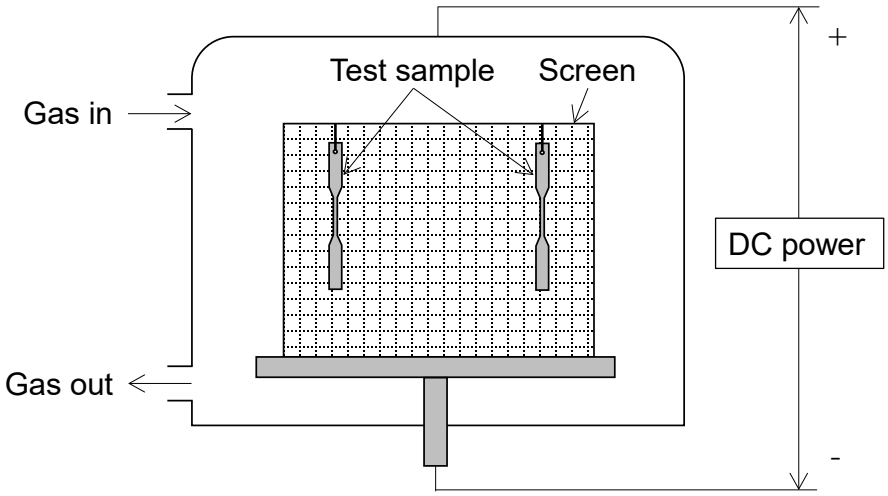

Fig. 2 Schematic diagram of an apparatus for ASPN of thin rolled plate test sample.

Table 1 Experimental conditions for ASPN of thin rolled plate test sample.

Processing temperature	400, 450 °C
Processing time	4 hrs.
Gas pressure	500 Pa
Gas flow ratio	50 % N_2 – 50 % H_2

Characterization. The surface modification layer thickness was characterized by analyzing the micrographs (GX71, Olympus Corporation, Tokyo, Japan) of nitrided samples etched in a solution of Marble's reagent (composed of 4 g $CuSO_4$, 20 mL HCl and 20 mL H_2O) at central cross section. The phase structure of surface modification layer was evaluated by X-ray diffraction (XRD, MiniFlex600, Rigaku Corporation, Tokyo, Japan). The surface hardness was measured under a load of 0.2 N using a Vickers microhardness tester (HM-211+AT-400, Mitsutoyo Corporation, Kanagawa, Japan). Furthermore, the tensile strength was evaluated by a tensile testing machine (AG-50kNXplus, SHIMADZU CORPORATION, Kyoto, Japan) at 5 kN load cell and 1 mm/min tensile speed condition and the fracture surface was observed by SEM images (ERA-600, ELIONIX INC., Tokyo, Japan).

Results and Discussions

Phase Structure and Nitrided Layer Thickness. Figure 3 shows the micrographs of the center cross sections around the edge of ASPN sample. A white layer that was not corroded by the Marble's reagent was generated at the surface. As the processing temperature increased, the white layer thickened. In plasma nitriding, there is a problem in which the modified layer becomes un-uniform around the edge due to concentration of discharge at the corners (edge effect). No edge effect was observed in ASPN processing in this study, and a uniform nitrided layer was formed even at the corners, similar to previous ASPN study [5].

Figure 4 shows the XRD patterns of the untreated and ASPN samples. The XRD pattern of the untreated sample showed three distinct peaks of γ-Fe. In XRD pattern of ASPN samples, these peaks were shifted to a lower angle, similar to our previous study on small-diameter thin pipe [6], indicating the formation of the S phase with N supersaturation. The amount of peak shift becomes larger as the processing temperature becomes higher because the amount of solid solution N increases. The lattice expansion rate of the ASPN sample calculated from the peak shift amount of the XRD pattern using Bragg's equation is 4.7 % at a processing temperature of 400 °C and 7.2 % at 450 °C.

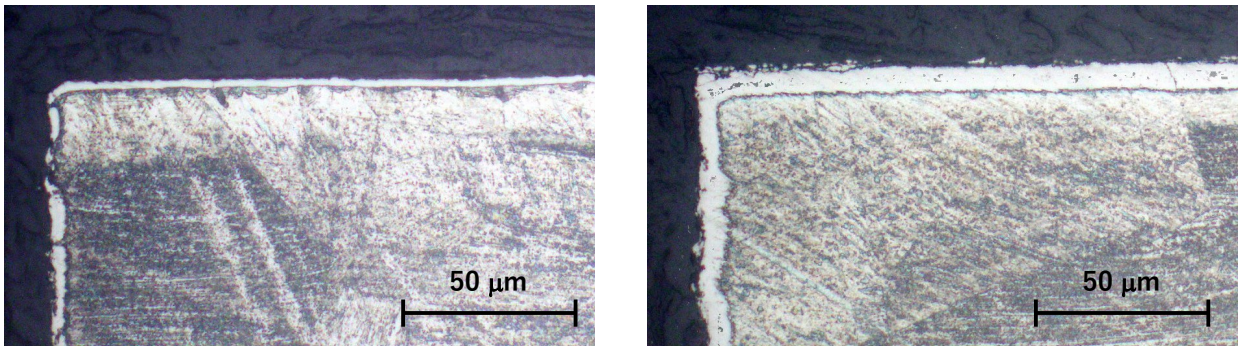

(a) Processing temperature: 400 °C (b) Processing temperature: 450 °C

Fig. 3 Micrographs showing the center cross sections around the edge of ASPN sample.

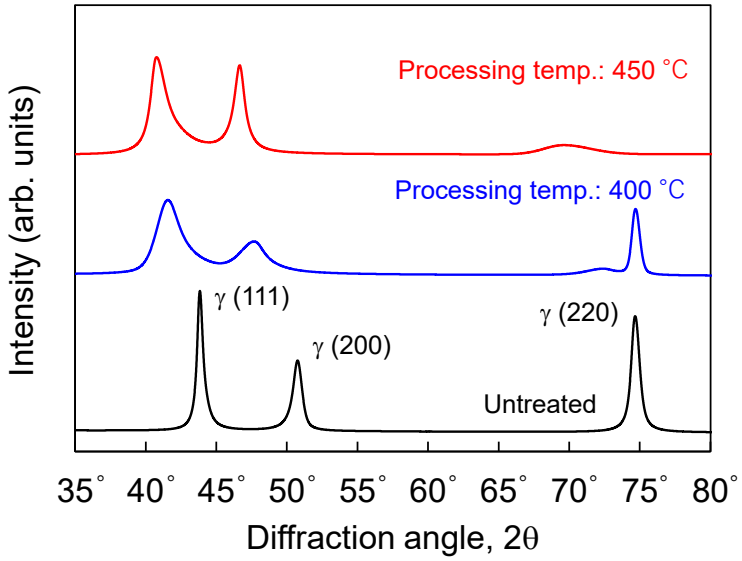

Fig. 4 XRD patterns of untreated sample and ASPN samples.

Figure 5 shows the layer thickness of S phase determined from the cross-sectional structure photograph in Fig. 3. When the processing temperature increased from 400 °C to 450 °C, the S phase thickness increased from 3 μm to 9 μm due to increasing nitrogen diffusion rate.

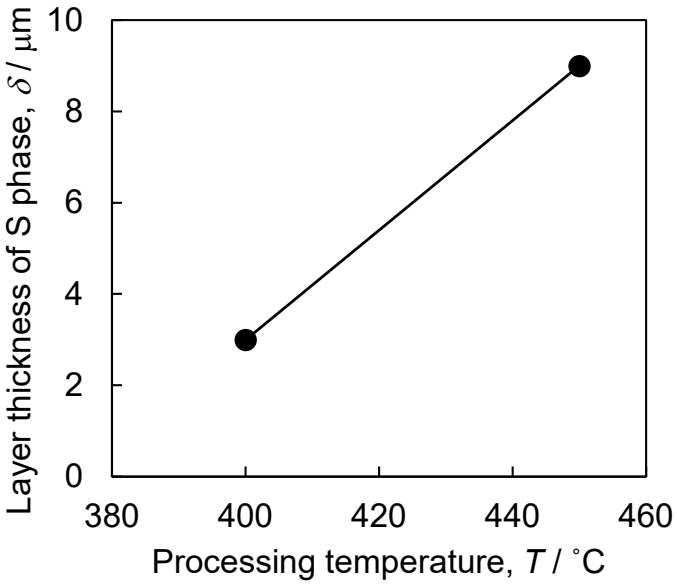

Fig. 5 Layer thickness of S phase.

Surface Hardness. Figure 6 shows the surface hardness of untreated sample and ASPN samples. The surface hardness was higher in ASPN samples than in the untreated sample. For the ASPN sample, the surface hardness increased from 650 HV to 1100 HV with increasing processing temperature up to 450 °C.

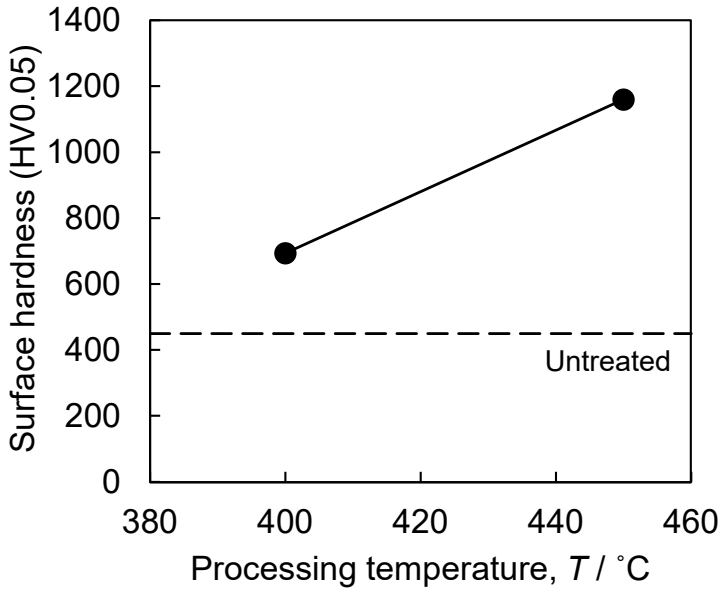

Fig. 6 Surface hardness of untreated sample and ASPN samples.

Tensile Strength. Figure 7 shows the relationship between stress and strain in a tensile test. For untreated sample, the stress increases monotonically up to a strain of 0.03, then becomes almost constant, and the material finally breaks when the strain exceeds 0.15. For the ASPN sample, the stress reached its peak around strain exceeded 0.03, and fracture occurs when the strain reaches around 0.05. The tensile strength (peak stress) of ASPN sample was higher than that of untreated sample because the ASPN sample maintains its slope longer than the untreated sample.

Figure 8 shows the tensile strength and fracture strain obtained from the results in Fig. 7. The tensile strength is increased in the ASPN sample compared to the untreated sample. This indicates that the tensile strength is improved due to the formation of the S phase. On the other hand, the fracture strain is decreased in the ASPN sample compared to the untreated sample, indicating a decrease in ductility. These parameters did not increase significantly when the processing temperature increased from 400 °C to 450 °C.

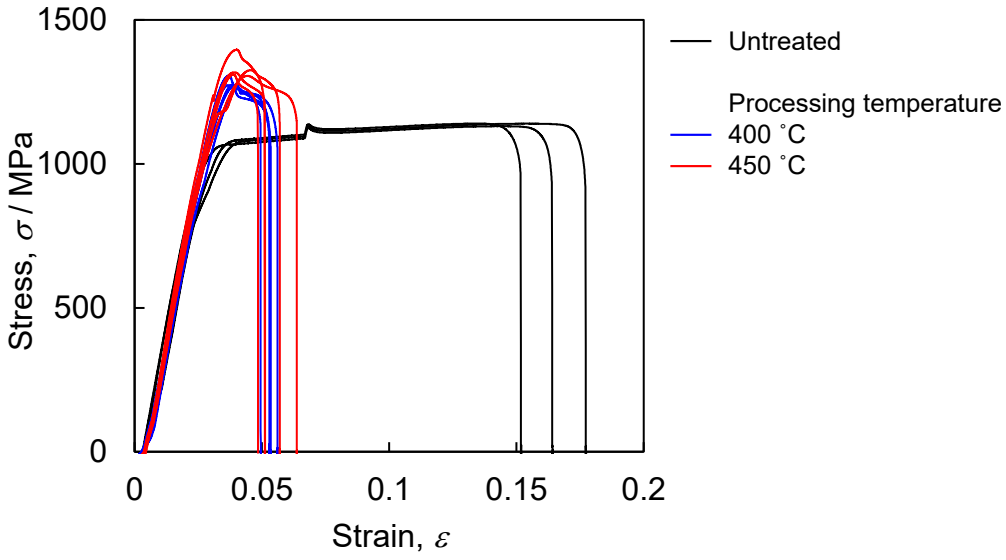

Fig. 7 Strain-stress diagram.

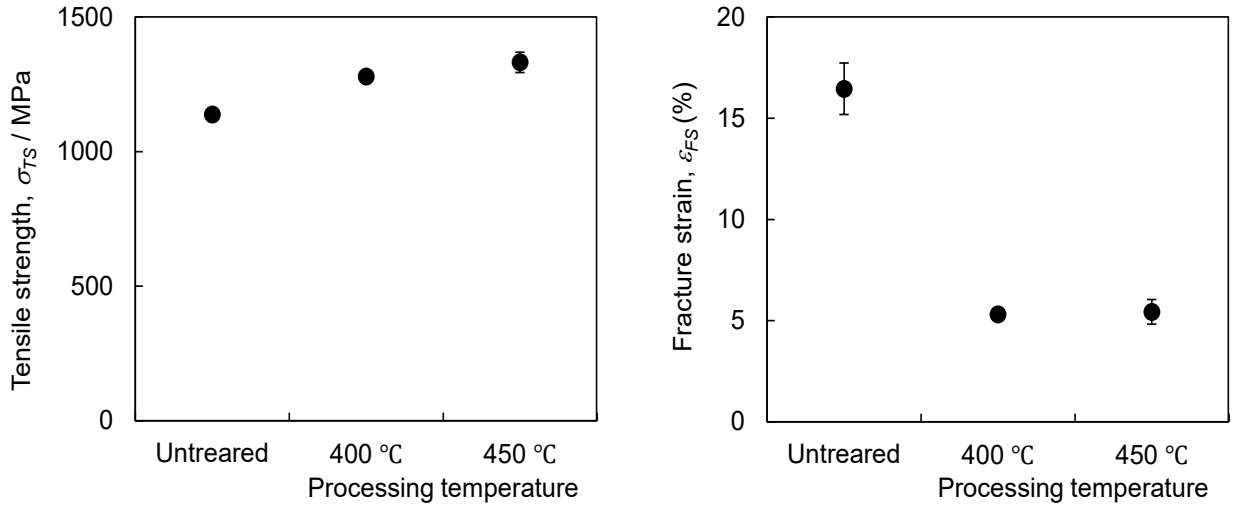

(a) Tensile strength (b) Fracture strain

Fig. 8 Strain-stress test result.

Figure 9 shows a SEM image taken from the front of the fracture surface near the edge. In the untreated sample shown in Fig. 9(a), dimples are observed over the entire fracture surface. On the other hand, in the sample treated at 400 °C in Fig. 9(b), a scale-like pattern can be seen from near the edges toward the center (toward the left side of the image). This is thought to be due to the elongation occurring from the edges toward the center, where the hardness has increased due to the formation of the S phase. In the sample treated at 450 °C in Fig. 9(c), the scale-like pattern can be seen more clearly, and its pattern is pulled from the edges toward the center.

Figure 10 shows the SEM images taken from the side of the fracture surface. For the ASPN samples in Figs. 10(b) and (c), crack occurred on the hardened surface (on the right side of the image) due to the tensile. This cracking was not observed in untreated sample in Fig. 10(a). Observation of these fracture surfaces suggests that the S phase formed on the surface by ASPN processing affects the tensile process, leading to the improvement in tensile strength shown in Figs. 7 and 8.

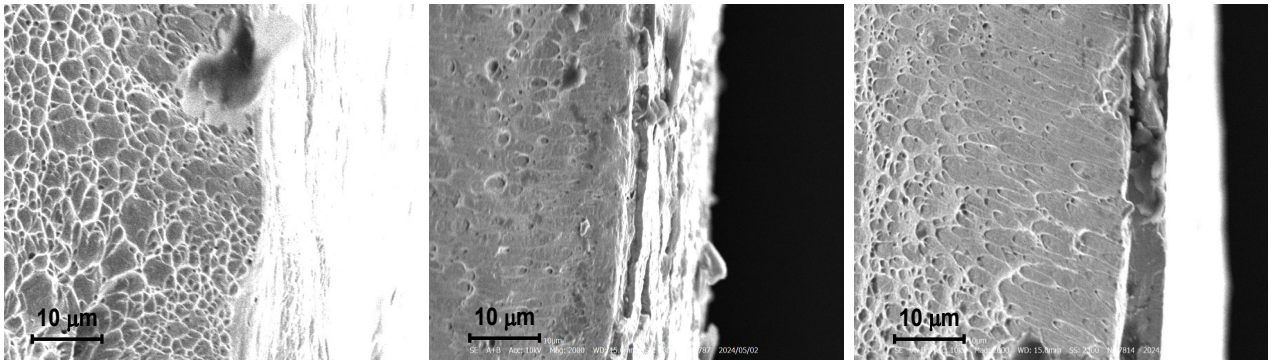

(a) Untreated sample (b) Processing temp. 400 °C (c) Processing temp. 450 °C

Fig. 9 SEM images of the fracture surface near the edge viewed from the front.

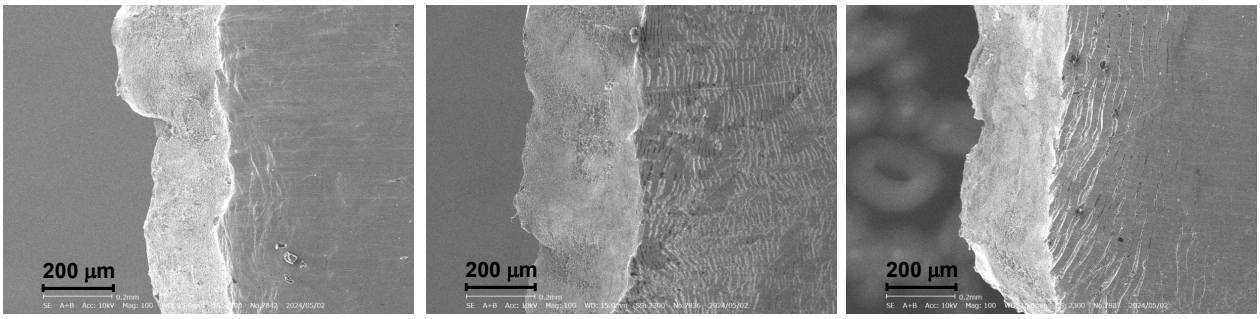

(a) Untreated sample (b) Processing temp. 400 °C (c) Processing temp. 450 °C

Fig. 10 SEM images of the fracture surface viewed from the side.

Summary

The purpose of this study is to clarify the mechanical properties of the S phase formed in ASS. A small thin ASS (SUS304) rolled plate with 0.5 mm thickness was treated by low-temperature ASPN. S phase was formed on the surface of the test sample, and S phase thickness was 9 μm at processing temperature of 450 °C and processing time of 4 hrs. Surface hardness increased with S phase formation. In the tensile test, it was shown that the S phase formed on the surface influenced the tensile and fracture process, and the tensile strength was improved.

Acknowledgments

The authors wish to express their gratitude to Motoo Egawa, ORIST (Osaka Research Institute of Industrial Science and Technology), for his valuable comments and direction. This paper is based on a new development of results obtained from a project subsidized by Sakai City.

References

[1] K. Ichii, K. Fujimura, T. Takase, Structure of the Ion-nitrided layer of 18-8 stainless steel, Technol. Rep. Kansai Univ., 27 (1986) 135-144.

[2] Z.L. Zhang, T. Bell, Structure and corrosion resistance of plasma nitrided stainless steel, Surf. Eng., 1 (1985) 131-136.

[3] T. Christiansen, M.A.J. Somers, Low temperature gaseous nitriding and carburising of stainless steel, Surf. Eng., 21 (2005) 445-455.

[4] F. Borgioli, The “expanded” phases in the low-temperature treated stainless steels: A review, Metals, 12 (2022) 331.

[5] A. Nishimoto, T.E. Bell, T. Bell, Feasibility study of active screen plasma nitriding of titanium alloy, Surf. Eng., 26 (2010) 79-84.

[6] K. Sumiya, S. Tokuyama, A. Nishimoto, J. Fukui, A. Nishiyama, Application of active-screen plasma nitriding to an austenitic stainless steel small-diameter thin pipe, Metals, 11 (2021) 366.

Published in: Key Engineering Materials
ISSN: 1662-9795, Vol. 1044, pp 67-73
doi:10.4028/p-7rsgMt

Submitted: 2025-05-30
Revised: 2025-12-10
Accepted: 2025-12-19
Online: 2026-03-03

Effect of Solution Annealing and Plasma Nitriding on the Fatigue Life Change of AISI 304 Austenitic Steel

Martin Slezák[1,a*], Milan Uhríčik[1,b], Veronika Chvalníková[1,c], Juraj Belan[1,d] and Tomáš Vlach[2,e]

[1]Faculty of Mechanical Engineering, Department of Materials Engineering, University of Žilina, Univerzitná 8215/1, 010 26 Žilina, Slovak Republic

[2]Faculty of Mechanical Engineering, Institute of Technology and Materials, Univesity Jana Evangelisty Purkyně in Ústí nad Labem, Pasteurova 3544/1, 400 96 Ústí nad Labem, Czech Republic

[a]*martin.slezak@fstroj.uniza.sk, [b]milan.uhricik@fstroj.uniza.sk, [c]veronika.chvalnikova@fstroj.uniza.sk, [d]juraj.belan@fstroj.uniza.sk, [e]tomas.vlach@ujep.cz

Keywords: Austenitic Stainless Steel, Solution Annealing, Plasma Nitriding, Microstructure, Fractography.

Abstract. Austenitic stainless steels are characterised by excellent corrosion resistance and good formability, but their low hardness and fatigue life are limitations in demanding applications. The aim of this study was to analyze the effect of solution annealing and plasma nitriding on the microstructure, hardness and fatigue properties of AISI 304 steel. The experimental material was examined in three states: initial, after solution annealing and after plasma nitriding. Solution annealing resulted in the removal of deformation martensite, giving a homogeneous austenitic structure with a decrease in hardness. On the contrary, plasma nitriding produced a hard nitride layer (1291 HV0.01), while no martensite retransformation took place. The results of the fatigue tests showed that the specimens after plasma nitriding reached the highest fatigue limit (878 MPa), while the specimens in the initial condition had the highest number of cycles to fracture. Fractographic analysis revealed typical fatigue failure characteristics in all conditions. The study highlights the possibility of optimising the fatigue properties of austenitic steels through an appropriate combination of thermal and chemical-heat treatments.

Introduction

Austenitic stainless steels are widely used in various industrial components. They are mainly used in industry because of their excellent corrosion resistance, paramagnetic properties (in the annealed state), biocompatibility, as well as their relatively low cost compared to their competitors [1, 2]. The disadvantages of austenitic stainless steels include low hardness, strength and rapid wear. The hardness can be increased by, for example, cold deformation. However, this process significantly changes the properties of austenitic steels. In the microstructure, α' martensite is formed, which results in a change from paramagnetic to ferromagnetic properties [3, 4]. Measurements have shown that the corrosion resistance of these steels changes with progressively increasing deformation, which is attributed to the formation of a martensitic phase [5, 6]. In order to reach again the paramagnetic state solution annealing is considered necessary. However, this process will again reduce the hardness. It is important to pay attention to the annealing temperature. It must be high enough to solve the phases in the material, but at the same time it must not be too high to prevent austenite grain growth [3]. A chemical and heat treatment process can be used to increase hardness, fatigue properties or wear resistance. An ideal candidate for this is plasma nitriding [1]. A prerequisite for plasma nitriding is that the nitrogen used for nitriding must be present in atomic form on the surface of the nitrided component. The nitrogen ions can then penetrate through the surface layer into the structure of the

base material. They then diffuse further into the material under elevated temperature and time conditions. In practice, a temperature ranges of 350–550 °C is used [7, 8]. At these temperatures, there are no changes in the shape and dimensions of the processed parts. At the same time, the process avoids plastic deformation. This means that deformation martensite formation does not occur during plasma nitriding. However, the formation of the CrN layer results in a reduction of the Cr content in the base matrix, which leads to a decrease in the corrosion properties of these steels [6, 9]. Interesting results were obtained in the research by Raman et al [10] where plasma nitriding was carried out at 420 °C with a nitriding time of 6 hours. The results of this research showed that nitriding resulted in an increase in hardness of the nitrided AISI 304 steel, also the surface roughness was reduced compared to the non-nitrided specimens. Nevertheless, the nitrided specimens achieved a lower fatigue life compared to the initial condition (annealed condition - annealing at 1050 °C, 0.5 h heat holding time, cooling in water). Raman et al. attributed this to chromium segregation at grain boundaries, which may have led to early crack initiation [10]. Different results were obtained by Varavallo et al. [11] who used nitriding at 400 °C with the same duration of 6 hours. In this case he obtained diametrically different results, where he obtained a 47 % increase in fatigue life with respect to the original condition [11].

Experimental Material and Experimental Methodology

The material used for the experiment AISI 304 was supplied in the form of 10x10 mm square bars and 3000 mm bar length. The bars were made by cold rolling. At the beginning of the experiment, the chemical composition was verified on a SPEKTROMAXx spark emission spectrometer. The results of the analysis are attached in Table 1. For the purpose of the experiment, the samples were cut to a length of 55 mm.

Table 1 Chemical composition of experimental material.

Type of steel	Concentration of chemical elements [mass. %]									
	C	Cr	Ni	Mn	Si	Mo	S	P	N	Fe
AISI 304	0.046	18.53	8.79	1.72	0.36	0.47	0.05	0.022	0.103	bal.

Solution annealing of the samples was carried out at the Department of Materials Engineering at the University of Žilina. The process was carried out in an electric resistance furnace without protective atmosphere. The annealing temperature was 1030 °C and the residence time was 30 minutes. This was followed by rapid cooling in water. The nitriding of the samples was made possible by Rübig SK. Micropulse plasma nitridation technology was used for nitridation. The nitriding temperature was maintained at 520 °C. The process time was 20 hours. The microstructure of AISI 304 austenitic steel of all states was observed on metallographically prepared samples. The preparation involved grinding, polishing and etching in an etchant consisting of glycerine + hydrofluoric acid + nitric acid. The etching time was approximately 10 seconds. The microstructure was observed on a NEOPHOT 32 light microscope. Photodocumentation was made using NIS Elements 4 software. A Tescan Vega LMU II electron microscope was used for EDX analysis and fractography. The Vickers test was used to measure the hardness. The samples in the initial state and after solution annealing were measured with a load of HV 0.5. For the nitriding layer, again a load of HV 0.01 was used. This loading was chosen in order to maintain the spacing between impressions in the nitriding layer. The loading time was 10 seconds and the measurements were carried out at a temperature of ± 22 °C. The fatigue life of the steel was carried out using a three-point cyclic load on a Zwick/Roell Amsler 150 HFP 5100 resonant pulsator.

Results and Discussion

The microstructure of all grades of AISI 304 austenitic steel is made up of polyhedral austenite grains, which have different sizes (Fig. 1a–c). The steel structure is complemented by annealing twins and twinning. the temperature and length of plasma nitriding was not sufficient to recrystallize the twinning back to pure austenitic grain. However, after the plasma nitridation process, a nitridation layer was formed (Fig. 1b). The twinning was removed only by the process of solution annealing (Fig. 1c).

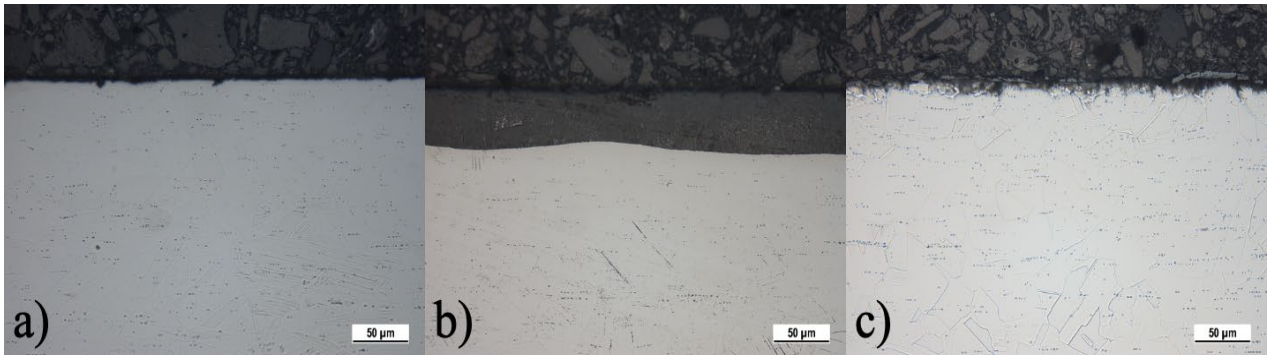

Fig. 1 Microstructure comparison of AISI 304 austenitic steel; a) initial state (IS), b) after plasma nitriding (PN), c) after solution annealing (SA).

EDX analysis – mapping was performed on an electron microscope (SEM) using a Bruker detector. Using this analysis, non-ferrous inclusions in the material were identified. The results (Fig. 2) show that it is manganese sulfide (MnS).

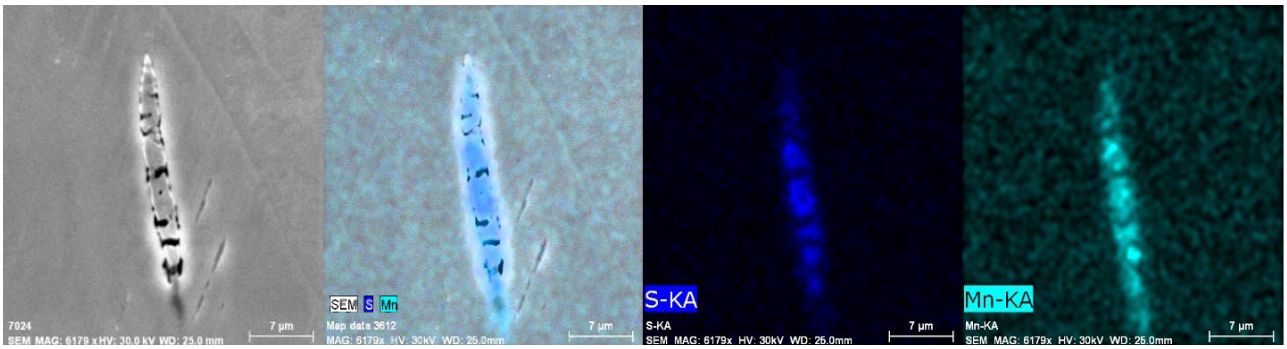

Fig. 2 EDX mapping analysis of manganese sulphide (MnS).

By comparing the hardnesses of all states, it can be evaluated that AISI 304 steel in the initial state and after plasma nitriding have approximately the same hardness throughout the measurement. After the solution annealing, the structure homogenized and thus the hardness decreased (Fig. 3). After the plasma nitriding process, a hard nitriding layer was formed. The microhardness value on this layer reached up to 1291 HV0.01 (Fig. 4). From the fatigue test results, Wöhler curves were constructed as a function of the top stress σ_h and the number of cycles to fracture N_f in semilogarithmic coordinates. The obtained values are plotted using Wöhler curves (Fig. 5) and show a decreasing character. The lifetime curves in the initial state and after plasma nitriding have a steeper character than after solution annealing. The stress amplitude for the initial condition was 180–450 MPa, for plasma nitriding 225–630 MPa and for solution annealing 279–360 MPa. The frequency used was 80 Hz. By comparing the results with the studies by Raman et al. [10] and Varavallo [11], it can be concluded that the results were close to the research by Varavallo, since in this case also the fatigue limit (fatigue life) increased after plasma nitriding.

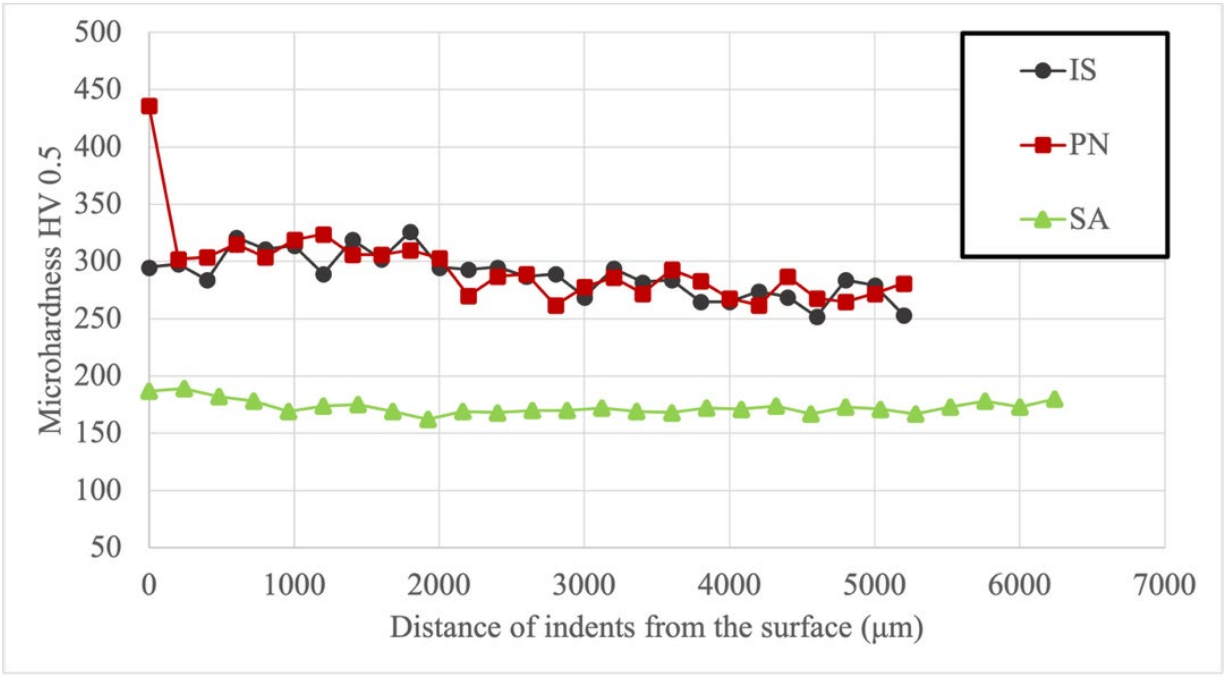

Fig. 3 Comparison of hardness from the surface to the core of the sample.

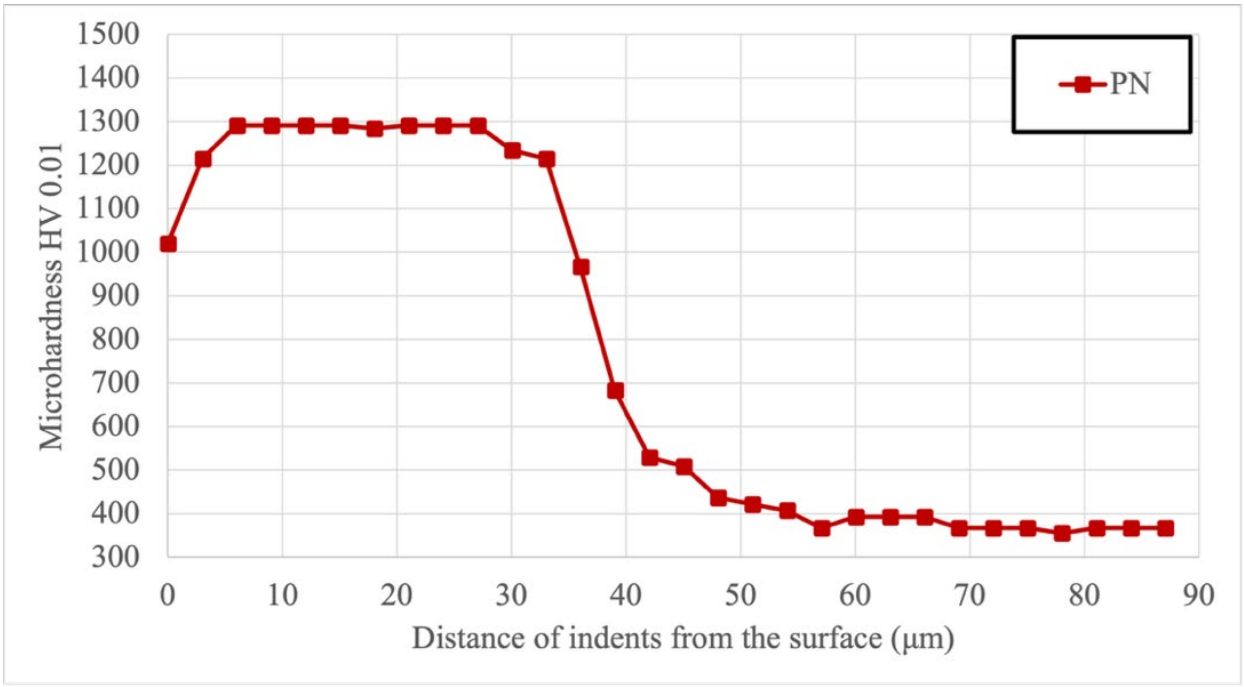

Fig. 4 Microhardness profile on the nitriding layer towards the core of the sample.

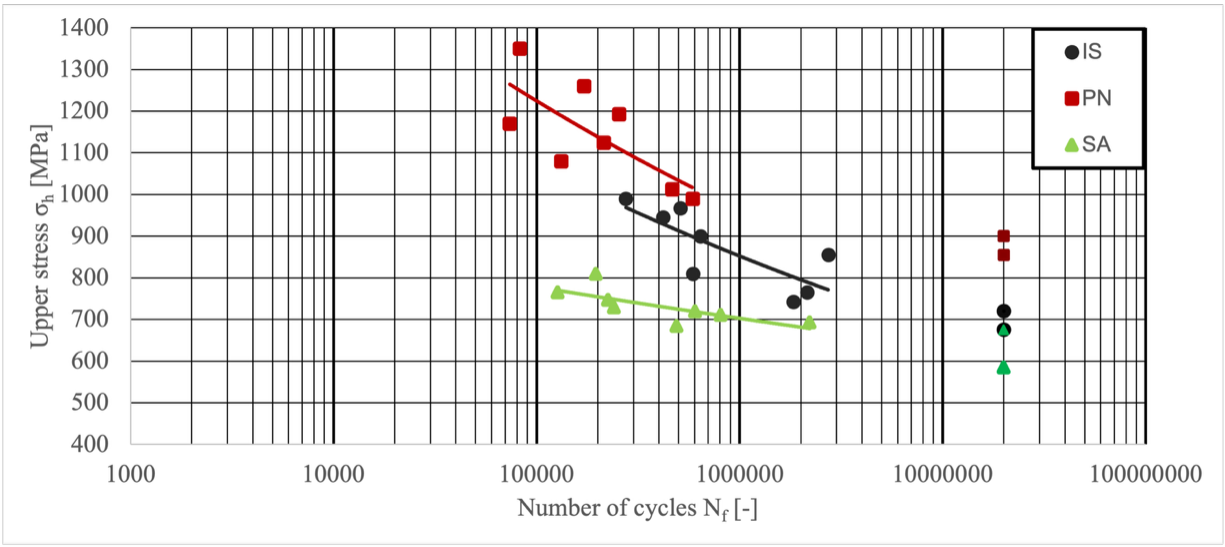

Fig. 5 Dependence of σ_h – N_f for AISI 304 steel at the initial condition, the condition after plasma nitriding and after solution annealing.

From a macrofractographic point of view, the fatigue surfaces after three-point cyclic bending can be divided into three regions: the fatigue area, the transition aera, and the static final fracture area, which represents the final fracture and the formation of the final fracture surface (Figs. 6a–c). From a microfractographic point of view, it was not possible to identify where the fracture initiated (only the initiation site could be determined). In the fatigue region of all states, striations were observed, which are a typical manifestation of fatigue of austenitic steels. Furthermore, pitting of dropped sulphide particles, secondary cracks, and intergranular cleavage failure of the austenitic grain were observed sporadically (Fig. 7).

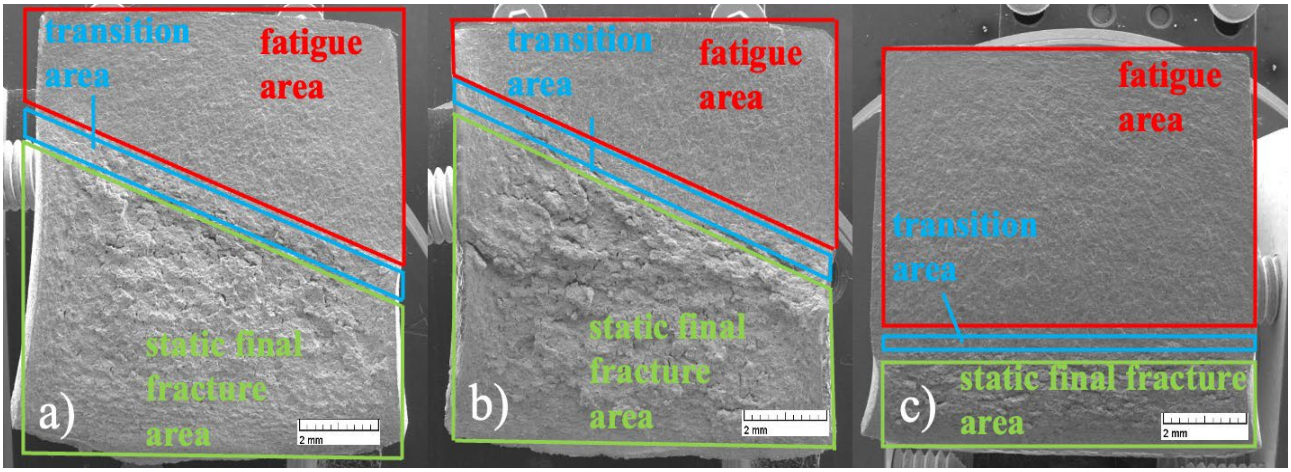

Fig. 6 View of the fracture area; a) initial state, b) after plasma nitriding, c) after solution annealing.

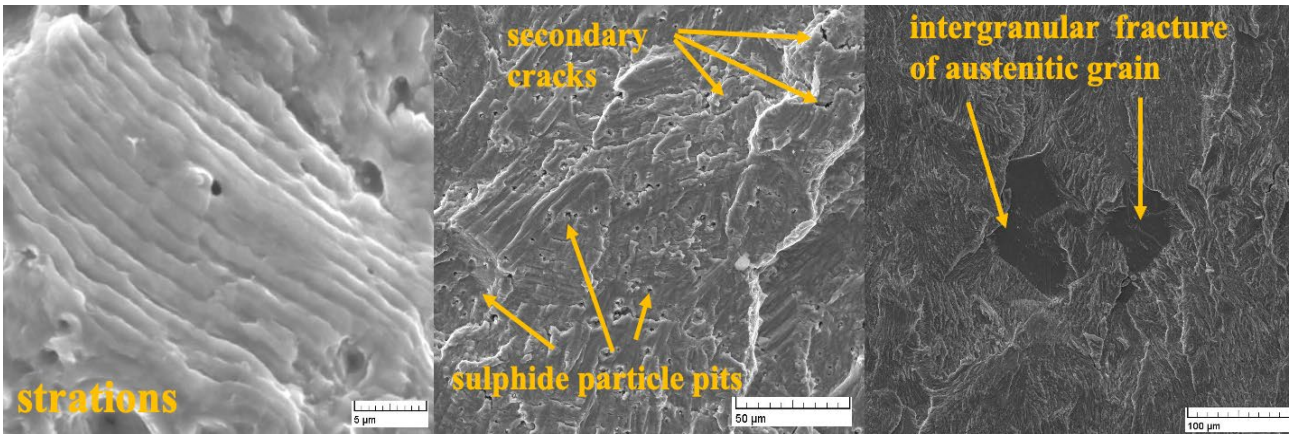

Fig. 7 Examples of fatigue characteristics.

Conclusions

From the analysis, which was focused on the influence of solution annealing and plasma nitriding on the fatigue properties of AISI 304 austenitic steel, the following conclusions can be drawn from the experimental results:

- The microstructure of all states is made up of polyhedral austenite grains, annealing twins and a large number of non-ferrous inclusions. Twinning were removed by solution annealing.
- The highest hardness was measured on the nitriding layer (1291 HV 0.01).
- The specimens in the initial condition withstood the highest number of cycles to fracture and reached the fatigue limit (718 MPa), however, the specimens after plasma nitriding withstood a lower number of cycles but reached a higher fatigue limit (878 MPa). The lowest fatigue limit was achieved by the samples after annealing (630 MPa).
- All conditions had similar fractographic characteristics.

Acknowledgment

Funded by the EU NextGenerationEU through the Recovery and Resilience Plan for Slovakia under the project No. 09I03-03-V05-00002. The research was also supported by the Scientific Grant Agency of the Ministry of Education of the Slovak Republic, KEGA 016ŽU-4/2023.

References

[1] de Araújo Junior, E., Bandeira, R.M., Manfrinato, M.D., Moreto, J.A., Borges, R., dos Santos Vales, S., Suzuki, P.A., Rossino, L.S., Effect of ionic plasma nitriding process on the corrosion and micro-abrasive wear behavior of AISI 316L austenitic and AISI 470 super-ferritic stainless steels, Journal of Materials Research and Technology, 8, 2 (2019) 2180-2191, ISSN 2238-7854.

[2] Godec, M., Donik, Č., Kocijan, A., Podogornik, B., Balantič. D.A.S., Effect of post-treated low-temperature plasma nitriding on the wear and corrosion resistance of 316L stainless steel manufactured by laser powderbed fusion, Additive Manufacturing, 32 (2020) 1-9, ISSN 2214-8604.

[3] Frizt, J., Practical guidelines for the fabrication of austenitic stainless steels. Encyklopedia. London. 2020. ISBN 978-1-907470-13-4.

[4] Cisquini, P., Ramos, S.V., Viana, P.R.P., de Freitas Cunha Lins, V., Franco Jr, A.R., Vieira, E.A., Effect of the roughness produced by plasma nitrocarburizing on corrosion resistance of AISI 304 austenitic stainless steel, Journal of Materials Research and Technology, 8, 2 (2019) 1897-1906, ISSN 2238-7854.

[5] Shit, G., Ningshen, S., The Effect of Severe Plastic Deformation on the Corrosion Resistance of AISI Type 304L Stainless Steel, Journal of Materials Engineering and Performance, 29 (2020) 5696-5709, ISSN 1059-9495.

[6] Talha, M., Ma, Y., Lin, Y., Pan, Y., Kong, X., Sinha, O.P., Behara, C.K., Corrosion performance of cold deformed austenitic stainless steels for biomedical applications, Corrosion Reviews, 37, 4 (2019) 283-306. ISSN: 2191-0316.

[7] Suzuki, K., Nakamura, Y., Nakajima, M., Bai, Y., Uematsu, Y., Improvement of Fatigue Properties by Solution Treatment in Nitrided Type 304 Stainless Steel, Procedia Materials Science, 3 (2023) 627-633, ISSN 2211-8128.

[8] Fernades, F.A.P., Heck, S.C., Pereira, R.G., Picon, C.A., Nascente, P.A.P., Casteletti, L.C., Ion nitriding of a superaustenitic stainless steel: Wear and corrosion characterization, Surface and Coatings Technology, 204, 18-19 (2010) 3087-3090, ISSN 0257-8972.

[9] Dalibon, E.L., Heim, D., Forsich, Ch., Brühl, S.P., Mechanical Behavior of Nitrided 316L Austenitic Stainless Steel Coated with a:C-H-Si, Procedia Materials Science, 9 (2015) 163-170, ISSN 2211-8128.

[10] Raman, S.G.S., Jayaprakash, M., Influence of plasma nitriding on plain fatigue and fretting fatigue behaviour of AISI 304 austenitic stainless steel, Surface and Coatings Technology, 201, 12 (2007) 5906-5911, ISSN 0257-8972.

[11] Varavallo, R., Manfrinato, M.D., Rossino, L.S., Spinelli, D., Riofano, R.M.M., de Souza, S.D., Plasma nitriding influence in the fatigue behavior of austenitic stainless steels AISI 304 and 316, Anais Proceedings, 48 (2006) 5163-5174, ISSN 1516-392X.

CHAPTER 2:

Surface Modification, Coatings and Corrosion Resistance

Published in: Solid State Phenomena
ISSN: 1662-9779, Vol. 386, pp 55-62
doi:10.4028/p-MNcxv1

Submitted: 2025-05-23
Revised: 2025-12-04
Accepted: 2025-12-19
Online: 2026-03-13

Influence of Thermal Treatments on the Corrosion Behaviour of Nickel-Aluminum Bronze in Freshwater-like Aqueous Environment

Paul Linhardt[1,a], Maria Victoria Biezma[2,b], Susanne Strobl[1,c] and Roland Haubner[1,d*]

[1]Technische Universität Wien, Institute of Chemical Technologies and Analytics, Getreidemarkt 9/164-03, A-1060 Vienna, Austria

[2]University of Cantabria, Dique de Gamazo 1, 39004 Santander, Spain

[a]paul.linhardt@tuwien.ac.at, [b]biezmav@unican.es, [c]susanne.strobl@tuwien.ac.at, [d*]roland.haubner@tuwien.ac.at

Keywords: Nickel-Aluminum-Bronze, Heat Treatment, Corrosion, Freshwater.

Abstract. Nickel-Aluminium Bronze is a copper alloy with excellent corrosion resistance in marine environments. However, there are also applications of NAB in freshwater and corrosion phenomena have been observed in such cases. To explore the effect of microstructure on the corrosion behaviour, heat treatments were applied to NAB samples, which were corrosion tested in electrolytes with a composition typical for freshwater. Depending on the presence of bicarbonate, sulfate, and chloride, different kinds of corrosion attack were observed. The mayor effect lies in minimization of the β-phase amount and increasing the portion of α- and κ-phases. Corrosion promoted by sulfate is the major hazard in fresh water, while the passivating effect of bicarbonate supports localization of the attack. Chloride plays an ambivalent role; it promotes the corrosion attack but limits the progressively penetrating evolution of localized corrosion. Since the composition of freshwater has a stronger impact on the corrosion phenomena of the NAB alloy, the influence of the heat treatments is not clearly evident. Compared to seawater, heat treatments have a lesser effect on the corrosion behaviour in freshwater.

Introduction

Nickel-Aluminium Bronze (NAB) Bronzes exhibit excellent corrosion resistance and are frequently used in applications where corrosion, erosion, and cavitation can occur. This applies to both seawater and freshwater. Typical examples include ship propellers, pumps, and turbines in hydroelectric power plants [1, 2]. Due to the complex alloy composition, these bronzes have a multi-phase microstructure, which also affects the corrosion behaviour [3–6]. In this respect, some studies have been carried out previously with Manganese-Aluminium bronzes (MAB) [7–9].

The microstructures of the NAB bronzes consist primarily of three easily distinguishable phases (α, β, and κ). The α and β phases form the matrix in which the κ phase is embedded. Heat treatments make it possible to influence the phase proportions, as well as their size, geometry and distribution [10, 11]. The phase diagram (Fig. 1) [12, 13] shows, that during solidification of the bronze melt only β-phase is formed in the first step. During further cooling the β-phase decomposes into α-phase and κ-phases below 940 °C. Between 940 °C and 800 °C a ternary phase region with α-, β- and κ-phases exists. Below 800 °C the β-phase gets completely converted and α- and κ-phases are present only in the NAB microstructure. Especially the κ-phases can show different morphologies and variable compositions between Fe_3Al and NiAl [14, 15]. By quenching from 1000 °C to room temperature, the formation of a martensitic phase, referred to as β′, is described. During a subsequent heat treatment, the β′-phase decomposes into fine-grained α- and κ-phases [16].

The corrosion behaviour of NAB in seawater has been repeatedly studied [17–19], mostly related to as-cast material. Its excellent resistance to high chloride environment is based on formation of a passivating layer consisting dominantly of copper and aluminum oxides. The multiphase structure bears the risk of dealloying or selective corrosion of the most reactive (anodic) phases [20].

Conversely, corrosion of NAB in fresh water is not much discussed in literature. Nevertheless, a specific case of NAB corrosion in river water has drawn our attention to this topic [21] and the corrosion behaviour of as-cast NAB in various fresh water compositions was investigated [22]. Based on these considerations, the influence of heat treatments on the NAB´s microstructures and its influence on the corrosion behaviour in freshwater are the objectives of this study.

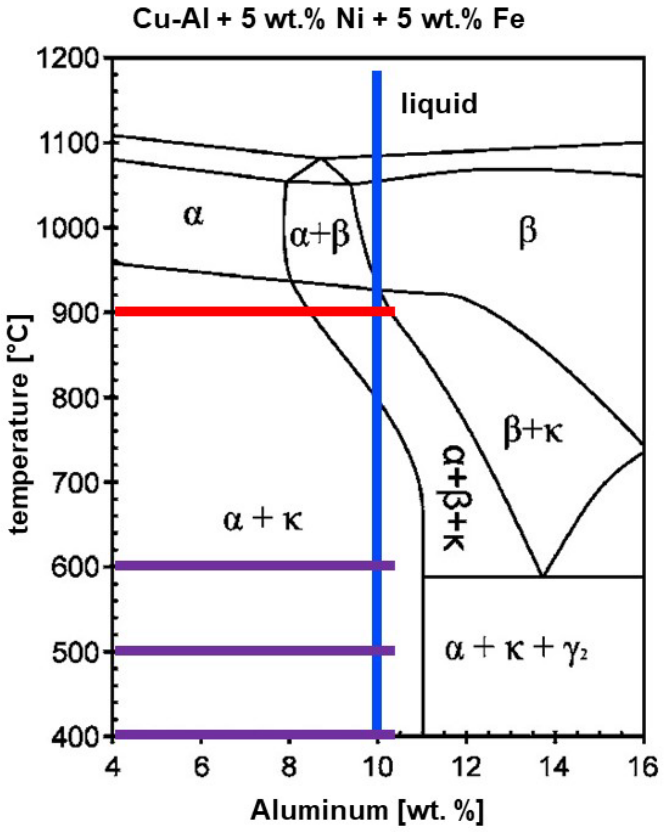

Fig. 1 Cu-Al + 5 wt.% Ni + 5 wt.% Fe phase diagram.

Experimental Procedure

NAB composition. type CuAl10Fe5Ni5 (analysis mass %: 80.53 Cu, 8.96 Al, 4.46 Fe, 4.60 Ni, 1.16 Mn, 0.07 Zn, 0.05 Sn, 0.01 Pb, 0.16 Si) (Table 1).

Heat treatments. The heat treatments were carried out in a muffle furnace, with the samples protected from oxidation by carbon grit. After annealing, the samples were quenched in water. NAB samples were solution annealed at 900 °C for 1 hour and then heat treated at 400, 500, or 600 °C for 45 min and 24 h respectively.

Metallography. The samples were embedded in epoxy resin. Metallographic preparation started with plane-grinding, followed by polishing with 9–1 μm diamond suspension. Etchant was $(NH_4)_2CuCl_4$.

Corrosion tests. Based on [22] potentiostatic corrosion testing at +194 $mV_{Ag/AgCl}$ was applied for 48 hours in solutions based on combinations of 0.5 mM SO_4^{2-}, 1 mM HCO_3^-, 0.5 mM Cl^- (Table 2). After the corrosion tests, the surfaces of the samples were examined in the SEM as well as metallographic cross sections were prepared and investigated in LOM.

Table 1 Composition of the NAB alloy CuAl10Fe5Ni5.

Element	Cu	Al	Fe	Ni	Mn	Zn	Sn	Pb	Si
wt. %	80.53	8.96	4.46	4.60	1.16	0.07	0.05	0.01	0.16

Table 2 Composition of the three electrolytes.

Electrolyte 1	Electrolyte 2	Electrolyte 3
48 mg/L SO_4^{2-}	48 mg/L SO_4^{2-} 61 mg/L HCO_3^-	48 mg/L SO_4^{2-} 61 mg/L HCO_3^- 17.5 mg/L Cl^-

Results and Discussion

Microstructural changes of NAB during heat treatments. As can be seen from the phase diagram (Fig. 1) at 900 °C, the 3 phases α-, β- and κ- are present.

Figure 2 shows the microstructure of the sample annealed and quenched at 900 °C. The light areas correspond to the α-phase, and the dark brown areas correspond to the β-phase. The κ-phases appear bright gray, with larger aggregates in the α-phase and smaller precipitates in the β-phase.

Starting with the sample annealed at 900 °C, annealing at lower temperatures should result in a transformation of the β-phase into the α-phase and κ-phases. This transformation is more slowly at lower temperatures (Fig. 3), while higher temperatures result in coarsening of the phases.

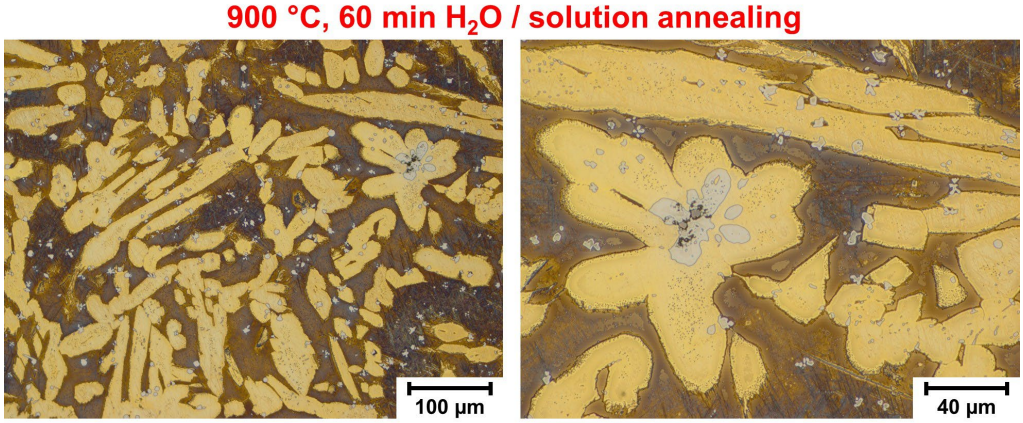

Fig. 2 Microstructures of the at 900 °C heat-treated NAB samples. Etchant $(NH_4)_2CuCl_4$.

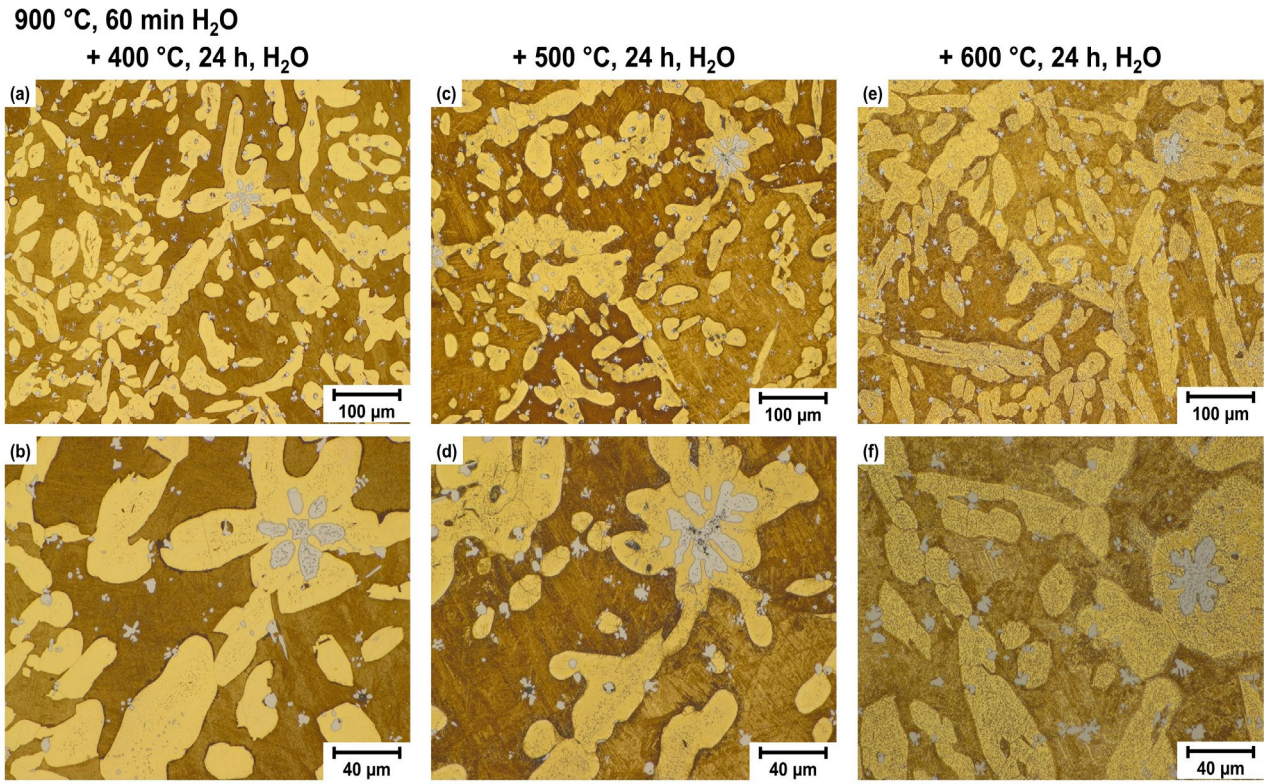

Fig. 3 Microstructures of the heat-treated NAB samples. Etchant $(NH_4)_2CuCl_4$.

In the sample annealed at 400 °C the α-phase and κ-phases appear unchanged, but darker and lighter areas are visible in the β-phase regions (Fig. 3a, b), and precipitation of fine κ-phase is observed. In a sample annealed at 500 °C, the darker and lighter regions of the original β-phase are contrasting better (Fig. 3c, d). After annealing at 600 °C, very fine κ-precipitates are visible additionally, in both the original β-phase and α-phase regions (Fig. 3e, f).

Potentiostatic electrochemical measurements. In sulfate electrolyte (electrolyte 1), a significant reduction in the corrosion current was observed as a result of the heat treatments compared to the solution-annealed sample (Fig. 4a). The attack appears as areas of rather uniform corrosion with adhering corrosion products with the solution-annealed sample (Fig. 5a). This is reflected in the rather steady current trend reached finally. In contrast, pitting-like corrosion was observed with all samples, corresponding with increasing trends of the currents, all at similar level. The attack is likely to have occurred preferentially in the vicinity of the large κ-aggregates within the α-phase (Fig. 5b–d).

In the sulfate-carbonate electrolyte (electrolyte 2), the corrosion currents were similarly low in all samples (Fig. 4b). This can be attributed to the effect of the carbonate, which forms a protective layer. Pitting-like corrosion, again corresponding with increasing current trends, was observed. The halos around the pits consist predominantly of Al corrosion products. Pitting corrosion is likely to originate from areas with κ-phase (Fig. 5e–h).

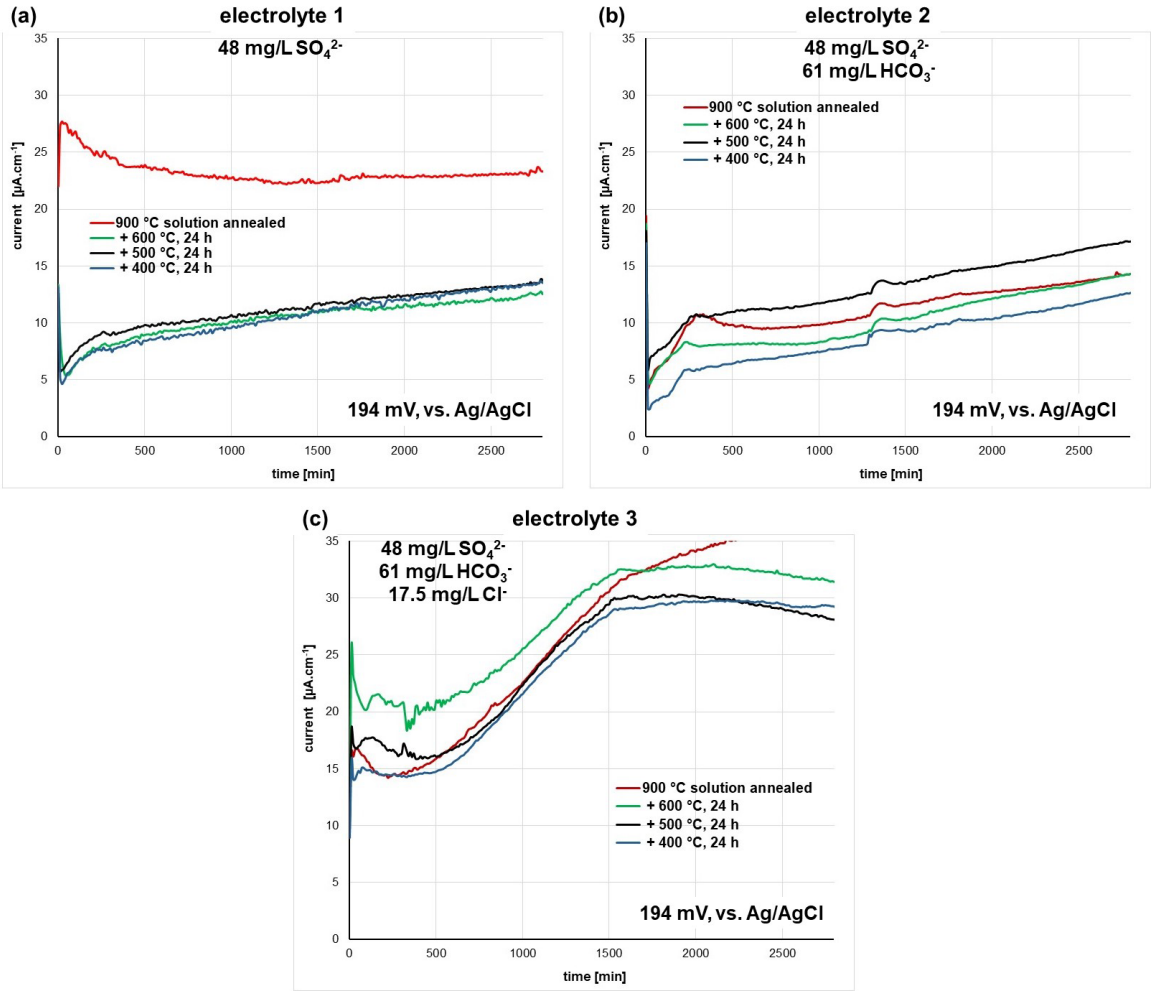

Fig. 4 Trends of current densities during on potentiostatic corrosion testing of heat treated NAB samples in three electrolytes.

If chloride was also present in the electrolyte in addition to sulfate and carbonate (electrolyte 3), the effects of the heat treatments were minimal, but the corrosion currents were significantly increased (Fig. 4c). These samples had poorly protective layers of corrosion products on the surfaces, which mainly contained aluminum compounds. Aluminum from the alloy is the most reactive element and corrodes easier. The attack appears as a kind of localized etching; no penetrating pitting was observed (Fig. 5i–l). This is reflected in increasing current trends in the beginning, which flatten and even get decreasing later on.

Cross sections of the corroded samples. Cross sections were taken from some samples after the potentiostatic corrosion tests to determine the degree of corrosion attack. Samples from the tests with electrolyte 3 were used for this purpose, as the corrosion current was highest in these tests and therefore the most metal loss from corrosion is expected (Fig. 6).

In general, it can be said that the localized corrosion attack was minor. It should also be noted that with localized corrosion, corrosion spots may not be easily detected in the metallographic section. In the sample annealed at 500 °C, corroded spots are visible that extend approximately 20 µm below the surface (Fig. 6a). The results for the sample annealed at 400 °C are similar, but dealloying, presumably due to corrosion of the β-phase, is also evident here (Fig. 6b). Furthermore, there are spots where the attack extends up to 50 µm below the surface, as well as crack-like phenomena (Fig. 6c).

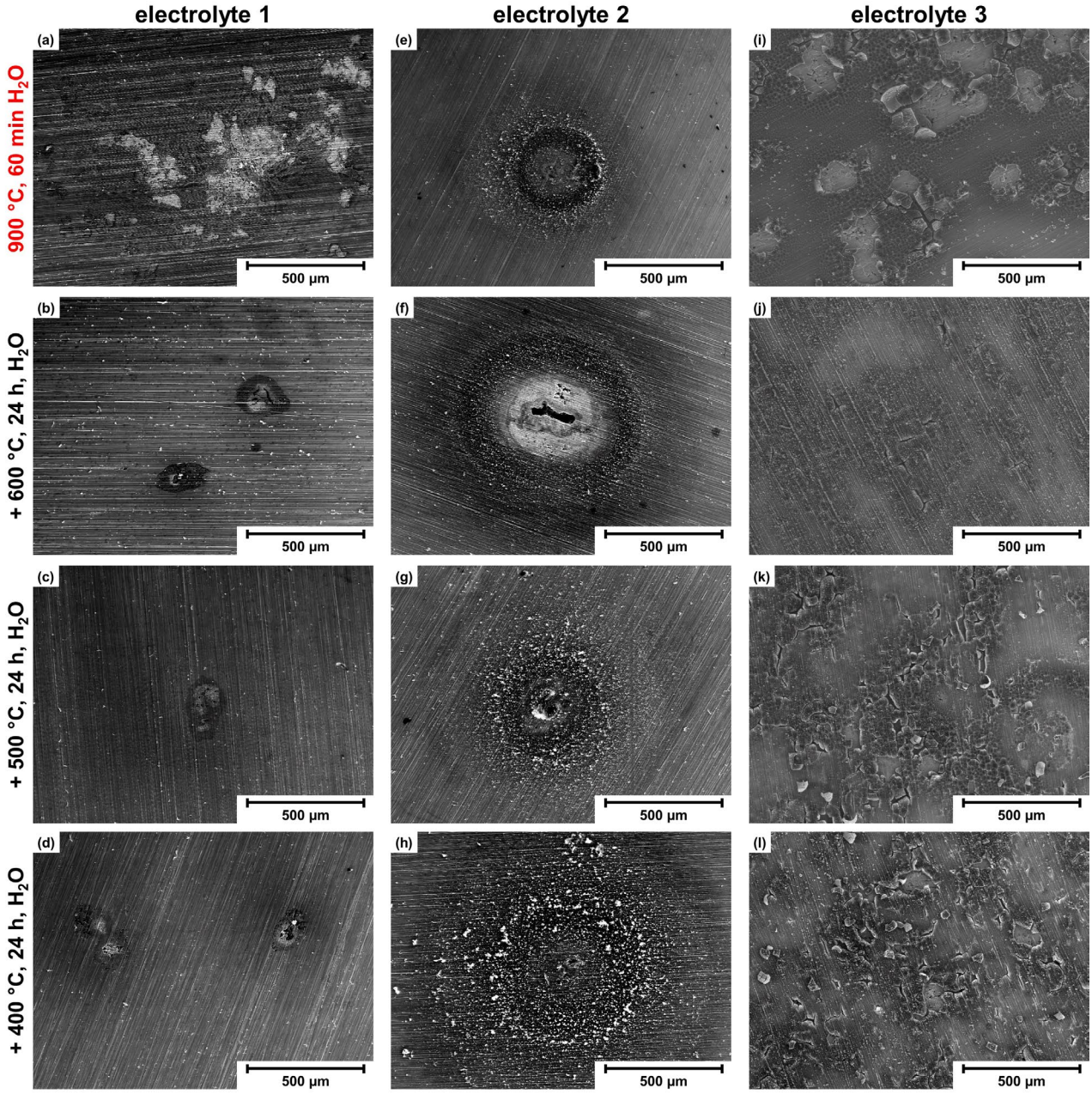

Fig. 5 Surfaces of the NAB samples after the potentiostatic corrosion tests in different electrolytes (SEM-BSE).

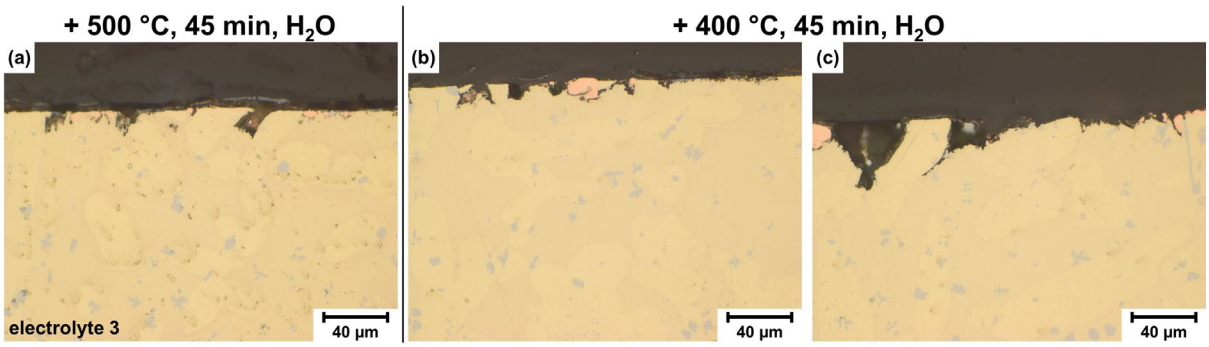

Fig. 6 Metallographic cross-sections of NAB samples after potentiostatic corrosion tests.

Summary

Nickel-Aluminium Bronze samples were tested for their corrosion resistance in synthetic freshwater after different heat treatments. Depending on the composition of this medium, different kinds corrosion attack was observed.

The influence of heat treatments on corrosion in freshwater is small compared to seawater [10]. In freshwater, the water composition primarily determines the corrosion behaviour.

The main effect of the heat treatments lies in minimization of the β-phase amount and increasing the amount of κ-phases and α-phase.

Corrosion promoted by sulfate is the major hazard in fresh water, while the passivating effect of bicarbonate supports localization of the attack. Chloride plays an ambivalent role; it promotes the corrosion attack, but limits the progressively penetrating evolution of localized corrosion. These observations agree with the findings reported previously [22].

Acknowledgements

The authors would like to thank the TU Wien Library for the financial support through its Open Access Funding Program.

References

[1] Z. Qin, Q. Zhang, Q. Luo, Z. Wu, B. Shen, L. Liu, W. Hu, Corros. Sci., 139 (2018) 255-266.

[2] P. Linhardt, S. Strobl, J. Böhm, M.V. Biezma Moraleda, R. Haubner, Pract. Metallogr., 58 (2021) 72-82.

[3] P. Brezina, Int. Met. Rev., 27 (1982) 77-120.

[4] E.A. Culpan, G. Rose, J. Mater. Sci., 13 (1978) 8, S. 1647-1657.

[5] P. Linhardt, S. Strobl, J. Böhm, M.V. Biezma Moraleda, R. Haubner, Pract. Metallogr., 58 (2021) 72-82.

[6] F. Hasan, A. Jahanafrooz, G.W. Lorimer, N. Ridley, Metall. Trans. A, 13A (1982) 1337-1345.

[7] M.V. Biezma, O. Gómez de la Rasilla, R. Haubner, P. Linhardt, Pract. Metallogr., 59, 5 (2022) 236-250.

[8] P. Linhardt, M.V. Biezma, S. Strobl, R. Haubner, Solid State Phenomena, 341 (2023) 25-30.

[9] R. Haubner, S. Strobl, G. Ball, P. Linhardt, M.V. Biezma, Pract. Metallogr., 61 (2024) 769-782.

[10] J. Böhm, P. Linhardt, S. Strobl, R. Haubner, M.V. Biezma Moraleda, Materials Performance and Characterization, 5 (2016) 689-700.

[11] I. Cobo Ocejo, M.V. Biezma Moraleda, P. Linhardt, Metals, 12 (2022) 380.

[12] Kupfer-Aluminium-Legierungen, Informationsdruck i.6, Deutsches Kupferinstitut, Auflage 03/2010.

[13] B.P. Pisarek, Archives of foundry engineering, 13 (2013) 72-79.

[14] E.A. Culpan, G. Rose, Journal of Material Science, 13 (1978) 1647-1657.

[15] R. Thomson, J.O. Edwards, The Kappa-Phase in Nickel-Aluminium Bronze, Part 2: Cast Microstructures and Properties, in AFS Transactions (1978) 395-400.

[16] P. Brezina, International Metals Reviews, 27 (1982) 77-120.

[17] J.A. Wharton, R.C. Barik, G. Kear, R. J. K. Wood, K.R. Stokes, F.C. Walsh, Corrosion Science, 47 (2005) 3336-3367.

[18] A. Al-Hashem, W. Riad, Materials Characterization, 48 (2002) 37-41.

[19] E.A. Culpan, G. Rose, British Corrosion Journal, 14 (1979) 160-166.

[20] J.A. Wharton, K. R. Stokes, Electrochim. Acta, 53 (2008) 2463-2473.

[21] P. Linhardt, Materials and Corrosion, 66 (2015) 1536-1541.

[22] P. Linhardt, S. Kührer, G. Ball, M.V. Biezma, Materials and Corrosion, 69 (2018) 358-364.

Published in: Solid State Phenomena
ISSN: 1662-9779, Vol. 386, pp 63-69
doi:10.4028/p-Gs146o

Submitted: 2025-06-20
Revised: 2025-12-09
Accepted: 2025-12-19
Online: 2026-03-13

New Approaches for Evaluating the Resistance of Clads under High Temperature Corrosion Conditions

Janette Brezinová[1,a*], Ján Viňáš[1,b] and Jakub Brezina[1,c]

[1]Technical University of Košice, Faculty of Mechanical Engineering, Košice, Slovakia

[a*]janette.brezinova@tuke.sk, [b]jan.vinas@tuke.sk, [c]jakub.brezina@tuke.sk

Keywords: High-Pressure Casting, Cladding, PVD Nanocoating, High Temperature Corrosion.

Abstract. The aim of the experimental work was to propose innovative procedures for the formation of renovation layers, to determine suitable material, modify the microgeometry and surface topography of new and renovated shaped parts of moulds for high-pressure casting of aluminium alloys. It has been designed and validated under laboratory and operational conditions a method of modifying the surface of the mould parts of moulds for casting aluminium alloys by forming stochastic texture by low energy laser in combination with duplex PVD coatings on the surfaces of mould parts in contact with the aluminium alloy melt. It has been verified the contact angle measurement methodology for determining the number of spurs by separation lubricant on the surface of the new or refurbished mould part before the first casting cycle. For the formation of the renovation layers, the additive materials were verified Dievar, Dratec, UTPA 702. A TruDisk 4002 solid-state disk laser with BEO D70 focusing optics was used for winding.

Introduction

Technology of pressure casting represents a complex of interrelationships between the properties of the alloy, the construction of the mold and the operation of the pressure casting stand. From the point of view of the efficiency of production and the improvement of the quality of castings, in addition to the technological parameters of metal casting under pressure, the design solution of the mold and its technological life are decisive. Technological lifetime of the mold is limited by the quality requirements prescribed for the casting and the tolerance range of the technological parameters for the pressure casting of the casting [1–3]. Shaped parts of molds and cores for casting aluminum alloys are usually made of chrome, tungsten and chrome molybdenum tool steels [4, 5]. Properties of the materials used for the production of molded parts of molds and cores for aluminum alloy die casting must take into account the stress of the molds in the aluminum alloy die casting itself. These are mainly thermal expansion, modulus of elasticity, mechanical properties at elevated temperatures, resistance to thermal fatigue and chemical stress of shaped parts of molds and cores. In the pressure casting process, the shaped parts of the molds and cores are exposed to intense thermal, mechanical and chemical stress. High melt flow velocities of aluminum alloys (up to 120 $m.s^{-1}$), high pressures (up to 120 MPa) and high maximum temperatures on the surface of shaped parts of molds (up to 550 °C) lead to erosion, abrasion, corrosion and thermal fatigue of the mold [6, 7]. The heat load of foundry cores is even higher (up to 600 °C), because they are not connected to the mold cooling system [8–11]. Thermal cyclic loading from 80 °C to 550 °C leads to high tensile stresses on the surface of shaped parts of molds/cores and subsequently to the formation and propagation of thermal cracks [12, 13]. Frequent contact of the surface of the shaped part of the mold with the melt causes the formation of growths (sticking) as a result of corrosion due to the influence of molten metals and consequently shortens the life of the shaped parts of the molds and cores. Aluminum alloy die casting molds and mold parts are exposed to abrasion and erosion in the high-pressure metal casting process. These phenomena are intensified in the case of injection of materials with a high Si content. At the same time, a physical-chemical reaction takes place on the surface of the mold to form intermetallic phases based on Fe-Al (melting). Intensity of both phenomena is conditioned by the initiation of surface cracks or cracks during the expansion of oxidized grains and the formation of weakened places responsible for aluminum sticking. Interaction of the Al melt with the steel material

of the mold, the kinetics of formation and the morphology of intermetallic phases on the basis of Fe-Al were devoted to works [14–17]. Any degradation change of the shape parts of the molds and cores will also affect the quality and dimensions of the castings. One of the solutions to extend the technological life of shaped parts of molds and cores on a global scale is their renovation with appropriate surface engineering technologies. Various measures can be implemented to increase the lifetime of the shaped parts of the molds and the resistance of the inner shaped surfaces of the mold, which are often eroded by the flow of molten aluminum. Their purpose is preventive - they are applied to a new form in critical places, or renovation – replenishment of eroded material or material broken by a network of thermal-mechanical cracks [18–19]. The most economical way of renovating shaped parts of molds and cores intended for pressure casting is cladding [20–22]. The main advantages of cladding are short downtimes and economic advantage compared to the production of a new part of the tool. Clad repair generally allows for higher added value in the foundry. Paper presents the results of research focused on surface modification by texturing and application of PVD coatings. Renovation of shaped parts of molds for high-pressure casting of aluminum alloys was realized by laser cladding.

Materials and Methods

From the group of shaped parts of molds for casting metal under high pressure on cold machines those molded parts (mold inserts) were selected by the filling chamber. Wear analysis was performed on the shaped parts that were discarded after 800 thousand casting of the mold cavity with a melt of aluminum alloy. On the surface of the molded parts, due to repeated impacts of the moving core on the surface of the molded parts of the mold, it caused intense plastic deformation associated with the separation of plastically deformed parts of the surface of the molded part, Fig. 1.

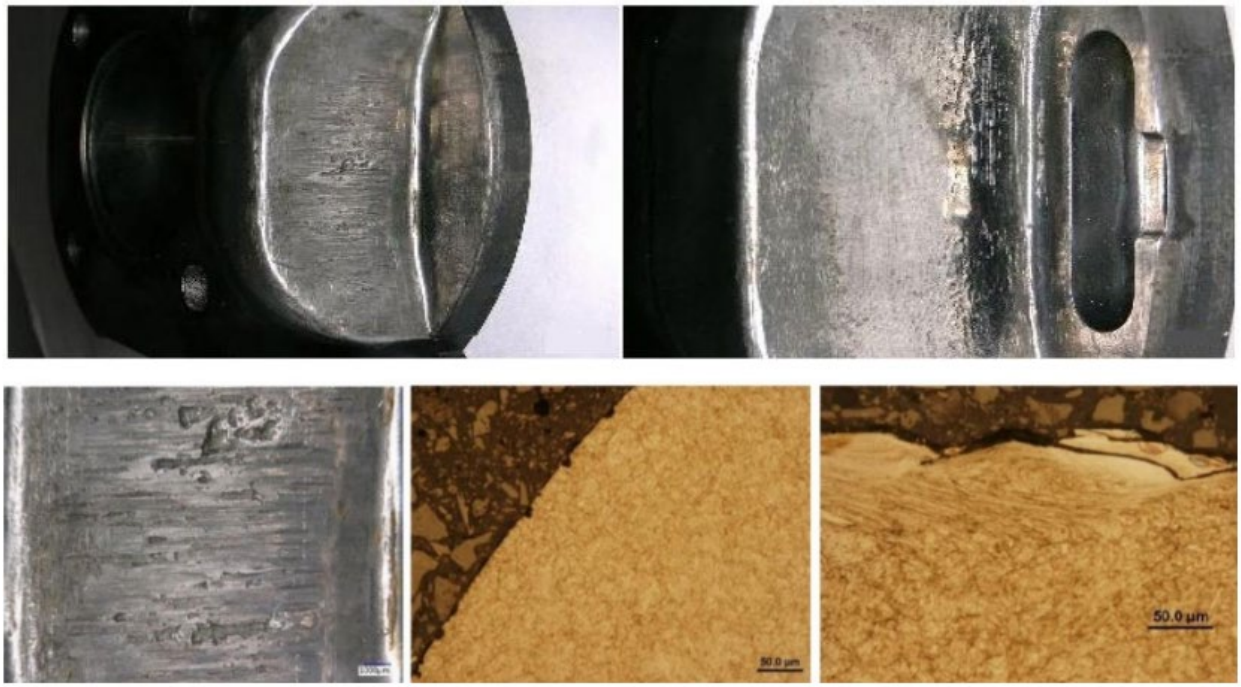

Fig. 1 Degradation of molds during the injection of Al alloys – cracks, adhesion of the separating agent, tearing of material on the surface of the molds

To repair and renovate the mold parts of molds for high-pressure casting of aluminum alloys, samples of experimental clads were prepared on the base material of grade 1.2343 (Dievar) with dimensions of 150×130×30 mm, which was refined to a hardness value of 44–48 HRC. Chemical composition of the base material is in Table 1, chemical composition of the filler materials is in Table 2.

Table 1 Chemical composition of the base material (wt.%), Fe balance

C	Mn	Si	P	S	Cr	Ni	Mo	V	Cu
0.382	0.377	0.914	0.002	0.002	4.893	0.199	1.277	0.499	0.077

Table 2 Chemical composition of the filler material (wt.%), Fe balance

Filler mat.	C	Si	Mn	Cr	Mo	Ni	Co	Ti	Al	Cu
1.2343 (Dievar)	0.4430	0.147	0.423	5.13	2.27	0.067	0.01	0.002	0.008	-
1.6356 (Dratec)	0.0005	0.200	0.50	0.15	4.0	18.0	12.0	1.60	-	-
1.6356 (A 702)	0.0200	-	-	-	4.0	18.0	12.0	1.60	0.10	-

In the presented experiment, the production of layers was realized by means of a TruDisk 4002 solidstate disk laser with BEO D70 focusing optics (Trumpf, Ditzingen, Germany). Three types of additive materials were used. Since the process was reimplemented on a robotic workstation, the additive materials used were in the form of wires with a diameter of ø 1.0 mm.

Cladding parameters were selected based on previously performed experiments on a given type of solidstate laser. Following experiments were analyzed:

- light microscopy, (etchant used – 3 % HNO_3 solution);
- microstructure in the area of drilled holes (for the drilling method);
- immersion test in a molten aluminum alloy AlSi, at a temperature of 680 °C – 60, 150 and 300 min;
- microtexturing of surface and
- contact angle measurement.

Microgeometry of the surface due to radiation - microtexturing. Grid and stochastic textures were created by laser radiation with the diameter of ablation craters of 50 micrometers, the depth of 5 to 8 µm, and the distance between the centers of the craters was modified with a low-energy laser of 100 µm and 200 µm. Integrity of the surfaces of the samples after the formation of ablation craters was checked using the scanning electron microscopy technique, Table 3.

Table 3 Distribution of ablation craters on the surface of the samples

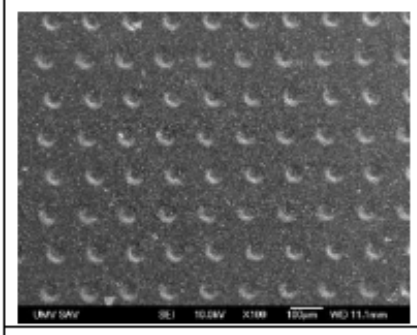	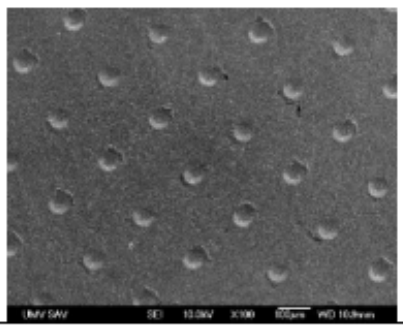	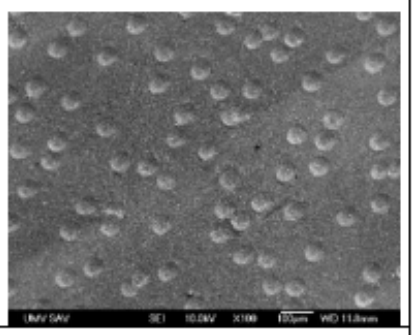
texture - grid 100x100 µm	texture - grid 200x200 µm	stochastic texture, maximum mutual distance of ablation craters 100 µm (texture random)

Dimensions of random texture craters on which duplex PVD coatings nACRo[4], AlTiN G and $AlXN_3$ were deposited using LARC technology were controlled by confocal microscopy. Dimensions and distribution of the ablation craters were: diameter 50 µm, depth 5–10 µm, average distance between the craters 200 µm.

Results and Discussion

Analyses of surface integrity were targeted to the area of ablation craters and their surroundings. The topography of the original surface after grinding and polishing was the same at the edges of the ablation craters, on the side of the craters, and in their center. There was no violation of the integrity of the surface of the samples in any crater. Based on the measurements, the creation of textures with a regular distribution of ablation craters is only possible on flat surfaces. Only textures with a stochastic distribution of ablation craters can be created on facially broken surfaces. To create a stochastic texture, also called a random texture, an interval of maximum crater distance of up to 200 μm was chosen. Inspection of the surface integrity of the samples with a stochastic distribution of ablation craters with a maximum mutual distance of 100 μm did not reveal damage to the integrity of the surface in the areas outside the ablation craters, in the crater walls and in their center. A multilayered nACRo^4 (a 4th generation nanocomposite layer) was deposited on a part of the samples with a textured surface in the regime of lattice textures and stochastic texture with a diameter of 50 μm ablation craters, a depth of 5 to 8 μm and a distance between the centers of the craters of 100 μm and 200 μm. It consists of nanocrystalline AlCrN grains embedded in an amorphous Si_3N_4 matrix. The aim of this surface treatment was to analyse the adhesion effect of commercially used lubricants in the technology of treatment of shaped parts of molds when casting aluminum alloys under high pressure on machines with a cold filling chamber. By checking the integrity of the textured surfaces with the deposited duplex PVD coating of the 4th generation nACRo^4, no failure of the integrity of the deposited PVD coating was detected. By semiquantitative EDX microanalysis, the elements forming the PVD coating nitrogen, aluminum, silicon and chromium were detected on the surface.

A stochastic texture of ablation craters was created by a low-energy laser on the surface of a hardened and tempered sample of Dievar material and experimental deposits. Duplex PVD coatings AlTiN G, $AlXN_3$ and nACRo^4 were deposited on such textured surfaces. The temperature of the PVD coating deposition process is higher than 500 °C. In this process, the elimination of residual stresses in the area of ablation craters can be assumed [23–25]. For all samples, the effectiveness of surface protection was investigated by the methodology used in tests of non-textured and laser-textured surfaces. Contact angle measurement criterion was selected as one of the control measurements. Aim was to obtain information about the resistance and effectiveness of the surface protection of the shaped part of the mold with SafetyLube 7815 lubricant in the "run-in" phase of the shaped part of the mold, which is in contact with the molten aluminum alloy. Test consisted of heating the samples to a temperature of 250 °C, applying a separating agent by spraying 10 times and 20 times and dipping for 15 seconds into a melt of an aluminum alloy based on Al-Si at a temperature of 680 ± 20 °C. With the increase in the number of spray cycles from 10x to 20x, higher values of the contact angle were measured for the laser random+duplex nACRo^4 system. This is because an increased number of spray cycles leads to more pronounced micro- and nanostructure formation on the surface and an increase in its roughness, which impairs the wettability of surfaces. After a short exposure of the treatment samples to the 250 °C/10x-spray SafetyLube 7815 and 250 °C/20x-spray SafetyLube 7815 treatment regimes and subsequent immersion in the aluminum alloy melt (680 °C/15 seconds), a decrease was measured with the laser random+duplex nACRo^4 system contact angle values (Fig.2). This decrease can be explained by the change in morphology and roughness of the layer formed after the application of SafetyLube 7815.

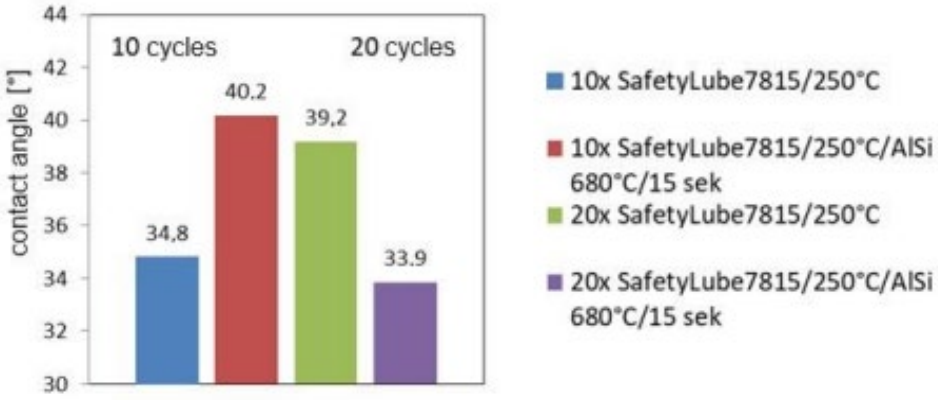

Fig. 2 Contact angle depending on the number of sprays with Safety Lube 7815. Surface Dievar+laser random+duplex nACRo[4].

Before the final application of the clads, corrosion tests of the clads (Dievar, Dratec, UTP A702) were performed in the melt of the Al-Si aluminum foundry alloy after complete immersion of the prismatic sample into the melt at a temperature of 680 °C ± 20 °C. The immersion time was 60, 150 and 300 min. The clads were processed according to the technical conditions prescribed by the drawing of the mold part or mold core. The samples with the clads were then immersed in the melt of the aluminum-silicon-based aluminum alloy at a temperature of 680 °C ± 20 °C so that the surface with the clads and the surface of the sample, which represented the basic steel material used for the production of mold parts and cores, were in contact with the melt. After 60 minutes, 150 minutes and 300 minutes, the samples with the clads were gradually removed from the melt and then cut transversely through the clads by electric spark. The samples for checking the microstructure were prepared in dentacryl, ground on sandpapers of grain size 240, 400, 600 and 800, moistened with water, polished with diamond paste, grain size 1/0 on satin moistened with kerosene, washed and rinsed with benzine. A light microscope was used to measure the thickness of the intermetallic layer. The thicknesses of the intermetallic layer on the side of the surface with the clads and on the surface of the adjacent side of the sample with the clads were measured. The thickness of the intermetallic layer on the surface opposite the clads provides information about the intensity of the reaction of the original material of the shaped part of the mold or cores with the melt of the aluminum alloy based on aluminum - silicon. The reaction of the clads deposit surface and the surface of the original material of the shaped part of the mold or cores was under the same experimental conditions. The thickness of the intermetallic layer on the clads deposit surface provides information about the intensity of the clads deposit reaction on the original material, Fig. 3. The dark areas in Fig. 3 represent microcavities that were created based on immersion tests. If the ratio of the thickness of the intermetallic phase on the surface of the plate and the thickness of the intermetallic phase on the opposite side to the clad is less than the number 1, then the clad is suitable for renovating shaped parts of the molds or cores. Given solution to the method of evaluating the resistance of clads in the aluminum alloy melt provides an effective method of selecting the clads for the renovation of shaped parts of molds and cores for casting aluminum alloys under high pressure. After immersion in Al-Si-based aluminum alloy melt at a temperature of 680 ± 20 °C; a) immersion for 60 minutes, h = 38 μm; b) immersion for 150 minutes, h = 110 μm; c) immersion for 300 minutes, h = 130 μm.

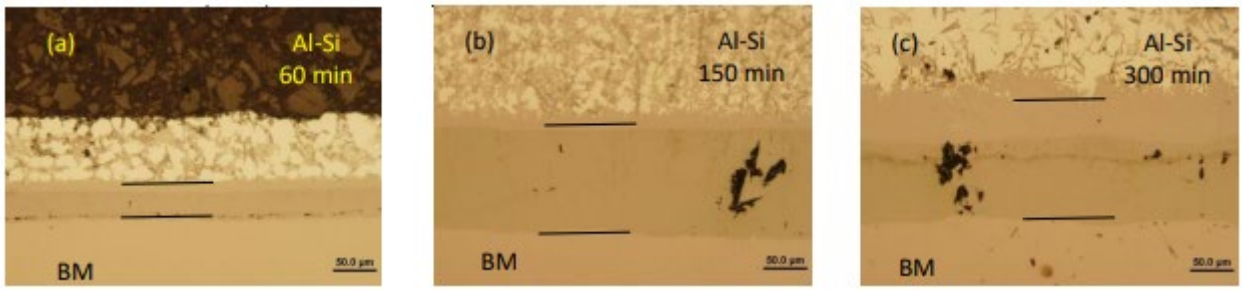

Fig. 3 Changes in the intermetallic layer after immersion in an Al-Si based aluminium alloy melt.

Conclusion

Microgeometry of the surface of the samples was modified by low-energy laser radiation - microtexturing. Grid and stochastic textures were created by laser radiation. Duplex PVD coatings AlTiN G, $AlXN_3$ and multilayer nanocrystalline coating $nACRo^4$ were deposited on random textures using LARC technology. The contact angle between the surface of the samples and the SafetyLube 7815 lubricant was NaCR determined. The goal was to obtain information about the resistance and effectiveness of the surface protection of the shaped part of the mold in the "run-in" phase of the shaped part of the mold, which is in contact with the molten aluminum alloy. The quality of the clads from Dievar, Dratec and UTPA 702 additive materials, which were produced by a TruDisk 4002 solid-state disk laser with BEO D70 focusing optics, was determined. A method of assessing the resistance of deposits in molten aluminum alloys based on aluminium-silicon based on the assessment of the size of intermetallic phases was proposed. Based on the results of immersion tests in the melt of the Al-Si-based alloy, laser cladding technology with additive material No. 1.6356 – Dratec. A coating was applied to the marked places, which was machined, and the shaped part of the mold was used for operational tests in the serial production of pressure castings.

For the purpose of determining the resistance to high-temperature corrosion of the clads deposit and the resistance to high-temperature corrosion of the base steel material of the shaped part of the mold and cores (BM) for high-pressure casting of aluminum alloys based on aluminum-silicon, we proposed to define the corrosion resistance coefficient as the ratio of the thickness of the intermetallic layer formed on the surface of the clads deposit to the thickness of the intermetallic layer formed on the surface of the base steel material.

Acknowledgment

This research was funded with the support of VEGA 1/0597/23, APVV-20-0303, APVV-24-0381 and KEGA 024TUKE-4/2025.

References

[1] Gerrard J., Kandlikar M., Journal of Cleaner Production, 15 (2007) 17-27.

[2] Hirsch J., Trans. Nonferrous Met. Soc. China, 24 (2014) 1995-2002.

[3] Ragan, E., et al., Liatie kovov pod tlakom, 1. vyd – Prešov, VMV (2007) s. 381.

[4] Xie, Y., Cheng, X., Wei, J., Luo, R., Materials, 15, 18 (2022) 6448.

[5] Maity, S.R., Chakraborty, S., Int. J. Adv. Manuf. Technol., (2015).

[6] Paiva, J.M., Fox-Rabinovich, G., Junior, E.L., Stolf, P., Ahmed, Y.S., Martins, M.M., Bork, C., Veldhuis, S., Materials, 11, 3 (2018) 358.

[7] Laemmle, J.T., Bohaychick, J., Lubr. Eng., (1992).

[8] Suraj R Marathe, Dr. Carmo Quadros, Int. J. Eng. Res., 9, 4 (2020) 1-10.

[9] Sands, M., Shivkumar, S., J. Mater. Sci., 38 (2003) 667-673.

[10] Tóth, J., Svidró, J.T., Diószegi, A., Stevenson, D., Int. J. Met., (2016).

[11] Shivkumar, S., Mater. Sci. Technol., 10 (1994) 986-992.

[12] Wu, F., Deng, X., Jie, X., Zheng, K., Luo, Z., Heat Treat. Met., 47, 3 (2022) 165-172.

[13] Pastirčák, R., Ščury, J., Fecura, T., In Proc. of the MATEC Web of Conferences; 2018.

[14] Sundqvist M., Hogmark S., Tribol. Int., 26 (1993) 129.

[15] Dingremont N., Bergmann E., Collignon P., Surf. Coat. Tech., 72, 3 (1995) 157-162.

[16] Bouayad A., Gerometta C, Belkebir A., Ambari A, Mater. Sci. Eng. A, 363, 1–2 (2003) 53-61.

[17] Chen Z.W., Mater. Sci. Eng. A, 397, 1–2 (2005) 356-369.

[18] Chen Ch. et al., Journal of Cleaner Production, 64 (2014) 13-23.

[19] Ferencz Peti, Lucian Grama, Ioan Solovăstru, Nonconventional Technologies Review. Romania, September, 2012, p. 10-14.

[20] K. Bobzin, T. Brögelmann, R.H. Brugnara, N.C. Kruppe, Surf. Coat. Tech., 284 (2015) 222-229.

[21] Li-qiong Chen, Li-jun Liu, Zhi-xin Jia, Ji-qiang Li, Yi-qiang Wang, Ning-bo Hu, Int. J. Adv. Manuf. Technol., 68 (2013) 2841-2848.

[22] Brezinová, J. et al., Metals, 8, 6 (2018) 399.

[23] Thuvander, A., 6th Int. Tool. Conf. 2002.

[24] Markežič, R., Naglič, I., Mole, N., Šturm, R., Eng. Fail. Anal., 95 (2019) 171-180.

[25] Zhang, X., Cheng, X., Stelson, K.A., Bhattacharya, M., Sen, A., Voller, V.R., J. Therm. Stress. 25, 6 (2002) 523-538.

Published in: Solid State Phenomena
ISSN: 1662-9779, Vol. 386, pp 71-76
doi:10.4028/p-Lf5jpA

Submitted: 2025-05-28
Revised: 2025-12-10
Accepted: 2025-12-19
Online: 2026-03-13

Novel ASC Refractory Design and Installation for Improved Energy Efficiency and Corrosion Resistance in Industrial Applications

Alica Mašlejová[1,a*], Dáša Chudíková[2,b], Branislav Buľko[1,c], Peter Demeter[1,d], Jaroslav Legemza[1,e], Martina Hrubovčáková[1,f] and Lydia Sobotova[3,g]

[1]Faculty of Materials, Metallurgy and Recycling, Technical University of Košice, Letná 1/9, 042 00 Košice-Sever, Slovak Republic

[2]RMS Košice,s.r.o. Vstupný areál U. S. Steel, 044 54 Košice, Slovak Republic

[3]Faculty of Mechanical Engineering, Technical University of Košice, Letná 1/9, 042 00 Košice, Slovak Republic

[a*]alica.maslejova@tuke.sk, [b]chudikova@rms-kosice.sk, [c]branislav.bulko@tuke.sk, [d]peter.demeter@tuke.sk, [e]jaroslav.legemza@tuke.sk, [f]martina.hrubovcakova@tuke.sk, [g]lydia.sobotova@tuke.sk

Keywords: Al_2O_3-SiC-C (ASC) refractory, corrosion resistance, energy efficiency.

Abstract. Al_2O_3-SiC-C (ASC) lining bricks for pouring ladle used in pre-treating molten (desulfurization) iron and molten iron ladles, which offer advantages such as high oxidation resistance, strong resistance to slag corrosion, good thermal shock resistance, and excellent resistance to mechanical wear and abrasion, have been investigated. It is expected that the combination of these new techniques will improve the energy and economic efficiency of the steel industry while also contributing to the decarbonization of both the refractory and steel industries. Additionally, the developed technology is expected to be applicable to other energy-intensive industries, such as cement, glass, pulp and paper, and non-ferrous metal processing. Investigating used samples is crucial for reducing wear on both ALKO60A and ALKO66ASC linings. The microstructures of laboratory prepared samples were analyzed using OLM, XRD, and SEM/EDS techniques. It is expected the formation of phases with low melting points, along with spinel solid solutions in the matrix and calcium di-aluminate near the alumina aggregates.

Introduction

Desulfurization of the iron performed in the pouring ladle using mixtures primarily composed of lime (67 % CaO), magnesium (30 % Mg), and minor components such as fluorspar (3 % CaF2). These materials react with sulfur to form sulfides, which are transferred into the slag. The slag is then mechanically removed from the surface of the iron, after which the iron is ready for further processing in the steelmaking oxygen converter. Ladle steel shells are characterized by high creep resistance and high strength at elevated temperatures [1]. Similarly, refractory materials used in such demanding processes must withstand chemical, thermal, and mechanical stresses. Their service life is directly affected by wear and the level of care taken during operation. Sulfur is the most detrimental element in iron, as it causes brittleness in steel and reduces its corrosion resistance. The most heavily worn areas of the pouring ladle are typically near the injection point or opposite the spout, where lining erosion occurs. Molten iron, at a temperature of 1430–1450 °C, is poured from the transport mixer into a relatively cold pouring ladle.

In external hot metal desulfurization, lime is the primary desulfurizing agent. Sulfur binds with calcium according to the following reaction:

$$(CaO) + [S] = (CaS) + [O] \quad (1)$$

Magnesium serves as another desulphurizing component, either reacting directly sulfur or acting as a deoxidizer by binding oxygen released during the lime reaction:

$$[S] + [Mg] + (CaO) = (CaS) + (MgO) \quad (2)$$

Fluorspar is added to the slag to lower the melting point, preventing the formation of high-melting complex compounds. High sulfur activity in hot metal, primarily due to its chemical composition, especially its carbon content (see Fig. 1) enables efficient and cost-effective desulfurization. These principles have been successfully applied in practice and now serve as the basis for AI models that use machine learning techniques based on PINNs (Physics-Informed Neural Networks). These models allow for precise and cost-effective predictions of target sulfur levels during external desulfurization, optimizing downstream converter treatment and the production of specific steel grades. Increasing the amount of desulfurization mixture is only to a point; beyond that, additional amounts yield diminishing returns. Efficient desulfurization can still be achieved with lower mixture consumption, depending on process control.

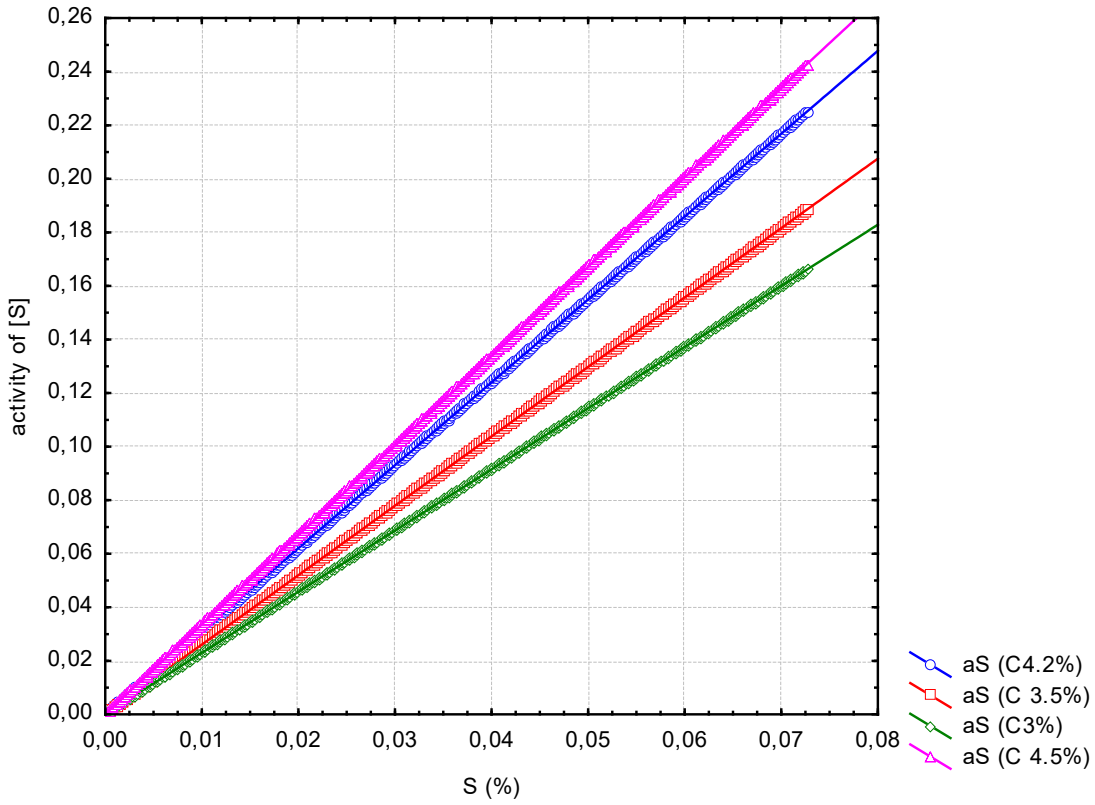

Fig. 1. Carbon content in hot iron influencing activity of sulfur.

Al_2O_3-SiC-C (ASC) refractory bricks are widely employed in blast furnace runners and/or ladle for their excellent thermal shock resistance and erosion resistance [2]. Favorable properties are mainly obtained from SiC and carbon additions. However, C is vulnerable to oxidation at higher temperatures and the volatiles generated during heat treatment leads to a decrease in the compactness and strength of the bricks in pouring ladle, where the hot metal desulphurization process is performed [3]. Simultaneously, the decarburized layer formed oxidation increases the brick corrosion by the blast furnace slag. Employing andalusite could improve the volume stability and thermal shock resistance of the bricks, due to mullitization of andalusite accompanied by a volume expansion [4]. The most castable pore channels are distributed in the matrix, so the silica-rich glass phase produced by andalusite aggregates cannot uniformly fill the pores in the castable matrix. Moreover, there is a higher probability that the exuded silica-rich glass in the matrix will combine with the nearby alumina powder to form secondary mullite [5]. The strain before the bricks break down completely increases because of the special pitch addition; and stress absorbing capability of the refractories increases slightly by reducing the amount of metal addition [6, 7]. Thermal shock tests coupled with the castable oxidation index were applied to evaluate the antioxidation impact [8–10].

Experimental

The company RMS Košice, s.r.o. Slovakia supplies ALKO60A refractory bricks – based on andalusite (see Table 1 for composition) to several steelworks for use in pouring ladles and transport mixers. The service life of these bricks varies depending on specific operating conditions.

Table 1. ALKO60A refractory brick properties.

Physical Properties			Chemical Composition, [%]	
Bulk density [kg.m^{-3}]	Porosity [%]	Compressive strength [MPa]	Al_2O_3	Fe_2O_3
min. 2440	max. 17	min. 55	min. 59	max. 1.2

ALKO60A exhibits low apparent porosity, high compressive strength, excellent thermal shock resistance and high hot load bearing capacity. Despite these favorable properties, its service life achieved at one steel plant is approximately 400–500 heats, while at another steel plant it reaches 900–1000 heats.

Several post-mortem examinations were conducted after the bricks reached the end of their service life. These results are summarized in the following sections. This study aims to evaluate the performance of ALKO60A (fired at 1550 °C) and propose a novel refractory material ALKO66ASC (tempered at 200 °C) which better suited for demanding operational conditions.

Results

Post-mortem samples of ALKO60A were analyzed using chemical methods and both qualitative and quantitative XRD analysis of the hot and cold faces (see Fig. 2). Visual inspection of the ladle revealed that after 300 heats, the remaining refractory thickness in high turbulence ranged from 0 to 60 mm, compared to an original thickness 177 mm. Penetration depth reached up to 90 mm, which is below the safety threshold. Samples with varying penetration and coloration were selected for further analysis. As shown in Table 2, chemical composition varied by depth, with decreasing Al_2O_3 and increasing Fe_2O_3 and MgO near the hot face-likely due to reactions with gunning materials and magnesium for the desulfurization mixture.

Fig. 2. ALKO60A postmortem samples.

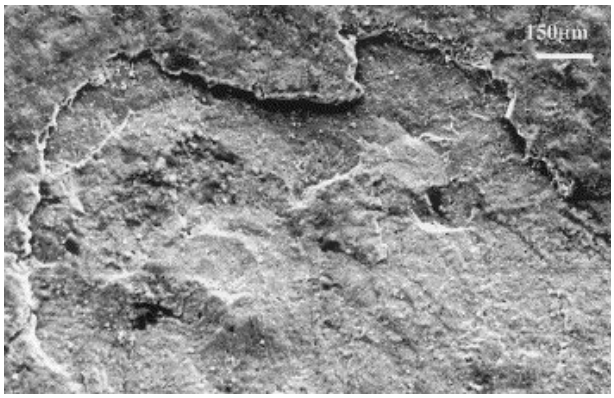

Fig. 3. Area of spalling wear of ladle.

Table 2. Chemical composition of postmortem samples hot and cold faces, [%].

Chemical Composition	SiO_2	Al_2O_3	Fe_2O_3	CaO	MgO	TiO_2	MnO	S
Hot face of sample	35.0	54.0	7.0	0.7	1.12	0.30	0.40	0.024
Cold face of sample	35.0	61.0	1.9	0.2	0.31	0.28	0.04	ND

**ND-not detected*

Main wear mechanism is spalling (Fig. 3), with around 0.5 mm of refractory peeling off per heat due to repeated thermal cycling. As crack forms, high-melting phases solidify and detach, while steel infiltrates the gaps and contributes to further wear. High Fe_2O_3 (7.0 %) and MgO (1.12 %) concentrations on the hot face led to the formation of phases just above the melting point of iron, facilitating structural disruption to further wear.

Detected oxides (Table 3) in the brick led to the formation of the phase above the melting point of iron. In this layer, melting may have occurred, allowing iron to infiltrate intergranular spaces, disrupting the structure and causing spalling.

Table 3. XRD phase composition – ALKO60A postmortem samples hot and cold faces, %.

Phase presence	Mullite $Al_6Si_2O_{13}$	SiO_2	Fe metal	Corund Al_2O_3	Hercynite $FeAl_2O_4$	Andalusite Al_2SiO_5
Hot Face	87.0	4.5	2.3	1.5	3.0	0.7
Cold Face	85.0	7.0	ND	4.19	0.12	3.6

The performance of the fired ALKO60A brick was not effective enough for hot metal treatment in the pouring ladle. Therefore, it was necessary to develop a new ALKO66ASC brick and test it under lab conditions to predict its performance under operational conditions. The crucible (100x100 mm with hole ϕ 50 mm) is suitable for lab static crucible corrosion test according to DIN 51069-2, see Fig. 4. Test run at 1550 °C for 5 hours at oxidation conditions, using fused desulfurization mixture as corrosion medium (67 % CaO, 30 % Mg and 3 % CaF2). Corrosion mechanisms preferent run through grain boundaries and show minimal values, see Fig. 5. EDX spectrum confirmed min. presence of corrosive attack by slag components at the grain boundary region.

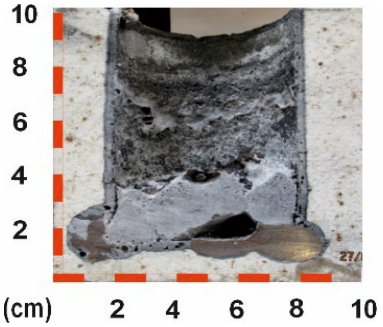

Fig. 4. ALKO66ASC corrosion test.

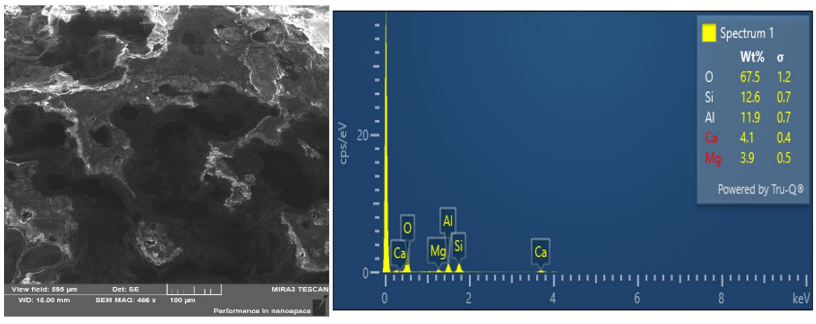

Fig. 5. Grain boundary corroded by blast furnace slag.

A novel ALKO66ASC (ASC) brick, which chemical and physical properties seen in Table 4 demonstrated lower energy consumption during production, with natural fossil gas consumption reduced by 10 times. The ASC brick is based on andalusite and additives, bonded with an eco-friendly, phenol-free resin system, and contains 10 % of carbon.

Table 4. Novel ALKO66ASC refractory brick properties.

Physical Properties			Chemical Composition, [%]		
Bulk density [kg.m^{-3}]	Porosity [%]	Compressive strength [MPa]	Al_2O_3	SiC	C
min. 2860	max. 7.5	min. 50.0	66.0	7.0	10.0

ALKO66ASC brick demonstrates excellent corrosion resistance to molten iron and slag and strong resistance to spalling per ASTM 1525 (tested at 1093 °C and then submerged in cold water). No cracks were observed after 12 thermal shock cycles; only some minor cracks appeared after 30 cycles (Fig. 6), without compromising structural integrity.

An oxidation resistance test (sample 50x50 mm) at 1480 °C for 5 hours showed 0.5 mm of decarbonized surface and 2.2 % volume change – likely due to the transformation of andalusite to mullite.

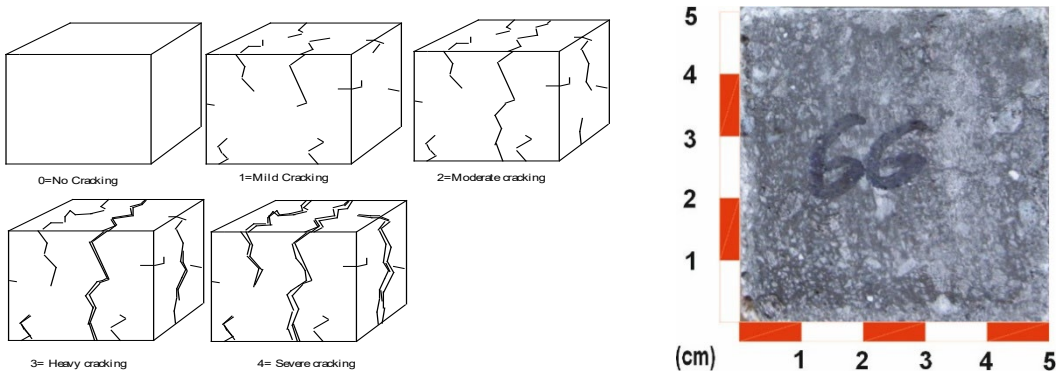

Fig. 6. Evaluation of spalling resistance and result of decarburizing test of ASC brick.

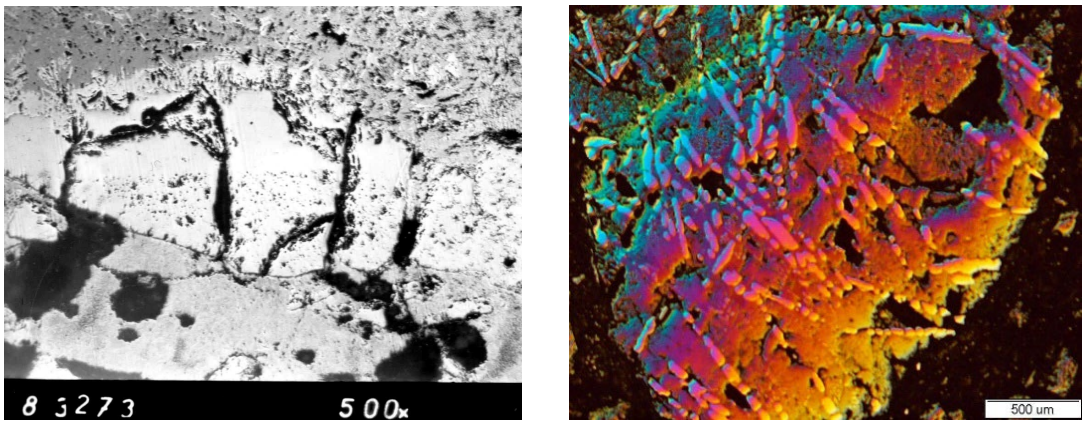

Fig. 7. Oxidation layer of ASC brick and andalusite transformation to mullite.

The refractoriness underload was measured too, and 0.5 % deformation was observed at high temperature around 1700 °C for ASC brick. The phase transformation of andalusite into mullite was detected and is visible in Fig. 7. The microstructural investigations showed that the depth of

infiltration of slag in sample was about 300 μm. The hot metal slag reacted mainly with alumina from the brick, not with silicon carbide or carbon. The dissolution of silicon carbide was attributed to the presence of iron. Forming a layer of calcium aluminate around the alumina aggregate could minimize the dissolution of the alumina in the slag.

Conclusion

Novel ALKO66ASC brick demonstrated excellent resistance to spalling, corrosion, mechanical wear, and abrasion in laboratory tests. These promising results support its use in operational trials. While the slag penetrates and reacts with the alumina aggregates, iron dissolves the silicon carbide and facilitates further slag penetration within the matrix of ASC bricks. The results also indicated that slag and iron tend to react with alumina and silicon carbide, respectively. Molten slag causes refractory failure through corrosion dissolution and spalling. Additionally, this technology producing new ALKO66ASC brick offers significant energy and cost savings and supports the decarbonization of both the refractory and steel industries.

Acknowledgement

This research was funded by the Ministry of Education, Science, Research and Sport of the Slovak Republic: VEGA 1/0199/24: "Development of mathematical control models and digital twins for individual steel production processes using machine learning to improve competitiveness and reduce the carbon footprint. Project 09I05-03-V02-00016: Smart-Steel: AI-Driven Control Models for Future Steel Production.

References

[1] M. Hagarová, et al., High temperature oxidation behavior of creep resistant steels in water vapor containing environments, Materials, 15 (2022) 616.

[2] X. Wang, et al., Enhancing the oxidation resistance of ASC castable, Materials, 14 (2021) 4775.

[3] N. Taki, et al., Improvement of refractory life for ladles, J. Techn. Assoc. Refract. Jpn., 37, 4 (2017) 236-244.

[4] Y. Matsuo, et al., Ladle refractory cost reduction, Refractories World Forum, 8, 1 (2016) 22-26.

[5] R. Dzurňák, et al., A device for dynamic testing on the refractory ceramics' resistance to biomass ash, Fuel, 374 (2024) 132491.

[6] T. Hattori, et al., Deformation behavior under load of Al_2O_3–SiC–C bricks for torpedo car, Taikabutsu Overseas, 15, 2 (1995) 42-47.

[7] N. Sahoo, et al., Development of improved quality alumina–silicon carbide–carbon bricks for hot metal transfer and torpedo ladles, UNITECR 07 Proceedings (2007) 381-383.

[8] R.C. Filho Joao, et al., Performance of Al_2O_3–SiC–C for torpedo car lining, UNITECR 93 Proceedings (1993) 1632-1640.

[9] S. Darbana, et al., Corrosion mechanisms of Al_2O_3–SiC–C refractory castables by iron and slag based on post-mortem analysis of industrial samples, Open Ceramics, 16 (2023) 100453.

[10] J. Hamacek, et al., On the high temperature bending strength of castable, Ceramics–Silikáty, 56, 3 (2012) 198-203.

Published in: Solid State Phenomena
ISSN: 1662-9779, Vol. 386, pp 77-83
doi:10.4028/p-3CElNJ

Submitted: 2025-05-13
Revised: 2025-12-12
Accepted: 2025-12-19
Online: 2026-03-13

The Impact of Final Turning on the SCC Susceptibility of Austenitic Stainless Steel AISI 304 and AISI 321

Marek Kudláč[1,a*], Mária Dománková[1,b], Katarína Bártová[1,c], Matúš Gavalec[1,d] and Dávid Slnek[1,e]

[1]Institute of Materials Science, Faculty of Materials Science and Technology in Trnava, Slovak University of Technology in Bratislava, J. Bottu 2781/25, 917 24 Trnava, Slovakia

[a*]marek.kudlac@stuba.sk, [b]maria.domankova@stuba.sk, [c]katarina.bartova@stuba.sk, [d]matus.gavalec@stuba.sk, [e]david.slnek@stuba.sk

Keywords: Austenitic Stainless Steel, Final Turning, Stress Corrosion Cracking, Corrosion, Surface.

Abstract. Final turning, which is a finishing process for obtaining components with specific precise parameters, affects the integrity of the surface and its properties, whether hardness or surface residual stresses. The synergistic effect of these factors affects the susceptibility of the material, to stress corrosion cracking. In this work, 2 types of austenitic stainless steel, namely AISI 304 and AISI 321, were turned. Tool with positive cutting geometry was used for turning. The cutting parameters that varied were the cutting speed (100 and 250 $m.min^{-1}$) and the tool feed (0.12, 0.2 and 0.3 $mm \cdot rev^{-1}$). The depth of cut was the same for all turnings (0.8 mm). Subsequently, the prepared samples were exposed in $MgCl_2$ solution based on the ASTM G36 for 96 hours. After this time, the samples were analysed using SEM, where the density of surface cracks was monitored. When comparing the crack density, an increase in density was visible for AISI 304 compared to AISI 321. It was shown that with increasing cutting speed, the density of cracks increased significantly, as well as with increasing tool feed. On the cross-sections the depth and length of the cracks were analysed. Crack depth and length increased with increasing feed too.

Introduction

Turning of austenitic stainless steels is a very demanding process, as they undergo strain hardening (slip bands or deformation twins are formed) of the surface grains, making machining difficult. In addition, mechanical stress and thermal treatment cause the formation of tensile residual stresses, which are highest near the surface and gradually decrease with depth to the area of effect of the compressive orientation of residual stresses. Turning also affects the surface integrity [1–3].

The finishing process associated with machining is final turning and final milling, which aims to smooth the surface and obtain precise dimensions of the product or semi-finished product. Since final machining is the final process in the production of components for primary water circuits of nuclear power plants, it is necessary that these components can withstand such extreme conditions (WWER reactor type where the temperature of primary circuit is 270 °C and the pressure is 12.26 MPa). However, in such an environment, there is a possibility of stress corrosion cracking (SCC) caused precisely by the presence of tensile residual stresses, surface integrity but also by microstructural changes in the surface areas after machining [3, 4].

In determining the susceptibility of such steels to SCC caused by machining or final surface treatment, exposure tests according to ASTM G36 are most often mentioned in the literature and articles, i.e. exposure tests in a boiling $MgCl_2$ solution at a temperature of 155 °C [4, 5], which causes the formation of corrosion cracks in a relatively short time, which is a convenient way to determine whether such a corrosion event can occur in the material prepared in this way.

In this work, turning with a tool with positive geometry was used (positive rake angle where the cutting edge slopes towards the workpiece), with a combination of parameters: 2 cutting speeds and 3 types of feeds. The influence of these parameters on the formation of corrosion cracking of two types of austenitic stainless steels (AISI 304 and AISI 321) in a boiling $MgCl_2$ solution was monitored. The results of both steels were subsequently compared.

Materials and Methods

The samples were prepared from two austenitic stainless steels AISI 304 and AISI 321. Table 1 and Table 2 show the standard chemical composition for both types of steel and the chemical composition of the material of the turned samples. Both austenitic steels were solution annealed at the temperature of 1050 °C. The surface hardness HV 0.1 of the steel bars (initial state) was 324 ± 13 for AISI 304 and 319 ± 6 for AISI 321.

Table 1 Chemical composition in wt.% of turned AISI 304 steel and standard AISI 304.

Steel brand	C	Si	Mn	P	S	Cr	Ni	Mo	Cu
Material of samples	0.026	0.33	1.78	0.044	0.025	18.40	8.01	0.28	0.45
AISI 304 standard	≤ 0.07	≤ 1.00	≤ 2.00	≤ 0.045	≤ 0.03	17.5–19.5	8.0–10.5	-	-

Table 2 Chemical composition in wt.% of turned AISI 321 steel and standard AISI 321.

Steel brand	C	Si	Mn	P	S	Cr	Ni	Ti	Cu
Material of samples	0.064	0.83	1.44	0.025	0.026	17.5	9.89	0.47	0.66
AISI 321 standard	≤ 0.08	≤ 1.00	≤ 2.00	≤ 0.045	≤ 0.03	17.0–19.0	9.0–12.0	5xC–0.70	–

Preparation of samples by final turning. AISI 304 and 321 steel bars with a diameter of 38 mm were turned using a DMG CTX alpha 500 lathe. The cutting tools used were VCGT 160408 indexable carbide cutting inserts with a sharp cutting edge and a tip radius r_ε of 0.8 mm, while the cutting parameters – cutting speed, feed and depth of cut – were varied (Table 3). The parameters were chosen to achieve graded roughness and at the same time obtain different values of residual stresses. The depth of cut was 0.8 mm for all samples, which was chosen to remove the previous deformed layer of original bars. In this way, a total of 12 samples were prepared for both types of steel. The turned rollers were cut and prepared for corrosion test. Before the test itself, they were observed using stereomicroscopy to detect possible surface defects.

Table 3 Turning parameters used for austenitic stainless steels AISI 304 and AISI 321.

Turning parameters					
Cutting speed v_c ($m \cdot min^{-1}$)		Feed f ($mm \cdot rev^{-1}$)			Depth of cut a_p (mm)
100	250	0.12	0.2	0.3	0.8

ASTM G36 and crack analysis. To perform the test according to ASTM G36, the apparatus was prepared (Fig. 1a). 500 g of $MgCl_2 \cdot 6H_2O$ was weighed into an Erlenmeyer flask and 12.5 ml of demineralized water was added and heating was started, ensuring that the heated solution had a temperature of 155 ± 1 °C. After the temperature had stabilized, samples of one type of steel were placed in the solution. The samples were placed in the rounded edge parts of the flask so that they were not directly on the heating element. The samples were boiled for 96 hours. After this time, the samples were removed, rinsed in demineralized water and cleaned in ultrasound. The procedure was repeated for another type of steel. The surface of the samples was first observed using a stereomicroscope to determine how cracks propagated within the turned surface. The surface of the samples was observed using SEM, where images with a magnification of 500x were used to evaluate the crack density. The crack density was determined using ImageJ software. This analysis is represented in Fig. 1b. On subsequent cross-sections, where the central surface area was observed, the crack lengths (CL – the sum of the lengths of the primary crack together with the lateral cracks) and crack depths (CD – the distance from the surface to the deepest point where the crack penetrated) were evaluated. In this case, the ImageJ software was used to determine the depth and length (Fig. 1c). The crack lengths and depths were divided into size categories of 5 μm, while their length and depth distributions were monitored.

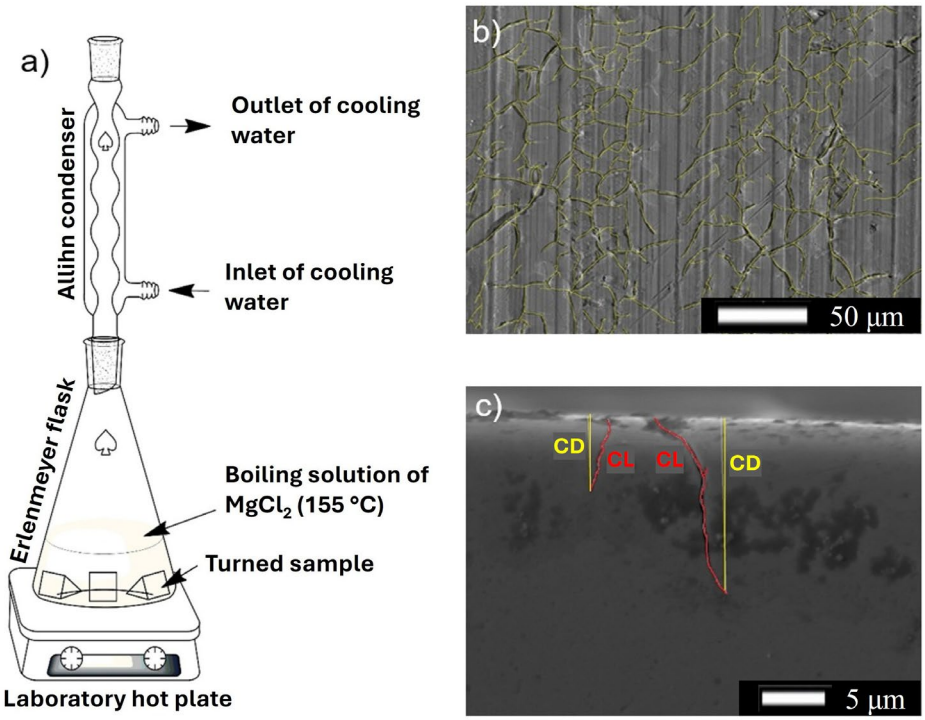

Fig. 1 Exposure test apparatus according to ASTM G36 (a), method of evaluating crack density from SEM image (b) and crack depth and crack length evaluation from SEM image (c).

Results and Discussion

After the ASTM G36, SEM images of density of cracks were evaluated, as well as the depth and length of cracks in cross-sections. The surface after the test was observed using a stereomicroscope.

Results of crack density. Stereomicroscopy showed the impact of $MgCl_2$ solution on sample surfaces. Selected topographic images of sample 3 before and after the test are shown in Fig. 2. In the image, regularly iterated feed marks of turning are visible. Within the cracks formed on the surface, the trend of cracks occurring mainly in the troughs themselves was repeated, and only a small part of the cracks was connected in the peaks, while these were thicker primary cracks and were in most cases perpendicular to the direction of turning. Signs of pitting were also observed.

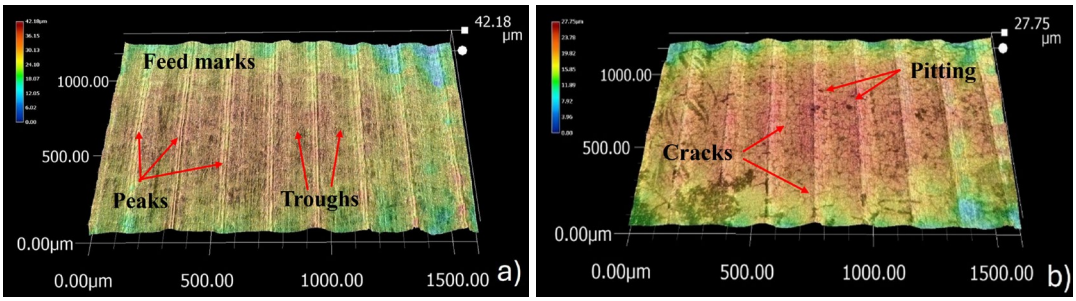

Fig. 2 Surface profile images of AISI 304 of sample 3 before (a) and after ASTM G36 test (b).

The network of cracks on the surface of the samples was also observed using SEM. Fig. 3 shows images of the surface of AISI 304 samples. With the cutting speed, an increase in the density of cracks was visible (the feed did not have a significant effect on the density). In terms of the highest crack density, it was sample 4, but also samples 2 and 6, i.e. samples where a higher cutting speed was used, i.e. 250 m·min^{-1}. Lower crack densities were at lower cutting speed (especially sample 3). As for the turned samples of AISI 321 steel, they are shown in Fig. 4. There is an obvious decrease in the crack density compared to AISI 304, while the trend in the influence of cutting parameters on the crack density was maintained. It is visible that the gradual increase in the cutting speed significantly influenced the formation of surface cracks. The lowest crack density is in sample 7, i.e. the sample with the lowest feed and cutting speed 100 m·min^{-1}. A low crack density was also recorded in sample 11. A gradual increase in cracks is visible, especially in samples 8 or 10. All crack density values are in Table 4. The table shows the cutting parameters and the resulting crack densities. The crack density is therefore the highest for AISI 304 samples, specifically sample 4 (127.4 ± 21.8 mm·mm^{-2}), the lowest value for sample 3. During the evaluation, there was a major problem with the significant variability of the crack density in different parts of the sample surface - which resulted in the standard deviations being much higher in these results. This could be caused by the uneven distribution of cutting forces during the cutting process and thus affecting the surface, especially in terms of residual stress but also hardness or roughness. Within AISI 321 steel, the lowest value was for sample 7 (63.1 ± 17.9 mm·mm^{-2}), where the crack density was the lowest, but in this case, it also varied in different surface areas. Sample 11 also had a low crack density value, namely 65.5 ± 5.1 mm·mm^{-2}.

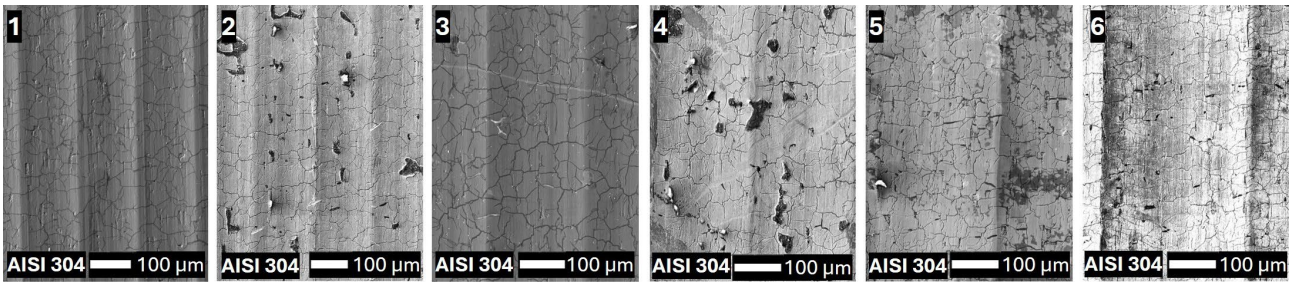

Fig. 3 SEM images of the surface of all AISI 304 samples after ASTM G36 corrosion test.

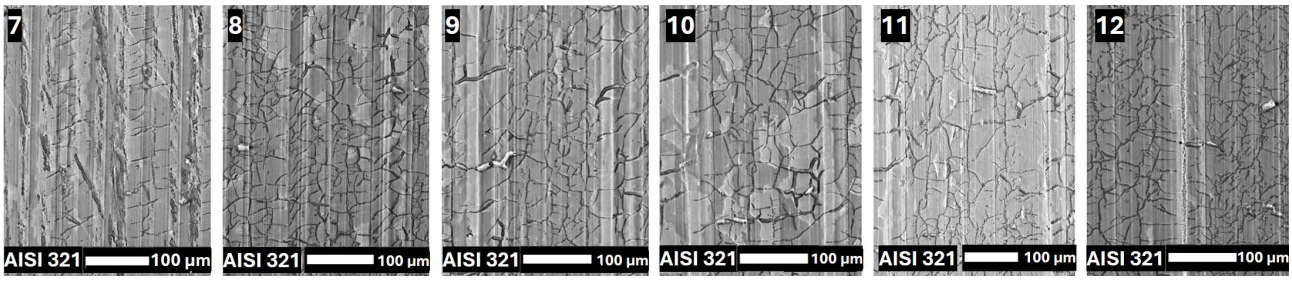

Fig. 4 SEM images of the surface of all AISI 321 samples after ASTM G36 corrosion test.

Table 4 Evaluation of crack density on the surface of samples of both steels.

Material of samples	Sample marking	Feed f (mm· rev^{-1})	Cutting speed v_c (m·min^{-1})	Crack density (mm·mm^{-2})
AISI 304	1	0.12	100	73.5 ± 4.9
	2	0.12	250	111.7 ± 10.4
	3	0.2	100	63.3 ± 8.9
	4	0.2	250	127.4 ± 21.8
	5	0.3	100	87.0 ± 9.4
	6	0.3	250	106.2 ± 17.6
AISI 321	7	0.12	100	63.1 ± 17.9
	8	0.12	250	104.4 ± 7.0
	9	0.2	100	83.4 ± 3.9
	10	0.2	250	102.1 ± 13.3
	11	0.3	100	65.5 ± 5.1
	12	0.3	250	100.4 ± 8.3

Results of crack length and depth. Cracks penetrating both steels were analysed using SEM while they had various morphologies from branched to simple magistral cracks without significant lateral cracks. Cracks were also initiated from the resulting pitting (Fig. 5a), or on some samples, subsurface cracks were formed, which interconnected with each other (Fig. 5b).

The lengths and depths of the cracks were measured and divided into size categories and their percentage representation was determined. Figure 6 shows distribution of crack depths and lengths for both types of steel. Figs. 6a and 6b shows the distribution of lengths and depths of AISI 304 steel samples, where shorter cracks were observed in samples 1 and 2, while with increasing tool feed the maximum decreased and the proportion of longer crack lengths increased (the largest in samples 4 or 5). The largest representation of crack lengths was from 5 to 35 μm. As for the depth of cracks, in samples 1 and 2 they penetrated to a maximum depth of 25 μm while gradually, with increasing feed, deeper cracks began to appear. In sample 5, cracks penetrating to a depth ranging from 30 to 35 μm were discovered.

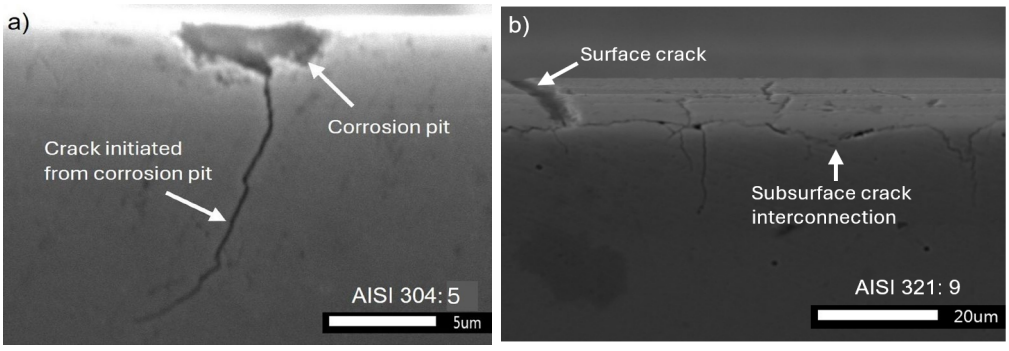

Fig. 5 SEM image of cross-section of AISI 304 sample 5 where crack initiated from corrosion pit (a) and cross-section of AISI 321 sample 9 showing subsurface crack networks that interconnect (b)

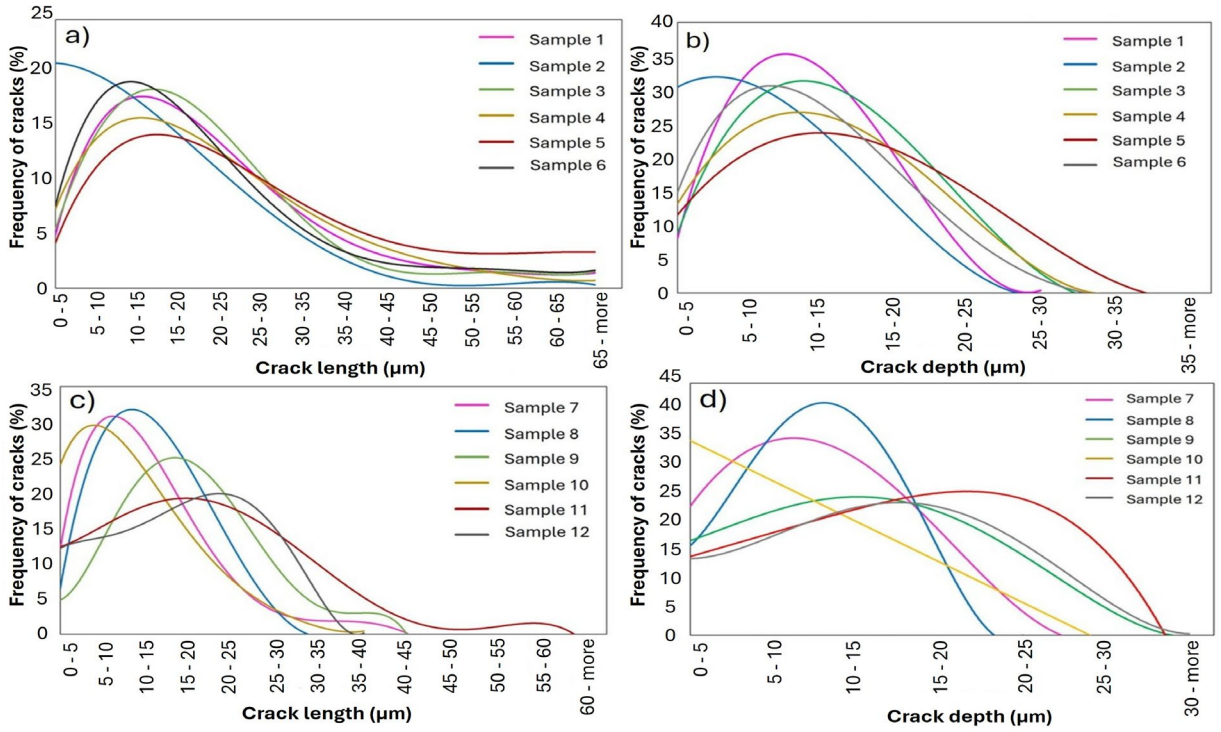

Fig. 6 Crack length (a) and depth (b) distribution of samples of AISI 304 and crack length (c) and depth (d) distribution of samples of AISI 321.

In Fig.6 c and Fig. 6d shorter crack lengths were observed in AISI 321 mainly in samples 7 and 8 but also in 10 (the largest length representation was from 5 μm to 25 μm), while in samples 9, 11 and 12 the range of lengths shifted (the largest representation from 10 μm to 30 or 35 μm, respectively) and a larger number of longer cracks appeared (especially sample 11). In terms of length and depth, a decrease was observed in the case of AISI 321 compared to AISI 304, while in terms of depth, sample 2 had the shallowest cracks. Comparing both steels, it was found that the distribution peaks in AISI 304 steel were more located in shorter or shallower cracks than in the case of AISI 321.

Discussion. The literature mentions that in terms of turning of austenitic stainless steel, it is most appropriate to use tools with a positive rake angle [6] and sharp cutting edge, which was also used in this work. This is due to the creation of small cutting forces and low heat generation. However, individual turning parameters showed how significantly they subsequently affected the surface and resistance to corrosion cracking in a $MgCl_2$ environment. Both parameters – feed and cutting speed – negatively affected the SCC resistance. In terms of obtaining a surface with the lowest residual tensile stresses, according to Jang et al. the following cutting parameters should be used: low feed (in the article 0.08 $mm \cdot rev^{-1}$), low cutting speed (approximately 28 $m \cdot min^{-1}$ with a sample diameter of 49 mm) [7]. The article also mentions a higher depth of cut, specifically 1 mm. However, at a depth of cut of 0.76 mm, a still high level of residual tensile stress of machined surface was recorded (around 500 MPa). Čička et al. mention in their article that the best parameters for final turning are minimum depth of cut, maximum spindle speed and low cutting speed [8]. The parameters in this article were used to obtain different types of sample surfaces and thus to influence these samples to SCC.

Summary

This work deals with the influence of final turning parameters on the susceptibility of two austenitic stainless steels AISI 304 and AISI 321 to stress corrosion cracking, and it was found that:

- The parameter that significantly increased the crack density was the cutting speed. The highest value 127.4 ± 21.8 $mm \cdot mm^{-2}$ was in turned AISI 304 sample with a feed of 0.2 $mm \cdot rev^{-1}$ and a cutting speed of 250 $m \cdot min^{-1}$. The feed was not shown to be a significant factor affecting the surface crack density.
- When comparing the steels, AISI 321 steel had a lower crack density rate than AISI 304 (exception sample 3) – the sample with the lowest crack density was the sample 7 turned with a feed of 0.12 $mm \cdot rev^{-1}$ and a cutting speed of 100 $m \cdot min^{-1}$ (63.1 ± 17.9 $mm \cdot mm^{-2}$).
- Within the dimensions of the cracks on the cross sections, the crack length and crack depth increased with increasing feed for both types of steel. AISI 321 showed shorter cracks compared to AISI 304, however, the distribution maxima in AISI 304 converged more to smaller lengths and depths than in AISI 321.

Acknowledgement

This work was supported by the Slovak Research and Development Agency under the Contract no. APVV-22-0146. Funded by the EU NextGenerationEU through the Recovery and Resilience Plan for Slovakia under the project No. 09I03-03-V05-00005.

References

[1] K. Kocman, Technological processes of machining, first ed., CERM, Brno, 2011.

[2] J. Beňo, I. Maňková, Technological and material factors of machining, first ed., Vienala, Košice, 2004.

[3] I. Korkut, M. Kasap, I. Çiftçi, U. Şeker, Determination of optimum cutting parameters during machining of AISI 304 austenitic stainless steel, J. Mat. & Des., 25 (2004) 303-305.

[4] H. Wu, Ch. Li, K. Fang, W. Zhang, F. Xue, G. Zhang, X. Wang, Effect of residual stress on the stress corrosion cracking in boiling magnesium chloride solution of austenitic stainless steel, Mat. and Cor., 25 (2018) 1572-1583.

[5] W. Zhang, Y. Li, H. Dong, Ch. Yang, X. Jiang, D. Lou, H. Xue, K. Fang, X. Wang, Correlation between machining-induced surface alterations and stress corrosion cracking susceptibility of austenitic stainless steels, J. Mat. Res. and Tech., 26 (2023) 5076-5094.

[6] AB SANDVIK COROMANT, Modern Metal Cutting – A Practical Handbook, first ed., Scientia, Praha, 1997.

[7] D.Y. Jang, T.R. Watkins, K.J. Kozaczek, C.R. Hubbard, O.B. Cavin, Surface residual stresses in machined austenitic stainless steel, Wear, 194 (1996) 168-173.

[8] M. Čička, R. Turisová, F. Kóča, H. Pačaiová, Machining of Austenitic Stainless Steels - the Influence of Various Factors on the Machining Result, Ac. Mech. Slov., 27 (2023) 18-26.

Published in: Solid State Phenomena
ISSN: 1662-9779, Vol. 386, pp 85-92
doi:10.4028/p-qr9MpO

Submitted: 2025-05-27
Revised: 2025-12-04
Accepted: 2025-12-19
Online: 2026-03-13

Effects of Composition and Layer Number on the Mechanical Properties of Multilayered Si-DLC / DLC Coatings

Atsuki Okano[1,a*] and Akio Nishimoto[2,b]

[1]Graduate School of Science and Engineering, Kansai University, 3-3-35 Yamate-cho, Suita, Osaka 564-8680, Japan

[2]Department of Chemistry and Materials Engineering, Kansai University, 3-3-35 Yamate-cho, Suita, Osaka 564-8680, Japan

[a]*k255579@kansai-u.ac.jp, [b]akionisi@kansai-u.ac.jp

Keywords: DLC Coating, Plasma CVD, Stainless Steel, Multilayer Structure, Surface Engineering.

Abstract. Diamond-like carbon (DLC) coatings are valued for their excellent wear resistance and ability to extend the life of mechanical components, supporting resource conservation. However, high residual stress and poor adhesion limit their practical use. Silicon-doped DLC (Si-DLC) can reduce stress and improve adhesion, though excess silicon lowers hardness, creating a trade-off. This study aimed to optimize both adhesion and hardness by adjusting the silicon-containing gas ratio and the number of stacked layers. Si-DLC was deposited on austenitic stainless steel (SUS304) using acetylene (C_2H_2) and tetramethylsilane (TMS) via plasma enhanced chemical vapor deposition (PECVD) at 170 °C with a 1.2 μm thickness. Higher TMS ratios increased silicon and hydrogen content in the Si-DLC layer. More layers reduced hardness and low-load wear resistance but enhanced durability under high loads.

Introduction

In recent years, environmental concerns have increased the demand for materials with longer service life and enhanced functionality. Surface modification technologies have become essential, enabling new surface properties without altering the base material. Desired properties include mechanical (wear resistance, lubricity), electrical, optical, thermal, chemical, and decorative functions. Established techniques like plating, thermal spraying, carburizing, and nitriding are widely used [1, 2].

This study focuses on diamond-like carbon (DLC), a high-performance coating known for its hardness, low friction, and resistance to wear and corrosion. DLC films, composed of sp^3 and sp^2 bonded carbon with hydrogen, can be deposited by chemical vapor deposition (CVD), plasma enhanced CVD (PECVD), physical vapor deposition (PVD), and other methods [3]. However, hard DLC films often suffer from high internal stress, leading to delamination due to thermal mismatch with substrates [4].

To address this, researchers have explored doping with elements like Si, Ti, or W (Me-DLC) to improve interface stability [5, 6], and multilayer structures to enhance durability [7–9]. Using Si-DLC interlayers and adjusting gas ratios during deposition have also proven effective in balancing adhesion and mechanical strength [10, 11].

In this study, we aimed to enhance both adhesion and durability of Si-DLC/DLC multilayer films by varying the precursor gas composition and the number of layers. Using C_2H_2 and tetramethylsilane (TMS) as source gases, the TMS ratio was set to 20 %, 60 %, and 100 %. A deposition using 100 % C_2H_2 was not performed because DLC films directly deposited onto SUS304 tend to delaminate due to poor adhesion caused by thermal expansion mismatch. Introducing Si into the DLC network forms longer C–Si bonds, relieving residual stress and improving adhesion. In this study, the TMS ratio was varied at equal intervals to systematically investigate the effects of Si incorporation and multilayer

structure on the mechanical properties of the coatings. While maintaining constant total film thickness, the number of layers was varied to create nine multilayer configurations. These were systematically analyzed to identify optimal deposition conditions.

Materials and Methods

Materials. Austenitic stainless steel SUS304 disk was used as the substrate. The sample material was 25 mm in diameter and 5 mm in thickness. The SUS304 samples were polished with wet emery paper from #220 to #2000. After polishing, the samples were ultrasonically cleaned with acetone, and dried in air.

Si-DLC / DLC coating condition. DLC films were deposited onto an SUS304 substrates through PECVD. Sputtering and PECVD were conducted at a 1×10^{-5} Pa base pressure and 443 K. Samples were cleaned for 10 min using Ar plasma generated at an applied bias of -380 V and a working pressure of 0.70 Pa. Details of the deposition conditions for Si-DLC intermediate layer and DLC films are presented in Table 1. Figure 1 shows a schematic illustration of the Si-DLC/DLC multilayer structure. The total film thickness was designed to be approximately 1.2 μm, consisting of 0.6 μm × 2-layers for the two-layer coating, 0.3 μm × 4-layers for the four-layer coating, and 0.2 μm × 6-layers for the six-layer coating. The thickness was measured using a surface profiler. A total thickness of around 1 μm is generally known to balance adhesion and durability for DLC coatings. In our previous study, increasing the TMS ratio improved durability but reduced adhesion [6, 9]. Therefore, the total thickness was fixed at 1.2 μm in this study while varying the multilayer structure to improve adhesion without compromising durability.

Surface characterization. The compositional analysis of the treated samples was performed using glow discharge optical emission spectroscopy (GD-OES; GD-profiler2, Horiba, Japan). The GD-OES conditions included a sputtering-mark diameter of 4 mm, a discharge pressure of 600 Pa, and a power of 35 W. The main elements measured were C, Si, and H.

Mechanical and functional properties evaluation. Mechanical properties were evaluated by nanoindentation using an ultra-micro hardness tester (ENT-2100, Elionix Co., Japan) under a 4.0 μN load, averaging the middle three of five measurements. Wear resistance was tested with a ball-on-disk tester (Anton Paar Japan) using an Al_2O_3 ball (ϕ6.35 mm), 5 N load, 0.1 m/s speed, 1000 m sliding distance, and 5 mm wear radius, following ISO 18535 [12]. Durability tests used the same device with a 10 N load and 7 mm wear radius, continuing until delamination occurred, defined by a friction coefficient (μ) reaching 0.4. Adhesion was evaluated by Rockwell indentation (1471 N, C-scale) using a diamond indenter. Delamination around the indentation was observed with an optical microscope (BX60M, Olympus) and ranked HF 1–6 per VDI 3198; HF 1–4 is considered acceptable.

Table 1 Coating conditions for Si-DLC / DLC multilayer.

Ar^+ bombard	Gas	Ar		
	Gas flow	40 sccm ($mLmin^{-1}$)		
	Time	10 min		
Si-DLC	Gas	**C_2H_2 + TMS**		
	Gas flow (TMS ratio)	40 sccm (20, 60, 100%)		
	Deposition rate	17, 30, 40 nm / min		
DLC	Gas	**C_2H_2**		
	Gas flow	100 sccm ($mLmin^{-1}$)		
	Thickness	2layers	4layers	6layers
		0.6 μm	0.3 μm	0.2 μm
	Time	18 min	9 min	6 min

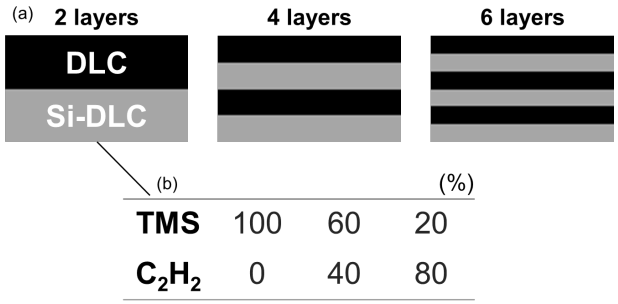

Fig. 1 Structural diagrams of Si-DLC/DLC multilayers. (a) Schematics of 2-, 4-, and 6-layer DLC structures. (b) TMS gas ratios for Si-DLC: 100 %, 60 %, and 20 %.

Results and Discussion

Figure 2 shows the presence of Si, C, and H peaks across all spectra. In Fig. 2(a)–(c), a single Si peak confirms the formation of a Si-DLC/DLC bilayer. Fig. 2(d)–(f) show two Si peaks, indicating a 4-layer structure with alternating Si-DLC and DLC films. Fig. 2(g)–(i) reveal three Si peaks, confirming a 6-layer structure. These results demonstrate the successful fabrication of 2-, 4-, and 6-layer multilayer films as intended. In addition, the Si and H contents increased with increasing TMS gas ratio up to 60 %, which is attributed to the higher Si and H content in the TMS precursor. However, the increase became negligible above 60 %, suggesting saturation of Si incorporation at higher TMS ratios.

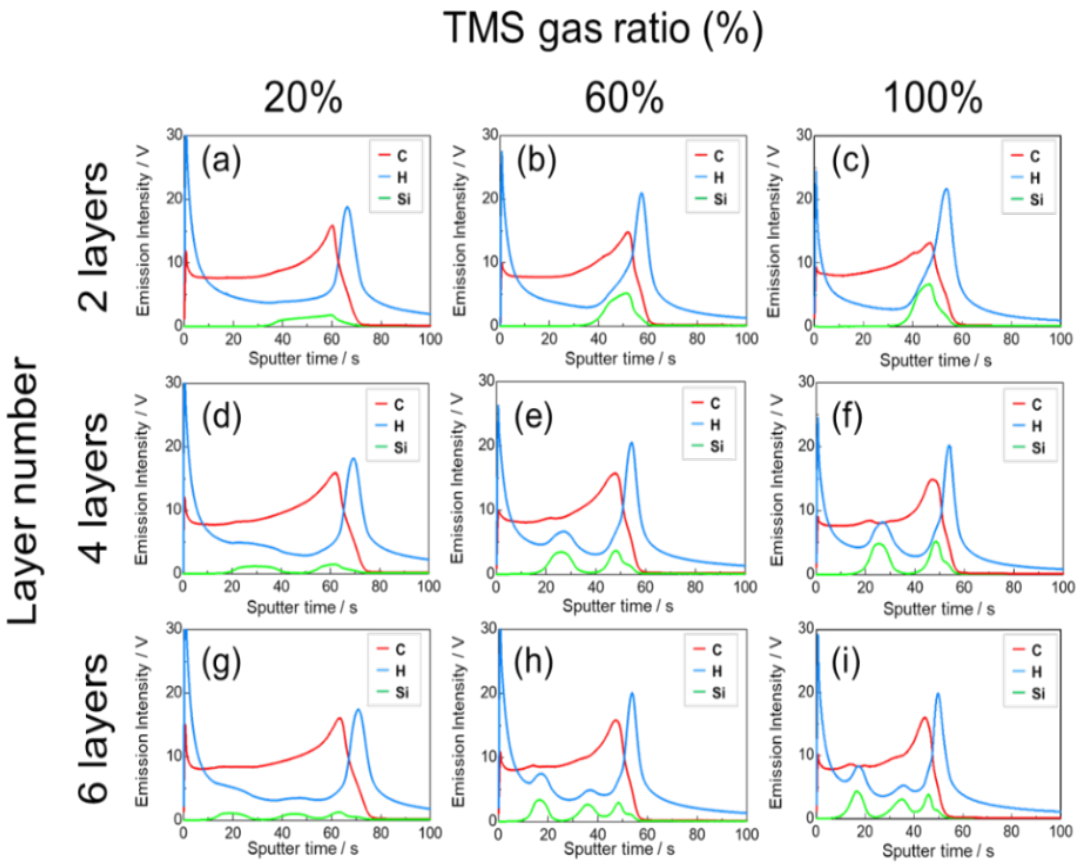

Fig. 2 GD-OES intensity profile of Si-DLC / DLC multilayer coated SUS304.

Figure 3(a) and (b) show the nano-hardness and Young's modulus under all conditions, both decreasing with increasing TMS ratio. This is attributed to the higher Si–C bonding and hydrogen content from TMS, as confirmed by GD-OES (Fig. 2). Hydrogen incorporation reduces DLC hardness by forming sp^3-CH_n ($n > 1$) structures, relaxing stress and decreasing film density through increased voids [13, 14].

In addition, both properties decreased with increasing number of layers. The sharper decline from 2- to 4-layers indicates that thinner layers and more interfaces enhance energy dissipation and the effect of softer Si-DLC layers. The smaller change between 4- and 6-layers suggests that mechanical properties tend to saturate with further layering [15, 16].

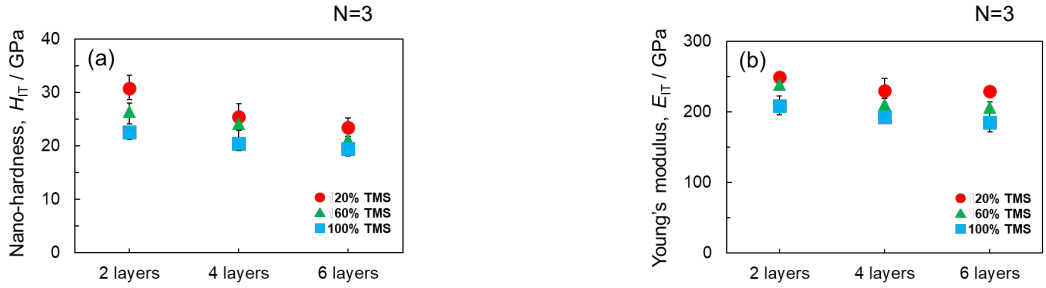

Fig. 3 (a) Nano-hardness and (b) Young's modulus of Si-DLC / DLC multilayer coated SUS304.

Figure 4 shows the wear scars and their profiles on both the samples and balls after testing. No penetration of the alumina ball into the substrate was observed. Figure 5(a) and Fig. 5(b) present the wear volumes of the samples and balls, respectively, for each TMS ratio and number of layers. These values were calculated from the wear scar profiles in Fig. 4. The ball wear volume, V_{ball}, was calculated using Equation (1), where A and B are the minor and major axes of the elliptical wear scar (mm), and D is the ball diameter (6.35 mm).

$$V_{ball} = \pi A^3 B / 32\, D \ (mm^3) \quad (1)$$

The wear volume V_{sample} of a sample is calculated according to Equation (2), where R is the wear scar radius (R = 7 mm) and S is the wear area of the sample surface (mm^2).

$$V_{sample} = 2\pi RS \ (mm^3) \quad (2)$$

$$S = wd / 2 \quad (3)$$

Figure 5 shows the variation of the friction coefficient during the test conducted under a 5 N load. The friction coefficients remained low and stable, indicating that the Al_2O_3 ball did not reach the substrate during sliding.

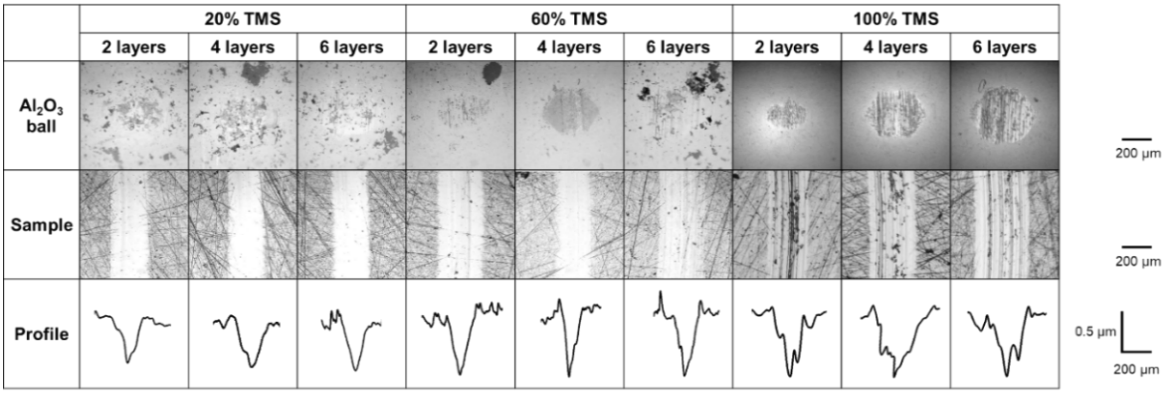

Fig. 4 Appearance of ball and wear tracks, cross-sectional profiles of samples.

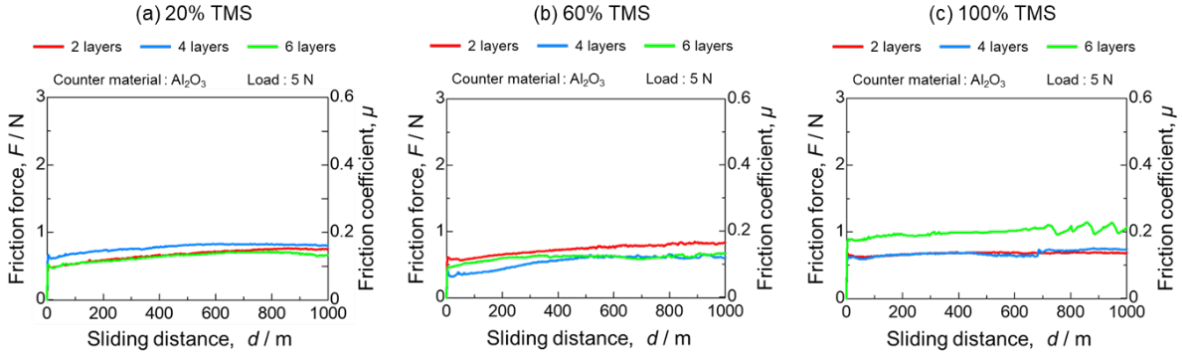

Fig. 5 (a–c) Friction force vs. sliding distance for Si-DLC/DLC-coated SUS304.

Figure 6(a) shows that under a 5 N load, the 2-layer Si-DLC with 20 % TMS had the lowest wear rate, while the 6-layer DLC had the highest. These differences arise from variations in surface hardness, film thickness, Si content, and interlayer interfaces. The excellent wear resistance of the 2-layer 20 % TMS sample is attributed to its thicker hard layer and balanced hardness–lubrication properties. In contrast, higher TMS ratios (60 % and 100 %) likely reduced hardness and increased plastic deformation, leading to higher wear. The 6-layer DLC wore rapidly because its thin layers exposed softer Si-DLC. As shown in Fig. 6(b), ball wear volume showed a similar trend, increasing with film wear due to larger contact area, while lower TMS content and fewer layers helped suppress ball wear.

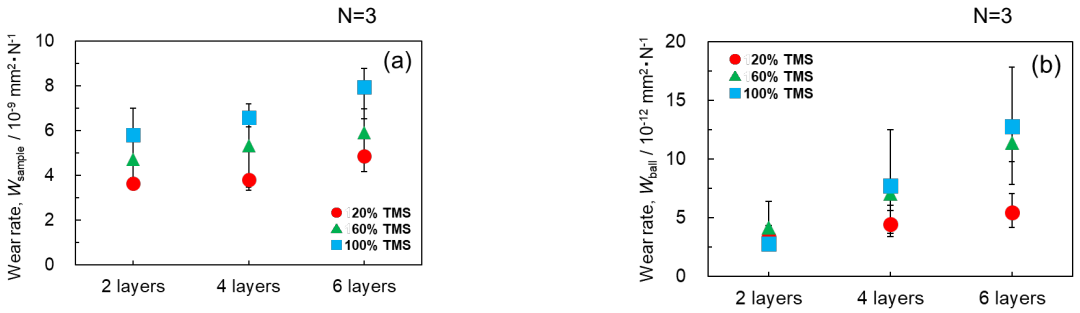

Fig. 6 (a) Wear rate of Si-DLC/DLC-coated SUS304 and (b) Al_2O_3 ball after wear test.

Figure 7(a)–(d) show friction force and sliding distance, indicating improved durability with lower TMS ratios due to reduced Si and H contents, which enhanced hardness and load-bearing capacity. In the 6-layer DLC, the multilayer structure likely helped distribute stress and suppress delamination by reducing stress concentration at interfaces, improving high-load performance [17]. At 10 N, where plastic deformation is more pronounced, both hardness and toughness are crucial. 2-layer films with thicker layers tend to fail quickly after delamination, while 6-layer DLC better resists damage due to thinner layers. Si-DLC films were more under high loads, as higher Si content reduced hardness and increased plasticity. At 100 % TMS, deep wear tracks formed. Si-DLC's oxygen affinity may have also promoted oxidation from frictional heat, accelerating wear. The friction coefficients of the coatings were approximately 0.1–0.2 under both 5 N and 10 N loads. Although slight variations were observed, they were attributed to environmental factors such as humidity and temperature during the tests.

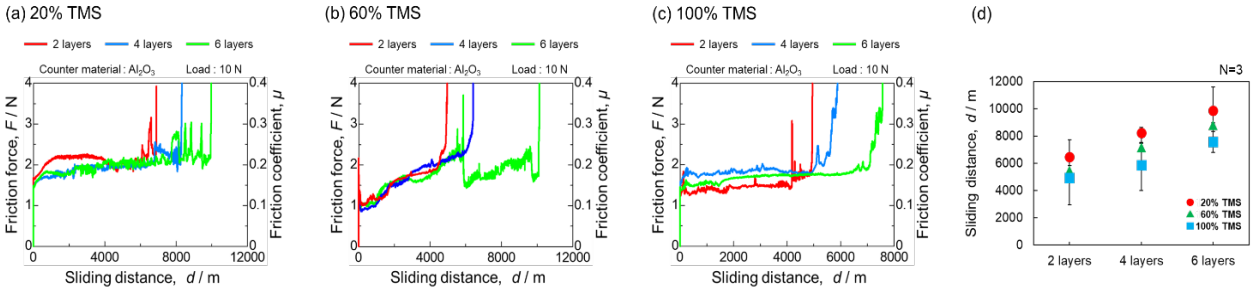

Fig. 7 (a)–(c) Friction force vs. sliding distance for Si-DLC/DLC-coated SUS304 against Al_2O_3 ball at room temperature and (d) delamination distance of each coating.

Figure 8 shows Rockwell indentation results, with all films displaying good adhesion (HF2 or better). Only the 2-layer films with 20 % and 100 % TMS showed HF2; all others achieved HF1. Lower adhesion at 20% TMS may result from insufficient stress relaxation due to low Si, while 100 % TMS may reduce hardness and wear resistance. Fewer interfaces in 2-layer structures likely limited stress dissipation. In contrast, multilayer structures improved adhesion by increasing interfaces and energy dissipation [18, 19]. These findings emphasize the need to optimize both TMS ratio and layer number for better adhesion.

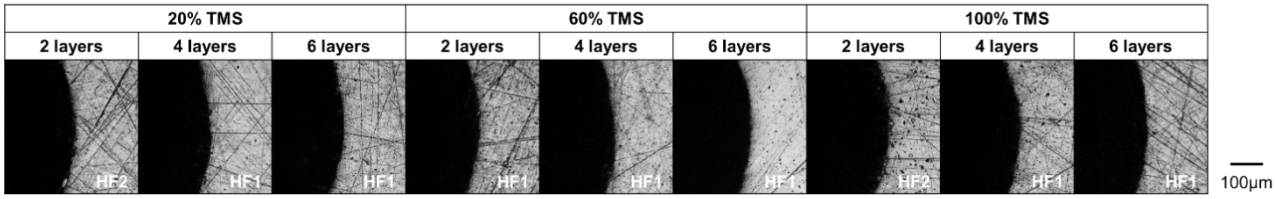

Fig. 8 Rockwell indentation of various Si-DLC / DLC multilayer coated SUS304.

Conclusions

This study investigated multilayer films of Si-DLC and DLC deposited using TMS and C_2H_2, under nine conditions varying TMS ratio and number of layers, to assess their effects on adhesion and mechanical properties. As a result, the following findings were obtained:

(1) Nanoindentation showed that increasing TMS ratio and number of layers reduced both hardness and Young's modulus.

(2) Under a 5 N load, wear increased with more layers and higher TMS due to exposure of softer Si-DLC. Under 10 N, multilayers improved durability by distributing stress, especially at lower TMS ratios.

(3) All samples showed good adhesion (HF2 or better). Only 2-layer films with 20 % or 100 % TMS showed HF2, likely due to limited stress relaxation or reduced hardness. Optimizing both TMS ratio and layer number is essential for improved performance.

References

[1] N. Nihira, A. Mitsuo, Surface treatment technology for beginners, Nikkan Kogyo Shimbun, (2012) 142-150.

[2] A. Nishimoto, T. Maruyama, T. Kobayashi, K. Akamatsu, Trends in surface modification technology of metallic materials, Eng. Technol., 14 (2007) 77-88.

[3] S. Aisenberg, R. Chabot, Ion-beam deposition of thin films of diamond like carbon, J. Appl. Phys., 42 (1971) 2953-2958.

[4] H. Saitoh, Handbook of DLC films, NTS, (2006) 414-417.

[5] F. Zhao, H. Li, L. Ji, Y. Wang, H. Zhou, J. Chen, Ti-DLC films with superior friction performance, Diam. Relat. Mater., 19 (2010) 342-349.

[6] H. Maruno, A. Nishimoto, Adhesion and durability of multi-interlayered diamond-like carbon films deposited on aluminum alloy, Surf. Coat. Technol., 354 (2018) 134-144.

[7] M.S. Kabir, Z. Zhou, Z. Xie, P. Munroe, Designing multilayer diamond like carbon coatings for improved mechanical properties, J. Mater. Sci. Technol., 65 (2021) 108-117.

[8] Y. Kobayashi, A. Nishimoto, Comparative investigation of the mechanical and wear properties of multilayer Si-DLC/DLC films, Mater. Trans., 62 (2021) 270-277.

[9] N. Fuyama, T. Nagaoka, K. Okada, A. Nishimoto, Improvement of surface properties of aluminum alloy-based composites by multi-layer DLC coating, Mater. Trans., 63 (2022) 1462-1468.

[10] M. Ikeyama, S. Nakao, Y. Miyagawa, K. Yoshimura, S. Miyagawa, Effects of Si content in DLC films on their friction and wear properties, Trans. Mater. Res. Soc. Jpn., 29 (2004) 635-638.

[11] R.K. Ghadai, S. Das, D. Kumar, S.C. Mondal, B.P. Swain, Correlation between structural and mechanical properties of silicon doped DLC thin films, Diam. Relat. Mater., 82 (2018) 25-32.

[12] ISO18535: Diamond-like carbon films - Determination of friction and wear characteristics of diamond-like carbon films by ball-on-disc method, (2016).

[13] P. Papakonstantinou, J.F. Zhao, P. Lemoine, E.T. McAdams, J.A. McLaughlin, The effects of Si incorporation on the electrochemical and nanomechanical properties of DLC thin films, Diam. Relat. Mater., 11 (2002) 1074-1080.

[14] S.S Camargo, R.A. Santos, A.L. Baia Neto, F.L. Freire, Jr, Jr, R. Carius, F. Finger, W. Beyer, Structural modifications and temperature stability of silicon incorporated diamond-like a-C:H films, Thin Solid Films, 332 (1998) 130-135.

[15] N. Kikuchi, E. Kusano, A. Kinbara, Plastic and elastic behavior of sputtered bilayered films by nanoindedtation, MRS Proc., 594 (1999) 513.

[16] J. Libardi, J.M.J. Ocampo, Comparative studies of the feed gas composition effects on the characteristics of DLC films deposited by magnetron sputtering, Thin Solid Films, 459 (2004) 282-285.

[17] M. Nakamura, S. Kubota, H. Suzuki, T. Haraguchi, Wear and friction characteristics of AlN/diamond-like carbon hybrid coatings on aluminum alloy, J. Mater. Eng. Perform., 24 (2015) 3789-3797.

[18] L. Ji, H. Li, F. Zhao, J. Chen, H. Zhou, Microstructure and mechanical properties of Mo/DLC nanocomposite films, Diam. Relat. Mater., 17 (2008) 1949-1954.

[19] J. Musil, P. Novák, R. Čerstvý, Z. Soukup, Tribological and mechanical properties of nanocrystalline-TiC/aC nanocomposite thin films, J. Vac. Sci. Technol. A, 28 (2010) 244-249.

Published in: Solid State Phenomena
ISSN: 1662-9779, Vol. 386, pp 93-98
doi:10.4028/p-bKn72U

Submitted: 2025-05-31
Revised: 2025-12-09
Accepted: 2025-12-19
Online: 2026-03-13

Investigation of Al-Si Coating Behavior on 22MnB5 Boron Steel During Heat Treatment

Alfred Ducháč[1,a*] and Pavel Kejzlar[1,b]

[1]Technical University of Liberec, Studentská 1402/2, 461 17 Liberec, Czechia

[a*]Alfred.duchac@tul.cz, [b]Pavel.kejzlar@tul.cz

Keywords: Al-Si, Al-Si-Fe, Fe-Al, intermetallic, iron aluminides, structure, microscopy, heat treatment, EDS, EBSD, 22MnB5.

Abstract. Steel 22MnB5 is widely used in the automotive industry for manufacturing high-strength structural car body parts. To achieve desired mechanical properties, hot-stamping is used, during which the Al-Si coating plays a critical protective role against oxidation. This study investigates the structural evolution of the Al-Si coating under various austenitization durations at 920 C. Intermetallic phase formation and coating morphology are analyzed.

Introduction

Due to the rising costs of advanced materials, there is increasing interest in using more affordable alternatives, often with surface modifications for specific applications. A typical example includes steels coated with hot-dip zinc or aluminum-silicon (Al-Si) layers, which provide protection against corrosion and high-temperature degradation. Al-Si coatings are commonly applied to high-strength martensitic steels such as 22MnB5, widely used in the automotive industry. Compared to Zn-based coatings, Al-Si offers superior barrier protection and prevents oxidation and scale formation during austenitization. When heated to approximately 900 °C, the Al-Si layer melts and intense elemental diffusion occurs between the coating and the substrate. This results in the formation of Fe-Al intermetallic phases (e.g., Fe_2Al_5, FeAl), which significantly influence the coating's morphology, mechanical behavior, and subsequent processing. While these phases improve oxidation resistance, they can also lead to internal stress, microcracking, and delamination. Understanding these phenomena requires knowledge of phase relationships in the Al-Fe-Si system and how they evolve during heat treatment. The binary Fe-Al phase diagram (Fig. 1) illustrates the formation of intermetallic phases depending on composition and temperature. During hot-dip coating (650 – 700 °C), τ5 (Al_7Fe_2Si) and $FeAl_3$ layers form. Austenitization at 900 – 950 °C enhances diffusion and leads to the formation of Fe-Al phases with higher melting points, preventing complete melting of the coating. After heat treatment, the Al-Si layer becomes heterogeneous: the surface contains Al_2O_3 and SiO_2 oxides that impair weldability, while subsurface regions show Kirkendall voids, microcracks, and brittle phases (e.g., Al_5Fe_2), which contribute to crack formation and delamination. These phenomena negatively affect processing [1–6].

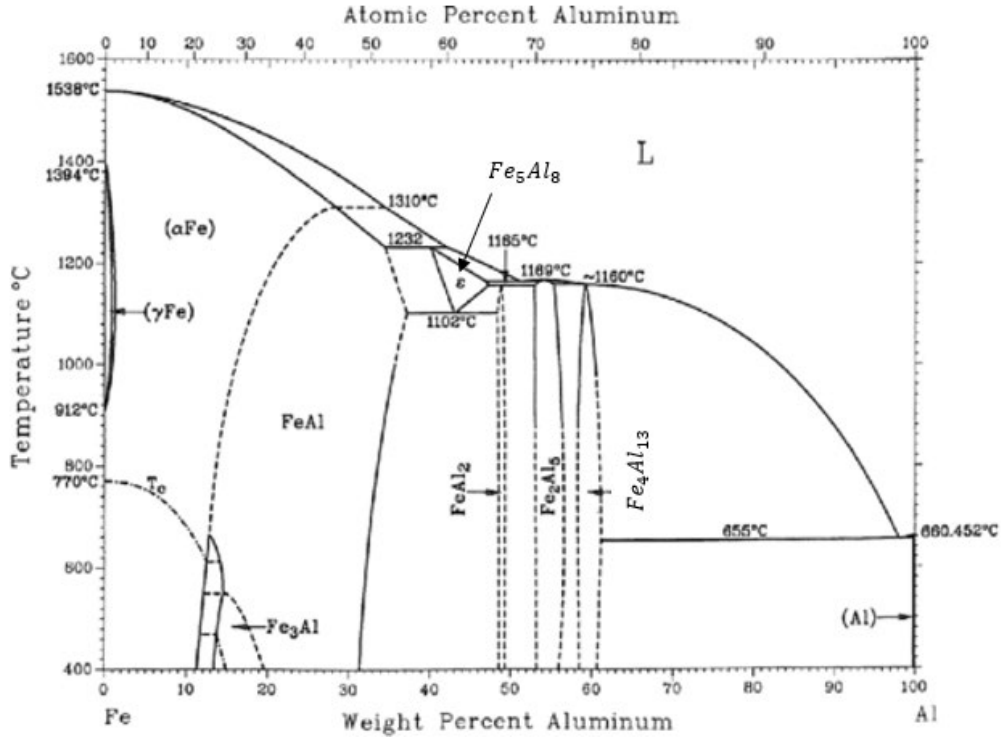

Fig. 1. Binary phase diagram Fe-Al [6].

Therefore, alloying modifications and detailed studies of intermetallic phase properties are being explored to improve coating performance.

Material and Methods

The experiments were conducted on 22MnB5 manganese-boron steel sheets (1.2 mm thick) coated with AS150Si10 (90 wt.% Al, 10 wt.% Si) [6, 7], with chemical composition conforming to DIN EN ISO 683-2 (see Table 1). The coil was sectioned into blanks, which were austenitized at 920 °C for 420, 600, and 840 s. One sample was retained in the as-received state. Final specimens were laser-cut to 18 × 25 mm (Fig. 2).

Table 1. Chemical composition of steel 22MnB5 according to DIN EN ISO 683-2.

Element	C	Si	Mn	P	S	Al	N	Cr	Ti	B	Fe
Min wt. %	0.21	0.15	1.10	-	-	-	-	0.10	0.015	0.0015	Rest
Max wt. %	0.25	0.40	1.35	0.023	0.010	0.080	0.010	0.25	0.045	0.0040	Rest

For EDS and EBSD analyses, metallographic cross-sections were prepared and finished using mechanical-chemical polishing with OP-S colloidal suspension (Struers). Elemental and crystallographic characterization was carried out using a Helios 5 PFIB FIB-SEM (ThermoFisher) equipped with Oxford Instruments detectors: EDS (Ultim Max100) and EBSD (Symmetry S3). Analyses were conducted at 20 kV and 26 nA. Light microscope images were acquired using Zeiss Axio Imager M2m.

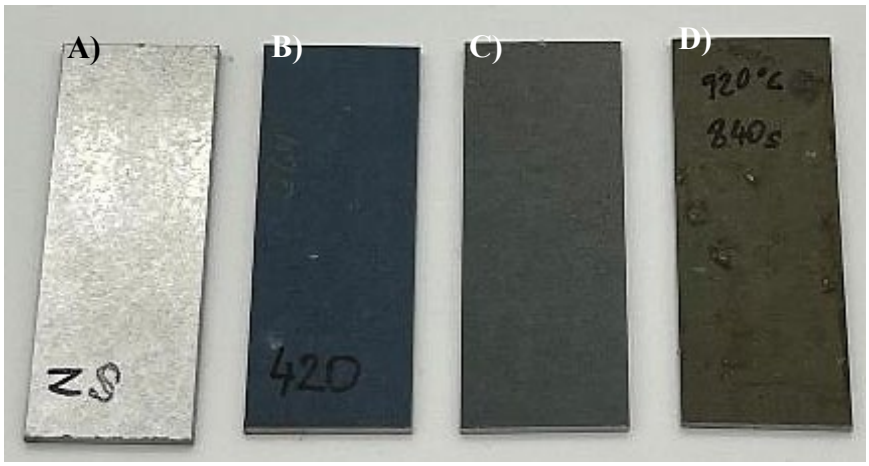

Fig. 2. Comparison of changes in the surface of the sample after heat treatment. A) Default state, B) 420 s, C) 600 s, D) 840 s.

Results and Discussion

Light microscopy revealed significant structural differences between the initial state and heat-treated samples (Fig. 3). The most pronounced morphological changes occurred between the 420 s and 600 s austenitization times, with the shorter duration resulting in a clearly defined multilayer intermetallic structure. In contrast, changes between 600 s and 840 s were less distinct.

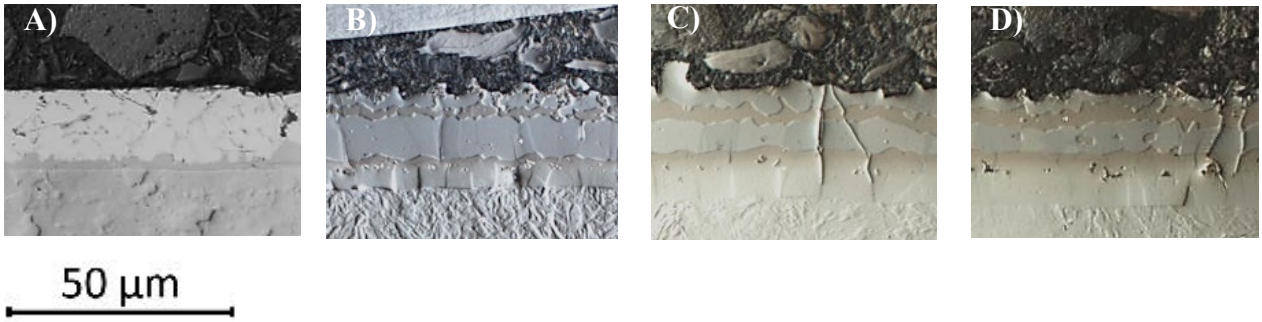

Fig. 3. Comparison of the structure of the intermetallic layer of a metallographic section using a light microscope. A) Default state, B) 420 s, C) 600 s, D) 840 s.

Heat treatment results in pronounced surface oxidation, also visible as a color change (Fig. 2). SEM analysis shows a thin, smooth oxide layer in the initial state, while longer austenitization at 920 °C produces a thicker and more complex oxide structure. EDS results (Fig. 4) confirm increased oxide content and enhanced iron diffusion into the coating with prolonged holding time.

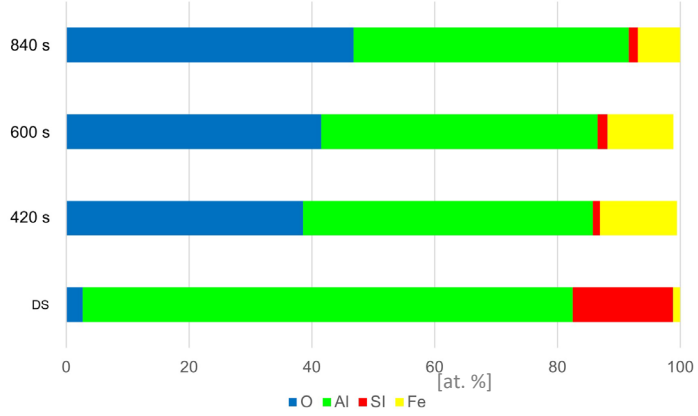

Fig. 4. EDS analysis of the chemical composition of the surface. With increasing time, surface oxidation and iron diffusion into the layer increase.

EDS maps (Fig. 5) reveal substantial changes in coating composition with increased heat treatment duration. The initial state features eutectic Si in an aluminum matrix and a thin τ5 layer. In heat-treated samples, a distinct diffusion transition zone forms between the substrate and the Al-Si coating, which broadens over time. Also a layered structure composed of FeAl and Fe_2Al_5 phases appears in the quenched samples.

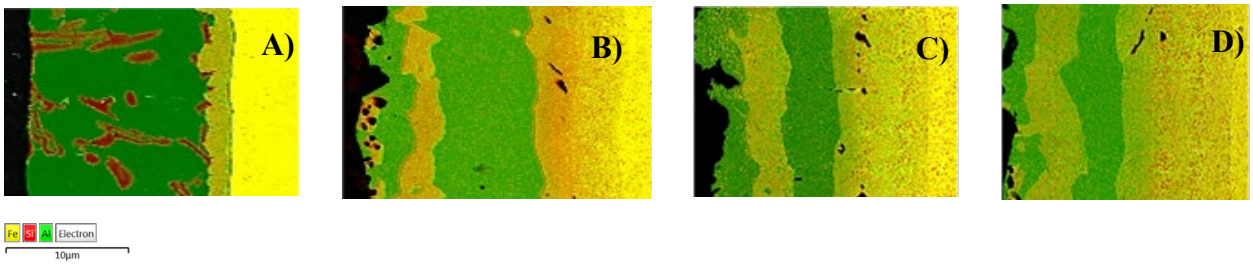

Fig. 5. Comparison of the intermetallic layer structure using EDS maps showing the distribution of selected elements such as aluminum (green), silicon (red), and iron (yellow). The comparison also shows that the thickness of the intermetallic phases varies in different positions along the y-axis. A) Default state, B) 420 s, C) 600 s, D) 840 s.

Defects such as microcracks, created during forming due to an uneven layer, were found on samples exposed to austenitisation for 420 seconds. Kirkendall pores, which are caused by different diffusion speeds of aluminium and iron, were also observed. Microcracks caused by different thermal expansion coefficients of individual intermetallic phases also occurred on the surface and below the surface of the layers. This results in the accumulation of internal stress and the formation of subsurface cracks. The spread of these cracks is stopped by ductile layers of Fe_3Al or α-Fe.

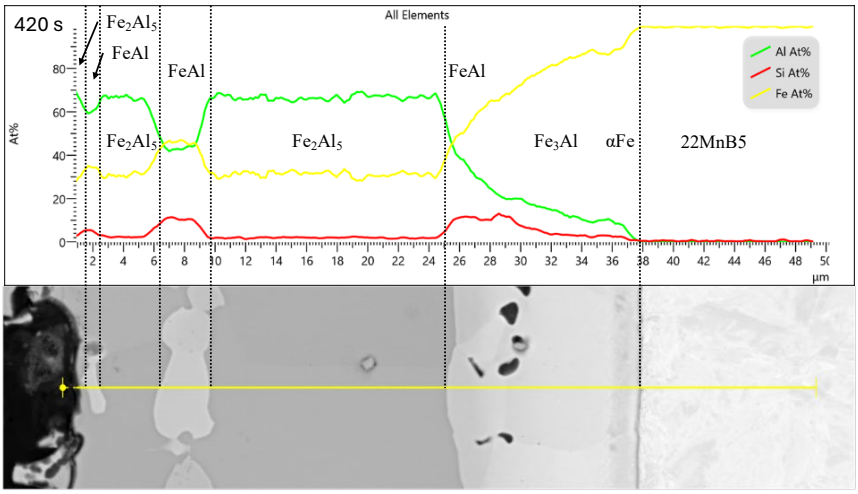

Fig. 6. EDS line analysis of chemical composition (holding time at austenitizing temperature 420 s).

Based on the chemical composition (Fig. 6) and binary diagram (Fig. 1), we can say that the phase composition of the surface layer changes from the substrate surface through α-Fe, which gradually transitions to Fe_3Al and then to FeAl, Fe_2Al_5, FeAl, Fe_2Al_5, FeAl, and in the last layer back to Fe_2Al_5. The width of the diffusion layer is 11 µm.

At an austenitizing temperature for 600 s, the phase composition of the layer is very similar to that of the 420 s layer, with differences only in the widths of the intermetallic layers and the diffusion layer. The thickness of the diffusion layer increased by 45 % (17 µm), Fe_2Al_5 decreased by 15 % (15 µm) and FeAl increased by 2.25 % (9 µm) compared to 420 s.

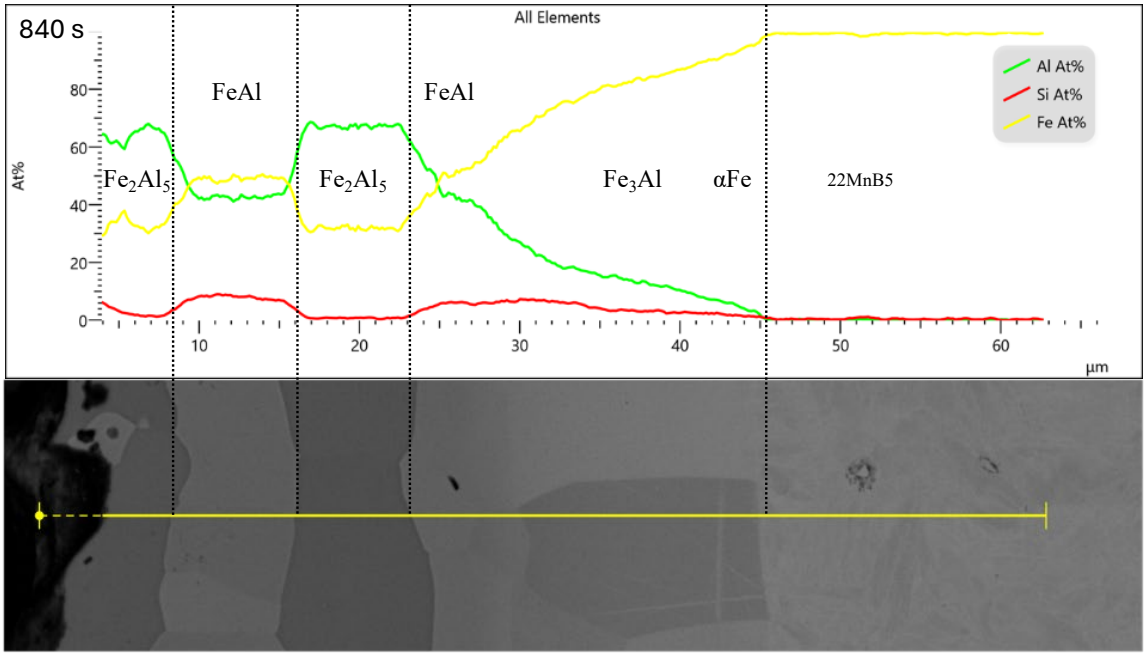

Fig. 7. EDS line analysis of chemical composition (holding time at austenitizing temperature 840 s).

According to the chemical composition diagram (Fig. 7), the composition of the phase layers is very similar to that of the layer with a holding time of 600 s, but the increase in the thickness of the diffusion layer is more noticeable here, increasing by 38 % (22 µm), which is 100 % more than at 420 s. The thicknesses of the Fe_2Al_5 and FeAl layers stabilized at 8 µm. Fe_2Al_5 decreased by 50 % (7 µm).

Samples with an austenitizing temperature for 420 s were examined by SEM-EBSD analysis to specify the phase composition. The individual phases analyzed by EBSD are shown in Fig. 8.

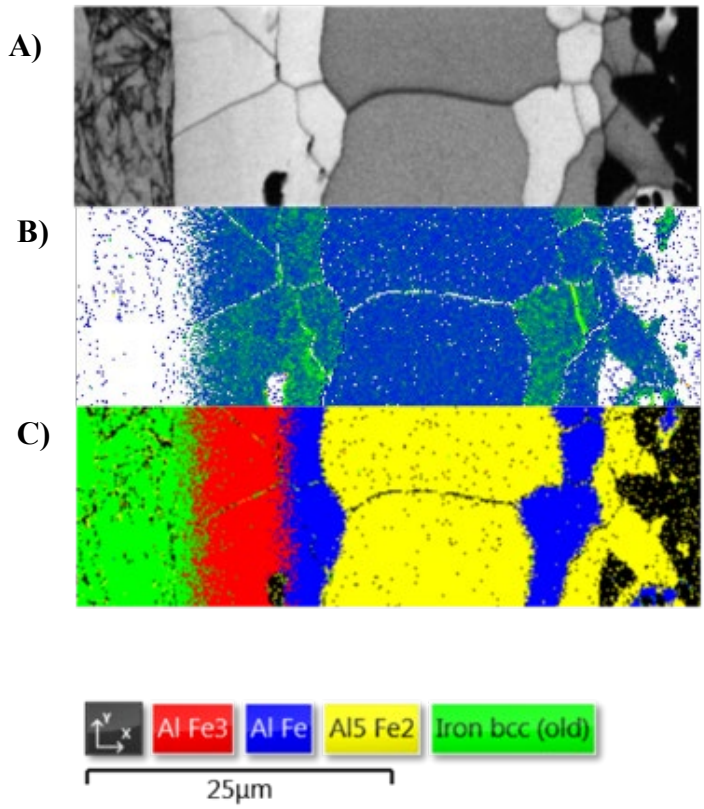

Fig. 8. Comparison of EBSD maps. A) Band contrast, B) KAM, C) Phase map.

As part of the EBSD analysis, an additional evaluation of the kernel average misorientation (KAM) was performed, see Fig. 8. The results showed an increased concentration of stress in the FeAl phase, which indicates its increased sensitivity to brittle fracture. This local increase in stress is likely to contribute to the brittle failure of the layers.

Conclusion

- Heat treatment of 22MnB5 steel with an Al-Si coating at a temperature of 920 °C leads to significant changes in the morphology and structure of the coating.
- Longer austenitization times (420 s, 600 s, 840 s) cause the formation of heterogeneous intermetallic multilayers with different physical properties. During heat treatment, significant surface oxidation occurs, the intensity of which increases with increasing holding time at the hardening temperature. This causes a significant increase in the thickness of the oxide layer, which in turn affects its structure and technological properties. Simultaneously with the increasing austenitization time, changes in the chemical composition of the surface layers and a significant expansion of the diffusion layer occur, where mainly FeAl and Fe_2Al_5 intermetallic phases are formed. The ratio of these phases changes depending on the holding time.
- In addition, EBSD analysis revealed an increased stress concentration in the FeAl phase, indicating a higher sensitivity of this phase to brittle fracture. Local stress increase is likely to be the main factor causing brittle failure and delamination of the layers.
- The results obtained by combining SEM, EDS, and EBSD methods provide a more detailed understanding of the formation, structure, and properties of intermetallic phases in Al-Si coatings. This information is essential for further research and optimization of surface layers to improve their stability and properties in subsequent technological operations.

References

[1] Huilgol, P., Bhat, S. and Bhat, K.U.: Hot-dip aluminizing of low carbon steel using Al-7Si-2Cu alloy baths, Journal of Coatings, 2013, 1 (2013) 180740.

[2] Fan, D.W., Kim, H.S., Oh, J.-K., Chin, K.-G. and De Cooman, B.C.: Coating degradation in hot press forming, ISIJ International, 50, 4 (2010) 561-568.

[3] Kolaříková, M., Chotěborský, R., Hromasová, M. and Linda, M.: The characteristics of Al-Si coating on steel 22MnB5 depending on the heat treatment, Acta Polytechnica, 59, 4 (2019) 352-358.

[4] Kučera, V., Cabibbo, M., Průša, F., Fojt, J., Petr-Soini, J., Pilvousek, T., Kolaříkova, M. and Vojtěch, D.: Phase composition of Al-Si coating from the initial state to the hot-stamped condition, Materials, 14, 5 (2021) 1125.

[5] Li, X., Scherf, A., Heilmaier, M. and Stein, F.: The Al-rich part of the Fe-Al phase diagram, Journal of Phase Equilibria and Diffusion, 37, 2 (2016) 162-173.

[6] Petr-Soini, J.: Vliv metalurgických faktorů na kvalitu svarového spoje u vysokopevných ocelových plechů s povlakem na bázi Al-Si, Fakulta strojní, Ústav materiálového inženýrství, České vysoké učení technické, 2022.

[7] Pourali, M., Abdollah-zadeh, A., Saeid, T. and Kargar, F.: Influence of welding parameters on intermetallic compounds formation in dissimilar steel/aluminum friction stir welds, Journal of Alloys and Compounds, 715 (2017) 1-8.

Published in: Solid State Phenomena
ISSN: 1662-9779, Vol. 386, pp 99-105
doi:10.4028/p-tF60oN

Submitted: 2025-05-29
Revised: 2025-12-12
Accepted: 2025-12-19
Online: 2026-03-13

Metallographic and Fractographic Analysis of Plastic Deformation of Austenitic Stainless Steel AISI 304 after Static and Dynamic Loading

Veronika Chvalníková[1,a*], Milan Uhríčik[1,b], Martin Slezák[1,c], Juraj Belan[1,d] and Tomáš Vlach[2,e]

[1]Faculty of Mechanical Engineering, Department of Materials Engineering, University of Žilina, Univerzitná 8215/1, 010 26 Žilina, Slovak Republic

[2]Faculty of Mechanical Engineering, Institute of Technology and Materials, University Jana Evangelisty Purkyňe in Ústí nad Labem, Pasteurova 3544/1, 400 96, Ústí nad Labem, Czech Republic

[a*]veronika.chvalnikova@fstroj.uniza.sk, [b]milan.uhricik@fstroj.uniza.sk, [c]martin.slezak@fstroj.uniza.sk, [d]juraj.belan@fstroj.uniza.sk, [e]tomas.vlach@ujep.cz

Keywords: Austenitic Steel, Sensitization, Microstructure, Fracture Surface, Mechanical Loading, Plastic Deformation.

Abstract. This paper presents a metallographic and fractographic study of AISI 304 austenitic stainless steel subjected to mechanical loading in the sensitized condition. Static three-point bending tests and impact tests were carried out to evaluate how sensitization affects the mechanical response and fracture behaviour of AISI 304. The study compares the initial state of the material with its condition after sensitization at 700 °C for 10 h, with emphasis on changes in plastic deformation and fracture mechanisms. Microstructural evaluation was performed using light microscopy, while Vickers microhardness measurements provided insight into local mechanical changes. Fractographic analysis using scanning electron microscopy revealed differences in fracture surface morphology. Results demonstrate a decrease in microhardness, reduced impact energy, and noticeable differences in fracture morphology following the sensitization treatment, indicating that the heat treatment influences both the mechanical response and failure behaviour of AISI 304.

Introduction

Austenitic stainless steels are widely used in chemical, automotive, energy, food-processing and aerospace industries due to their favourable combination of corrosion resistance, weldability, high ductility and stability over a wide temperature range. Their corrosion resistance is governed mainly by chromium, which forms a passive oxide layer on the surface, while nickel promotes the formation and stability of the austenitic phase. Additional alloying elements such as molybdenum, niobium and titanium further improve resistance to localized corrosion or stabilize the microstructure against sensitization [1–4].

Molybdenum is added to austenitic steels to improve resistance to pitting. Niobium is added to cast and formed austenitic steels as a stabilizer to reduce the risk of intergranular corrosion. Basic austenitic steels such as AISI 304, 316 and 347 are widely used for power plant components. Recently developed super austenitic stainless steels can contain up to six percent molybdenum. The term 'super austenitic' refers to austenitic stainless steels containing high levels of chromium, nickel, molybdenum and nitrogen, with an iron content of around fifty per cent [3–6].

The chromium content of alloys is important in ensuring the corrosion resistance of steels, as it forms a passive protective layer on the surface. Nickel is an important austenite forming element. At the same time, Cr-Ni and Ni-Mo steels are the most widely used group of stainless steels. The steels are stabilized with niobium, titanium, etc. In order to maintain a stable austenitic structure, the balance between the contents of the different elements is important. With a carbon content ranging from 0.1 % to 0.12 % and a chromium content of 18 %, 9 % nickel is sufficient. By increasing the amount of

molybdenum and other ferrite-forming elements such as silicon, niobium and titanium, an increase in austenite-forming elements is also required. Molybdenum increases the strength and corrosion resistance of steels. Increasing nickel content is also important in reducing the amount of carbon in alloys. Silicon is also an important element in steels and its effects at high temperatures limit melt carburization and oxidation. The group of austenitic stainless steels also includes Cr-Mn steels, which have lower corrosion resistance. They are therefore not used in aggressive and highly corrosive equipment [7–9].

To evaluate mechanical changes associated with sensitization, the present work focuses on microstructural alterations, microhardness, static bending behaviour and impact energy absorption.

Experimental Material

The test material was AISI 304 austenitic stainless steel supplied by Novel s.r.o. in the form of three-meter-long rods with a cross-section of 10x10 mm. For experiments, specimens were cut to the required length of 55 mm, machined with V-notches with an angle of 45° and a depth of 2 mm. The chemical composition of AISI 304 is shown in Table 1.

Table 1 Chemical composition of austenitic steel [wt. %].

	C	Mn	Si	Cr	Ni	Mo	S	P	Fe
AISI 304	0.03	1.44	0.32	18.87	7.80	0.24	0.05	0.02	balance

Sensitization was chosen to determine the susceptibility of the steel to intergranular corrosion. This heat treatment was carried out at 700 °C with a holding time at this temperature of 10 hours, followed by cooling in the furnace until complete cooling.

Microhardness was measured on metallographically prepared surfaces using a Zwick/Roell ZHVμ tester, by the Vickers method. A diamond four-sided needle with a tip angle of 136° was driven into specimens with a load of 0.5 kp and a loading time of 10 seconds. Indentations were placed along a line perpendicular to the longitudinal specimen axis.

Specimens were subjected to static three-point bending tests and impact (Charpy) tests. At the end of tests, specimens were observed under a scanning electron microscope, where fractographic evaluations of the fracture surfaces were made after tests. The observed fracture surfaces were analyzed in terms of the propagation of plastic zones.

Results and Discussion

In the sensitized condition, the microstructure shows a visibly increased contrast along grain boundaries compared to the initial state (Fig. 1a, b). Such boundary decoration is consistent with the formation of chromium-rich precipitates reported in the literature during sensitization of AISI 304. However, in this study no EDS or TEM analysis was performed, and therefore the presence of chromium carbides cannot be conclusively confirmed. The micrographs indicate only that the grain boundaries exhibit altered etching response after heat treatment, suggesting microstructural changes associated with sensitization.

After sensitization, electrolytic etching according to ASTM A262 Practice A (Fig. 1c) revealed grooves and discontinuities along grain boundaries, which qualitatively indicate sensitization-related chromium depletion [10, 11].

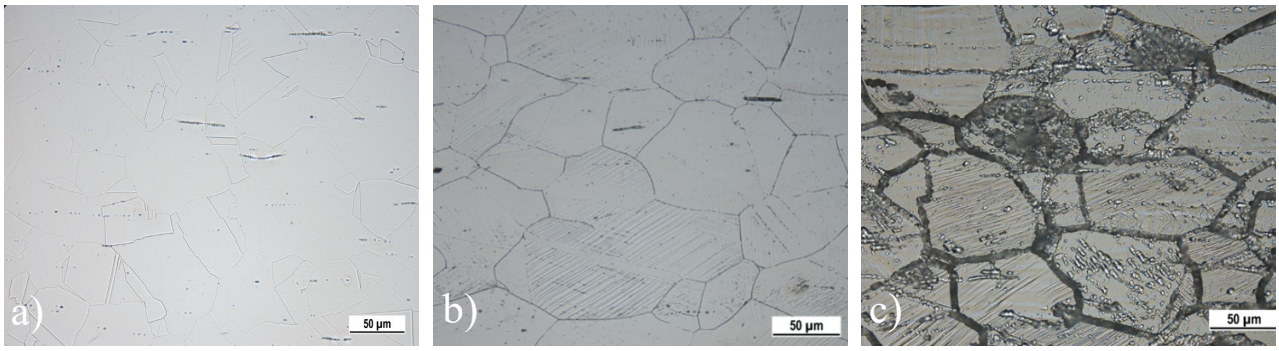

Fig. 1 Microstructure of 304 austenitic steel, a) in the initial state, b) after sensitization, etch. G+HF+HNO_3, c) after sensitization, etch. 10 % oxalic acid.

The average microhardness value of the 304 test material in the initial state (Fig. 2) is not uniform along the length of the measured area, where the lowest microhardness value recorded was 251 HV 0.5 and the highest measured value was 337 HV 0.5. From the microhardness curve of the austenitic steel 304 after sensitization (Fig. 3) that the curve indicates lower values than the initial state and is not uniform along the length of the measured area, where the minimum measured microhardness value was 212 HV 0.5 and the maximum measured microhardness value was 262 HV 0.5.

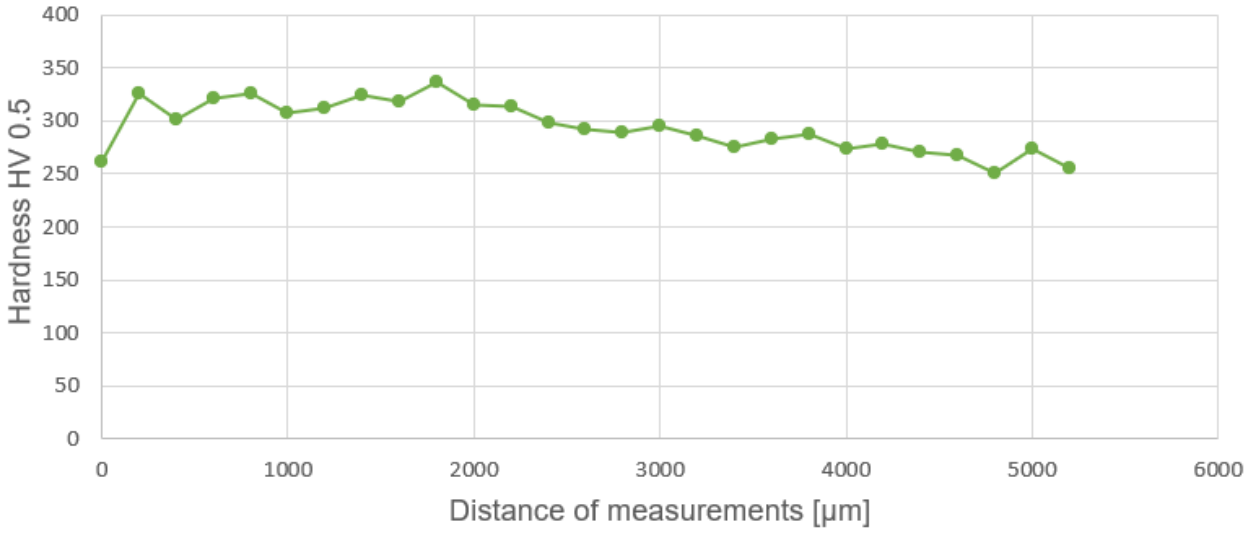

Fig. 2 Microhardness profile of 304 austenitic steel in the initial state.

The microhardness measurements of the sensitized material exhibit a smaller scatter compared to the initial state. This variation is consistent with the known microstructural heterogeneity that develops during sensitization. Although indentations located near grain boundaries depleted with precipitates could contribute to such scatter, this was not directly verified in the present study, as no post-indentation metallographic examination was performed. Therefore, the interpretation is limited to the observation that sensitization decreases hardness and also decreases measurement variability, which is commonly reported for AISI 304 after heat treatment [12, 13].

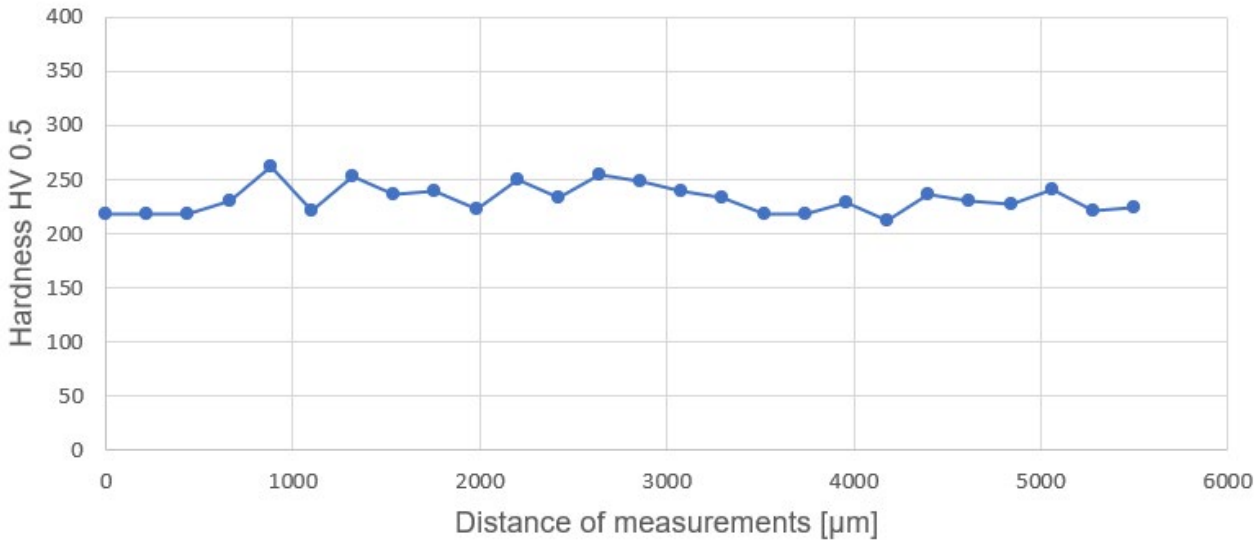

Fig. 3 Microhardness profile of AISI 304 austenitic steel after sensitization.

Before the bending impact test, the specimen surfaces were metallographically prepared and imaged with a scanning electron microscope. Then, an impact (Charpy) tests was performed and these surfaces and the fractures themselves were observed after the test (Fig. 4a). The average absorbed energy of the sensitized samples is 163.3 J.

After the bending impact test, a plastic region near the notch close to the crack was identified in the fractured specimens. Deformation-induced slip features and line-like contrast appear within the grains, consistent with localized plastic deformation. Plastically deformed annealing twins were also clearly observed, which contained distinct thicker slip bands (Fig. 4b).

Fractographic analysis allowed to determine the nature of the fracture and to assess the ductility of the material. The fracture surface exhibited a predominantly ductile morphology characterized by shallow dimples formed by microvoid coalescence (Fig. 4c). Several inclusions, likely oxide or sulphide particles, were observed at the base of some dimples. No brittle cleavage features were detected [14, 15].

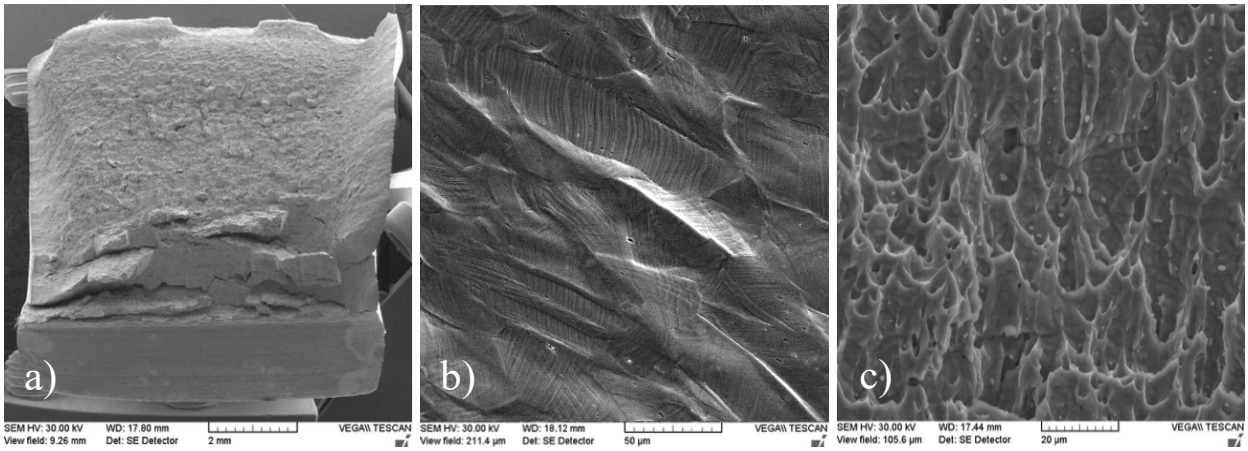

Fig. 4 Fracture surface after bending impact test, a) fracture surface, b) deformation-induced slips, c) shallow dimples.

The static three-point bending test allows observing the development and propagation of deformation processes under the notch of the specimen by a slow process of increasing the loading force. In this way, it was possible to evaluate the manifestation of plastic deformation on the surface of the specimen material (Fig. 5a). Before the static three-point bending test, the surfaces of the

specimens were metallographically prepared after sensitization, especially around the notch, in order to better observe the surface changes after loading. The maximum static loading force was 32 800 N, at which a crack appeared under the root of the notch and the loading deformed the grains in different crystallographic directions. The plastic deformation was manifested by deformation-induced slip features and line-like contrast appear within the grains, consistent with localized plastic deformation. (Fig. 5b).

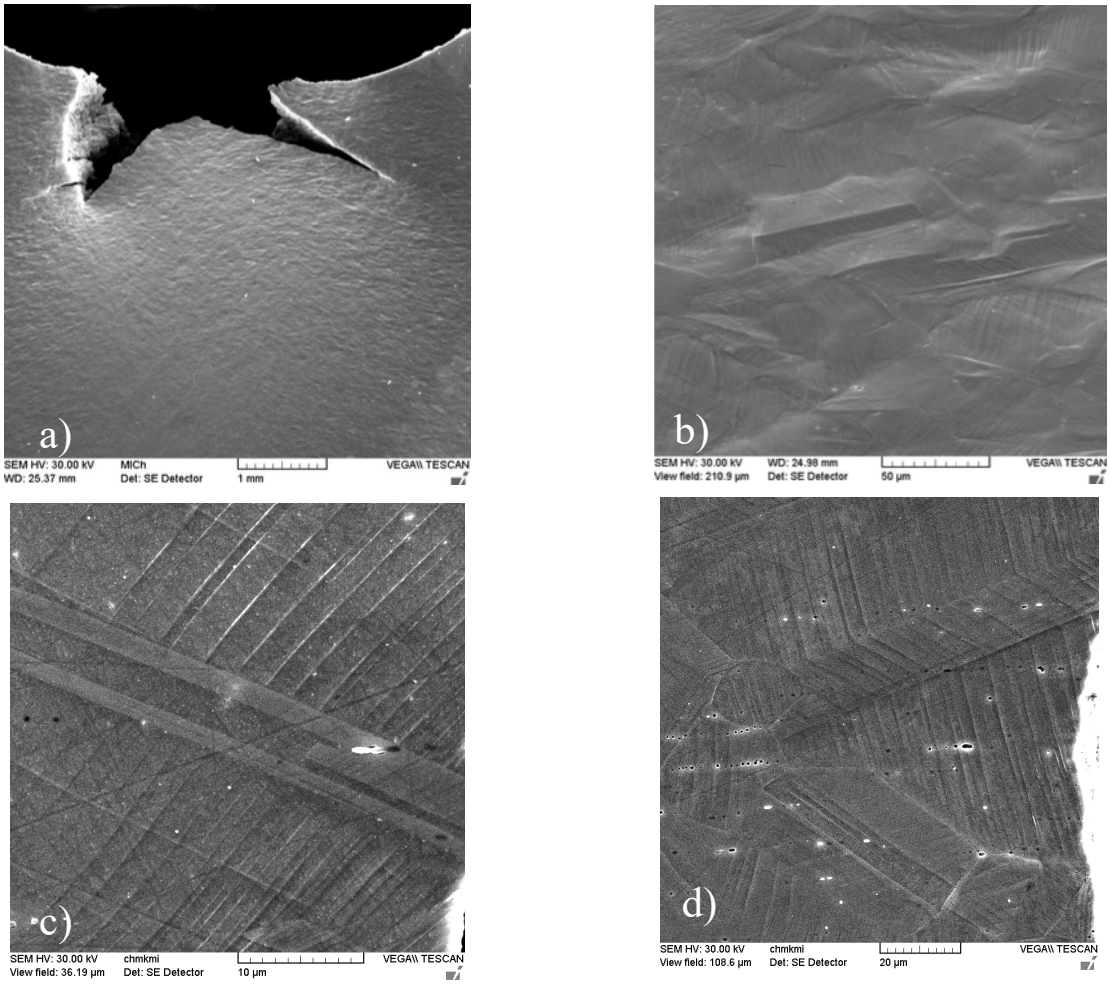

Fig. 5 AISI 304 after sensitization, a) crack formed during static test, b) detail of plastically deformed grains, c) interruption of the plastic deformation process in the grain by annealing twinning, d) annealing twinning with ongoing plastic deformation at the edge of a propagating crack

The length and width of these slip bands gradually increase and widen. The slip lines have different distances and orientations from each other, but sometimes they are almost parallel as documented in Fig. 5c [16]. In some cases, such as at the edge of a crack that has grown and spread, there is a gradual increase in plastic deformation even through annealing twins as seen in Fig. 5d. In materials with low energy stacking faults, dislocations find almost no obstacles and planar transverse crossing prevails in many slip planes close to each other [16].

Conclusion

The research consisted of obtaining and processing data on the chemical analysis of the tested material, microstructure, microhardness and static and dynamic testing. The fracture surfaces after tests were also evaluated.

- The austenitic steel 304, after sensitization and subsequent cooling in the furnace, has a microstructure formed by polyhedral austenite grains of various sizes, with annealing twins and also deformable martensite. At the grain boundaries by segregation, there were a visibly increased contrast along grain boundaries. A definitive confirmation of grain-boundary carbide precipitation would require compositional or diffraction-based techniques such as EDS, TEM, or EBSD phase mapping, which were beyond the scope of the present work.
- From the microhardness history of austenitic steel 304 after sensitization, the minimum measured microhardness value was 212 HV 0.5 and the maximum measured microhardness value was 262 HV0.5.
- All test specimens after the impact test in bending had a ductile fracture with shallow dimples, with an average absorbed energy of 163.3 J.
- The static test was able to evaluate the manifestation of plastic deformation on the surface of the specimen material. The maximum static loading force was 32800 N, because at this force a crack was formed on the notch. The specimen showed a deformation surface on which deformed grains could be observed.
- For comparison, the reference measurements for the initial (non-sensitized) state were: average absorbed energy of 123.3 J and maximum static loading force of 35 000 N.

Acknowledgements

The research was supported by the Scientific Grant Agency of the Ministry of Education of the Slovak Republic and the Slovak Academy of Sciences, No. 004ŽU-4/2023, No. 009ŽU-4/2023, No. 016ŽU-4/2023, No. 1/0461/24, APVV-20-0427 and by the Project for the Support of Young Scientists at UNIZA, Project ID 20422.

References

[1] Milad, M., Zreiba, N., Elhalouani, F., Baradai, C., Journal of Materials Processing Technology, 203, 1-3 (2008) 80-85.

[2] Srinivasan, N., Metallography, Microstructure, and Analysis, 10, 2 (2021) 133-147.

[3] Tao, H., et al., Journal of Materials Engineering and Performance, 29, 7 (2020) 4515-4528.

[4] Gajjar, P.K., et al., Transactions of the Indian Institute of Metals, 75, 6 (2022) 1411-1427.

[5] Belyakov, A., Sakai, T., Miura, H., Materials Science and Engineering: A, 319-321 (2021) 867-871.

[6] Leiva-García, R., et al. Electrochimica Acta, 70 (2012) 105-111.

[7] Murr, L.E., et al. Materials Characterization, 39, 2 (1997) 575-598.

[8] Ahmedabadi, P.M., et al., Journal of Materials Engineering and Performance, 28, 11 (2019) 7036-7046.

[9] Shirzadi, A., Jackson, S., Structural alloys for Power plants. Elsevier. 2014. ISBN 978-0-85709-238-0.

[10] Gaudett, M.A., Scully, J.R., Journal of the Electrochemical Society, 140, 12 (1993) 3425-3435.

[11] Koscisová, E., et al., Research Papers Faculty of Materials Science and Technology Slovak University of Technology, 21, 341 (2014) 131-136.

[12] Schweitzer, E.W., Göken, M., International Journal of Materials Research, 95 (2004) 492-498.

[13] Slezák, M., et al., Manufacturing Technology, 23, 6 (2023) 909-916.

[14] Das, A., Materials Science and Technology, 32 (2016) 1366-1373.

[15] Bunchoo, N., et al., Engineering Failure Analysis, 141 (2022) 106672.

[16] Milella, P.P., Fatigue and corrosion in metals, Springer Science & Business Media. 2013. ISBN 9788847023352.

Published in: Solid State Phenomena
ISSN: 1662-9779, Vol. 386, pp 107-112
doi:10.4028/p-hSwSa6

Submitted: 2025-05-21
Revised: 2025-12-12
Accepted: 2025-12-19
Online: 2026-03-13

Metallographic Analysis of the Cutting Zone and Comparison with Numerical Simulation

Maroš Martinkovič[1,a*], Martin Necpal[1,b], Tomáš Vopát[1,c] and Mária Dománková[2,d]

[1]Institute of Production Technologies, Faculty of Material science and Technology in Trnava, Slovak University of Technology in Bratislava, Trnava Slovakia

[2]Institute of Materials, Faculty of Material science and Technology in Trnava, Slovak University of Technology in Bratislava, Trnava Slovakia

[a*]maros.martinkovic@stuba.sk, [b]martin.necpal@stuba.sk, [c]tomas.vopat@stuba.sk, [d]maria.domankova@stuba.sk

Keywords: Turning, Cutting Zone, Metallography Analysis, Numerical Simulation.

Abstract. In the paper the detailed structural changes in the cutting zone were determined using metallography. Accurate determination of parameters such as shear angle, slip angle, chip thickness, cutting ratio, chip separation point, etc. required metallographic analysis on a relatively complex sampling of the cutting area. We performed the analysis on an orthogonal cutting. We achieved orthogonal cutting by turning a thin-walled Inconel 718 and C45 alloy tubes and setting the lath bit cutting edge perpendicular to the tube axis. In real state, the shapes in the cutting zone are more complicated therefore the chip thickness was determined using quantitative metallography from the equality of areas and the resulting point of transition between the chip and the machined surface. The shear angle starts from this point and is a tangent to the cutting edge, the direction of which was determined using the Thales circle. The distance between this point and the machined surface which represents a layer which is not separated from the machined material but is planar deformed was determined too. The depth of the deformed layer and the value of deformation on the machined surface was determined by quantitative metallography. A much simpler numerical simulation was performed with the same parameters using Deform 2D/3D software package. Numerical simulation could not fully replace metallographic analysis, but to some extent numerical simulation can be used instead of metallographic analysis.

Introduction

Structural changes in the cutting zone during turning are significantly influenced by the technological conditions of the machining process. A detailed understanding of these changes – particularly in terms of chip formation and material flow – is essential and can be achieved through metallographic analysis. Accurate determination of key parameters such as the shear angle, slip angle, chip thickness, and cutting ratio typically requires sectioning and analysis of specimens obtained through interrupted cutting, a procedure that is both complex and time-consuming. Under ideal conditions, the cutting zone exhibits a smooth, continuous chip, a sharp tool edge, and a clearly defined transition between the chip and the machined surface, as illustrated in Fig. 1. In such cases, fundamental parameters like chip thickness and shear angle can be determined relatively easily and used to calculate key process characteristics. However, under real-world machining conditions, the geometry of the cutting zone is considerably more complex [1], as shown in Fig. 2. In these cases, parameter determination often requires the application of specialized algorithms [2], or the development of new methods tailored to the specific cutting scenario. Numerical simulation offers a more accessible and time-efficient alternative for studying cutting phenomena [3]. Nevertheless, the reliability of simulation outcomes depends critically on validation against experimental data. Only when a simulation model has been verified through experimental comparison can it be considered a valid substitute for metallographic analysis.

Metal cutting, when analyzed as a plastic deformation process, is characterized by highly localized and asymmetric material flow occurring at extremely large strains and exceptionally high strain rates. Within the cutting zone, three distinct regions of intensive plastic deformation can be identified. The tertiary deformation zone, found at the contact area between the tool flank and the freshly machined surface. The Saltykov stereological method, using oriented test lines, enables quantification of grain boundary orientation [4], thus allowing indirect measurement of plastic deformation [5].

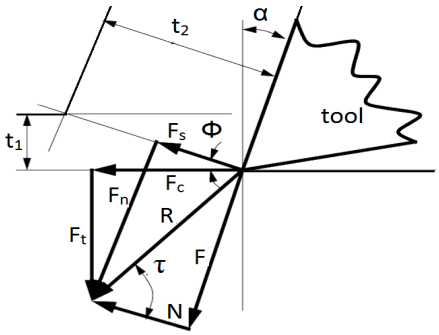

Fig. 1 Cutting zone ideal state and its geometry.

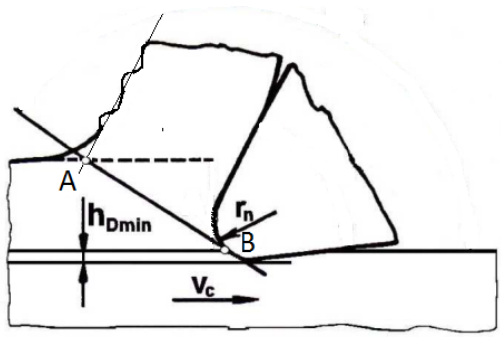

Fig. 2 Cutting zone real state.

Experimental Procedures and Results

The experimental investigation was conducted on CK45 (1.0503) carbon steel, a medium-carbon alloy commonly employed as a reference material in machining studies due to its well-characterized behavior under cutting conditions. The cutting analysis was performed under orthogonal cutting conditions, which simplify the mechanics of the process and allow more direct interpretation of deformation and chip formation. The tool used for turning was a clamped carbide insert, specifically the SECO DNMG150608-M3, TP3500 grade, known for its stability in finishing operations and reliable performance in steel machining. The process was carried out using standard cutting parameters: cutting speed v_c = 175 m.min^{-1}, feed f = 0.1mm, rake angle α = -1°, clearance angle γ = 6°, cutting edge radius r_n = 19 µm. To obtain metallographic specimens from the cutting zone, the internal stress method was applied. This approach involves the interruption of the cutting process at a precise moment, allowing for preservation and extraction of the deformed zone for subsequent microstructural analysis. This technique ensures minimal disruption to the material state during sampling, preserving the geometry and microstructure of the chip–tool–workpiece interface.

Following the cutting tests, the obtained chip specimens were preserved together with the machined surface for further analysis. Microstructural evaluation was performed on transverse sections through the cutting zone using metallographic cross-sections, allowing for detailed observation of chip morphology, deformation zones, and the interface between the chip and workpiece. To determine the chip thickness (t_2), a quantitative metallographic method was employed. This approach is based on the principle of area equivalence between the cut chip cross-section and a rectangle of known width and unknown thickness. By equating the area of the deformed chip to that of a rectangle with a width equal to the cutting feed, the chip thickness can be precisely estimated. This method, introduced here, represents a novel approach to measuring chip thickness from microstructural data (Fig. 3). A critical geometric feature – the point of transition between the chip and the machined surface – was denoted as point A. To determine the shear plane angle (Φ), a tangent was constructed from point B, lying on the cutting edge radius, such that it passes through point A. This tangent is geometrically defined as a tangent to the cutting edge radius, forming the shear plane. To achieve this, a Thales circle was constructed over the diameter connecting point A and the center of the cutting edge radius, enabling a precise graphical determination of the shear angle. This geometrical construction also represents a new method developed in the present study. The vertical distance from point B to the machined surface, denoted as h_d, corresponds to a material layer that is not removed as chip but instead experiences planar plastic deformation. This layer, referred to as t_1, represents the beginning of the tertiary deformation zone, as seen in Fig. 5. In addition to the shear

angle, the slip plane angle (Φ_1) was measured directly from the microstructure, yielding a value of 45.5° (Fig. 4). Unlike the shear angle, this value is easier to measure due to the distinct orientation of grain elongation. The difference between the slip angle and shear angle provides a useful indicator of material plasticity – ranging from zero in fully ductile materials to approximately 30° in brittle ones. All experimentally determined parameters are summarized in Fig. 4 – shear plane angle $\Phi = 27.5°$, $t_1 = 90$ µm, $t_2 = 140$ µm, $h_d = 7$ µm, tertiary deformed layer 10 µm, plastic deformation in tertiary area $\varepsilon = 0.44$.

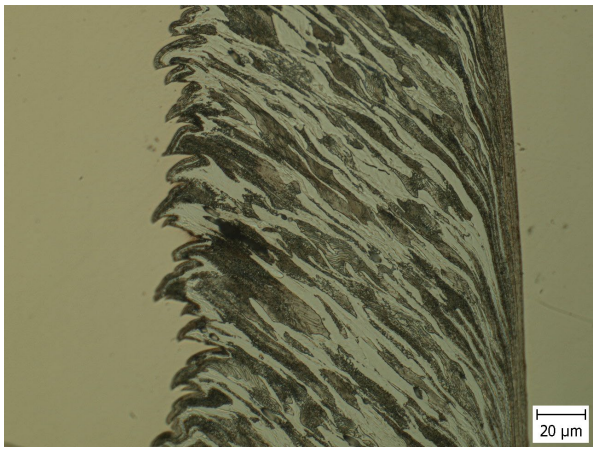

Fig. 3 Cut of chip.

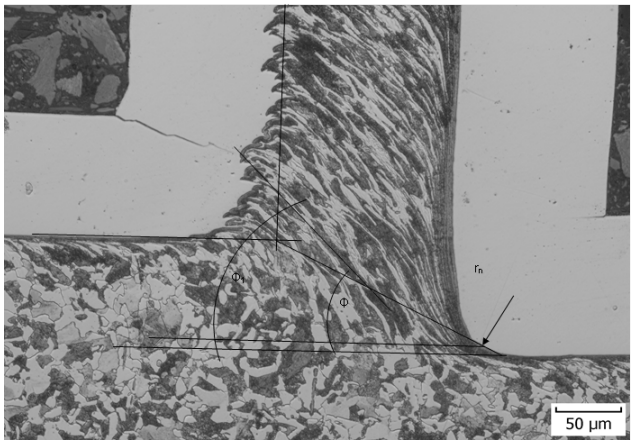

Fig. 4 Cutting zone parameters.

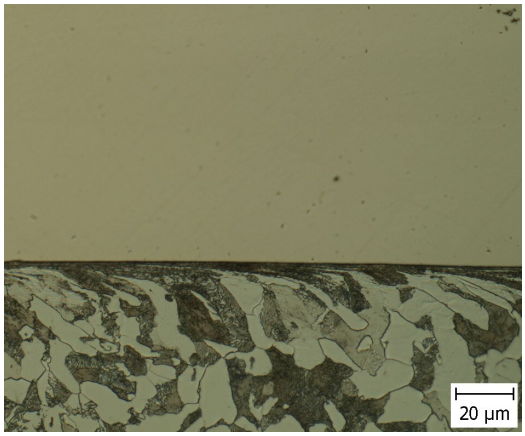

Fig. 5 Machined surface.

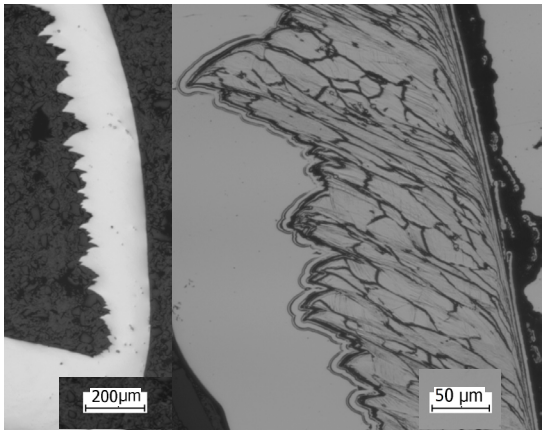

Fig. 6 Chip of Inconel 718.

The second workpiece was the bulk from Inconel 718. We performed the analysis on an orthogonal cutting. CNMG 120408 SM cemented carbide cutting inserts (WC+Co10%) were used as samples in the experimental research and PCLNL 2020K12 tool holder. Standard cutting parameters were used: cutting speed $v_c = 50$ m.min^{-1}, feed $f = 0.1$ mm, rake angle $\alpha = -1°$, clearance angle $\gamma = 6°$, cutting edge radius $r_n = 19$ µm.

Internal stress method for cutting zone specimen obtaining was used as in previous case. The chip thickness t_2 was determined using quantitative metallography from Fig. 6. Slip plane angle Φ_1 was 30° (measured directly in Fig. 7).

All above mentioned parameters are in Fig. 7 – shear plane angle $\Phi = 20°$, $t_1 = 88$ µm, $t_2 = 200$ µm, $h_d = 2.5$ µm, tertiary deformed layer 10 µm, plastic deformation in tertiary area $\varepsilon = 0.23$ (Fig. 8). In this case cutting forces were measured. Kistler (Type 9257B) dynamometer was used to measure cutting force components during the turning. Geometry of cutting forces is in Fig. 1 (R – total force, F_c – cutting force F_t – tangential force, F_s – shear force, F_n – normal to shear force, τ – friction angle, F – friction force, N – normal force to friction force, Φ – shear angle, α – tool rake angle, t_1/t_2 – chip thickness undeform/deformed). Measured forces were $F_c = 412$ N, $F_t = 227$ N. Forces F and N determined according Fig. 1 were F = 220 N, N = 416 N, friction coefficient $\mu = 0.53$. To determine

all other parameters it is necessary to know the shear angle Φ, which was metallographic determined, e.g. $F_s = 310$ N. As can be seen, metallographic analysis of the cutting zone is relatively complex both during sample preparation and evaluation. Therefore, an attempt is made to replace it with a simpler numerical simulation.

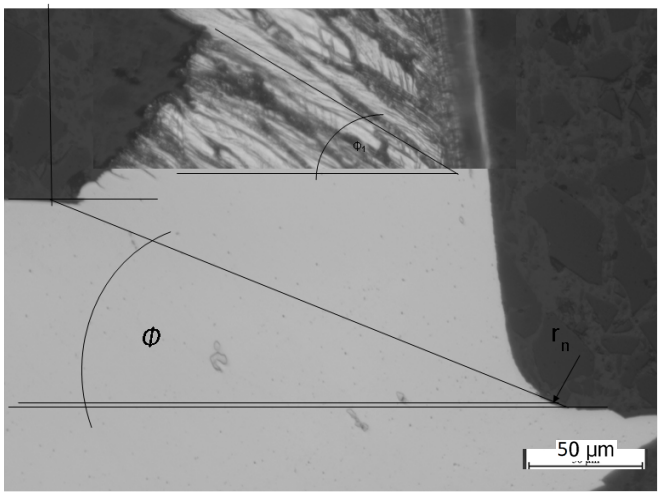

Fig. 7 Cutting zone parameters Inconel 718.

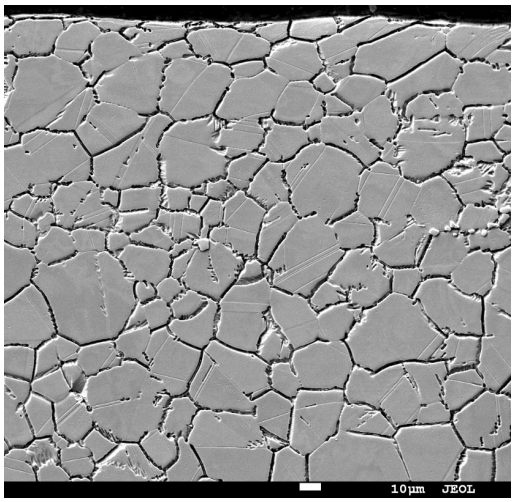

Fig. 8 Machined surface Inconel 718.

Numeric Simulation and Results

To support the experimental observations and validate the newly proposed geometrical methods for chip analysis, a finite element simulation of the orthogonal cutting process was performed using DEFORM-2D. The simulation focused on reproducing the essential features of chip formation, enabling the evaluation of the shear plane angle, chip thickness, the tertiary deformed layer, and cutting force components under conditions identical to the experimental setup.

The numerical model adopted a two-dimensional orthogonal cutting configuration, with the cutting tool positioned perpendicularly to the workpiece surface [6]. The workpiece material, CK45 carbon steel, was modeled as a plastic, thermoviscoplastic deformable body using temperature- and strain rate-dependent data from the DEFORM material database . The cutting tool was treated as a rigid object, consistent with standard modeling practice in metal cutting simulations. Tool geometry and contact conditions matched those used in the experiment. Boundary conditions and cutting parameters were defined to replicate the experimental machining process. A Lagrangian incremental approach was used, with refined meshing applied in the primary shear zone and tool–chip interface to ensure accurate resolution of deformation and temperature gradients. Thermomechanical coupling was included to account for the heat generated through plastic deformation and frictional contact. The tool–workpiece interaction was modeled using a Coulomb friction model, with friction coefficients obtained from the material database [7].

To complement the experimental investigation, a series of finite element simulations were conducted using DEFORM-2D, with the aim of replicating chip formation and quantitatively evaluating key machining parameters. These included the shear plane angle, chip thickness, tertiary deformation layer thickness, and cutting forces, all under orthogonal cutting conditions corresponding to the experimental setup.

The simulation adopted a two-dimensional orthogonal cutting configuration. The tool was positioned perpendicular to the axis of the workpiece, mirroring the experimental turning setup of thin-walled tubes. The workpiece material was modeled as a deformable viscoplastic solid, with properties drawn from the DEFORM material database. The tool was assumed rigid, and real tool geometry was applied, including rake and clearance angles, as well as cutting edge radius. Thermomechanical coupling was used throughout, incorporating plastic deformation heating and frictional sliding, based on database-defined contact properties.

The first simulation used C45 (1.0503) carbon steel as the workpiece material, corresponding to the material used in the physical experiment. A standard Lagrangian time-incremental formulation was used, with refined meshing in the cutting zone to capture the steep gradients in strain and temperature. The simulation successfully replicated continuous chip formation, as shown in Fig 9.

The simulated chip geometry and deformation fields were used to extract cutting parameters. The shear plane angle was found to be 24.5°, which is close to the experimentally determined value. The chip thickness at steady-state cutting was measured as 0.32 mm, consistent with the flow-based deformation behavior of ductile C45. A distinct tertiary deformation layer of 0.01 mm thickness was observed near the machined surface. The simulation also provided reliable values for the cutting force (Fc = 222 N) and passive force (Ft = 121 N), data that will be used in future validation with force measurement instrumentation.

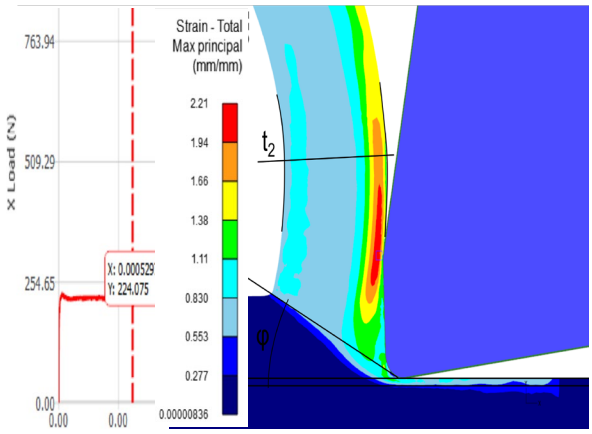

Fig. 9 Simulation results for C45 carbon steel.

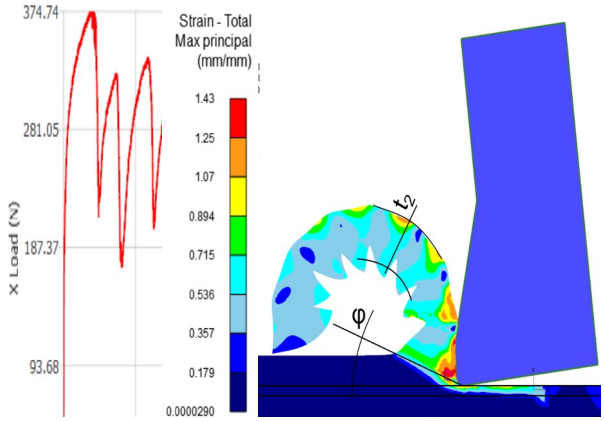

Fig. 10 Simulation results for Inconel alloy.

A second simulation was carried out for Inconel, a high-temperature nickel-based alloy known for its poor machinability. In this case, additional mesh refinement and remeshing criteria were applied to manage the high gradients in strain and to maintain mesh quality in the primary shear zone.

The simulation results for Inconel showed a markedly different deformation response compared to C45. Due to the alloy's higher strength and strain hardening rate, the shear plane angle was reduced to 21°, indicating a more compact and intense shear zone. The chip thickness was measured at 0.22 mm, reflecting stronger material resistance and lower ductility. The tertiary deformation layer was visibly thicker, measured at 0.025 mm, which is consistent with increased surface strain accumulation in difficult-to-cut materials. Notably, the cutting force increased significantly to 332.7 N, with a corresponding thrust force of 172.4 N. These values confirm the higher energy requirements and tool loading conditions when machining superalloys like Inconel. The chip formation and thermal–mechanical response are illustrated in Fig. 10.

Summary and Conclusion

Comparing the experimental and numerical simulation results clearly shows a qualitative agreement between the two analyzed materials, which implies that the numerical simulation correlates with the experimentally determined parameters, but there are quantitative differences.

The combination of experimental analysis and numerical simulation provided a comprehensive understanding of the orthogonal cutting process, including chip formation mechanisms, shear angle evolution, tertiary deformation behavior, and cutting force development. However, both approaches present distinct advantages and inherent limitations. From the experimental side, while the observations are grounded in physical reality, preparing specimens and acquiring reliable data – such as shear plane angles or tertiary deformation layers – requires extensive time, precision, and effort. Metallographic preparation, microstructural interpretation, and manual measurements introduce variability and demand significant operator expertise.

Conversely, the finite element simulation offers a fast and repeatable means of accessing internal variables like stress, strain, temperature, and force, which are often inaccessible in experiments. Nonetheless, the reliability of simulation outcomes is highly dependent on the accuracy of boundary conditions, tool–workpiece interaction definitions, and especially the material model. In the absence of well-defined material behavior under high strain rates and elevated temperatures, the simulated results may deviate significantly from physical reality. Thus, while experiments provide trustworthy validation, simulations offer efficient predictive power. The two methods are best viewed as complementary: experiments are critical for validating new modeling approaches, and simulations are essential for extending insights beyond the reach of conventional measurement techniques. Successful integration of both requires careful calibration, thorough material characterization, and clear understanding of process physics.

Numerical simulation could not fully replace metallographic analysis, but to some extent numerical simulation can be used instead of metallographic analysis for process optimization, i.e. mutual comparison of results for different machining parameters. There are several such parameters and performing experiments with their combination is practically impossible, but with numerical simulation it is relatively easy.

Acknowledgment

This work was supported by the Slovak Research and Development Agency under the contract No. APVV-21-0071.

References

[1] L. Gu, Study on white layer formation during machined surface evolutionin high-speed machining of rail steel, The International Journal of Advanced Manufacturing Technology, 125 (2023) 2503-2516.

[2] A.S. Siju, S.D. Waigaonkar, Effects of rake surface texture geometries on the performance of single-point cutting tools in hard turning of titanium alloy, Journal of Manufacturing Processes, 69 (2021) 235-252.

[3] M. Mustafa, S. Pervaiz, I. Deiab, The Effect of Rake Angle and Cutting Edge Radius on the Orthogonal Cutting, Recent Progress in Materials, 6, 2 (2024).

[4] S.A. Saltykov, Stereometric metallography, third ed., Metallurgia, Moskva, 1970.

[5] M. Martinkovic, S. Vaclav, Estimation of local plastic deformation of polycrystalline materials, Key Engineering Materials, 586 (2014) 39-42.

[6] H. Miguelez, R. Zaera, A. Rusinek, A. Moufki, A. Molinar, Numerical Modelling of Orthogonal Cutting: Influence of Cutting Conditions and Separation Criterion. Journal de Physique IV, 134 (2006) 417-422.

[7] N. Sridhar, M.S. Aezhisai Vallavi, T. Mugilan, An integrated approach of FEM analysis using DEFORM 3D and experimental investigation of forces developed in Al-Si7Mg, Materials Today: Proceedings, 80 (2023) 888-895.

CHAPTER 3:

Microstructure Evolution in Advanced Materials

Published in: Defect and Diffusion Forum
ISSN: 1662-9507, Vol. 448, pp 101-106
doi:10.4028/p-86TaGl

Submitted: 2025-05-14
Revised: 2025-12-08
Accepted: 2025-12-19
Online: 2026-03-03

Enhancement of Mechanical Properties in $Al_{0.35}CoCrFeNi$ Complex Concentrated Alloys Through Grain Size Tailoring

Kateryna Ulybkina[1,2,a*], Kateryna Kamyshnykova[1,b], Tatiana Pelachová[1,c] and Alena Klimová[1,d]

[1]Institute of Materials and Machine Mechanics, Slovak Academy of Sciences, Dúbravská cesta 9, 845 13 Bratislava, Slovak Republic

[2]Faculty of Materials Science and Technology in Trnava, Slovak University of Technology, Jána Bottu 24, Trnava, Slovak Republic

[a*]kateryna.ulybkina@savba.sk, [b]kateryna.kamyshnykova@savba.sk, [c]tatiana.pelachova@savba.sk, [d]alena.klimova@savba.sk

Keywords: Complex Concentrated Alloy, Recrystallization, Grain Growth, Activation Energy, Hall-Petch Relationship.

Abstract. This paper presents experimental results on the processing of complex concentrated alloy with a nominal composition of $A_{0.35}CoCrFeNi$. The alloy was produced by vacuum induction melting and tilt casting. The microstructure of the as-cast CCA consists of dendritic and interdendritic regions homogenized by heat treatment at 1360 °C. After rotary swaging at room temperature, the microstructure is characterized by an abundance of dislocations and continuously intersecting slip bands. Annealing experiments were carried out in the temperature range of 1150 °C – 1300 °C and different holding times to determine the parameters of grain growth kinetics. Phase and chemical analysis were investigated using XRD and EDS methods. The activation energy of recrystallization in the studied composition was 458 kJ mol^{-1}. The influence of grain size on room temperature mechanical properties and tensile properties was determined. The hardening coefficients k_h and k_σ, calculated using the Hall-Petch relation, were 277.5 HV $\mu m^{-1/2}$ and 655 MPa $\mu m^{-1/2}$, indicating the effectiveness of grain boundary hardening in the studied single-phase CCA.

Introduction

High-entropy alloys (HEAs) have attracted considerable interest since their discovery, but despite an impressive amount of research, much remains to be fully understood. Characterized by their multicomponent nature, these alloys typically consist of four or more elements forming a single-phase solid solution [1]. This unique characteristic gives HEAs exceptional mechanical properties compared to traditional alloys, such as a high strain hardening coefficient and ductility in FCC structures or excellent yield strength in BCC structures [2, 3]. However, HEAs often require additional improvement to achieve an optimal balance between strength and ductility - key properties for structural materials. This is usually accomplished by introducing various intermetallic phases into a single-phase alloy. This type of HEAs is called complex concentrated alloys (CCAs) [4].

Equimolar CoCrFeNi alloy with FCC structure exhibits excellent uniform deformation and a relatively low yield strength of 160 MPa but a high tensile strength of 718 MPa [5]. It is, therefore, an excellent basis for further precipitation hardening. Adding Al, even in small quantities, can significantly change this alloy's structure and mechanical properties, forming secondary phases such as B2, $L1_2$, or σ-phase [6]. For example, creating the B2 phase in the structure of CoCrFeNi HEA with the addition of 0.7 mol. % aluminum increases the yield strength (YS) and ultimate tensile strength (UTS) to 770 MPa and 1090 MPa, respectively, with an elongation of ~17 %. The release of finely dispersed $L1_2$ precipitates leads to an even more significant increase in the YS and UTS to 990 MPa and 1400 MPa, respectively, while maintaining plasticity at a level of ~13 % [7]. In addition to promoting the formation of secondary phases, the addition of aluminum also contributes to the solid solution hardening due to lattice distortion. Grain boundary strengthening is another key factor in improving the mechanical properties of HEAs/CCAs by creating grain boundaries that impede

dislocation motion [8]. Various plastic deformation techniques followed by recrystallization annealing are used to achieve a fine-grained structure [9]. Research shows that HEAs/CCAs exhibit slower grain growth and higher activation energy than conventional alloys, attributed to their compositional complexity [10].

This study aims to develop a CCA based on an Al-doped equiatomic CoCrFeNi alloy to enhance its strength while maintaining acceptable ductility. By combining rotary swaging and controlled annealing, the study seeks to optimize the relationship between grain size and mechanical properties in a single-phase $Al_{0.35}$CoCrFeNi CCA for further research to improve the alloy's strength.

Methods of Obtaining and Studying the Material

A CCA with the nominal composition $Al_{0.35}$CoCrFeNi (mol.%) was prepared using the methods of vacuum induction melting (VIM) in a graphite crucible and inclined casting into a graphite mold in an IT-KTV-20/1.5 unit (LINN High Therm GmbH). The charge was heated to a melt temperature of 1580 °C and held for 10 min to completely dissolve all components. To minimize the loss of reactive elements due to evaporation, the melting was carried out in an argon atmosphere at pressure 10 kPa. Cast ingots with a diameter of 25 mm and a length of 140 mm were subjected to solid solution annealing at a temperature of 1360 °C for 6 h in a protective dynamic argon atmosphere in a Nabertherm resistance furnace, LHT08/17, followed by stepwise rotary swaging at room temperature to a final diameter of about ~8 mm. Annealing experiments were carried out at 1150 °C, 1200 °C, 1250 °C and 1300 °C under argon atmosphere using rapid cooling. The annealing times were 3 min, 20 min, 120 min, and 480 min. After appropriate metallographic preparation of the samples, microstructural studies were carried out using scanning electron microscopy (SEM) using a JEOL 7600F microscope, and transmission electron microscopy (TEM) using a JEOL 1200 FX microscope operating at 80 kV. The chemical composition of the as-cast alloy was measured using energy dispersive spectroscopy (EDS). The morphology and grain size were measured using a computer image analyzer and SigmaScanPro software. X-ray diffraction (XRD) analysis was performed using a Bruker D8 diffractometer operating at 12 kW with a copper anode.

Hardness testing was performed using a Zwick Roell ZHμ Vickers indenter with a load of 98 N. Tensile tests were performed on cylindrical specimens with the diameter of the gauge part was 4.5 mm, and the gauge length was 22.5 mm at room temperature and a $2 \times 10^{-3} s^{-1}$ strain rate using a Zwick/Roell Z100 universal testing machine. For each alloy microstructure, two samples were used. Elongation was measured using a MAYTEC PMA-12/V7 high-temperature extensometer with ceramic sensor arms.

Discussion of the Obtained Results

Fig. 1a shows a typical as-cast microstructure, which consists of dendritic and interdendritic regions due to segregation during solidification. The chemical composition, measured by EDS, indicates an increased concentration of Ni and Al in the interdendritic region, and Cr and Fe in the dendritic region, respectively [11]. After casting, the structure's X-ray diffraction pattern shows single-phase diffraction peaks corresponding to the FCC (A1) phase (Fig. 1b).

Before swaging, homogenization annealing was performed at 1360 °C for 6 h to eliminate segregation. Fig. 1c illustrates the SEM microstructure of the alloy following plastic deformation, which enabled the accumulation of a high degree of deformation and the introduction of numerous nuclei for subsequent recrystallization. Fig. 1d shows a more detailed structure after rotary swaging, including the TEM microstructure with the corresponding diffraction pattern. The structure contains many dislocation walls formed by slip planes restricting the movement of accumulated dislocations during deformation. Due to the high degree of deformation, it is also possible to observe the formation of curved, intersecting, deformed slip bands.

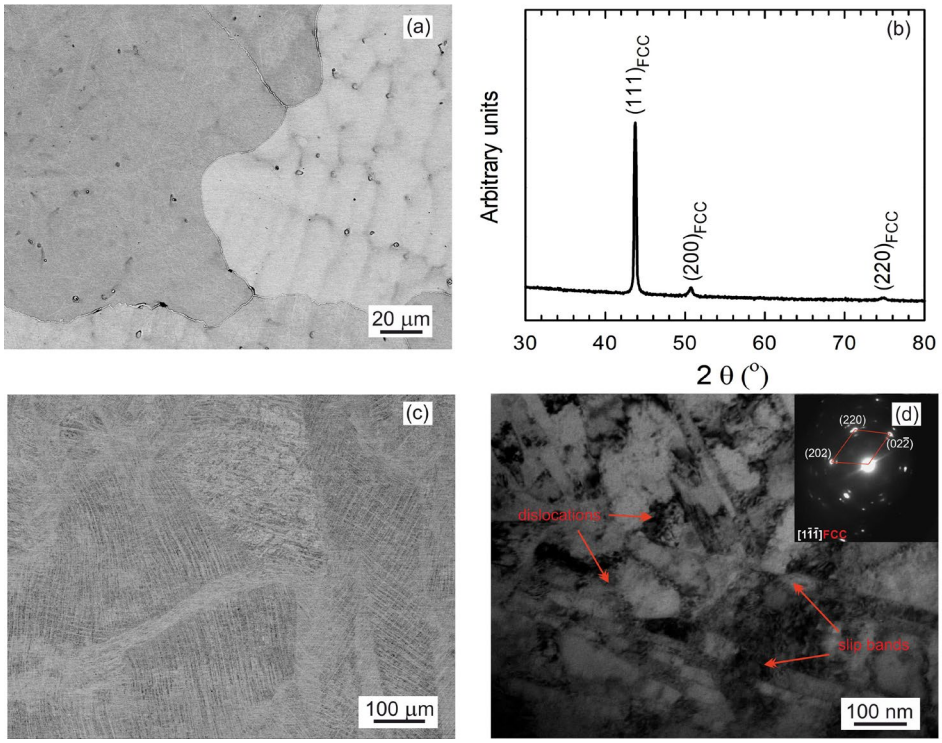

Fig. 1 The typical microstructure of the $Al_{0.35}CoCrFeNi$ CCA: (a) SEM micrograph showing detail of the as-cast dendritic microstructure of the transversal section; (b) XRD pattern of the studied as-cast alloy; (c) SEM micrograph showing detail of the swaged microstructure of the transversal section; (d) TEM bright-field images of the swaged alloy with corresponding selected-area diffraction pattern (SADP).

To study the grain growth kinetics and the effect of grain size on the mechanical properties of a single-phase solid solution, the alloy was heat-treated according to the phase diagram [12] in the temperature range of 1150 °C – 1300 °C with a step of 50 °C, with different holding times. Fig. 2 shows the structures of the alloy annealed at 1150 °C for 3 min and 480 min. As shown in Fig. 2a, after 3-minute annealing, the deformation structure disappears, and a microstructure with an average grain size of about 35 μm appears. With annealing time increasing to 480 min, the average grain size increases to 126 μm (Fig. 2b). The annealing twins are also observed in the structures (Fig. 2a and b), the formation of which is maintained by a high level of stored energy and is strongest at the beginning of recrystallization.

The grain growth kinetics were evaluated quantitatively by analyzing the grain size as a function of isothermal annealing time and described using expressions for polycrystalline materials (Eq.1) and the Arrhenius equation (Eq.2):

$$d^n - d_0^n = kt, \tag{1}$$

$$k = k_0 \, exp(-Q/RT), \tag{2}$$

where n is the grain growth index, which determines the growth mechanism; k is the kinetic constant, which determines the diffusion processes and depends on the temperature T and grain boundary energy; t is the holding time, d is the grain size; d_o is the initial grain size, k_o is the pre-exponential factor, Q is the recrystallization activation energy, and R is the universal gas constant.

The grain growth index n for this alloy was 2.9, indicating that the grain growth is controlled by diffusion only, which agrees with the results of other studies for HEAs/CCAs [13]. Determining the dependence of the kinetic constants on annealing temperatures and using Eq. 2 allowed us to determine the recrystallization activation energy for the studied CCA, which was 458.65 $kJ.mol^{-1}$ [11]. Similar activation energy values were obtained for the CoCrFeNi alloy doped with 0.3 mol.%

and 0.2 mol.% aluminum [14]. At the same time, the activation energy of the single-phase CoCrFeNi alloy is 221 kJ.mol^{-1} [15]. Such high activation energy values are most likely due to alloying with aluminum, which introduces even more significant lattice distortion due to its larger atomic radius.

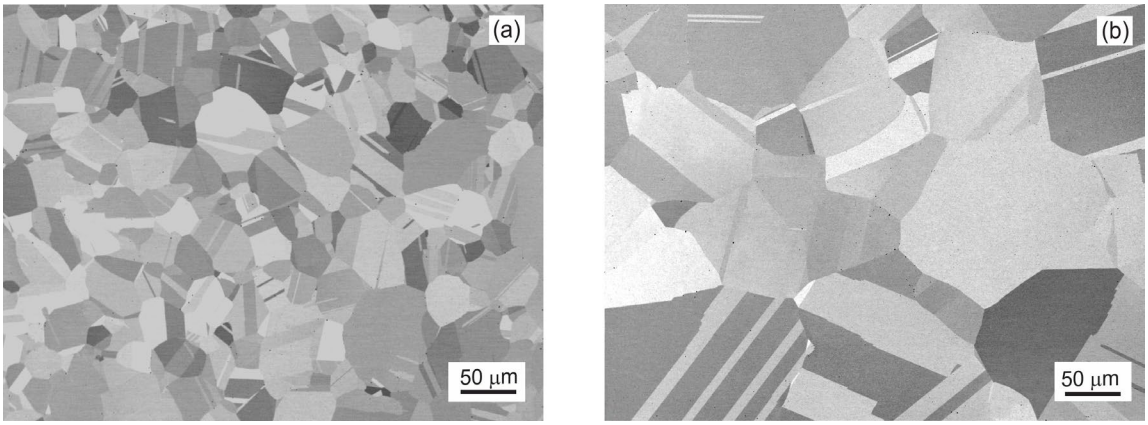

Fig. 2 SEM micrographs of $Al_{0.35}CoCrFeNi$ CCA annealed at 1150 °C for various times: (a) 3 min, (b) 480 min.

The measured hardness of the studied $Al_{0.35}CoCrFeNi$ alloy after casting was (140 ± 0.5) HV [12]. Plastic deformation at room temperature led to an increase in hardness to (260 ± 0.5) HV. Further annealing of the quenched material at 1150 °C for 3 min reduced the hardness values to the initial value due to recovery and recrystallization processes. The increase in average grain size explains the insignificant decrease in hardness with an increase in annealing time to 480 min. The Hall-Petch relationship was used to describe the dependence of hardness on the average grain size, which allows one to determine the efficiency of grain boundaries in strengthening the alloy (Eq.3):

$$H = H_0 + k_h d^{-1/2}. \quad (3)$$

The values of intrinsic hardness H_0 and Hall-Petch hardening coefficient k_h for the studied CCA with single-phase FCC structure were estimated as 99.13 HV and 277.5 HVµm$^{-1/2}$, respectively. Compared with the results of previously published studies for similar aluminum-alloyed alloys, minor discrepancies in the values were observed [16, 17], which may be due to the difference in the pre-treatment stages. For the single-phase alloy, the k_h parameter was 165 HVµm$^{-1/2}$ [18], which is more than one and a half times lower than the value obtained in this study, demonstrating the effectiveness of aluminum alloying for strengthening the alloy.

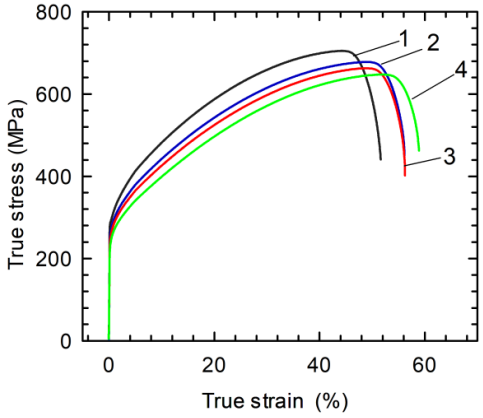

Fig. 3 Compressive true stress–true strain curves for annealed specimens at 1150°C: 1 – 3 min, 2 – 20 min, 3 – 120 min, 4 – 480 min.

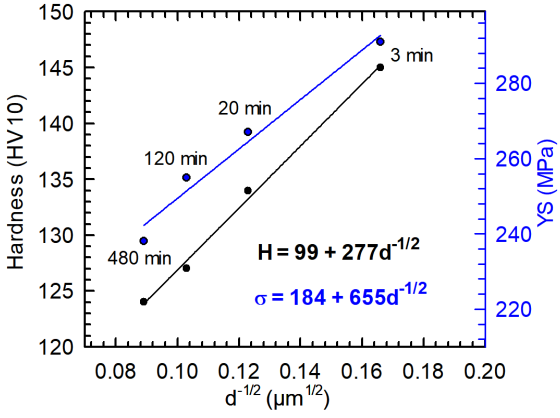

Fig. 4 Hall-Petch relationship (hardness and yield strength as a function of grain size) for annealed CCA at 1150 °C for different times.

Typical engineering stress-strain curves of the studied single-phase $Al_{0.35}CoCrFeNi$ CCA are shown in Fig. 3. To investigate the effect of grain size on the strength and relative elongation of the alloy with a single-phase FCC structure, tensile tests were conducted at room temperature on annealed samples with varying holding times. The obtained data for all four alloys are in agreement with the measured hardness. According to the results, high values of relative elongation before failure indicate that the obtained FCC single-phase alloy has a good strain-hardening ability. Additionally, it is observed that with a decrease in annealing time, the relative elongation decreases slightly. Despite this, the alloy still demonstrates more than 50 % high ductility. Conversely, the tensile strength and yield strength values increase with decreasing annealing time, reaching 705 MPa and 291 MPa, respectively. As in the case of hardness, the tensile yield strength can also be expressed using the Hall-Petch relationship (Eq.4). In this case, the equation takes the form:

$$\sigma = \sigma_0 + k_\sigma d^{-1/2}, \quad (4)$$

σ_0 is the alloy's intrinsic yield strength, and k_σ is the Hall-Petch hardening coefficient. The values for σ_0 and k_σ were obtained using linear regression as 184 MPa and 655 MPa $\mu m^{1/2}$, respectively (Fig. 4). For example, J. Yang et al. [19] found that the value of the hardening coefficient k_σ for the single-phase $Al_{0.1}CoCrFeNi$ alloy was 464 MPa $\mu m^{1/2}$.

Comparing the results obtained with those of other studies, it is evident that aluminum alloying enhances the strength characteristics of HEAs/CCAs. This is explained by the additional lattice distortion introduced due to the much larger atomic radius, the low shear modulus of aluminum compared to other alloy elements, and the reduction in the stacking fault energy (SFE). All this leads to limited dislocation movement due to lattice and elastic mismatch.

Summary

The main objective of the current study was to investigate the effect of the applied technological processes on the microstructure and mechanical properties of the obtained single-phase CCA with the nominal composition $Al_{0.35}CoCrFeNi$. Additionally, the impact of the average grain size on the mechanical properties of the alloy was also examined.

To summarize, the following conclusions can be drawn:

- The segregation of elements in the alloy after vacuum induction melting and casting methods completely disappears during solution annealing, and the structure becomes homogeneous.
- Rotary swaging at room temperature obtained a highly deformed structure and introduced nuclei for recrystallization.
- After recrystallization annealing, the samples' structure consists of equiaxed grains with annealing twins.
- Grain growth is controlled by both the solute resistance and the effects of grain boundary tension and is described by a classical power law with an exponent n = 3.
- The high calculated values of the recrystallization activation energy and hardening coefficients in the resulting alloy are explained by the influence of aluminum additives. These additives introduce additional lattice distortions, slowing grain growth and increasing the efficiency of grain boundary hardening in the single-phase $Al_{0.35}CoCrFeNi$ alloy.

Acknowledgements

This work was financially supported by the Slovak Research and Development Agency under the contract APVV-23-0206 and by the Slovak Grant Agency for Science under contract VEGA 2/0018/22. The EU NextGenerationEU supported this work through the Recovery and Resilience Plan for Slovakia under projects No. 09I03-03-V01-00037 and No. 09I04-03-V02-00005.

References

[1] J.W. Yeh, S.K. Chen, S.J. Lin, S.J. Gan, T.S. Chin, T.T. Shun, C.H. Tsau, S.Y. Chang, Adv. Eng. Mater., 6 (2004) 299-303.

[2] J.Y. He, C. Zhu, D.Q. Zhou, W.H. Liu, T.G. Nieh, Z.P. Lu, Intermetallics, 55 (2014) 9-14.

[3] C.C. Juan, M.H. Tsai, C.W. Tsai, C.M. Lin, W.R. Wang, C.C. Yang, S.K. Chen, S.J. Lin, J.W. Yeh, Intermetallics, 62 (2015) 76-83.

[4] D.B. Miracle, O.N. Senkov, Acta Mater., 122 (2017) 448-511.

[5] W.H. Liu, T. Yang, C.T. Liu, Mater. Chem. Phys., 210 (2018) 2-11.

[6] B. Gwalani, S. Gorsse, D. Choudhuri, Y. Zheng, R. S. Mishra, R. Banerjee, Scr. Mater., 162 (2019) 18-23.

[7] B. Gwalani, S. Gangireddy, Y. Zheng, et al., Sci. Rep., 9 (2019) 6371.

[8] S. Gorsse, D.B. Miracle, O.N. Senkov, Acta Mater., 135 (2017) 177-187.

[9] P. Thirathipviwat, Y. Onuki, G. Song, J. Han, S. Sato, J. Alloys Compd., 890 (2022) 161816.

[10] Y.C. Huang, C.H. Su, S.K. Wu, C. Lin, Entropy, 21, 3 (2019) 297.

[11] K. Ulybkina, K. Kamyshnykova, A. Klimová, T. Pelachová, A. Školáková, J. Pinc, Intermetallics, 175 (2024) 108456.

[12] C. Zhang, F. Zhang, H. Diao, M.C. Gao, Z. Tang, J.D. Poplawsky, P.K. Liaw, Mater. Des., 109 (2016).

[13] M. Vaidya, A. Anupam, J.V. Bharadwaj, C. Srivastava, B.S. Murty, J Alloys Compd., 791 (2019) 1114-1121.

[14] C.S. Wu, P.H. Tsai, C.M. Kuo, C.W. Tsai, Entropy, 20, 12 (2018) 967.

[15] Z. Yang, F. He, Q. Wu, K. Zhang, D. Cui, B. Guo, B. Han, J. Li, J. Wang, Z. Wang, Metall Mater Trans A Phys Metall Mater Sci,, 52 (2021) 3799-3810.

[16] M. Annasamy, N. Haghdadi, A. Taylor, P. Hodgson, D. Fabijanic, Materials Science and Engineering: A, 754 (2019) 282-294.

[17] B. Gwalani, V. Soni, M. Lee, S.A. Mantri, Y. Ren, R. Banerjee, Mater. Des., 121 (2017) 254-260.

[18] Z. Wu, H. Bei, F. Otto, G.M. Pharr, E.P. George, Intermetallics, 46 (2014) 131-140.

[19] J. Yang, J.W. Qiao, S.G. Ma, G.Y. Wu, D. Zhao, Z.H. Wang, J. Alloys Compd., 795 (2019) 269-274.

Published in: Defect and Diffusion Forum
ISSN: 1662-9507, Vol. 448, pp 107-112
doi:10.4028/p-6UBnSm

Submitted: 2025-05-30
Revised: 2025-12-08
Accepted: 2025-12-19
Online: 2026-03-03

Influence of Growth Rate on the Microstructure and Properties of EuBCO Bulk Superconductors Prepared by Top Seeded Melt Growth Process

Liudmila Vojtkova[1,a*], Pavel Diko[1,b] and Marek Vojtko[2,c]

[1]Institute of Experimental of Physics, Slovak Academy of Sciences, Watsonova 47, 040 01, Košice, Slovakia

[2]Institute of Materials Research, Slovak Academy of Sciences, Watsonova 47, 040 01, Košice, Slovakia

[a*]vojtkova@saske.sk, [b]dikos@saske.sk, [c]mvojtko@saske.sk

Keywords: Bulk Superconductors, EuBCO, Single Crystal, Single-Direction Melt-Growth (SDMG), Top Seeded Melt Growth (TSMG), Microstructure, Subgrains, Pores, Cooling Rate, Growth Rate, Eu211 Size Particles.

Abstract. To prepare bulk single-crystal REBCO superconductors by the new single-direction growth method (SDMG: Single-Direction Melt-Growth), it is necessary to produce a large-area seed of high quality, for example, based on EuBCO. Since the samples prepared by the SDMG method copy the structure of the seed, for the production of large-area seeds it is necessary to optimize the time-temperature regime in order to grow seeds with a suitable structure and composition and minimize structural defects (limiting the amount of subgrains and others). A higher growth rate was used in comparison with the standard growth rates used to produce EuBCO seeds of larger dimensions. The increased growth rate in the crystal growth window reduces the outflow of the melt from the sample, and thus it is possible to achieve a single-crystal sample in the entire volume of the precursor. The samples were produced at different growth rates: 1; 2; 3 and 5 °C/h. The microstructure of the samples was studied by polarized light microscopy and scanning electron microscopy. The size and distribution of Eu211 particles in the sample volume and the subgrain structure were studied on the fabricated samples.

Introduction

Single-crystal REBCO ($REBa_2Cu_3O_7$, RE: rare earth element) bulk superconductors are promising materials for practical applications. At present, REBCO bulk single-crystal superconductors (MMS) are produced by the Top-Seeded Melt-Growth (TSMG) process or by the new Single-Direction Melt-Growth (SDMG) technique. TSMG is the most common used method for preparing bulk superconductors grown from a small REBCO seed. Resulting single-crystal sample usually consists of four a-growth sectors and one c-growth sector [1–5]. A new superconductor growth technique, the SDMG method of single-direction growth of bulk REBCO crystal, uses a large-area seed [6–8]. By this process, the bulk crystal is formed by only one c-growth sector. Since the single crystal grown by SDMG technique copies the crystal structure of the large-area seed, it is necessary to have a high-quality seed.

The desired microstructure of REBCO seed-samples should have reduced proportion of subgrains, minimal subgrain disorientation and suitable volume fraction of cracks and porosity. Moreover, prepared seed-sample should have the same dimensions than the subsequently prepared sample by SDMG process. Study of crystal growth rate should help to find suitable parameters of time-temperature process of preparation of that type of microstructure.

The seed-samples, which should be used as large-area seeds for SDMG process, were produced by TSMG process from EuBCO materials, because they have a higher peritectic temperature than most prepared REBCO bulk superconductors [9]. Eu123 single crystals were prepared at growth rates of 1, 2, 3 and 5 °C/h in the peritectic growth temperature window. A higher cooling rate in the growth temperature window was used in comparison with the standard cooling rates used to grow

EuBCO bulk crystals. A higher cooling rate leads to a higher growth rate and shortens the time required for bulk crystal growth. Their properties and microstructure were analysed.

The prepared samples were also analysed not only as seed-samples but also as classical samples of superconducting materials, in which the desired microstructure should contain small homogeneously distributed Eu211 particles serving as pinning centres. Also, small amount of CeO_2 was added to the samples, which refines the Eu211 particles and increases the growth rate of the Eu123 single crystal [10–11]. The porosity of the samples was also evaluated.

Experimental Materials and Methods

Experimental material. The samples were prepared from commercially available solid phase powders $EuBa_2Cu_3O_{7-\gamma}$ (Eu123) (Solvay Fluor GmbH, Germany, maximum particle size $d_{max.} = 5$ μm), $Eu_2Ba_1Cu_1O_5$ (Eu211) (Solvay Fluor GmbH, Germany, maximum particle size $d_{max.} = 5$ μm) and CeO_2 (Aure Remy).

Growth of bulk crystals. Four samples were prepared with the same mass ratio of Eu123:Eu211 phases 78.3:21.7. 0.5 wt.% CeO_2 was added to all samples. The mixed powders were uniaxially pressed in the form of pellets with a diameter of 30 mm and a weight of 25 g. $Nd_1Ba_2Cu_3O_{7-\gamma}$ (Nd123) thin film seeds were placed on top of the samples. The whole arrangement was placed on an aluminum oxide plate (Fig. 1, left). All four samples (samples K, M, O and P) intended for preparation by TSMG process were heat treated with four different cooling rates in the temperature window of peritectic single crystal growth. First, the samples were heated to 350 °C at a rate of 100 °C/h, followed by a holding time of 1 hour. The samples were then heated to the melting temperature T = 1118 °C, with a holding time of 1 hour to ensure the formation of a liquid pellet phase. The cooling of the samples consisted of cooling the sample near the perectic reaction temperature of 1081 °C at a rate of 100 °C/h. Then, the samples were slowly cooled from 1081 °C to 1046 °C at four different rates of 1, 2, 3 and 5 °C/h, and the last step was the cooling of the samples in the furnace. The scheme of the time-temperature regime is shown in Figure 1 on the right.

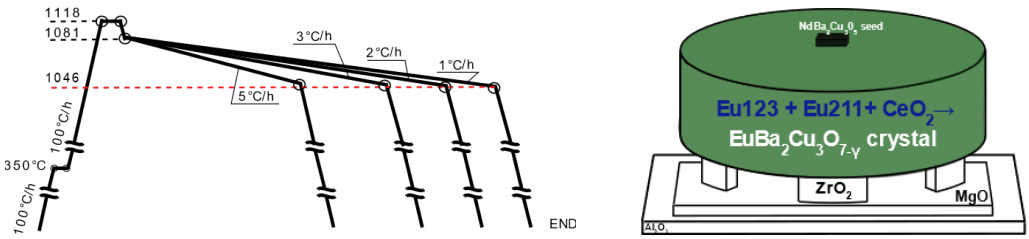

Fig. 1. The schematic assembly of pellet layers and time-temperature regime for prepared EuBCO single crystal by top seeded melt growth method.

The prepared bulk crystals were oxygenated in a tube furnace with a flowing oxygen atmosphere at a temperature of 410 °C for 336 hours.

Results and Discussion

Results of single crystal growth. Figure 2 shows the macroscopic images of the top surface morphology of bulk EuBCO samples P, K, M and O fabricated by TSMG technique with NdBCO seed film. The samples were grown using different growth rates in the peretectic crystal growth temperature range. The epitaxial growth of EuBCO crystals successfully occurred from the seed, and therefore it is possible to confirm the feasibility of growth from NdBCO film seed in TSMG technique using different crystal growth rates. However, in the case of crystals grown at higher growth rates, M and O samples of 3 °C/h and 5 °C/h, respectively, the presence of larger subgrains can be seen on the crystal surface.

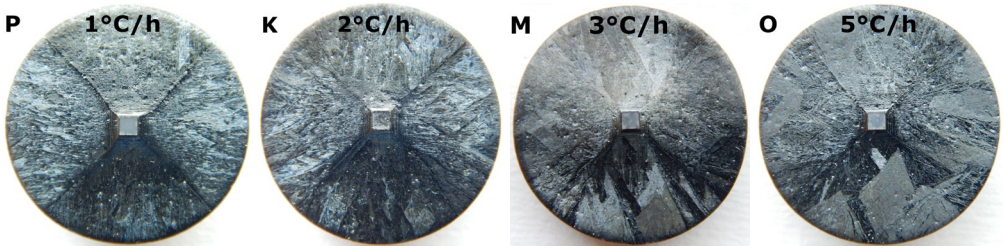

Fig. 2. The macrophotograph of the top surface of EuBCO samples prepared by growth rate 1, 2, 3 and 5 °C/h.

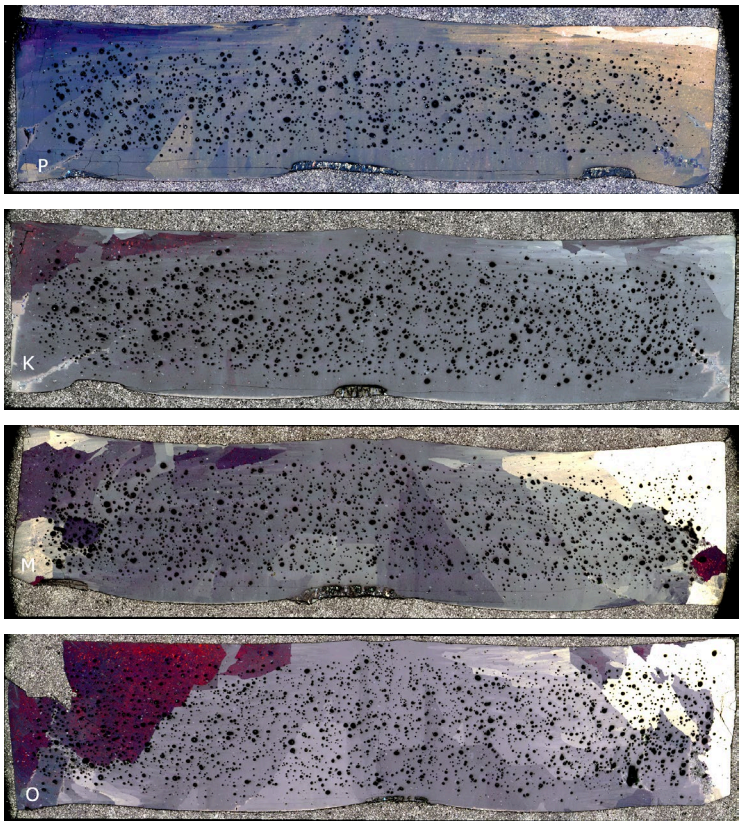

Fig. 3. The microstructure of cross section with subgrains of the samples prepared by different growth rate in polarised light.

Micrographs of the structure of samples P, K, M and O after the oxidation process in a section parallel to the (100) plane are shown in Fig. 3. The structure of the samples is different. It is known that an increase in supercooling (in our case the growth rate) has an effect on the formation of greater disorientation in the lattice and the formation of a subgrain structure in the crystal. The addition of CeO_2 to the samples also has an impact on crystal preparation because it refines the Eu211 particles. Smaller Eu211 particles dissolve more easily in the reverse peritectic reaction, causing an increase in the growth rate of bulk crystals [11, 12]. When we compare the prepared samples produced with the same composition and with different time-temperature regimes, it is obvious that the single crystal of sample P prepared at a growth rate of 2 °C/h contains the less subgrain structure in comparison with sample O grown at a rate of 5 °C/h (Fig. 3). The higher crystal growth rate caused a structure with a more pronounced disorientation of subgrains. The micrographs show a gradually increasing disorientation of subgrains in the samples as the crystal growth rate increases. They are most visible near the sample surface and at the edges of the crystals. But it is also seen that the single crystal in all cases grew into the very bottom end and also to the edges, probably due to the higher growth temperature. During faster growth, the melt needed for crystal growth did not have time to leave the sample and a relatively large sample was grown. Regarding the quality of the microstructure, as the proportion of pores in the sample volume, it

changes and increases from lower to higher growth rates (Table 1). The volume fraction of pores in crystals grown at 1 and 2 °C/h was the lowest. The porosity of sample P is 7.01 %, sample K 7.34 %, sample M 8.16 % and sample O has the highest porosity of 8.53 %. It can be assumed that during the TSMG process, pores are formed from O_2 due to a peritectic reaction during the melting of the sample (formula 1). At a higher cooling rate and subsequently a higher growth rate, the sample is in the molten state for a shorter time. Since oxygen from the bubbles (pores) escapes from the sample by diffusion through the melt, more of it remains in the sample at higher cooling rates.

$$2(RE)Ba_2Cu_3O_{7-\gamma}(s) \leftrightarrow (RE)_2BaCuO_5\ (s) + Ba_3Cu_5O_8(l) + yO_2(g) \quad (1)$$

Table 1. Eu211 particle size and pore volume fraction in Eu123 bulks (samples P, K, M and O) fabricated by different growth rate.

Sample	EqDiameter, d211, μm						Pores
	a1	a2	a3	c1	c2	c3	%
P	0.66	0.73	0.77	0.64	0.68	0.76	7.01
K	0.68	0.74	0.8	0.68	0.69	0.77	7.35
M	0.73	0.81	0.79	0.76	0.72	0.85	8.16
O	0.72	0.8	0.83	0.7	0.74	0.82	8.53

Microscopic observation of studied samples. The shape of the pores is spherical, and such porosity is typical for samples prepared by the classic process of melt growth with a seed placed on the surface (TSMG). Pores are useful for the oxygenation process of bulk crystals. However, they reduce the volume of the superconducting material, thereby reducing the macroscopic superconducting properties.

Microstructural analysis of EuBCO samples was performed at the beginning, middle and end of a-growth sector and c-growth sector. The positions of the performed microstructure analysis and the evaluation of the size distribution of Eu211 particles in the samples are shown in Fig. 4.

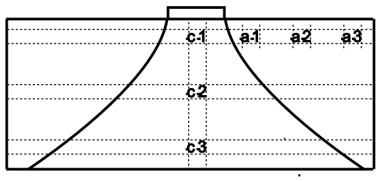

Fig. 4. Schematic illustration of the location of microstructural analysis in a/c-section.

Figure 5 shows SEM photographs of the microstructures taken in bulk Eu123 crystals prepared with different growth rates by the TSMG process. The particle sizes were evaluated by image processing software. Fine and spherical Eu211 particles are evenly distributed in the Eu123 matrix in all samples. There are a few large particles in the samples, but the average size of most particles is in the range of 0.64 to 0.85 μm. The average particle size in the samples increases with increasing crystal growth rate. This can be observed in both crystal growth directions “a” and “c” (Table 1). The percentage of Eu211 particles also increases in the samples with increasing crystal growth rate (Fig. 6). Similarly, the volume fraction of particles increases in all samples in both growth sectors, also depending on the distance from the seed. But the most evenly distributed particles can be seen in the sample prepared with a growth rate of 3 °C/h in growth sector “a” (Fig. 6). The finest particles are in samples P and K prepared with slow growth rates of 2 and 3 °C/h, respectively. At slow growth rates, the radius of Eu211 particles decreases and the volume fraction of Eu211 particles slightly increases with higher growth rates. Moreover, the smallest amount of subgrains was observed in sample P prepared at a rate of 2 °C/h, and therefore I consider that combination of time-temperature regime and Eu211 particle content of sample P is the most suitable for the preparation of bulk superconducting materials.

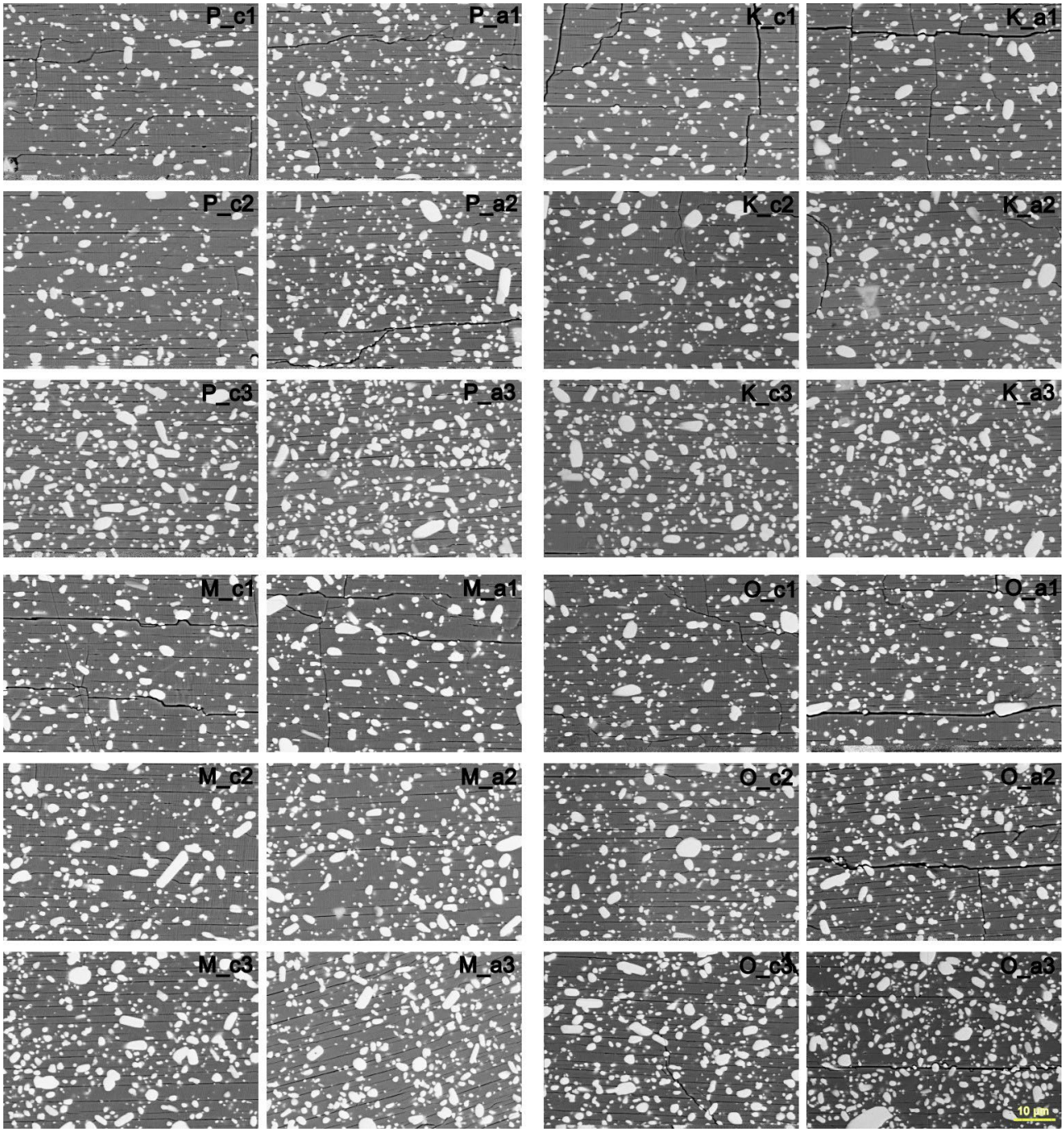

Fig. 5. Microstructures of the EuBCO single crystals with 211 particles of samples P, K, M, O, taken at the beginning, in the middle and at the end of a- and c-growth sector.

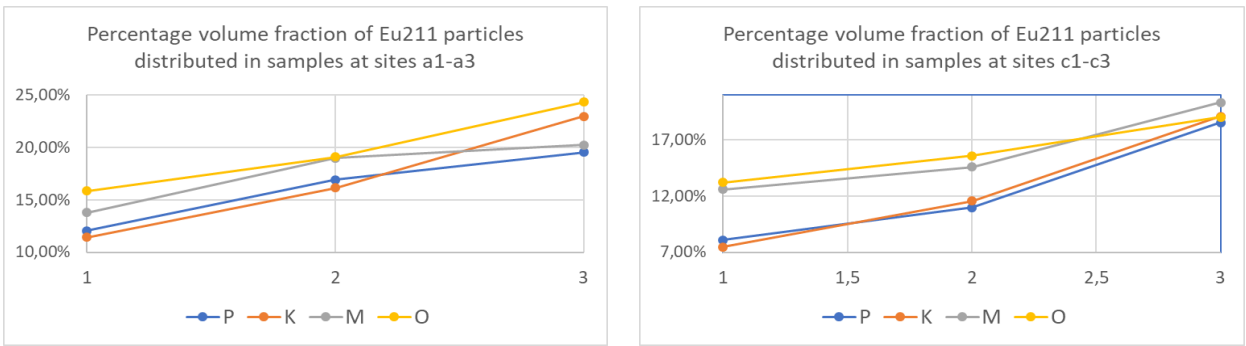

Fig. 6. Distribution and volume fraction Eu211 particle in studied samples.

Summary

In this work, Eu123 crystals were grown at different growth rates by the TSMG process. The used growth rates were 1, 2, 3 and 5 °C/h. We found that the Eu123 crystal grown at 1 and 2 °C/h contained the smallest pores. The higher crystal growth rate caused a structure with more pronounced subgrain disorientation.

Analysis of the size and volume fraction of Eu211 particles in the bulk crystal showed that at a slow growth rate, the radius of Eu211 particles decreases and also volume fraction of Eu211 particles slightly increases with higher growth rate.

The volume fraction of particles increases in all samples in both growth sectors depending on the distance from the seed.

Acknowledgement

This work was supported by Slovak Grant Agency APVV-17-0625, APVV-21-0387, No. 2/0094/22, No. 2/0152/25 and by NPS Vojtkova 2025.

References

[1] D.K. Namburi, Y. Shi, A.R. Dennis, J.H. Durrell, D.A. Cardwell, Supercond. Sci. Technol., 31, 427 (2018) 19.

[2] X. Wang, X. Liu, D. Wei, Y. Shi, C. Cai, Y. Zhang, K. Zhang, D. Zhou, Supercond. Sci. Technol., 37, 8 (2024) 12.

[3] K.N. Batur, Ş. Duman, B. Çakir, M. Başoğlu, Journal Metrics: physica status solidi (b), Nov. 2024.

[4] T. Motoki, T. Kii, J.-I. Shimoyama, IEEE Transactions on Applied Superconductivity, 35, 5 (2025) 6800305.

[5] T. Motoki, R. Sasada, T. Tomihisa, S.-I. Nakamura, J.-I. Shimoyama, Superconductor Science and Technology, 35, 9 (2022) 094003.

[6] M. Radušovská, P. Diko, D. Volochová, R. Smolko, V. Kuchárová, J. Bednarčík, Ceramics International, 51, 18 (2025) 24699-24706.

[7] Yuanyuan Chena, Xiangxiang Cuia, Xin Yaoa, Progress in Materials Science, 68 (2015) 97-159.

[8] D.K. Namburi, Y. Shi, D.A Cardwell, Supercond. Sci. Technol., 34 (2021) 053002, 51.

[9] P.-W. Chen, I.-G. Chen, S.-Y. Chen, M.-K. Wu, Supercond. Sci. Technol., 24 (2011) 085021, 1-8.

[10] D. Volochová, M. Radušovská, P. Diko, Journal of the American Ceramic Society, 108, 6 (2025) e20435.

[11] A. Mahmooda, S.D. Parka, B.H. Juna, J.S. Younc, Y.H. Hanb, T.H. Sungb, C.J. Kim, Physica C: Superconductivity, 469, 15-20 (2009) 1165-1168.

[12] D. Volochová, P. Diko, V. Antal, M. Radušovská, S. Piovarči, Journal of Crystal Growth, 356 (2012) 75.

Published in: Defect and Diffusion Forum
ISSN: 1662-9507, Vol. 448, pp 113-118
doi:10.4028/p-I7mFRW

Submitted: 2025-10-26
Revised: 2025-12-08
Accepted: 2025-12-19
Online: 2026-03-03

Comparison of Properties of CeO_2 Doped ZrO_2 Samples Prepared by Conventional Sintering and by SPS

Marek Vojtko[1,a*], Peter Tatarko[2,b] and Viktor Puchý[1,c]

[1]Institute of Materials Research of SAS, Watsonova 47, Košice, Slovak Republic

[2]Institute of Inorganic Chemistry of SAS, Dúbravská cesta 9, 845 36 Bratislava 45, Slovak Republic

[a*]mvojtko@saske.sk, [b]peter.tatarko@savba.sk, [c]vpuchy@saske.sk

Keywords: CeO_2-Doped ZrO_2, Sintering, SPS, Grain Size, Fracture, Hardness.

Abstract. The aim of the study was to prepare samples suitable for testing the shape memory phenomenon in ceramic systems. Testing would be carried out by preparing micro-objects with dimensions in the order of micrometers using SEM/FIB techniques, and subsequent testing using a nanoindenter. The article deals with the influence of the preparation method on the properties of samples prepared by conventional annealing and spark plasma sintering. Two commercial powders were used, namely PSZ-10C and PSZ-20C. The microstructure of the samples, fracture surfaces and HV hardness, as well as indentation hardness were evaluated on the prepared samples. It was shown, that both conventional annealing and SPS can be used for preparation of samples with a suitable grain size, but also that the preparation method has a significant impact on the properties of the sample. Depending on the preparation method, the grain size varied from approximately 1 μm to 50 μm. There is also difference in the character of the fracture surfaces and in the hardness of the samples, where a difference in indentation hardness from approximately 10 GPa to approximately 20 GPa was measured.

Introduction

Zirconium oxide (ZrO_2) can exist in one of three modifications depending on the conditions (monoclinic below 1170 °C, tetragonal between 1170 °C and 2370 °C and cubic above 2370 °C). By adding some oxides, such as CaO, MgO, CeO_2 and Y_2O_3, or by refining the grain to the nanoscale, it is possible to stabilize the tetragonal or cubic phase at room temperature [1, 2]. Tetragonally stabilized zirconium oxide exhibits the transformation toughening phenomenon [3] and also the shape memory phenomenon has also been observed in such a system [4].

It is well known that ceramic materials are inherently brittle along grain boundaries, therefore it is appropriate to study the shape memory phenomenon in ceramic materials within a single grain. The shape memory effect on micro-objects prepared by SEM/FIB techniques was observed in 2013 by Lai et al. [5] on yttrium and cerium stabilized ZrO_2. In the same system, Du et al. [6] studied the effect of grain size on the application of the shape memory effect.

The aim of this work is to prepare samples from cerium stabilized zirconia for studying the shape memory effect in ceramic materials with appropriate grain size (some microns) and phase composition (tetragonally stabilized zirconia), and to compare possibilities of preparation such samples by conventional sintering and spark plasma sintering (SPS).

Experimental Material and Methods

Commercial cerium-stabilized ZrO_2 powders, namely PSZ-10C and PSZ-20C (Stanford Advanced Materials, ZrO_2 – 10 wt.% CeO_2 and ZrO_2 – 20 wt.% CeO_2, Particle Size: D50 = 0.5–1 μm) were used to prepare the samples. Two methods of sintering the powder samples were used, conventional sintering (samples E2, I and J) and SPS (Spark Plasma Sintering, SPS HP D10-SD) (samples N, B and B1). Sample E2 (ZrO_2 – 10 wt.% CeO_2) was cold pressed and sintered at 1400 °C for 20 hours. Similarly, samples I (ZrO_2 – 10 wt.% CeO_2) and J (ZrO_2 – 20 wt.% CeO_2) were cold pressed and sintered at 1600 °C for 20 hours. Samples N (ZrO_2 – 10 wt.% CeO_2) and B (ZrO_2 – 10 wt.% CeO_2)

were prepared by SPS at 1600 °C, 60 minutes (sample N) and 2000 °C, 10 minutes (sample B), respectively. Sample B1 (ZrO_2 – 10 wt.% CeO_2) was prepared in the same way as sample B, but after SPS it was further annealed in an oxide atmosphere at 1400 °C for 4 hours. The processing of the samples is summarized in Table 1.

Table 1 Used regimes for prepared samples.

Sample	Composition	Sintering	Temp. [°C]	Time [min.]	Temp. [°C]	Time [min.]
E2	ZrO_2 – 10 wt.% CeO_2	conventional	1200	1200	-	-
I	ZrO_2 – 10 wt.% CeO_2	conventional	1600	1200	-	-
J	ZrO_2 – 20 wt.% CeO_2	conventional	1600	1200	-	-
N	ZrO_2 – 10 wt.% CeO_2	SPS	1600	60	-	-
B	ZrO_2 – 10 wt.% CeO_2	SPS	2000	10	-	-
B1	ZrO_2 – 10 wt.% CeO_2	SPS + conv.	2000	10	1400	240

The samples for observation were prepared by grinding and polishing, or a fracture surface was created. A Zeiss Axio Observer 1M light microscope and a Zeiss Auriga Compact 45–76 electron microscope were used for observation. The average grain size was evaluated by the Saltykov method from approximately 50 grains.

The Vickers hardness HV1 to HV30 (WILSON-WOLPERT hardness tester Tukon 1102) and the indentation hardness (Nanoindenter TTX NHT) at a load 100 mN were measured on the polished surfaces.

Results

The microstructures of the prepared samples at different magnifications are presented in Fig. 1. The microstructure of the samples is single-phase, with the exception of sample N (Fig. 1d), where two structural components can be observed. For this reason, the grain size of sample N was not evaluated. In samples prepared by conventional sintering increased porosity was observed, probably associated with insufficient processing control. In samples B and B1 (Fig. 1e and 1f), chipping on grain boundaries occurred during their preparation by grinding and polishing was observed.

The results of measured grain size is presented in Table 2. In terms of the grain size of the prepared samples, samples I, J, B and B1 are suitable for studying the shape memory in individual grains. It is evident from the results, that the increasing of temperature during conventional annealing led to an increasing of the grain size, namely from 0.8 μm at temperature 1400 °C to almost 5 μm at 1600 °C, both for samples with 10 and 20 % of CeO_2.

Table 2 Grain size of prepared samples.

Sample	E2	I	J	N	B	B1
Grain size [μm]	0.8	4.7	4.5	-	50.4	48.2

The SPS preparation of the samples yielded completely different results. At temperature 1600 °C, the single-phase structure decomposed into two structural components, one rich in Zr and the other rich in Ce, as presented in Fig. 1d and 2. SPS preparation at 2000 °C resulted in grain coarsening to approximately 50 μm. Also, SPS preparation resulted in a decrease in the oxygen content of the sample (sample B). Subsequent annealing in an oxide atmosphere resulted in re-oxygenation of the sample (sample B1), as it was described earlier [7].

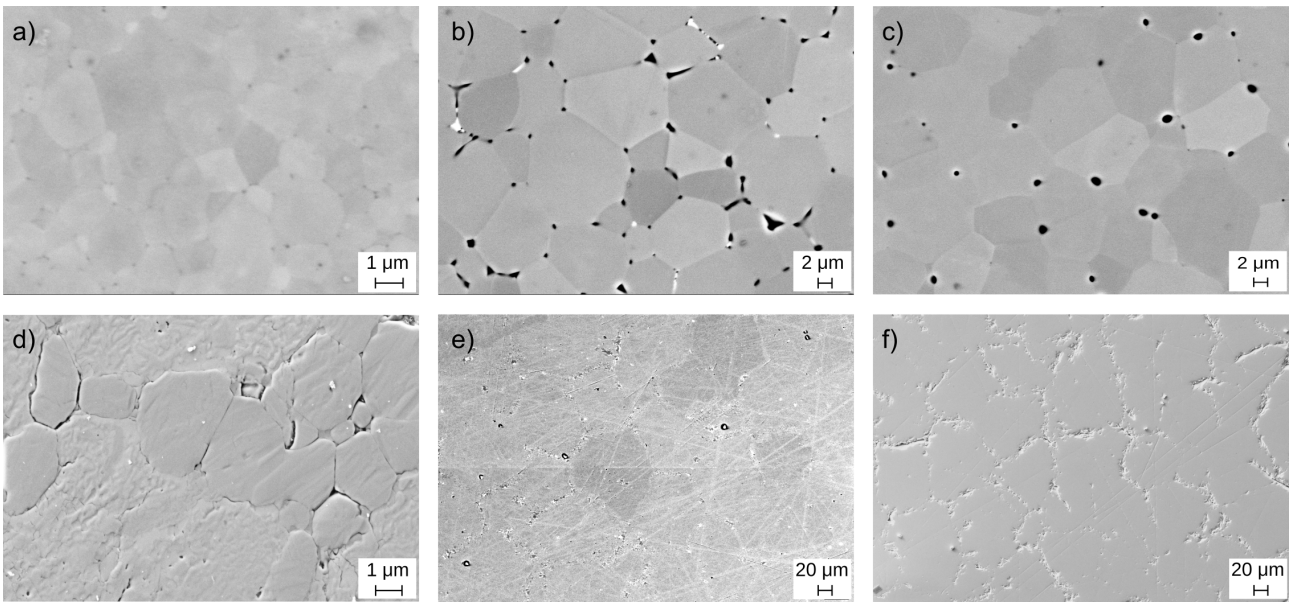

Fig. 1 Microstructures of prepared samples, a) sample E2, b) sample I, c) sample J, d) sample N, e) sample B and f) sample B1.

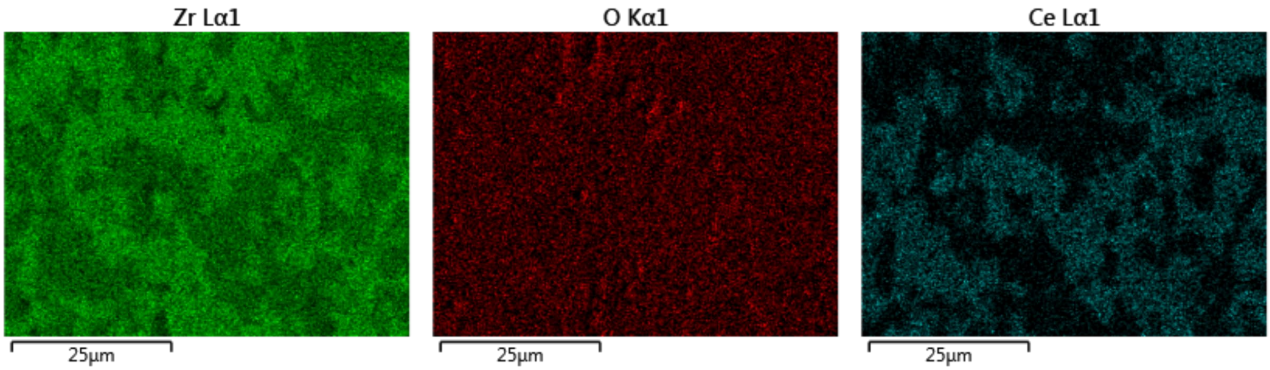

Fig. 2 EDX maps of sample N.

The fracture surfaces of the prepared samples are presented in Fig. 3 and the proportion of intercrystalline and transcrystalline fracture of the samples is presented in Table 3. In samples E2, I, J and N, a mixed fracture occurred with a proportion of transcrystalline fracture of about 40 %. The fracture surface of sample B has a transcrystalline character, which after annealing the sample in an oxide atmosphere (sample B1) changes to intercrystalline. Porosity can also be seen on the fracture surfaces in samples I and J. The fractures of samples E2, I and J contain relatively smooth surfaces of intercrystalline cleavage, and conversely, the transcrystalline cleavage has a rugged character. In sample N, structural features similar to twinning or martensitic transformation are visible on the intercrystalline facets. In contrast to samples E2, I, J and N, sample B has relatively smooth transcrystalline surfaces with some transverse cracks. On the intercrystalline surfaces of sample B1 there are particles of contamination and higher amount of transverse cracks than in sample B.

The hardness of the samples was measured by several methods. The results of the measurements are presented in Table 4 and in graphic form in Fig. 4. The highest values of the measured hardness were achieved for samples I, J and B, while the lowest hardness was measured for sample N. The hardness of sample B was significantly reduced after annealing in an oxide atmosphere (sample B1). As expected, the samples showed a decrease in hardness with increasing load at measurement. The exception was observed in sample N, where there was an increase in hardness with increasing load, which could be caused by the two-phase structure. After hardness test, indents were checked by light microscopy. Some chipping at indents was visible on samples B and B1. Near the indents of I and J

samples martensitic transformation by polarized light was observed. Martensitic transformation is a basic condition for the application of the shape memory phenomenon in a sample. Since the martensitic transformation was observed in samples I and J and their average grain size is almost 5 μm, these samples should be suitable for the preparation of small pillars in one grain (with dimensions of approximately 2 μm in diameter and 5 μm in height) by the FIB technique. Martensitic transformation in grains near the indent of sample I is presented in Figure 5.

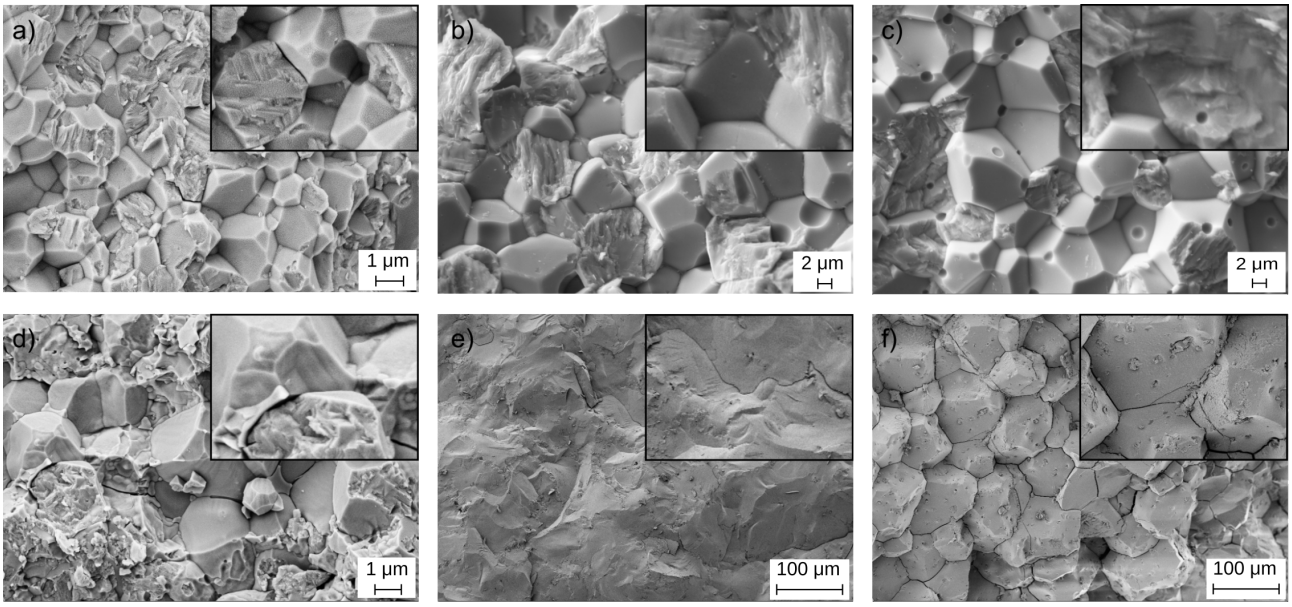

Fig. 3 Fracture surfaces of prepared samples with details, a) sample E2, b) sample I, c) sample J, d) sample N, e) sample B and f) sample B1.

Table 3 Transgranular and intergranular fracture ratio.

Sample	E2	I	J	N	B	B1
Transgranular fracture ratio [%]	37	43	39	40	95	5
Intergranular fracture ratio [%]	63	57	61	60	5	95

Table 4 Indentation hardness and Vickers hardness of samples.

Sample	Hit(O&P) [GPa]	Eit(O&P) [GPa]	HV(O&P) [GPa]	HV1	HV10	HV30
E2	13.72	203.2	1271	938	916	905
I	19.88	235	1841	944	867	861
J	21.18	212.9	1960	998	917	912
N	10.4	168.4	963	612	663	685
B	20.27	215.3	1877	1169	836	775
B1	13.36	168.4	1237	902	827	700

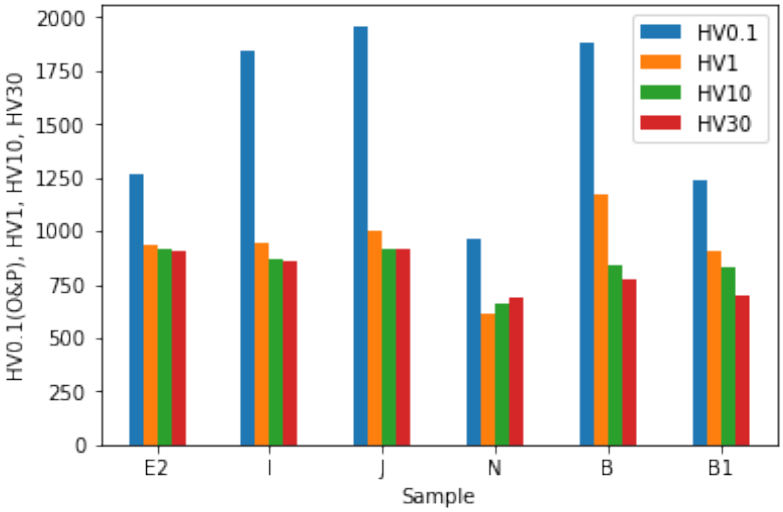

Fig. 4 Influence of applied force on result of hardness.

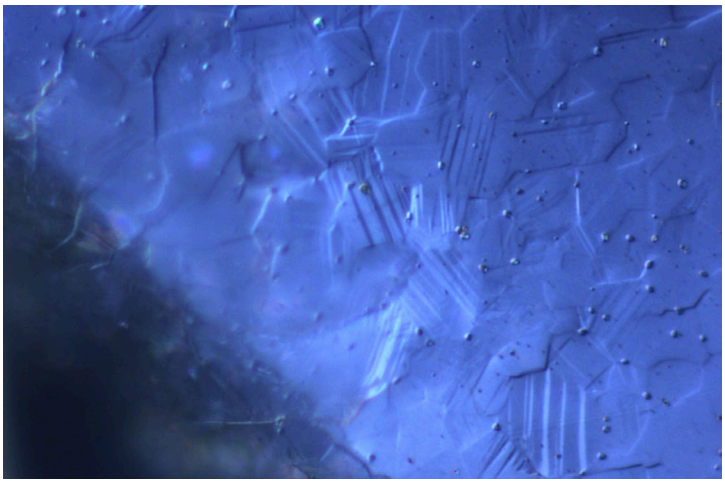

Fig. 5 Martensitic transformation near the indent (sample I).

Summary

Both methods, conventional sintering and SPS, can be used to prepare a sample (ZrO_2 doped with CeO_2) with a suitable grain size and structure for further investigation of the shape memory phenomenon. With conventional sintering, there is a problem with higher porosity and time and energy consumption. SPS process caused problem with decomposition into two phases at some temperatures and a decrease in oxygen content. Depending on the preparation method, the grain size varied from approximately 1 μm to 50 μm. There is also difference in the character of the fracture surfaces and in the hardness of the samples. Indentation hardness varied from approximately 10 GPa to 20 GPa. On the samples I and J prepared by conventional sintering at 1600 °C for 60 min. a martensitic transformation was observed near the indents. These samples have sufficient grain size for the preparation of small pillars by FIB technique and thus they are suitable for further study of shape memory phenomenon in the presented ceramic system.

Acknowledgment

This work was supported by Scientific grant agency of The Ministry of Education, Research, Development and Youth of the Slovak Republic and Slovak Academy of Sciences (VEGA grant No. 2/0152/25).

References

[1] J.R. Kelly, I. Denry, Dental Materials, 24 (2008) 289-298.

[2] R.C. Garvie, Journal of Physical Chemistry, 69, 4 (1965) 1238-1243.

[3] R.H.J. Hannink, P.M. Kelly, B.C. Muddle, Journal of the American Ceramic Society, 83, 3 (2004) 461-487.

[4] M.V. Swain, Nature, 322 (1986) 234-236.

[5] A. Lai, Z. Du, C.L. Gan, C.A. Schuh, Science 27, 341, 6153 (2013) 1505-1508.

[6] Z. Du, X.M. Zeng, Q. Liu, A. Lai, S. Amini, A. Miserez, Ch.A. Schuh, Ch.L. Gan, Scripta Materialia, 101 (2015) 40-43.

[7] M. Vojtko, V. Puchý, E. Múdra, O. Milkovič, A. Kovalčíková, Journal of the European Ceramic Society, 40, 14 (2020) 4844-4852.

Published in: Defect and Diffusion Forum
ISSN: 1662-9507, Vol. 448, pp 119-124
doi:10.4028/p-hkPl0d

Submitted: 2025-05-30
Revised: 2025-12-08
Accepted: 2025-12-19
Online: 2026-03-03

The Influence of the Final Machining Process on the Change of the Microstructure in the Surface Region of Austenitic Stainless Steels

Katarína Bártová[1,a*], Marek Kudláč[1,b], Mária Dománková[1,c], Tomáš Vopát[1,d], Matúš Gavalec[1,e] and Dávid Slnek[1,f]

[1]Faculty of Materials Science and technology in Trnava, Slovak University of Technology in Bratislava, Jána Bottu 25, 917 24 Trnava, Slovak Republic

[a*]katarina.bartova@stuba.sk, [b]marek.kudlac@stuba.sk, [c]maria.domankova@stuba.sk, [d]tomas.vopat@stuba.sk, [e]matus.gavalec@stuba.sk, [f]david.slnek@stuba.sk

Keywords: Austenitic Stainless Steels, Turning, Microstructure, TEM, Texture, Corrosion.

Abstract. Austenitic stainless steels (ASSs) are characteristic with a combination of good mechanical and corrosion properties. Therefore, they are used in the primary circuits of nuclear power plants. Under the influence of a corrosive environment containing chloride ions and mechanical loading, the phenomenon of stress corrosion cracking occurs in ASSs. SCC can also be initiated by the surface condition of ASSs. Machining is usually the last stage of production, during which a significant deformed zone with high residual tensile stresses can be created, which can accelerate the initiation of stress corrosion cracking. Research is focused on analyzing the influence of final turning on microstructural changes of the surface-machined layer caused by various turning parameters (e.g.: cutting speed, feed, depth of cut, cutting tool geometry). No significant microstructure changes were observed between the samples by light microscopy, so we focused on transmission electron microscopy (TEM) on thin lamellas prepared using the focus ion beam (FIB) technique. TEM observation confirmed the presence of a deformed zone and a passivation layer. In the case of the sample that was turned with a higher feed and cutting speed, the passivation layer was discontinuous. Such a microstructural change can significantly affect the corrosion resistance of ASS.

Introduction

One of the safety problems in nuclear power plants (NPPs) is stress corrosion cracking (SCC), which can be defined as an environmentally sensitive form of material degradation caused by the synergistic action of tensile stresses and a corrosive environment [1–5]. ASSs, which are used as the most common structural material for NPPs, are highly susceptible to chloride SCC [6–8]. The current state of nuclear and energy safety can be classified as satisfactory. However, from the perspective of reliability, safety and economics of operation, knowledge about materials applied in NPPs and the impact of long-term operation (LTO) on their properties must be constantly expanded. Today's operating nuclear reactors were originally designed for 30 to 40 years of operation. In EU countries, 19 water-water energetic reactors 440 units are in operation. The high level of safety, effective, reliability, and LTO behind the projected lifetime up to 60–80 years is the real and very actual challenge for the European nuclear community. A very important factor is also the nature of the microstructure of ASSs, which can significantly influence their corrosion resistance.

A serious problem can be the integrity of the surface of ASSs due to the final machining, which can create extremely high levels of tensile residual stresses on the surface of the material (on the order of up to 1000 MPa) [9]. In addition, a strain-strengthened layer with large plastic deformation and the presence of strain-induced martensite can be formed [10, 11]. Final machining, depending on the parameters used, can increase the surface roughness of ASSs, which has a direct impact on their electrochemical behavior [2, 12].

Published works have confirmed that surface working operations such as grinding, turning, milling, cause a significant change in the microstructure, which is associated with the formation of deformation texture and deformation-induced martensitic transformation near the machined surface. The nature of the machined surface has a significant impact on the resistance to chromium-induced

SCC. The formation of strain-induced martensite causes not only an increase in hardness but also increased dissolution in chloride environments. The observed microstructural changes were significantly sensitive to the final machining technology used and the applied parameters [1, 2, 7, 13, 14]. The authors found that the roughness, residual stress and thickness of the deformation zone are proportional to the material removal rate. However, a deeper understanding of the microstructure of the machined deformation zone is still lacking.

Therefore, this study, which aims to expand the knowledge of microstructure formation during machining of AISI 321 austenitic stainless steel, was carried out with respect to the used final turning parameters, which were cutting speed, feed, depth of cutting and cutting tool geometry.

Experimental Procedure

The chemical composition of the AISI 321 steel and the standard is given in Table 1. The steel was turned on a DMG CTX 500 alpha lathe using a single-sided indexable carbide cutting insert with positive geometry, a tip radius of 0.8 mm and no rounding of the cutting edge. Table 2 shows the turning parameters of individual samples. Cutting speeds of 100 and 250 m/min and feed of 0.12, 0.2 and 0.3 mm/rev were used during experiment. The depth of cut was chosen based on the depth of the deformation texture present on the surface semi-finished producted. In order to evaluate the effect of parameters, we needed to get into a material where the grains weren't deformed by rolling process.

Table 1 Chemical composition [wt.%] of turned AISI 321 steel and standard AISI 321.

Steel brand	C	Si	Mn	P	S	Cr	Ni	Ti	Cu
Material of samples	0.064	0.83	1.44	0.025	0.026	17.5	9.89	0.47	0.66
AISI 321 standard	≤ 0.08	≤ 1.00	≤ 2.00	≤ 0.045	≤ 0.03	17.0 19.0	9.0 12.0	5xC 0.70	–

Table 2 Turning parameters used for austenitic stainless steels AISI 321.

Turning parameters					
Cutting speed v_c [m/min]		Feed f [mm/rev]			Depth of cut a_p [mm]
100	250	0.12	0.2	0.3	0.8

The appearance of the surface after turning was observed using Zeiss Stemi 2000-C stereomicroscope the surface roughness of individual samples was subsequently measured. The roughness was measured using a Mitutoyo SJ 210 roughness meter at three different locations on each sample. The average roughness for individual sample was calculated.

The samples for light microscopy were prepared using standard metallographic procedures and were electrolytically etched in 10 % oxalic acid at 10 V for 15 seconds.

Microhardness was measured with Hanemann's method, which uses Vickers' pyramid shape indenter mounted in a special lens. The evaluation was performed using Neophot 21 device. A loading force of 50 p for 10 s load time was applied during measurement. Microhardness was measured on cross-sections near the turned surface (approximately 25 μm below the surface). To obtain the average value, 10 measurements were realized on each sample and the standard deviation was calculated.

Subsequent analysis was focused on observing the changes in the surface microstructure caused by turning. The samples were nanomachined by focused ion beam (FIB) on a Thermo Scientific Scios 2 DualBeam high-resolution scanning electron microscope. TEM was applied to thin lamella prepared by the FIB method. A JEM ARM 200cF analytical transmission electron microscope with atomic resolution was used for detailed observation of the subsurface microstructure.

Results and Discussion

The surface appearance after turning of samples 1 to 6 is shown in the Fig. 1. Samples 1 and 2 have a similar surface appearance, as do samples 3 and 4. The most significant tool mark can be seen on samples 5 and 6, where the highest feed of 0.3 mm/rev was used during turning.

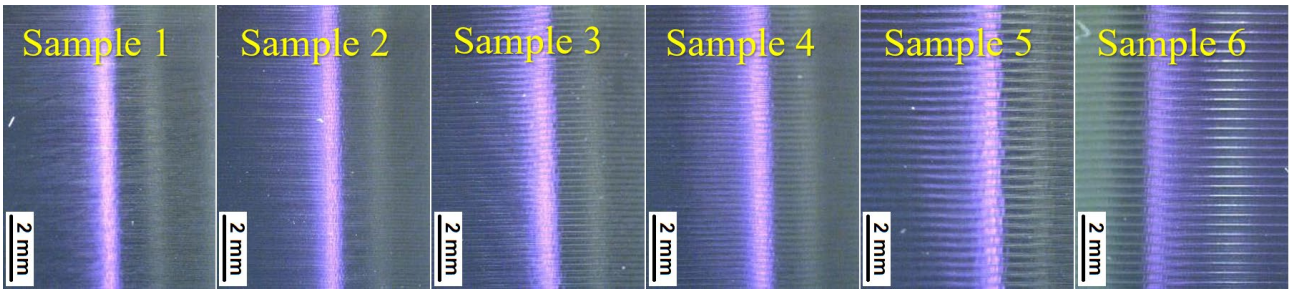

Fig. 1 The surface appearance after turning of samples 1 to 6.

The average roughness for each sample is summarized in Table 3. Sample 1 had an average roughness value of 0.7. The lowest average roughness value of 0.5 was measured for sample 2. In the case of samples 3 and 4, a similar average roughness value of 1.65 was measured. The highest value of roughness around 3.7 was observed for samples 5 and 6.

Table 3 Turning parameters + roughness + microhardness.

Sample	Cutting speed v_c [m/min]	Feed f [mm/rev]	Average roughness Ra	Roughness Rz	Microhardness HV 0.05
1	100	0.12	0.708	3.982	338 ± 12
2	250	0.12	0.499	2.841	343 ± 12
3	100	0.2	1.655	7.281	375 ± 15
4	250	0.2	1.663	7.109	377 ± 12
5	100	0.3	3.765	15.493	372 ± 18
6	250	0.3	3.697	15.904	366 ± 13

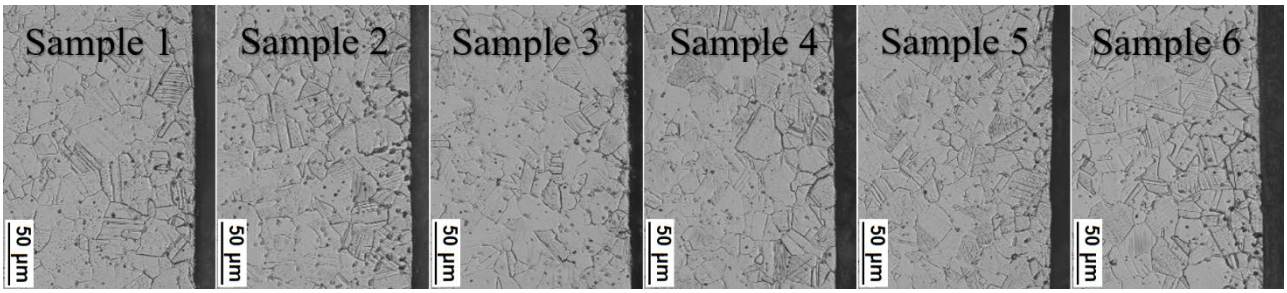

Fig. 2 Microstructure below the turned surface of samples 1 to 6.

The microstructure of investigated steel cross-sections (Fig. 2) consisted of polyhedral austenite grains with annealing twins. Grain boundaries were etched with higher intensity below the turned surface. In austenitic stainless steel, deformation twins with different orientations were observed below the turned surface. These deformation twins were observed to a depth of 80-100 µm from the turned surface. Precipitates were also present. These are probably carbides of stabilizing elements.

The microstructure below the surface was examined using a scanning electron microscope. Deformation twins were observed in the austenitic grains, and these twins intersected in some grains. Precipitates were observed excluded at the grain boundaries as well as inside the austenitic grains. EDS analysis revealed that the precipitates are rich in Cr. No significant differences were observed between the individual samples. For this reason, we focused on TEM, which allowed us to achieve higher resolution.

Table 3 shows the average microhardness values with standard deviation for individual samples. The lowest microhardness of around 340 HV0.05 was measured for samples 1 and 2, which had the lowest roughness. Samples 3 to 6 had a microhardness in the range of 366 to 377 HV0.05.

Subsequent analysis was focused on observing the changes in the surface microstructure caused by turning. For this reason, transmission electron microscopy was applied on a thin lamella (Fig. 3a) prepared by the focused ion beam (FIB) method. Lamellas from sample 1 and 6 were prepared by this method, with the lamella oriented perpendicular to the turned surface. These samples were selected to compare the extremes. On the one hand, a sample with the lowest feed (0.12 mm/rev) and cutting speed (100 m/min) was selected, on the other hand, a sample turned with the highest values of these parameters (f = 0.3 mm/rev, v_c = 250 m/min). Fig. 3b,c shows the microstructure of sample 1 and 6 near the turned surface to a depth of approximately 1.6 μm (Fig. 3b) and 0.5 μm (Fig. 3c), respectively, which cannot be seen using light or scanning electron microscopy. Fig. 3b shows a significant deformed zone that was located up to a depth of 1.1 μm below the surface.

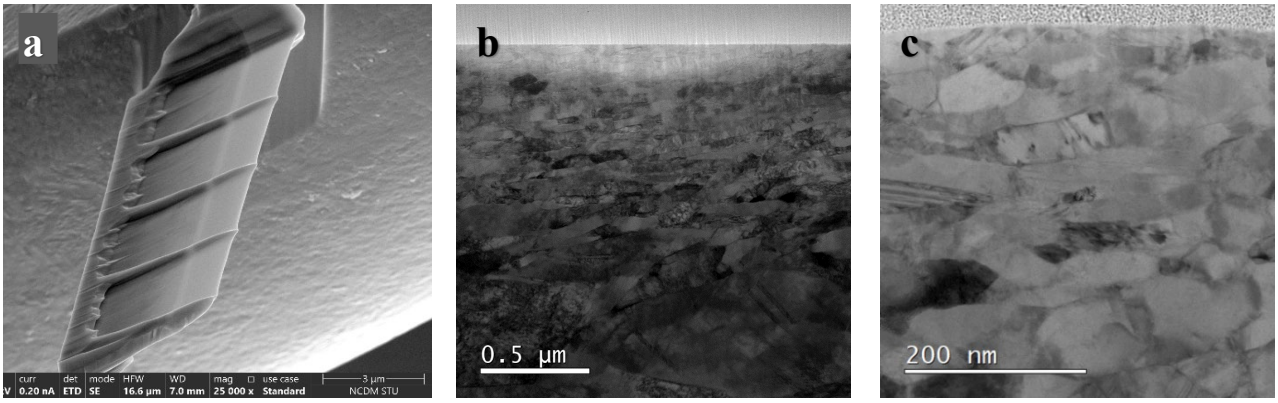

Fig. 3 Prepared lamella of sample 1 by the FIB method (a), Microstructure of sample 1 (b) and sample 6 (c) close to the surface.

Yang et al. [12] investigated the effect of turning parameters (v_c= 128 m/min, f_l= 60 mm/min, a_p= 0.5 mm), milling parameters (v_c 15 m/min, f_l= 150 mm/min, a_p= 0.5 mm) and subsequent surface mechanical grinding treatment (SMGT) on the microstructure changes near the surface of AISI 316L steel. The authors observed a plastic deformed region extending to a depth of 40 μm into the matrix, and an ultrafine grain (UFG) layer with a thickness of approximately 1 μm was present on the turned surface. In the case of milling, a plastic deformed region of 35-40 μm depth and a UFG layer of 0.5 μm were also induced. Wu et al. [14] milled (v_c= 300 m/min, a_p= 0.5 mm, a f= 0.08 mm per tooth) AISI 316L steel, achieving a roughness Ra of around 1 μm. These authors observed gradually deformed zone with a thickness of around 100 μm and a fine-grained layer in the range of 2 μm to 5 μm from the milled surface.

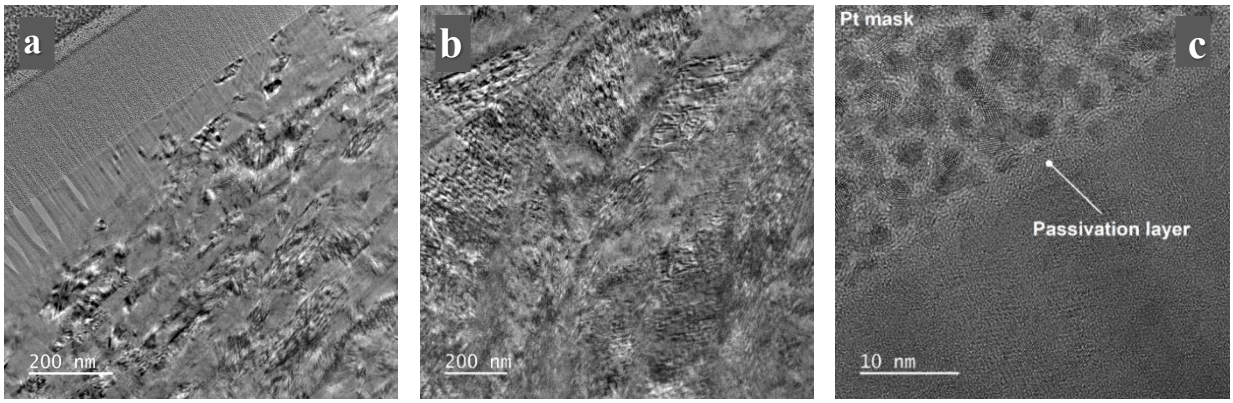

Fig. 4 Detail view of a sample 1 microstructure: near the surface (a), approximately 2.2 μm below the turned surface (b), passivation layer (c).

A detail view of a sample 1 and sample 6 microstructure at different distances from the turned surface is shown on Fig. 4 and Fig. 5. The microstructure analysis showed a significant deformation region below the turned surface. Both samples had deformed grains near the turned surface, with the grain size of approximately 50 to 70 nm in the direction perpendicular to the surface. With increasing distance from the surface, the grain size increased, but they still had a deformation character. In the case of sample 6, the microstructure was affected to a greater depth compared to sample 1. With increasing distance from the surface, an increased density of deformation twins can be observed (Fig. 4b, Fig. 5b). Wu et al. [14] found that the highest density deformation bands and band intersections are located in the region of 3-5 μm from the milled surface. In Fig. 4c, a thin layer can be observed on sample 1 under the platinum mask. The layer is continuous and it is probably a passivation layer. The thickness of the passivation layer was measured 10 times and the average thickness was 2.5 nm ± 0.3 nm. In the case of sample 6, an insignificant passivation layer was observed under the platinum mask compared to sample 1. High-resolution images (Fig. 5c) document a continuous passivation layer on the surface of sample 6 at a different location. The measured passivation layer thickness in Fig. 5c was in the range of 1.8 to 3.1 nm. The average passivation layer thickness was 2.5 ± 0.5, which is the same as in sample 1.

Solution of the electron diffraction pattern (Fig. 6b), we identified ε-martensite in deformed zone. Wu et al. [14] in AISI316L steel, which was milled, did not identify martensite in the whole deformation layer.

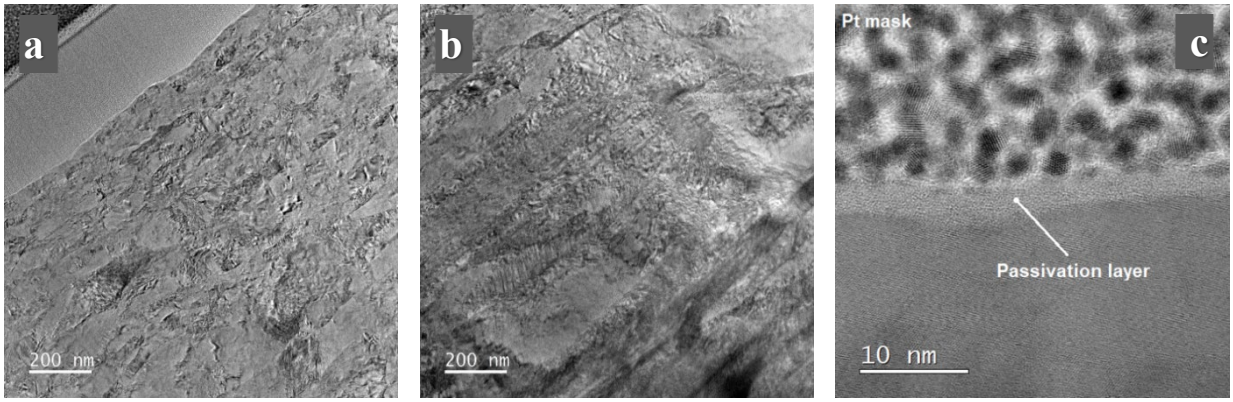

Fig. 5 Detail view of a sample 6 microstructure: near the surface (a), approximately 3.8 μm below the turned surface (b), passivation layer (c).

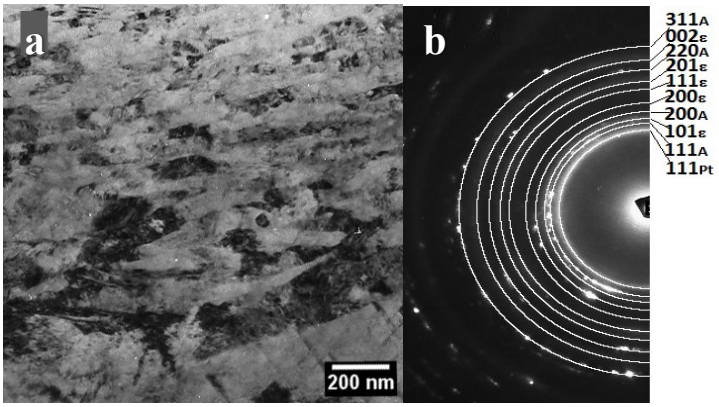

Fig. 6 Microstructure of sample 1 (a), electron diffraction pattern of ε-martensite, Pt- platinum mask, A-austenite (b).

Summary

Based on the results, we can make the following conclusions:

- No significant changes were observed by light microscopy between samples 1 to 6. In addition to annealing twins, deformation twins were also present in the austenitic grains.

- Samples 1 and 2, which had the lowest roughness, showed a microhardness close to the turned surface of around 340HV.
- In the case of samples 3 to 6, the microhardness did not change (370 HV) even though the samples had different roughness.
- TEM observed microstructure to a depth of 5 μm from the turned surface, which we could not observe by light microscopy. The grains showed a significant deformation structure. The grain sizes were around 50-70 nm in the direction perpendicular to the surface. In the case of sample 6, significant deformed grains were observed to a greater depth.
- By electron diffraction, ε-martensite was identified in deformed zone.
- Both samples had approximately 2.5 nm thick passivation layer on the turned surface.
- In the case of sample 6, which was turned at a cutting speed of 250 m/min and a feed of 0.3 mm/rev, the passivation layer was discontinuous. Sample 6 will likely be less corrosion resistant compared to sample 1.

Acknowledgment

This work was supported by the Slovak Research and Development Agency under the Contract no. APVV-22-0146.

References

[1] W. Zhang, K. Fang, Y. Hu, S. Wang, X. Wang, Corros. Sci., 108 (2016) 173-184.

[2] S.G. Acharyya, A. Khandelwal, V. Kain, A. Kumar, I. Samajdar, Mater. Charact., 72 (2012) 68-76.

[3] P.L. Andresen, M.M. Morra, J. Nucl. Mater., 383 (2008) 97-111.

[4] T. Terachi, T. Yamada, T. Miyamoto, K. Arioka, J. Nucl. Mater., 426 (2012) 59-70.

[5] L. de L. e Silva, N. Ducommun, L. Jubin, R. Mainguy, Y. Thebault, E. Andrieu, Ch. Blanc, Corros. Sci., 244 (2025) 112629.

[6] R. Roy, H.J. Qu, K.S. Mao, J.P. Wharry, Scrip. Mater., 262 (2025) 116652.

[7] P.S. Kumar, S.G. Acharyya, S.V.R. Rao, K. Kapoor, Mater. Scien. Engin. A, 687 (2017) 193-199.

[8] Z. Hou, S. Xiu, C. Sun, X. Zou, Y. Yao, J. Mat. Resear. and Techn., 25 (2023) 2890-2902.

[9] A. Turnbull, K. Mingard, J.D. Lord, D.R. Tice, K.J. Mottershead, N.D. Fairweather, A.K. Bradbury, Corros. Sci., 53 (2011) 3398-3415.

[10] Z. Fan, X. Gong, B. Li, P. Yu, X. Liu, H. Zhou, Y. He, W. Zheng, J. Scien: Advan. Mater. And Devic., 10 (2025) 100842.

[11] J. Lv, H. Luo, Mater. Scien. and Engin.: C, 34 (2014) 484-490.

[12] Ch. Yang, X. Jiang, W. Zhang, X. Wang, Mater. Charac., 194 (2022) 112493.

[13] K.N. Lyon, T.J. Marrow, S.B. Lyon, J. Mater. Proces. Techn., 218 (2015) 32-37.

[14] T. Wu, Ch. Liu, L. Chang, H. Wang, L. Zhang, X. Zhou, MTLA, 31 (2023) 101866.

Published in: Defect and Diffusion Forum
ISSN: 1662-9507, Vol. 448, pp 125-130
doi:10.4028/p-gmBT5y

Submitted: 2025-05-09
Revised: 2025-12-05
Accepted: 2025-12-19
Online: 2026-03-03

Microstructure and Hardness Distribution of Laser Powder Bed Fusion-Produced AISI 2507 Super Duplex Stainless Steel

Mengistu Jemberu Dagnaw[1,a*], Zbigniew Brytan[1,b], Dominik Cimbala[2,c], Vladimir Simkulet[2,d] and Sichale Worku Fita[1,e]

[1]Silesian University of Technology, Faculty of Mechanical Engineering, Department of Engineering Materials and Biomaterials, ul. Konarskiego 18a, 44-100, Gliwice, Poland

[2]Faculty of Manufacturing Technologies of the Technical University of Košice with the seat in Prešov, Bayerova 1, 080 01, Prešov, Slovakia

[a*]Mengistu.Jemberu.Dagnaw@polsl.pl, [b]zbigniew.brytan@polsl.pl, [c]dominik.cimbala@tuke.sk, [d]vladimir.simkulet@tuke.sk, [e]sichale.fita@polsl.pl

Keywords: SDSS, AISI 2507, LPBF, Microstructure, Hardness Distribution.

Abstract. This study investigated the impact of as-printed and heat-treated additively produced 2507 super duplex stainless steel (also known as SDSS) on microstructure and hardness distribution. Optical microscopy was used to examine the phase transformations of the steel during the as-printed (untreated) and solution-annealed treatment stages of samples. The relationship between microstructure and hardness distribution (center and edge) was studied. Because the LPBF process cools rapidly, the SDSS shows that the main phase in as-printed samples is ferrite, with 5 % austenite. The fully balanced microstructure is forming when the solution annealing is performed, with austenite content about 52 %. The hardness of SDSS is strictly related to the material microstructure, where the fully ferritic structure shows higher hardness 50.16–46.18 HRC, while the balanced duplex microstructure reveals lower values 34.58–32.26 HRC.

Introduction

Additive manufacturing (AM) is expanding rapidly, particularly for metallic components with defined geometries and mechanical properties. It enables efficient production of prototypes, customized parts, and digital spare part inventories. Research focuses on improving 3D printing techniques for better precision and cost-effectiveness [1, 2].

Duplex stainless steels (DSS), containing nearly equal ferrite and austenite phases, exhibit superior corrosion resistance and higher strength than austenitic steels. Super-DSS, with increased alloying, are suited for harsh environments such as marine and petrochemical sectors, offering material savings due to their strength. Although DSSs have been used for decades, their complex processing and high costs drive interest in AM, which remains underdeveloped for Super-DSS despite rising demand. DSS is also valued for its recyclability and low environmental impact [3, 4].

The development of AM-grade Super-DSS 2507 (EN 1.4410) reflects growing interest, though its properties and heat treatment protocols are not well established [5]. Therefore, further investigation of structure–property relations in AM DSS is necessary.

Hardness is commonly used to assess mechanical properties due to its simplicity and correlation with strength [6] and wear resistance [7]. Unlike yield strength, which is sensitive to internal defects, micro-hardness reflects actual microstructural features, such as phase distribution and grain size, both influenced by AM parameters.

Most studies report hardness in the as-fabricated state, allowing insight into how AM conditions affect properties before post-processing. Fast thermal cycles often prevent equilibrium microstructures. Comparing data across studies helps evaluate the impact of AM methods and alloy selection on hardness [8].

While previous reviews address mechanical properties [9–12], microstructures [13, 14], AM methods [15–20], and alloys [9, 11], a systematic assessment of processing microstructure property relationships is still needed. This work compiles hardness data across various alloys to analyze the

effects of cooling rate, composition, and post-processing, supporting optimal material and process selection in AM).

Materials and Methods

Super duplex stainless steel, grade 2507 (EN 1.4410), produced by Sandvik Osprey Ltd., with the chemical composition given in Table 1, was utilized to fabricate rectangular samples for the Charpy impact test (10x10x55 mm) by the laser beam powder bed fusion (L-PBF) method. The 2507 powder is a gas-atomized material having particle sizes between 15 and 45 μm.

Table 1 Chemical composition of AISI 2507 super duplex stainless-steel powder [wt. %].

Elements	Fe	Cr	Ni	Mo	Mn	Si	N	Cu	C	P	S	O
[wt. %]	Bal.	24.44	9.11	3.68	0.38	0.29	0.30	0.14	0.016	0.023	0.001	0.017

The L-PBF printing process utilized an AM125 RENISHAW printer equipped with a Yb fiber laser, with a maximum power of 200 W, a scanning speed of 2,000 mm/s, and a wavelength of 1.074 nm. The components were produced on a mild steel platform in an argon inert gas environment with an oxygen concentration below 10 ppm. A meander scanning approach was employed, with a rotation of 67° after the application of each layer. The employed printing settings were laser power P = 180 W, hatch distance h = 120 μm, layer thickness t = 30 μm, and scan speed V = 300 mm/s. The energy density of the applied parameters was computed using the formula $Ed = P/(V \cdot h \cdot t)$ J/mm³, resulting a value of 166 J/mm³.

The DSS investigated in this research underwent post-processing heat treatment, and two conditions were examined:

- As printed, without any further post processing (AS),
- Solution annealing at 1100 °C/15 min, rapid cooling in water (SA).

X-ray diffraction (XRD) patterns were collected using an X-Pert PRO instrument. For the X-ray diffraction analysis, a Co target, and a scan rate of 0.01 step/s and a scan range for 2θ between 30 to 110° were used. The X'Pert HighScore Plus was used for phase identification and quantitative analysis.

Metallography was performed using a 4K digital microscope (Keyence VHX-7000). Samples were ground, polished, and etched in 10 % oxalic acid (3–6 V, 5–60 s).

Hardness was measured using a CV Instruments CV400DAT tester (HRA, HRC) on surface and cross-sectional areas. Vickers microhardness (HV0.1, 100 gf, 15 s) was used to assess the hardness profile. Additional HRC values were obtained using an Insize ISH-RSR400 Rockwell tester (max. 1471 N, 0–60 s load delay).

Results and Discussion

Microstructure Analysis. Due to the rapid cooling inherent in the LPBF process, the as-printed SDSS samples exhibit a predominantly ferritic microstructure (Fig. 1). X-ray diffraction confirms strong ferrite peaks Fe-α (110), (200), (211) and a weak austenite peak Fe-γ (111). After solution annealing, a balanced duplex structure is achieved, with clear austenite peaks including Fe-γ (111), (200), (220), (311), and (222), indicating the coexistence of both phases. The austenite fraction increases to approximately 52 % after annealing.

Figure 2 shows the microstructure evolution. In the as-printed state, the microstructure is mostly ferritic with minor austenite at ferrite grain boundaries. Typical defects, such as partially unmelted powder particles, are present. Ferrite grains are elongated along the build direction (Fig. 2a). After annealing, a near-equilibrium duplex structure forms, where ferritic grains are interspersed with grain boundary austenite and intragranular Widmanstätten austenite (Fig. 2b).

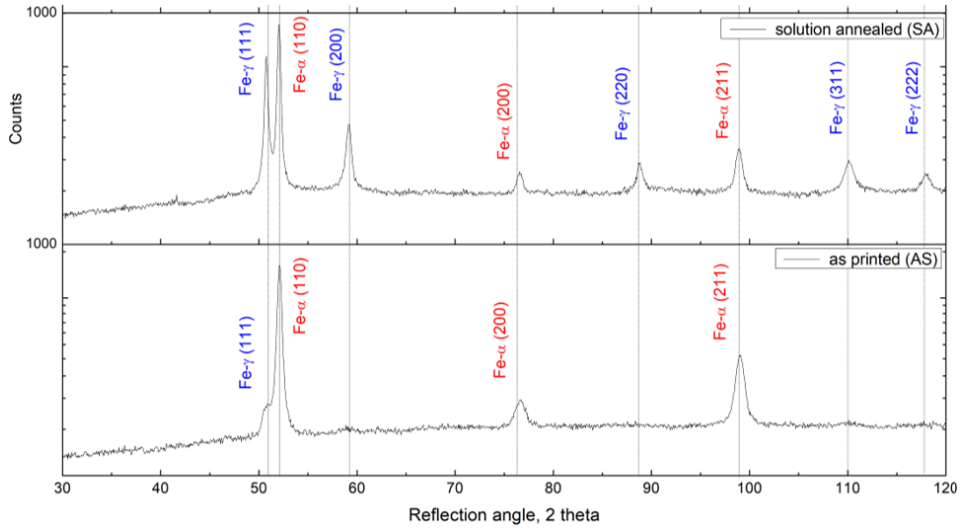

Fig. 1 X-ray diffraction patterns for the as printed and solution annealed samples.

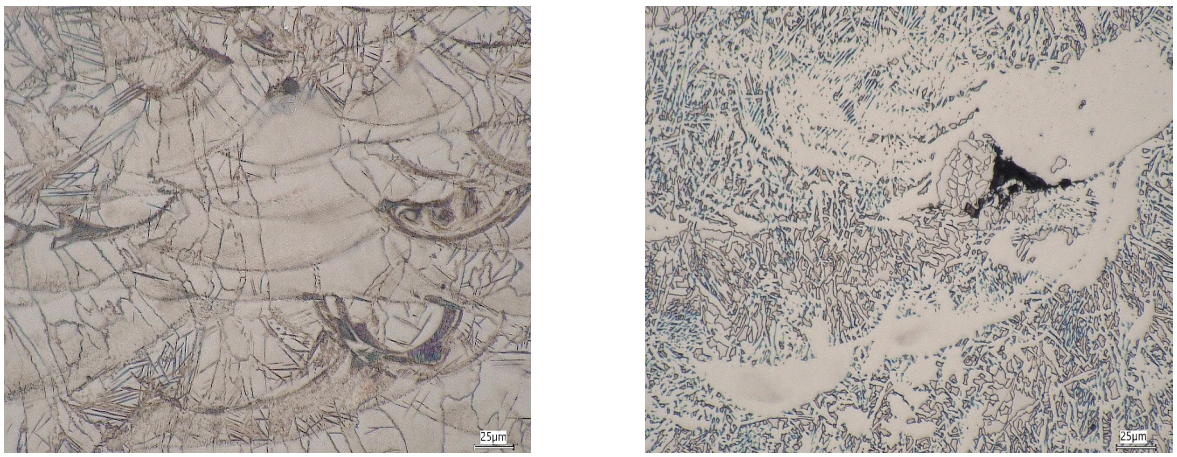

(a) As printed (b) Solution annealed

Fig. 2 Light optical microscope microstructure of SDSS (transverse to build direction XZ).

Hardness Evaluation. Hardness measurements of printed SDSS samples revealed comparable values for both surface and core regions (Table 2). In the as-printed (AS) state, hardness ranged from approximately 50.16 to 46.18 HRC, decreasing to 34.58–32.26 HRC after solution annealing (SA). The elevated surface hardness in the AS condition aligns with previous findings on LPBF-fabricated duplex and super duplex stainless steels, attributed to rapid solidification, high dislocation density, and fine microstructures induced by repeated laser scanning [21]. Additionally, layer-by-layer thermal cycling introduces localized residual stresses and uneven phase distributions, further contributing to surface hardening [22]. Slightly lower core hardness indicates a more thermally stabilized duplex microstructure due to prolonged exposure during processing [23]. Solution annealing significantly reduced hardness by relieving internal stresses, decomposing metastable phases (such as ferrite/martensite), and promoting a reversion to the thermodynamically stable austenite–ferrite duplex structure [24]. A notable difference in hardness between edge and center regions was observed in the as-printed samples, with higher values at the edge. This variation results from microstructural gradients driven by rapid solidification and thermal history [25]. Solution annealing mitigated this disparity, leading to a more uniform hardness distribution and refined microstructure [26]. Vickers hardness measurements across the cross-section (Fig. 3) followed a similar trend. In the AS state, values ranged from 320 to 470 HV0.1, reflecting significant microstructural inhomogeneities caused by localized residual stresses, thermal gradients, and phase imbalances [27]. In contrast, SA samples exhibited lower and more uniform values (250–320 HV0.1), indicating microstructural homogenization and stress relief [28]. The pronounced reduction in edge

hardness after annealing confirms the influence of rapid cooling and residual stresses in the initial hardening. Overall, SDSS hardness strongly correlates with microstructure: fully ferritic structures are harder, while balanced duplex structures resulting from annealing are comparatively softer.

Table 2 Hardness of LPBF-produced SDSS under two different specimen conditions.

Sample conditions	Surface hardness		Core hardness		Hardness from edge-to-center	
	HRC	SD*	HRC	SD	HV0.1	SD*
As printed (AS)	50.16	5.30	46.18	4.11	407.71	25.75
Solution annealed (SA)	34.58	0.97	32.26	1.67	232.91	34.49

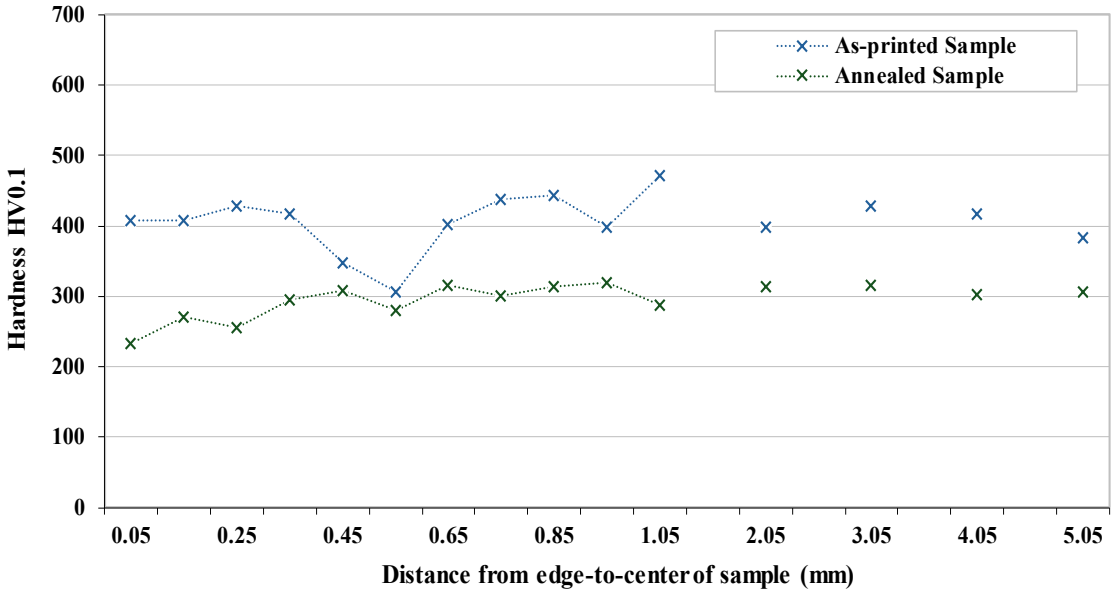

Fig. 3 Hardness distribution from the edge to center of samples.

Conclusions

Heat treatment was tested on L-PBF-printed super duplex stainless steel 2507 microstructure and hardness. The following conclusions from the results can be drawn:

- When 2507 SDSS is printed, its microstructure is mostly ferritic, with about 5 % weak austenite at the ferrite grain boundaries. SDSS exhibits a balanced microstructure with 52 % austenite after solution annealing. Austenite is equally distributed in ferritic grains' edges, gaps, and Widmanstätten laths.
- The printed SDSS showed almost consistent core and surface hardness values. As-printed specimens are 50.16–46.18 HRC, but post-solution annealing reduces them to 34.58–32.26 HRC. The balanced duplex microstructure (SA) is softer than the fully ferritic structure, which is harder.

Acknowledgment

This work was supported by the Slovak Research and Development Agency under contract No APVV-20-0514.

References

[1] Y. Bai, C. Zhao, J. Yang, R. Hong, C. Weng, H. Wang, Microstructure and machinability of selective laser melted high-strength maraging steel with heat treatment, J. Mater. Process. Technol., 288 (2021) 116906.

[2] Y. Kaynak, O. Kitay, Porosity, surface quality, microhardness and microstructure of selective laser melted 316L stainless steel resulting from finish machining, J. Manuf. Mater. Process., 2 (2018) 36.

[3] J. Charles, P. Chemelle, The history of duplex developments, nowadays DSS properties and duplex market future trends, World Iron Steel, 6 (2011) 1-21.

[4] J. Charles, P. Chemelle, The history of duplex developments, nowadays DSS properties and duplex market future trends, World Iron Steel, 1 (2012) 46-57.

[5] Osprey® 2507 super-duplex stainless steel for additive manufacturing, Datasheet, Available: https://www.additive.sandvik/en/super-duplex/super-duplex-powder-for-additive-manufacturing/.

[6] J.S. Keist, T.A. Palmer, Development of strength-hardness relationships in additively manufactured titanium alloys, Mater. Sci. Eng. A, 693 (2017) 214-224.

[7] H. Attar, S. Ehtemam-Haghighi, D. Kent, I.V. Okulov, H. Wendrock, M. Bönisch, A.S. Volegov, M. Calin, J. Eckert, M.S. Dargusch, Nanoindentation and wear properties of Ti and Ti-TiB composite materials produced by selective laser melting, Mater. Sci. Eng. A, 688 (2017) 20-26.

[8] J.S. Zuback, T. DebRoy, The hardness of additively manufactured alloys, Materials, 11 (2018) 2070.

[9] F. Cao, T. Zhang, M.A. Ryder, D.A. Lados, A review of the fatigue properties of additively manufactured Ti-6Al-4V, JOM, 70 (2018) 349-357.

[10] Y. Kok, X.P. Tan, P. Wang, M. Nai, N.H. Loh, E. Liu, S.B. Tor, Anisotropy and heterogeneity of microstructure and mechanical properties in metal additive manufacturing: A critical review, Mater. Des., 139 (2018) 565-586.

[11] D. Agius, K.I. Kourousis, C. Wallbrink, A review of the as-built SLM Ti-6Al-4V mechanical properties towards achieving fatigue resistant designs, Metals, 8 (2018) 75.

[12] S.M. Yusuf, N. Gao, Influence of energy density on metallurgy and properties in metal additive manufacturing, Mater. Sci. Technol., 33 (2017) 1269-1289.

[13] M. Easton, M. Qian, A. Prasad, D. StJohn, Recent advances in grain refinement of light metals and alloys, Curr. Opin. Solid State Mater. Sci., 20 (2016) 13-24.

[14] P. Collins, D. Brice, P. Samimi, I. Ghamarian, H. Fraser, Microstructural control of additively manufactured metallic materials, Annu. Rev. Mater. Res., 46 (2016) 63-91.

[15] K. Derekar, A review of wire arc additive manufacturing and advances in wire arc additive manufacturing of aluminium, Mater. Sci. Technol., 34 (2018) 1-22.

[16] H. Shipley, D. McDonnell, M. Culleton, R. Lupoi, G. O'Donnell, D. Trimble, Optimisation of process parameters to address fundamental challenges during selective laser melting of Ti-6Al-4V: A review, Int. J. Mach. Tools Manuf., 128 (2018) 1-20.

[17] L. Hitzler, M. Merkel, W. Hall, A. Öchsner, A review of metal fabricated with laser-and powder-bed based additive manufacturing techniques: Process, nomenclature, materials, achievable properties and its utilization in the medical sector, Adv. Eng. Mater., 20 (2018) 1700658.

[18] L.C. Zhang, Y. Liu, S. Li, Y. Hao, Additive manufacturing of titanium alloys by electron beam melting: A review, Adv. Eng. Mater., 20 (2018) 1700842.

[19] B. Song, X. Zhao, S. Li, C. Han, Q. Wei, S. Wen, J. Liu, Y. Shi, Differences in microstructure and properties between selective laser melting and traditional manufacturing for fabrication of metal parts: A review, Front. Mech. Eng., 10 (2015) 111-125.

[20] N. Shamsaei, A. Yadollahi, L. Bian, S.M. Thompson, An overview of Direct Laser Deposition for additive manufacturing; Part II: Mechanical behaviour, process parameter optimization and control, Addit. Manuf., 8 (2015) 12-35.

[21] B. Wu, Z. Pan, D. Ding, D. Cuiuri, H. Li, J. Norrish, A review of the wire arc additive manufacturing of metals: Properties, defects and quality improvement, J. Manuf. Process., 35 (2018) 127-139.

[22] S. Gorsse, C. Hutchinson, M. Gouné, R. Banerjee, Additive manufacturing of metals: A brief review of the characteristic microstructures and properties of steels, Ti-6Al-4V and high-entropy alloys, Sci. Technol. Adv. Mater., 18 (1) (2017) 584-610.

[23] Karlsson, M. Thuvander, S. Wessman, Microstructural evolution and mechanical performance of super duplex stainless steel produced by laser powder bed fusion, Mater. Des., 192 (2020) 108728.

[24] Z. Sun, X. Tan, S.B. Tor, W.Y. Yeong, Selective laser melting of stainless steel 316L with low porosity and high build rates, Mater. Des., 104 (2019) 197-204.

[25] J.S. Zuback, T. DebRoy, The hardness of additively manufactured alloys, Materials, 11 (2018) 2070.

[26] H. Li, J. Ma, G. Li, W. Zhang, X. Bao, Y. Shi, Effect of solution annealing time on the microstructure and mechanical properties of selective-laser-melted 2205 duplex stainless steel, Crystals, 14 (2024) 229.

[27] J. Karlsson, M. Thuvander, S. Wessman, Microstructural evolution and mechanical performance of super duplex stainless steel produced by laser powder bed fusion, Mater. Des., 192 (2020) 108728.

[28] Z. Sun, X. Tan, S.B. Tor, W.Y. Yeong, Selective laser melting of stainless steel 316L with low porosity and high build rates, Mater. Des., 104 (2016) 197-204.

CHAPTER 4:

Welding

Published in: Key Engineering Materials
ISSN: 1662-9795, Vol. 1046, pp 27-33
doi:10.4028/p-N5Ea4h

Submitted: 2025-05-31
Revised: 2025-12-05
Accepted: 2025-12-19
Online: 2026-03-16

Microstructure Characterization of a Dissimilar 14MoV6-3/T91 Weld after Long-Term Service Exposure at 580 °C

Vlastimil Vodárek[1,a*], Renáta Palupčíková[1,b] and Petra Váňová[1,c]

[1]Department of Materials Engineering and Recycling, Faculty of Materials Science and Technology, VŠB-Technical University of Ostrava, 17. listopadu 15, Ostrava-Poruba, Czech Republic

[a*]vlastimil.vodarek@vsb.cz, [b]renata.palupcikova@vsb.cz, [c]petra.vanova@vsb.cz

Keywords: Dissimilar Ferritic Welds, Microstructural Stability, Precipitation, Hardness, Degradation.

Abstract. Applications of advanced heat resistant ferritic steels in boiler repairs require detailed information on the creep behaviour of welds made of various combinations of steels. The paper deals with the results of hardness and microstructure characterization of a dissimilar circumferential weld of 14MoV6-3 and P91 tubes after about 10 years of service exposure in a boiler operated at 580 °C and steam pressure of 10.3 MPa. The P91 tube (ϕ38x4 mm) was welded to the 14MoV6-3 tube (ϕ38x6.3 mm) using the GTAW (141) technology. Bőhler-FOX IN 9-IG (3Cr0.5Mo0.3V) wires were applied as a filler material. Microhardness evaluation after long-term service exposure revealed two carburized zones, values in these zones did not exceed 350 HV0.5. The slowdown of recrystallization in partially decarburized areas of the 14MoV6-3 and the WM suppressed the formation of soft ferritic bands along fusion lines. This phenomenon is related to the high thermodynamic stability of V(C,N) particles in vanadium-bearing low alloy heat resistant ferritic steels at temperatures below 600 °C.

Introduction

Very complex manufacturing and repair practices in power boilers require to use components made from different steels. In components that have to operate for long times periods in the creep regime, welds between different ferritic steels introduce a number of challenges [1, 2]. In replacement of tube sections, the designer may benefit from higher allowable stress values and better steam-side and fire-side corrosion resistance of advanced (9–12) % Cr martensitic steels. Although many combinations exist for ferritic heterogeneous welds there is no standard approach to the design of these welds in the power generation industry [2]. The most important degradation mechanism in heterogeneous welds during their exposure in the creep regime is the redistribution of interstitial elements in the direction of their chemical potential/activity gradients.

There are three basic concepts for the design of heterogeneous ferritic butt welds between low Cr and high Cr base materials [2]:

- Filler metal matches to the lower alloy material. In this case the critical area is the fusion line between the high Cr base material and the lower Cr filler material. On the opposite side of this weld there is only a low driving force for significant microstructure changes.
- Filler metal matches to the higher alloy material. The fusion line between the low Cr base material and the weld metal is of special importance. The matching chemistry on the opposite side of the weld will result in similar microstructures and a low driving force for microstructure changes.
- In the case of filler material with an intermediate Cr content there will be a gradient of chemical composition at both fusion lines. The rate of interstitial redistribution will depend on the difference in thermodynamic activities of these elements across the weld. These are not only a function of the Cr content but also of other alloying elements.

The main goal of this contribution is to describe microstructure and property changes in a 14MoV6-3/T91 butt circumferential weld made using an intermediate Cr filler material. The replacement of the low alloy steel 14MoV6-3 with T91 steel made it possible to reduce the wall thickness of the tube. The repair weld was tested in a steam boiler at a temperature of 580 °C for about 95,000 hours.

Experimental Material

The butt circumferential weld between 14MoV6-3 and T91 tubes was manufactured by using TIG (141) welding technology with a Bőhler-FOX IN 9-IG (3Cr0.5Mo0.3V) as the filler material. The dimensions of the 14MoV6-3 and T91 tubes were ϕ38x6.3 mm and ϕ38x4 mm, respectively. The quality heat treatment of both base materials consisted of normalizing followed by tempering at 730–750 °C.

In the weld under study it can be expected:

- carbon diffusion from 14MoV6-3 steel into the weld metal (WM), resulting in the formation of a partly decarburized area in the coarse-grained heat affected zone (CG HAZ) of 14MoV6-3 steel and a carburized area in the WM adjacent to the fusion line.
- carbon redistribution from the WM into T91 steel accompanied by the formation of a partially decarburized zone in the WM and a carburized area in the WM/T91 fusion zone.

Figure 1 shows the schema of the heterogeneous weld investigated. The chemical compositions of the base materials are shown in Table 1. The field post weld heat treatment (PWHT) regime was 740 °C/1 hour/air.

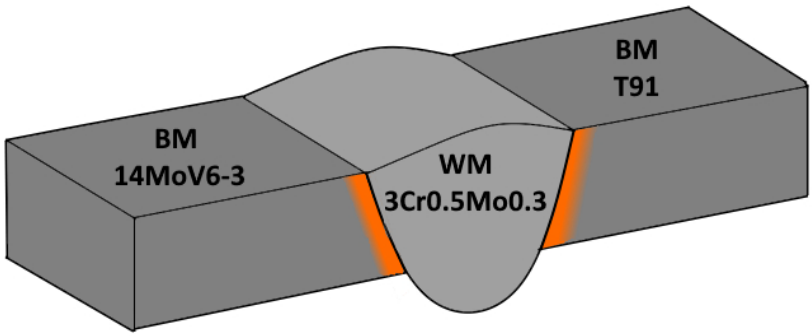

Fig. 1 Schema of the heterogeneous ferritic weld investigated; orange bands represent areas of carbon redistribution.

Table 1 Chemical compositions of base materials, wt. %.

Grade	C	Si	Mn	Cr	Mo	V	Nb
14MoV6-3	0.11	0.26	0.56	0.63	0.51	0.28	-
T91	0.11	0.32	0.73	8.94	0.93	0.21	0.08

The microstructure of the weld was studied after service exposure in a power plant boiler at a temperature of 580 °C and steam pressure of 10.3 MPa for about 95,000 hours. The microhardness profile across the weld was evaluated. Microstructure characterization was carried out using light microscopy (LM) and transmission electron microscopy (TEM). Carbon extraction replicas were prepared for minor phase identification in critical parts of the weld. Identification of minor phases was performed using electron diffraction (SAED) and energy dispersive X-ray (EDX) microanalysis.

Results and Discussion

Figure 2 shows the longitudinal section through the weld. The macroetch assessment did not reveal creep defects in any part of the weldment. The profile of HV0.5 microhardness across the weld is shown in Fig. 3. The WM was harder than both base materials (BM). Microhardness measurement was performed in the middle thickness of the weld with a step of 1 mm. The HV0.5 microhardness of the WM is higher than that in both base materials. The CG HAZ of the T91 tube exhibits the highest microhardness level. Microhardness in the HAZ of 14MoV6-3 steel is significantly higher than that in the BM.

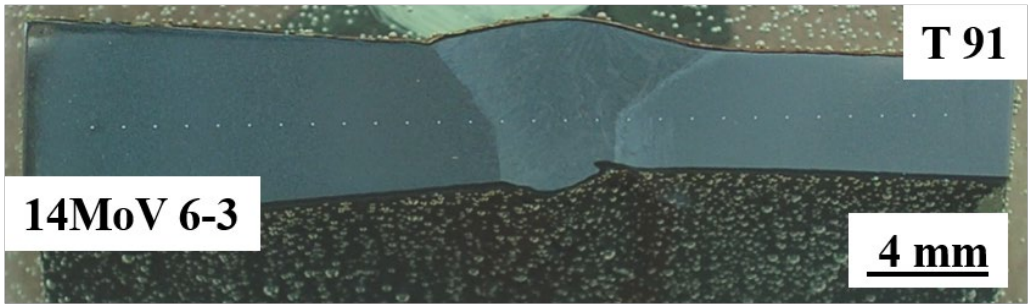

Fig. 2 Longitudinal section through the weld; indents of microhardness in the middle thickness.

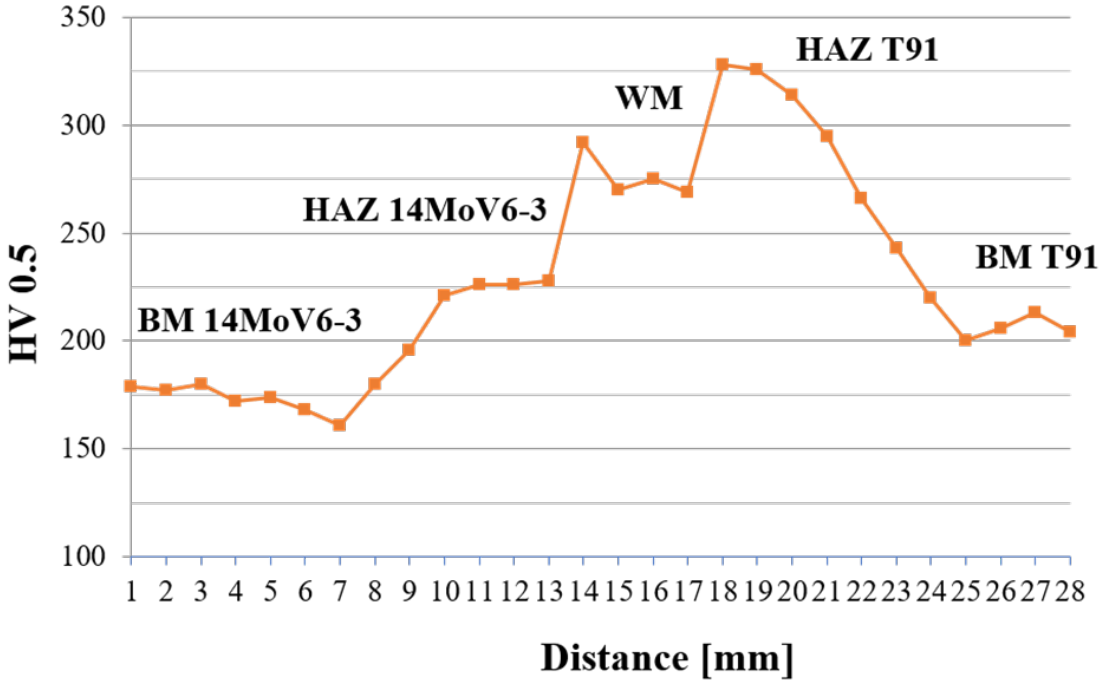

Fig. 3 Microhardness HV0.5 profile across the weld; see Fig. 2.

The step of the line profile was not fine enough to reveal local changes in microhardness. Therefore, five HV0.5 measurements were carried out in the basic parts of the weldment. Results shown in Table 2 prove the existence of two carburized areas. Despite the fact that in the CG HAZ of 14MoV6-3 steel partial decarburization took place during the PWHT and service exposure, the microhardness level in this area is higher than that in the 14MoV6-3 BM.

Table 2 HV0.5 microhardness values across the weld.

Area	HV0.5 ± STD
BM 14MoV6-3	186 ± 18
CG HAZ 14MoV6-3	252 ± 25
Carburized WM	337 ± 17
WM	301 ± 13
Decarburized WM	253 ± 5
CG HAZ P91	348 ± 10
BM P91	224 ± 11

Microstructure of the 14MoV6-3 BM was formed by a mixture of bainite and ferrite (Fig. 4). TEM analysis revealed heavy precipitation. Two minor phases were identified: cementite and V(C,N). Precipitation strengthening of this steel is mainly controlled by the precipitation of the MX phase, where M is vanadium and X can be carbon and/or nitrogen [3–5]. Fig. 5 shows that particles of V(C,N) were relatively coarse – up to 150 nm. Such microstructure corresponds to the low level of the 14MoV6-3 BM microhardness reported in Table 2. In the fine grained (FG) part of the HAZ the fraction of ferrite in the ferritic-bainitic microstructure was significantly lower than that in the BM. In the CG HAZ the microstructure was fully bainitic. The thermal cycle during welding resulted in partial or full dissolution of precipitates that were present in the BM after quality heat treatment. Re-precipitation processes occurred in the HAZ during the PWHT and the long-term service exposure. The service exposure was significantly lower than the tempering temperature during the quality heat treatment. V(C,N) particles in the HAZ were much finer than those in the BM not affected by welding (Fig. 6). Higher hardness in the 14MoV6-3 HAZ as compared to the BM can be explained by different products of austenite decomposition and differences in precipitation of V(C,N) particles. Recovered bainite was present in the CG HAZ up to the fusion line (Fig. 7). This means that partial decarburization of 14MoV6-3 steel did not result in dissolution of most precipitates and the formation of a band of soft ferrite along the fusion line as it is typical for 2.25CrMo steels [1].

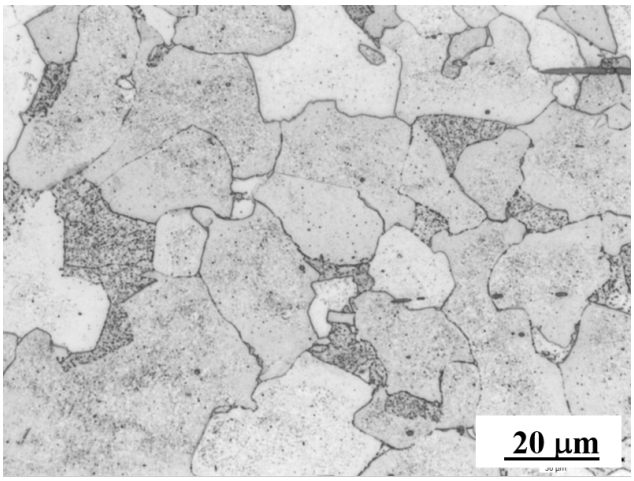

Fig. 4 Microstructure of the 14MoV6-3 BM: a mixture of ferrite and bainite.

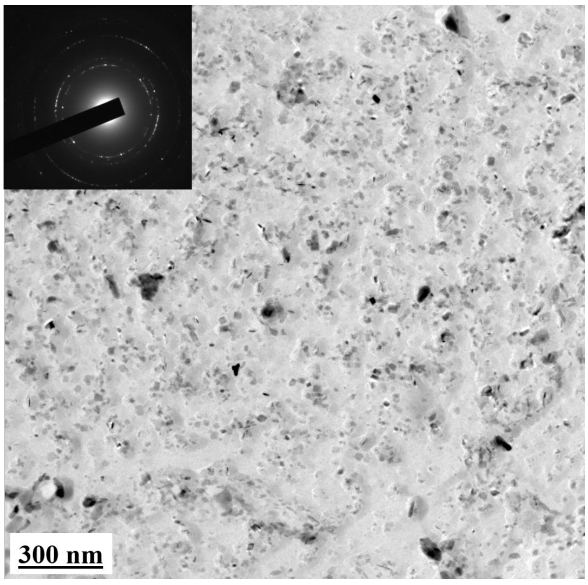

Fig. 5 Typical distribution and size of V(C,N) particles in bainite of the 14MoV6-3 BM; insert: ring diffraction pattern of V(C,N).

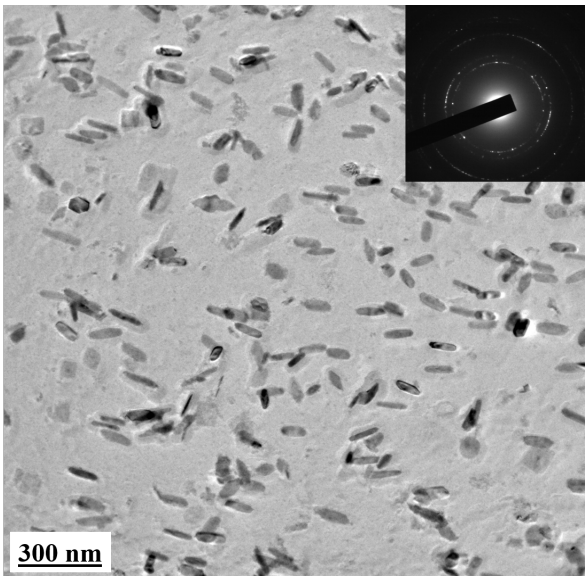

Fig. 6 Typical distribution and size of V(C,N) particles in bainite of the HAZ in 14MoV6-3 steel, insert: ring diffraction pattern of V(C,N).

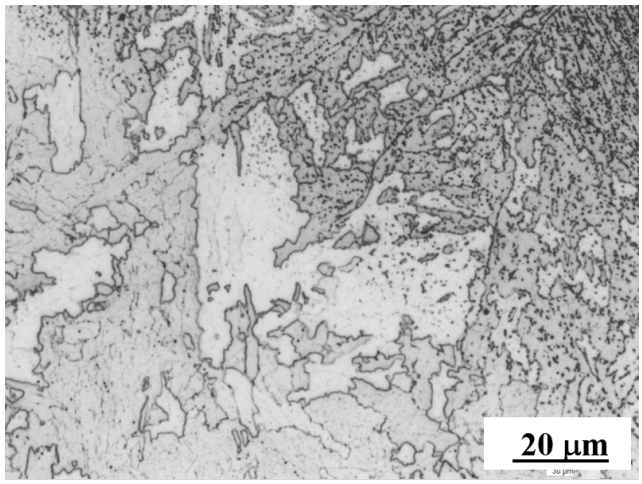

Fig. 7 Recovered bainite in the partially decarburized CG HAZ of 14MoV6-3 steel along the fusion line.

TEM study revealed that in the CG HAZ of 14MoV6-3 steel particles of cementite dissolved but V(C,N) particles were preserved. Fig. 8 shows precipitation of fibre-like V(C,N) particles along the fusion line. These particles probably formed during austenite decomposition in the weld by the mechanism of interphase precipitation. Detail of these particles is shown in Fig. 9. Partial decarburization of the CG HAZ during long-term service exposure at 580 °C did not result in their dissolution.

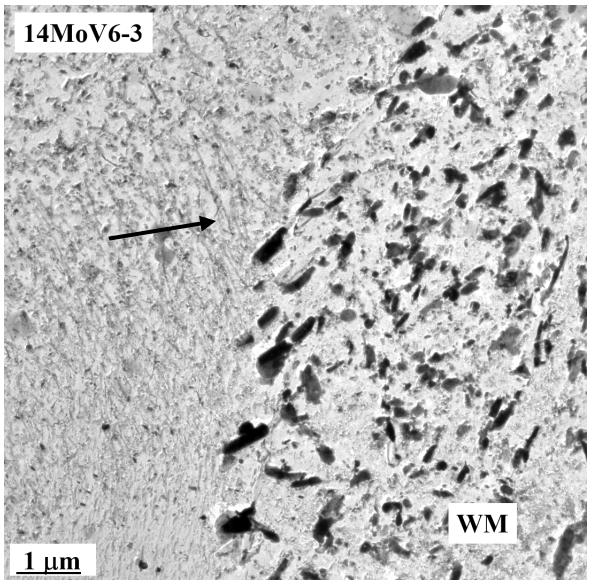

Fig. 8 Precipitation along the 14MoV6-3/WM fusion line; an arrow shows fiber-like V(C,N) particles in the CG HAZ.

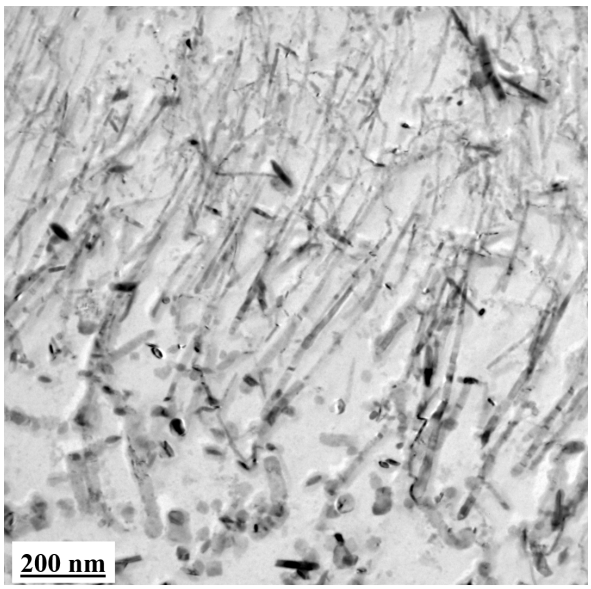

Fig. 9 Detail of fiber-like V(C,N) particles along the 14MoV6-3/WM fusion line.

In the carburized zone of the WM heavy precipitation of $M_{23}C_6$ and V(C,N) particles was present. The microstructure of the WM consisted of tempered bainite. The PWHT and the service exposure at 580 °C resulted in the precipitation of $M_{23}C_6$ and V(C,N) particles in bainitic ferrite. Fig. 10 shows the microstructure of the WM/T91 fusion zone and the surrounding partly decarburized WM.

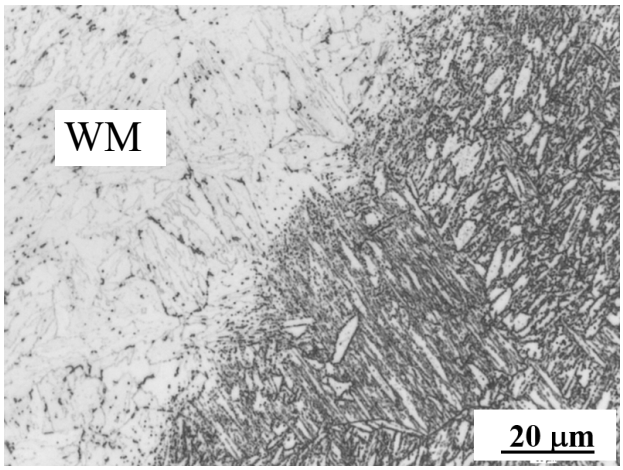

Fig. 10 Microstructure along the WM/T91 fusion line.

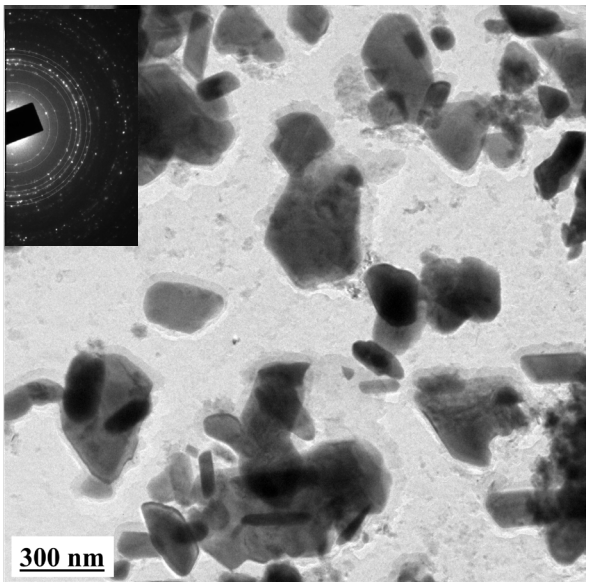

Fig. 11 Heavy precipitation in the carburized zone of the WM/T91 fusion zone, insert: ring diffraction pattern of $M_{23}C_6$.

The microstructure of the partially decarburized zone of the WM consisted of recovered bainite. Grain boundaries were decorated by coarse precipitates. The microstructure of the fusion zone was formed by tempered bainite with a heavy precipitation of $M_{23}C_6$ particles (EDX in wt.%: 62 Cr, 33 Fe, 5 Mo) and a smaller fraction of V(C,N) particles (Figs. 10 and 11). The carburization process in heterogeneous welds mainly takes place in the concentration gradient of solutes in the fusion zone [6]. The microstructure of the T91 tube, which was not affected by welding, corresponded to tempered martensite. Precipitates in the T91 BM were identified as $M_{23}C_6$ carbides, Laves phase of Fe_2Mo type (EDX in wt.%: 4 Si,7 Cr, 35 Fe, 54 Mo) and VN (EDX in wt.%: 63 V, 13 Cr, 8 Fe, 12 Mo, 4 Nb) phase. The beginning of partial in-situ transformation of VN to modified Z-phase was not observed.

Summary

The results of hardness and microstructural characterization of the 14MoV6-3/3Cr0.5MoV/T91 heterogeneous weld after service exposure in a boiler at a temperature of 580 °C and steam pressure of 10.3 MPa for about 95,000 hours can be summed up as follows:

- Service exposure did not result in the formation of creep defects in any part of the weldment.
- Partial decarburization of 14MoV6-3 steel along the 14MoV6-3/WM fusion line was not accompanied by the formation of a soft ferritic band. Particles of cementite dissolved, but particles of V(C,N) were stable and slowed down the recovery/recrystallization of bainite. Similarly, partial decarburization of the WM along the WM/T91 fusion line did not cause the formation of a ferritic band. The cause of this phenomenon is the high thermodynamic stability of the V(C,N) phase in vanadium-bearing ferritic steels below approximately 600 °C.
- Maximum microhardness in both carburized zones of the weld investigated did not exceed 350 HV0.5.

Acknowledgement

This article was supported by project No.CZ.02.01.01/00/22_008/000463 ′Materials and technologies for sustainable development‘ within the Jan Amos Komensky Operational Program financed by the European Union and the Czech Republic's state budget and the project SP2025/076 ′Material and technological properties of construction materials in relation to their production method, processing and the effect of degradation mechanisms′.

References

[1] Allen, D.J., Creep Performance of Dissimilar P91 to Low Alloy Steel Weldments. In Proceedings of the Power Plant and Renewables; Strang, A. et al., Eds.; IOM: London, UK, 2003; Volume 6, pp. 281-294.

[2] Mayr, P., Schlacher, C., Siefert, J.A., Parker, J.D., Microstructural Features, Mechanical Properties and High Temperature Failures of Ferritic to Ferritic Dissimilar Welds, Int. Mater. Rev., 64 (2018) 1-26, https://doi.org/10.1080/09506608.2017.140943.

[3] Abe, F., Tabuchi, M., Microstructure and Creep Strength of Welds in Advanced Ferritic Power Plant Steels, Sci. Technol. Weld. Join., 9 (2004) 22-30. https://doi.org/10.1179/136217104225017107.

[4] Purmenský, J., Foldyna, V., Prnka, T., Einfluß der Wärmebehandlung auf das Mikrogefüge und die mechanischen Eigenschaften des Stahles 14 MoV63, Stahl und Eisen, 94, 23 (1974) 1155-1160.

[5] Sobotka, J., Prnka, T., Einfluß des Gefügezustandes und der Gefügebeständigkeit auf die Zeitstandfestigkeit niedriglegierten vanadincarbidhaltigen Schweißgutes, Arch. Eisenhüttenwes, 45, 9 (1974) 629-634.

[6] Vodárek, V., Holešinský, J., Kuboň, Z., Palupčíková, R., Váňová, P., Malcharcziková, J., Creep Resistance and Microstructure Evolution in P23/P91Welds, Materials, 18 (2025) 194. https://doi.org/10.3390/ma18010194.

Published in: Key Engineering Materials
ISSN: 1662-9795, Vol. 1046, pp 35-40
doi:10.4028/p-r2L8v8

Submitted: 2025-06-11
Revised: 2025-12-09
Accepted: 2025-12-19
Online: 2026-03-16

Evaluation of the Operational Degradation of ESW Pipeline Welds

Zuzana Vávrovcová[1,a*], Zbyněk Veselka[1,b] and Jan Bajer[1,c]

[1]ÚJV Řež, a.s., Hlavní 130, Řež, 250 68 Husinec, Czech Republic

[a*]zuzana.vavrovcova@ujv.cz, [b]zbynek.veselka@ujv.cz, [c]jan.bajer@ujv.cz

Keywords: Microbial Corrosion, MIC, Manganese-Oxidizing Microorganisms, MOMO.

Abstract. This study presents the results of both non-destructive (radiography and computed tomography) and destructive (light optical and scanning electron microscopy) evaluations of operational degradation in welded joints of ESW (electroslag welding) pipelines. Microbiologically influenced corrosion (MIC), potentially induced by manganese-oxidizing microorganisms (MOMOs), was investigated as a plausible degradation mechanism. Extensive subsurface corrosion cavities were identified beneath the internal surface of the pipelines. The presence of MnO_2 globules near these cavities supports the hypothesis of MOMO-induced corrosion.

Introduction

Three DN 125 pipeline segments, each containing welded joints and flanges, were submitted for analysis to determine the underlying degradation mechanisms (see Fig. 1). The segments were designated as 'left weld (LS)', 'central weld (SS)', and 'right weld (PS)'. According to the provided specifications, the base material of the flanges and pipes is titanium-stabilized austenitic stainless steel, grade 1.4571 (equivalent to 316Ti), as detailed in Table 1.

The pipeline system transports an aqueous solution devoid of H_3BO_3 for approximately 10–11 months annually. During the remaining period, the system is either stagnant or drained. The pipeline has been in service since 2008, following the replacement of DN200 carbon steel pipes with austenitic stainless steel due to severe surface corrosion.

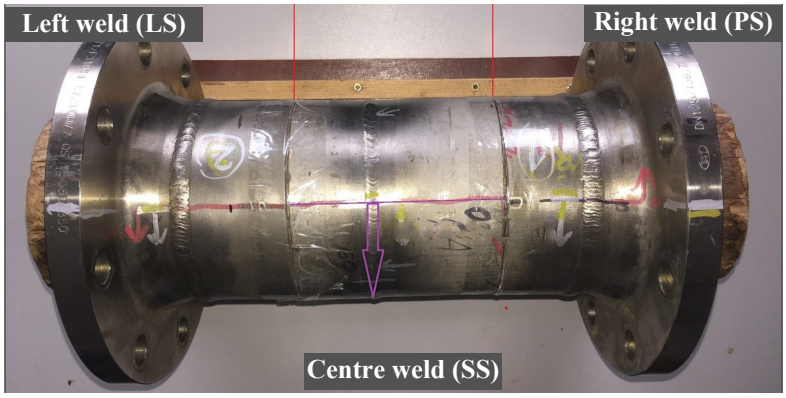

Fig. 1 Samples LS, SS, PS.

Table 1 Chemical composition of 1.4571 material according to standard ČSN EN 10088-3 [wt. %].

	C	Si	Mn	P	S	Cr	Mo	Ni	Ti
1.4571	0.08	1	2	0.045	0.03	16.5-18.5	2-2.5	10.5-13.5	5xC up to 0.7

While microbial corrosion has traditionally been associated with sulfate-reducing bacteria, recent studies have demonstrated that other microorganisms, including manganese-oxidizing microorganisms (MOMOs), can also contribute to MIC [1–5]. Under aerobic conditions and in the presence of manganese ions, MOMOs catalyze the oxidation of Mn^{2+} to higher-valence manganese oxides (Mn (III/IV)) or hydroxides [1, 2]. These oxidation products are typically amorphous and non-

stoichiometric [1–3], complicating their identification via X-ray diffraction. For simplicity, they are often represented by the formulas MnO_2 and MnOOH [1, 3].

MnO_2, in particular, is known for its high electrochemical reactivity and strong oxidative potential [1, 3]. The corrosion process initiated by MOMOs involves a biotic phase, during which microbial metabolic by-products accumulate on the stainless steel surface, followed by an abiotic phase driven by the electrochemical activity of MnO_2. This sequence results in a shift of the corrosion potential of the passive stainless steel towards more anodic values, thereby lowering the critical chloride concentration required to initiate pitting corrosion [1–3]. The lowest reported chloride concentration at which such damage has been observed is 65 mg/L. Under the influence of MnO_2, the material is unable to repassivate effectively [1, 3].

MOMO-induced MIC has been documented in freshwater environments and is known to affect both martensitic and, more significantly, austenitic stainless steels. Affected pipeline surfaces typically exhibit a black, slimy biofilm rich in MnO_2, along with thick layers of biomineralized Mn(IV) oxide deposits.

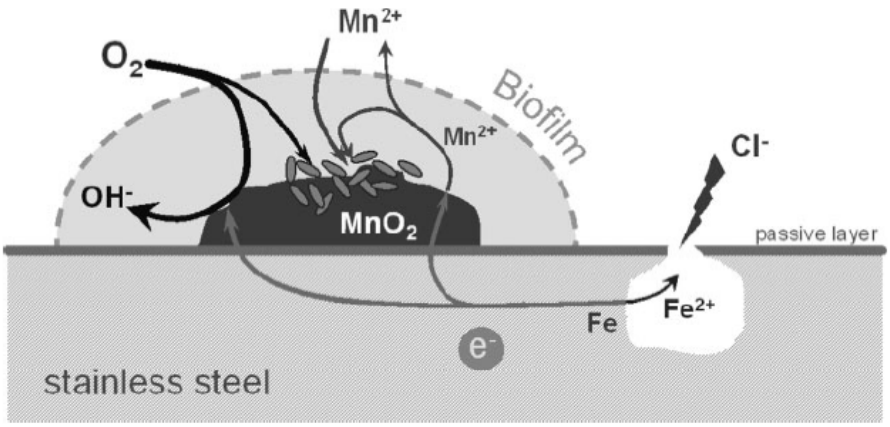

Fig. 2 Diagram of MOMO microbial corrosion mechanism [2].

Methodology

A comprehensive non-destructive evaluation was conducted on the provided pipeline samples. This included detailed visual inspection and dye penetrant (capillary) testing. Subsequently, the original specimens were sectioned into ring-shaped cut-outs containing circumferential welds. These were submitted to Gamalux Plzeň, spol. s r.o., for radiographic examination of the weld joints.
Based on the radiographic findings, selected specimens exhibiting indications of internal anomalies were extracted for further analysis. These were forwarded to CEITEC for high-resolution computed tomography (CT) to document the internal defects in detail, with particular focus on cavities suspected to originate from microbiologically influenced corrosion (MIC).

Following the CT analysis, specific regions were identified for further surface and cross-sectional evaluation. Non-destructive surface characterization was performed using scanning electron microscopy (SEM), while destructive analysis of longitudinal sections was carried out using light optical microscopy (LOM) and SEM.

Finally, the chemical composition of the materials was verified using X-ray fluorescence (XRF) spectroscopy.

Results

XRF analysis confirmed that the chemical composition of the samples corresponds to the declared titanium-stabilized austenitic stainless steel grade 1.4571.

The microstructure of all segments was austenitic, characterized by mechanical twinning and the presence of delta ferrite. The weld metal exhibited an austenitic, predominantly dendritic FA-type microstructure.

Visual and dye penetrant inspections confirmed that the external surfaces were free from service-induced damage. However, several manufacturing-related weld defects were identified on both the inner and outer surfaces. The most frequently observed defects included lack of fusion, incomplete root penetration, and weld overlap.

The internal surfaces of all specimens were coated with grey-black deposits, which may indicate the former presence of a slimy biofilm rich in MnO_2 oxides [1–4]. Nevertheless, the expected thick layers of corrosion products, primarily composed of MnO_2, were not preserved – likely due to mechanical cleaning, as evidenced by visible abrasion marks. In several areas, brown-orange corrosion staining was observed on the internal surfaces. Notably, voids were detected in the specimen containing the right-side weld, located adjacent to these corroded regions (see Fig. 3).

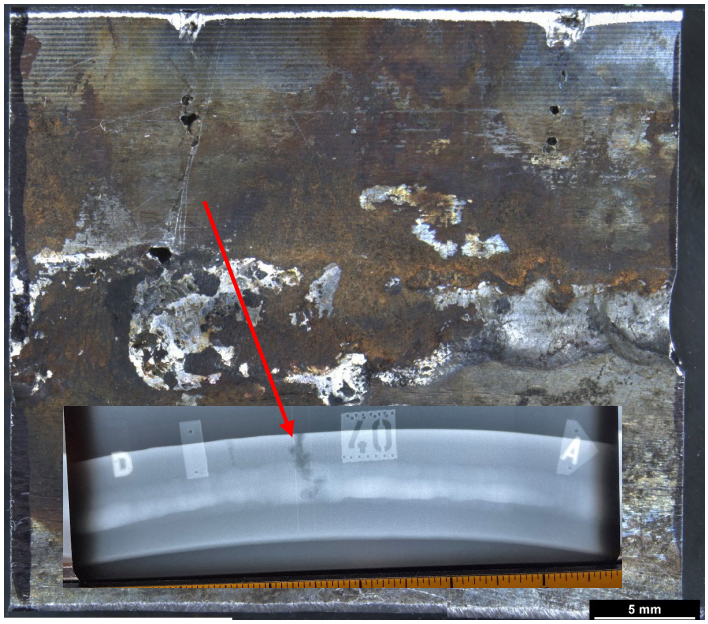

Fig. 3 Detail of the inner surface weld with cavities, PS2 specimen with radiographic image of the outer surface.

Radiographic inspection of the welded joints confirmed the presence of typical manufacturing defects originating from the welding process. These defects were determined to be unrelated to operational degradation. In contrast, voids resembling cavities caused by microbiologically influenced corrosion (MIC) were detected in regions exhibiting brown-orange discoloration – corrosion stains, (see Fig. 3).

Based on the radiographic findings, several areas of interest were selected for further investigation using computed tomography (CT). The CT scans corroborated the visual inspection results, revealing extensive sub-surface caverns at the locations of the corrosion stains across all welds. These caverns are predominantly subsurface, interacting with the inner surface at only a few isolated points.

The most extensive void, located in the base material of the right-side flange, measured approximately 3.2 cm in length. In this instance, the voids could be seen on the internal surface with the naked eye (Figs. 3 and 4). Figure 5 presents a tomographic cross-section of the specimen at the location of the assumed maximum dimension of defect V1. The voids were primarily situated within or adjacent to the weld metal but were also observed in the base metal and its heat-affected zone (HAZ). All voids originated at the internal surface, lacked corrosion products, and exhibited similar morphological characteristics.

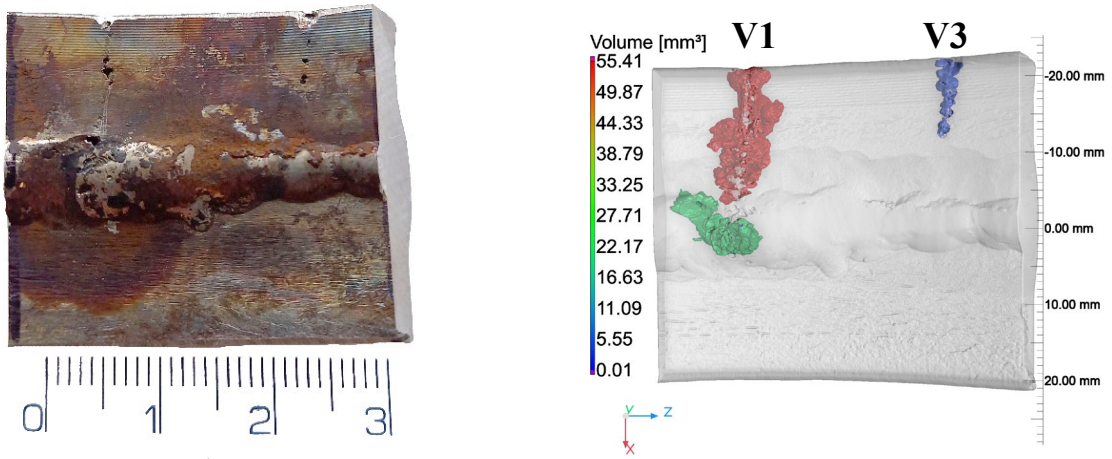

a) b)

Fig. 4 Inner surface of PS-2 specimen (a) and its CT tomography (b).

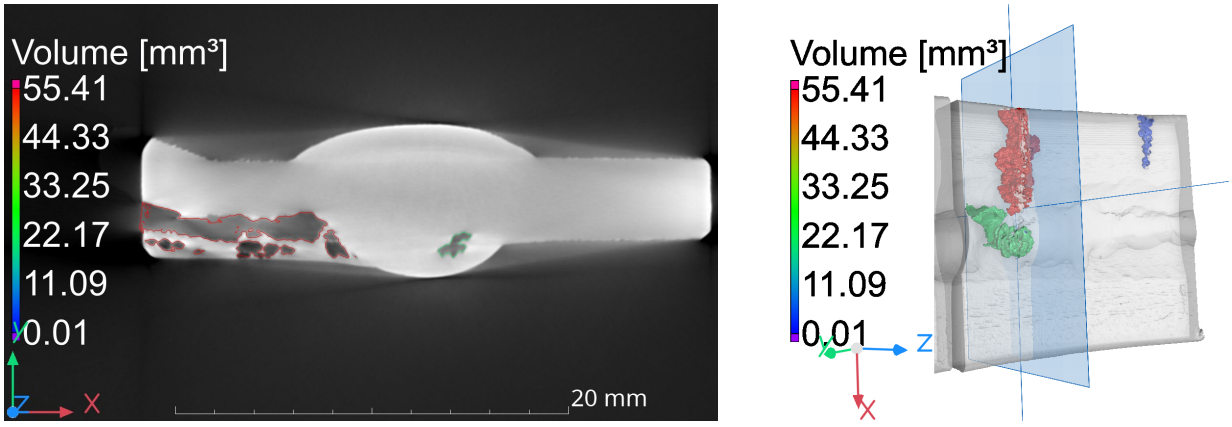

a) b)

Fig. 5 Appearance of red and green defect in cross section.

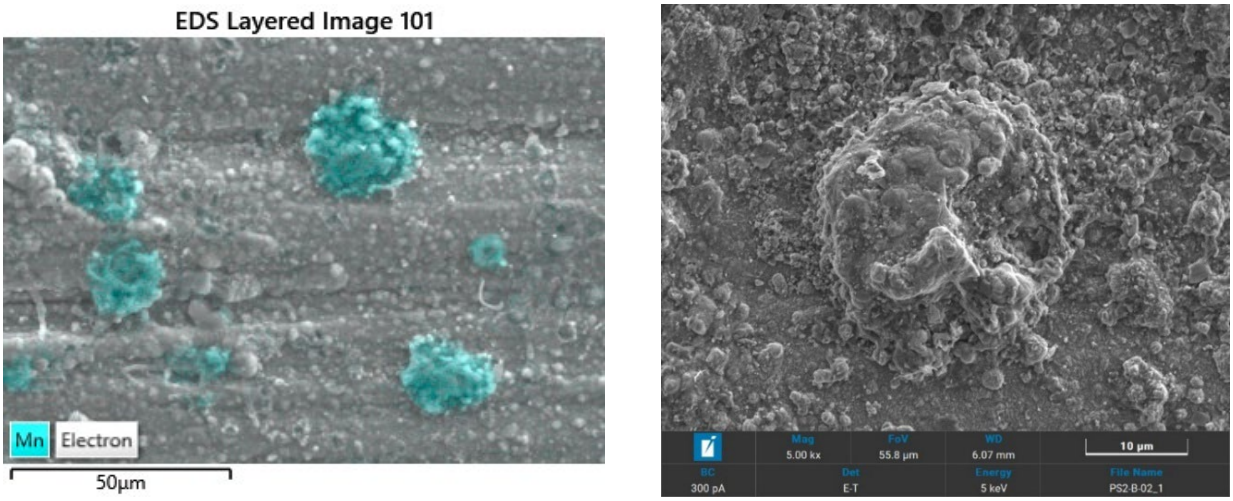

a) b)

Fig. 6 MnO_2 globules. X-ray elemental composition maps SEM-EDS (a), SE (Everhart-Thornley detector) mode (b).

Stereomicroscopic examination revealed that the internal surface of the pipeline was coated with grey-black to grey-brown deposits. Scanning electron microscopy (SEM) analysis of these deposits suggests they may represent remnants of a black mucilaginous biofilm [1–3], likely present prior to the extraction of the samples from the TVD assembly. However, due to prior mechanical cleaning –

evidenced by surface abrasion marks – the surface was only available for analysis in a post-cleaned state, which significantly limited the ability to detect intact MnO_2 globules.

Despite this limitation, localized SEM inspection near defect V1 revealed the presence of MnO_2 globules (see Fig. 6). Their detection supports the hypothesized mechanism of microbiologically influenced corrosion (MIC) caused by manganese-oxidizing microorganisms (MOMOs).

Conclusions

Operational degradation of ESW pipelines was assessed using three DN 125 welded pipeline samples, extracted from a system in service between 2008 and 2021. Microbiologically influenced corrosion (MIC) caused by manganese-oxidizing microorganisms (MOMOs) was hypothesized as the primary degradation mechanism.

The evaluation involved a combination of non-destructive techniques – visual inspection, dye penetrant testing followed by radiography, and computed tomography of several picked defects. The internal surface condition was evaluated as well on a few selected specimens. The metallographic cross sections at the weld joint's locations were prepared for a LOM and SEM evaluation. The chemical composition was verified via X-ray fluorescence (XRF). The key findings are summarized as follows:

- Material Verification: XRF analysis confirmed that the flanges and pipes were composed of titanium-stabilized austenitic stainless steel grade 1.4571 (equivalent to 316Ti).
- Microstructural Characterization: A Microstructure of all components is austenitic with characteristic twinning and varying amounts of delta ferrite. The weld metal has an austenitic, predominantly FA-type dendritic microstructure.
- Surface Condition: Visual and capillary inspections revealed no signs of operational damage on the external surfaces.
- Internal Deposits: Grey-black deposits were observed on the internal surfaces, potentially indicative of a previously present MnO_2-rich biofilm. However, mechanical cleaning prior to sample delivery removed any significant layers of corrosion products.
- Subsurface Cavities: Radiographic and CT analyses confirmed the presence of large subsurface caverns at locations corresponding to corrosion stains. These cavities were primarily located beneath the internal surface, with only a few isolated connections to the surface.
- Cavern Dimensions: The largest detected void, approximately 3.2 cm in length, was found in the base material of the right-side flange in an area where voids were visible to the naked eye. Additional cavities were observed in the weld metal, base metal, and heat-affected zones. All voids originated at the internal surface, were devoid of corrosion products, and exhibited similar morphology.

Due to the mechanical cleaning of the pipeline prior to laboratory analysis, direct evidence supporting the MIC mechanism is not sufficient. Nevertheless, SEM inspection near defect V1 revealed MnO_2 globules within black surface deposits, supporting the hypothesis of corrosion induced by manganese-oxidizing microorganisms.

A definitive confirmation of MOMO-induced corrosion would require further investigation, including analysis of the aqueous medium, observation of uncleaned pipeline surfaces, and verification of manganese presence within its biofilm.

This study contributes to ongoing efforts by the Primary Circuit Systems, Chemical Regimes, Equipment Care, and Ageing Management departments at EDU and ETE to understand and mitigate localized corrosion phenomena in operational systems.

References

[1] Vávrovcová, Z., Krpec, M., Veselka, Z., Brabec, P., Vlček, P., Laboratorní hodnocení provozní degradace potrubí se svary TVD EDU 2. ÚJV Řež, a.s., 2022. Technická zpráva.

[2] Linhardt, P., Twenty years of experience with corrosion failures caused by manganese oxidizing microorganisms, Materials and Corrosion, 61, 12 (2010) 1034-1039, ISSN 09475117, doi:10.1002/maco.201005769Linhardt 2004.

[3] Linhardt, P., Microbially influenced corrosion of stainless steel by manganese oxidizing microorganisms, Materials and Corrosion, 55, 3 (2004) 158-163, ISSN 09475117, doi:10.1002/maco.200303782.

[4] The Role of Manganese Dioxide (MnO_2) Deposition in Microbiologically Influenced Corrosion. EPRI, Palo Alto, CA: 2004. 1009597.

[5] Linhardt, P., MIC of stainless steel in freshwater and the cathodic behaviour of biomineralized Mn-oxides. Electrochimica Acta. 2006, č. 51, s. 6081-6084.

Published in: Key Engineering Materials
ISSN: 1662-9795, Vol. 1046, pp 41-46
doi:10.4028/p-9lUn7r

Submitted: 2025-06-02
Revised: 2025-12-10
Accepted: 2025-12-19
Online: 2026-03-16

Evaluation of Interface between Alumina Dispersion Strengthened Copper Composite and Precipitation Strengthened Copper

František Kromka[1,a*], Ondrej Milkovič [2,1,3,b], Juraj Szabó[1,c], Katarína Ďurišinová[1,d], Juraj Ďurišin[1,e] and Ivan Pethryshynets[1,f]

[1]Institute of Materials Research of Slovak Academy of Sciences, Watsonova 47, Košice, Slovakia

[2]RVmagnetics, a.s., Košice, 30, Košice, Slovakia

[3]Institute of Experimental Physics of Slovak Academy of Sciences, Watsonova 47, Košice,

[a*]fkromka@saske.sk, [b]omilkovic@saske.sk, [c]jszabo@saske.sk, [d]kdurisinova@saske.sk, [e]jdurisin@saske.sk, [f]ipethryshynets@saske.sk

Keywords: Alumina Dispersion Strengthened Copper, Spark Plasma Sintering, Spot Welding, Copper Alloy.

Abstract. Alumina dispersion strengthened copper (ADSC) is nowadays well-researched material. Its properties make it an excellent candidate for use in electrical engineering applications such as material for welding electrodes. The subject of this study was a joint of ADSC and precipitation-strengthened Cu-Cr alloy. ADSC was prepared by powder metallurgy method using Spark Plasma Sintering (SPS). While SPS allows the preparation of low porosity compacts it's limited by the size and shape of compacts it can prepare. This work aimed to prepare different joints between ADSC and Cu-Cr alloy and examine their properties as well as chemical composition and microstructures. Three types of joints were tested. A joint made by pressing ADSC into Cu-Cr sleeve shows the forming of oxides in the joint as well as the hardening of Cu-Cr on the contact surface due to deformation strengthening. Joint made by SPS flash sintering showing the formation of relatively big cavities and the formation of oxides on the materials interface. The in-situ joint was produced using a method where a Cu-Cr sleeve replaced the bottom punch in SPS compaction. The In-situ interface shows very little change in chemical composition and seemingly made a diffusion connection. However, these samples show higher porosity of composite compared to regularly SPS prepared compacts.

Introduction

Dispersion-strengthened metal matrix materials are composites of usually metal matrix strengthened by dispersion of small stable particles. For the preparation of ADSC were researched various dispersion particles such as Al_2O_3, Y_2O_3, TiO_2, WC, SiC [1]. For this study was chosen Al_2O_3 dispersion as best candidate to prepare good composite. This type of oxide was used for its relative ease of introduction to the matrix, previous experience with the process of introducing dispersion into the matrix as well as economic feasibility of using this oxide in comparison with Y_2O_3 or WC. Introduction of Al_2O_3 into the matrix forms $Cu_xAl_yO_z$ [2] interphase which further increases Al_2O_3 potential to make a good dispersion composite with copper.

ADSC owes its excellent mechanical properties such as tensile strength and hardness to Hall-Petch strengthening mechanism. Dispersion particles of Al_2O_3 form barriers against grain growth during material preparation by Zener-pinning mechanism [3]. This way we can prepare a composite that has comparable mechanical properties to precipitation-strengthened copper such as CuCo alloys while retaining their mechanical properties even in elevated temperatures. Such thermal stability is very important in applications where heightened temperatures and high mechanical strains are present such as spot welding applications.

Composites strengthened by the Al_2O_3 have the advantage of reaching nanocrystalline dispersions which significantly increases their hardness. The possibility of preparing nanocrystalline structures with 9–15 nm [4] crystalline crystalline sizes of copper matrix allowed the preparation of high-strength copper composite. Composites prepared by Ďurišin et. al. [4] exhibited 160 HB and ultimate tensile strength up to 436 MPa retaining its mechanical properties up to 900 °C.

Tanaka et al. [5] showed a comparison between ADSC and copper chromium precipitation strengthened copper chromium alloy. Electrodes from ADSC were prepared by copper powder mixed with alumina complex which were hot extruded into copper billet sleeves forming copper bar with ADSC core. Experimental electrodes exhibit a gradual very low decrease of hardness and electrical conductivity up to 900 °C namely 127–100 HV for hardness and 90–85 % IACS for conductivity. Compared to precipitation-strengthened Cu-Cr which showed a significant decrease of hardness from 160–80 HV in a span from 500–700 °C as well as a decrease of conductivity from 83–45 % IACS in the span of 700–900 °C we can see that precipitation strengthened Cu-Cr is nowhere near thermal stability of ADSC.

Furthermore, Tanaka et. al. [5] tested the life span of electrodes comparing ADSC electrodes with conventional Cu-Cr electrodes. This comparison was done indirectly by measuring the weld nugget diameter and observing at what point the nugget diameter dips below the diameter deemed as inadequate for making food weld. Results show that the ADSC electrode has a twice longer lifespan than the chromium copper electrode. Furthermore, the ADSC electrode made much more consistent welds in comparison with Cu-Cr.

Experimental Materials

Samples were prepared by powder metallurgy method. ADSC in all cases was prepared by the process of mixing CuO powder with a water solution of aluminum nitrate $Al(NO_3)_3 \cdot 9H_2O$. Aluminum nitrate was measured and mixed with water in order to yield 2 vol. % Al_2O_3 in the resulting composite. The mixed slurry was afterward dried which resulted in the coating of CuO particles with Al_2O_3 and forming of $Cu(NO_3)_2$. Afterward, powders were ground in an attirtor 10 min 60 Hz 1:1 weight ratio balls to powder then calcined at 500 °C for 1 hour to get rid of chemically bound water and nitrates. A dried mixture of Al_2O_3 and CuO were after calcination cooled to room temperature and milled by vibration milling method for 50 min at 20 Hz and weight ratio balls to powder 1:1. After first vibration milling powder was reduced in H_2 atmosphere for approximately 1h. The first reduction occurred at a temperature around 150 °C until all of the oxygen present in CuO was reduced. After the first reduction metal copper powder was cooled, and milled again in a vibration mill this time for 30 minutes at 20 Hz and a 1:1 ball-to-powder ratio. Copper alumina powder was green compacted, and reduced in the H_2 atmosphere for another hour at 800 °C in order to get rid of most of the introduced oxygen from the composite.

The green compacted powder was then compacted and sintered to the final composite by the SPS method. There were two instances of preparation of the composite by SPS. The first method involved performing SPS in a cylindrical graphite mold with a 10 mm diameter. The sintering process lasted an overall 20 minutes with a steady increase of temperature and pressing force up to 800 °C and force of 5 kN at low vacuum 5×10^{-1} bar where the sample was compacted without further increase of temperature and pressure for 10 minutes. In the second process instead of a lower graphite press an electrode body prepared from Cu-Cr alloy with a chemical composition in Table 1. The powder was compacted and sintered in the Cu-Cr alloy sleeve with the sintering setting set to the same parameters as in the previous two cases and the final result is called an “in-situ” sample.

Table 1 Chemical composition of Cu-Cr electrodes in wt. %.

Si	Cr	Cu	Fe	Zr
0.002	0.934	98.96	0.015	0.083

For purposes of this study were prepared three samples. The first sample further called “pressed” was prepared by pressing on 7 mm diameter billet into the Cu-Cr sleeve. Sample “welded” was prepared by flash plasma sintering where between the composite and Cu-Cr electrode body was put a thin layer of Cu + 2 vol. % Al_2O_3 powder. Powder served as a high-resistance place for two surfaces to weld together. The flash process occurred for 10 seconds at full power setting of the machine which was 37 kW at 5 kA and 7 V.

All samples were sectioned and prepared for scanning electron microscopy to evaluate their microstructure and chemical composition. In order to find the boundary between Cu-Cr precipitation strengthened copper and Cu + Al_2O_3 composite was also performed line EDX chemical analysis. Nano-indentation was used to discover changes in the hardness across the interface area and how does hardness of both materials changes.

Results and Discussion

Microstructures of the interfaces between ADSC and Cu-Cr can be seen in Fig. 1 were evaluated for their chemical composition by EDX semi-quantitative line analyses.

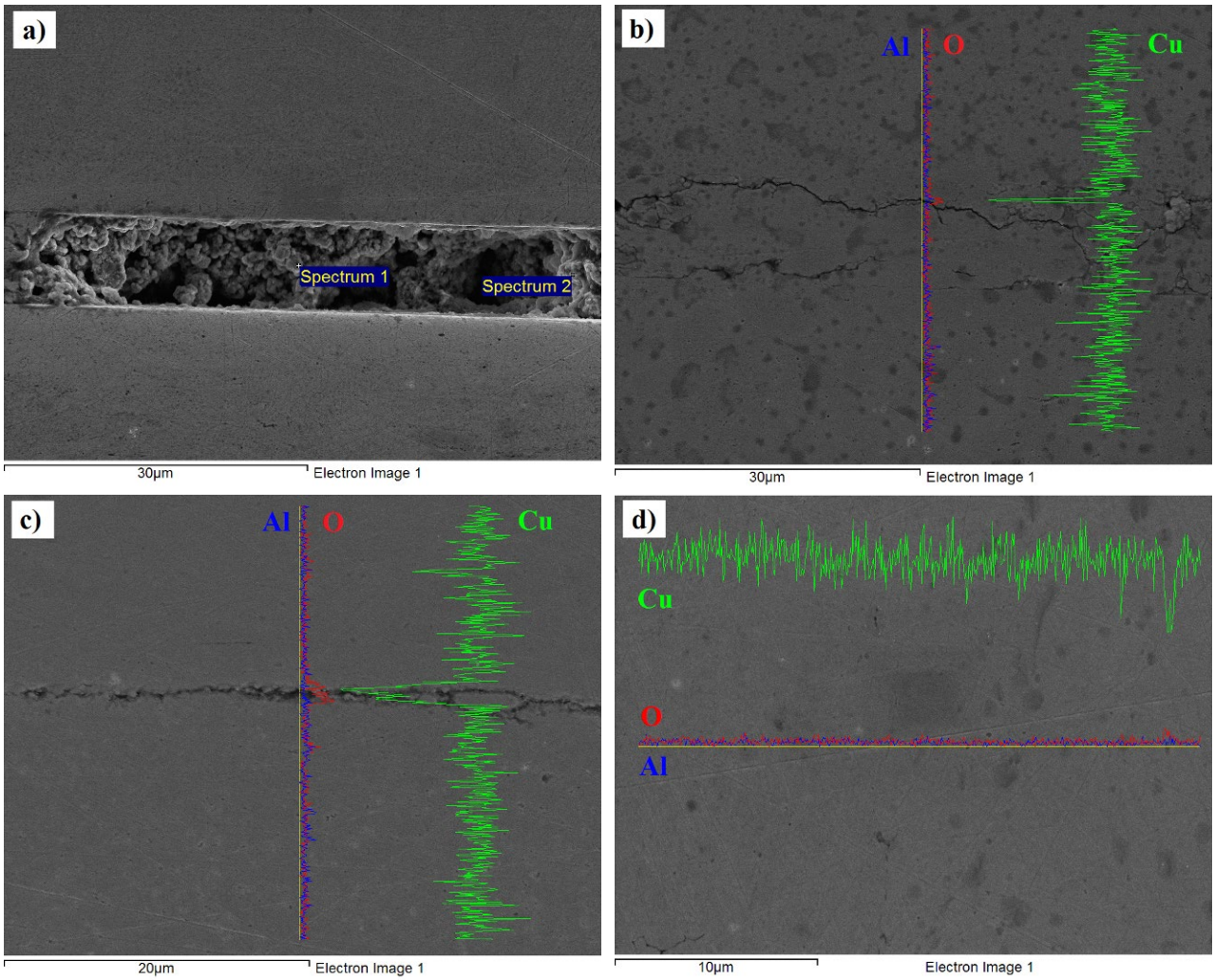

Fig. 1 a) cavity on the interface of welded sample; b) line analysis of welded sample Cu-Cr up ADSC down; c) line analysis of pressed sample Cu-Cr up ADSC down; d) in-situ sample ADSC left Cu-Cr right.

Table 2 Point EDX analysis of cavity in the welded sample (wt. %) in Fig1 a).

Spectrum 1	Cu	O	Spectrum 2	Cu	O
	96.63	3.37		89.66	10.34

From Fig. 1b, c the pressed sample and welded sample had a visible interface while the in-situ sample had no apparent boundary between materials. That is also supported by line analysis which shows in the case of welded and pressed samples heightened levels of oxygen in the boundary between materials. In the case of the welded sample, the line analysis crossed a good connection between ADSC and Cu-Cr, Fig. 1b. The formed joint exhibits a visible boundary between ADSC and

Cu-Cr. This was caused by the uneven distribution of powder between both materials and caused weakening which will be described further. In the welded sample was detected also cavities, on the boundary between ADSC and Cu-Cr were detected heightened presence of oxides (Table 2) which indicated oxidation of powder prior to SPS further weakening the joint. The absence of detected aluminum in the composite was caused due to the low amount (2 vol. %) of Al_2O_3 in the composite.

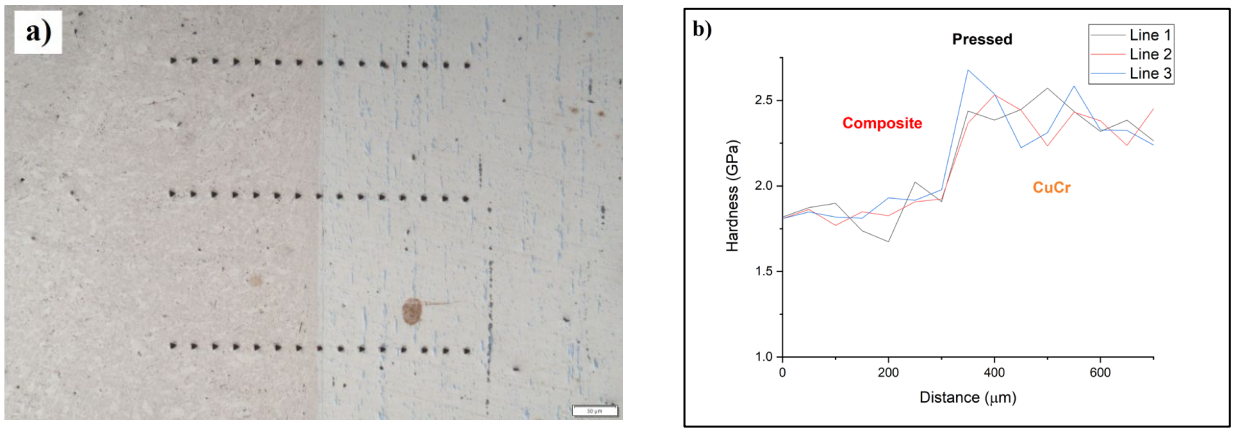

Fig. 2 Nanoindentation of pressed sample: a) microstructure and nanoindents; b) graph of microhardness change.

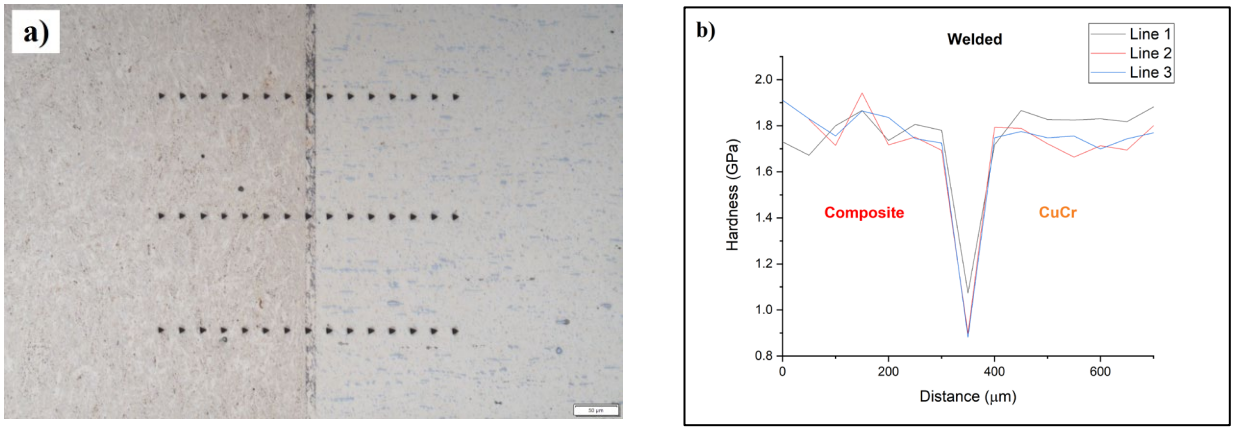

Fig. 3 Nanoindentation of weld sample: a) microstructure and nanoindents; b) graph of microhardness change.

Nanoindentation experiments were performed using Nano Indenter G200 produced by Agilent Technologies (Chandler, AZ, USA) equipped with a Berkovich-type diamond indenter. Poisson's ratio (v) of 0.35 is used, for all samples, assuming a quasi-isotropic behavior. Measurements were done using both single loading–unloading indentation measurements. Nanoindentation hardness was measured always in the places where the best connection was found between composite and Cu-Cr as visible in Fig. 2–4a to mitigate error from cavities. Three lines of indents perpendicular to the joint between composite and Cu-Cr were performed to get a statistical evaluation of hardness differences on the joint. From Fig. 2–4b it's clear that all methods used to join materials had vastly different properties. Pressed sample Fig. 2b has shown an interesting increase of the Cu-Cr micro-hardness in comparison with other cases. That is most likely caused by the manufacturing process where the composite was pressed into the sleeve of the Cu-Cr electrode. The pressing process caused deformations around the sleeve which can result in Cu-Cr hardening. The pressed sample was evaluated after the welding tests; therefore, additional deformation associated with the characteristics of spot welding may have been induced, leading to an increase in microhardness.

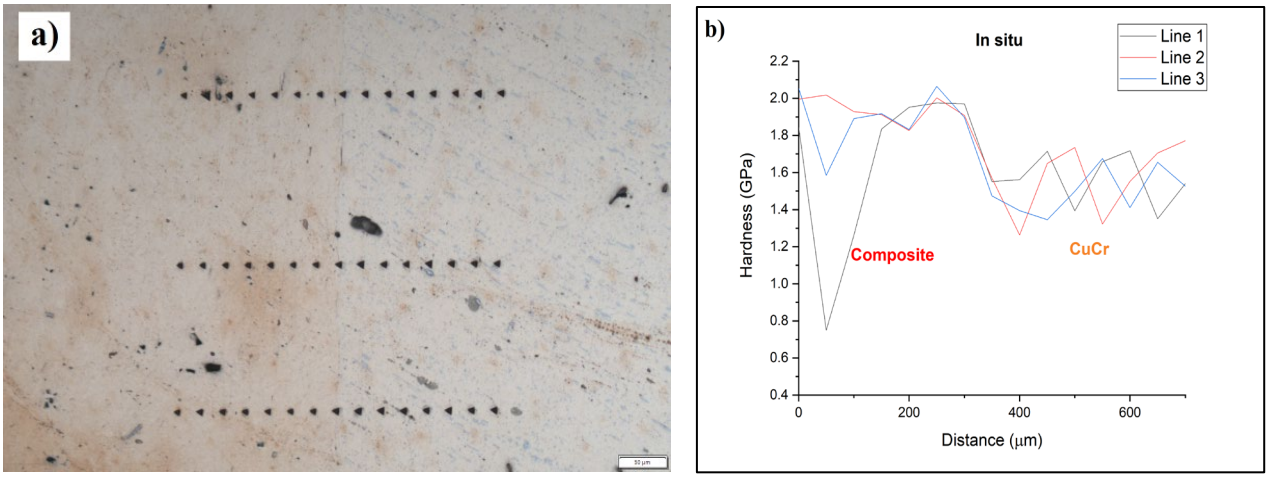

Fig. 4 Nanoindentation of in-situ sample: a) microstructure and nanoindents; b) graph of microhardness change.

Figure 3b shows the microstructure of the flash-welded sample with visible joints between materials. Despite our efforts to make indents in part of the sample without cavities such as on resulting hardness in the connection between composite and Cu-Cr shows a significant decrease, Fig. 3b. That is most likely caused by improper connection between materials and the presence of cavities as is visible on its microstructure. Figure 4a shows the microstructure of the in-situ joint. By light microscopy we were able to see the place of joining of both materials without any significant faults however in the ADSC we can see pores and cavities. This was the result of the SPS process since the same conditions were used for manufacturing billets as well as the in-situ method. Given that this was the first prototype it's obvious that more attention should be given to changing SPS conditions in order to get rid of the porosity and manufacture much better compact. These pores caused also visible significant inconsistencies in composite-Cu-Cr joint (Fig. 4b) roughly 300 μm from the joint into the composite.

Summary

Prepared alumina dispersion copper composites containing 2 vol. % Al_2O_3 were successfully joined with chromium copper alloy. Three different methods of making the joint between ADSC and Cu-Cr were evaluated. It was apparent that making joints by pressing or by flash welding in SPS was an insufficient method for further use causing the formation of cavities and oxides. The presence of these cavities causes low hardness in the joint area and the presence of oxides will decrease joint electrical conductivity. Microhardness tests prove no visible gradient of lowering or increasing hardness depending on the distance to the joint. Novel in-situ method preparation of ADSC in Cu-Cr sleeve posed promising way to mitigate problems with cavities and oxide formation making diffusion joint however, compaction SPS conditions have to be adjusted to get rid of pores formed in ADSC prepared by this method.

Acknowledgement

This work was carried out within the research project Funded by the EU NextGenerationEU through the Recovery and Resilience Plan for Slovakia under the project No. 09I03-03-V04-00314.

References

[1] J.R. Groza, J.C. Gibeling, Principles of particle selection for dispersion-strengthened copper, Mater. Sci. Eng. A, 171, 1-2 (1993) 115-125, doi:10.1016/0921-5093(93)90398-X.

[2] P.K. Jena, E.A. Brocchi, I.G. Solórzano, M.S. Motta, Identification of a third phase in Cu-Al2O3 nanocomposites prepared by chemical routes, Mater. Sci. Eng. A, 371, 1-2 (2004) 72-78, doi:10.1016/S0921-5093(03)00642-7.

[3] K. Huang, R.E. Logé, Zener Pinning, Ref. Modul. Mater. Sci. Mater. Eng., (2016) 1-8, doi:10.1016/b978-0-12-803581-8.03211-2.

[4] K. Ďurišinová, J. Ďurišin, M. Orolínová, M. Ďurišin, J. Szabó, Microstructure and Mechanical Properties of Nanocrystalline Dispersion Strengthened Copper, Powder. Met. Prog., 14, 1 (2014) 58-63.

[5] Y. Tanaka, M. Noguchi, An alumina dispersion strengthened copper composite electrode for spot welding, Weld. Int., 1, 11 (1987) 1074-1078, doi:10.1080/09507118709449392.

CHAPTER 5:

Tribology

Published in: Key Engineering Materials
ISSN: 1662-9795, Vol. 1044, pp 77-82
doi:10.4028/p-P5xO1G

Submitted: 2025-05-30
Revised: 2025-12-09
Accepted: 2025-12-19
Online: 2026-03-03

Tribological Behavior of Al_2O_3-ZrO_2 + 3Y_2O_3 Composites

Jana Andrejovská[1,a], Dávid Medveď[1,b*], Marek Vojtko[1,c] and Viktor Puchý[1,d]

[1]Institute of Materials Research of Slovak Academy of Sciences, Watsonova 47, 040 01 Košice, Slovakia

[a]jandrejovska@sake.sk, [b*]dmedved@sake.sk, [c]mvojtko@sake.sk, [d]vpuchy@saske.sk

Keywords: Tribology, ZTA – Zirconia-Toughened Alumina, Wear.

Abstract. This study investigates the tribological behavior of composites based on Al_2O_3–ZrO_2 stabilized with 3 mol. % Y_2O_3 (ZTA – zirconia-toughened alumina), prepared using spark plasma sintering (SPS) technology. The composites were characterized in terms of microstructure, mechanical properties, and wear resistance in a dry ball-on-flat configuration. SEM analysis confirmed a homogeneous and fine-grained microstructure without porosity, with Al_2O_3 grain sizes of 200–400 nm and ZrO_2 grain sizes of 100–200 nm. Measurements revealed high Vickers hardness (1566.7 ± 133.6 MPa), fracture toughness (6.4 ± 0.29 MPa·$m^{1/2}$), nanoindentation hardness (25.94 ± 2.35 GPa), and Young's modulus (365.9 ± 18.2 GPa). The coefficient of friction ranged from 0.40 to 0.53 depending on the load, and the specific wear rate was extremely low (4.81 × 10^{-7} to 5.08 × 10^{-7} mm^3/Nm). Analysis of the wear track revealed predominantly abrasive wear without significant fragmentation or delamination. The results demonstrate that optimized microstructure, proper phase stabilization, and a high degree of densification enable the preparation of composites with an excellent combination of hardness, toughness, and tribological resistance. These materials are suitable for demanding applications in industry, energy, and biomedicine.

Introduction

Tribological systems in energy, the automotive industry, medical implants, and precision manufacturing equipment place high demands on wear resistance, the stability of the coefficient of friction, as well as the mechanical reliability of materials [1, 2]. Ceramic composites based on Al_2O_3 and tetragonal ZrO_2 stabilized with yttria (ZTA – zirconia-toughened alumina) represent the current state-of-the-art in this field, thanks to the synergistic effect of combining hardness, thermal stability, and fracture toughness [3, 4]. The foundation of their unique properties is the phase transformation of zirconia from the tetragonal to the monoclinic phase, accompanied by a volume expansion (3–5 %), which acts as a barrier to crack propagation, known as transformation toughening [4, 5]. For practical applications, however, this transformation must be controlled and stabilized – the addition of yttria stabilizes the tetragonal phase up to room temperature, which prevents spontaneous microcracking during cooling and loading of the material [4, 6]. The ability to precisely adjust the phase ratio and microstructure is a decisive tool for designing a composite with an optimized combination of hardness and toughness [7, 10]. The microstructure of ZTA composites is fundamentally determined by the preparation and sintering technologies used, where advanced techniques (e.g., SPS) make it possible to achieve submicron grain size, homogeneous phase distribution, and a high degree of densification without significant porosity [5, 10]. Precisely controlled microstructure minimizes weak spots (grain boundaries, pores), thereby increasing both wear resistance and fracture toughness [5, 10]. The tribological properties of ZTA composites depend not only on composition but also on the mutual arrangement of phases, surface morphology, and grain boundary characteristics. Fine-grained structures contribute to reducing the rate of abrasive wear and to the formation of a protective tribolayer during sliding, as confirmed by extensive studies in the energy, automotive, and biomedical sectors [2, 5, 8, 9]. Advanced measurement methods, especially nanoindentation and optical profilometry, allow for detailed quantification of Young's modulus, hardness, fracture toughness, and the coefficient of friction, which is essential for scientific optimization of these systems [6, 7]. The aim of this work is to comprehensively investigate the

influence of microstructure, phase composition, and experimental parameters on the tribological and mechanical properties of ZTA composites, to analyze wear mechanisms, and to discuss their significance for applications under extreme conditions.

Experimental Methods

The starting materials were fine α-Al_2O_3 powder with a particle size of approximately 150 nm (TAIMICRON TM DAR, TAIMEI CHEMICALS CO.) and tetragonal ZrO_2 powder stabilized with 3 mol. % Y_2O_3 with a particle size of 30–60 nm (Inframat Corporation). Powder mixtures were prepared by weighing mass fractions corresponding to a composition of 50 vol. % Al_2O_3 and 50 vol. % ZrO_2 + $3Y_2O_3$ with an accuracy of ±10 mg. These powders were then dispersed in approximately 40 vol.% isopropanol and homogenized in a planetary mill PULVERISETTE 6 (FRITSCH, Germany) for 2 hours at 200 rpm in a zirconia container with 10 mm diameter balls, maintaining a ball-to-powder ratio of 10:1 and reversing the direction of rotation every 30 minutes. After homogenization, the suspension was evaporated in a rotary evaporator, the powder was thoroughly dried, sieved through a 200 μm mesh, and stored in a desiccator.

The powder mixtures were sintered using an HP D10-SD device (FCT Systeme, Germany). The powder was pressed into a graphite mold with an inner diameter of 20 mm, lined with graphite foil 0.5 mm thick. The SPS process involved linear heating from room temperature to 400 °C at a rate of 100 °C/min, followed by a five-minute isothermal hold to remove residual moisture. The temperature was then increased at the same rate up to 1400 °C and held for five minutes. After sintering, the samples were cooled in a controlled manner to 400 °C, then left to cool freely in air. The pressing force during sintering was gradually increased up to a maximum of 20 kN and was gradually reduced during cooling.

The resulting samples had a cylindrical shape with a diameter of 20 mm and a height of approximately 4 mm. Sample surfaces were prepared using standard metallographic procedures: coarse grinding with SiC papers of grit sizes 320 to 1200, followed by fine polishing with diamond suspensions of 9 μm, 3 μm, and 1 μm, and final polishing with colloidal silica (0.05 μm, 3 minutes at 150 rpm). Surface roughness was verified with a confocal microscope Sensofar PLu Neox, with a resulting Ra value of approximately 0.06 μm.

The microstructure was analyzed using an environmental scanning electron microscope EVO MA15 (Carl Zeiss, Germany) in backscattered electron (BSE) mode. Vickers microhardness was measured using a Vickers 432SVD microhardness tester (Wolpert Wilson Instruments) at a load of 49.05 N (HV5), with a dwell time of 15 s and at least five indents per sample.

Nanoindentation was performed with an Agilent G200 instrument using a Berkovich tip (100 indents, 200 nm depth, continuous stiffness measurement mode). Young's modulus and nanohardness were determined according to the Oliver–Pharr method [9]. Fracture toughness (K_{IC}) was calculated based on the length of cracks emanating from the corners of Vickers indents using the Niihara equation [2], with the modulus of elasticity obtained from nanoindentation measurements.

Tribological properties were evaluated using a Bruker UMT-3 tribometer in a ball-on-flat configuration, with a 6 mm SiC ball as the counterpart. Tests were carried out in dry conditions at laboratory temperature (22 ± 1 °C) and relative humidity (40 ± 5 %). The movement was reciprocal with a 5 mm amplitude, 10 Hz frequency, and normal loads of 5, 10, and 25 N. The average sliding speed was 0.1 m/s, and the total sliding distance was 500 m. The coefficient of friction was recorded continuously during the test.

The wear volume (V) was determined from 3D profilometry of the wear tracks using the Sensofar PLu Neox. The specific wear rate (W_s) was calculated according to equation (1), where the volume loss (V) was divided by the product of applied load (F) and sliding distance (L):

$$Ws = \frac{V}{F.L} \left[\frac{m\mathrm{m}^3}{Nm}\right] \quad (1)$$

The morphology of the wear track and the presence of tribolayers were analyzed using SEM/FIB-SEM (ZEISS Auriga Compact) in SE and BSE modes and using EDX spectroscopy (energy-dispersive X-ray analysis).

The mechanical properties of the studied ZTA_3 composite were characterized using multiple methods, providing a comprehensive overview of its strength parameters. The average Vickers microhardness reached 1566.7 ± 133.6 MPa, indicating high resistance to plastic deformation and confirming high microstructural homogeneity.

Results and Discussion

Basic mechanical properties such as indentation fracture toughness (K_{IC}) and Vickers microhardness were determined at a load of 5 N. Similarly, nanoindentation parameters such as nanohardness and Young's modulus were measured. The results are summarized in Table 1.

Table 1 Values of Vickers hardness and indentation fracture toughness at a load of 5 N.

Mechanical property	Value
Vickers hardness HV [MPa]	1566.7 ± 133.6
Indentation fracture toughness according to Niihara K_{IC} [MPa·m$^{1/2}$]	6.4 ± 0.29
Nanoindentation hardness [GPa]	25.94 ± 2.35
Young's modulus [GPa]	365.9 ± 18.2

The measured indentation fracture toughness K_{IC} = 6.4 ± 0.29 MPa·m$^{1/2}$ represents a significant increase compared to monolithic alumina ceramics (typically 3–4 MPa·m$^{1/2}$), which is the result of the effective transformation toughening mechanism in the ZTA system [4, 10]. The presence of metastable tetragonal ZrO_2 grains allows for local phase transformation in the vicinity of a propagating crack, leading to local volume expansion and effectively hindering crack growth [4]. This transformation is the main reason for the high toughness of ZTA composites and has been repeatedly confirmed in experimental studies (e.g., Basu et al., 2004) [10].

The measured Vickers hardness HV = 1566.7 ± 133.6 MPa is typical for highly densified fine-grained ZTA composites. It is higher than that of pure zirconia ceramics (1200–1400 MPa) and comparable to values reported for submicron ZTA materials [5, 10]. The increased hardness is a result of the fine-grained microstructure, homogeneous distribution of hard phases, and the absence of significant porosity [5]. According to the literature (e.g., He et al., 2004), similar composites exhibit values in the range of 1500–1700 MPa, which confirms the quality of the prepared samples [5].The nanoindentation hardness of 25.94 ± 2.35 GPa and Young's modulus of 365.9 ± 18.2 GPa correspond with results obtained for fine-grained ZTA composites in leading studies [6, 7, 10]. The higher value of nanoindentation hardness compared to conventional Vickers hardness is due to the local measurement in very small volumes, where the contribution of hard phases is higher and the influence of defects or grain boundaries is minimal [6]. Such values of nanoindentation parameters indicate high microstructural quality, strong grain boundaries, and effective stress transfer within the material. A fine-grained and homogeneous microstructure with an optimized Al_2O_3:ZrO_2 ratio directly supports high values of both hardness and toughness [5, 10]. Compared to the literature (Basu et al., 2004; Vasylkiv et al., 2003), these values are above average for this type of composite, which is a result of high-quality preparation and effective phase stabilization [7, 10]. Furthermore, the presence of yttria-stabilized ZrO_2 prevents undesirable grain growth during sintering, preserving the fine-grained character, which is essential for maintaining high hardness and fracture toughness [4, 5, 10]. In tribological tests (see Table 2), the composites exhibited a stable and relatively low coefficient of friction: 0.51 at 5 N, 0.48 at 10 N, and 0.44 at 25 N. Such a decrease in COF with increasing load is in agreement with Ghaemi et al. (2017), who report COF values for similar systems in the range of 0.45–0.65 [2].

Table 2 Coefficient of friction (COF) and wear rate (Ws) at different loads.

Sample	Load [N]	COF [-]	Ws [mm³/Nm]
Al_2O_3-ZrO_2+3Y_2O_3	5	0.51	4.81×10^{-7}
	10	0.48	4.99298×10^{-7}
	25	0.44	4.23639×10^{-7}

The specific wear rate (W_s) ranged from 4.81×10^{-7} to 5.08×10^{-7} mm³/Nm, which is comparable to or better than values reported for ZTA composites in the literature [2, 10].

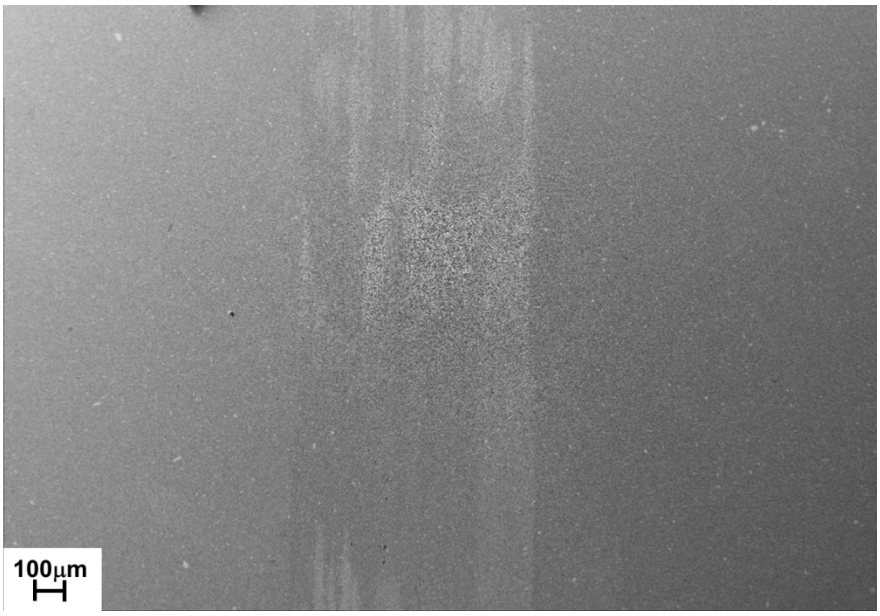

Fig. 1 SEM micrographs with typical damage mechanism in the wear tracks after the wear test with 25 N.

The SEM image of the wear track (Fig. 1) shows a smooth surface with fine parallel grooves typical of abrasive wear. The edges are slightly raised due to plastic deformation, and the formation of a tribolayer can be observed in the central part, which contributes to reduced friction and protects the surface from further damage [9, 10]. More pronounced defects, such as delamination or fragmentation of the surface, were not observed, indicating high microstructural integrity [5]. The absence of pores or segregation confirms the high degree of densification and optimal SPS sintering parameters, in line with the best results in the field [5, 10].

The results for indentation fracture toughness, hardness, and nanoindentation parameters clearly confirm the high degree of optimization achieved in the prepared ZTA composites. The indentation fracture toughness $K_{IC} = 6.4 \pm 0.29$ MPa·m$^{1/2}$ significantly exceeds the values typical for monolithic alumina (3–4 MPa·m$^{1/2}$), which is a direct result of the effective phase transformation of tetragonal zirconia grains to the monoclinic phase near a propagating crack [4, 10]. This transformation leads to volumetric expansion and crack closure, effectively inhibiting crack growth and increasing the overall toughness of the system [3, 4].

The Vickers hardness of 1566.7 ± 133.6 MPa ranks among the highest values reported for ZTA composites in the literature (He et al., 2004; Basu et al., 2004). An important factor is the fine-grained, homogeneous microstructure and high degree of densification, which suppress the formation of defects and allow for uniform stress distribution throughout the volume. Fine phase boundaries additionally enhance resistance to initiating defects and microcracks, increasing both hardness and wear resistance [5, 10].

The nanoindentation hardness of 25.94 ± 2.35 GPa and Young's modulus of 365.9 ± 18.2 GPa represent top values compared to similar composites and demonstrate the high microstructural quality of the prepared materials [6, 7]. Nanoindentation measurements reveal the true potential of local mechanical response, where the influence of macroscopic defects or grain boundaries is minimized and the synergy of hard phases is maximized [6, 7]. The difference between nanoindentation and macroscopic hardness is typical for ceramic systems with a fine microstructure and is also discussed in works by Basu et al. (2004) and Vasylkiv et al. (2003) [7, 10].

In comparison with the literature, the obtained mechanical parameter values are above average for ZTA composites, demonstrating the effectiveness of the applied SPS sintering method, the high purity of the powders, and precise phase stability control [5, 10]. This combination of high Young's modulus, hardness, and toughness ensures long-term reliability under intensive tribological loading and allows for extended application in extreme conditions in energy, transport, and biomedicine [1, 2]. The results confirm that the optimized fine-grained microstructure, stabilization of ZrO_2 with yttria, and correctly set processing conditions lead to a significant enhancement of the mechanical and tribological properties [5, 10]. The COF and wear rate values are equal to or better than those reported in the literature, which can be attributed to the effective formation of a tribolayer at higher loads and homogeneous distribution of hard phases [2, 9, 10].

Vickers hardness and fracture toughness are consistent with the best reported data for ZTA systems (Basu et al., 2004; He et al., 2004), where the submicron microstructure enables an excellent compromise between hardness and resistance to crack propagation [5, 10]. The presence of a fine tribolayer in the wear tracks reduces friction, which is in line with the conclusions of Ghaemi et al. (2022) and Chevalier et al. (2007), who state that such a protective layer is key to reducing abrasive wear and extending component lifetime [1, 2].

The abrasive character of the wear, absence of delamination, and stable COF even at higher loads confirm the advantages of the fine-grained structure and strong phase bonding [2, 5]. Microstructural integrity is thus the foundation that enables wide-ranging applications, from energy systems to orthopedic implants and precision engineering [1, 2, 5].

Conclusions

ZTA composites prepared by SPS technology achieve outstanding parameters: Vickers hardness of 1566.7 MPa, fracture toughness of 6.4 $MPa \cdot m^{1/2}$, a stable coefficient of friction of 0.40–0.53, and a very low specific wear rate (around 5×10^{-7} mm^3/Nm). The morphology of the wear track demonstrates a predominantly abrasive mechanism, formation of a protective tribolayer, and absence of serious surface defects, resulting from the optimized microstructure and phase stability. The results demonstrate that these composites are suitable for the most demanding tribological applications in industry and biomedicine, where the decisive factors are the combination of high strength, toughness, and wear resistance [1-2, 10].

Acknowledgements

The work was Funded by the EU NextGenerationEU through the Recovery and Resilience Plan for Slovakia under the project No. 09I03-03-V04-00260.

References

[1] J. Chevalier, L. Gremillard, Ceramics for Medical Applications: A Picture for the next 20 years. Journal of the European Ceramic Society, 29, 7 (2009), https://doi.org/10.1016/j.jeurceramsoc. 2008.08.025.

[2] M.H. Ghaemi, S. Reichert, A. Krupa, M. Sawczak, A. Zykova, K. Lobach, S. Sayenko, Y. Svitlychnyi, Zirconia ceramics with additions of Alumina for advanced tribological and biomedical applications, Ceramic International 43, 13 (2017) 9746-9752, https://doi.org/10.1016/j.ceramint. 2017.04.150.

[3] Lawn, B.R., Principles of Fracture Toughness Measured by Indentation and Calibration Approaches, Journal of Materials Science, 33, 20 (1998) 4947-4956.

[4] R.H.J. Hannink, P.M. Kelly, B.C. Muddle, Transformation Toughening in Zirconia-Containing Ceramics, Journal of the American Ceramic Society, 83, 3 (2000) 461-487. https:// doi.org/10.1111/j.1151-2916.2000.tb01221.x.

[5] Y.J. He, A.J.A. Winnubst, A.J Burggraaf, H. Verweij, P.G.T. Van der Varst, G de With, Sliding Wear of ZrO_2-Al_2O_3 Composite Ceramics, Journal of the European Ceramic Society (1997) 1371-1380.

[6] W.C. Oliver, G.M. Pharr, An Improved Technique for Determining Hardness and Elastic Modulus Using Load and Displacement Sensing Indentation Experiments, Journal of Materials Research, 7, 6 (1992) 1564-1583, https://doi.org/10.1557/JMR.1992.1564.

[7] O.O. Vasylkiv, Y. Sakka, V.V. Skorokhod, Hardness and fracture toughness of alumina-doped tetragonal zirconia with different yttria contents, Journal of the European Ceramic Society, 23, 10 (2003) 1669-1676, https://doi.org/10.2320/matertrans.44.2235.

[8] J. Chevalier, L. Gremillard, S. Deville, Low-temperature degradation of zirconia and implications for biomedical implants, Biomaterials, 30, 8 (2007) 1558-1566, https:// doi.org/10.1146/annurev.matsci.37.052506.084250.

[9] Y.M. Chen, B. Rigaut, F. Armanet, Wear Behaviour of Partially Stabilized Zirconia at High Sliding Speed, Journal of the European Ceramic Society, 6 (1990) 383-390. https://doi.org/10.1016/0955-2219(90)90006-2.

[10] Basu, B., Vleugels, J., Van Der Biest, O., Microstructure–toughness–wear relationship of tetragonal zirconia ceramics, Journal of the European Ceramic Society, 24, 7 (2004) 2031-2040, https://doi.org/10.1016/S0955-2219(03)00355-8.

Published in: Key Engineering Materials
ISSN: 1662-9795, Vol. 1044, pp 83-89
doi:10.4028/p-UI9lc1

Submitted: 2025-07-14
Revised: 2025-12-10
Accepted: 2025-12-19
Online: 2026-03-03

Tribological Behavior of ZrO_2-3Y_2O_3 Ceramics in Dry Reciprocating Sliding Against SiC Counterparts

Dávid Medveď[1,a], Jana Andrejovská[1,b*], Marek Vojtko[1,c] and Viktor Puchý[1,d]

[1]Institute of Materials Research of Slovak Academy of Sciences, Watsonova 47, Košice, 040 01, Slovakia

[a]dmedved@saske.sk, [b]*jandrejovska@saske.sk, [c]mvojtko@saske.sk, [d]vpuchy@saske.sk

Keywords: Tribology, Yttria-Stabilized Zirconia, Wear.

Abstract. In this study, the mechanical and tribological properties of 3 mol. % yttria-stabilized tetragonal ZrO_2 (3Y-TZP) prepared by spark plasma sintering (SPS) were investigated. Nanoindentation revealed a high hardness of 16.51 ± 0.86 GPa and an elastic modulus of 250 ± 8.8 GPa. The low scatter of these values provides strong evidence for a homogeneous, fine-grained microstructure. Vickers microhardness at a 5 N load was 1382 ± 14 and indentation fracture toughness (K_{IC}, Niihara) was 5.2 ± 0.03 MPa·$m^{1/2}$, confirming the material's high mechanical resilience. Dry reciprocating sliding against a SiC counterface exhibited a stable coefficient of friction (COF) of 0.37–0.39, with a slight decrease to 0.37 at 25 N load attributed to the formation of a thin protective tribolayer. Wear track depth increased from ~0.8 μm (5 N) to ~2.8 μm (25 N), and width from ~1.400 μm to ~ 1.600 μm, while the specific wear rate rose only marginally from 9.28 × 10^{-8} to 5.05 × 10^{-7} mm^3/N·m, demonstrating excellent wear resistance. SEM/EDX analysis revealed predominant abrasive wear with microcracking, alongside tribochemical oxidation layers rich in SiO_2 and carbon that contribute to surface protection. Stabilization of the tetragonal phase and a fine-grained microstructure are key factors enabling the superior hardness, elasticity, and tribological performance of 3Y-TZP for applications demanding low friction and high wear resistance.

Introduction

Yttria-stabilized tetragonal zirconia polycrystal (3Y-TZP) is an advanced structural ceramic with exceptional mechanical and chemical properties, including high hardness, fracture toughness, flexural strength, wear resistance, chemical inertness, and low thermal conductivity [1–3]. These properties enable demanding applications: cutting tools, bearings, seals, thermal barriers (energy/automotive), and biocompatible medical implants/surgical instruments valued for reliability under cyclic loading [1, 2, 4]. Its chemical stability and thermal resistance also suit sensors, fuel cell membranes, and devices in extreme conditions [2]. Fine-grained, homogeneous 3Y-TZP resists undesirable phase transformations, unlike coarse-grained/heterogeneous materials prone to spontaneous transformation, excessive crack propagation, wear and delamination [5–7]. High fracture toughness stems from transformation toughening: stress-induced tetragonal-to-monoclinic ZrO_2 phase transformation consumes energy and hinders crack propagation. This involves ≈ 4 % volumetric expansion near crack tips, generating compressive stresses, increasing fracture toughness and wear resistance [1, 8, 9], earning it the name "ceramic steel" [2, 9]. Transformation toughening is influenced by microstructure (grain size, tetragonal phase fraction, density) [3, 6, 7]. Modern methods like SPS yield fine-grained, high-density 3Y-TZP, preserving the transformable tetragonal phase [7, 10]. Yttria content/distribution is crucial for tetragonal phase stabilization per the ZrO_2–Y_2O_3 phase diagram [11]. Tribological behavior is linked to microstructure; fine-grained homogeneous 3Y-TZP resists undesirable phase transformations, wear and microcracking, unlike coarse/heterogeneous structures [3, 5, 15]. Phase transformation during friction can be self-healing, preventing damage [9, 12, 13],

and tribochemical oxidation forms protective layers [13]. However, excessive/environmental transformation or moisture exposure (LTD : Low - Temperature Degradation) can cause degradation, grain pull-out, friction fluctuations, microcracking, and fatigue failure [12]. Monolithic zirconia exhibits higher resistance to abrasive wear under dry conditions than composite materials [15]. Interaction with SiC counterface materials represents a specific case since SiC is characterized by high hardness and wear resistance, significantly influencing wear mechanisms and service life of both components [15]**.** Nanoindentation allows precise measurement of mechanical parameters such as hardness (H), elastic modulus (E), and microdeformation [14]. Well-prepared ZrO_2–3 mol. % Y_2O_3 can achieve H up to 16.8 GPa and fracture toughness of 5.2 $MPa \cdot m^{1/2}$ [6, 11]. This article experimentally investigates the tribological behavior of ZrO_2–$3Y_2O_3$ under dry reciprocating sliding against SiC at various loads. The goal is to study load-friction-wear relationships, identify dominant wear mechanisms, understand contact pressure effects on zirconia's tribological properties, and provide a basis for optimizing applications requiring high dry sliding wear resistance.

Materials and Methods

The starting material was a commercial powder of yttria-stabilized tetragonal zirconia polycrystal containing 3 mol. % Y_2O_3 (3Y-TZP, Tosh Corporation, Japan). The 3Y-TZP powder was dispersed in isopropanol (~40 vol. %) and homogenized in a planetary ball mill (Retsch PM 100) for 2 hours at 200 rpm. Zirconia oxide containers and balls were used as the milling medium in a ball-to-powder weight ratio of 10:1. The rotation direction was reversed every 30 minutes to ensure uniform particle distribution. After milling, the suspension was evaporated, the powder dried, and sieved through a 200 μm mesh. The prepared powders were stored in a desiccator. The powder mixtures were sintered using an HP D10-SD SPS device (FCT Systeme, Germany). The powder was pressed into a graphite die (Ø 20 mm), lined with a 0.5 mm graphite foil. The SPS process involved linear heating from room temperature to 400 °C at a rate of 100 °C/min, followed by a 5-minute dwell to remove residual moisture. Subsequently, the temperature was increased to 1400 °C at the same heating rate and held isothermally for 5 minutes. After sintering, the samples were cooled in a controlled manner to 400 °C and then allowed to cool freely in air. The applied pressure was gradually increased to a maximum of 20 kN and reduced progressively during cooling. The resulting samples were cylindrical, with a diameter of 20 mm and a height of approximately 4 mm. Sample surfaces were prepared by standard metallographic procedures: coarse grinding using SiC papers with grit sizes ranging from 320 to 1200, fine polishing with diamond suspensions (9 μm, 3 μm, 1 μm), and final polishing with colloidal silica (0.05 μm, 3 min, 150 rpm). Surface roughness was verified using a confocal microscope (Sensofar PLu Neox), resulting in an average Ra value of approximately 0.06 μm. The morphology of the wear track and the state of the adjacent unworn surface were analyzed using an environmental scanning electron microscope (EVO MA15, Carl Zeiss, Germany) in backscattered electron (BSE) mode. Vickers microhardness measurements were conducted on a Wolpert Wilson Instruments Vickers hardness tester (model 432SVD) under a load of 49.05 N (HV5) with a dwell time of 15 s and a minimum of 5 indentations per sample. Nanoindentation tests were carried out using an Agilent G200 nanoindenter equipped with a Berkovich tip (100 indents per sample, maximum depth 1200 nm, continuous stiffness measurement mode). Young's modulus and nanohardness were determined according to the Oliver–Pharr method [14]. Fracture toughness (K_{IC}) was calculated from the crack lengths emanating from the corners of Vickers indentations using the Niihara equation, where the modulus of elasticity was taken from nanoindentation measurements. Tribological properties were evaluated on a Bruker UMT-3 tribometer in a ball-on-flat configuration, with a 6 mm diameter SiC ball as the counterface. Tests were performed under dry conditions at room temperature (22 ± 1 °C, 40 ± 5 % relative humidity). The reciprocating sliding amplitude was 5 mm with a frequency of 10 Hz and normal loads of 5, 10, and 25 N. The average sliding speed was 0.1 m/s, and the total sliding distance was 500 m. The friction coefficient was recorded continuously. Wear volume (V) was

determined from 3D profilometry of the wear tracks using the Sensofar PLu Neox system. The specific wear rate (Ws) was calculated based on the volume loss (V), sliding distance (L), and applied load (F), according to Equation (1):

$$Ws = \frac{V}{F.L} \left[\frac{mm^3}{Nm}\right] \quad (1)$$

The morphology of the wear track and the presence of tribofilms were analyzed using SEM/FIB-SEM (ZEISS Auriga Compact, SE/BSE modes) and EDX (energy-dispersive X-ray spectroscopy).

Results

The results of nanoindentation measurements on ZrO_2–$3Y_2O_3$ samples prepared by the SPS method confirm a high level of hardness and elastic modulus of the material. After an initial increase caused by surface effects, the hardness curves stabilize at approximately 16.5 GPa. Similarly, the elastic modulus stabilizes at about 250 GPa. The results exhibit low scatter, which strongly suggests a homogeneous microstructure. The average values and standard deviations of hardness and elastic modulus are summarized in Table 1.

Table 1 Mechanical properties of ZrO_2–$3Y_2O_3$ ceramics obtained by nanoindentation.

Nanomechanical Property	Value [GPa]
Hardness	16.51 ± 0.86
Elastic modulus	250 ± 8.8

The values in Table 1 are representative and corresponding to typical characteristics of fine-grained yttria-stabilized tetragonal zirconia. Such values contribute to the material's high resistance to microcracking and wear. In addition to nanoindentation parameters, Vickers microhardness and indentation fracture toughness (K_{IC}) at a load of 5 N were also measured on the samples. These results are presented in Table 2.

Table 2 Vickers microhardness and indentation fracture toughness (load 5 N).

Mechanical property	Value
Vickers hardness HV	1382 ± 14
Indentation fracture toughness K_{IC} [MPa·m$^{1/2}$] according to Niihara	5.2 ± 0.03

High values of hardness, elastic modulus, and fracture toughness indicate a well-developed microstructure of the material, where the fine-grained structure and stabilized tetragonal zirconia phase jointly contribute to enhanced mechanical strength and improved tribological resistance of the material under extreme operating conditions. The COF during reciprocating dry sliding exhibits a typical behavior with an initial running-in and stabilization phase, followed by a steady-state COF. As shown in Fig. 1, at lower loads of 5 N and 10 N, the COF stabilizes at approximately 0.39, whereas at the highest load of 25 N, a slight decrease in COF to about 0.37 is observed.

Stable COF values of 0.37–0.39 throughout the test indicated good tribological stability, suiting ZrO_2–$3Y_2O_3$ for applications requiring low friction and high wear resistance. The specific wear rate (Fig. 2) slightly increased with load (from ~9.28×10^{-8} mm³/N·m at 5 N to ~5.05×10^{-7} mm³/N·m at 25 N) but remained relatively stable, confirming the ceramic's good wear resistance. An SEM image of the wear track (Fig. 3, 25 N), with EDX analysis of selected areas (Spectra 1–4), revealed elemental compositional variability within the worn zone.

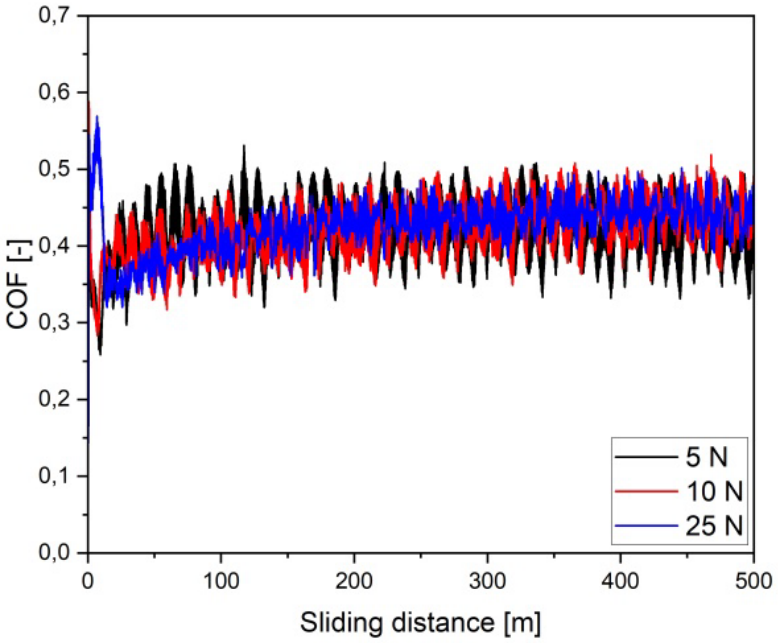

Fig. 1 COF vs. sliding distance of the investigated material after the wear test at 5 N, 10 N, and 25 N applied loads.

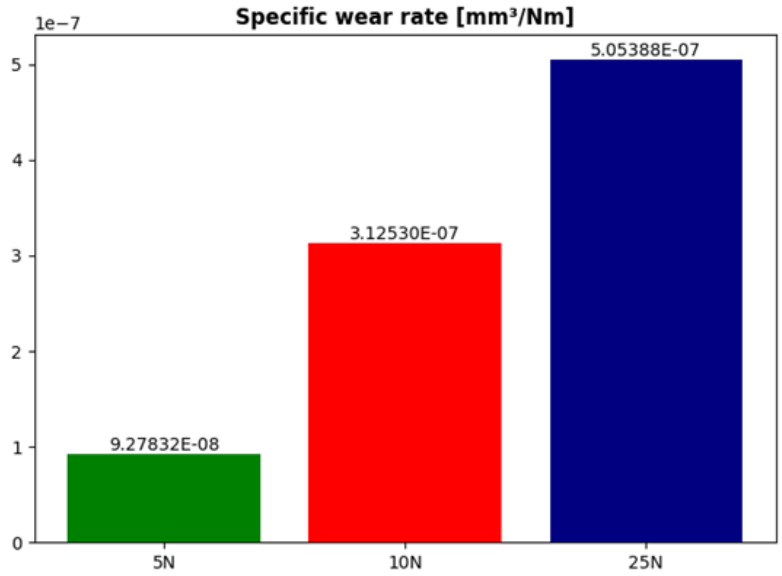

Fig. 2 Wear rates of the $ZrO_2 + 3Y_2O_3$ at applied loads of 5 N, 10 N and 25 N.

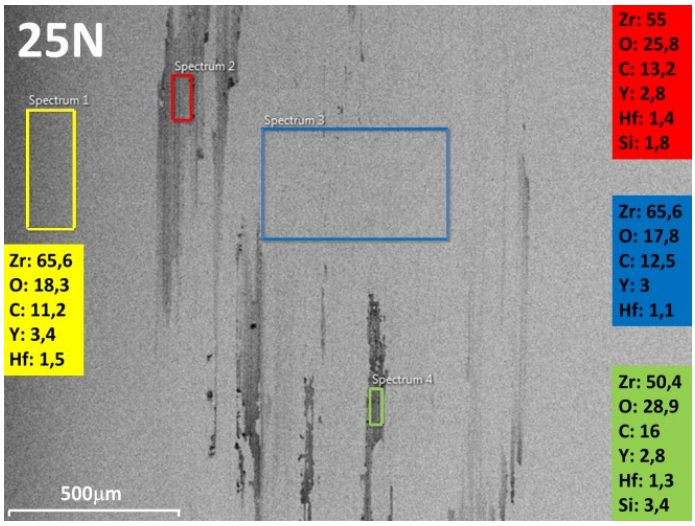

Fig. 3 EDX analysis of the chemical composition of the worn track of ZrO_2 + $3Y_2O_3$ after wear test with 25 N load.

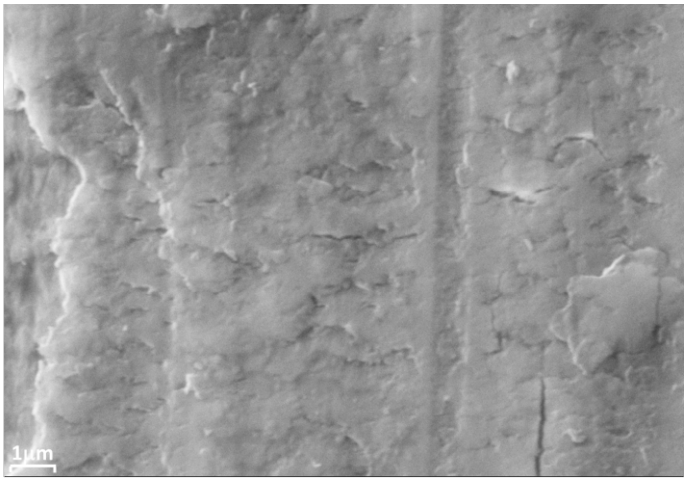

Fig. 4 SEM micrographs with typical damage mechanism in the wear tracks after the wear test with 25 N.

EDX analysis (Fig. 3) of the worn ZrO_2 + $3Y_2O_3$ surface confirmed the base ceramic matrix composition (Spectrum 1), while other areas (Spectra 2 and 4) exhibited increased oxygen and carbon content along with silicon. This indicates tribochemical oxidation and material transfer from the SiC counterface, leading to tribolayer formation. Spectrum 3 showed a composition similar to the base material but with slightly less oxidation. The presence of yttria confirmed zirconia stabilization, and trace hafnium likely originated from the SiC ball. SEM micrographs (Fig. 4) of the worn surface displayed fine, irregular microdefects and microcracks, characteristic features of a dominant abrasive wear mechanism caused by the hard SiC counterbody.

Discussion

Nanoindentation confirmed high hardness (~16.5 GPa) and elastic modulus (~250 GPa) for 3Y-TZP ceramics. While a dedicated microstructural image was not captured, the combination of high mechanical properties and their extremely low scatter serves as powerful indirect evidence for a highly homogeneous, fine-grained microstructure, free of significant defects. This interpretation aligns with literature [6, 7] emphasizing the importance of a fine-grained microstructure and high density. The low scatter of values indicates a homogeneous microstructure without significant defects [1, 9, 15].

Vickers microhardness (1382) and fracture toughness K_{IC} (5.2 MPa·m$^{1/2}$) confirm the material's good mechanical durability. Slightly lower K_{IC} values compared to some of the highest reported may be influenced by specific sintering parameters and grain size [6, 11].

Tribological tests showed a stable COF of 0.37–0.39 at all loads, with a slight decrease at the highest load, potentially due to thin tribolayer formation. This phenomenon agrees with observations by Che et al. [13] regarding the self-lubricating effect of tribochemical oxidation during dry sliding. The COF stability throughout the test also indicates good tribological stability of 3Y-TZP under dry reciprocating sliding conditions, consistent with results from He and de Wit [5] and Esposito and Tucci [9].

Specific wear rate values show only a slight increase with load, confirming the material's ability to withstand higher contact pressures without significant deterioration of tribological properties. Such resistance is typical for yttria-stabilized tetragonal zirconia ceramics, which, due to transformation toughening and microstructural homogeneity, effectively mitigate friction-induced damage [1, 3].

Microscopic analysis of the wear track revealed microcracks and defects typical for dry wear of ZrO_2–$3Y_2O_3$ ceramics, suggesting a dominant abrasive wear mechanism. Chemical EDX analysis confirmed the presence of a carbon-containing tribolayer, likely formed by tribochemical oxidation during sliding [13]. This tribolayer may act as a passive barrier between the ceramic substrate and the hard SiC counterface, contributing to improved tribological performance [14]. A combined wear mechanism was demonstrated: dominant abrasive wear (microcracks, grooving) due to hard contact with SiC, and simultaneous tribochemical reactions forming a protective tribolayer (oxide layers with Si and C). The presence of yttria in the surface layer indicates the preservation of the tetragonal phase, crucial for the transformation toughening mechanism, and thus for maintaining high fracture toughness and wear resistance [1, 9].

Overall, the results confirm that stabilization of the tetragonal phase and a fine-grained microstructure are key factors for the successful application of 3Y-TZP in tribological environments, especially in contact with hard counterfaces such as SiC.

Conclusion

This study investigated the tribological behavior of ZrO_2–$3Y_2O_3$ ceramics prepared by SPS during dry reciprocating sliding against a SiC counterface. An optimized fine-grained microstructure led to high hardness (~16.5 GPa), a stable elastic modulus (~250 GPa), and adequate fracture toughness ($K_{IC} \approx 5.2$ MPa·m$^{1/2}$). Tribological tests showed a stable COF of 0.37–0.39, with a slight decrease at the highest load (25 N), likely due to tribolayer formation. Although wear increased with load, the specific wear rate remained relatively stable, indicating good wear resistance. EDX analysis confirmed tribochemically formed oxide layers rich in silicon oxide and carbon, acting as protective barriers. Surface imaging revealed typical signs of abrasive wear (microcracks). The wear mechanism combined abrasive damage from the SiC counterface with tribochemical formation of protective oxide layers. The findings highlight the potential of 3Y-TZP ceramics for applications requiring high wear resistance under dry conditions, including precision mechanical systems, energy, and biomedical fields.

Acknowledgements

The work was funded by the EU NextGenerationEU through the Recovery and Resilience Plan for Slovakia under the project No. 09I03-03-V04-00260.

References

[1] R.H.J. Hannink, P.M. Kelly, B.C Muddle, Transformation toughening in zirconia-containing ceramics, J.Amer. Ceram. Soc., 83, 3 (2000) 461-487.

[2] R.C. Garvie, R.H.J. Hannink, R.T. Pascoe, Ceramic steel, Nature, 258 (1975) 703-704.

[3] B. Basu, B. Sreenivasulu, A. Kumar, S. Basu, Microstructure–toughness–wear relationship of tetragonal zirconia ceramics, J. Europ. Ceram. Soc., 24, 9 (2004) 1563-1570.

[4] J. Chevalier, What future for zirconia as a biomaterial, Biomaterials, 27, 4 (2006) 535-543.

[5] W. He, de J. H. W. Wit, Grain-size dependence of sliding wear in tetragonal zirconia ceramics. Wear, 217, 1-2 (1998) 144-150.

[6] M. Trunec, P. Stastny, J. Kastyl, P. Roupcova, Z. Chlup, 2Y-TZP ceramics with high strength and toughness by optimizing the microstructure, J. Europ. Ceram. Soc, 44, 5 (2024) 3258-3266.

[7] A. Palmeira, M.P. Cangani, D. Rodrigues Jr, K. Strecker, Influence of sintering parameters on the microstructure and mechanical properties of nanosized 3Y-TZP ceramics. Ceram. Inter., 42, 1 Pt A (2016) 123-131.

[8] F. Egilmez, G. Ergun, I. Cekic-Nagas, P.K. Vallittu, L.V.J. Lassila, Factors affecting the mechanical behavior of Y-TZP, J. Mech. Behav. Biomed. Mater., 37 (2014) 78-87.

[9] A. Tucci, L. Esposito, Microstructure and tribological properties of ZrO_2 ceramics, Wear, 172, 2 (1994) 111-119.

[10] M. Díaz, Microstructure and mechanical properties of zirconia (3Y-TZP)/Zr composites prepared by wet processing and subsequent spark plasma sintering. Mater. Sci. Forum, 1016 (2022) 621-626.

[11] O.O. Vasylkiv, Y. Sakka, V.V. Skorokhod, Hardness and fracture toughness of alumina- doped tetragonal zirconia with different yttria contents, J. Europ. Ceram. Soc., 23, 10 (2003) 1669-1676.

[12] J. Chevalier, L. Gremillard, S. Deville, Low-temperature degradation of zirconia and implications for biomedical implants. Biomaterials, 30, 8 (2009) 1558-1566.

[13] Y. M. Chen, B. Rigaut, F. Armanet, Wear Behaviour of partially Stabilized Zirconia High Sliding Speed, Europ. Ceram. Soc., 6 (1990) 383-390.

[14] W.C. Oliver, G.M. Pharr, An improved technique for determining hardness and elastic modulus using load and displacement sensing indentation experiments, J. Mater. Research, 7, 6 (1992) 1564-1583.

[15] B. Basu, J. Vleugels, O. Van Der Biest, Microstructure–toughness–wear relationship of tetragonal zirconia ceramics, J. Europ. Ceram. Soc., 24, 7 (2004) 2031-2040.

CHAPTER 6:

Applied Materials and Engineering Applications

Published in: Materials Science Forum
ISSN: 1662-9752, Vol. 1179, pp 29-34
doi:10.4028/p-15bSzd

Submitted: 2025-05-31
Revised: 2025-12-04
Accepted: 2025-12-19
Online: 2026-03-03

Polycrystalline Thermoelectric Materials with Observed Anisotropy

František Mihok[1,2,a*], Viktor Puchý[1,b], Juraj Szabó[1,c], Beáta Ballóková[1,d], Róbert Džunda[1,e] and Karel Saksl[2,1,f]

[1]Institute of Material Research SAS, Watsonova 47, 04001 Košice Slovakia

[2]Faculty of Materials, Metallurgy and Recycling TUKE, Letná 9, 04200 Košice Slovakia

[a*]frantisek.mihok@tuke.sk, [b]vpuchy@saske.sk, [c]jszabo@saske.sk, [d]bballokova@saske.sk, [e]rdzunda@saske.sk, [f]karel.saksl@tuke.sk

Keywords: Thermoelectric Generator, SnSe, Ag_2S, Anisotropy, Doping.

Abstract. Thermoelectric generators (TEGs) are vital, reliable energy sources for both extreme environments such as deep space exploration and off-grid terrestrial applications, as well as emerging fields like wearable energy harvesters and biocompatible medical sensors. This study focuses on tin selenide (SnSe) combined with ductile silver sulfide (Ag_2S) to leverage their complementary properties: SnSe's promising thermoelectric performance and mechanical robustness for homojunction TEGs, and Ag_2S's exceptional ductility and thermal sensitivity ideal for flexible, biocompatible devices. Materials were synthesized using scalable powder metallurgy and spark plasma sintering (SPS) techniques, ensuring reproducibility and microstructural control tailored for these diverse applications. Our Bi-doped polycrystalline SnSe exhibits a unique polarity switching phenomenon and anisotropic behavior influenced by dopants (Bi, Ag, In), enabling optimized thermoelectric and mechanical properties that reduce interfacial stresses and enhance durability in harsh conditions. Meanwhile, the Ag_2S materials combine thermoelectric efficiency with fast thermal response and flexibility, suited for continuous physiological monitoring in wearable systems. The hybrid integration of SnSe homojunctions with flexible Ag_2S devices opens new possibilities for durable, efficient thermoelectric energy harvesting across wide temperature gradients in aerospace and biomedical fields.

Introduction

Thermoelectric generators (TEGs) represent a critical energy harvesting technology for extreme environments, from deep-space probes to autonomous terrestrial sensors, due to their reliability and predictable operation without moving parts. Conventional TEG designs rely on heterojunction couples of dissimilar materials (e.g., Bi_2Te_3 alloys), but these systems face inherent limitations: thermal expansion mismatches induce interfacial stresses that degrade performance over time, while brittle thermoelectric materials complicate integration into flexible applications. Recent advances in homojunction TEG pairs using tin selenide (SnSe) offer a promising solution to these challenges, as single-material systems inherently minimize interfacial stresses while maintaining performance parity.

The layered orthorhombic structure of SnSe enables rare anisotropic thermoelectric properties, with reported zT values exceeding 2.6 along specific crystallographic directions [1]. Figure of merit zT is used to determine efficiency of thermoelectric materials:

$$zT = \frac{\alpha \,.\, \sigma}{\kappa} \tag{1}$$

where α stands for Seebeck coefficient, σ for electrical conductivity and κ for thermal conductivity. However, practical implementation requires scalable synthesis of polycrystalline materials with controlled dopant distributions. Our previous work demonstrates that Bi doping induces a unique polarity switching phenomenon in SnSe, transitioning from p-type to n-type conduction at concentrations >0.5 at. %, while maintaining mechanical integrity through powder metallurgy and spark plasma sintering (SPS) [2].

Complementary to high-temperature SnSe systems, ductile silver sulfide (Ag_2S) emerges as a novel material for flexible thermoelectrics. Unlike conventional brittle semiconductors, Ag_2S exhibits metallic-like ductility (failure strain >20 %) while retaining a relatively high Seebeck coefficient. This unique combination enables novel applications in wearable energy harvesters and implantable medical sensors, where mechanical compliance and fast thermal response (<1 s) are critical. Recent studies confirm that Ge doping in Ag_2S can optimize the carrier concentration balance between electrical conductivity and Seebeck coefficient, making it suitable for low-grade heat recovery [3].

The object of this study is to develop and characterize polycrystalline SnSe doped with various elements via powder metallurgy and spark plasma sintering (SPS), alongside Ge-doped Ag_2S synthesized by solid-state reaction and cold extrusion, focusing on their thermoelectric, electrical, mechanical, and microstructural properties including observed anisotropy. The primary goals were to demonstrate polarity switching in doped SnSe for enabling durable thermoelectric generators with homojunctions by minimizing thermal expansion mismatch stresses. Another goal was to quantify the anisotropic thermoelectric behavior arising from layered microstructure and sintering-induced preferred orientation in doped SnSe. Lastly, our goal was to improve thermoelectric properties of ductile Ag_2S for flexible applications. These advancements target hybrid TEG designs for extreme environments (space, high ΔT) and low-gradient uses (wearables, sensors), enhancing reliability without compromising performance.

Materials and Methods

Both SnSe and Ag_2S were prepared from pure elemental powders with a purity of at least 99.9 %. SnSe was prepared via powder metallurgy. Elemental powders were mixed together and then placed into a circular furnace. Doping element was also in the form of a powder and was thoroughly mixed with other elements. They were heated up to 500 °C (5 °C/min) for 12 hours under an Ar atmosphere. Cooling was performed at the same rate. The prepared polycrystalline melts were crushed and analyzed. Afterwards, the crushed powders were sintered using spark plasma sintering (SPS, 650 °C, 50 MPa, 10 minutes) into discs. The thermoelectric properties of these discs were determined. A single step sintering of discs with contact plates was also explored. The sintered materials can be seen in Fig. 1a–c, and the sintering scheme in Fig. 1d.

Ag_2S was synthesized from pure elemental powders. Dopant was also in the form of powder and was mixed with Ag and S powders. After mixing, the powders were placed into a steel container and heated to 160 °C under an Ar atmosphere. The mixture was kept at 160 °C for 10 hours while the solid-state reaction occurred. The last step was cold extrusion of the Ag_2S to obtain rods with a 4 mm diameter. The thermoelectric properties of these rods were determined.

Before sintering and cold extrusion, each material underwent chemical and phase analysis using EDX (Tescan Mira, Czechia) and XRD (Philips XPert Pro, The Netherlands) techniques. Determination of thermoelectric properties was carried out on in-house developed instruments for measuring the Seebeck coefficient and electrical conductivity at room temperature. Mechanical properties were determined using depth-sensing indentation on a TTT-NHT instrument (CSM Instruments, now Anton Paar, Austria). The tests were conducted in linear mode with a Berkovich pyramid diamond tip. Forces of 50 mN (for Ag_2S) and 10 mN (for SnSe) were applied to each sample for a duration of 10 s. The load-penetration depth (P-h) profiles obtained were analyzed following the Oliver and Pharr method. More details about material synthesis, characterization, and instrumentation can be found in our previous works [2, 3].

Results and Discussion

Doped materials based on SnSe showed a rising concentration of Bi dopant in material characterization. In all materials, there was a noticeable loss of Sn based on the elemental analysis. This effect is well-known in SnSe alloys and is difficult to resolve [1, 8, 9]. Phase analysis confirmed the presence of a majority SnSe phase with some $SnSe_2$ present. Doping concentration did not affect the unit cell parameters as confirmed by XRD analysis and Rietveld refinement, and EDX confirmed

uniform distribution of elements across the whole sample (more details can be found in our previous work [2]). Doping elements were therefore not incorporated into the unit cell but instead were present in interstitial positions. We combined two steps during the sintering process: pressing the powders into discs and the addition of electrical contacts. Contact plates were added to the top and bottom of the powder during the sintering step. Graphite paper was used to protect dies and ease separation. It was put in between contact plates and graphite dies. Graphite paper was also used around the circumference (Fig. 1d). Copper was initially used, but even a 0.5 mm thick layer dissolved into our material during sintering. Stainless steel was tried with unsatisfactory results (Fig. 1b). Brass was tested next and proved to be an effective material to create an electrical contact layer on the SnSe material (Fig. 1c). This layer is required for effective construction of thermoelectric modules and generators. It enables efficient soldering of components and helps with homogeneous current transfer.

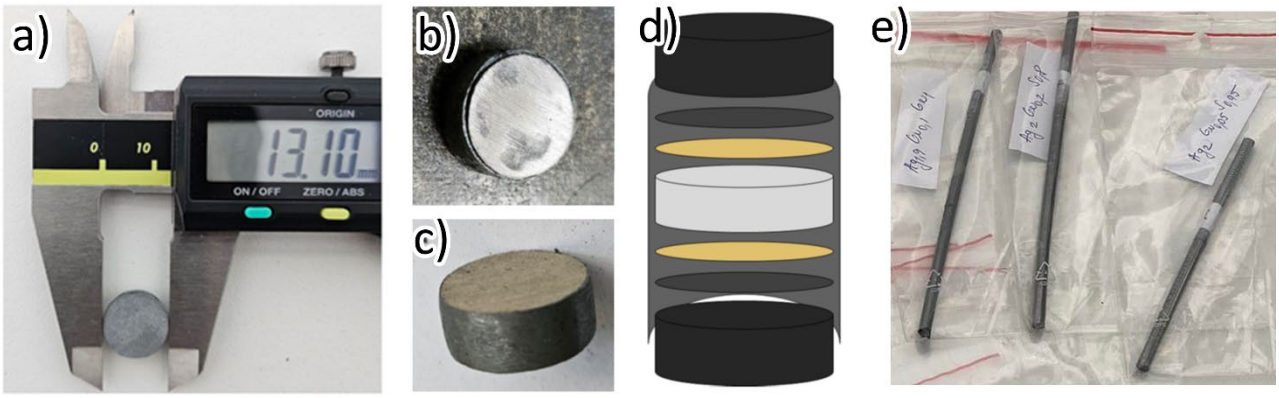

Fig. 1 Sintered SnSe disk (a), sintered disk with stainless steel layer (b), sintered disk with brass layer (c), SPS sintering scheme (d), extruded 4 mm Ag_2Se rods (e).

Pure SnSe is a p-type semiconductor, resulting in a positive Seebeck coefficient. By doping this material with Bi (replacing Sn), we managed to flip the Seebeck coefficient into negative values. Even though the synthesized materials are polycrystalline and elements are spread out homogeneously, we observed significant anisotropy of the Seebeck coefficient. Depending on the measured plane, the difference was as high as 75 % (Fig. 2). This anisotropy is caused mainly by the layered structure, apparent from optical, SEM, and XRD analysis. More detailed microstructure analysis can be found in our other works [2, 7]. Layer planes are mostly aligned perpendicularly to the sintering direction. Anisotropy was reduced but still noticeable in In doped samples. Changes in Seebeck coefficient, across different orientations, were up to 18 %. Ag doping significantly improved the material's homogeneity with only 8.5 % change in Seebeck coefficient across different orientations. More details about these materials can be found in our other work [7]. Unfortunately, the electrical conductivity of SnSe was reduced by Bi doping and was comparable only at the highest doping concentration. To further study the cause of this lower electrical conductivity, we used the Van der Pauw four-probe method on our disc samples. A Hall constant close to zero indicates very complex charge carrier transport with contributions from both electrons and holes. Additionally, low carrier mobility indicates the presence of heavy charge carriers (Fig. 3). Heavy charge carriers in semiconductors can cause an elevated Seebeck coefficient and suppressed electrical conductivity [5, 6]. The layered structure of our SnSe materials was also apparent from their mechanical properties. The materials were both soft and brittle, which became apparent even when handling them. Nanoindentation confirmed improvement of mechanical properties (both hardness and elastic modulus) with the addition of dopant (Fig. 4a).

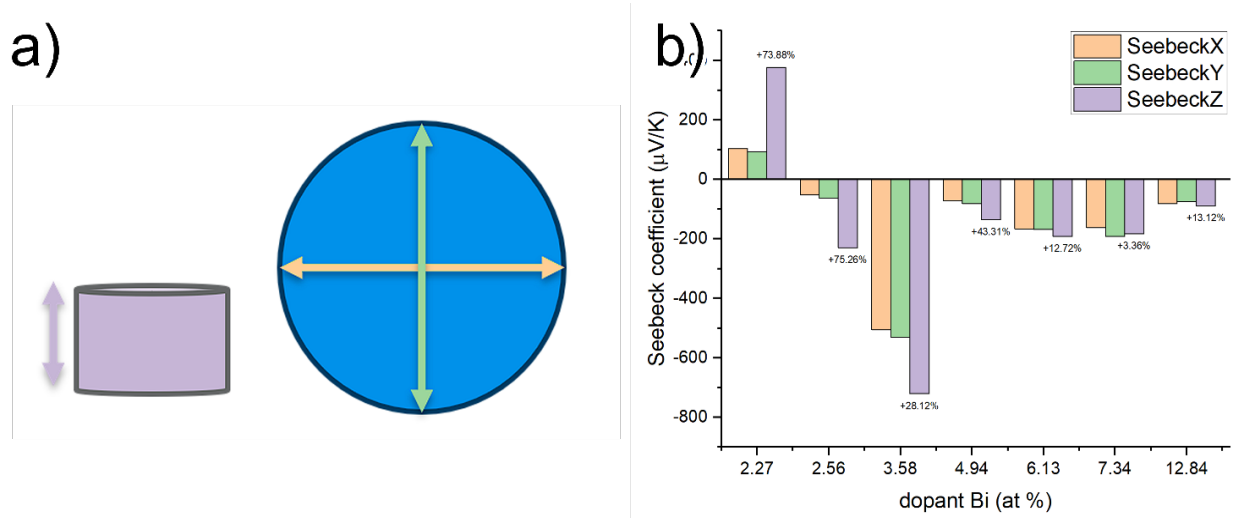

Fig. 2 Measuring directions (a), anisotropy of Seebeck coefficient in Bi doped materials (b).

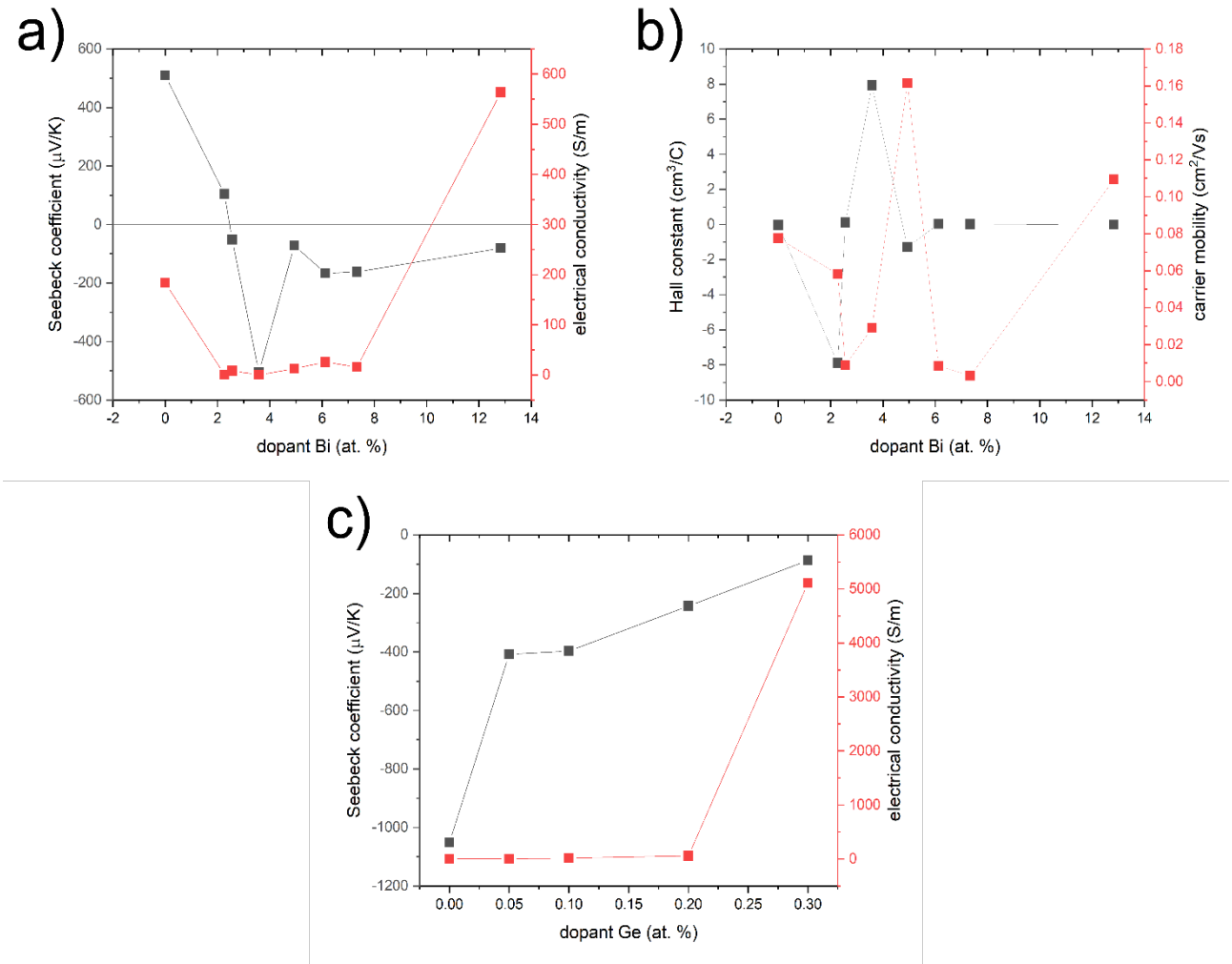

Fig. 3 Seebeck coefficient and electrical conductivity (a), Hall constant and carrier mobility (b) of Bi doped SnSe, Seebeck coefficient and electrical conductivity of Ge doped Ag_2S (c).

Ag_2S has significantly different mechanical properties. It is tough and ductile, allowing its use in flexible thermoelectrics. Based on the nanoindentation, hardness is vastly improved and the elastic modulus is roughly the same as SnSe (Fig. 4b). Similarly to SnSe, chemical and phase composition was verified using the same techniques. The presence of the α-Ag_2S phase was confirmed. Pure Ag_2S is a strong n-type semiconductor. However, its main drawback for use in thermoelectrics is very low

electrical conductivity. We tried to mitigate this by Ge doping and we were successful [3]. When Ge was doped replacing S, the electrical conductivity was even lower than that of pure Ag_2S. When Ag was being replaced, we eventually managed to achieve a rise in electrical conductivity. From the drop in Seebeck coefficient and previous SnSe results, we can assume that the charge carrier transport mechanism was changing with the addition of Ge. Heavy charge carriers were being replaced by light carriers, eventually resulting in a significant electrical conductivity jump at the 0.3 Ge sample. The remaining heavy charge carriers allowed this material to retain a usable Seebeck coefficient value, achieving noteworthy thermoelectric performance overall.

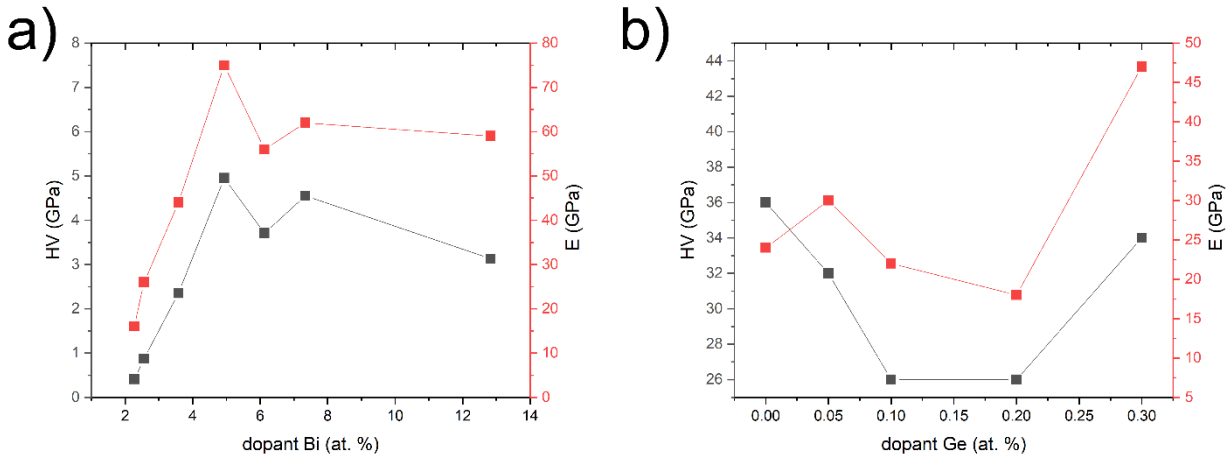

Fig. 4 Hardness and elastic modulus obtained via nanoindentation method for Bi doped SnSe materials (a), Ge doped Ag_2S (b).

Summary

This study advances thermoelectric by developing and characterizing two doped polycrystalline material systems: tin selenide (SnSe) and silver sulfide (Ag_2S). Bi doping in SnSe enables a unique polarity switching from p-type to n-type conduction, paving the way for durable homojunction thermoelectric generators that reduce mechanical stresses caused by thermal expansion mismatch. The anisotropic thermoelectric behavior linked to SnSe's layered microstructure and dopant concentration is quantified, demonstrating how preferred orientation influences performance optimization. Separately, Ge doping in Ag_2S results in biocompatible, ductile materials that retain strong thermoelectric performance, enabling flexible and wearable energy harvesting applications. These findings open new avenues for robust, efficient thermoelectric devices applicable across a broad range of conditions – from extreme aerospace environments to biocompatible medical sensors.

Acknowledgment

This work was supported by the Slovak Research and Development Agency under Contract no. APVV23-0030, VEGA project No. 2/0039/23 and KEGA project No. 011TUKE-4/2025. This research was funded in part by the international project M-ERA.NET 3/2022/235/H2MobilHydride.

References

[1] C. Zhou, et al., Nat. Mater., 20, 10 (2021) 1378-1384.

[2] F. Mihok, et al., Inorganics, 12, 4 (2024) 103.

[3] G. Hrickova, et al., Inorganics, 12, 4 (2024) 98.

[4] W.C. Oliver, G.M. Pharr, J. Mater. Res., 7 (1992) 1564-1583.

[5] H. Namiki, M. Kobayashi, K. Nagata, Y. Saito, N. Tachibana, Y. Ota, Materials Today Sustainability, 18 (2022) 100116.

[6] P. Sun, et al., Nat Commun, 6, 1 (2015).

[7] F. Mihok, et al., Inorganics, 13, 10 (2025) 333.

[8] W. Shi, et al., Adv Sci (Weinh), 5, 4 (2018) 1700602.

[9] G. Hema Chandra, Journal of Crystal Growth, 306, 1 (2007) 68-74.

Published in: Materials Science Forum
ISSN: 1662-9752, Vol. 1179, pp 35-41
doi:10.4028/p-E6D3ot

Submitted: 2025-05-31
Revised: 2025-07-18
Accepted: 2025-12-19
Online: 2026-03-03

Gas Pressure Infiltration of Porous Ni-Al_2O_3-Al Compacts with Molten Aluminium

Andrej Opálek[1,a*], Stanislav Kúdela j.r.[1,b], Matej Štěpánek[1,c], Naďa Beronská[1,d] and Karol Iždinský[1,e]

[1]Institute of Materials and Machine Mechanics, Slovak Academy of Sciences, Dúbravská cesta 9/6319, 845 13 Bratislava, Slovakia

[a*]andrej.opalek@savba.sk, [b]stanislav.kudela-ml@savba.sk, [c]matej.stepanek@savba.sk, [d]nada.beronska@savba.sk, [e]karol.izdinsky@savba.sk

Keywords: Nickel Aluminides, Gas Pressure Infiltration, Uniaxial Pressing, Thermocycling, Microstructure.

Abstract. This paper presents a method for fabricating a porous Ni-Al_2O_3-Al compact using uniaxial double-action pressing, which was subsequently infiltrated with molten aluminium. Al_2O_3 ceramic particles primarily serve to create porosity within the composite compact. Due to the difficulty pressing hard metal powders, aluminium powder was introduced into the Ni+Al_2O_3 mixture to act as a plasticizer, improving the material's compressibility. Experiments indicated that the optimal infiltration temperature was 750 °C with an infiltration duration of 300 seconds. To evaluate the reaction extent among the initial components, a subset of infiltrated samples underwent annealing at 800 °C for 3 hours under an inert argon atmosphere. Both annealed and reference samples were subjected to thermal cycling. The microstructure and thermal stability of the resulting composite materials were analyzed and characterized using scanning electron microscopy with energy-dispersive spectroscopy, respectively.

Introduction

Nickel aluminides, a recognized class of intermetallic compounds, have rapidly gained attraction across various industries, such as aerospace, automotive, and energy. This considerable interest primarily stems from their outstanding physical and mechanical properties. These include low density, high thermal stability, and a relatively high specific strength, distinguishing them from traditional metallic materials. Additionally, their superior resistance to corrosion and oxidation, especially at elevated temperatures, unequivocally positions nickel aluminides for industrial applications in demanding operating conditions [1, 2].

When pressing hard metal powders such as Ni and Al_2O_3, manufacturers often encounter difficulties related to poor flowability and resistance to densification. These powders tend to form green bodies with inadequate density or cracking if processed without modification. To address these challenges, plasticizers (or binding agents) are introduced into the powder mixture to enhance its flexibility, workability, and cohesion during compaction. In powder metallurgy – particularly for hard metal systems – plasticizers serve to improve compressibility, increase green strength, ensure more uniform pressure transmission, and reduce common defects like cracking and lamination. Although plasticizers are well-known in the plastics and ceramics industries, in this context they specifically refer to additives that impart temporary plasticity to the powder bed, making it behave more like a deformable mass during pressing. Common examples include metallic soaps (e.g., zinc stearate, stearic acid), waxes, and various polymers [3–5]. Their use contributes to producing higher-quality green bodies and enhances overall process efficiency. However, these additives also pose challenges, particularly during post-compaction steps, where they may influence the final sintered properties or raise environmental and health concerns.

In this study, Al powder was used as a plasticizer. Using aluminum (Al) powder as a plasticizer in the context of compacting Ni-Al or Ni-Al_2O_3 powder mixtures is an interesting and somewhat unique approach compared to traditional organic plasticizers. Its "plasticizing" effect primarily stems from its ductility and lower melting point relative to nickel and alumina. The fabrication of Ni-Al-Al_2O_3 multiphase composites is inherently complex, not least because the Ni-Al interaction is strongly exothermic. In this study, a porous Ni framework reinforced with Al_2O_3 particles was pressure infiltrated with molten Al. Although intermetallic phases form during infiltration, they may be metastable; subsequent high-temperature thermocycling can drive further phase transformations or trigger reactions involving any residual Al.

The main aim of this study is to develop and characterize porous Ni-Al_2O_3-Al composite compacts by utilizing aluminum powder as a plasticizer for improved press ability, followed by gas pressure infiltration with molten aluminum, and to investigate the resulting microstructure, intermetallic phase formation, and thermal stability under cyclic heat exposure.

Material and Methods

For green body preparation, the following powders were used:

- **Nickel (Ni):** 99.3 % purity, Metco 56C-NS, OC Oerlikon Corporation, Pfäffikon, Switzerland; particle size <75 µm.
- **Aluminum oxide (Al_2O_3):** 95.50 % purity, Metco Amdry 6060, OC Oerlikon Corporation, Pfäffikon, Switzerland; particle size <45 µm.
- **Aluminum (Al):** 95.50 % purity, Alpoco A1050, AMG Alpoco UK Limited, UK; particle size <63 µm.

Initially, a mixture of Ni powder with 12.87 wt.% Al_2O_3 (corresponding to 25 vol.%) was prepared. This specific composition was selected based on prior experiments, which showed that higher Al_2O_3 content reduced compact cohesion after pressing. To improve compressibility, 3 g of aluminum powder was added to the Ni-Al_2O_3 blend, taking advantage of Al's relatively ductile nature. This amount proved optimal for enhancing compactness without significantly reducing porosity. The resulting powder blend (hereinafter referred to as the "powder mixture") had a volumetric composition of 68.76 % Ni, 22.95 % Al_2O_3, and 8.29 % Al.

Particle size distribution for each powder was determined using laser diffraction (Analysette 22 NanoTec, Fritsch, Germany) in water. The measured D_{50} values were:

- Ni: 69.91 µm
- Al_2O_3: 33.17 µm
- Al: 30.32 µm

Finally, the powder mixture was thoroughly homogenized for 30 minutes using a Turbula T2F mechanical mixer (WAB, Muttenz, Switzerland).

Porous Ni-Al-Al_2O_3 compacts were fabricated by uniaxial double-action pressing and then infiltrated with molten aluminum. The Al_2O_3 particles act as a pore-forming phase, creating a controlled porous network within the compact. To overcome the poor compressibility of the Ni-Al_2O_3 blend, ductile aluminum powder was added as a plasticizer, thereby enhancing the material’s packability during pressing.

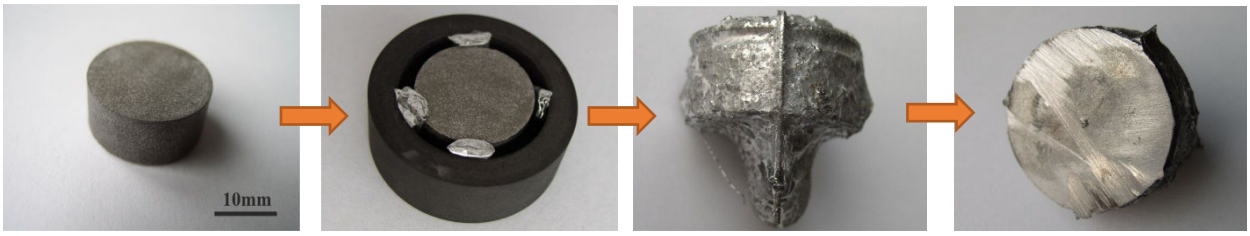

Fig.1 Procedure for Liquid Al Infiltration of the green compact.

The powder blend was uniaxially pressed at 250 MPa. The green compact was then infiltrated at 750 °C for 300 sec. under a 5 MPa argon atmosphere.

The porosity of green compacts was calculated from the known mass and volume of green compact. The rule of mixture was used to determine theoretical density of bulk composite considering mass fractions of used powders and their densities. The microstructure was analyzed by SEM EDS utilizing JEOL JSM 6610 (Jeol, Tokyo, Japan). Aztec software, Oxford instruments, UK was used to investigate the intensity in keV of EDS peaks of individual elements (Ni, Al) and according to the ratio of elements Ni-Al in at.% the types of intermetallic compounds NiAl, Ni_2Al_3, Ni_5Al_3 and $NiAl_3$ were determined. Thermal stability was measured by DTA/TG/Dil combined apparatus (Linseis Thermal Analyser L75/L81/2000, Selb, Germany) was. The sample temperature was measured by an S-type thermocouple located in close vicinity to the sample. The samples were heated from 30 °C to 630 °C at a heating rate of 3 °C/min in an inert argon atmosphere.

Results and Discussion

A detailed analysis was performed to evaluate the microstructure and chemical composition of the Ni-Al_2O_3-Al compacts after molten aluminum infiltration. Special attention was given to the distribution of phases and the extent of reaction among the constituents under the selected processing conditions. To determine the degree of reaction A more detailed study of phase formation in both of the initial components, one of the infiltrated tablets was annealed for 3 hours at 800 °C in an argon atmosphere. Subsequently, a sample cut from it underwent three thermal cycles up to 630 °C (3 °C/min) in a dilatometric device (referred to as the "annealed sample"). The results from this sample were compared with an infiltrated sample that had not been subjected to annealing (the "reference sample"). Based on previous findings, it is clear that the most significant volume changes occur during the first annealing cycle, which was also confirmed for the reference sample (Fig. 2). The elongation after the third cycle was minimal and at approximately the same level for both compared samples. The coefficients of thermal expansion (CTEs) also confirm progressive stabilization of the samples during repeated thermal cycling. While the reference sample requires more cycles to reach thermal equilibrium compared to the annealed sample, their CTE values converge closely by the third cycle.

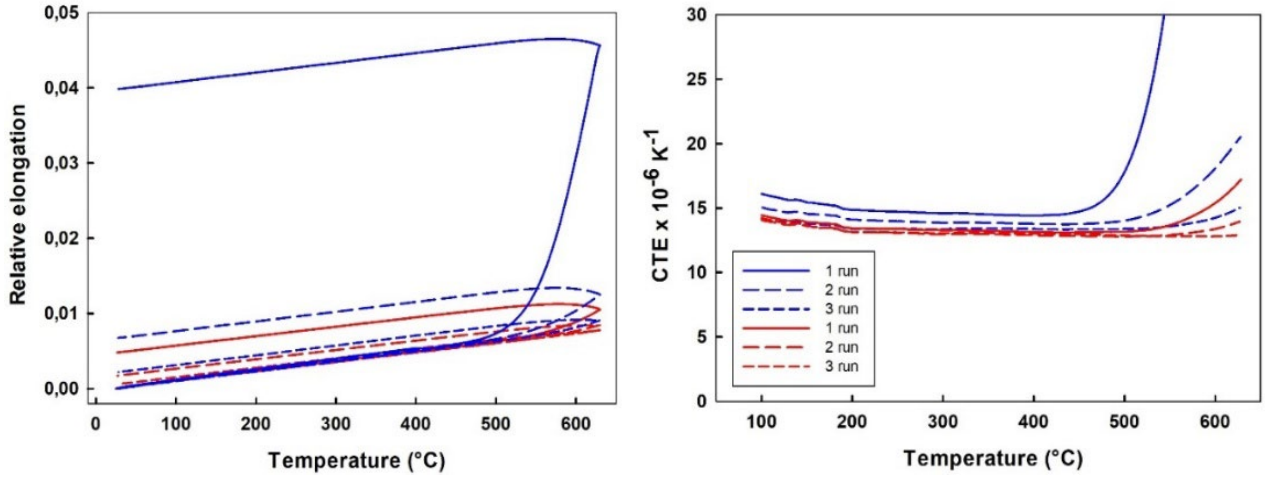

a) b)

Fig. 2 Dependence of relative elongation (a) and coefficient of thermal expansion (b) on temperature for a sample formed by infiltrating a pressed powder mixture with liquid Al at a temperature of 750 °C for 300 s in an Ar atmosphere (3 °C/min), reference sample (blue line) and after infiltration in Ar atmosphere – annealed sample (3 hrs. 800 °C) (red line).

The microstructure of the prepared composites before and after thermal cycling is shown in Fig. 3 a homogeneous distribution of ceramic particles and the newly formed phases was observed practically throughout the entire cross-section of the samples. The results indicate that the volume of Ni particles significantly decreases after infiltration, yet the porosity remains minimal. This suggests that during infiltration, the Al melt penetrates the entire volume of the prepared sample, and the consumed Al is replenished. Upon heating the sample to 630 °C in the dilatometer, the porosity of the reference sample increased (Fig. 3b), and further thermal cycling led to an even greater increase (Fig. 3c). A substantially lower porosity was observed in the sample that was first annealed for 3 hours at 800 °C and only then subjected to thermal cycling. This points to the fact that phase formation after sample infiltration can also influence the course of subsequent annealing. If the composite is subjected to longer-term annealing at 800 °C, the porosity is lower compared to when the annealing process is interrupted by cooling to laboratory temperature.

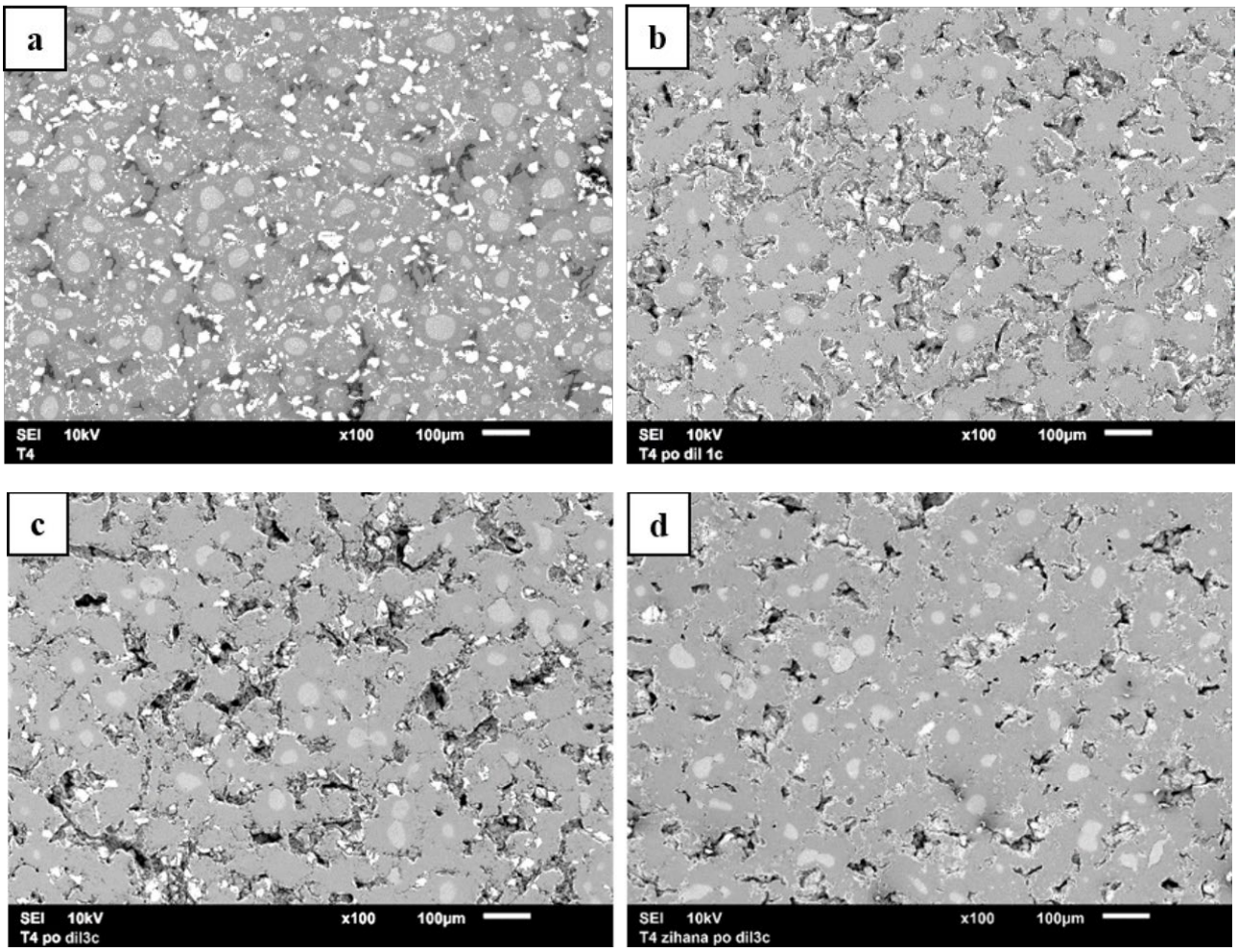

Fig. 3 Sample structure (reference) after infiltration (a), after the first annealing cycle to 630 °C (b), after three annealing cycles to 630 °C (c) and after infiltration annealed for 3 h in Ar at 800 °C and after 3 cycles to 630 °C (d) (SEM image in the secondary electron field).

Types of samples is illustrated in Fig. 4. After infiltration, a small amount of unreacted Al is still observed, which is entirely consumed during the first cycle up to 630 °C. The volume of unreacted Ni particles significantly decreases; these particles are surrounded at their periphery by the Ni_2Al_3 phase. This phase forms via the reaction between Ni and Al at high Al concentration and low temperatures. Al atoms diffuse towards the center of the Ni particles, leading to the formation of the Ni_2Al_3 phase, which is thermodynamically most favorable under these conditions [7]. Further within the volume, the $NiAl_3$ phase is present. After five cycles up to 630 °C, practically only the Ni_2Al_3 phase was observed, in addition to any remaining unreacted Ni.

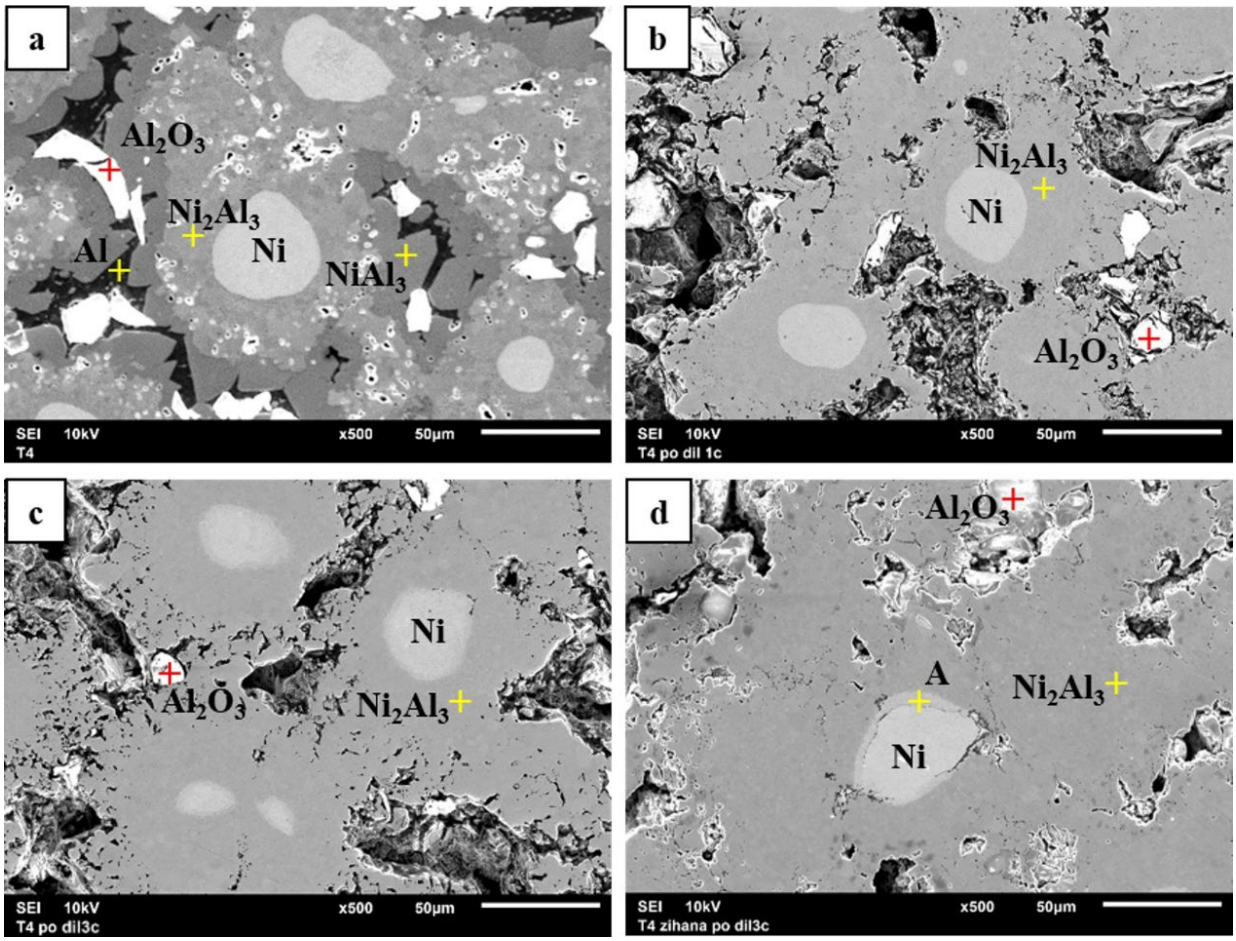

Fig. 4 Structure of samples from a pressed powder mixture with liquid Al after infiltration at 750 °C and a holding time of 300 seconds (a), after the first annealing cycle to 630 °C in Ar atmosphere (dilatometer) (b), after three annealing cycles to 630 °C in Ar atmosphere (dilatometer) (c) and 3 h annealing in Ar atmosphere to 800 °C + annealing in dilatometer 3 cycles to 630 °C in Ar atmosphere (d) (SEM, secondary electron field imaging; EDS point analysis).

If the sample was first annealed for a more extended period (3 hours) at 800 °C after infiltration, the higher Al content ($NiAl_3$) phase is no longer observed. Another change compared to the non-annealed sample is forming a thin phase, close to Ni_5Al_3, around some Ni particles, indicated by point A (Fig. 4.d). The primary disadvantage of the Ni_2Al_3 phase is its brittleness. To prevent the formation of this phase, systems with, a lower Al concentration and higher annealing temperatures, typically in the range of 1000 to 1100 °C, are preferred, as this leads to the dominant formation of the NiAl phase [8]. In our experiments, we infiltrated preforms where we deliberately created sufficient porosity, ensured by the pressing pressure and Al_2O_3 particles. This allowed enough Al to enter the sample to form the Ni_2Al_3 phase under the given infiltration conditions. The reactions forming aluminides in Ni and Al_2O_3 powder compacts infiltrated with molten Al are very rapid, occurring even during infiltration and continuing at elevated temperatures thereafter. It's not feasible to halt these reactions at an intermediate phase. Consequently, a protective barrier layer on their surface is essential if the goal is to preserve unreacted nickel (Ni) particles.

Conclusions

- Incorporating ductile Al as a plasticizer allows the otherwise difficult-to-press Ni-Al_2O_3 powders to be compacted at significantly lower pressing forces.
- Upon molten Al infiltration, the composite develops a uniformly homogeneous microstructure, with Al_2O_3 particles evenly distributed throughout.

- Aluminide formation during infiltration is extremely rapid and continues unabated during any subsequent high temperature exposure, so the intermetallic reactions cannot be arrested at an intermediate stage.
- Thermal cycling demonstrated that manufacturing-induced internal stresses were progressively relieved, resulting in enhanced sample stability.

Acknowledgment

The authors gratefully acknowledge the financial support from the Slovak Grant Agency for Science under the project VEGA No. 2/0061/22. Corresponding author*: email: andrej.opalek@savba.sk.

References

[1] S. Sampath, V.P. Ravi, S. Sundararajan. An overview on synthesis, processing and application of nickel aluminides: from fundamentals to current prospects. Crystals, 13 (2023), 435.

[2] Ş. Talaş. 3-Nickel aluminides, in: R. Mitra (Ed.), Intermetallic Matrix Composites, Elsevier Ltd. Amsterdam, The Netherlands, 2018, pp. 37- 69.

[3] Q. Xu, B. Gabbitas, S. Matthews, D. Zhang. The effect of binder and plasticizer on porous titanium compacts prepared by slip casting. Proc. Mat. Sci., 4 (2014) 81-84.

[4] Y. Thomas, V. Paris, S. St-Laurent, U.S. Patent 2015/0068361 A1. (2015)

[5] S. Russo, L. Brambilla, J.B. Thomas, E. Joseph. But aren´t soaps metal soaps? A review of applications, physico-chemical properties of metal soap and their occurrence in cultural heritage studies. Herit. Sci., 11 (2023) 172.

[6] A. Opálek, S. Kúdela, M. Nosko, K. Iždinský, P. Štefánik, F. Simančík. Forming of intermetallic phases during infiltration of nickel rods and powders with molten aluminium. Acta Metall. Slovaca Conf., 3 (2013) 247-252.

[7] M. Konieczny, R. Mola, P. Thomas, M. Kopcial. Procesing, microstructure and properties of laminated Ni-intermetallic composites synthesised using Ni sheets and Al foils. Arch. Metallurg. Mat., 56 (2011) 693-702.

[8] J. Angenete, K. Stiller. Comparison of inward and outward grown Pt modified aluminide diffusion coatings on a Ni based single crystal superalloy. Surf. Coat. Tech., 15 (2002) 107-118.

Published in: Materials Science Forum
ISSN: 1662-9752, Vol. 1179, pp 63-69
doi:10.4028/p-oUmYc0

Submitted: 2025-05-28
Revised: 2025-12-10
Accepted: 2025-12-19
Online: 2026-03-03

Transition Metal Phosphide-Based Membrane Electrode Assembly for Cost-Effective Production of H_2

Cyril Bera[1,a*], Alexandra Gubóová[1,b], Magdaléna Strečková[1,c] and Alexandra Kovalčíková[1,d]

[1]Institute of Materials Research, Slovak Academy of Sciences, Watsonova 1935/47, Košice, Slovakia

[a*]cbera@saske.sk, [b]aguboova@saske.sk, [c]mstreckova@saske.sk, [d]akovalcikova@saske.sk

Keywords: PEM Electrolyzer, Green Hydrogen, Non-Platinum Catalysts, Membrane Electrode Assembly, Optimization, Renewable Energy.

Abstract. This paper demonstrates the potential use of affordable, and efficient electrocatalysts, which can maintain the efficiency and stability of platinum-group metals in water-splitting. The study focuses on the optimization and setup of a PEM electrolyzer, alongside the development of new methods for preparing membrane electrode assemblies (MEA) using cost-effective and efficient catalyst materials. The integration of a fibrous membrane layer into the MEA architecture represents a promising design strategy, offering excellent structural and transport properties. Herein, a simple preparation method for modified NiCoP electrocatalysts in the form of carbon fibers is presented, using needleless electrospinning combined with airbrush spraying of an Ir-black solution onto a perfluorosulfonic membrane (Nafion), later pressed together with NiCoP carbon fibers to form a custom-made MEA. For electrochemical testing, custom made MEA was directly evaluated in the PEM electrolyzer setup, providing a preliminary demonstration of overall performance and stability.

Introduction

Research in proton exchange membrane (PEM) electrolyzers is tied to developing cost-effective, more efficient electrocatalysts that maintain the stability of platinum group metals (PGM) in water splitting reactions – hydrogen evolution reaction (HER) and oxygen evolution reaction (OER) [1]. Non-platinum catalysts, like transition metal phosphides (TMPs), are being explored and characterized. Hydrogen is emerging as a new type of fuel for energy storage and emission reduction [2]. Notably, green hydrogen with high energy density and low emissions is vital for decarbonizing industries but faces challenges in cost, availability and efficient production. Water electrolysis remains the most common H_2 production method [3]. The European Energy Directive aims for 14 % renewable energy use by 2030 [2]. Hydrogen versatility across multiple sectors such as transport, industry, energy and heating strengthen its role as a future fuel [4]. However, current production of 50 billion cubic meters per year is insufficient for rising global energy demands. This research aims to develop cost-effective fabrication methods of MEA to enhance PEM electrolyzer efficiency and stability during HER and OER, thus increasing production of green hydrogen. PEM electrolysis is a modern, efficient method for H_2 production, using a proton-conducting polymer membrane to split water at low temperatures (50–80 °C). It offers high efficiency and rapid response to power fluctuations, making it well-suited for integration with intermittent renewable sources like solar and wind [4]. Unlike alkaline electrolyzers, which have longer start up times, PEM systems can quickly adapt to dynamic operating conditions and energy storage needs. However, reliance on costly PGM catalysts limits scalability [5]. Developing non-PGM alternatives is critical for economic viability [8]. Recent research shows that TM-based catalysts – such as Ni, Co, Fe, and Mn oxides - offer promising performance, improved stability, and lower cost [6, 7].

Optimization of Single Cell PEM Electrolyzer

Optimizing a single-cell PEM electrolyzer for green hydrogen production involves several challenges [8]. The high costs of materials like Nafion membranes and Pt/Ir catalysts affect economic

viability. Proper MEA fabrication, sealing, and balanced gas/water distribution are critical to prevent inefficiencies such as gas crossover and flow imbalances. Performance depends on minimizing ohmic and overpotential losses, maintaining membrane hydration, and avoiding electrode flooding or dehydration [9]. Efficient gas bubble removal is necessary to sustain electrochemical activity. Temperature and pressure must be carefully managed – higher values improve performance but can accelerate degradation. Durability is limited by catalyst loss, membrane thinning, and corrosion. Integration with variable renewable energy sources adds complexity, requiring advanced control systems. Maintaining H_2 purity and effective cooling is also essential at high current densities. Addressing these issues through improved materials, design, and operation is key to achieving efficient, durable, and scalable green hydrogen production [10].

Materials

Parts of Laboratory PEM Electrolyzer

In this paper, two components were prepared: an experimental laboratory PEM electrolyzer and a MEA with a layer of carbon fibers (CF) doped by NiCoP nanoparticles. To evaluate our materials, an experimental PEM electrolyzer (Fig. 1) was constructed to prove best properties of studied catalysts, regarding its stability and activity in both acidic and alkaline environments [11]. The electrolyzer consists of membrane electrode assembly (MEA), current collectors (CC), gas diffusion layers (GDL), insulation layers made of polytetrafluoroethylene (PTFE) and end plates (EP).

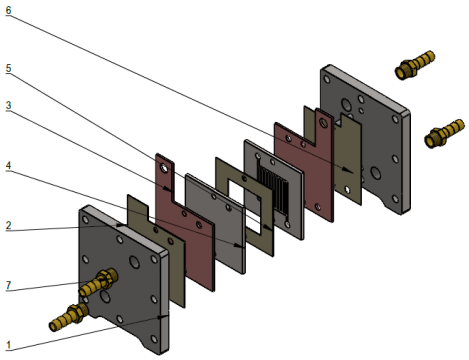

Fig. 1 Experimental PEM electrolyzer: (1) End plates, (2) Anode insulation plate (expanded PTFE), (3) Current collector plates, (4) Bipolar plates with flow field, (5) MEA, (6) Cathode insulation plate (expanded PTFE), (7) Connector terminals for water feed and gas removal.

The main important part is the MEA, which divides the cell of PEM electrolyzer into two half cells: the anode and the cathode side. MEA consists of a membrane that serves as an ion-exchange medium for the passage of H^+ ions, and catalysts that are closely bonded to the membrane and represent 24 % of the total cost of the electrolyzer. This membrane/catalyst assembly is the central part of the PEM. The most used materials are perfluorosulfonic acids, such as Nafion (Nafion 115, 117, and 212) [12]. These membranes exhibit high strength, activity, oxidative stability, thermal dimensional stability, and excellent proton conductivity. The two most common methods for preparing MEAs are the catalyst-coated membrane (CCM) and catalyst-coated substrate (CCS) techniques [13]. In the CCM method, the electrocatalyst suspension is applied directly to the membrane and hot-pressed at 120 °C under 60 $kg \cdot cm^{-2}$ to ensure strong adhesion. In contrast, the CCS method applies the catalyst to the gas diffusion layer (GDL), typically porous carbon paper or titanium mesh. The suspension – comprising electrocatalyst, ionomer (e.g., Nafion), isopropanol, and water – is ultrasonically homogenized for 30 minutes before application. Once assembled, this structure offers two main benefits for PEM electrolysis: the ionomer enhances proton transport, reduces ohmic losses, and the suspension reinforces electrode durability. Developing durable, cost-effective materials remains a key research focus [14].

Experimental

Activation of Nafion Membrane

To assemble the modified MEA, the first step was to prepare a catalytic membrane consisting of a cathode and anode side, known as a MEA. The MEA was made from Nafion™ 117, cut to a size of 3 × 3 cm. Nafion activation was carried out at 80 °C for 2 hours in demineralized water, followed by treatment at 60 °C for 30 minutes in a 3 % H_2O_2 solution. The penultimate step involved activation in 0.05 M H_2SO_4 at 60 °C for 30 minutes. Finally, the membrane was cleaned of any remaining H_2O_2 and H_2SO_4 in demineralized water at 80 °C for 1 hour.

Preparation of NiCoP CF Layer

In this study, CF doped with bimetallic TMPs were synthesized using needless electrospinning (NLE) method from a polymer-based solution (Fig. 2). 1:1 molar ratio of metals in the final binary phosphides, concentrations of $CoCl_2 \cdot 6H_2O$ (Sigma-Aldrich, ACS reagent, 98 %) and $NiCl_2 \cdot 6H_2O$ (Sigma-Aldrich, ACS reagent, 98%), were precisely adjusted according to the literature [7]. Polyacrylonitrile (PAN, Mw = 150.000 $g \cdot mol^{-1}$, Sigma-Aldrich) served as the primary polymer for precursor fiber formation. Phosphoric acid (H_3PO_4, Merck, 85 %) was used as the phosphorus source and to improve the solution's viscosity and conductivity, thereby enhancing its spinnability. N,N-dimethylformamide (DMF, Acros Organics, 99.8 %) acted as the solvent for the spinning solution. Fibers were produced using the NLE method with a Nanospider™ NS LAB device (Elmarco, Czech Republic). A 30 ml polymer solution was poured onto a rotating electrode, with a spinning distance of 180–190 mm and a rotation speed of 9 rpm. A high voltage of 70–80 kV induced a current of ~100 mA. The resulting polymer precursor fibers (PPF) formed coloured polymer wool. 1g of precursor wool was folded, placed between Al_2O_3 ceramic plates, and stabilized at 270 °C into a sheet. It was then sintered in an Ar atmosphere at 1200 °C and reduced in H_2 at 780 °C to form the final modified CF.

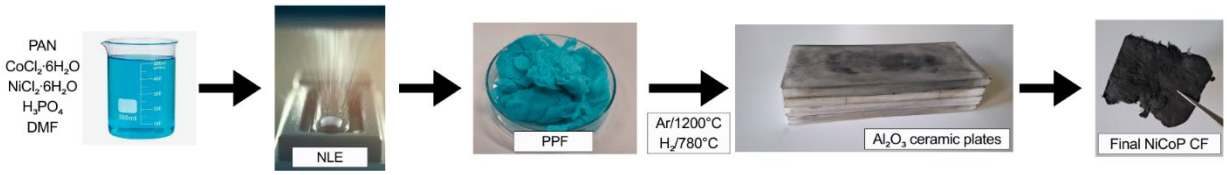

Fig. 2 Schematic process of synthesis for NiCoP CF layer.

Preparation of IrO_2 Suspension

To verify catalytic properties on the anodic side of MEA in laboratory electrolyzer, a suspension made of commercial anodic catalyst IrO_2 (Sigma-Aldrich, ≥99 % TMB) was prepared. Catalytic suspension consisted of 0.08 g of IrO_2, 6.17 ml of isopropyl alcohol (FCC, 99.8 %) and LIQUION™ Nafion™ (20 wt. %, PFSA). Mixture was poured into vial and homogenized using ultrasound homogenizer with elongated needle sonification probe for 30 minutes. Following homogenization, the resulting suspension was ready for application by air brush.

MEA fabrication

IrO_2 suspension, as an anode catalyst, was applied by air brush in layers, on the sheet of Nafion (3x3 cm) and stored in a drying oven for about 5 minutes. After that, the process was repeated. A total of 10 coatings were applied. The next step was to prepare layers represented by CoP/CF which were separated from anode catalysts with Nafion. The Nafion membrane was the same size (3x3 cm) using a scalpel and ruler. Then these sheets were bonded with 1 ml of liquid Nafion to connect them into a single layer and pressure pressed on a heated plate (70 °C) to create MEA. Prepared MEA was left to settle for 24 hours, each layer to properly bind with each other.

Methods

XRD analysis was performed using a Philips X'Pert Pro with CuKα radiation. The morphology of the modified NiCoP CF was examined using a high-resolution scanning electron microscope (FIB-SEM ZEISS AURIGA Compact). To determine the chemical composition, energy-dispersive X-ray spectroscopy (EDS) was used – specifically, the SDD-EDS analytical system Oxford Instruments X-MaxN 80 mm² for SEM (AZtec evaluation software). To establish a baseline performance reference, electrochemical tests were performed using a VIONIC potentiostat. Ultrapure water was supplied to the anode side at room temperature at a flow rate of 5 $mL.min^{-1}$. All measurements were performed under ambient pressure and temperature. Chronoamperometric measurements were carried out by applying fixed cell potentials ranging from 1.4 to 2.0 V, allowing the system to stabilize at each voltage until a steady-state current was reached. Additionally, short-term dynamic performance was assessed via triangular voltage cycling between 1.4 V and 2.0 V at a scan rate of 50 $mV.s^{-1}$ over 10 cycles to evaluate the stability and response of the system.

Results and Discussion

Structural and Morphological Characterization

Figure 3 shows the XRD pattern of NiCoP CF synthesized from PAN. The diffraction peaks for NiCoP at positions 40.01°, 44.99°, 47.64°, 54.46°, 54.86°, and 55.26° correspond to the crystallographic planes (111), (201), (210), (300), (002), and (211), which precisely match the hexagonal structure of NiCoP according to the COD database, entry number 01-071-2336 [15]. Two broad diffraction lines at 23.86° and 43.27° confirmed CF matrix [16].

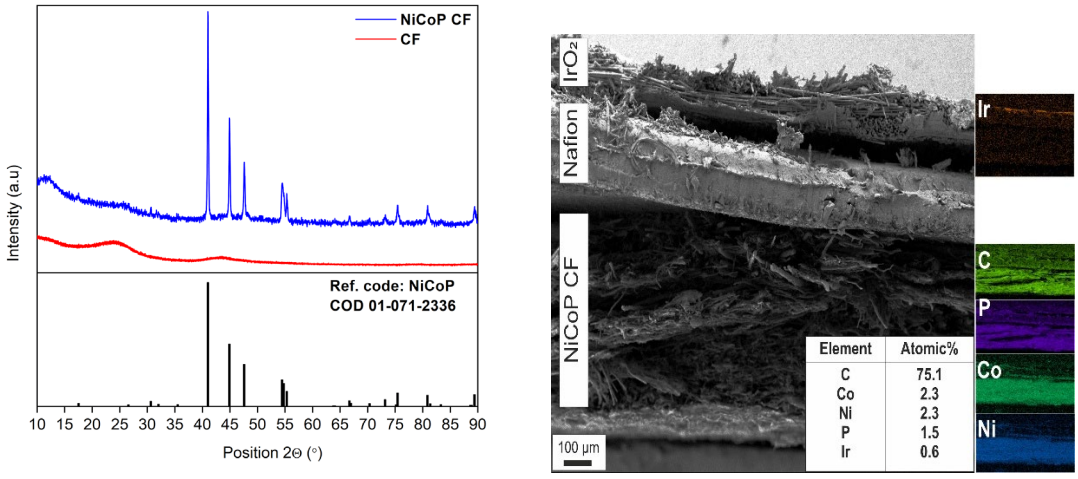

Fig. 3 XRD analysis of NiCoP CF and SEM image of optimized MEA with elemental mapping.

SEM provided a closer look on the cross-section of each MEA layer. NiCoP CF layer exhibits finely fibrous structures with an average fibre diameter of ~1 µm, as observed. NiCoP nanoparticles are uniformly distributed both within and on the surface of the carbon matrix [14]. The chemical composition was investigated by SDD-EDS mapping analysis (Fig. 3), confirming the presence of C, P, Ni, and Co within the MEA sample [17]. The elements Ni, Co, and P were homogeneously distributed within their presented layers, with Ni and Co present in nearly equal atomic ratios, indicating an equimolar metal composition. Note, fibers of NiCoP CF are embedded onto the surface of IrO_2 layer due to cutting of the membrane by scalpel for the purpose of SEM imaging.

Electrochemical Characterization

Electrochemical evaluation was conducted on the fibres without catalytic coating on the cathode side. Chronoamperometric measurements were performed by applying fixed cell potentials between 1.4 V and 2.0 V. As shown in Fig. 4a), the current density progressively increased with applied potential, reaching a maximum of ~21 mA.cm^{-2} at 2.0 V under ambient temperature and pressure. For comparison, a commercial PGM-based MEA at optimized conditions can deliver up to 200 mA.cm^{-2} at 2.0 V [18]. This means that the performance of the NiCoP-based MEA represents ~10 % of the activity of commercial systems. While significantly lower in absolute terms, this baseline activity is noteworthy given the non-optimized composition, absence of PGM, and ambient testing conditions. The results confirm that the fibrous NiCoP structure exhibits measurable electrocatalytic activity toward HER and is a suitable candidate for further development. The low-pressure, room-temperature testing conditions serve as a stringent benchmark, underscoring the importance of catalyst layer tuning, membrane optimization, and operational parameter adjustment to unlock the full potential of the system [19].

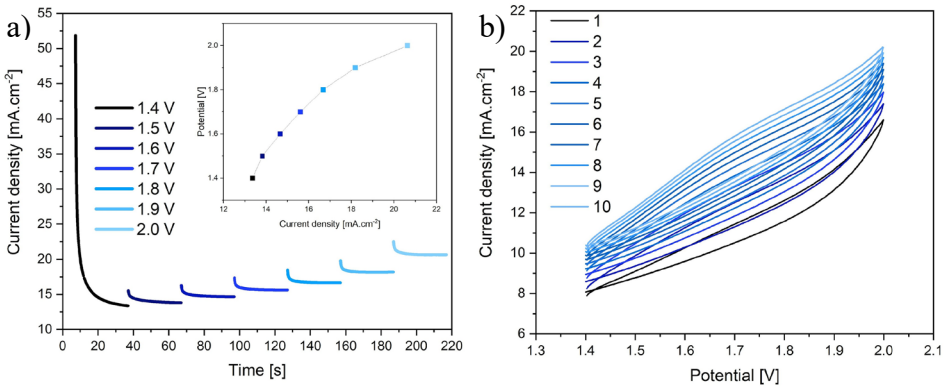

Fig. 4 a) Chronoamperometric measurement of NiCoP MEA recorded in range from 1.4 V to 2.0 V and potential-current density plot, b) CV measurement recorded in range from 1.4 V to 2.0 V.

Additionally, cyclic voltammetry was conducted for 10 consecutive cycles. The CV profiles (Fig. 4b) show stable and reproducible behavior. The current response increased progressively with applied potential, reflecting the onset of water oxidation and confirming the activity of the system. The stable CV behavior also suggests that the NiCoP layer retains electrochemical integrity under repeated cycling, which is a key consideration for long-term electrolyzer operation.

Conclusion

This study demonstrates the optimization of the MEA for enhancing the economic feasibility of PEM electrolyzers. NiCoP catalysts were synthesized in the form of modified CF and integrated into MEAs. The successful incorporation of these materials into the MEA structure was confirmed by XRD and SEM, revealing phase-pure phosphide formation and uniform catalyst distribution across the fibrous network. Comprehensive optimization of the catalyst layer (mechanical stability, facile fabrication and catalyst dispersion inside the CF matrix) can lead to improved interfacial contact, increased electrochemical surface area, and enhanced proton/electron transport. The incorporation of a fibrous membrane layer into the MEA offers a promising structural platform, providing high surface area and favourable mass transport pathways, even though catalytic enhancement is essential to achieve significant current densities. Electrochemical measurements demonstrated moderate current densities under ambient conditions. These findings validate the concept of using phosphide-based materials for MEA integration and establish a foundation for further improvements. The results confirm that the NiCoP MEA exhibits promising properties for application in PEM electrolyzer systems. Overall, this study highlights the importance of targeted material design in advancing non-PGM catalysts and supports the feasibility of transitioning toward more affordable and sustainable hydrogen generation pathways.

Acknowledgements

This work was funded by the EU NextGenerationEU through the Recovery and Resilience Plan for Slovakia under the project No. 09I03-03-V04-00109.

References

[1] C. Bera et al., NiCoP fibers as novel catalysts for hydrogen evolution in alkali and acidic environment, Int. J. Hydrogen Energy, 60, 1 (2024) 118-132, doi: 10.1016/j.ijhydene. 2024.02.195.

[2] D. Siegmund et al., Crossing the Valley of Death: From Fundamental to Applied Research in Electrolysis, JACS Au, 1, 5 (2021) 527-535, doi: 10.1021/jacsau.1c00092.

[3] H.M. Zhang, et al., Recent advances in amorphous metal phosphide electrocatalysts for hydrogen evolution reaction, Int. J. Hydrogen Energy, 47, 85 (2022) 36084-36097, doi: 10.1016/j.ijhydene.2022.08.184.

[4] S. Sikiru et al., Hydrogen-powered horizons: Transformative technologies in clean energy generation, distribution, and storage for sustainable innovation, Int. J. Hydrogen Energy, 56, 1 (2024) 1152-1182, doi: 10.1016/j.ijhydene.2023.12.186.

[5] M. Han, et al., Retrospect and Prospect: Nanoarchitectonics of Platinum-Group-Metal-Based Materials, Adv. Funct. Mater., 33, 44 (2023) doi: 10.1002/adfm.202301831.

[6] A. Gubóová, et al., Iron-nickel metal foams modified by phosphides as robust catalysts for a hydrogen evolution reaction, Mater. Today Chem., 34, 8 (2023), doi: 10.1016/j.mtchem.2023.101778.

[7] M. Streckova, et al., Nanoarchitectonics of binary transition metal phosphides embedded in carbon fibers as a bifunctional electrocatalysts for electrolytic water splitting, J. Alloys Compd., 923 (2022) 166472, doi: 10.1016/j.jallcom.2022.166472.

[8] C.W. Wu, et al., A systematic review for structure optimization and clamping load design of large proton exchange membrane fuel cell stack, J. Power Sources, 476, 7 (2020), doi: 10.1016/j.jpowsour.2020.228724.

[9] M.N.I. Salehmin, et al., High-pressure PEM water electrolyser: A review on challenges and mitigation strategies towards green and low-cost hydrogen production, Energy Convers. Manag., 268, 6 (2022) 115985, doi: 10.1016/j.enconman.2022.115985.

[10] J. Lauri, et al., Design of a PEM electrolyzer test station for experimentation on power quality induced efficiency loss and cell degradation, Thesis, 2020.

[11] C. Bera and M. Streckova, Carbon Fibers Doped by Binary Phosphides as an Electrocatalytic Layer for PEM Electrolysers, J. Nano Res., 78, 3 (2023) 97-102, doi: 10.4028/p-o8u8bx.

[12] K. Jiao, et al., Designing the next generation of proton-exchange membrane fuel cells, Nature, 595, 7867 (2021) 361-369, doi: 10.1038/s41586-021-03482-7.

[13] N. Mohamed Aslam, et al., Preparation of Membrane Electrode Assembly for High Performance of Formic Acid Fuel Cell, Malaysian J. Anal. Sci., 20, 3 (2016) 678-686, doi: 10.17576/mjas-2016-2003-29.

[14] S. Battiato, et al., Superior Performances of Electroless-Deposited Ni-P Films Decorated with an Ultralow Content of Pt for Water-Splitting Reactions, ACS Appl. Energy Mater., 5, 2 (2022) 2391-2399, doi: 10.1021/acsaem.1c03880.

[15] H. Liang, et al., Plasma-Assisted Synthesis of NiCoP for Efficient Overall Water Splitting, Nano Lett., 16, 12 (2016) 7718-7725, doi: 10.1021/acs.nanolett.6b03803.

[16] S. Anantharaj, et al., Recent Trends and Perspectives in Electrochemical Water Splitting with an Emphasis on Sulfide, Selenide, and Phosphide Catalysts of Fe, Co, and Ni: A Review, ACS Catal., 6, 12 (2016) 8069-8097, doi: 10.1021/acscatal.6b02479.

[17] J. Zhu, et al., Recent Advances in Electrocatalytic Hydrogen Evolution Using Nanoparticles, Chem. Rev., (2019), doi: 10.1021/acs.chemrev.9b00248.

[18] A.M.I. Noor Azam, et al., Parametric Study and Electrocatalyst of Polymer Electrolyte Membrane (PEM) Electrolysis Performance, Polymers, 15, 3 (2023), doi: 10.3390/polym15030560.

[19] J.K. Lee, J.H. Seo, J. Lim, S. Park, H.W. Jang, Best Practices in Membrane Electrode Assembly for Water Electrolysis, ACS Mater. Lett., 6, 7 (2024) 2757-2786, doi:10.1021/acsmaterialslett. 4c00699.

Published in: Materials Science Forum
ISSN: 1662-9752, Vol. 1179, pp 71-77
doi:10.4028/p-d7iDgG

Submitted: 2025-05-27
Revised: 2025-12-08
Accepted: 2025-12-19
Online: 2026-03-03

Recycling of Zinc-Based Industrial Waste into Nanostructured Material for Potential Wastewater Treatment Applications

Erika Mudra[1,a*], Ivan Shepa[1,b], Kateryna Nemesh[1,2,c], Jana Piroskova[2,d], Jakub Klimko[2,e], Petra Hviscova[1,f] and Ondrej Petrus[1,g]

[1]Institute of Materials Research, Slovak Academy of Sciences, Watsonova 47, 040 01 Kosice, Slovak Republic

[2]Faculty of Materials, Metallurgy and Recycling, Technical University of Kosice, Letna 9, 040 01 Kosice, Slovak Republic

[a*]emudra@saske.sk, [b]ishepa@saske.sk, [c]knemesh@saske.sk, [d]jana.piroskova@tuke.sk, [e]jakub.klimko@tuke.sk, [f]phviscova@saske.sk, [g]opetrus@saske.sk

Keywords: recycling waste, electrospinning, zinc oxide, photocatalytic activity, ceramic fibers.

Abstract. This work demonstrates the successful preparation of two types of photocatalytically active nanostructured materials from an industrial waste product – Sal Ammonia Skimming – using hydrochloric acid as a leaching medium. The whole production process was developed to prepare valuable ZnO nanomaterials in both fibrous and powdered forms. This involved a sequence of hydrometallurgical processing, needle-less electrospinning, and conventional calcination of recycled environmentally polluting industrial waste. The morphologies and phase composition of the resulting ZnO powder and ZnO fibers were analyzed using SEM, EDS, and XRD analyses. The impact of the morphology of the prepared nanomaterials on the photocatalytic efficiency of the ZnO-based photocatalyst – powder versus ZnO nanofibers – was evaluated through decolorization experiments of the commonly used methylene blue dye in batch mode. Methylene blue was chosen as a model substance for toxic industrial pollutants. A 25 W UVA lamp with an emission maximum at 365 nm was used as a light source. Removal efficiencies were carefully tested and compared for different nanomaterial morphologies and preparation conditions. The most photocatalytically active ZnO-based nanomaterial was the electrospun nanofibrous one calcined at 600 °C for 1 h. This material achieved 100 % removal of a 10^{-5} mol/L methylene blue dye from the solution within 700 minutes at an increased catalyst-to-dye ratio of 500 mg/50 ml. Based on the obtained results, it can be stated that the prepared materials exhibit high photocatalytic activity under UV light irradiation and have a potential for photocatalytic water remediation applications.

Introduction

The constant development of new technologies increases the demand for metals on a global scale. In the European Union, the consumption of materials is currently higher than the extraction from the primary raw materials, so most countries depend on the import of metals from other countries of the world. Zinc has an important position in the industry. Almost 60 % of the world's Zn production is consumed for galvanizing. Approximately 34 % of the world's Zn production comes from recycling materials [1]. Wet batch hot dip galvanizing uniquely produces a waste called Sal Ammoniac Skimming, resulting from the reaction between molten zinc and the flux, ammonium chloride (NH_4Cl), within the bath. This material consists mainly of Zn(OH)Cl, NH_4Cl, ammonium chloride, oxides, sulfides, and trace amounts of other substances [2]. Alarmingly, this particular waste stream is presently not processed and ends up being discarded in landfills. Considering the amounts of heavy metals, zinc-containing wastes are evaluated as among the solid wastes that cause the most damage to the environment [3]. However, the high amount of zinc found in these wastes also makes them an economically valuable resource [3]. To obtain metals of interest such as Zn from industrial waste, recycling is possible by hydrometallurgical processing using aqueous solutions based on alkalis and

acids. The recovery of the metals with relatively high yields by leaching with the given method from secondary sources was investigated in the literature before [4]. The method can effectively convert individual metals into a solution, which can then be used as an essential component of the precursor solution for the preparation of nanofibers of oxides of the metals of interest. In this way, waste is recovered and a material with high added value is prepared. One of the techniques for the preparation of one-dimensional nanomaterials is electrospinning (ES). This method can produce nano/microfibers with diameters ranging from 50 nm to 2 μm of polymer and ceramic nature, not limited by the composition: from simple to compositionally complex or even high entropy ceramic fibers with precisely tuned morphological and phase designs. The use of recycled raw materials often brings with it the disadvantage of quantitative deviations in chemical composition. The utilization of electrospinning offers the possibility of adjusting the fluctuating chemical composition of the resulting fibers by simply adding/compensating the missing elements in the spinning solution. In ref. [3], the preparation of ZnO fibers from waste brass flue dust through ammonium acetate-assisted leaching is investigated. This study provides a waste disposal method combined with an efficient method to transform Zn as a value-added functional material [3].

Advanced oxidation processes utilizing materials such as zinc oxide are considered a promising avenue for the removal of emerging water pollutants. Contemporary strategies focus on engineering materials with high surface areas and efficient light absorption, ideally extending into the visible range, while mitigating material loss through tailored morphologies and minimizing electron losses during light-induced excitation and electrochemical processes [5]. Although nanoparticulate catalysts have generally proven to be highly effective, despite inherent drawbacks [6], the nanofibrous nanoarchitecture holds the potential to play a crucial role in achieving even greater catalytic performance with the same material composition.

The presented work aimed to develop a method for the preparation of photocatalytically active nanostructured materials from recycled environmentally polluting industrial waste using hydrometallurgical processing, needleless electrospinning, and conventional calcination. At the same time, this study evaluates the influence of the morphology of the prepared nanostructures on the photocatalytic efficiency of ZnO powder and ZnO fibers.

Experimental Materials and Methods

The zinc source for the preparation of ZnO nanofibers was a recycled Zn-enriched solution obtained from the hydrometallurgical processing of Sal Ammoniac Skimming, an industrial waste generated during galvanized steel production. Scanning electron microscopy (SEM) image (Fig. 1a) reveals the dendritic structure of the as-received Sal Ammoniac Skimming sample. A detailed view of the marked area (Fig. 1b) shows the presence of small particles on the surface. Energy-dispersive X-ray spectroscopy (EDS) analysis indicated the presence of chlorine (Cl), carbon (C), zinc (Zn), oxygen (O), nitrogen (N), sodium (Na), and aluminum (Al). Due to its hygroscopic nature, the as-received sample was dried at 105 °C for 24 hours before use.

Leaching experiments were conducted in an 800 ml glass reactor using 80 g of the Sal Ammoniac Skimming, resulting in a liquid-to-solid (L:S) ratio of 10. The mixture was continuously stirred at 300 rpm using a glass stirrer. Zinc extraction was investigated using distilled water and a 0.01 M HCl solution as leaching media. The leaching medium was maintained at a constant temperature of 50 °C using a water-circulating thermostat (Fig. 1c). The total duration of the leaching process was limited to 30 minutes. Following preparation and chemical analysis, the resulting leachate was used to prepare the electrospinning precursor solution, which subsequently served for the fabrication of both final ZnO products: nanopowder and nanofibers.

The precursor solution was prepared by adding 1.1 g of citric acid monohydrate (Centralchem, p.a.) to 20 g of the Zn-enriched leachate and stirring until complete dissolution. Subsequently, 2.5 g of polyvinylpyrrolidone (PVP, Acros Organics, Mw = 360,000 g·mol^{-1}), 2.5 g of absolute ethanol (MICROCHEM), and 1 ml of acetic acid (Acros Organics, 99.7+%) were added to the solution. The final mixture was stirred for 3 hours at room temperature to ensure complete homogenization.

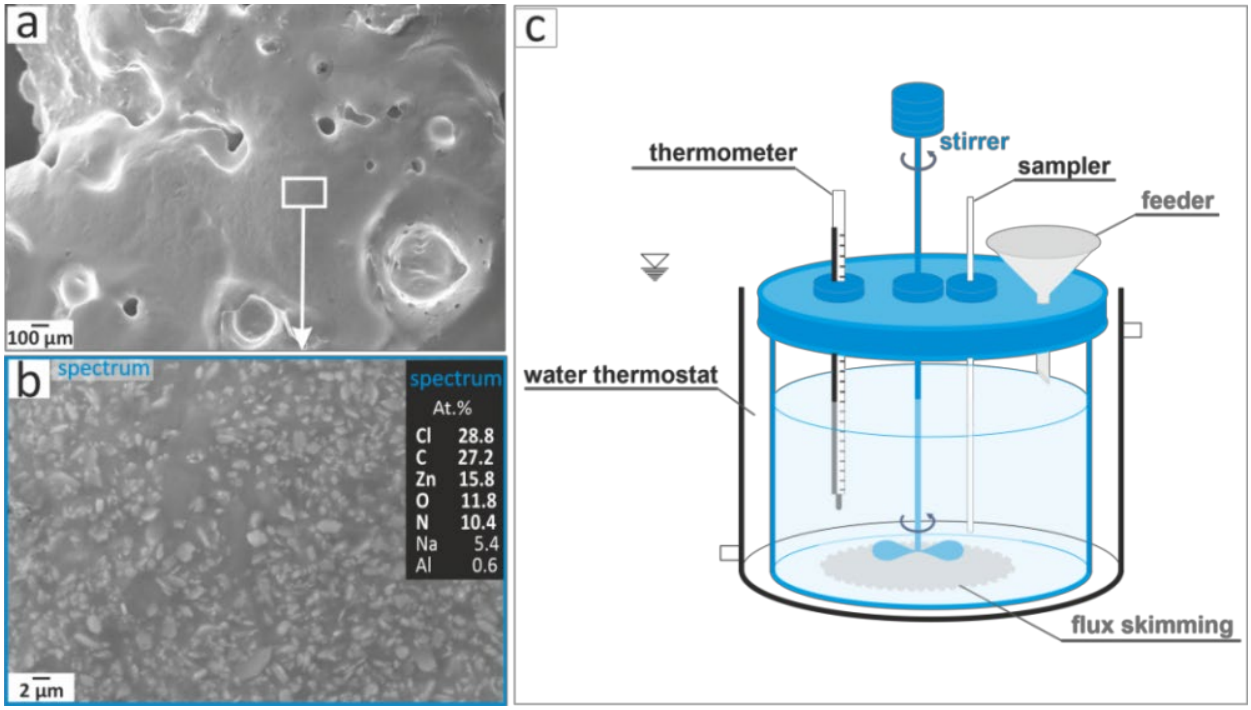

Fig. 1. SEM micrographs of a) Sal Ammoniac Skimming sample; b) detail of recycling sample surface. c) The scheme of the leaching apparatus.

ZnO powder: The part of the prepared solution was used to form a precursor of ZnO powder. The solution was left in a Petri dish at room temperature to complete evaporation of the solvent, dried solid, and then crushed into a fine powder containing a significant amount of polymer.

ZnO fibers: The remaining prepared solution was used to produce precursor fibers by needle-less electrospinning technology on the Nanospider NS-Lab 200, ELMARCO, Czechia. The applied voltage was 70 kV and the distance between the spinning electrode and collector – 150 mm.

The final samples – ZnO powder and ZnO fibers were obtained by calcination of precursors in the temperature-controlled furnace at 600 °C with 1 h dwelling time and forced air circulation to provide full removal of carbon residues. The resulting ceramic samples were labeled as – ZnO powder and ZnO fibers and have been subjected to detailed characterization and testing of the photocatalytic activities.

The initial chemical analysis of recycling Sal Ammoniac Skimming samples was performed by the classical wet method using atomic absorption spectrometry (AAS) with a Varian SpectrAA20+-type spectrophotometer (Varian, detection limit: 0.3–6 ppb; slit width 0.2–1 µm; wavelength 213.9–422 nm and lamp current 4–12 mA, Belrose, Australia). The phase composition of ZnO samples was analyzed using the X-ray diffraction method (XRD). The diffraction pattern was obtained using a SEIFERT X-ray diffractometer 3003/PTS (Seifert, Germany) with CoKα radiation. The diffraction patterns were analyzed by DIFFRAC.EVA with PDF2 database, and TOPAS program refined by the Rietveld method. The morphology analysis was observed by scanning electron microscopy (SEM/FIB ZEISS-AURIGA Compact). The average grain size was measured by ImageJ software. Spectrophotometric analyses and photocatalytic activity tests were performed on a Biochrom WPA Lightwave II UV/Vis Spectrophotometer. The photocatalytic activity of the prepared ZnO samples

was evaluated by measuring the decomposition rate of cationic dye methylene blue (MB) under UVA lamp irradiation (25 W, with maximum wavelength at 365 nm). Initially, the dye photolysis was studied without the catalyst addition, confirming the neglectable degradation rate of pure MB solution. Subsequently, 200 or 500 mg of powder or shredded fibers were added to the 50 ml of dye solutions with an initial concentration of 10^{-5} mol/L and mixed for 2 hours in the dark to ensure the dye adsorption. Samples were taken every 10 minutes for up to 700 minutes, centrifuged to speed up the catalyst separation, and analyzed using UV-visible spectrophotometry to determine the actual concentration and thus the degradation rate of MB. The photocatalytic efficiency was tested at two catalyst-to-dye ratios by taking 200 mg and 500 mg of the catalyst.

Results and Discussion

The only source of Zn for the preparation of photocatalytic active ZnO nanostructures was Sal Ammoniac Skimming. After its processing, there was a quantitative transfer of metal into the solution and the chemical composition of Zn-enriched leachate obtained by AAS analysis demonstrated the presence of 12.32 g/L Zn, 0.2 g/L Pb and trace elements of Fe (0.003 g/L), Cu (0.006 g/L), Cr (0.001 g/L), Ca 0.03 g/L), and Si (0.011 g/L). Two distinct morphologies of ZnO nanostructures were synthesized, and their phase composition was subsequently evaluated via XRD analysis. Fig. 2a shows the XRD diffraction pattern confirming the presence of ZnO single phase structure in both cases (2Θ = 36.9°; 38.0°; 40°; 42.2°; 55.6°; 66.5°; 74.2°; 78.6°; 80.6°; 82°; 86.4°; 92.2°; 98.1°; 109.3°; 113.9°;117.7°; ICOD 01-079-0207).

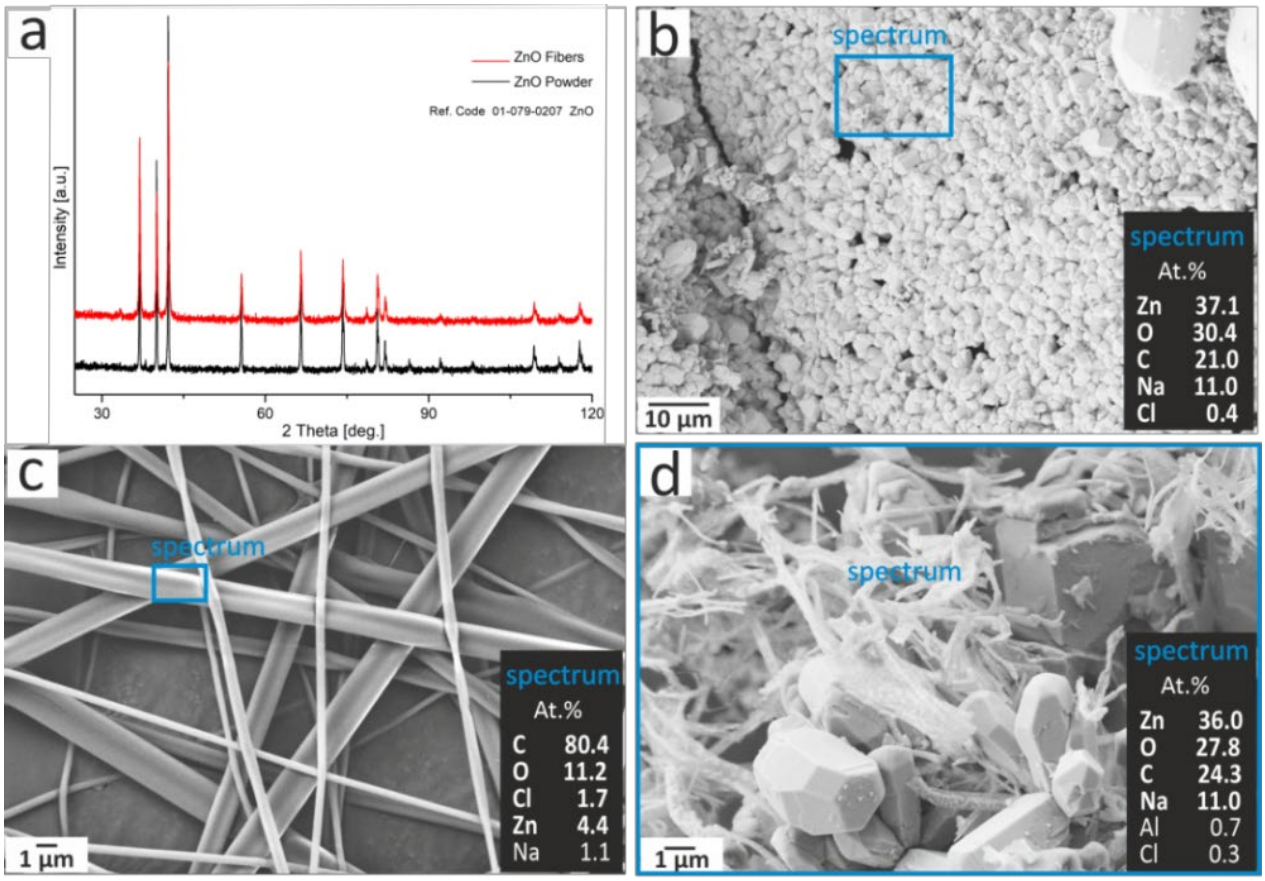

Fig. 2. a) X-ray diffraction patterns of prepared samples. SEM micrographs coupled with EDS analysis of b) ZnO powder c) precursor PVP/Zn-based fibers and d) ceramic ZnO fibers.

Prepared precursor and ceramic samples were morphologically analyzed using SEM. Fig. 2b shows the ZnO powder after final calcination. The structure was formed by ZnO crystals with a wide size range: small grains with a size below 1 μm were present as well as large, single ones larger than 20 μm. The average grain size of the powder was still about 1.5 μm. EDS analysis revealed that ZnO powder contained Zn, O, Na, and Cl. The calcination conditions as final temperature and dwell time, were carefully optimized so that the final material did not contain any carbon residues. Therefore, it must be mentioned that the signal for C in the EDS results originates from the conductive carbon tape used for SEM sample preparation. The precursor fibers (Fig. 2c) based on PVP/Zn had a continuous fibrous morphology with individual nanofibers with a diameter of about 300 nm. Ribbon-like fibers with a width of 1–2 μm were also present as artifacts of the needle-less electrospinning. After the final calcination, which led to the removal of the polymer component and the crystallization of the ZnO phase, the sample consisted of a combination of rod-shaped ZnO single crystals with a length of up to 10 μm and fine ceramic polycrystalline fibers with a thickness of approximately 100 nm, as shown in Fig. 2d. Thus, the ceramic material retained its fibrous morphology even after heat treatment. The large rod-shaped ZnO grain formations probably arose due to the preferential growth of appropriately oriented ZnO grains. EDS analyses confirmed a significant decrease in the amount of carbon originating from the polymer precursors and the formation of zinc oxide fibers with the presence of a small amount of impurities (Na, Al, Cl) originating from the waste recycling process.

The photocatalytic activities of the two types of ZnO samples were tested for degradation of MB under UV light irradiation. The efficiency of the dye degradation was evaluated through UV-Vis spectroscopy based on the equation (Eq. 1) [7]:

$$\%D = 100 \times (A_0 - A_t)/A_0 \quad (1)$$

Obtained dye degradation profiles were recorded, analyzed, and visualized in Fig. 3. Based on the obtained results, it can be stated that the prepared materials exhibit high photocatalytic activity under UV light irradiation and have a potential for photocatalytic water remediation applications. In the case of comparison of the same material with different morphology, it can stated that ZnO fibers were able to adsorb more MB in the initial stage of the test, assumably due to the larger surface area. ZnO fibers and ZnO powder showed somehow comparable photocatalytic activity towards the decomposition of MB dye at a higher catalyst-to-dye ratio of 500 mg/50 ml, while at a low value of 200 mg/50 ml, ZnO fibers showed significantly higher activity, as can be seen from the steeper profile and thus was able to remove the more dye at the same time. At an increased catalyst-to-dye ratio of 500 mg/50 ml the MB dye was removed 100 % within 700 min by the ZnO fibers sample.

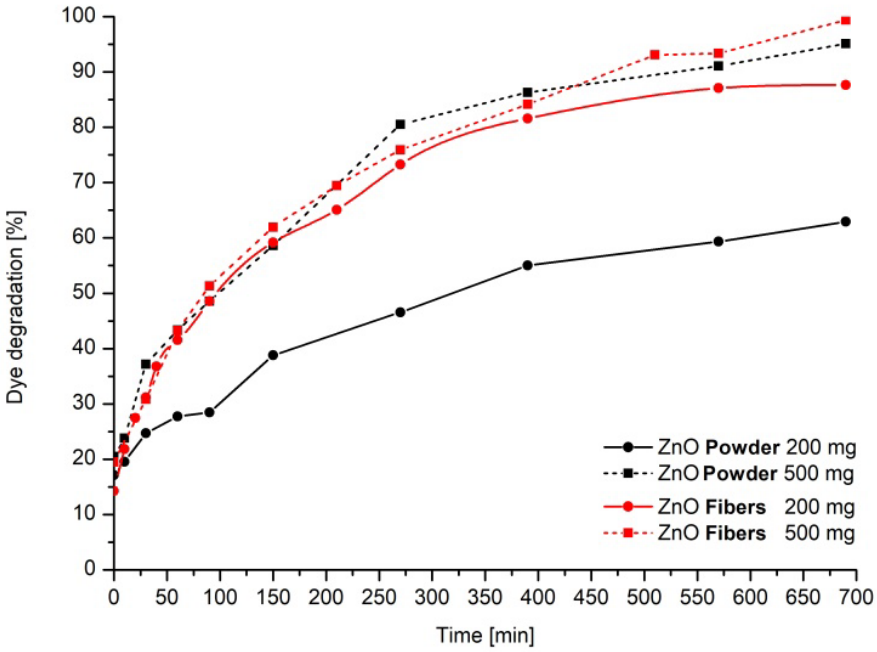

Fig. 3. The photocatalytic dye degradation profiles measured for the prepared ZnO powder and ZnO fibers at 200 mg and 500 mg of catalysts amounts in 50 ml MB under UV radiation.

At a low catalyst-to-dye ratio of 200 mg/50 ml, ZnO fibers reached the max dye degradation efficiency of about 85 % at 570 min. The ZnO powder was able to remove a smaller amount of MB 65 % at 700 minutes. The reason is probably that the size of the ZnO powder grains determines the smaller specific surface of the given catalyst. In previous works, it was described that the large specific surface area of ZnO enables more contaminants to be adsorbed onto its active surface and thus leads to more pollutants being attacked by the formed hydroxyl radicals. The chain reaction that then occurs at the surface enhances the degradation rate of the contaminants [8]. As the catalyst-to-dye ratio increases, this difference in the photocatalytic efficiency decreases. An increase in the catalyst dosage will enhance the total active surface area and the number of reaction sites on the catalyst surface [5]. As a result, the number of hydroxyl and superoxide radicals increased as well, which facilitated the degradation of the organic pollutants [5]. Thus, the degradation efficiency was enhanced. The production of zinc oxide (ZnO) nanostructures utilizing industrial waste streams presents a compelling strategy for several reasons. Firstly, it offers access to inexpensive precursor materials, significantly reducing manufacturing costs. Secondly, and perhaps more importantly, this approach provides a valuable pathway for mitigating environmental pollution by transforming waste products into a high-value material.

The resulting ZnO nanostructures, when employed in photocatalytic wastewater treatment, offer a suite of advantages. These include inherent low toxicity, intrinsic antibacterial properties, and significant biodegradability, which facilitates the eventual bioavailability of zinc for living organisms. Furthermore, the utilization of a nanofiber morphology in these applications offers the practical benefit of straightforward separation of the photocatalyst from the treated water, simplifying the overall process.

Conclusion

In this work, two types of photocatalytically active nanostructures were successfully prepared from an industrial waste product – Sal Ammoniac Skimming – using hydrochloric acid as a leaching medium. The morphologies, and phase composition of the resulting ZnO powder and ZnO fibers were evaluated utilizing SEM, and XRD analyses. Decolorization tests on the MB dye were performed

utilizing 200 mg and 500 mg of the catalysts. The most active material was electrospun ZnO nanofibers calcined at 600 °C with 1 h dwelling time. At an increased catalyst-to-dye ratio of 500 mg/50 ml the MB dye was removed 100 % within 700 min. Although the ZnO nanofibers show a comparable activity at a higher amount of catalyst as ZnO powder, their morphology makes them a more prospective alternative due to simple separation from the reactive media.

Acknowledgment

This work was supported by the Scientific Grant Agency of the Ministry of Education, Science, Research and Sport of the Slovak Republic and the Slovak Academy of Sciences, project No. VEGA 2/0080/23, by the Slovak Research and Development Agency under contract no. APVV-20-0299. The work was funded by the EU NextGenerationEU through the Recovery and Resilience Plan for Slovakia under project No. 09I03 03 V02 00013.

References

[1] Zinc facts. Government of Canada. Online 07.04.2025 Information on https://natural-resources.canada.ca/minerals-mining/mining-data-statistics-analysis/minerals-metals-facts/zinc-facts.

[2] J. Piroskova, J. Trpcevska, D. Orac, M. Laubertova, H. Horvathova, B. Holkova, Production of zinc oxide from hazardous waste - Sal Ammoniac Skimming, J. Min. Metall. Sect. B Metall., 54 (2018) 377-384.

[3] M.A. Topçu, Production and characterization of zinc oxide nanofibers derived from waste material as precursor, Process Safety and Environmental Protection, 175 (2023) 150-159.

[4] X. Liu, et al., Towards sustainability: A novel process for recycling vanadium and molybdenum from waste hydrogenation catalysts. Journal of Environmental Chemical Engineering, 12 (2024) 6.

[5] K.M. Lee, C.W. Lai, K.S. Ngai, J.C. Juan, Recent developments of zinc oxide based photocatalyst in water treatment technology: A review, Water Res., 88 (2016) 428-448.

[6] B. Srikanth, R. Goutham, R. Badri Narayan, A. Ramprasath, K.P. Gopinath, A.R. Sankaranarayanan, Recent advancements in supporting materials for immobilised photocatalytic applications in waste water treatment, J. Environ. Manage., 200 (2017) 60-78.

[7] P. Ramesh, A. Rajendran, Green synthesis of manganese dioxide nanoparticles: photocatalytic and antimicrobial investigations, Int. J. Environ. Anal. Chem., 00 (2023) 1-13.

[8] C.B. Ong, L.Y. Ng, A.W. Mohammad, A review of ZnO nanoparticles as solar photocatalysts: Synthesis, mechanisms and applications, Renew. Sustain. Energy Rev., 81 (2018) 536-551.

Published in: Materials Science Forum
ISSN: 1662-9752, Vol. 1179, pp 81-87
doi:10.4028/p-0LJrGa

Submitted: 2025-05-26
Revised: 2025-12-05
Accepted: 2025-12-19
Online: 2026-03-03

The Importance of Dislocations in the Work Hardening of Low-Carbon Steel during Cold Plastic Deformation

Tin Brlić[1,a*], Miloš Matvija[2,b], Stoja Rešković[1,c] and Maksym Lisnichuk[3,4,d]

[1]Faculty of Metallurgy, University of Zagreb, Aleja narodnih heroja 3, 44000 Sisak, Croatia

[2]Institute of Materials, Faculty of Materials, Metallurgy and Recycling, Technical University of Košice, Letná 9, 04200 Košice, Slovakia

[3]Faculty of Science, University of Pavol Jozef Safarik Kosice, Park Angelinum 9, 04001, Košice, Slovakia

[4]Institute of Materials Research, Slovak Academy of Sciences, Watsonova 47, 04001 Košice, Slovakia

[a]*tbrlic@simet.unizg.hr, [b]milos.matvija@tuke.sk, [c]reskovic.stoja@gmail.com, [d]maksym.lisnichuk@upjs.sk

Keywords: Cold Plastic Deformation, Low Carbon Steel, Digital Image Correlation, Thermography, Microstructure, TEM, STEM, Dislocation Density.

Abstract. It is well known that the work hardening process of low-carbon steels is highly dependent on the movement and accumulation of dislocations in the crystal grains, which affect the stress and strain magnitudes and their distribution. The aim of this paper is to explain the importance of dislocation movement and density on the temperature, i.e. stress and strain changes during cold plastic deformation of low-carbon steels. Therefore, tests were carried out in this paper using the methods of static tensile testing, thermography, digital image correlation (DIC) and microstructural analysis. The microstructure analysis was carried out using a light and transmission electron microscope (TEM). The transmission electron microscope analysis was performed in two different modes, the TEM and scanning TEM (STEM). The results of static tensile testing, thermography and digital image correlation (DIC) are related to the microstructural changes that occur during the work hardening process of low-carbon steel. At the moment of maximum work hardening (immediately before fracture), significant grain elongation and high dislocation density of low-carbon steel were observed.

Introduction

Work hardening of metals is one of the most important phenomena in the forming of metallic materials, which leads to an increase in their strength and internal stress. The work hardening of metallic materials during plastic deformation limits their deformation degree. Dislocations are one of the most important internal defects in the plastic deformation of metallic materials, as they affect the hardening of the metals, but at the same time also enable plastic deformation [1–3].

Dislocations move through the crystal lattice, interact with each other and create new dislocations during the plastic deformation of steel. As the plastic deformation of steel progresses, the dislocation density increases [4, 5].

Various test methods are used to examine the plastic deformation of steel. Thermography and DIC are most commonly used in the plastic deformation of steel as they allow detailed monitoring and analysis of plastic deformation. The use of thermography and DIC enables a detailed investigation of the plastic flow of metallic materials. These methods enable the prediction of new findings on the deformation behavior of metallic materials during plastic deformation [6]. In addition to thermography and digital image correlation, metallographic analysis of steel is also frequently used to investigate the plastic deformation of steel [7, 8]. Well-known methods for

analyzing the microstructure during the plastic deformation of steel are light optical microscopy, scanning electron microscopy (SEM) and transmission electron microscopy [9].

Thermographic and DIC studies are combined with metallographic analysis to relate microstructural changes to the deformation behavior of steel under plastic deformation [10]. Therefore, the ability to relate microstructural changes to local stress and strain changes can contribute to the investigation of the mechanism of work hardening and the importance of dislocations during plastic cold deformation of low-carbon steel.

The aim of this article is to explain the importance of dislocation movement and density for the temperature, i.e. stress and strain changes during cold plastic deformation at the moment of maximum work hardening of low-carbon steels.

Experimental Procedure

The tests were carried out on low-carbon steel with a chemical composition of 0.13 wt% C, 0.77 wt% Mn, 0.18 wt% Si, 0.010 wt% P, 0.019 wt% S and 0.020 wt% Al. The dimensions of the low-carbon steel sample were: length 45 mm, width 20 mm and thickness 3 mm.

The tests were carried out using the static tensile test, thermography, digital image correlation (DIC) and microstructural analysis methods. The static tensile test was carried out using the Hegewald & Peschke Inspect table 100 kN testing machine. The stretching rate was 10 mm/min. The LabMaster 2.9.4.9 software package was used during the static tensile test.

The thermographic tests were carried out with a JENOPTIK VarioCAM M82910 thermal camera. The thermal camera had a temperature sensitivity of 80 mK and the results were analyzed using the IRBIS3 professional software package. The black matte coating ColorMatic RAL 9005, LECHSYS 29141 was used to prepare the test samples. Digital image correlation was carried out using a Basler acA2500 digital camera. 5 images per second were taken during the test. The results were analyzed using the Zeiss Quality Suite: Inspect Correlate software package. The white coating Bianco Opaco RAL 9010 was used to prepare the test samples by applying white markers.

The microstructural analysis was carried out using a light and transmission electron microscope (TEM), Fig. 1. The microstructural analysis was carried out in the initial state (before deformation) and immediately before fracture of the low-carbon steel test sample (maximum work hardening). The metallographic analysis was performed at magnifications of 500x and 1000x using an Olympus GX51 light optical microscope with a DP27 digital camera and the Olympus Stream Motion 2.4.3. software package (Fig. 1a).

A standard metallographic sample preparation was carried out. Grinding was performed using 120, 400, 600, 800 and 1200 grit sandpaper with constant water cooling for 5 minutes per grit. After grinding, the samples were polished with an aqueous suspension of aluminum oxide (Al_2O_3). Finally, the samples were etched with 5 % nital for 5 seconds.

Transmission electron microscope (TEM) analysis was performed in two different modes, TEM and scanning TEM (STEM) mode using the Jeol JEM 2100F UHR, Fig. 1b. Specimen preparation for transmission electron microscopy consisted of mechanical fine grinding with SiC abrasive papers up to P1500, mechanical polishing with a 1 μm diamond paste and electrolytic polishing with a Struers TenuPol-5 device. Automatic electrolytic thinning of the samples on both sides was performed using an electrolyte of methanol with perchloric acid $HClO_4$ (9:1) at room temperature and a voltage of 20 V.

a) b)

Fig. 1 a) Light optical microscope Olympus GX51 and
b) transmission electron microscope Jeol JEM 2100F UHR.

Results and Discussion

Thermography and digital image correlation analysis was carried out at the moment of maximum work hardening of the low-carbon steel. The results of thermography and digital image correlation analysis are shown in Fig. 2.

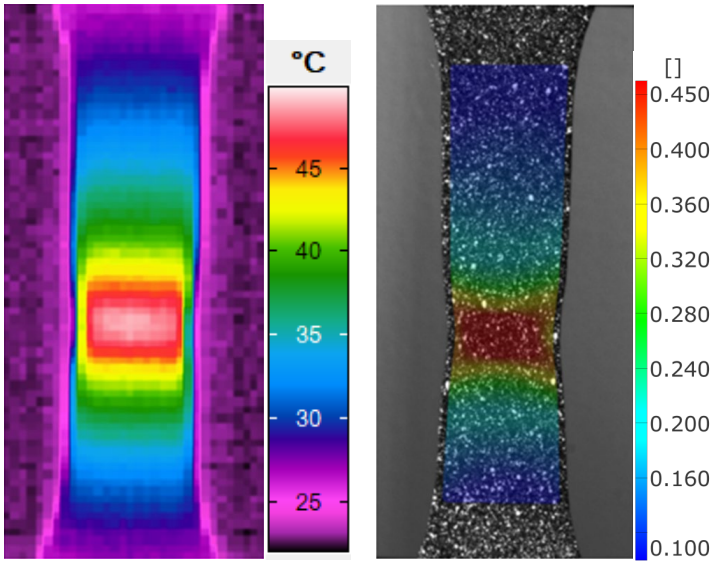

a) b)

Fig. 2 Temperature change and strain distribution during the maximum work hardening of low-carbon steel during cold deformation.

The maximum temperature change (stress) and strain were determined in the central narrowed part of the test sample, Fig. 2. Therefore, the results of the static tensile test, thermography and digital image correlation are related to the microstructural changes that occur during the maximum work hardening of low-carbon steel, Figs. 3–5.

Metallographic analysis was used to investigate the importance and influence of dislocations on the work hardening mechanism of low-carbon steel. The microstructural analysis of the low-carbon steel was carried out before deformation and at the moment of maximum work hardening, immediately before fracture of the test sample, Fig. 3 and 5.

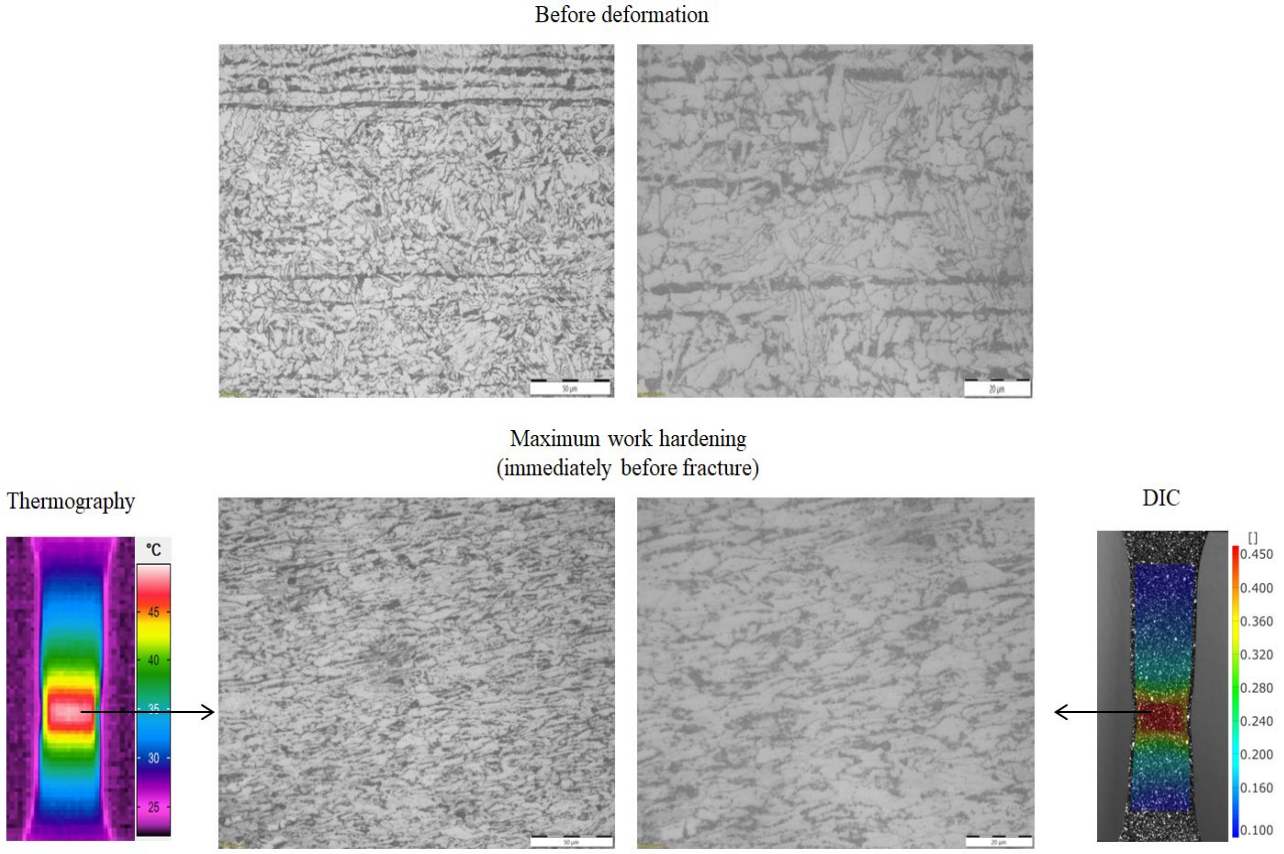

Fig. 3 Results of thermography and digital image correlation in relation to microstructural changes before deformation and immediately before fracture of the sample.

The metallographic analysis of low-carbon steel revealed significant differences in the microstructure of the steel before deformation and at maximum work hardening. Significant crystal grain elongation was found prior to fracture of the sample in relation to the microstructure of the steel before deformation, Fig. 3.

A detailed microstructural analysis on a transmission electron microscope was carried out using TEM and STEM modes. In STEM mode, the dislocations were more contrasted (Fig. 4b). Therefore, a further microstructural analysis was carried out in STEM mode to analyze the maximum work hardening of the specimens.

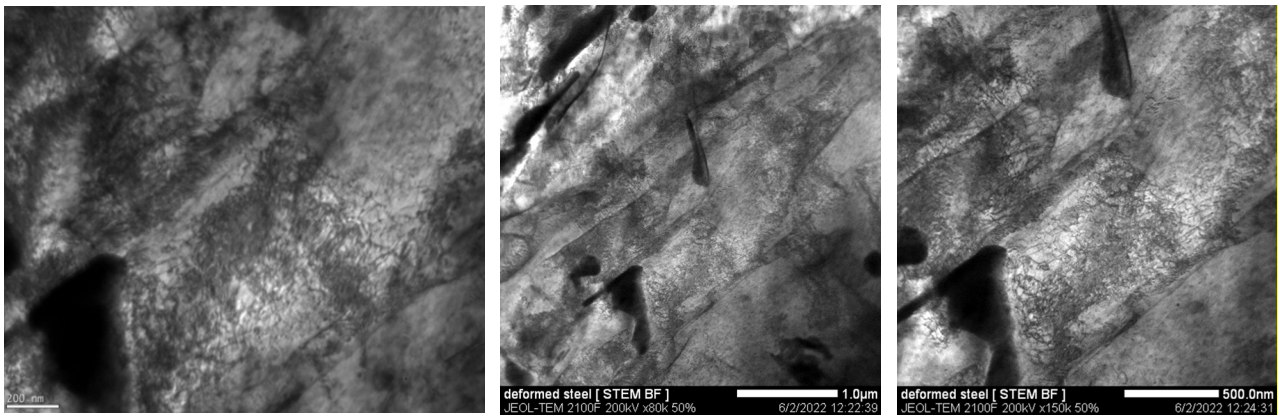

a) b) c)

Fig. 4 a) TEM (bright field) and b) STEM analysis at maximum work hardening of low-carbon steel at a magnification of 80 000x and 150 000x.

A high dislocation density and their accumulation within the crystal grains were observed during the maximum degree of cold plastic deformation immediately before fracture of the test sample, Fig. 4. The accumulation of dislocations and their mutual interaction were observed in most of the elongated crystal grains. The results of thermography, digital image correlation, metallographic and STEM analysis are related and are shown in Fig. 5.

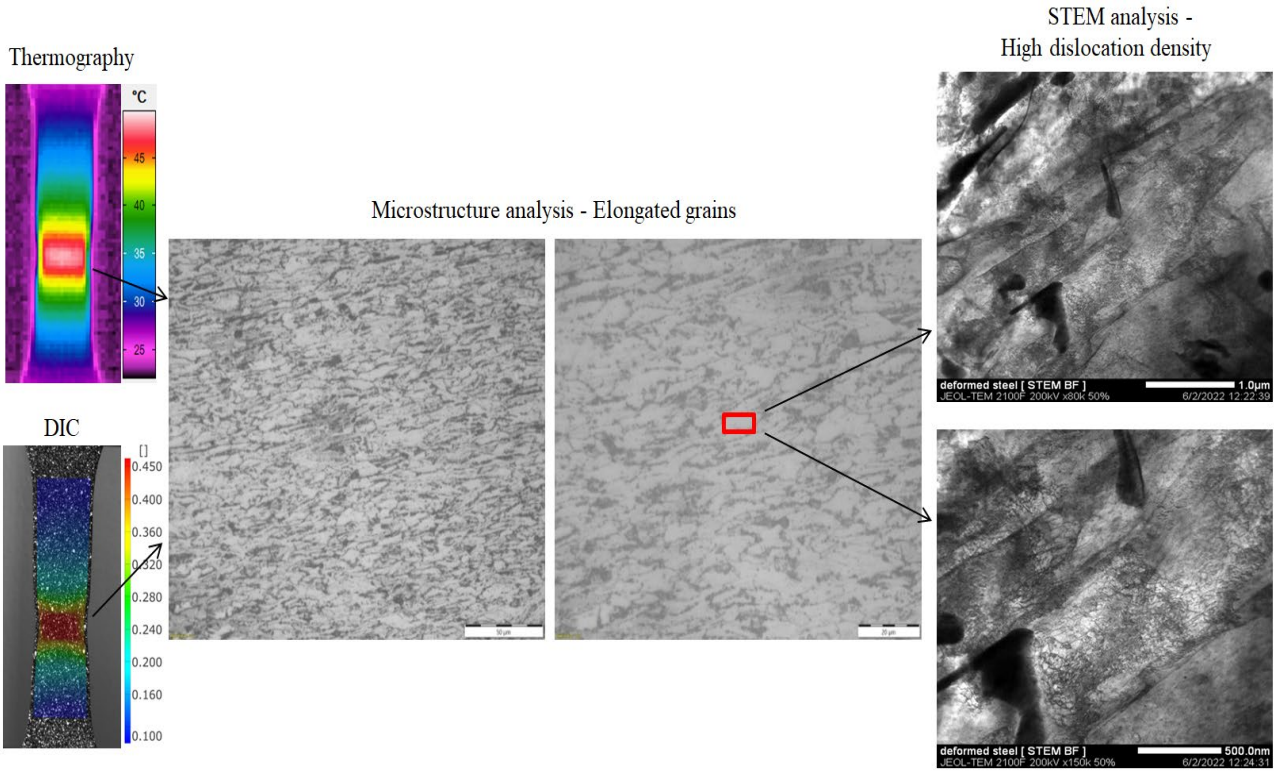

Fig. 5 Maximum work hardening of low-carbon steel.

Microstructural analysis has shown that work hardening of low-carbon steel during plastic cold deformation is largely dependent on movement and dislocation density. As a result of their movement and local accumulation, there is a higher work hardening, internal stresses and local strains of the low-carbon steel. The dislocation density and the internal stresses increase significantly and thus also the work hardening of low-carbon steel during the increase in the degree of deformation of the plastic cold deformation.

The maximum stress and strain changes were observed in the narrowed central part of the test sample (Fig. 2), which is due to the significant density and mutual interaction of the dislocations (Fig. 5). The movement of dislocations in the narrowed central part of the test sample leads to their significant mutual interaction and higher accumulation, which causes maximum work hardening of the low-carbon steel.

Conclusion

The results of static tensile testing, thermography and digital image correlation (DIC) are related to the microstructural changes that occur during maximum work hardening of low-carbon steel. Significant grain elongation and high dislocation density of low-carbon steel were observed at the moment of maximum work hardening (immediately before the sample fractured) compared to the initial state of the microstructure before deformation.

It was found that the high dislocation density, their movement and accumulation in local areas of the microstructure are of great importance and lead to work hardening, stress rise and increase in local strain during the increase in the degree of deformation of low-carbon steel. The highest dislocation density, area of maximum work hardening, internal stresses and local strains were found in the narrowed central part of the low carbon steel test sample.

Acknowledgment

This paper has been performed within infrastructural scientific projects Centre for Foundry Technology - SIMET, KK.01.1.1.02.0020 and VIRTULAB - Integrated Laboratory for Primary and Secondary Raw Materials, Code: KK.01.1.1.02.0022.

References

[1] S. Rešković, Osnove teorije oblikovanja deformiranjem. Sveučilište u Zagrebu, Metalurški fakultet, Sisak, 2020.

[2] T. Matković, P. Matković, Fizikalna metalurgija I. Sveučilište u Zagrebu, Metalurški fakultet, Sisak, 2009.

[3] B. Grizelj, Oblikovanje metala deformiranjem, Umformtechnik, Metal Forming. Sveučilište Josipa Jurja Strossmayera u Osijeku, Strojarski fakultet u Slavonskom Brodu, Slavonski Brod, 2018.

[4] C. Liang, Understanding Plastic Deformation: Principles, Mechanisms and Applications, Adv. Mate. Sci. Res., 7 (2024) 229-230.

[5] Y. Tomota, M. Ojima, S. Harjo, W. Gong, S. Sato, T. Ungár, Dislocation densities and intergranular stresses of plastically deformed austenitic steels, Mat. Sci. Eng. A, 743 (2019) 32-39.

[6] T. Brlić, S. Rešković, I. Deanović, I. Samardžić, Line Analysis of Changes in the Deformation Zone During Lüders Band Propagation, Teh. Vjesn., 31 (2024) 881-884.

[7] S. Kumar, E. Povoden-Karadeniz, Chapter: Plastic Deformation Behavior in Steels during Metal Forming Processes: A Review. From the Edited Volume: Material Flow Analysis, IntechOpen, 2021.

[8] X. Zhang, L. Zhang, C. Ma, X. Hai, K. Song, 316L Austenitic Stainless Steel Deformation Organization and Nitriding-Strengthened Layer Relationships, Appl. Sci., 15 (2025) 2352.

[9] P. Dolzhenko, M. Tikhonova, M. Odnobokova, R. Kaibyshev, A. Belyakov, Ultrafine-Grained Stainless Steels after Severe Plastic Deformation, Metals, 13 (2023) 674.

[10] T. Brlić, T. Rodič, I. Samardžić, M. Marciuš, M. Matvija, S. Rešković, The Deformation Behavior of Niobium Microalloyed Steel during Lüders Band Formation, Metals, 13 (2023) 1678.

Published in: Materials Science Forum
ISSN: 1662-9752, Vol. 1179, pp 89-95
doi:10.4028/p-xq7Xuj

Submitted: 2025-05-26
Revised: 2025-12-05
Accepted: 2025-12-19
Online: 2026-03-03

Application of Industrial Computed Tomography (iCT) in Dentistry on 3D Printed Co-Cr Dental Bridge

Andreja Brlić[1,a], Samir Čimić[2,b*], Josip Kos[3,c], Ivan Salarić[2,4,d], Igor Keser[5,e] and Tin Brlić[6,f*]

[1]Dental Practice, Ulica Stjepana i Antuna Radića 5, 44000 Sisak, Croatia

[2]School of Dental Medicine, University of Zagreb, Ivana Gundulića 5, 10000 Zagreb, Croatia

[3]Topomatika Ltd., Industrijska ulica 3, Novaki, 10431 Sveta Nedelja, Croatia

[4]Department of Maxillofacial and Oral Surgery, University Hospital Dubrava, Avenija Gojka Šuška 6, 10000 Zagreb, Croatia

[5]Keser Dental Studio, Medveščak 47, 10000 Zagreb, Croatia

[6]Faculty of Metallurgy, University of Zagreb, Aleja narodnih heroja 3, 44000 Sisak, Croatia

[a]dental.brlic@gmail.com, [b]*scimic@sfzg.unizg.hr, [c]j.kos@topomatika.hr, [d]salaric@sfzg.unizg.hr, [e]keserdental@gmail.com, [f]*tbrlic@simet.unizg.hr

Keywords: 3D Printing, Industrial Computed Tomography (iCT), 3D Scanning, Co-Cr Alloy, Dental Bridge.

Abstract. Quality control of dental bridges in dentistry is an important area for several key reasons such as meeting high quality standards, identification of imperfections and volume defects (e.g. microcracks, porosity, irregularities), dimensional accuracy, etc. In this paper, tests were performed on additively manufactured 3D-printed and cast Co-Cr dental bridges. Surface comparison of Co-Cr dental bridges (3D-printed and cast) was carried out by checking the possibility of dimensional accuracy determination. Precise analysis of the 3D-printed Co-Cr dental bridge internal structure was performed using industrial computed tomography (iCT). The iCT analyzes were carried out from different observing perspectives of the 3D-printed Co-Cr dental bridges. The results from this study showed different applications of iCT and 3D scanning in quality control of dental bridges. The importance of iCT application in the field of dental bridges quality control was established.

Introduction

Today, the quality control of metal products using different digital technologies has an increasing importance and significance, considering its wider application in various fields such as dentistry [1]. It is possible to improve the quality of dental products using the methods of digital 3D scanning by determining their dimensional deviations and volume defects [2].

Different digital methods and techniques are often used in the dentistry, such as 3D scanning and computed-tomography (CT) tests, in order to determine different dimensional characteristics and changes in various dental products. The digital 3D scanning is used in comparing various dental products such as dental bridges [2, 3], dental crowns [4], various denture types [5], dental casts [6], etc.

In dentistry the quality control of dental bridges should be an important area for several key reasons such as meeting high quality standards, identification of imperfections and volume defects (e.g. microcracks, porosity and irregularities), dimensional accuracy, etc. This is important to ensure optimal durability of prosthetic restorations and to avoid discomfort for patients and therapists. In the oral cavity, high masticatory forces and constant temperature fluctuations are expected, which put the various materials used to the test, especially in the case of (even minor) imperfections and inaccuracies.

The CT is used for various purposes in dentistry. It is used as micro-computed tomography (μ-CT) [7, 8] and cone-beam computed tomography (CBCT) [9] for different types of examinations in dentistry. Since the production of dental bridges is one of the important areas in dentistry, it is of great importance for the patients to produce high quality dental bridges. In this sense, in the field of the quality control of dental bridges internal structure, in addition to the use of micro-CT and CBCT, there are potential benefits for use of industrial computed tomography (iCT). The application of iCT is significantly increasing [10] and can be useful for examining the volume defects such as microcracks, porosity and irregularities since it is a non-destructive method.

A literature review shows that digital 3D scanning and iCT tests of dental bridges or crowns are carried out on different types of dental materials, such as Co-Cr alloys [11], zirconia [4] and produced by various methods and techniques such as additive manufacturing, traditional casting and milling [11]. However, there is a lack of research in the available literature on quality testing of metallic dental bridges assessed by iCT.

The aim of this study is to research the possibility of iCT application in quality control of 3D-printed Co-Cr dental bridges. Dimensional geometry comparison, between 3D-printed and cast Co-Cr dental bridge, and quality control of 3D-printed Co-Cr dental bridge internal structure (volume defects) were carried out.

Experimental Procedure

The tests in this paper were conducted on 3D-printed Co-Cr metal framework of dental bridge produced from the original plaster dental cast. The reference 3D cast (STL file) of dental bridge for printing process was obtained using software package 3Shape. The Co-Cr dental bridge was produced using the 3D printer DMP dental 100 (3D Systems, Inc.).

Wirobond C+Co-Cr powder was used for additive manufacturing of Co-Cr dental bridge. The 3D-printed Co-Cr dental bridge is shown in Fig. 1. In some parts of paper, a Co-Cr dental bridge obtained by the traditional Co-Cr alloy casting process was used.

Fig. 1 Additively manufactured 3D-printed Co-Cr dental bridge.

ICT of Co-Cr dental bridge was carried out using iCT system Zeiss Metrotom scout 6 which had power of 50 W and 225 kV, Fig. 2. The testing procedure for iCT was as follows: define the product for digitalization; define the dimensions of defects which are expected; define the resolution which would be needed for expected defects; digitalization and evaluation process. The software package Zeiss Inspect X-Ray, part of Zeiss Quality Suite, was used for CT system control and data evaluation. The following setting was used: tube voltage of 200 kV and voxel size data of 42 μm with 752 image projection.

Fig. 2 Zeiss Metrotom 6 scout.

Results and Discussion

The quality of dental bridges largely depends on their dimensional and geometric accuracy. Therefore, the research of 3D-printed Co-Cr dental bridge dimensional accuracy was conducted. The tests were conducted in different positions of dental bridge to show the different possibilities of dental bridges quality control using the results of iCT digitization for the analysis and dimensional accuracy comparison. The digital twin, i.e. digital copy, of real 3D-printed Co-Cr dental bridge obtained by iCT digitization is shown in Fig. 3. The dimensional deviation analysis, using the option Surface comparison, between 3D-printed Co-Cr dental bridge actual geometry and reference 3D model, generated by software package, for 3D printing is shown in Fig. 4.

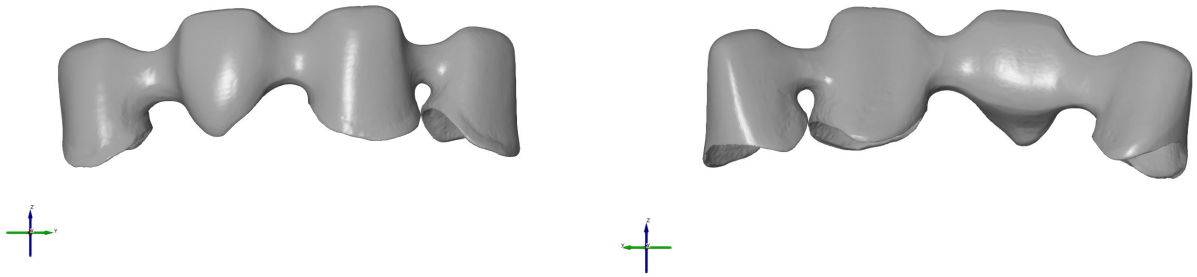

Fig. 3 3D model of digital twin – additively manufactured Co-Cr dental bridge.

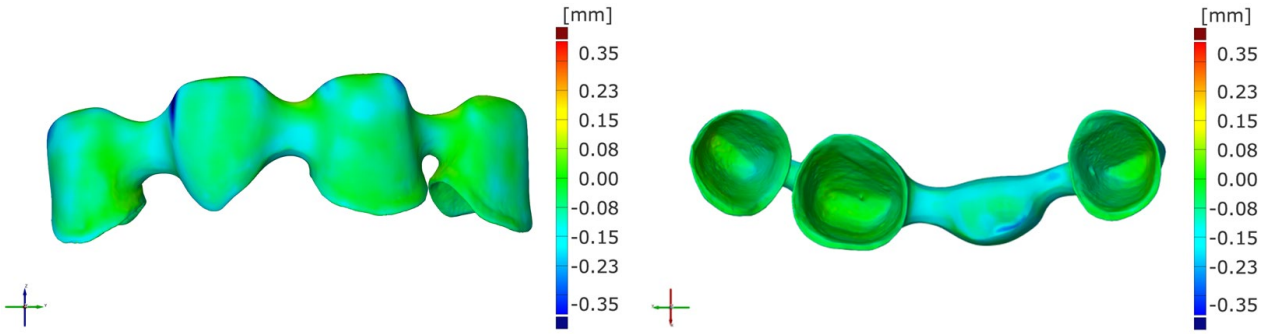

Fig. 4 Deviations in color map between 3D-printed Co-Cr dental bridge geometry and referent 3D model (used for 3D printing as reference).

Figure 4 showed that it is possible to carry out a dimensional geometry comparison between the outer and inner part of the 3D-printed Co-Cr dental bridge digital twin and the reference 3D model. A more detailed analysis was carried out on the inner part of dental bridge. In dentistry, the quality and dimensional geometry accuracy of dental bridges is more important in the inner part of the dental bridge. Therefore, the possibility of a more detailed examination of dimensional accuracy was demonstrated by a point analysis of the inner part of the dental bridge shown in Fig. 5.

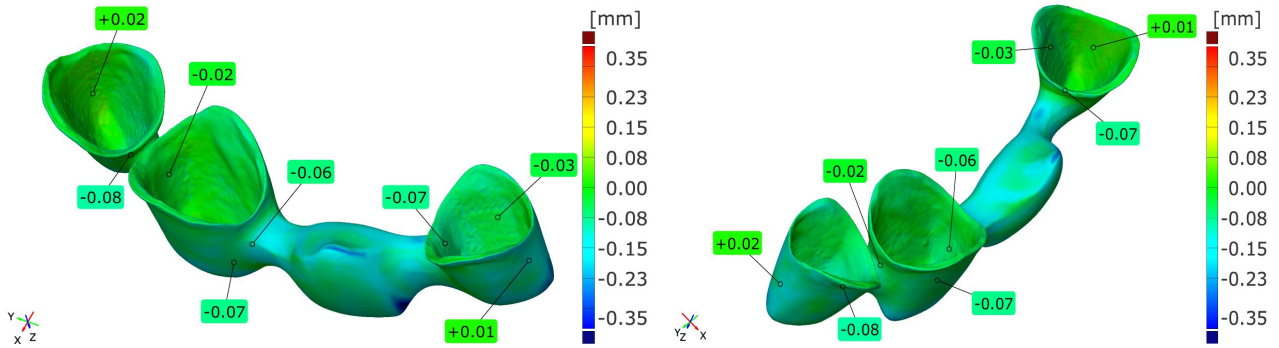

Fig. 5 Point analysis of the inner part of the 3D-printed Co-Cr dental bridge.

The obtained results clearly show that it is possible to accurately determine the exact dimensional geometry deviations of any internal part of the dental bridge between the actual geometry of 3D-printed Co-Cr dental bridge and reference 3D model for 3D printing process. This part of dimensional accuracy quality control is very important in dentistry for the proper fit of the dental bridge onto the patient's previously prepared tooth crowns. Another significance and possibility is the dimensional geometry comparison between additively manufactured 3D-printed Co-Cr dental bridge and dental bridge obtained by traditional casting process. The qualitative results of the surface comparison of outer and inner parts of the dental bridge between the 3D-printed and cast Co-Cr dental bridge are shown in Fig. 6.

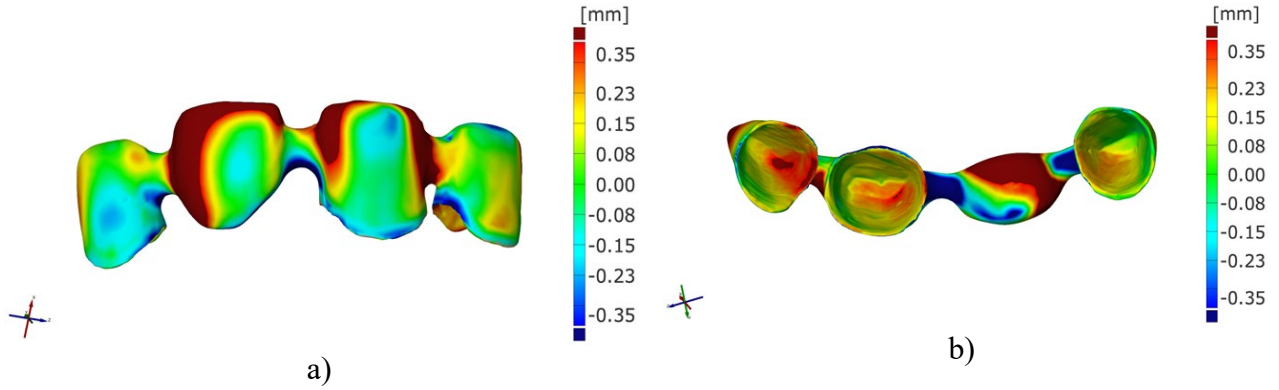

a) b)

Fig. 6 Color map deviations between 3D-printed and cast Co-Cr dental bridge geometry of a) outer part and b) inner part

Color difference maps were set from -0.35 (dark blue) to +0.35 mm (red). Negative deviations (blue) indicated smaller parts of 3D-printed compared to cast dental bridge, while positive deviations (yellow to red) indicated larger parts of cast compared to 3D-printed dental bridge. Qualitative results of surface comparison showed that dimensional geometry deviations exist between 3D-printed and cast Co-Cr metal framework of dental bridge. Thus, iCT was confirmed as a valid method for dimensional comparison quality control of dental bridges in dentistry. In addition to the dimensional geometry deviation analysis between the digital twin of reference 3D model and digital twin of dental bridges obtained by various production methods (3D printing and casting), it is possible to determine and measure the gap area between the dental bridge and the original plaster dental model (Fig. 7).

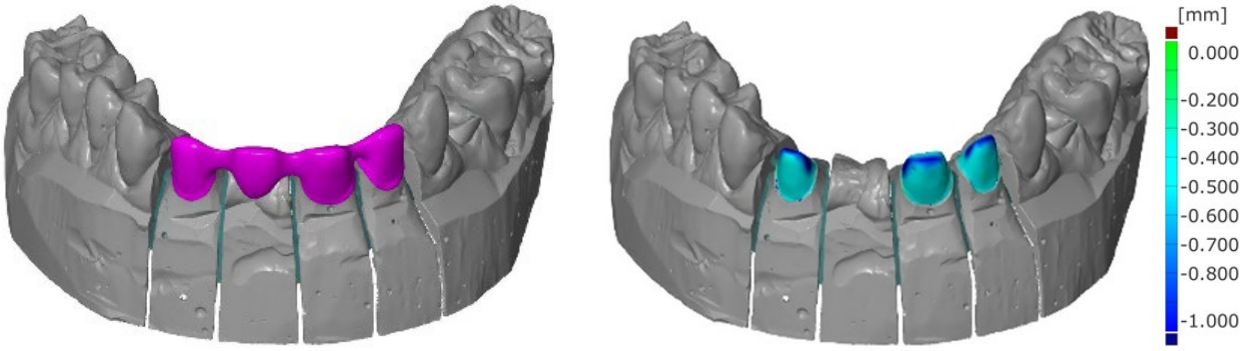

a) b)

Fig. 7 a) Digitally assembled 3D-printed Co-Cr dental bridge on the original plaster dental model and b) gap area between digital twin of the original plaster dental model and the 3D-printed Co-Cr dental bridge according to the color map legend.

As shown in Fig. 7, it is possible to determine lower and higher gap areas between digital twin of the original plaster dental model and the 3D-printed Co-Cr dental bridge. The lower gap areas are shown as green parts respectively and higher gaps are marked with blue according to the color map legend (Fig. 7b).

Precise and more detailed analysis of the 3D-printed Co-Cr dental bridge was carried out using iCT analysis. The iCT analysis was performed to detect volume defects (such as microcracks, porosity, irregularities) across the volume cross-section of 3D-printed Co-Cr dental bridge.

The iCT analysis results of internal structure from the lateral side and entire cross-section of the 3D-printed Co-Cr dental bridge are shown in Figs. 8 and 9.

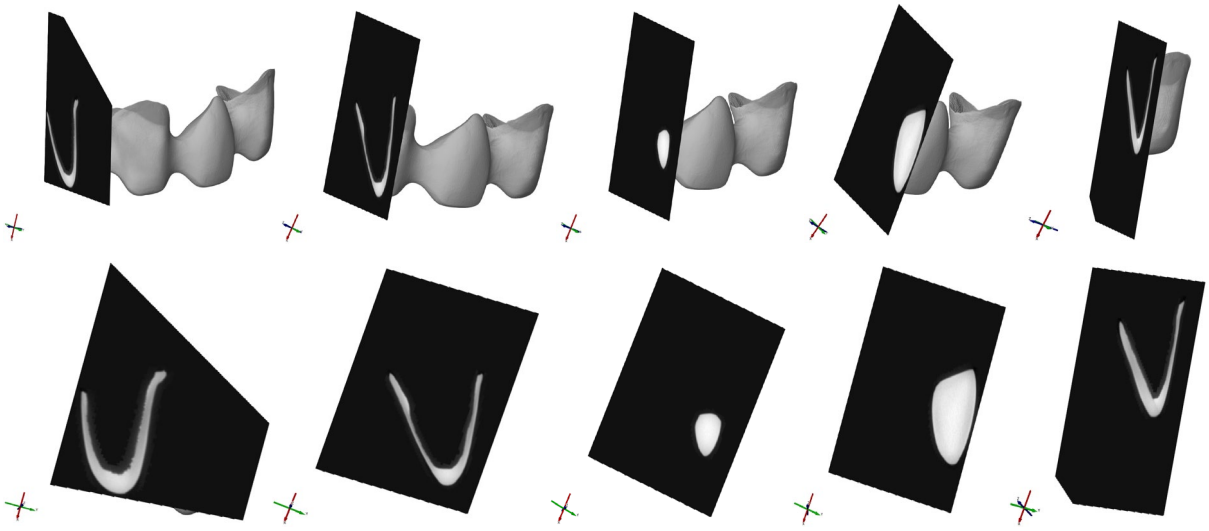

Fig. 8 ICT analysis of a 3D-printed Co-Cr dental bridge from the lateral side of dental crowns.

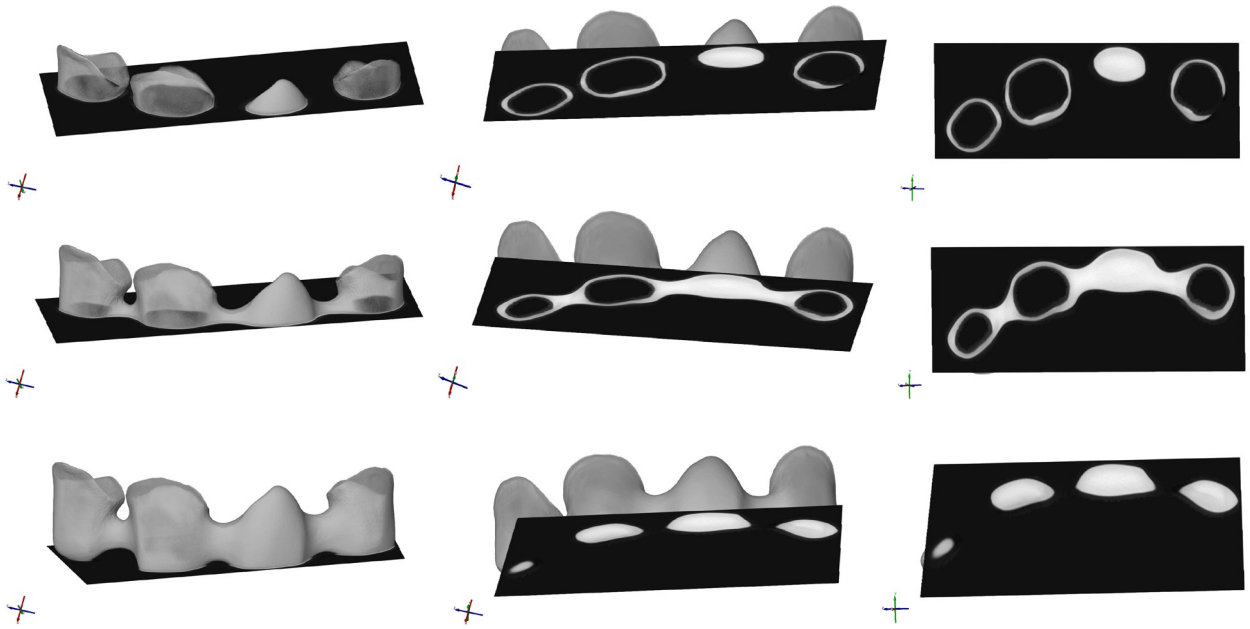

a) b)

Fig. 9 ICT analysis of 3D-printed Co-Cr dental bridge: a) top and b) bottom view of entire cross-section.

The iCT analysis of 3D-printed Co-Cr dental bridge showed that it is possible to accurately analyze the internal structure of the metallic dental bridge. It was determined that the analyzed 3D-printed Co-Cr dental bridge had no volumetric defects (micro-cracks, porosity, irregularities) that could have had an impact on its quality and application.

A detailed volume analysis of the 3D-printed Co-Cr dental bridge using the iCT in different sections showed that it is possible to analyze different parts of the dental bridge, such as the various sections of the teeth, intermediate members, joints between teeth as shown in Figs. 8 and 9.

Although the iCT analysis confirmed the absence of volumetric defects in the tested 3D-printed Co-Cr dental bridge, it is important to acknowledge certain limitations inherent to the iCT method. One of the primary constraints is factors such as scanning cost and the limited availability of iCT equipment that may restrict its widespread use in routine dental practice. Despite these limitations, iCT remains a valuable non-destructive tool that could assess the internal quality of additively manufactured dental bridges.

It can be concluded that the use of the iCT for dimensional geometry comparison and analysis of the internal structure of dental bridges can be helpful in order to determine their final quality before application. Therefore, it can be assumed that in the future iCT could have an application and a significant role in the quality control of dental bridges made from various metal alloys and other materials used for manufacturing of dental bridges.

Conclusion

Research has shown various potential applications of iCT in dentistry. The importance of using iCT in the field of dental bridges quality control was established. It was determined that is possible to analyze the dimensional geometry comparison (between 3D-printed and cast Co-Cr dental bridge) and internal structure of the 3D-printed Co-Cr dental bridge. Furthermore, the results from this study had shown that observed 3D-printed Co-Cr dental bridges had no volumetric defects such as microcracks, porosity and irregularities.

References

[1] L. Lin, Y. Fang, Y. Liao, G. Chen, C. Gao, P. Zhu, 3D Printing and Digital Processing Techniques in Dentistry: A Review of Literature., Adv. Eng. Mater., 21 (2019) 1801013.

[2] M. Javaid, A. Haleem, L. Kumar, Current status and applications of 3D scanning in dentistry, Clin. Epidemiol. Glob., 7 (2019) 228-233.

[3] L. Du, Y. Lai, C. Luo, Y. Zhang, J. Zheng, X. Ge, Y. Liu, E-quality Control in Dental Metal Additive Manufacturing Inspection Using 3D Scanning and 3D Measurement, Front. Bioeng. Biotechnol., 8 (2020) 1038.

[4] J.-H. Cho, H.-I. Yoon, J.-S. Han, D.-J. Kim, Trueness of the Inner Surface of Monolithic Crowns Fabricated by Milling of a Fully Sintered (Y, Nb)-TZP Block in Chairside CAD–CAM System for Single-visit Dentistry, Materials, 12 (2019) 3253.

[5] B. Stawarczyk, N. Lümkemann, M. Eichberger, T. Wimmer, Accuracy of Digitally Fabricated Wax Denture Bases and Conventional Completed Complete Dentures, Dent. J., 5 (2017) 36.

[6] Ž. Santoši, I. Budak, M. Šokac, T. Puškar, Đ. Vukelić, B. Trifković, 3D Digitization of featureless dental models using close range photogrammetry aided by noise-based patterns, Facta Univ. Ser.: Mech. Eng., 16 (2018) 297-305.

[7] B. Erpaçal, Ö. Adigüzel, S. Cangül, The use of micro-computed tomography in dental applications, International Dent. Res., 9 (2019) 78-91.

[8] E.F. Alsubaiy, Micro-CT analysis of 3D printed provisional crowns fitting, Technol. Health Care, 31 (2023) 259-268.

[9] J. Minnema, M. van Eijnatten, A.A. Hendriksen, N. Liberton, D.M. Pelt, K.J. Batenburg, T. Forouzanfar, J. Wolff, Segmentation of dental cone-beam CT scans affected by metal artifacts using a mixed-scale dense convolutional neural network, Med. Phys., 46 (2019) 5027-5035.

[10] L. De Chiffre, S. Carmignato, J.-P. Kruth, R. Schmitt, A. Weckenmann, Industrial applications of computed tomography, CIRP Ann. - Manuf. Technol., 63 (2014) 655-677.

[11] M. Averyanova, P. Bertrand, B. Verquin, Manufacture of Co-Cr dental crowns and bridges by selective laser Melting technology, Virtual and Physical Prototyping, 6 (2011) 179-185.

CHAPTER 7:

Metallographic Studies of Archaeological Metals

Published in: Materials Science Forum
ISSN: 1662-9752, Vol. 1180, pp 53-59
doi:10.4028/p-Is6WLJ

Submitted: 2025-05-27
Revised: 2025-12-04
Accepted: 2025-12-19
Online: 2026-03-04

Copper Test Melts with Additions of Pb, Bi, As, Sb and Sn

Roland Haubner[1,a*] and Susanne Strobl[1,b]

[1]Technische Universität Wien, Institute of Chemical Technologies and Analytics, Getreidemarkt 9/164-03, A-1060 Vienna, Austria

[a*]roland.haubner@tuwien.ac.at, [b]susanne.strobl@tuwien.ac.at

Keywords: copper, test melts, bismuth, arsenic, antimony, tin.

Abstract. Archaeometallurgical copper-artefacts contain a wide variety of metal admixtures (e.g. Pb, Bi, As, Sb, Sn) which either originate from the ores or were intentionally added. When the melt solidifies, these elements can accumulate in different structural areas and form special phases. The different alloying elements also interact with each other. In order to be able to examine these interactions, model alloys with different elements (Pb, Bi, As, Sb, Sn) and concentrations (5 or 10 wt.% each) were produced. More simple alloys show a dendritic microstructure and the added elements accumulate in the interdendritic areas. This is clearly visible for Pb and Bi additions, as both metals are not soluble in copper. As and Sb form compounds with Cu which precipitate mainly in the interdendritic regions. Sn is soluble in Cu at lower concentrations and Cu-Sn phases are formed only at higher concentrations. The resulting microstructures become very complex if more elements are involved. Finally, they enable us to have a better understanding for microstructures of ancient copper alloys.

Introduction

The beginnings of copper metallurgy are essentially determined by the available copper ores and the methods used to extract the metallic copper [1]. Accompanying elements play an important role, because they remain in the copper to a greater or lesser extent (e.g. Fe, S, As, Sb, Pb) [2, 3]. During a subsequent production of bronze, the constituents of the two source ores are mixed and can react with each other (e.g. Sn, Pb) [4]. Further interactions can occur when ores are added intentionally or unintentionally (e.g. PbS, ZnS, Sb_3S_2) [5, 6].

This means that a prehistoric bronze can contain many elements that interact with each other [7]. The goal of producing test melts is to document and study such interactions and to get a better assessment for the measured results of historical bronzes.

Experimental Procedure

Melting of the samples.

The individual metal powders were weighed in appropriate ratios, transferred to a quartz crucible and slightly mixed. This mixture was then covered with carbon powder to prevent oxidation. It was then heated to approximately 1100 °C in a chamber furnace. When this temperature was reached, the mixture was left for approximately 15 minutes and subsequently air cooled.

Metallography.

After cutting the samples were cold mounted in epoxy resin. Metallographic preparation started with plane-grinding, followed by polishing with 9–1 µm diamond suspensions.

For etching Klemm 2 and $(NH_4)_2CuCl_4$ solutions were used.

It should be noted, that due to segregation, the composition of the alloys shown in the images, may not correspond to the initial concentrations.

A light optical microscope (LOM) and a scanning electron microscope (SEM) with backscattering electron (BSE) detector were used. X-ray analysis (EDX) was performed to measure the local elemental compositions.

Results and Discussion

The interactions between the different metals are based on thermodynamic data illustrated by phase diagrams. The binary phase diagrams of the investigated metals are all available [8], but not the ternary or quaternary ones. Therefore, attempts are made to explain the observed microstructures from the analytical results.

Alloy 10 % Bi, 10 % Pb, balance Cu.

Bi and Pb are insoluble in Cu [8]. Dendritic solidification of copper occurs from the melt and Bi-Pb are present in the interdendritic regions (Fig. 1a). The dendrites have a length of up to 1 mm. After etching different coloured dendritic cells are visible due to the diverse orientation of copper (Fig. 1b–d). Pb is insoluble in Bi, but in the binary system a Pb-Bi phase is formed. Finally, the Pb-Bi phase and Bi should be present. In the SEM-BSE images, the interdendritic regions of Pb and Bi are visible as a bright “network” (Fig. 1e, f).

Alloy 10 % Sb, 10 % Pb, balance Cu.

Sb forms the intermetallic phase Cu_3Sb and Pb is insoluble in Cu [8]. This is already visible at the polished sample where Cu_3Sb appears light grey and Pb black (Fig. 2a, b). During solidification of the melt Cu dendrites are formed first and Sb as well as Pb concentrate in the remaining melt. The concentration gradients are clearly visible at the etched samples (Fig. 2c, d). The SEM images and the EDX element distribution obviously show that Cu_3Sb and Pb are separated (Fig. 2e–g).

Alloy 10 % As, 10 % Sn, balance Cu.

The interactions of As and Sn in copper are of striking interest for ancient bronzes [3, 9]. Again, a dendritic structure is formed, but no identification of the individual phases is possible from the etched samples. (Fig. 3a–d). Sn concentration in Cu increases with progressive solidification. Cu_3As forms in the interdendritic regions. The $Cu_{41}Sn_{11}$ phase is subsequently formed during a eutectoid transformation (Fig. 3e–g).

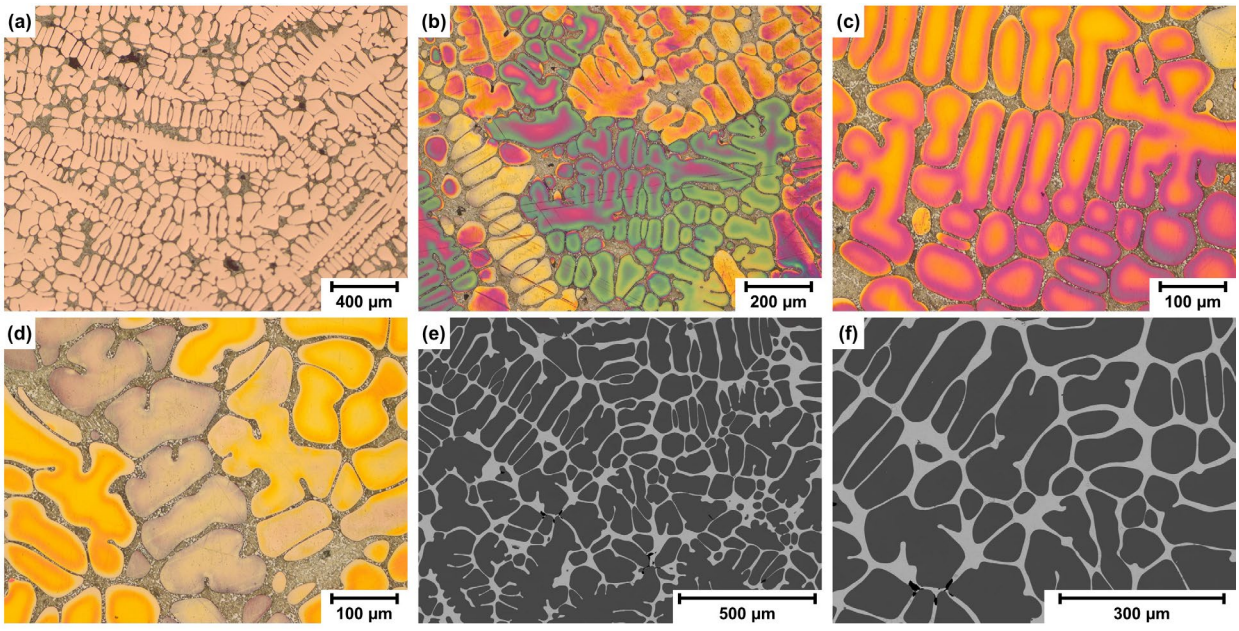

Fig. 1. Alloy 10 % Bi, 10 % Pb, balance Cu. (a) polished, (b–d) Klemm 2 etched, (e, f) SEM.

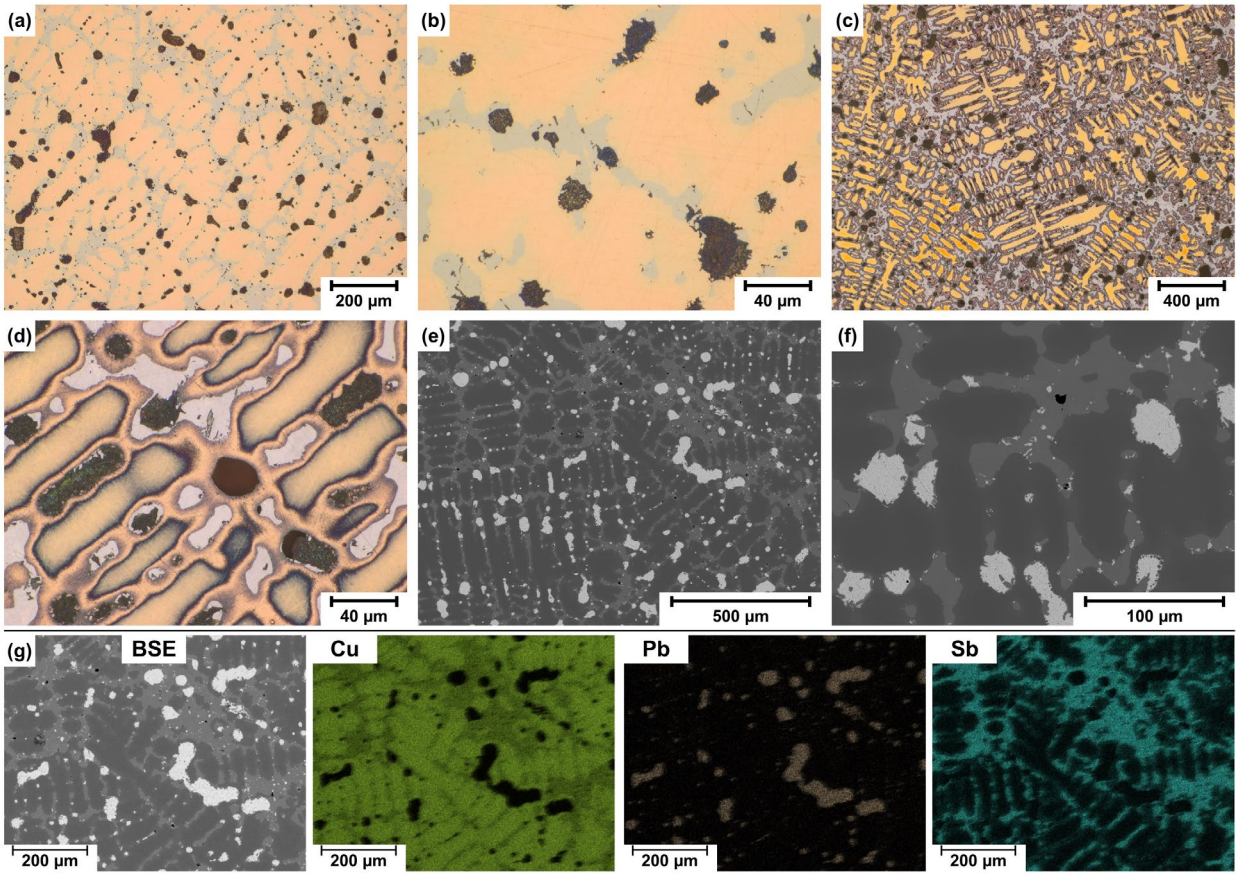

Fig. 2. Alloy 10 % Sb, 10 % Pb, balance Cu. (a, b) polished, (c, d) $(NH_4)_2CuCl_4$ etched, (e, f) SEM, (g) SEM-BSE element distribution.

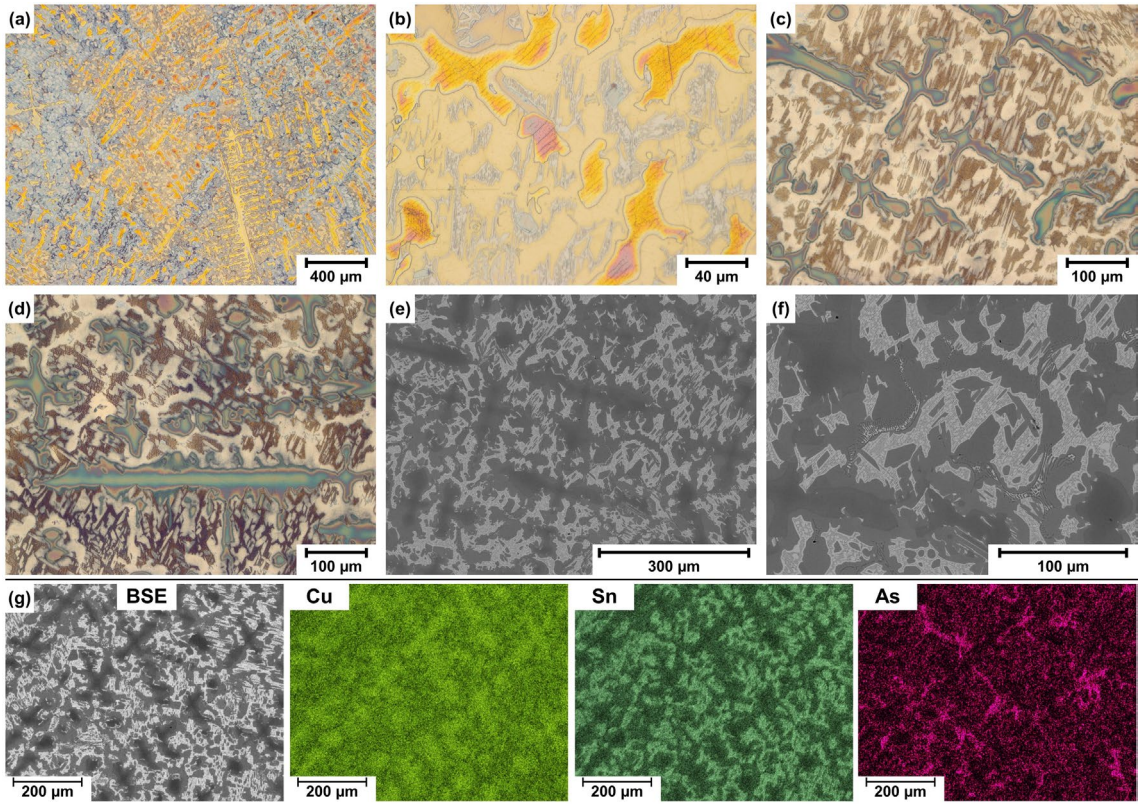

Fig. 3. Alloy 10 % As, 10 % Sn, balance Cu. (a, b) Klemm etched, (c, d) $(NH_4)_2CuCl_4$ etched, (e, f) SEM, (g) SEM-EDX element distribution.

Alloy 10 % Sb, 10 % Sn, balance Cu.

All binary phase diagrams between Cu, Sb and Sn are very complex, and many intermetallic phases are possible [8, 10]. Cu forms the dendritic structure and the alloying elements are enriched in the interdendritic regions (Fig. 4a–d). In the SEM-BSE images, the interdendritic areas appear homogeneous (Fig. 4e, f). According to the EDX element distribution, the elements Sb and Sn are present side by side in the interdendritic regions and are not separated (Fig. 4g). It is assumed that the phases Cu_3Sb and $Cu_{41}Sn_{11}$ are present. It cannot be determined whether or not an Sb-Sn phase had been formed.

Alloy 5 % Sb, 5 % As, 5 % Pb, balance Cu.

In this alloy, four elements already interact, making the system considerably more complex. Looking at the individual elements, Cu_3As and Cu_3Sb are formed. Pb and As form an eutectic at 2.6 wt.% As, Pb and Sb form one at 11.1 wt.% Sb [8].

Again, in this alloy Cu dendrites are formed first and the alloying elements accumulate in the melt to solidify in the interdendritic areas (Fig. 5a–d). The intermetallic phases Cu_3Sb, Cu_3As and Pb are expected (Fig. 5e, f). Based on the EDX element mappings one can see that As is associated with both Pb and Sb (Fig. 5g). Since Pb is insoluble in Cu, it is separated.

Alloy 5 % As, 5 % Sb, 5 % Sn, balance Cu.

This Cu alloy contains As, Sb and Sn, each 5 wt.%, but no typical solidification structure was obtained. This quaternary system probably has multiple eutectics and other phase transitions unknown to us.

The typical dendritic solidification structure of Cu is not observed, but Cu forms elongated bars instead of dendrites (Fig. 6a–f). Similar to the ternary Sb-Sn-Cu system, the Sb and Sn phases are co-localized (Fig. 6g).

Complete different is the behaviour of the As compounds: they solidify from a residual melt.

Thus, various microstructures are present, which can be explained by eutectic solidification or eutectoid transformations. These microstructures overlap, but it was not possible to identify the individual phases by EDX.

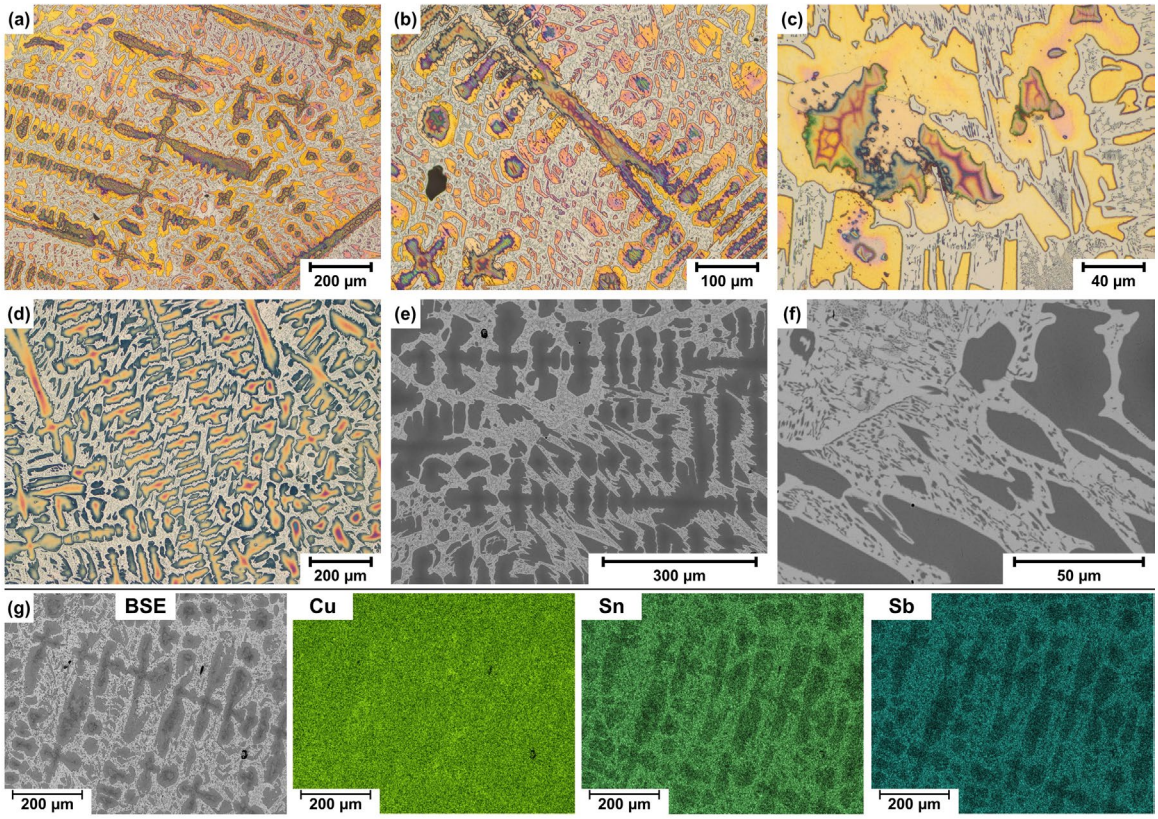

Fig. 4. Alloy 10 % Sb, 10 % Sn, balance Cu. (a, b) Klemm etched, (c, d) $(NH_4)_2CuCl_4$ etched, (e, f) SEM, (g) SEM-EDX element distribution.

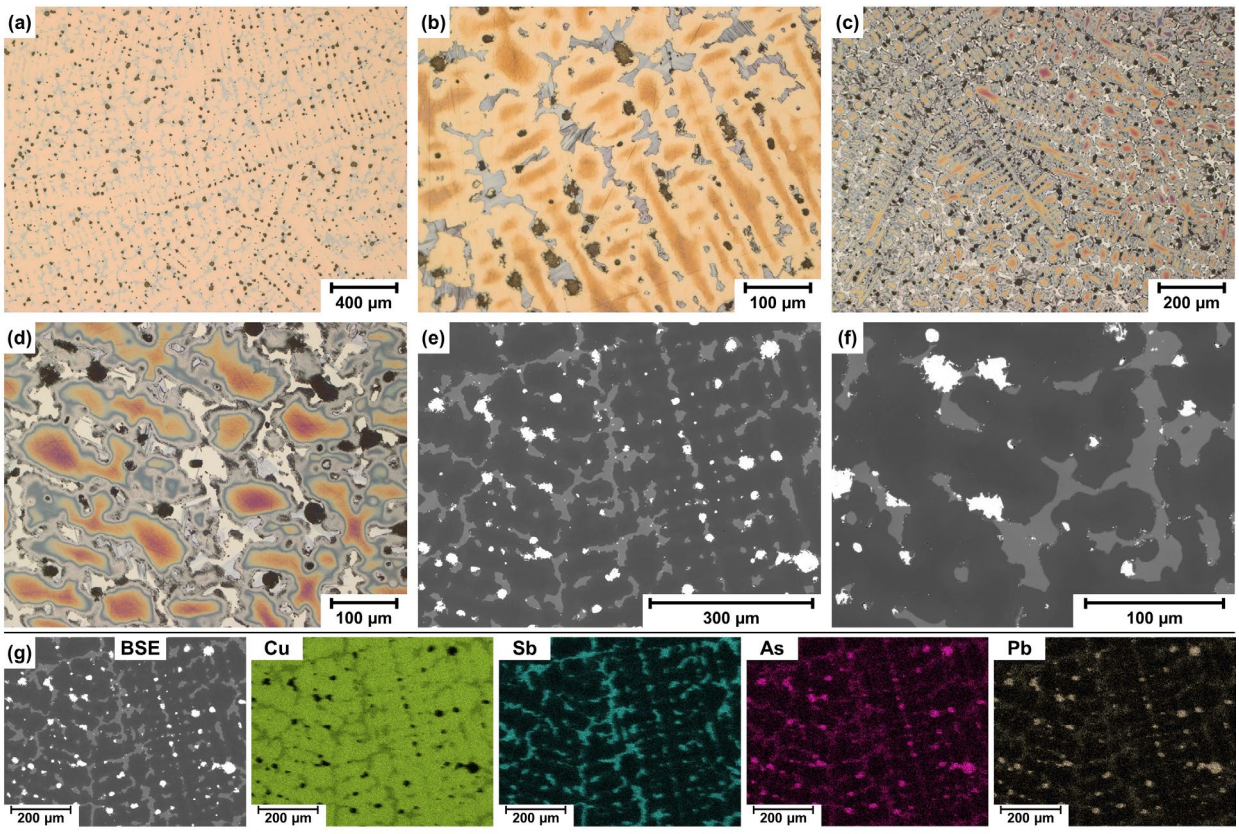

Fig. 5. Alloy 5 % Sb, 5 % As, 5 % Pb, balance Cu. (a) polished, (b) Klemm etched, (c, d) $(NH_4)_2CuCl_4$ etched, (e, f) SEM, (g) SEM-EDX element distribution.

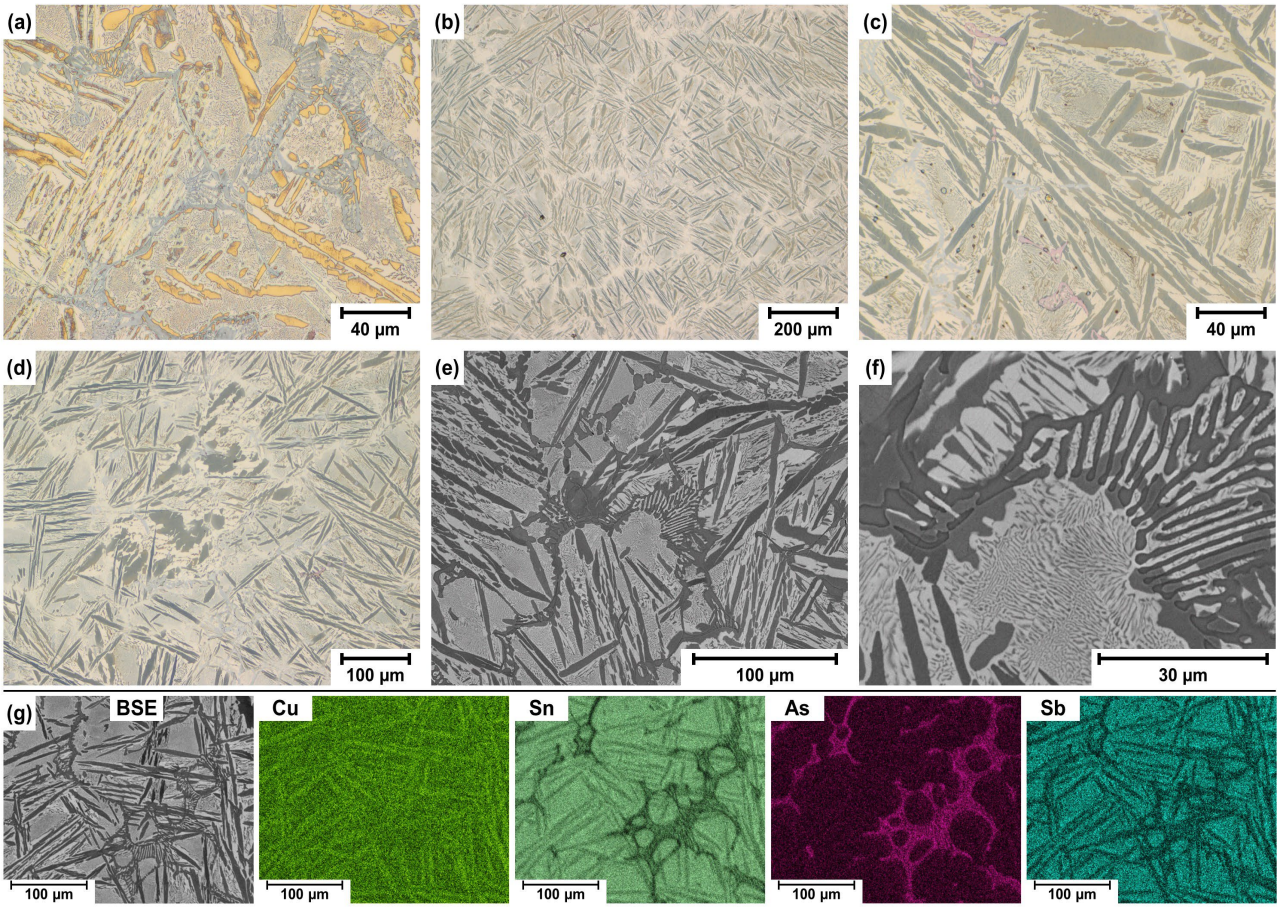

Fig. 6. Alloy 5 % As, 5 % Sb, 5 % Sn, balance Cu. (a) Klemm etched, (b–d) $(NH_4)_2CuCl_4$ etched, (e, f) SEM, (g) SEM-EDX element distribution.

Summary

For a better understanding of historical copper alloys, various model alloys with Pb, Bi, As, Sb and Sn additives were molten and investigated by metallography.

Typically, Cu solidifies first, forming dendrites, while the alloying elements are concentrated in the interdendritic areas. The microstructure of the alloy depends on the amount of Cu, which is involved in the formation of intermetallic phases. Since Pb and Bi do not form phases with Cu, and the metals are not soluble in Cu, the interdendritic regions are small. But As, Sb and Sn form corresponding cupreous phases (Cu_3As, Cu_3Sb and $Cu_{41}Sn_{11}$) and so the proportion of Cu dendrites is reduced and the interdendritic regions increase.

In ternary copper alloys, with a ratio of 10:10:80, a dendritic microstructure is observed, and the alloying elements accumulate in the interdendritic regions.

This phenomenon is further amplified in quaternary systems with a ratio of 5:5:5:75.

In the system As-Sb-Sn-Cu no dendritic growth is observed due to the formation of different Cu-containing intermetallic phases.

Acknowledgement

The authors would like to thank the TU Wien Library for the financial support through its Open Access Funding Program.

References

[1] R. Haubner, Die prähistorische Kupfermetallurgie - allgemeine Betrachtungen, BHM Berg- und Hüttenmännische Monatshefte, 166 (2021) 343-351, doi: 10.1007/s00501-020-01056-0.

[2] R. Haubner, S. Strobl, Considerations on Copper Smelting from Fahlores and the Metallurgy of Cu-As Bronzes, BHM Berg- und Hüttenmännische Monatshefte, 168 (2023) 434-444, doi: 10.1007/s00501-022-01230-6.

[3] F. Ertl, S. Strobl, R. Haubner, An ancient bronze ingot smelted from fahlore, Materials Science Forum, 891 (2017) 613-617, doi:10.4028/www.scientific.net/MSF.891.613.

[4] R. Haubner, S. Strobl, Direct Production of Tin Bronzes from Copper and Cassiterite, Materials Science Forum, 1081 (2023) 137-142, doi:10.4028/p-s4jt77.

[5] R. Haubner, S. Strobl, Microstructure of an extraordinary Bronze Age copper ingot with a high antimony content, Pract. Metallogr., 59 (2022) 732-748, doi: 10.1515/pm-2022-1004.

[6] R. Haubner, S. Strobl, M. Thurner, H. Herdits, Ein Kupfergusskuchen mit hohem Antimongehalt aus Velem/Westungarn, BHM Berg- und Hüttenmännische Monatshefte, 165 (2020) 453-460, doi: 10.1007/s00501-020-01017-7.

[7] R. Haubner, S. Strobl, Investigations on Copper Cast Cakes, Sickle Fragments and a Spout Axe of the Hoard Find from Drassburg/Burgenland, Metallography, Microstructure, and Analysis, 12 (2023) 187-201, doi: 10.1007/s13632-023-00936-4.

[8] T.B. Massalski, Binary Alloy Phase Diagrams. ASM International, Metals Park OH (1990).

[9] R. Haubner, S. Strobl, The Copper-Arsenic eutecticum and the Cu_3As phase, Defect and Diffusion Forum, 405 (2020) 19-25, doi: 10.4028/www.scientific.net/DDF.405.19.

[10] R. Haubner, S. Strobl, Microstructural Examinations of Copper Antimony Alloys, Pract. Metallogr., 58 (2021) 620-629, doi: 10.1515/pm-2021-0054.

Published in: Materials Science Forum
ISSN: 1662-9752, Vol. 1180, pp 61-67
doi:10.4028/p-eykX5A

Submitted: 2025-05-27
Revised: 2025-12-10
Accepted: 2025-12-19
Online: 2026-03-04

A Bronze Button from Late Bronze Age Site of Inzersdorf ob der Traisen

Roland Haubner[1,a*] and Susanne Strobl[1,b]

[1]Technische Universität Wien, Institute of Chemical Technologies and Analytics, Getreidemarkt 9/164-03, A-1060 Vienna, Austria

[a*]roland.haubner@tuwien.ac.at, [b]susanne.strobl@tuwien.ac.at

Keywords: bronze, button, bronze age.

Abstract. In the region of Inzersdorf ob der Traisen in Lower Austria, 273 cremation graves from the late Bronze Age (ca. 1300–800 BC) were recovered. Also, various bronze artefacts were found in some graves, including a button which was analyzed by metallography. It should be determined how the button was manufactured, for example by casting or soldering, and microstructural changes can be detected due to temperature effects by cremation. The button is made of bronze whose composition was determined by XRF: 87 wt.% Cu, 9 wt.% Sn and 1 wt.% Pb. The microstructure of the bronze clearly shows a temperature influence during cremation. The bronze microstructure is recrystallized as well as parts were melted, causing oxidation at the grain boundaries. Also, some areas of the bronze show small shrink holes. Further corrosion took place during long-term storage of the button in the soil.

Introduction

During the construction of the S33 expressway, large-scale rescue excavations were carried out in Inzersdorf ob der Traisen, Lower Austria [1, 2], because an Urnfield period cemetery was detected. In one of the graves the investigated bronze button was found.

About 273 graves were documented in the cemetery of Inzersdorf ob der Traisen. The cemetery was used from the earliest Urnfield period (about 1300 BC) to the late Urnfield period (about 800 BC). The majority of the graves date back to the early Urnfield period (1300–1000 BC), when small urn graves were used [3–5].

During a cremation the deceased persons are burnt on a pyre together with their clothing, jewellery and other grave goods. Then the cremated residuals are placed in a grave, usually in an urn [6].

Large quantities of bronze artefacts were found in some of the graves. These were primarily costume objects such as bracelets, pins and buttons, while tools such as knives were in the minority and weapons were completely absent [5].

During cremation a heat influence on the metallic objects can be expected and their microstructure will change depending on the local temperature and the duration of the heat exposure. Depending on the bronze composition, the alloy melts between 900 and 1000 °C. As a part of experimental archaeology, cremation experiments were carried out with pigs and bronze parts, which were subsequently examined [6–8].

This work is a continuation of studies on prehistoric buttons [9, 10].

Experimental Procedure

The button was photographed and was subsequently examined using micro-computed tomography (micro-CT) [11]. It was then cold mounted in epoxy resin under vacuum. Once hardened, a cut was made parallel to the eyelet of the button. This cross-section was again cold mounted. The metallographic preparation was carried out in stages by grinding and polishing up to a diamond grain

size of 1 µm. The sections were analyzed in the as-polished state and after etching with Klemm 2 solution.

A light optical microscope (LOM) and a scanning electron microscope (SEM) with energy dispersive X-ray analysis (EDX) were used. To determine the overall chemical composition of the samples, measurements were additionally carried out on the metallographic sections using X-ray fluorescence analyses (XRF).

Results and Discussion

Non-destructive testing methods.

The button face is a flat disc whose edge is bent inwards. The eyelet is not centered. The button is entirely covered with a greenish-brown patina (Fig. 1). The button plate appears homogeneous in the CT sections. In the area of the eyelet inhomogeneities are visible, which can be attributed to defects during manufacture or corrosion (Fig. 2).

Fig. 1. Photos of the knob from different perspectives. (a) avers, (b) reverse, (c) side view.

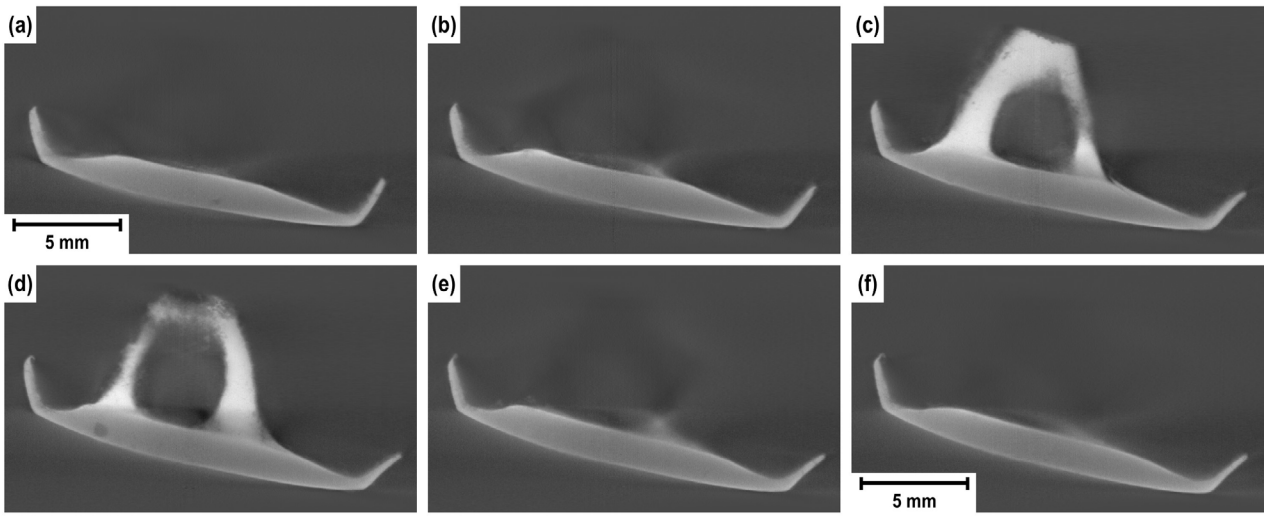

Fig. 2. Images of CT cuts through the button.

The bronze alloy.

The button consists of a bronze alloy with approximately 9.5 wt.% Sn and 1.2 wt.% Pb (Table 1). From the CT sections and the overview images of the metallographic sections no evidence of a joint is observable. Consequently, this button was cast (Fig. 3).

One would expect a dendritic solidification structure of a cast bronze [12–14], but this is not the case. Instead, the microstructure is coarsely crystalline and has isolated annealing twins. One explanation is that the button was heat-treated during cremation [9, 15].

Table 1. XRF on the metallographic sample of the button.

Element	Cu	Sn	Pb	Ni	Fe	S	Ca	Si	Al
wt.%	87.34	9.51	1.24	0.35	0.18	0.09	0.29	0.86	0.12

Observed bronze microstructures.

At the bent-up edge of the button, which has a thickness of approximately 400 µm, the microstructure is very coarse with grain sizes of up to 400 µm (Fig. 4a, b). Annealing twins are occasionally visible (Fig. 4c). Also, corrosion products can be seen along grain boundaries and at the surface.

In the thicker area of the eyelet, grain sizes of up to 500 µm are observed (Fig. 4d, e). Corrosion products are present at the surface (Fig. 4f).

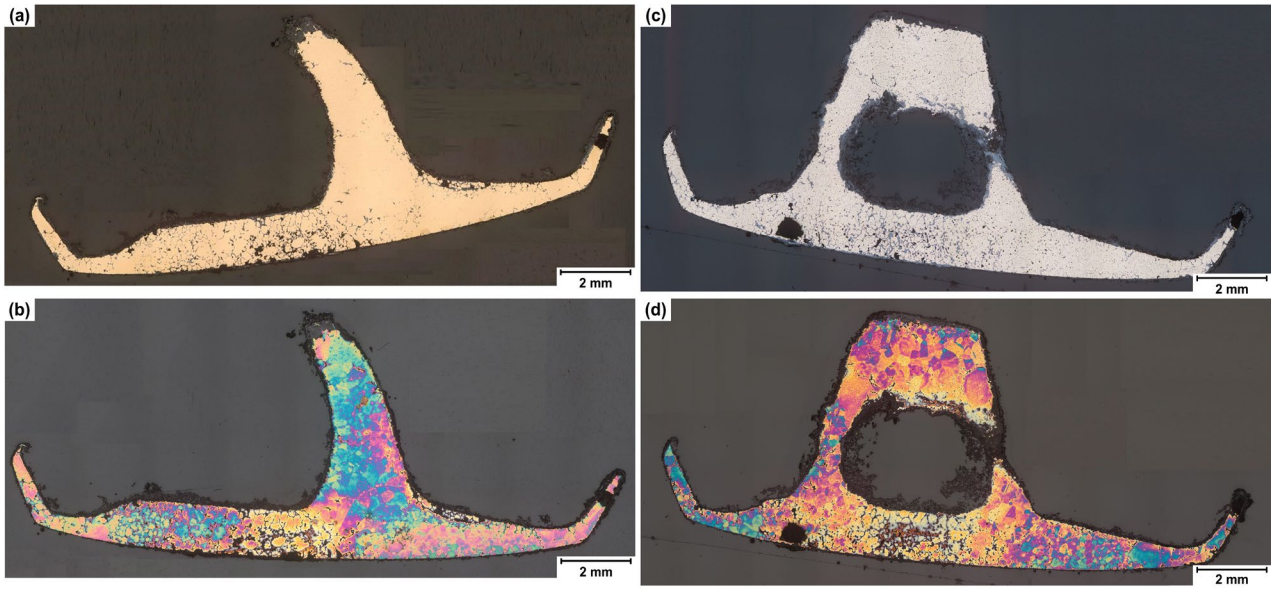

Fig. 3. Different metallographic grinding levels of the button. (a, b) 1st grinding level, (c, d) 2nd grinding level, (a, c) polished, (b, d) Klemm 2 etched.

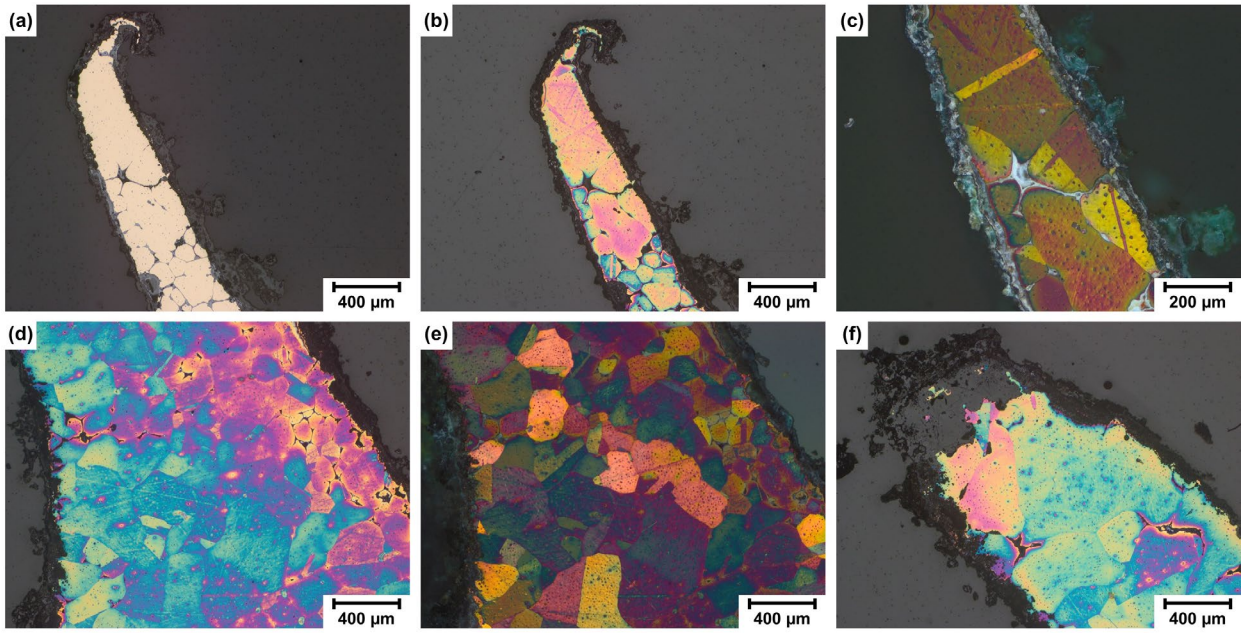

Fig. 4. 1st grinding level. (a–c) bent-up edge of the button, (d–f) eyelet region. (a) polished, (b–f) Klemm 2 etched, (c, e) polarized light.

In the button´s center the bronze had melted partially during cremation (Fig. 5). These areas have shrinkholes and the grain boundaries are oxidized partially (Fig. 5a–d). Due to these grain boundary oxides, the grain size in these areas is low with about 200 µm (Fig. 5d–f), because oxidation along the original grain boundaries of the bronze occurred faster than the recrystallization of the structure. A SEM-EDX element distribution shows that Sn is enriched in the oxidation products at the grain boundaries. Also, local enrichments of S were detected, but no metal can be assigned to S. Possible are PbS or Cu_2S precipitates (Fig. 6).

In the slightly thicker areas of the button, at the 2nd grinding level, spheric inclusions within the bronze grains were observed (Fig. 7). These inclusions are completely or partially filled. Additionally, some holes are visible (Fig. 7b, e, f) which could be shrinkholes. The inclusions may consist of PbS or Cu_2S. By a SEM-EDX element distribution S was detected in areas of the holes but no Pb, which could be due to the lower detection limit for Pb (Fig. 8). However, the Sn enrichment in the oxides at the grain boundaries is clearly observable.

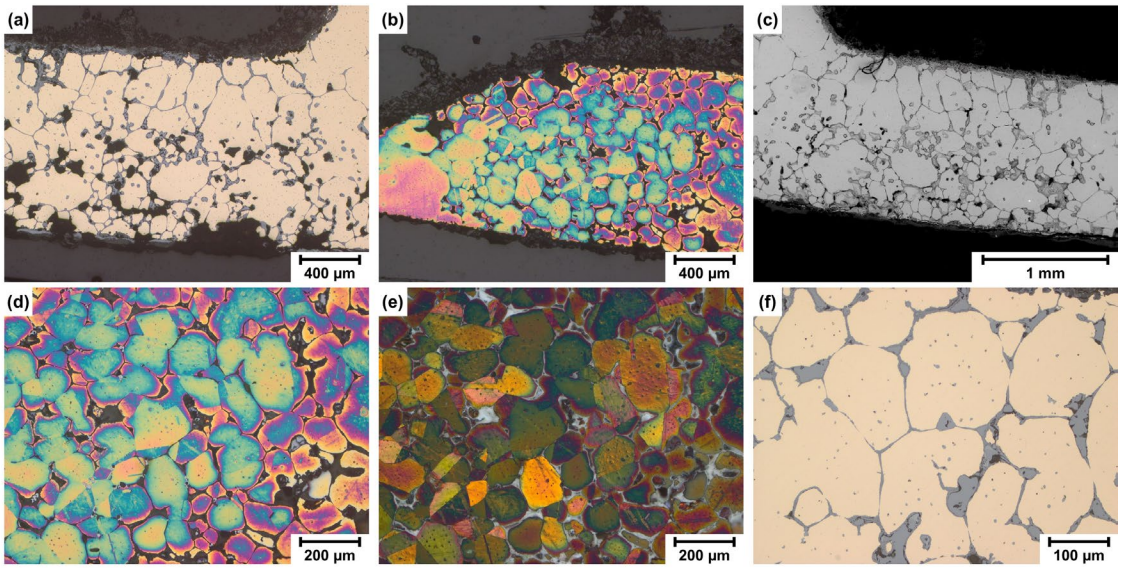

Fig. 5. Partially molten area of the button. (a, f) as-polished. (b, d) Klemm 2 etched, (c) SEM, (f) polarized light.

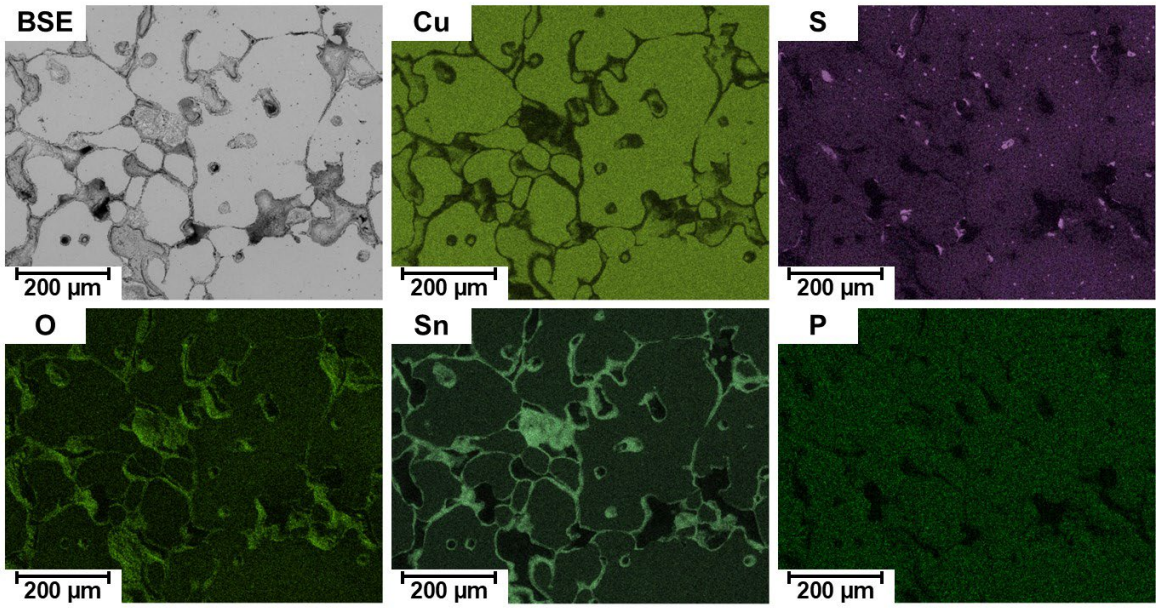

Fig. 6. SEM-EDX element distribution.

The oxidation along the grain boundaries during cremation is due to high-temperature corrosion as well as scaling and Cu_2O (cuprite) is formed. Cuprite appears red in polarized light (Fig. 7c, Fig. 9c) [9]. However, aqueous corrosion also occurred during long-term storage of the bronze in the soil, resulting in the formation of malachite at the surface (Fig. 9a–c). Malachite appears green in polarized light (Fig. 7c, Fig. 9c).

The formation of the surface layer shown in Fig. 9b and Fig. 9c can be explained as follows: during cremation oxidation occurred along the grain boundaries resulting in the formation of Cu_2O (red in polarized light) (Fig. 9c). Later the malachite layer was formed at the surface (green in polarized light) [16].

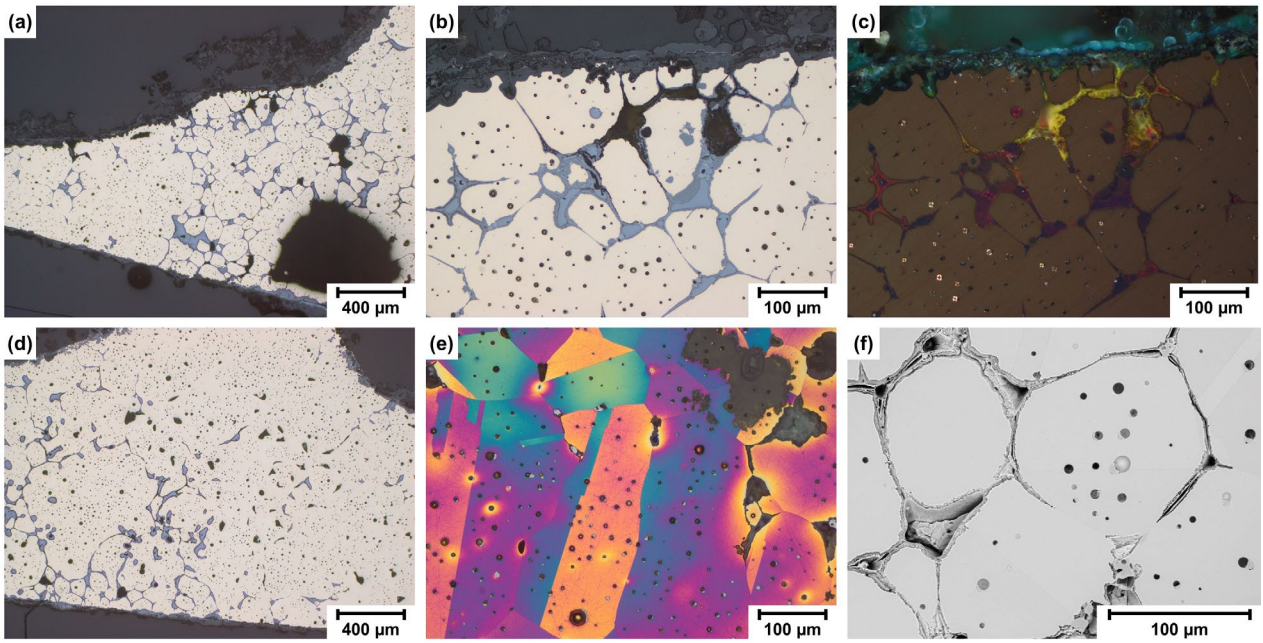

Fig. 7. 2nd grinding level. Small holes in the bronze grains. (a, b, d) as-polished, (c) polarized light, (e) Klemm 2 etched, (f) SEM.

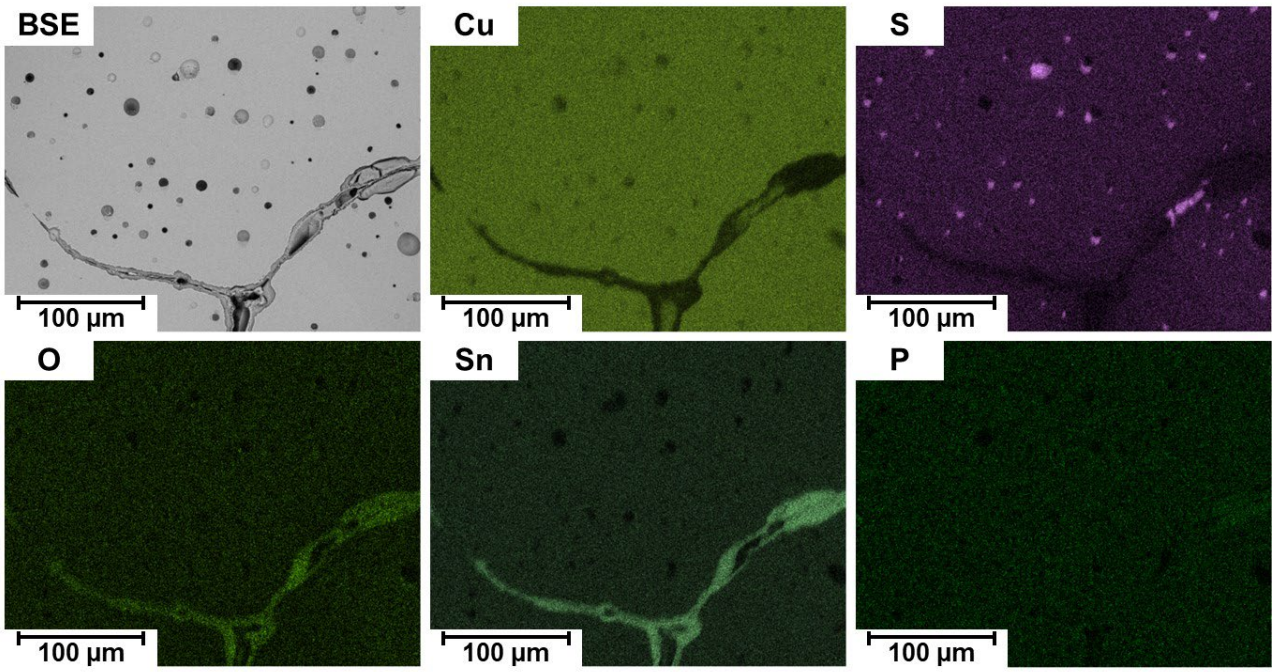

Fig. 8. SEM-EDX element distribution.

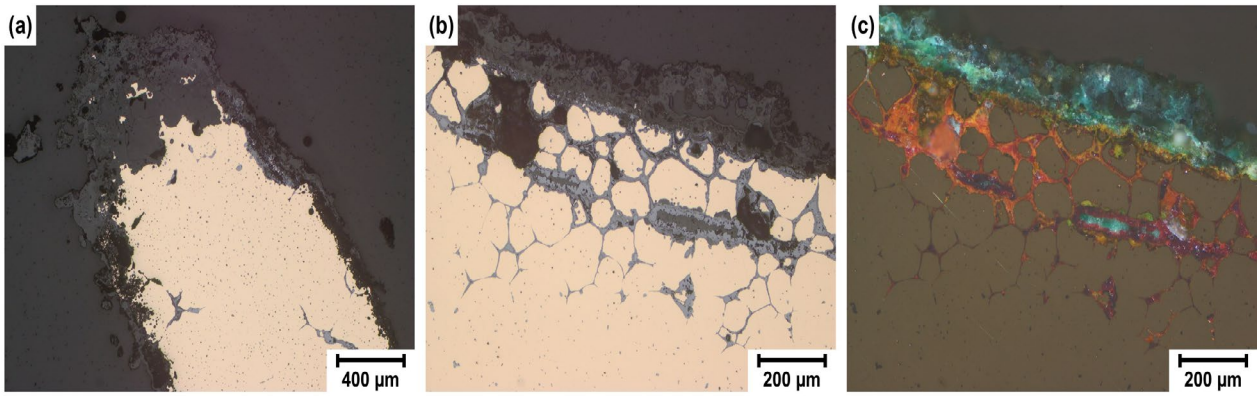

Fig. 9. Corroded surfaces of the bronze. (a) edge of the button, (b) surface, (c) polarized light.

Summary

A bronze button from the late Bronze Age (ca. 1300–800 BC) was investigated.

The button was made by casting, which is consistent with the buttons from Schandorf [9] and Mitterkirchen [10] examined so far.

During cremation the button partially melted resulting in the formation of Cu_2O at the grain boundaries. In other areas the structure recrystallized resulting in grain growth of the bronze and sizes up to 1 mm were formed.

Also, small spherical shrink holes, partially filled with Cu_2S, were observed in the bronze grains of the melted regions.

Sn is enriched in Cu_2O, which had developed by scaling, and at the bronze surface malachite had formed.

Acknowledgement

The authors would like to thank the TU Wien Library for the financial support through its Open Access Funding Program.

References

[1] J.-W. Neugebauer, A. Gattringer, Fundberichte aus Österreich, 28 (1989) 55-61.

[2] A. Gattringer, J.-W. Neugebauer, Fundberichte aus Österreich, 20 (1982) 157-190.

[3] M. Lochner, Brandbestattung und Bronzemetallurgie - Die Urnenfelderkultur in Niederösterreich (1300–800 v. Chr.), Archäologie Niederösterreichs, 5 (2021) Verlag der Österreichischen Akademie der Wissenschaften, Wien.

[4] J.-W. Neugebauer, Bronzezeit in Ostösterreich. Wissenschaftliche Schriftenreihe Niederösterreich, Verlag Österreichisches Pressehaus (1994).

[5] M. Fritzl, Die mehrfach belegten Gräber des urnenfelderzeitlichen Gräberfeldes von Inzersdorf ob der Traisen, Niederösterreich. MA Thesis, University of Vienna (2017).

[6] M. Fritzl, M. Konrad, K. Grömer, A. Stadlmayr, Rituale in der mitteldonauländischen Urnenfelderzeit: Eine Annäherung durch experimentelle Kremationen. In: Pieler F, Nowotny E (eds) Beiträge zum Tag der Niederösterreichischen Landesarchäologie 2019, Asparn an der Zaya, (2019) 42-54.

[7] R. Haubner, S. Strobl, M. Fritzl, M. Konrad, BHM Berg- und Hüttenmännische Monatshefte, 169 (2024) 104-110.

[8] R. Haubner, S. Strobl, Metallography, Microstructure, and Analysis, (2025) (in press). doi:10.1007/s13632-025-01195-1

[9] R. Haubner, Garment buttons from a Hallstatt period tumulus, Pract. Metallogr., 60 (2023) 276-288.

[10] R. Haubner, S. Strobl, J. Leskovar, Metallography, Microstructure, and Analysis, 13 (2024) 1119-1130.

[11] R. Haubner, S. Strobl, Pract. Metallogr., 61 (2024) 216-231.

[12] R. Haubner, S. Strobl, BHM Berg- und Hüttenmännische Monatshefte, 169 (2024) 483-489.

[13] R. Haubner, S. Strobl, Metallography, Microstructure, and Analysis, 12 (2023) 187-201.

[14] R. Haubner, S. Strobl, J. Leskovar, Pract. Metallogr., 61 (2024) 630-641.

[15] M. Fritzl, M. Konrad, S. Strobl, R. Haubner, BHM Berg- und Hüttenmännische Monatshefte, 169, 9 (2024) 470-482.

[16] R. Haubner, S. Strobl, P. Trebsche, Materials Science Forum, 891 (2017) 41-48.

Published in: Materials Science Forum
ISSN: 1662-9752, Vol. 1180, pp 69-75
doi:10.4028/p-O3Bp7s

Submitted: 2025-05-27
Revised: 2025-12-05
Accepted: 2025-12-19
Online: 2026-03-04

Roman Bronze Objects from the Archaeological Site of Burg in Burgenland, Austria

Susanne Strobl[1,a] and Roland Haubner[1,b*]

[1]Technische Universität Wien, Institute of Chemical Technologies and Analytics, Getreidemarkt 9/164-03, A-1060 Vienna, Austria

[a]susanne.strobl@tuwien.ac.at, [b*]roland.haubner@tuwien.ac.at

Keywords: bronze, small parts, roman, microstructures.

Abstract. Several Roman bronze objects were confiscated from a digger, which had been collected illegally at the archaeological site of Burg, Burgenland. Since these parts are archaeologically worthless, they were allowed to be examined with destructive analysis methods. The investigative results of five parts are presented. The surface of the parts is covered with a green patina which contains mainly Cu and smaller amounts of Sn, Pb, P, Ca, Al, S and Fe. If XRF analyses are performed, it must be taken into account that elements such as Sn accumulate in the patina. The average XRF analyses of the hook showed a content of 0.8 wt.% Sn and about 2 wt.% Pb, but in the fibular parts and the button up to 42 wt.% Pb were detected. Due to very different compositions of the samples, the microstructures are also appropriate miscellaneous. It is possible to distinguish between cast, recrystallized and deformed microstructures. These investigations show that the Roman metallurgist used a wide variety of copper alloys, because raw and recycled materials were probably processed together.

Introduction

It is usually difficult to obtain historical objects for examination using destructive testing methods, as such objects possess cultural value and must be preserved. Exceptions exist, e.g. when objects are on hand in large numbers [1–4] or their origin is not clearly established [5–7].

In this work the investigated samples were confiscated from a metal detectorist and were available for examination. The objects have been classified by an archaeologist as Roman and it was reported that they come from the Burg archaeological site in Burgenland, Austria [8].

So far, we had the possibility to examine by metallography a Roman bronze fibula [6], a bronze tip – the producer is uncertain [7], probably Roman provenance - and several objects made of copper or copper alloys from the Bronze Age [9–11].

For bronze objects, it seems to be necessary to produce several metallographic sections, because inhomogeneities can occur due to the bronze casting process, which can pervert the results of localized sampling [12]. Furthermore, analysis should not be performed solely on the surface, as corrosion leads to an accumulation of Sn in the corrosion products and you get no information about the bulk microstructure [13].

Experimental Procedure

First the objects were photographed and subsequently cold mounted in epoxy resin under vacuum. Once hardened, the metallographic preparation was carried out in stages by grinding and polishing up to a diamond grain size of 1 µm. The sections were analyzed in the as-polished state and after etching with Klemm 2 or $(NH_4)_2CuCl_4$ solution.

A light optical microscope (LOM) and a scanning electron microscope (SEM) with Electron Backscattering Detector (BSE) and with energy dispersive X-ray analysis (EDX) were used. To determine the overall chemical composition of the samples, measurements were additionally carried out on the metallographic sections using X-ray fluorescence analyses (XRF).

Results and Discussion

XRF measurements.

The XRF analyses performed on the metallographic sections are summarized in Table 1. It should also be noted that minor errors may occur, because the corrosion layer is partially included. In these measurements it is already noticeable that the Pb contents are high (up to 42 wt.%) and fluctuate extremely (minimum: 2 wt.%). The contents of Sn and Zn also vary remarkably.

Table 1. XRF results of the bronzes (wt.%) measured at the metallographical cross sections.

Element	Burg 1	Burg 2	Burg 3	Burg 4	Burg 5
Cu	96.4	56.66	69.65	56.82	48.87
Sn	0.79	12.86	3.73	8.71	6.5
Pb	1.92	26.82	22.88	30.07	41.78
Sb	0.4	0.87	0.09	0.7	0.2
Zn	n.n.	1.93	1.42	3.33	1.62
S	n.n.	0.12	1.55	n.n.	0.06
P	0.09	0.3	0.07	n.n.	0.16
Si	0.13	0.2	0.11	n.n.	0.31
Fe	0.27	0.24	0.27	0.38	0.42
Al	n.n.	n.n.	0.05	n.n.	0.08

A copper hook (Burg 1).

According to XRF measurements (Table 1), the hook examined consists predominantly of copper with approximately 0.8 wt.% Sn and 2 wt.% Pb.

Corrosion products with Sn enrichments are visible on the surface (Fig. 1a–c), which were detected by EDX. Elevated concentrations of P (up to 5 wt.%) and Ag (up to 0.9 wt.%) were locally measured. Also, boron was detected at some locations, but a quantification with EDX measurements is impossible. May be the elements Ag, B, and P reached the surface due to a soldering process, but this is not certain.

The cross-section shows that the bent part of the hook is significantly thicker than the straight part (Fig. 1d). This indicates that the hook was manufactured by forging and is additionally confirmed by the microstructure. In the undeformed part the grain size is up to 100 µm (Fig. 1e). In the deformed part the grain size is significantly smaller with up to 20 µm (Fig. 1f), but elongated inclusions of lead are visible (Fig. 1f–h). The corrosion layer can be seen on the surface (Fig. 1i).

A fibula pin catch (Burg 2).

The XRF measurements show that the fibula pin catch is made of bronze with 13 wt.% Sn and 27 wt.% Pb (Table 1) (Fig. 2a). These values could be somewhat too high, if the proportion of corrosion products was measured simultaneously.

In the as-polished condition dark Pb and gray corrosion products can be identified (Fig. 2b, c) and after etching a dendritic microstructure is observed (Fig. 2d–f), indicating a production by casting.

Small and bright precipitates of the intermetallic phase $Cu_{41}Sn_{11}$ are visible additionally (Fig. 2e). Polarized light clearly shows different orientated dendritic regions formed during solidification, as well as the corrosion product malachite, which appears green (Fig. 2f).

A fibula head (Burg 3).

According to XRF measurements the fibula head contains 4 wt.% Sn and 23 wt.% Pb (Table 1) (Fig. 3a). The Sn content is somewhat low for a bronze.

A cross-section through the head appears rather homogeneous with large black spots, which were identified as Pb inclusions (Fig. 3b). A closer look reveals the presence of large and small Pb aggregates (Fig. 3c, f, g). The large aggregates are usually oval with a size up to 300 µm. The small ones are irregularly shaped in the range of 10 µm (Fig. 3g). It is assumed that this distribution of Pb is a result of the high Pb content and segregation effects during solidification of the melt.

The Cu-Pb phase diagram is unique, because it exhibits a monotectic behavior in the concentration range between 37.4 and 86 wt.% Pb in Cu [14]. This means that two melts of different compositions exist side by side. The ternary Cu-Pb-Sn phase diagram is somewhat more complex: the addition of Sn increases the region containing two melts and simultaneously reduces the temperature range of solidification [15]. The linear arrangement of Pb aggregates (Fig. 3d) can be explained by the fact, that the melt solidifies from the rim to the core resulting in an enrichment of alloying elements at the solidification front. Copper exhibits a dendritic solidification structure (Fig. 3e), and an additional bright phase is visible, which can be interpreted as Cu-Sn phase (Fig. 3h). The large, partially Pb-filled, oval inhomogeneity could be a mixture of shrinkage cavity and Pb precipitation (Fig. 3g).

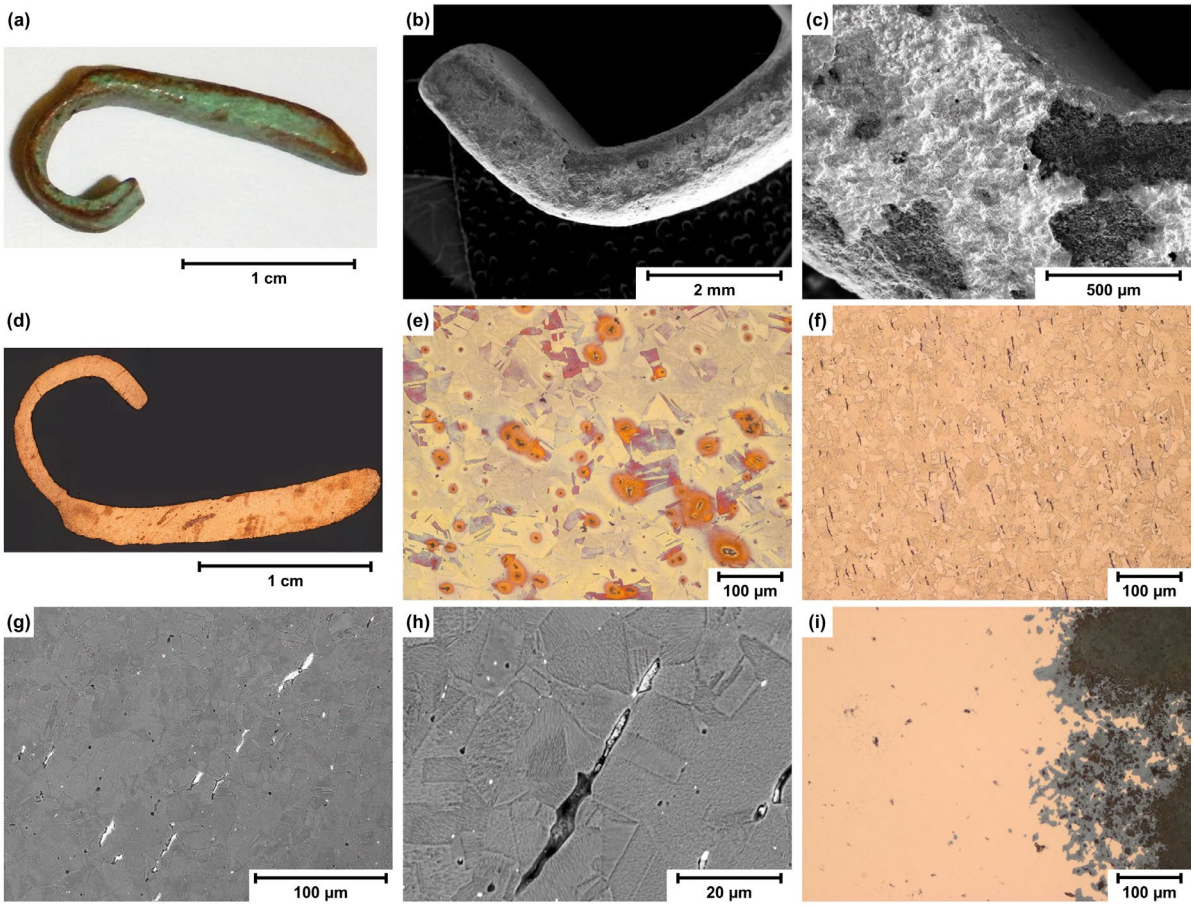

Fig. 1. Copper hook (Burg 1). (a) photo, (b, c) surface, SEM (d–f) cross section, LOM, (d–f) $(NH_4)_2CuCl_4$ etched, (g, h) SEM, (i) polished, LOM.

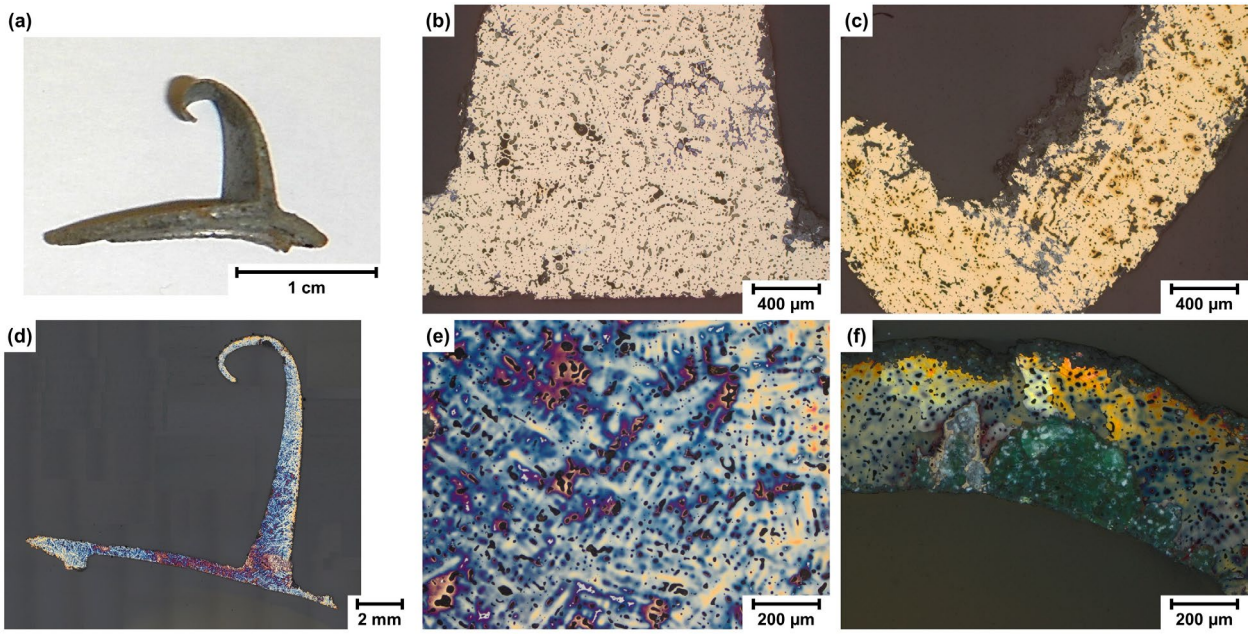

Fig. 2. Fibula pin catch (Burg 2). (a) photo, (b, c) polished, LOM, (d, e) Klemm 2 etched, LOM (f) polarized light, LOM.

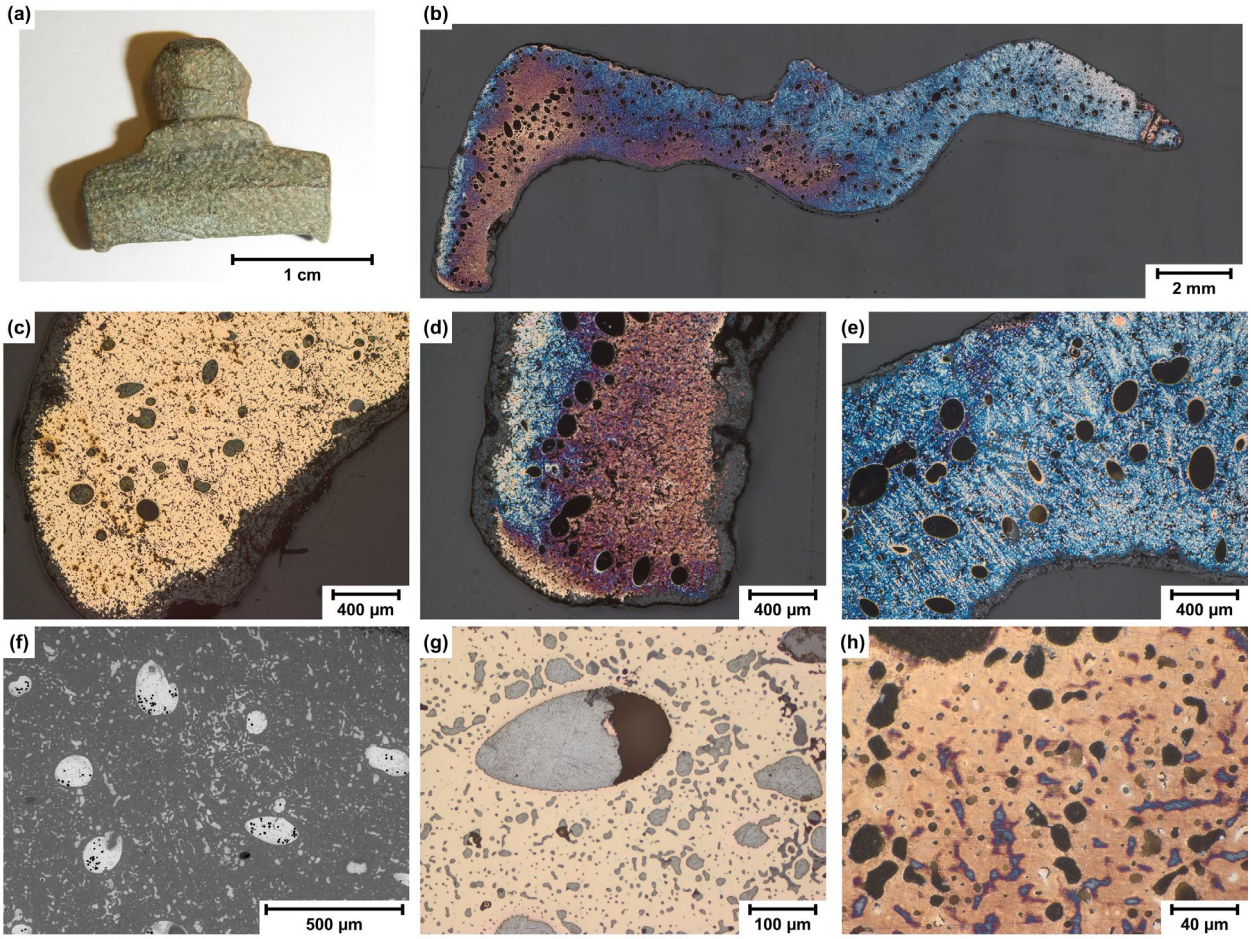

Fig. 3. Fibula head (Burg 3). (a) photo, (b) cross section, Klemm 2 etched, LOM, (c, g) polished LOM, (d, h) Klemm 2 etched, (f) SEM.

A fibula food (Burg 4).

The fibula food contains 9 wt.% Sn and 30 wt.% Pb, more of both elements than the previously described fibula head. It contains additionally 3 wt.% Zn (Table 1) (Fig. 4a).

As expected from the XRF analysis, this alloy contains numerous precipitates of Pb and a Cu-Sn phase (Fig. 4d, f). Also the dendritic solidification of copper is clearly visible (Fig. 4c, f), but large Pb inclusions - seen in the fibula head - are not visible.

The hook shown in Fig. 4b is the catch of the fibula foot. Increased corrosion is visible inside (Fig. 4b, e) and a distinct corrosion layer is also visible outside (Fig. 4f). The enrichment of Pb and Sn in the corrosion products may have led to relative high XRF values.

A bronze button (Burg 5).

The investigated button has a central pin and no eyelet (Fig. 5a). The pin and the extraordinary high Pb content (42 wt.% Pb, 6.5 wt.% Sn) distinguishes it from previously examined buttons from the Iron and Bronze Ages (Table 1) [16, 17].

The microstructure is homogeneous over the cross-section (Fig. 5b). The microstructure shows a dendritic solidification (Fig. 5c–e) of copper and numerous precipitations in the interdendritic areas (Fig. 5f–h). Although the Pb content measured by XRF is approximately twice that of the fibula head, the Pb inclusions are relatively small with a size up to 40 µm.

These results indicate that the button underwent no further heat treatment after its casting.

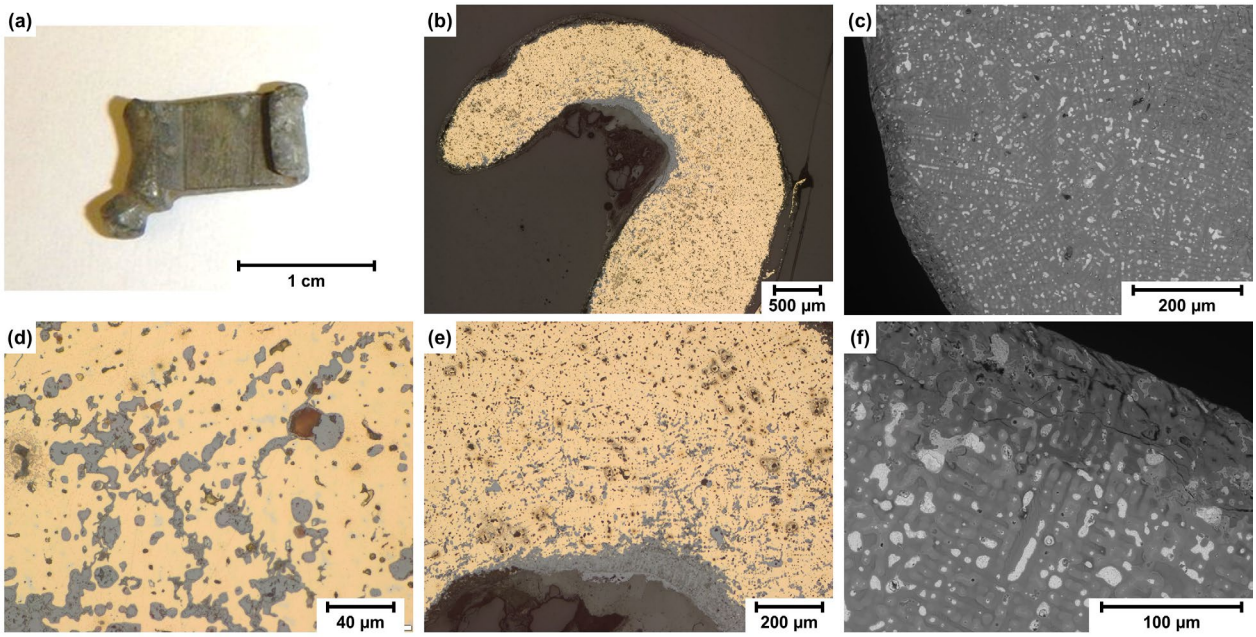

Fig. 4. Fibula food (Burg 4). (a) photo, (b, d, c) polished, LOM, (c, f) SEM.

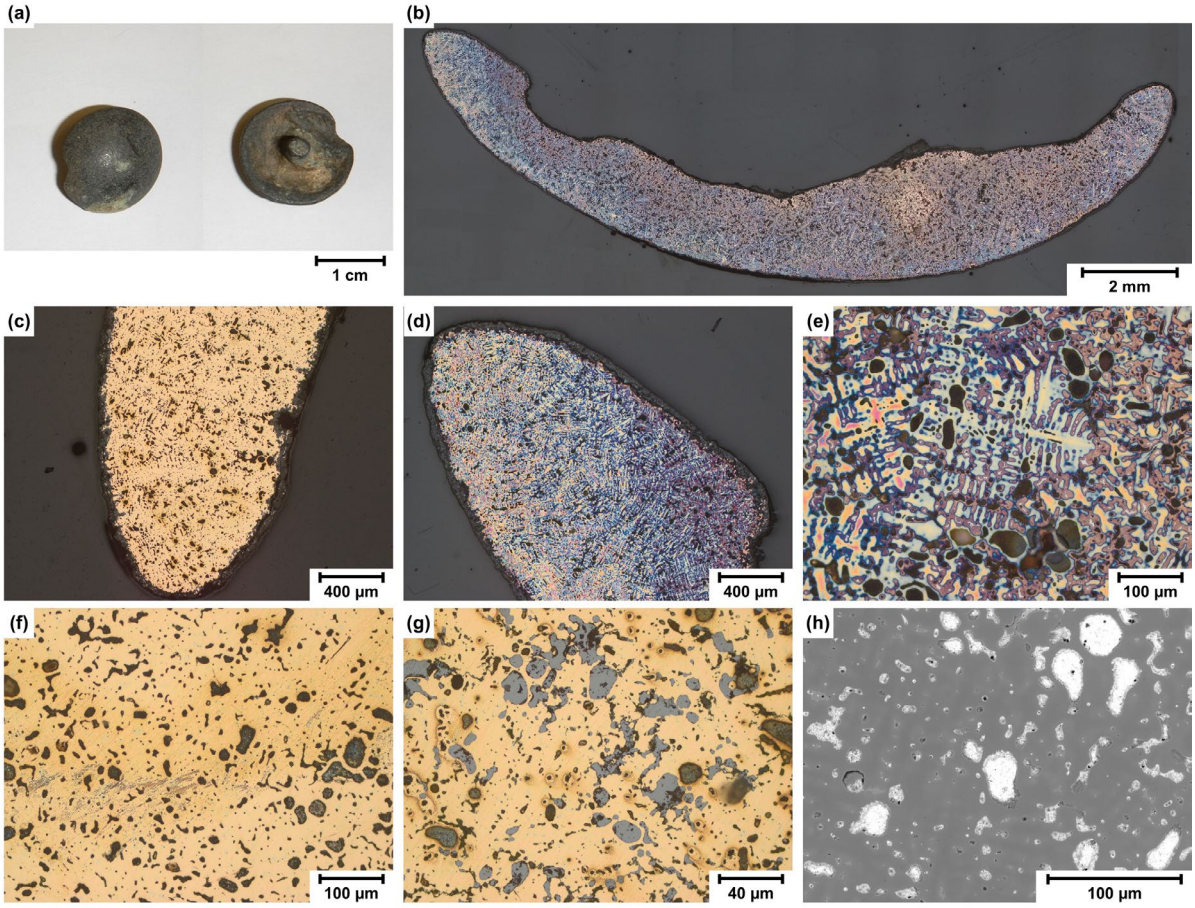

Fig. 5. Bronze button (Burg 5). (a) photos avers and revers, (b) overview, (b, d, e) Klemm 2 etched, LOM, (c, f, g) polished, LOM, (h) SEM.

Summary

A prerequisite for these investigations was that the objects could be destroyed to carry out metallographic examinations. The analyzed samples were a bronze hook, a fibula pin catch, a fibula head, a fibula food and a bronze button.

The examined hook consists of copper with small amounts of Pb and Sn. Its microstructure is recrystallized and deformed.

The fibula parts and the button are quite different from the hook, because all of them contain more than 23 wt.% Pb. The button had the highest Pb content with 42 wt.% Pb.

Since the other components of the bronze influence the microstructures, there are some differences among the examined samples. However, it is suspected that at high concentrations of Pb and Sn, large Pb aggregates can be formed due to the melting behavior of the alloy.

The patina of all parts is green, but it should be noted that in particular Sn and Pb can be concentrated in the corrosion products. This can lead to misinterpretation of the measurement results.

Regardless of the alloy composition, it is possible to distinguish between cast, recrystallized and deformed microstructures.

These investigations show that the Roman metallurgist used a wide variety of copper alloys, because raw and recycled materials were probably processed together.

Acknowledgement

The authors would like to thank the TU Wien Library for the financial support through its Open Access Funding Program.

References

[1] R. Haubner, S. Strobl, Materials Science Forum, 782 (2014) 635-640.

[2] R. Haubner, S. Strobl, Pract. Metallogr., 59 (2022) 720-731.

[3] W. Scheiblechner, S. Karl, D. Modl, S. Strobl, R. Haubner, BHM Berg- und Hüttenmännische Monatshefte, 166 (2021) 363-369.

[4] R. Haubner, S. Strobl, J. Leskovar, Pract. Metallogr., 61, 9-10 (2024) 630-641.

[5] R. Haubner, F. Ertl, S. Strobl, Pract. Metallogr., 54 (2017) 107-117.

[6] R. Haubner, A. Pronina, S. Strobl, Metallography, Microstructure, and Analysis, 14 (2025) 652-662.

[7] R. Haubner, S. Strobl, BHM Berg- und Hüttenmännische Monatshefte, 169, 9 (2024) 483-489.

[8] W. Meyer, Burgenländische Heimatblätter, 46 (1984) 145-167.

[9] R. Haubner, S. Strobl, Metallography, Microstructure, and Analysis, 12 (2023) 187–201.

[10] R. Haubner, S. Strobl, M. Thurner, H. Herdits, BHM Berg- und Hüttenmännische Monatshefte, 166 (2021) 352-357.

[11] R. Haubner, S. Strobl, Pract. Metallogr., 59 (2022) 749-760.

[12] R. Haubner, S. Strobl, Pract. Metallogr., 59 (2022) 732-748.

[13] R. Haubner, S. Strobl, P. Trebsche, Materials Science Forum, 891 (2017) 41-48.

[14] T.B. Massalski, Binary Alloy Phase Diagrams. ASM International, Metals Park OH (1990).

[15] R. Cayumil, R. Khanna, M. Ikram-Ul-Haq, R. Rajarao, A. Hill, V. Sahajwalla, Waste Management, 34 (2014) 1783-1792.

[16] R. Haubner, Pract. Metallogr., 60 (2023) 276-288.

[17] R. Haubner, S. Strobl, J. Leskovar, Metallography, Microstructure, and Analysis, 13 (2024) 1119-1130.

CHAPTER 8:

Fatigue, Fractography and Failure Analysis

Published in: Key Engineering Materials
ISSN: 1662-9795, Vol. 1043, pp 75-80
doi:10.4028/p-3Oq9Pr

Submitted: 2025-05-27
Revised: 2025-12-04
Accepted: 2025-12-19
Online: 2026-02-27

Effects of Ball Milling Time on CoCrFeNiTi High Entropy Sintered Alloys

Akito Fujii[1,a*] and Akio Nishimoto[2,b]

[1]Graduate School of Science and Engineering, Kansai University, Suita, Osaka 564-8680, Japan

[2]Department of Chemistry and Materials Engineering, Faculty of Chemistry, Materials and Bioengineering, Kansai University, Suita, Osaka 564-8680, Japan

[a*]k099325@kansai-u.ac.jp, [b]akionisi@kansai-u.ac.jp

Keywords: High Entropy Alloy, Spark Plasma Sintering, Mechanical Alloying, Powder Metallurgy.

Abstract. In this study, CoCrFeNiTi high entropy alloy (HEA) powder was treated by ball milling (BM) for up to 50 hours and sintered compacts were fabricated by spark plasma sintering (SPS). XRD analysis confirmed that the BM powder formed a single BCC solid solution phase after 25 hours, and a nanocrystalline structure was obtained due to the reduction in crystallite size and increase in dislocation density. Meanwhile, after sintering, the main phase changed to FCC, and secondary phases such as $CoTi_2$, CrFe, and TiC were precipitated. Carbon analysis by EMIA and EPMA showed that the carbon content in the powder and sintered compact increased with increasing BM time, which is considered to be the cause of TiC formation. Micro-Vickers hardness tests showed maximum hardness at the initial state, decreased at 5 hours, and then recovered after 15 hours due to the effect of secondary phase precipitation and microstructure. The effects of BM treatment and sintering conditions on phase structure, microstructure, element distribution, and mechanical properties were clarified, suggesting that it is an effective method for controlling the properties of HEA.

Introduction

In recent years, the demand for advanced metallic materials has grown significantly in the aerospace, semiconductor, and electronics industries, where both long service life and high functionality are essential. In particular, space applications pose extreme challenges, including vacuum irradiation and repeated cryogenic-to-high-temperature cycles, that exceed the capabilities of conventional binary and ternary alloys in terms of durability and mechanical stability [1, 2].

High-Entropy Alloys (HEAs), composed of five or more principal elements in near-equiatomic ratios, have emerged as promising alternatives due to their unique properties, such as high-temperature strength, enhanced tensile strength, and reduced diffusion rates [3]. Among them, CoCrFeNi-based systems alloyed with elements like Ti, Mn, Mo, or Al have demonstrated notable performance improvements. For example, CoCrFeNiTi HEAs exhibit hard intermetallic phases (e.g., Fe-Cr, NiTi), achieving tensile strengths of 700–800 MPa and Vickers hardness exceeding 800 HV, although with limited ductility [4, 5]. Ti addition also promotes the formation of protective TiO_2 films, significantly enhancing corrosion resistance in acidic and chloride environments [4]. In contrast, CoCrFeNiMn HEAs maintain a single FCC phase with exceptional ductility (> 80 %) and corrosion resistance similar to Ni-Cr alloys, especially in seawater [6]. CoCrFeNiMo HEAs show sigma-phase precipitation at higher Mo contents, yielding compressive strengths over 1400 MPa, hardness above 400 HV, and excellent thermal and oxidation resistance [7]. Meanwhile, CoCrFeNiAl HEAs exhibit a phase shift from FCC to FCC + BCC to single BCC as Al content increases, sustaining high strength above 800 °C, though excessive Al may reduce ductility and corrosion resistance [8].

This study focuses on CoCrFeNiTi HEAs, which offer a favorable balance of surface hardness and corrosion resistance. Using powder metallurgy, we aim to optimize powder preparation and sintering conditions to control densification and microstructure. In particular, we investigate how varying ball milling durations affect carbon uptake in powders and sintered bodies, and we evaluate the resulting mechanical properties.

Experimental Methods

Sample

Powder. Co powder (400 mesh, 99.8 % purity) from Strem Chemicals, Cr powder (45 μm, 99.5 % purity), Fe powder (45 μm, 99.9 % purity), Ti powder (45 μm, 99.9 % purity) from Fujifilm Wako Pure Chemicals Co., and Ni powder (45 μm, 99.9 % purity) from Nilaco Co. were used. These five types of powders were weighed using an electronic balance to produce the CoCrFeNiTi alloy.

Ball Milling. Ball milling (BM) was conducted on the weighed powder using a 250 mL stainless steel vessel (Fritsch Japan) with 3/8-inch (~9.5 mm) Cr steel balls. Prior to milling, the powder was weighed so that the five constituent elements had an equiatomic composition of 20 at% each, and then loaded into the vessel. The powder was placed on top of the balls, followed by the addition of 75 mL of heptane to prevent agglomeration, oxidation, and to improve powder recovery. The powder-to-ball weight ratio was fixed at 10:1 to ensure consistent energy input. The sealed vessel was purged and filled with argon gas for approximately 5 minutes to establish an inert atmosphere. Milling was performed using a planetary ball mill (Pulverisette 6, Fritsch Japan), with weight balancing applied. The process followed a cycle of 30 minutes milling and 10 minutes rest, for total durations of 0 (as-received), 5, 10, 15, 25, and 50 hours.

Spark Plasma Sintering. Spark plasma sintering (SPS) was carried out as follows. A graphite die (φ = 20 mm) and punches were coated with boron nitride spray as a release agent, and 15.0 g of BM powder was loaded inside. Graphite spacers were placed between the electrodes and punches. The chamber was evacuated to below 10^{-2} Pa, and SPS was conducted. To monitor sintering temperature, a φ = 4 mm hole was drilled into the side of the die at sample height, and a K-type thermocouple was inserted. Pulsed DC current was applied to generate Joule heating between the die, punches, and powder. After sintering, the system was cooled to room temperature under vacuum, then vented to air. The sintered sample was removed, ground to #2000 grit, polished with 1.0 μm Al_2O_3 powder, ultrasonically cleaned, and air-dried.

Analysis.

X-ray diffraction (XRD). An X-ray diffractometer (MiniFlex 600, Rigaku Corp.) equipped with a HyPix-400 MF 2D detector was used to identify the compound phases in the BM-treated powders and their sintered compacts. Cu Kα radiation (λ = 1.54184 Å) served as the X-ray source, operated at 40 kV and 15 mA. Diffraction measurements were conducted over a 2θ range of 20°–140°, with a step size of 0.02° and a scan rate of 1°/min.

Phase identification was based on Bragg's law and the interplanar spacing relation for cubic systems. Lattice constants were determined by extrapolating the Nelson–Riley function due to the broad and weak diffraction peaks at high angles in both BM powders and sintered samples.

The lattice constants were determined by extrapolating the Nelson–Riley function [9], which was necessary due to the broad and weak diffraction peaks observed at high angles in both BM-treated powders and sintered samples. Additionally, the Williamson–Hall method [10] was employed to estimate both crystallite size and lattice strain, based on the relationship between the full width at half maximum (FWHM, β) and the diffraction angle (θ) using the following equation (1):

$$\beta \frac{\cos\theta}{\lambda} = \frac{0.9}{D} + 2\varepsilon \frac{\sin\theta}{\lambda} \quad (1)$$

where β is in radians, λ is the X-ray wavelength, D is the crystallite size, and ε is the lattice strain.

Using the calculated crystallite size (D), the dislocation density (ρ) was estimated by equation (2) [11]:

$$\rho = \frac{1}{D^2} \quad (2)$$

Elemental Analysis. The elemental composition of the BM-treated sintered bodies was analyzed using an electron probe microanalyzer (EPMA, JEOL JXA-8230) and a wavelength dispersive spectrometer (WDS) attached to the device. The analysis was performed under conditions of an accelerating voltage of 15 kV and a probe current of 3.0×10^{-8} A. The crystals used for analysis of each element were LIF crystals (LiF: lithium fluoride) for Cr, Fe, Co, and Ni, PET crystals (polyethylene glycol terephthalate) for Ti, and LDE crystals (Low-Diffraction-Efficiency crystals) for C. In addition, a carbon and sulfur analyzer (EMIA, manufactured by HORIBA) was used to quantify the carbon concentration in the powder with high accuracy.

Micro-Vickers hardness test. In order to measure the hardness of sintered alloys at various BM times, hardness tests were conducted using a micro-Vickers hardness tester (model: PMT-X7A) manufactured by Matsuzawa Co. The specimens were polished to #2000 using wet emery paper, buffed to a mirror finish using Al_2O_3 powder with a grain size of 1.0 μm, and ultrasonically cleaned in acetone to degrease them before conducting the hardness test. The test conditions were a constant load of 0.98 N (100 gf) and a constant loading time of 15 s. The hardness value was determined as the average of three hardness values measured five times.

Results and Discussion

X-ray diffraction (XRD). XRD measurements were conducted on each powder sample and its corresponding sintered body to investigate phase structure evolution as a function of BM time. The XRD patterns of the powders are shown in Fig. 1(a). For the 0 hrs. sample, distinct peaks corresponding to pure Ni, Co, Cr, Fe, and Ti were observed, indicating that mechanical alloying had not yet occurred. As BM time increased, these peaks gradually weakened and completely disappeared by 25 h, indicating the formation of a dominant single-phase BCC structure (space group: Im-3m), consistent with the formation of a multicomponent solid solution. In contrast, the XRD patterns of the sintered samples (Fig. 1(b)) revealed a main FCC phase (space group: Fm-3m) for all BM conditions. Additionally, peaks corresponding to secondary phases, $CoTi_2$, CrFe intermetallic compounds, and TiC carbides, were observed. These secondary phases are attributed to the presence of excess Ti beyond its solubility limit and to carbon uptake from the organic solvent during BM processing [12]. The lattice constants of the powder and sintered samples, calculated using the Nelson–Riley method, are listed in Tables 1(a) and 1(b), respectively. As shown in Table 1(a), the BCC lattice constant of the powder stabilized at approximately 2.884 Å between 5 h and 25 hrs., with a slight contraction to 2.8806 Å at 50 hrs. Table 1(b) shows that the FCC lattice constant of the sintered samples ranged from 3.590 Å to 3.607 Å, reaching a minimum at 25 hrs. and slightly increasing again at 50 hrs. The crystallographic features obtained using the Williamson–Hall method are summarized in Fig. 2. Lattice strain (ε), crystallite size (D), and dislocation density (ρ) were evaluated based on Eq. (1) and Eq. (2), respectively. In the powder samples (Figs. 2(a) to 2(c)), ε and ρ increased significantly with longer BM time, while D decreased, reaching approximately 2.1 nm and 0.24 nm^{-2}, respectively, at 50 h. These results confirm that intense plastic deformation during BM led to nano crystallization and the formation of a dense dislocation network [13]. In contrast, the sintered samples exhibited significantly reduced ε and ρ, and an increase in D (up to ~27 nm), across all BM durations. These trends were especially pronounced at longer BM times. The observed microstructural recovery is attributed to recrystallization induced by rapid heating and applied pressure during SPS processing [14].

Table 1 Lattice constants of (a) BCC phase in powder (b) FCC phase in sintered sample at each BM time. (Calculated using the Nelson–Riley extrapolation method.)

(a)

BM time [h]	Lattice constant a_{BCC} [Å]
5	2.8841
10	2.8829
15	2.8854
25	2.8842
50	2.8806

(b)

BM time [h]	Lattice constant a_{FCC} [Å]
5	3.6007
10	3.6070
15	3.6061
25	3.5903
50	3.6002

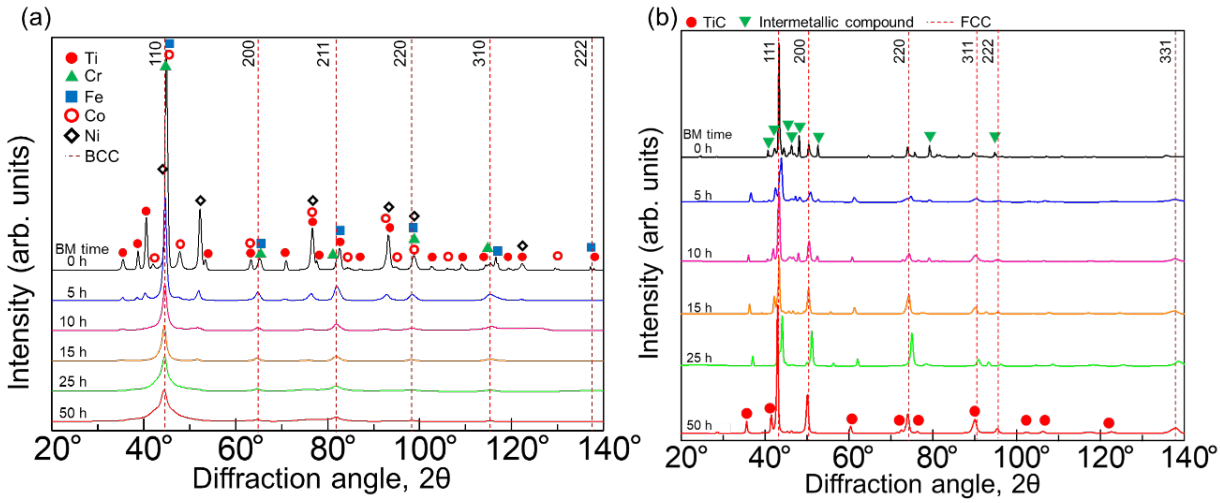

Fig. 1 XRD patterns of (a) powder and (b) sintered samples at various BM times.

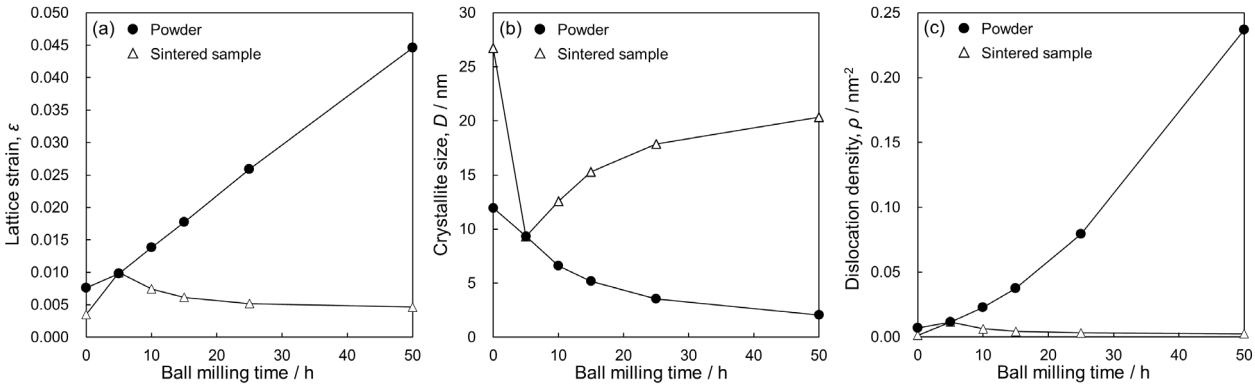

Fig. 2 (a) Lattice strain, (b) crystallite size, and (c) dislocation density as functions of BM time for both powder and sintered samples, all derived from the Williamson–Hall analysis.

Elemental Analysis. The carbon content in the powder and sintered body was quantitatively compared by EMIA and EPMA as shown in Fig. 3. The average carbon concentration of the powder measured by EMIA was only 0.02 wt.% at 0 hrs. without BM treatment, but gradually increased with the BM time, reaching 0.40 wt.% at 5 hrs., 0.81 wt.% at 10 hrs., 1.03 wt.% at 15 hrs., 1.21 wt.% at 25 hrs., and 1.40 wt.% at 50 hrs., the longest time. This is thought to be the result of the accumulation of carbon contamination from the organic solvent during mechanical alloying and the die during sintering [13]. On the other hand, quantitative point analysis of the sintered body by EPMA showed that the carbon content increased from 0.29 wt.% at 0 hrs. to 0.93 wt.% at 5 hrs. and 1.26 wt.% at 10 hrs., then temporarily decreased to 0.96 wt.% at 15 hrs. and 0.54 wt.% at 25 hrs., and then jumped significantly to 2.34 wt.% at 50 hrs. This localized heterogeneity is interpreted as the carbon dispersed in the BM powder precipitating as TiC during SPS sintering and forming local carbide clusters [15]. In fact, TiC peaks and clusters were confirmed in XRD and EPMA mapping, and the EPMA value fluctuates greatly due to the localization of carbon as a second phase, while the EMIA shows a smoother increase because it reflects the average concentration of the whole powder. From these results, it is considered that the extension of the BM time increases the carbon content in both the

powder and the sintered body, and that the hard phase can be strengthened through TiC precipitation, especially during long-term BM, but it is also necessary to consider interface design to suppress local segregation.

Vickers hardness test. The results of the micro-Vickers hardness test are shown in Fig. 4. The sintered compact without BM treatment (0 hrs.) exhibited the highest hardness, averaging approximately 895 HV. However, the hardness significantly decreased to approximately 721 HV after 5 h of BM. It then gradually recovered to 766 HV at 10 h, 838 HV at 15 h, 804 HV at 25 h, and 834 HV at 50 h, ultimately stabilizing around 830 HV from 15 h onward. Three main factors are considered responsible for these variations in hardness: (1) crystallite size, (2) dislocation density, and (3) precipitation of second phases ($CoTi_2$, CrFe, and TiC). As shown in Figs. 2(b) and (c), the sample at BM 5 h had the smallest crystallite size (~9 nm) but also the highest dislocation density. However, significant reduction of dislocation networks due to recovery and recrystallization, associated with severe grain refinement, likely diminished the expected contributions from grain boundary strengthening (Hall–Petch effect [16]) and dislocation strengthening [17], leading to lower hardness. After 10 h of BM, hard second phases such as $CoTi_2$, CrFe intermetallic compounds, and TiC carbides began to precipitate more noticeably during SPS sintering, supplementing the multi-element solid solution formed in the powder stage. These precipitates contributed to Orowan-type strengthening [18], which played a major role in restoring hardness to ~830 HV after 15 hrs. Although crystallite size increased to 15–20 nm and dislocation density decreased beyond 15 hrs., the hardness remained relatively high due to the balanced contributions of precipitation and moderate grain refinement strengthening. These findings suggest that extending the BM time to 15 hrs. or longer facilitates the recovery and retention of high hardness through the synergistic effects of second-phase precipitation and the Hall–Petch mechanism, following the recovery phase of extreme nano crystallization.

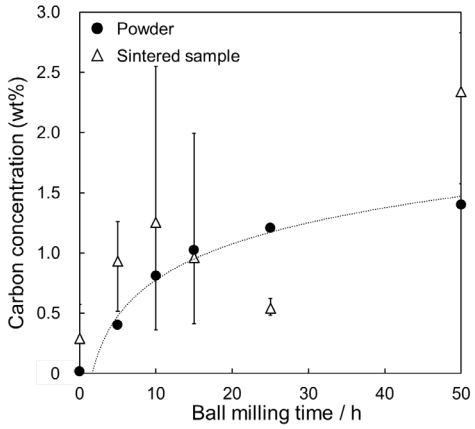

Fig. 3 Carbon concentration as a function of BM time measured by EMIA and EPMA.

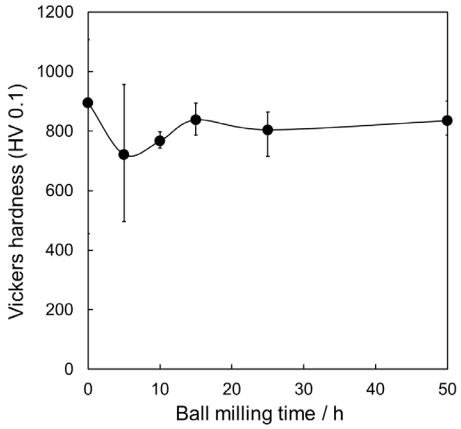

Fig. 4 Micro-Vickers hardness of sintered samples as a function of BM time.

Conclusions

In this study, we investigated the changes in phase structure, microstructure, carbon concentration, and mechanical properties of powders and sintered bodies of CoCrFeNiTi high entropy alloys with different ball milling (BM) times. With increasing BM time, the powders formed a BCC nanocrystalline structure, which transformed to the FCC phase after sintering, and secondary phases such as $CoTi_2$, CrFe, and TiC precipitated. In particular, carbon was thought to originate from the solvent in the BM, and reacted with Ti to produce TiC. Notably, the 15 hrs. BM condition introduced the least amount of carbon while maintaining the highest hardness, making it the most optimal processing time in this study. Lattice strain and dislocation density increased in the BM, and recovery and recrystallization progressed with SPS sintering. Hardness maintained a high level (approximately 830 HV) after BM 15 hrs. due to the synergistic effect of secondary phase precipitation and grain refinement. These results indicate that the optimization of BM processing and sintering conditions can increase the hardness and control the microstructure of CoCrFeNiTi alloys.

Acknowledgment

This work was supported by JKA and its promotion funds from KEIRIN RACE.

References

[1] J.W. Yeh, S.K. Chen, S.J. Lin, J.Y. Gan, T.S. Chin, T.T. Shun, C.H. Tsau, S.Y. Chang, Nanostructured high-entropy alloys with multiple principal elements: novel alloy design concepts and outcomes, Adv. Eng. Mater., 6 (2004) 299-303.

[2] H. Nakajo, A. Nishimoto, Producing CrFeCoNiSi-based high entropy alloy by spark plasma sintering, Mater. Trans., 62 (2021) 1231-1238.

[3] Y. Zhang, T.T. Zuo, Z. Tang, M.C. Gao, K.A. Dahmen, P.K. Liaw, Microstructures and properties of high-entropy alloys, Prog. Mater. Sci., 61 (2014) 1-93.

[4] Z. Li, K.G. Pradeep, Y. Deng, D. Raabe, Metastable high-entropy dual-phase alloys overcome the strength–ductility trade-off, Nature, 534 (2016) 227-230.

[5] A. Fujii, A. Nishimoto, CoCrFeNiTi high-entropy sintered alloy with metal screen direct current plasma nitriding, Heat Treat. Conf. Proc., 84901 (2024) 97-106.

[6] X. Wang, Q. Liu, Y. Huang, L. Xie, Q. Xu, T. Zhao, Effect of Ti content on the microstructure and corrosion resistance of CoCrFeNiTix high entropy alloys prepared by laser cladding, Materials, 13 (2020) 2209.

[7] T.T. Shun, L.Y. Chang, M.H. Shiu, Microstructure and mechanical properties of multiprincipal component CoCrFeNiMox alloys, Mater. Charact., 70 (2012) 63-67.

[8] M. Tokarewicz, M. Grądzka-Dahlke, Review of recent research on AlCoCrFeNi high-entropy alloy, Metals, 11 (2021) 1302.

[9] J.B. Nelson, D.P. Riley, An experimental investigation of extrapolation methods in the derivation of accurate unit-cell dimensions of crystals, Proc. Phys. Soc., 57 (1945) 160.

[10] G.K. Williamson, W.H. Hall, X-ray line broadening from filed aluminium and wolfram, Acta Metal, 1 (1953) 22-31.

[11] K. Edalati, N. Enikeev, dislocation density in ceramics processed by severe plastic deformation via high-pressure torsion, Materials, 17 (2024) 6189.

[12] P. Kratochvil, H. Thürlová, V. Nováček, A. Strakošová, J. Čech, M. Karlík, P. Haušild, J. Čapek, F. Průša, Understanding the influence of Ti content on mechanically alloyed and sintered CoCrFeNiTix high entropy alloy, J. Mater. Res. Technol., 35 (2025) 7371-7383.

[13] C. Suryanarayana, Mechanical alloying and milling, Progress Mater. Sci., 46 (2001) 1-184.

[14] R. Kumar, S.R. Bakshi, J. Joardar, S. Parida, V.S. Raja, R.K. Singh Raman, structural evolution during milling, annealing, and rapid consolidation of nanocrystalline Fe–10Cr–3Al powder, Materials, 10 (2017) 272.

[15] I. Moravcik, A. Kubicek, L. Moravcikova-Gouvea, O. Adam, V. Kana, V. Kana, V. Pouchly, A. Zedera, I. Dlouhy The origins of high-entropy alloy contamination induced by mechanical alloying and sintering. Metals, 10 (2020) 1186.

[16] Y.T. Zhu, X. Liao, Retaining ductility, Nature Materials, 3 (2004) 351-352.

[17] Y. Zhang, T.T. Zuo, Z. Tang, M.C. Gao, K.A. Dahmen, P.K. Liaw, Z.P. Lu, Microstructures and properties of high-entropy alloys, Prog. Mater. Sci., 61 (2014) 1-93.

[18] E.P. George, D. Raabe, R.O. Ritchie, High-entropy alloys, Nat. Rev. Mater., 4 (2019) 515-534.

Published in: Key Engineering Materials
ISSN: 1662-9795, Vol. 1043, pp 83-89
doi:10.4028/p-dtPp9Y

Submitted: 2025-05-18
Revised: 2025-12-05
Accepted: 2025-12-19
Online: 2026-02-27

Fracture Surface Morphology and Roughness of Ti-Scaffold Filaments

Jaroslav Pokluda[1,2,a*], Jana Escherová[1,b] and Marta Kianicová[1,c]

[1]Faculty of Special Technology, Alexander Dubček University of Trenčín, Ku kyselke 469, 911 06 Trenčín, Slovakia

[2]Central European Institute of Technology, Brno University of Technology, Purkyňova 123, 612 00 Brno, Czechia

[a*]jaroslav.pokluda@tnuni.sk, [b]jana.escherova@tnuni.sk, [c]marta.kianicova@tnuni.sk

Keywords: titanium scaffold, fatigue, fracture morphology, roughness, filament porosity.

Abstract. Titanium scaffolds produced by additive manufacturing were studied using the scanning electron microscopy (SEM) and the confocal optical microscopy (COM). The previous research has shown that the titanium scaffolds with porous filaments (14 % porosity) exhibited markedly better fatigue resistance than those with compact filaments (6 % porosity). This article is devoted to macroscopic and microscopic images of fracture surfaces of both types of scaffolds after cyclic compression (CC) tests and after cyclic three-point bending tests (CTPB). A high density of cracks and broken filaments was indicated particularly in scaffolds with porous filaments. The fatigue crack growth was highly affected by the microporosity. Fracture facets were smaller and rougher for the porous filaments compared to the compact ones. Values of roughness parameters S_a and S_v for porous filaments were significantly higher than those for compound fibres. Both SEM and COM studies confirmed an important role of crack-pore interactions especially in the porous filaments.

Introduction

Advanced 3D metallic porous structures produced by additive manufacturing, known as scaffolds, find applications in biomedicine as the bone implants (e.g. [1]). The previous research [2] has shown that the titanium scaffolds produced by the direct ink writing (DIW) technique with higher (open 14 %) porosity of filaments exhibited superior fatigue strength, well comparable to Ti lattices with dense filaments fabricated using powder bed fusion AM methods, and markedly better than the fatigue strength of DIW scaffolds with smaller (closed 6 %) porosity. This improvement was attributed to crack-tip shielding mechanisms [2, 3], such as crack deflection and branching induced by interactions between micropores and the advancing crack front. Similarly, high normalized fatigue strength was reported for DIW iron–manganese lattices with ~22 % open microporosity [4].

Given the limited number of findings and the complexity of fracture processes in scaffolds, it was useful to find out whether the higher fatigue strength observed in DIW Ti-scaffolds with porous filaments can be reproduced by CTPB experiments on individual filaments, prepared under the same sintering conditions and with similar microporosities. This study presents the results of SEM and COM investigations of crack distribution within the scaffolds volume as well as of fracture surfaces of their filaments fractured by CTPB tests.

Experimental Samples and Methods

The scaffolds and filaments were printed using a robotic deposition device (BSN3D+, Fundación CIM, Spain). The Ti ink consisted of commercially pure argon-atomised titanium spherical powder particles with a size range of 20–63 μm. The printed filaments were dried at room temperature for 12 h, debinded at 350 °C for 12 h, and sintered at 1300 °C for 3 h (porous) or 1400 °C for 10 h (compact) in argon. The final filament samples had a functional length of approximately 32 mm and a diameter of 1.7 mm.

The crack distribution and fracture surface morphology were examined using the scanning electron microscope Tescan Mira3, Czech Republic. Standard procedures of sample manipulation within the vacuum chamber were applied. The fracture surface morphology and roughness of broken filaments was studied by the confocal laser microscope Olympus LEXT™ OLS5100, Japan and the software OLS5100 - Analysis application, version 3.1.1.296. Each of 6 samples was subjected to 7 measurements on small surfaces of size 4500 μm^2 spread over the fatigue fracture surface and the average value with the standard deviation was computed.

Stress-controlled 3PB fatigue tests of filaments were performed within the fatigue life range of 10^2–10^6 cycles using a machine equipped with a 10 kN dynamic load cell (Instron E3000; USA) at a constant stress amplitude, the stress ratio R = 0.1 and frequency f = 2 Hz. The supports had the diameter of 10 mm and the span of 20 mm.

Results of SEM and COM Studies

The first part of investigations was made on cylindrical scaffolds previously fractured by CC. Here we focused on the macroscopic SEM images showing the volume distribution of cracks. The second part concerns SEM of scaffold filaments fractured by CTPB tests, and the third part presents COM measurement of fracture surface roughness of fibres. These SEM and COM results document differences in the morphology and roughness of fracture surfaces of scaffolds with compound and porous fibres.

Scaffolds fractured by cyclic compression (SEM).

The macroscopic view of parts of fractured scaffolds is shown in Fig. 1. The higher damage of scaffolds with porous filaments is caused by a higher volume density of fatigue cracks. Surface cracks and fibre fractures at the scaffold critical sites are depicted in Fig. 2a) for compound and in Fig. 2b) for porous filaments. Note that the porous scaffold contains more surface cracks and fractured fibres occurring near the contact points of overlapping orthogonal filaments in both types of scaffolds. Indeed, exactly these sites correspond to tensile stress zones under CC loading, as revealed by the finite element modelling [5]. Since the cracks initiated at many large surface pores, tens of fatigue cracks propagated even in the scaffolds with compact fibres. The fastest crack broke the first filament to start the scaffold fracture process. This elucidates an observed high scatter of CTPB tests of compact fibres as well as a less difference in S-N curves of compact and porous fibres compared to the CC tests of scaffolds [6]. Indeed, the probability of a pore occurrence directly at the point of the maximum tensile stress on the compact surface during CTPB tests is much smaller than that within the scaffold and on the porous surface. This leads to a high data scatter and a longer average fatigue life of compact filaments in CTPB tests.

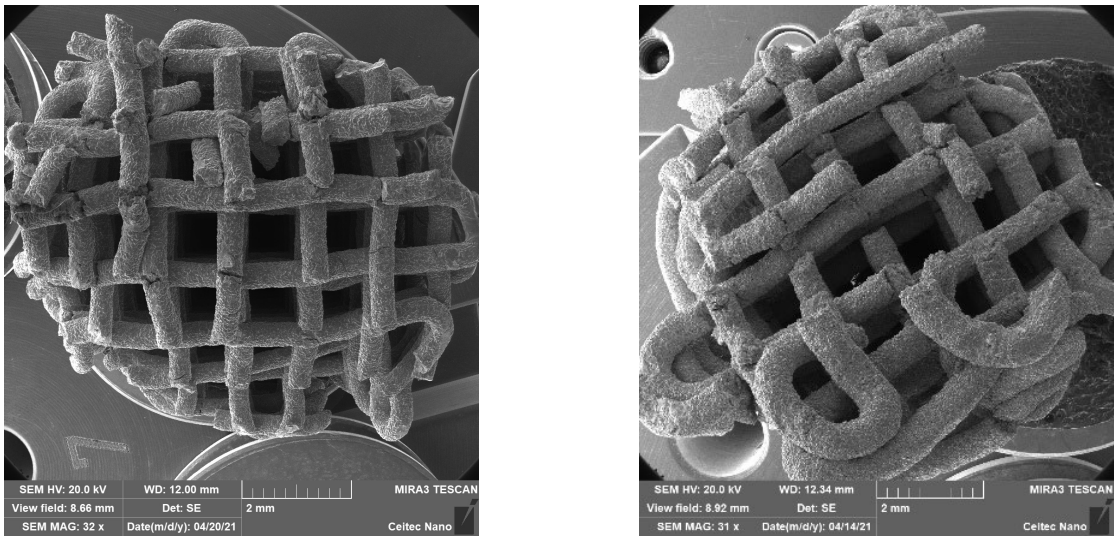

a) b)

Fig. 1. The broken parts of scaffolds with: a) compact fibres and b) porous fibres. Note the higher fatigue damage of the lattice with porous filaments.

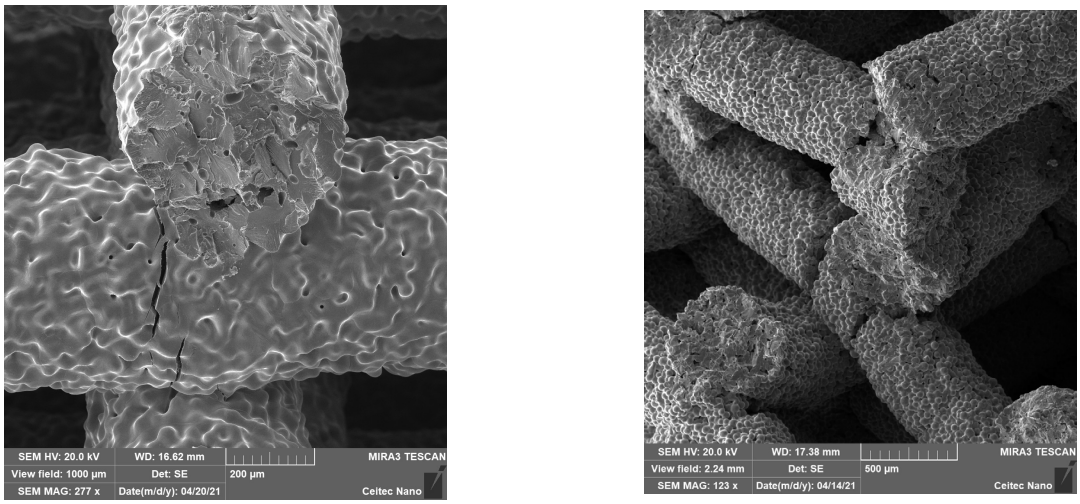

a) b)

Fig. 2. Surface cracks and fibre fractures at critical sites in a) compound filaments and b) porous filaments. Note that the surface cracks and fracture surfaces in both types of fibres occur at the locations of tensile stresses near the contact points of overlapping filaments.

Filaments fractured by cyclic three-point bending (SEM).

The typical fracture morphology for both types of filaments is in Fig. 3. The compound fibres (Fig. 3a) exhibited rather flat and large fracture facets comparable with the mean grain size of 90 µm. The crack growth was strongly affected by the microporosity as evidenced by a higher number of pores on fracture surfaces when compared with the cross-sectional porosity [2]. In the case of porous fibres (Fig. 3b), the facets are smaller and rougher, sometimes fracturing the sintering ligaments in between grains with the mean size of 50 µm.

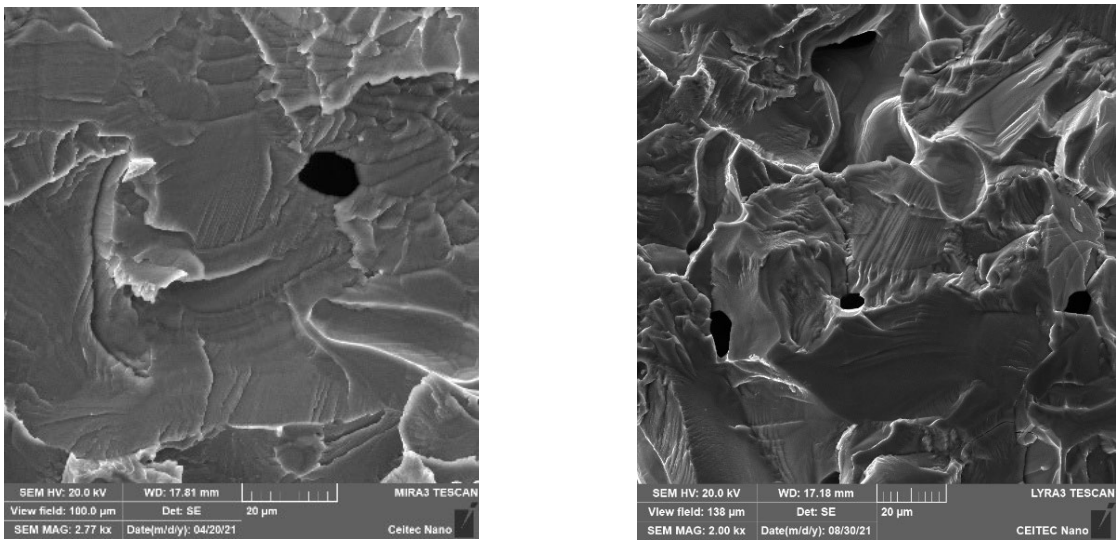

a) b)

Fig. 3. The typical fracture surface morphology of a) compound filaments and b) porous filaments. Note the larger and flatter facets on the compound fracture surface and pores on both fracture surfaces.

Occasionally, the cracks followed the pore clusters at grain boundaries to create intergranular facets, as seen in Fig. 4a). The detail of these facets in Fig. 4b) reveals fine, often periodical patterns, which are probably the result of sintering diffusion processes occurring on the particle surfaces. The periodical patterns might be confused with striations on smooth transgranular facets (Fig. 5). The hexagonal close-packed (alpha) titanium crystal structure does not possess enough independent slip systems to enable a complete plastic accommodation of neighbouring grains. Thus, the quasi-cleavage facets on suitable crystallographic planes associated with typical river patterns at grain boundaries could also be occasionally observed, as seen in Fig. 6.

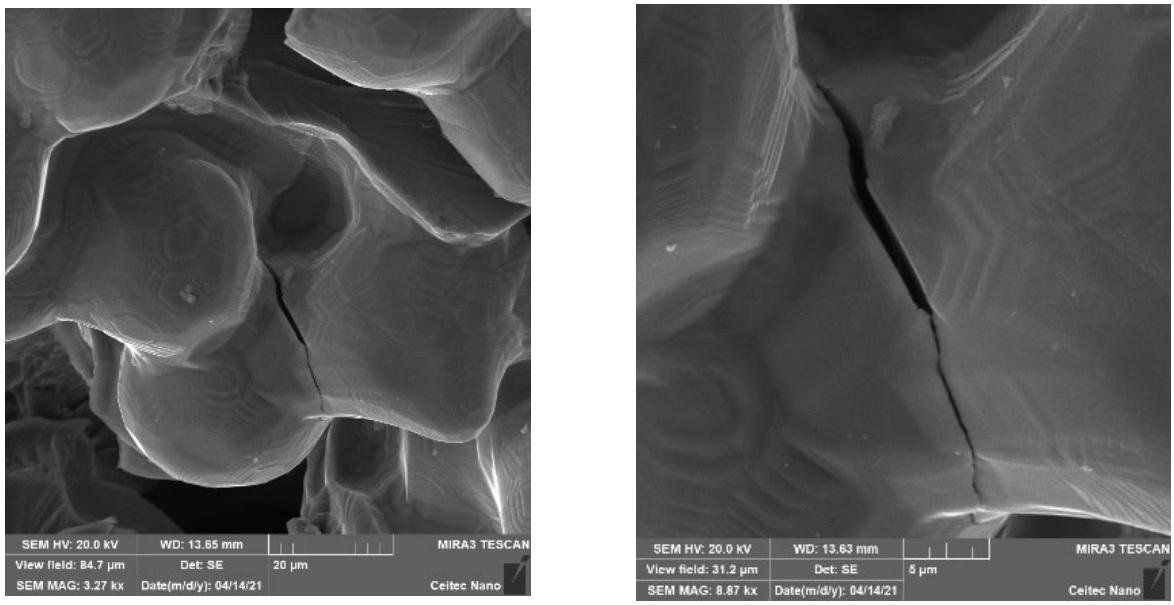

a) b)

Fig. 4. Intergranular facets and the secondary crack on the fracture surface of a porous fibre. The fine patterns visible in the detail b) are probably the result of sintering diffusion processes on particle surfaces.

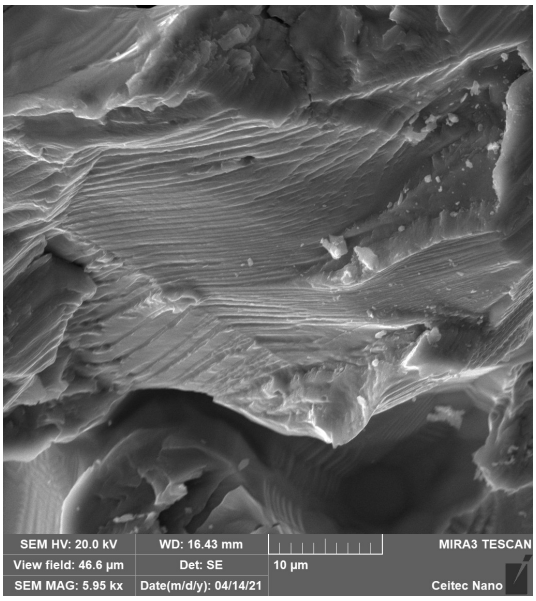

Fig. 5. Morphological patterns on the fracture surface with fatigue striations.

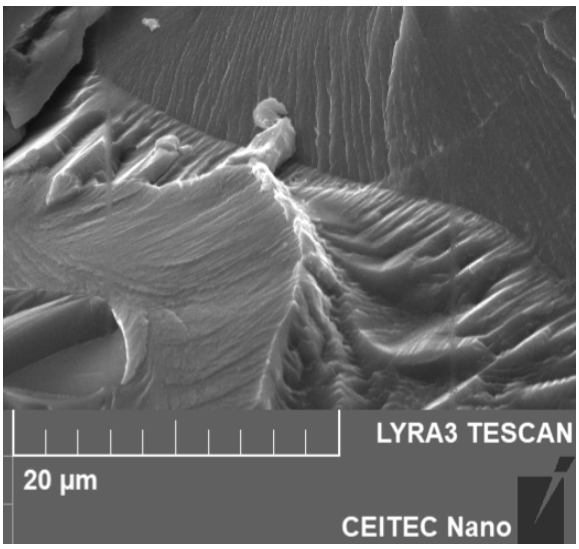

Fig. 6. Morphological patterns on the fracture surface with quasi-cleavage facets associated with river patterns at the grain boundary.

Filaments fractured by cyclic three-point bending (COM).

The COM analysis was preferentially employed to determine the fracture surface topology and roughness. Coloured topology of semi-elliptical parts of fatigue fracture surfaces of selected compound and a porous filaments fractured at a nearly equal number of cycles is depicted in Fig. 7 (elevations red and valleys blue).

The fracture surfaces of compound fibres were less rough than those of porous ones, as confirmed by the related arithmetical mean height $S_{a,c} = 4.1 \pm 3.3$ µm and the maximum pit height $S_{v,c} = 28 \pm 15$ µm, unlike $S_{a,p} = 5.5 \pm 3.4$ µm and $S_{v,p} = 37 \pm 12$ µm for porous fibres.

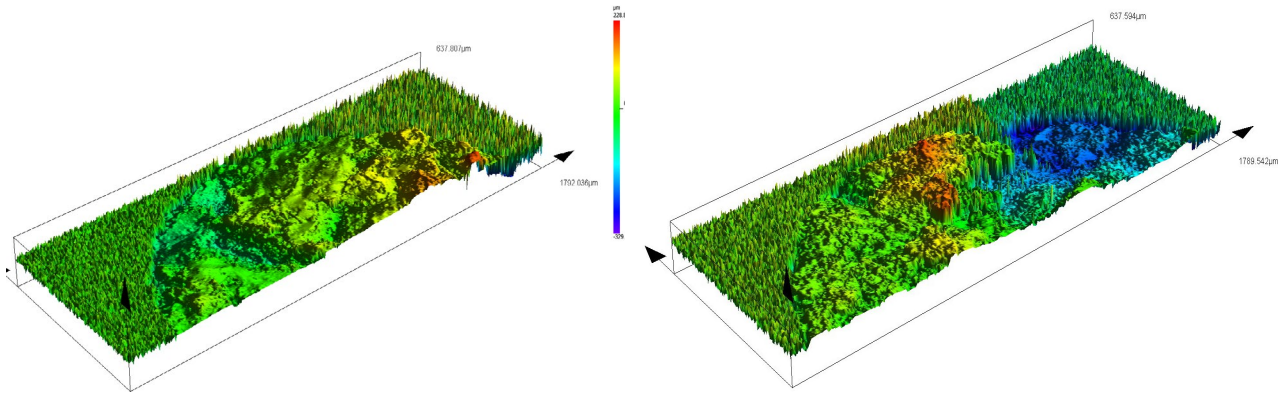

a) b)

Fig. 7. The coloured topology of semi-elliptical parts of fatigue fracture surfaces of selected a) compound and b) porous filaments. Note the higher roughness of the porous fibre.

Summary

The results of SEM a COM studies on Ti-scaffolds and filaments, fractured by respective CC and CTPB tests, can be summarized as follows:

(i) A high density of cracks and broken filaments in the scaffold volume was observed. The crack density in scaffolds with porous fibres was higher than that in the scaffolds with porous fibres.

(ii) The crack growth was highly affected by the porosity, and the fracture facets were smaller and rougher for the porous filaments than for the compact ones.

(iii) Values of roughness parameters S_a and S_v for the fracture surface of porous filaments were significantly higher than those of the compound ones.

Both SEM and COM analysis conformed an important role of crack-pore interactions particularly in the porous filaments.

Acknowledgement

The authors thank to Dr. Karel Slámečka from the Institute of Physics of Materials, AS CR in Brno, for his help with SEM studies. The work was supported by the Ministry of Education, Research, Development and Youth of the Slovak Republic under the project VEGA 1/0080/24.

References

[1] Q. Han, C. Wang, H. Chen, X. Zhao, J. Wang, Porous tantalum and titanium in orthopedics: a review, ACS Biomater. Sci. Eng., 5 (2019) 5798-5824.

[2] K. Slámečka, A. Kashimbetova, J. Pokluda, T. Zikmund, J. Kaiser, E. B. Montufar, L. Čelko, Fatigue behaviour of titanium scaffolds with hierarchical porosity produced by material extrusion additive manufacturing, Mater. Des., 225 (2023) 111453.

[3] J. Pokluda, P. Šandera, Micromechanisms of Fracture and Fatigue: In a Multiscale Context, Springer Ltd, London, 2010.

[4] N.E. Putra, V. Moosabeiki, M.A. Leeflang, J. Zhou, A.A. Zadpoor, Biodegradation-affected fatigue behavior of extrusion-based additively manufactured porous iron–manganese scaffolds, Acta Biomater., 178 (2024) 340-351.

[5] K. Slámečka, P. Skalka, J. Pokluda, Modeling mechanical properties of titanium scaffolds with variable microporosity, Adv. Eng. Mater., (2024) 2400535.

[6] K. Slámečka, et al., will be submitted for publication.

Published in: Key Engineering Materials
ISSN: 1662-9795, Vol. 1043, pp 91-97
doi:10.4028/p-uNNa0z

Submitted: 2025-06-11
Revised: 2025-12-05
Accepted: 2025-12-19
Online: 2026-02-27

Metal Dusting Failure in an Aniline Processing Plant

Zdeněk Kuboň[1,a*], Jana Kosňovská[1,b] and Gabriela Rožnovská[1,c]

[1]MATERIÁLOVÝ A METALURGICKÝ VÝZKUM s.r.o., Pohraniční 693/31, Vítkovice, CZ-703 00 Ostrava, Czech Republic

[a*]creep.lab@mmvyzkum.cz, [b]jana.kosnovska@mmvyzkum.cz, [c]gabriela.roznovska@mmvyzkum.cz

Keywords: Corrosion, Carburizing Atmosphere, Austenitic Stainless Steel, Metal Dusting.

Abstract. The paper summarizes the results of the analysis made on the ruptured tube of the reactor made of austenitic stainless steel in which the conversion of aniline to diphenylamine occurs at elevated temperature and pressure and in the presence of a catalyst. The tube wall perforation occurred in the piping used to measure the pressure in the reactor and a fire occurred after an aniline, ammonia and catalyst vapour leak. The material analyses carried out clearly showed that the thinning and subsequent perforation of the tube wall was due to a specific corrosion attack, so-called metal dusting, which occurs at elevated temperatures and in the presence of a carburizing atmosphere.

Introduction

Metal dusting is a catastrophic form of carburization attack leading to the decomposition of metals and alloys into dust of metal particles, oxides, and graphite. It occurs at relatively high temperatures (typically from 400 to 800 °C) and in carburizing atmospheres or, more commonly, in carburizing and selectively oxidizing atmospheres. The low partial pressure of oxygen in carburizing atmospheres allows the breakdown of the protective oxide layer on the metal surface at elevated temperatures. It happens even in the case of high-alloy steels and nickel alloys which are not immune to this specific type of corrosion attack. While at carbon activity $a_C < 1$ carburization occurs and carbon deposition in steels leads to internal formation of M_7C_3 and $M_{23}C_6$ carbides, metal dusting occurs in active atmospheres containing CO and/or hydrocarbons at carbon activity $a_C > 1$, i.e. under conditions where there is a tendency to form graphite (in equilibrium with graphite, $a_C = 1$). Metals and alloys in which carbon dissolves, i.e. mainly Fe, Ni, Co and their alloys, are particularly susceptible to this damage. Carbon is transferred from the surrounding gaseous atmosphere and dissolves in the metal at $a_C > 1$ until supersaturation, which leads to the growth of graphite particles that destroy these materials [1,2].

Chromium-alloyed steels are often used in the critical temperature range for the occurrence of this phenomenon. Low-alloy steels, such as 1%Cr-0.5%Mo, 2.25%Cr-1%Mo, etc., are heat and creep resistant up to a temperature of approximately 600 °C, but under metal dusting conditions ($a_C > 1$) they can only be used in an atmosphere with a sufficiently high content of H_2O and/or CO_2, where magnetite can form. However, process conditions in chemical reactors are often more severe and metal dusting begins immediately and evenly with these steels. Metal dusting starts by local attack on the metal surface at points where the protective oxide layer is broken through, leading to pitting corrosion. A corrosion product (graphite) then grows from these pits, which is usually carried away by fast-flowing process gases. Typical for Cr steels and alloys are areas with increased concentrations of carbides precipitated along the boundaries, but also inside the grains, which precede the final corrosion attack. To increase protection against this phenomenon, it is necessary to form a compact layer of Cr-rich oxides on the metal surface. Ferritic (martensitic) steels with more than 11 % Cr and austenitic steels with a Cr content above 17 % Cr are therefore more resistant, but not immune. [3] The lower amount of chromium required to achieve the resistance of ferritic steels is due to the higher diffusivity of Cr in the ferritic lattice and thus its faster replenishment on the surface of the component. The rapid supply of Cr to the surface enables to form a protective corrosion layer, which consists of an outer layer of spinel phase $(Mn,Fe)O{\cdot}Cr_2O_3$ and an inner (very compact) layer of Cr_2O_3 oxide.

Even high-alloy steels with sufficient Cr content exhibit this form of attack after a more or less long period of exposure. In principle, the same mechanism applies to high-alloy steels as to carbon steels or nickel, but the details of the attack may differ, see Fig. 1 [4]:

- The attack begins with local penetration through the protective oxide layer on the metal surface at the points of local defects and/or weakness.
- Carbon passes into the metal phase at this point, where the carburizing gas has access to the bare metal surface (Fig. 1a).
- Carbon diffuses into the material and firstly reacts with alloying elements to form stable carbides ($M_{23}C_6$ and M_7C_3 with Cr as the main component, MC with Ti, Zr, V, Nb, W, and Mo_2C). A zone with internal carbides is formed (Fig. 1b), but these carbides are still very fine in the metal dusting temperature range. This zone is then supersaturated with dissolved carbon.
- After supersaturation with dissolved C, graphite nuclei form, which grow both inward (Fig. 1c) and, with continued carbon supersaturation, also outward from the metal surface (Fig. 1d).

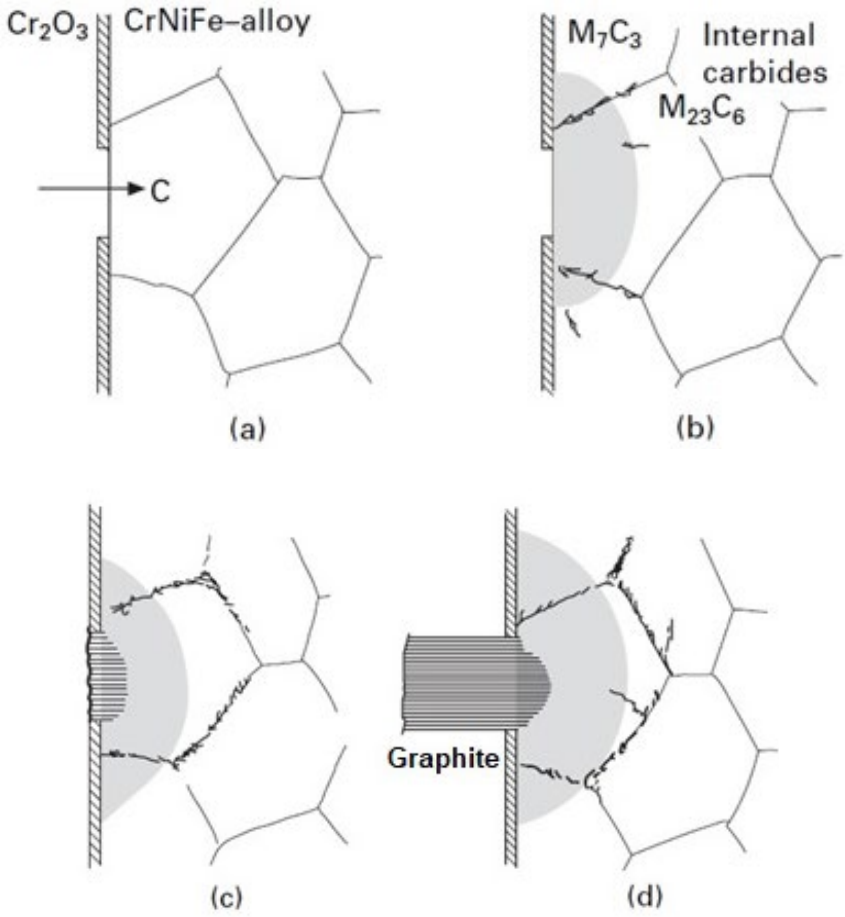

Fig. 1 Scheme of processes during metal dusting of high-alloy steels and Ni-based alloys: (a) defect in the protective oxide layer, allowing carbon penetration; (b) formation of carbides towards the interior of the material ($M_{23}C_6$ and M_7C_3 (M = Cr, Fe, Ni)); (c) after supersaturation with dissolved C, graphite nuclei form and grow inward; (d) outward growth of particles composed of graphite fibers, metal, carbides, and oxides [4].

Experimental Material and Results

Complex material analyses were aimed at determining the causes of the rupture and the subsequent fire of the tube used for the pressure measurement inside the aniline processing reactor. The reactor is a vertical pressure vessel with a volume of approximately 30 m^3, working at temperature of 342 °C and pressure 2.3 MPa. The pressure measurement tube operates in a vertical position and is connected to the reactor by a side flange. The bottom flange is blinded and there is a pressure gauge tap at the top. A primary leak occurred between the side and bottom flanges, and unreacted products (aniline, ammonia, and water vapor with catalyst) began to leak and subsequently to burn.

After the fire, the entire section of the fire-damaged tube was delivered for the material expertise, Fig. 1. This was a Ø 58 mm tube made of stainless steel 1.4539 (X1NiCrMo-CuN25-20-5), a superaustenitic Cr-Ni-Mo steel further alloyed with copper, which is resistant to various organic and inorganic acids as well as seawater and also has high resistance to pitting corrosion. This steel is also known as AISI 904L. The tube had been in operation for a total of 8 years.

Fig. 1 Delivered tube with perforated wall.

Visual analysis showed thinned tube wall around the perforation and, apart from the crack itself, also very irregular wall thickness and a heavily rough and wrinkled inner surface, Fig. 2 and 3. Based on visual observation, the real wall thickness of the tube was from 3 to 5 mm, while the original thickness should be 8 or 9 mm, so it is clear that the tube wall was heavily thinned during operation.

Fig. 2 Cross section of the tube wall in the perforation.

Fig. 3 Cross section of the tube wall outside perforation.

The control chemical analysis was performed on the ARL RTG Advant'X and LECO CS 230 instruments and the results shown in Table 1 revealed material substitution, when probably AISI 316 steel was used instead of declared 1.4539 steel. Also, unusually (and also absurdly) high carbon content indicated at least the possibility of carburization of the steel.

Table 1 Chemical composition of the tube [wt. %].

	C	Mn	Si	P	S	Cr	Ni	Mo	Cu	N	Ti	Nb	W	Co
Tube	0.31	1.10	0.50	0.021	0.001	17.03	12.04	1.98	0.30	0.023	0.39	0.007	0.040	0.063
1.4539	max. 0.020	max. 2.00	max. 0.70	max. 0.030	max. 0.010	19.0 21.0	24.0 26.0	4.00 5.00	1.20 2.00	max. 0.15	-	-	-	-

The assumption of possible carbonization was clearly confirmed by measuring the hardness profile, where the maximum hardness near the inner surface was approximately about 200 HV10 higher than around the circumference of the tube, Table 2.

Table 2 Results of hardness HV10 measurement.

Around the tube [°]								Across the wall [mm]		
0	45	90	135	180	225	270	315	1	2	3
199	205	184	171	173	181	186	179	239	240	385

Metallographic analysis then confirmed the extensive and deep corrosion attack reaching up to half the original wall thickness and forming even empty holes, Fig. 4. The attack then progressed from the inner surface of the tube into the material, which was associated with intensive carburization. The increasing concentration of carbon in the microstructure of the tube was clearly reflected on the metallographic section prepared through the tube wall, Fig. 5. While the original austenitic microstructure outside the attack was nearly free of carbides, Fig. 6, towards the inner surface of the tube, chains of carbides decorated the grain boundaries, Fig. 7. Then carbides spread over the whole grain interior and coarse carbides continuously decorate grain boundaries, Fig. 8. Increasing amount of fine carbides inside grains changes the colour into dark with light chains of coarser carbides decorating grain boundaries, Fig. 9. Still increasing carbon content and coarsening carbides then again change the contrast back to light with coarse and clearly distinguishable carbide particles, Fig. 10. Immediately on the inner surface of the tube, the coarse carbide particles eventually reach the character of eutectic carbides, Fig. 11.

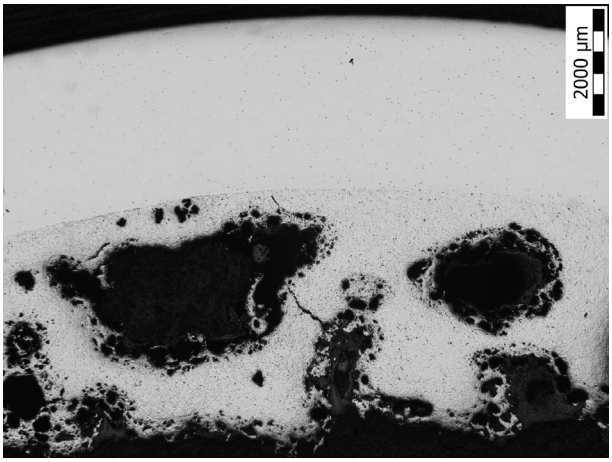

Fig. 4 Metal dusting attack extending into more than half the tube wall thickness.

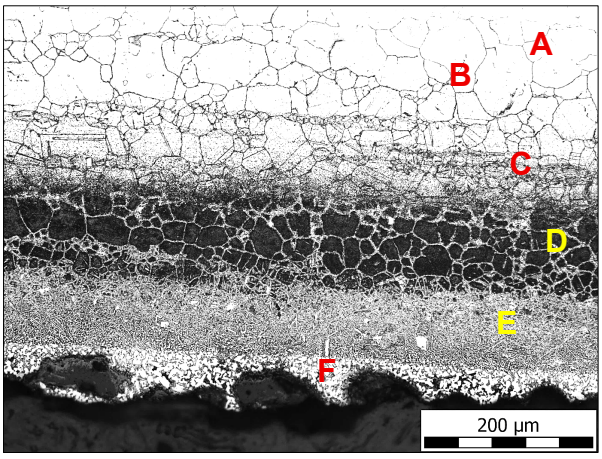

Fig. 5 Change of the microstructure under the inner surface of the tube.

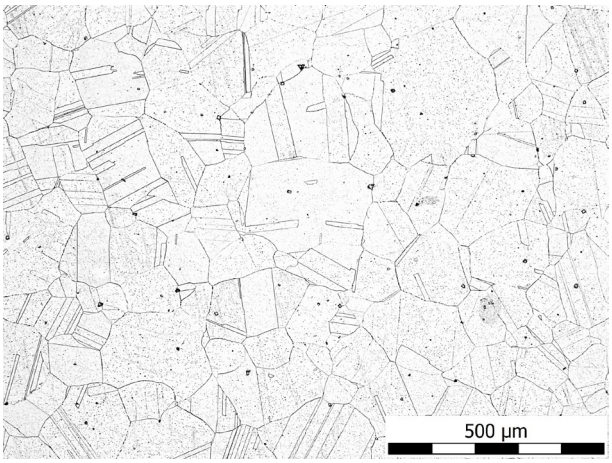

Fig. 6 Original microstructure of the tube outside of the attack by metal dusting – A.

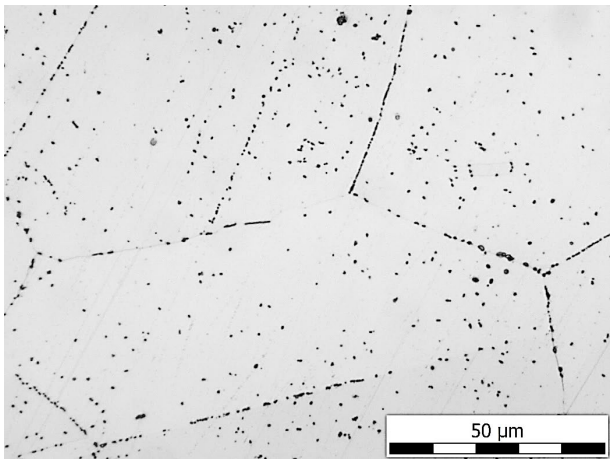

Fig. 7 Grain boundaries decorated by carbide chains, carbides also already inside grains – B.

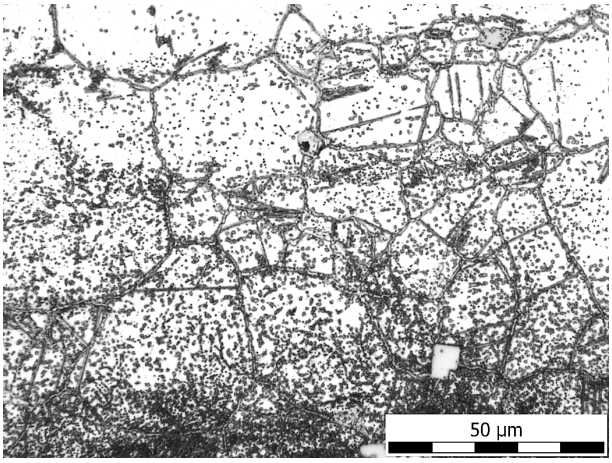

Fig. 8 Strongly decorated grain boundaries and intense precipitation inside the grains – C.

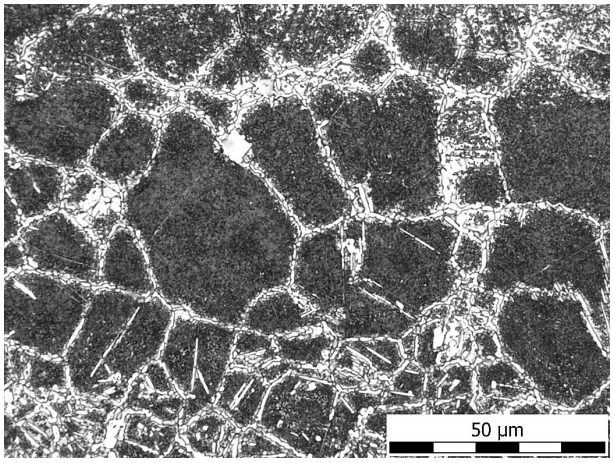

Fig. 9 Coarse carbide chains on grain boundaries and dark carbide precipitates inside grains – D.

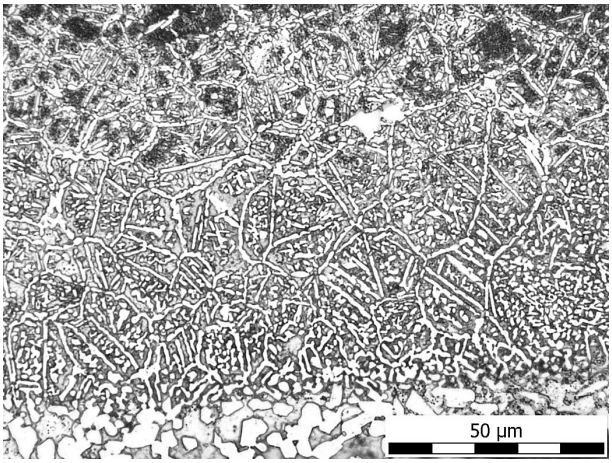

Fig. 10 Coarse carbide particles inside grains and on the grain boundaries – E.

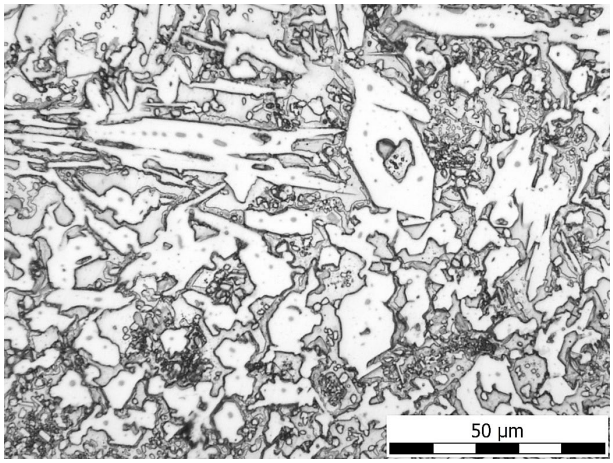

Fig. 11 Eutectic form of extra heavy carbides – F.

The confirmation that the damage of the tube was indeed caused by metal dusting is the result of the EDX microanalysis of the chemical composition performed on the edge of a large defect (hole) on the inner surface of the tube, Fig. 12. Around the hole there is a ring of anthracite shade, which is

formed by practically pure carbon in the form of graphite, inside the hole there were even small graphite sticks, Figs. 13 and 14.

Fig. 12 Corroded area on the inner surface of the tube, graphite forms rings around holes.

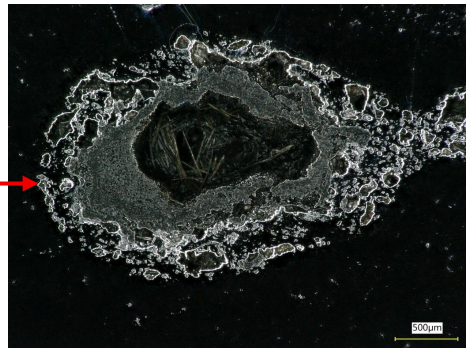

Fig. 13 Detail of the hole surrounded by graphite ring and sticks inside.

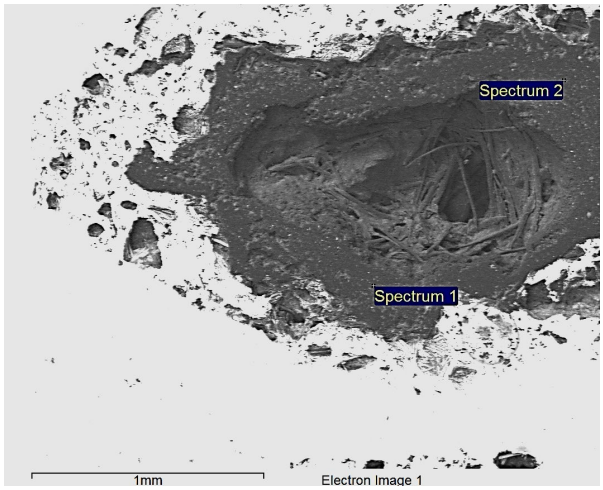

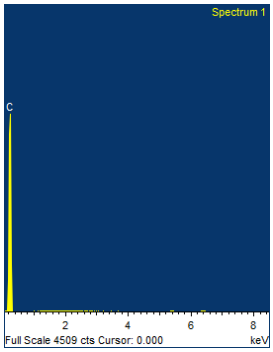

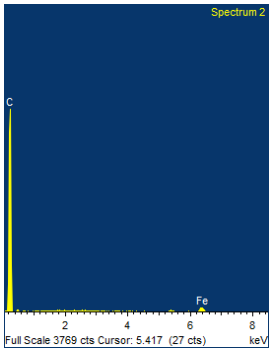

Spectrum	Fe	C
	[wt. %]	
1	-	100.0
2	2.7	97.3

Fig. 14 Results of EDX microanalysis of non-metallic filling around the hole in the tube wall.

Discussion

The fact that the perforation damage of the tube wall occurred after 9 years of operation can be probably related to the relatively low operating temperature and possibly also to the low reactivity of the reaction mixture, which is not a typical carburizing agent. Low operating temperature, on the other hand, makes it more difficult to heal the protective oxide layer on the metal surface by chromium diffusion from the grain interior. The essential role in damage development can also play the substitution of the material, when steel of the AISI 316 type (17 % Cr, 12 % Ni, 2.5 % Mo) was used instead of the originally declared 904L steel (21 % Cr, 25 % Ni, 4.5 % Mo, 1.5 % Cu). The higher chromium, nickel and also molybdenum content in the latter steel increases the stability of the oxide layer. In steels with more than 25 % Cr, a compact layer of practically pure Cr_2O_3 can form on the metal surface, which has minimal permeability for oxygen atoms. Nickel, altogether with copper and also tin, that forms no carbide also greatly decreases graphite nucleation. [5] Higher content of Mo increases not only the stability of the oxide layer but also the resistance to pitting corrosion, which very often precedes and starts metal dusting. Possible strategies for metal dusting control can be divided into *alloying for improved oxide scale*, *alloying to decrease carbon precipitation* and *surface engineering*. The first assumes to add secondary oxide forming elements such as Si or Al that will improve scale barrier properties, or, in the FeCrAlY alloys, will form compact alumina scale. The second approach relies mainly on the positive effect of Cu, but due to its low solubility in ferrite, it is

more suitable for austenitic steels with higher nickel content. The last possibility is based on suppression of the catalytic decomposition of CO or hydrocarbons on the material surface and provision of a surface material which does not dissolve or absorb carbon. Coatings based on Al and Cr rich phases represent promising perspectives [6].

Conclusion

The analysis of a ruptured aniline reactor tube confirmed the danger of metal dusting at relatively low temperature (~350 °C), which was counterbalanced by the long service life. The same problem with tube wall thinning by metal dusting was confirmed also in other reactors at the same location. Therefore, it was recommended both to verify the tube material used in the other reactors and to focus on regular inspection of the tube wall thickness as well as the reactor bodies themselves.

Acknowledgment

This paper was created with the Institutional support for long-term and conceptual development of a research organization in 2025, provided by the Ministry of Industry and Trade of the Czech Republic.

References

[1] T.S. Hummelshøj, C.C. Appel, M.A. J. Somers, T. Christiansen, C.C. Appel, Mechanisms of metaldusting corrosion. Kgs. Lyngby, Denmark: Technical University of Denmark (DTU). (DCAMM Special Report No. S115. 2010.

[2] A. Agüero, M. Gutiérrez, L. Korčáková, T.T.M. Nguyen, B. Hinnemann, S. Saadi, Metal Dusting Protective Coatings. A Literature Review, Oxid Met, 76 (2011) 23-42.

[3] H.J. Grabke, Metal Dusting of Low- and High-Alloy Steels, Corrosion, 51, 9 (1995) 711-720.

[4] H.J. Grabke, M. Schütze, Corrosion by carbon and nitrogen. Metal dusting, carburisaton, and nitridation. Woodhead Publishing Ltd, Cambridge, 2007 (e-book).

[5] D.J. Young, J. Zhang, Metal Dusting: Catastrophic Corrosion by Carbon, JOM, 64, 12 (2012) 1461-1469.

[6] D.J. Young, J. Zhang, C. Geers, M. Schütze, Recent advances in understanding metal dusting: A review, Materials and Corrosion, 62 (2011) 7-28.

Published in: Key Engineering Materials
ISSN: 1662-9795, Vol. 1043, pp 99-105
doi:10.4028/p-oGeKA5

Submitted: 2025-06-12
Revised: 2025-12-12
Accepted: 2025-12-19
Online: 2026-02-27

Fractography and Microstructural Analysis of Fatigue Crack Propagation in Beta-Annealed Ti6Al4V Alloy after Fatigue Test

Juraj Belan[1,a*], Milan Uhríčik[1,b], Martin Slezák[1,c] and Veronika Chvalníková[1,d]

[1]Department of Materials Engineering, Faculty of Mechanical Engineering, University of Žilina, Univerzitná 8215/1, 010 26 Žilina, Slovakia

[a*]juraj.belan@fstroj.uniza.sk, [b]milan.uhricik@fstroj.uniza.sk, [c]martin.slezak@fstroj.uniza.sk, [d]veronika.chvalnikova@fstroj.uniza.sk

Keywords: Ti6Al4V alloy, beta-annealing, alpha-case layer, fatigue crack initiation, propagation, SEM fractography.

Abstract. Titanium alloy Ti6Al4V was oxidation annealed in the beta-phase region (1050 °C/3 hours + WQ) in a furnace under a non-protective atmosphere. The above treatment caused the formation of an alpha-case layer on the surface. The above layer, because of its high hardness and strength, has a significant effect on the surface properties of the alloy. However, undesirable effects include the formation of cracks in this layer and a change in the mechanism of initiation and propagation of fatigue cracks. Based on the above findings, it is also very complicated to predict the fatigue life of Ti alloys processed in this way because of the presence of cracks in the alpha-case layer and the varying thickness of this layer. From the fractography and microstructural point of view, the initiation of fatigue cracks in the heat-treated alloy is realized by transcrystalline cleavage and the formation of pronounced fracture facets as a consequence of surface cracks in the alpha-case layer. Fatigue crack propagation (in the alpha-case layer region) is realized along the interface of the alpha-phase needles and the beta-phase primer grain without the significant presence of so-called fatigue striations.

Introduction

Pure titanium is a polymorphic metal that crystallizes in two allotropic modifications, Fig. 1: low-temperature Ti-α (up to about 882 °C), which crystallizes in a HCP lattice and high-temperature Ti-β (up to a melting temperature of about 1670 °C), which crystallizes in a BCC lattice [1–3]. The most commonly used titanium alloy Ti-6Al-4V includes the two-phase α + β.

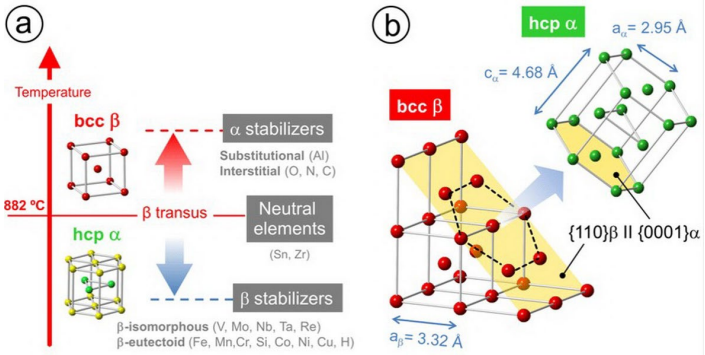

Fig. 1. a) Classification of the alloying elements of titanium according to their influence on the β-transus temperature, T_β. b) Lattice correspondence between the α – HCP and β – BCC structures. The lattice parameters correspond to the values of pure titanium at RT and 900 °C for α and β, respectively.

This alloy exhibits an excellent strength-to-density ratio, as well as outstanding mechanical properties and corrosion resistance. Because of these properties, it is widely used in the aerospace industry and as a biomedical material. However, a significant drawback of this alloy is its high affinity for atmospheric oxygen and nitrogen, which can lead to the formation of a hard but brittle layer known as the α-case layer at higher temperatures. The maximum oxygen solubility in the Ti-α phase is approximately 14.5 wt.% and is not significantly dependent on temperature. Oxides such as Ti_3O (8–

13 wt.% O) or Ti_2O (10–14.4 wt.% O) form at around 400 °C (some references reports temperatures over 480 °C [4, 5]). The oxygen solubility in the Ti-α phase does not change with temperature until around 600 °C. In contrast, the maximum oxygen solubility in the Ti-β phase increases with temperature and reaches approximately maximum 3 wt.% at 1720 °C, Fig. 2 [6].

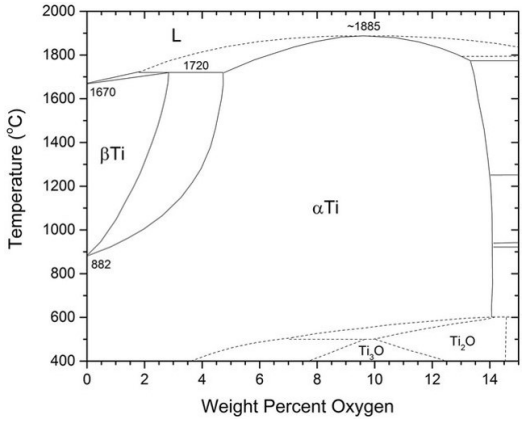

Fig. 2. A binary phase diagram Titanium – Oxygen.

Several authors have studied diffusion kinetics in Ti-6Al-4V alloy at different temperatures [7–9]. According to Du et al. [5], the kinetics of oxygen diffusion in the formation of Al_2O_3 and TiO_2 oxides in the alloy is parabolic at lower temperatures (ranging from 650 to 700 °C) with an activation energy value of Q = 276 kJ.mol^{-1}, and linear at higher temperatures (ranging from 700 °C to 850 °C) with an activation energy value of Q = 191 kJ.mol^{-1} [8].

The formation of the α-case layer is solely related to the oxygen diffusivity in the aforementioned alloy. Poquillon et al. [10] found a correlation between the oxygen content of the oxygen-influenced layer and hardness during the oxygen-phase-oxidation process of the oxide layer. Dong et al. [11] investigated the effect of diffusion temperature on the grain morphology of the α-case layer. They discovered that the grains of the α-case form of fine polygonal needles or plates, depending on the dwell time at the diffusion temperature, in the region surrounding the β-transus temperature. The similar results about formation of α-case layer and its morphology after oxidation annealing at 1050 °C and various cooling rates were confirmed by Belan et al. [12].

Numerous researchers have examined how the presence of the α-case layer affects both static and dynamic mechanical behavior, including under high-temperature conditions. Chan et al. [13] explored how α-case formation influences the mechanical response of titanium alloy cast components. Their findings indicate that slower cooling rates lead to a thicker α-case layer, which correlates with increased microhardness and reduced toughness. This decline in toughness is attributed to micro crack initiation at the boundary between the α-phase and the retained β-phase. The role of the α-case layer in the initiation and propagation of fatigue cracks has been studied by Yan et al. [14] and Gaddam et al. [15]. These investigations consistently demonstrate that the presence of an α-case layer significantly shortens the fatigue life of the alloy, with cracks commonly initiating from micro cracks within the α-case. Furthermore, changes in the base microstructure – from bimodal and lamellar to equiaxed, during fatigue testing result in a shift in fracture mode, moving from ductile toward entirely brittle failure.

The main goal of this study is microstructure and fractography analysis of β-annealed Ti-6Al-4V alloy with presented α-case layer and its effect on fatigue crack propagation mode and fatigue life as well.

Experimental Material and Methods

The titanium alloy Ti-6Al-4V as the experimental material from the supplier BIBUS Metals AG, Brno CZ was used, see Table 1. The alloy was delivered in annealed conditions (that was statement from material sheet).

Table 1. The chemical composition (wt. %) and selected mechanical properties of Ti6Al4V alloy (*Ti content is a balance; **Own hardness measurement).

Fe	C	N	H	O	Al	V	UTS [MPa]	YS 0.2% [MPa]	Elongation [%]	Hardness HRC
0.16	0.025	0.009	0.0049	0.164	6.112	4.105				
Long. (not applicable to hardness measurements)							1023	994	12.13	32.5
Trans. (not applicable to hardness measurements)							1185	1152	11.73	57**

Specimens were heat-treated (HT) by oxidation annealing (OA) at 1050 °C (which is a temperature over β-transus temperature for this alloy) with a dwell time of 3 hrs., followed by WQ (water quenching – cooling rate was 500 °C.s^{-1}).

Specimens for metallography evaluation were prepared via regular metallographic procedures: wet sanding and wet polishing on Struers TEGRASYSTEM, etched by 10 % HF or 1.5 ml HF + 2ml HNO_3 + 10 ml H_2O (this reagent provides better results). Microstructures, the α-case layer, were evaluated on NEOPHOT 32 optical microscope (OM), and fractography analysis was done at TESCAN Vega II (SEM).

Fatigue testing under three-point bending conditions was conducted at ambient temperature (22 °C ± 5 °C) using a ZWICK / ROELL Amsler 150HFP 5100 resonance pulsator. The Amsler 150HFP 5100 is designed for fatigue assessment using sinusoidal loading based on the resonance principle. It operates within a frequency range of 35–300 Hz and allows testing with both constant and variable amplitude, supporting maximum force amplitudes of ±75 kN and mean loads up to ±150 kN. This equipment enables fatigue evaluations on both materials and components and complies with standards such as DIN 50100 for S/N curve generation in tensile, compressive, and alternating stress regimes.

The test parameters were configured as follows:

i) for specimens without HT (no α-case layer presented), a static preload of F_{static} = –15.0 kN; a dynamic loading range from –7.0 kN to –13.5 kN; frequency varied between 102.0 Hz and 108.6 Hz;

ii) for specimens after applying HT (with α-case layer presented), a static preload of F_{static} = –10.0 kN; a dynamic loading range from –5.0 kN to –8.0 kN; frequency varied between 68.5 Hz and 70.0 Hz,

The stress ratio R < 1 in both cases. Testing was terminated after 2.0×10^7 cycles, which is considered the fatigue limit for titanium alloys. Samples, measuring 10 mm×11 mm×50 mm, with the primary load applied at the midpoint. To mitigate thermal effects from cyclic loading, external fans were used for specimen cooling. The stress amplitude (σ_a) was calculated via Eq. 1:

$$\sigma_{a\,max} = \frac{3.F.L}{2.b.h^2}\ [MPa] \quad (1)$$

where F represents the applied dynamic force [N], L is the support span (30 mm), b is the width (10 mm), h is the height (11 mm), and σ_a is the resulting stress amplitude in MPa.

An S–N diagram was created to represent the fatigue data. While axial (push-pull) fatigue testing with a stress ratio R = –1 is more typical, three-point bending introduces additional complexity. This method induces a negative mean stress due to the static preload exceeding the dynamic stress amplitude, leading to a non-symmetric stress cycle (R < 1). As a result, the central region of the sample experiences more complex stress states, potentially reducing the fatigue life compared to conventional push-pull testing.

Results and Discussion

The microstructure of the starting stage and after applied β-transus oxidative annealing is shown in Fig. 3. The microstructure of the starting stage (Fig. 3a) is characterized by quasi-polyhedral grains (without distinct grain boundaries – difficult to observe) of the original β phase with excluded α phase lamellae. After HT (OA), the grain boundaries are clearly identifiable and are characterized by varying sizes. The original lamellar form of the α-phase precipitation changed to α′-martensite needles (the cooling rate after HT (OA) was approximately 500 °C.s^{-1}), and a distinct α-case layer with needle morphology and size (length) up to 250 μm. The above-mentioned change in structure and the formation of the α-case layer also had an impact on the increase in the hardness of the sample surfaces. A secondary, undesirable factor in the formation of the α-case layer is the formation of cracks in this surface layer.

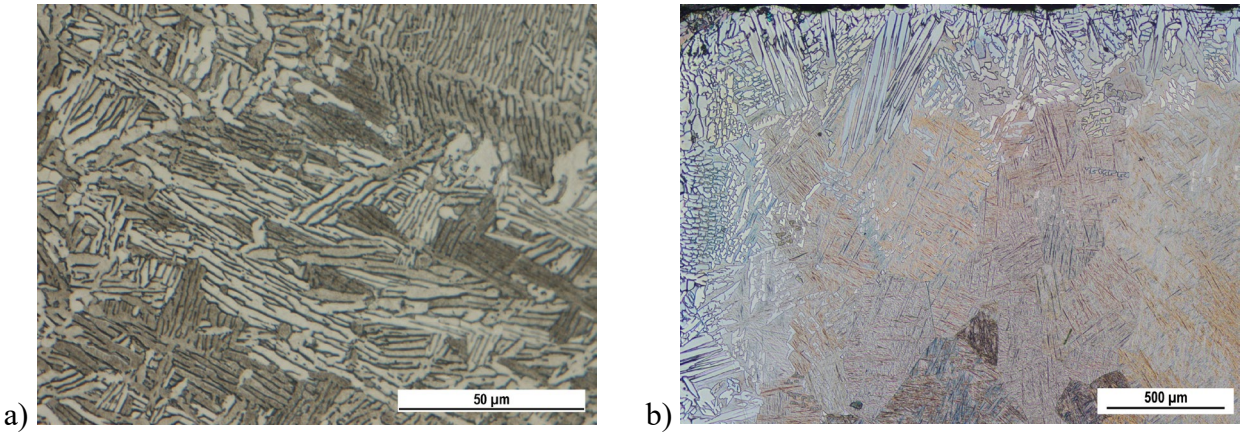

Fig. 3. Microstructure of Ti-6Al-4V alloy a) as a starting stage, etch. 10 % HF, b) after applied HT (OA), etch. 10 % HF + polarized light.

The results of fatigue tests are presented in the form of S-N curves, Fig. 4.

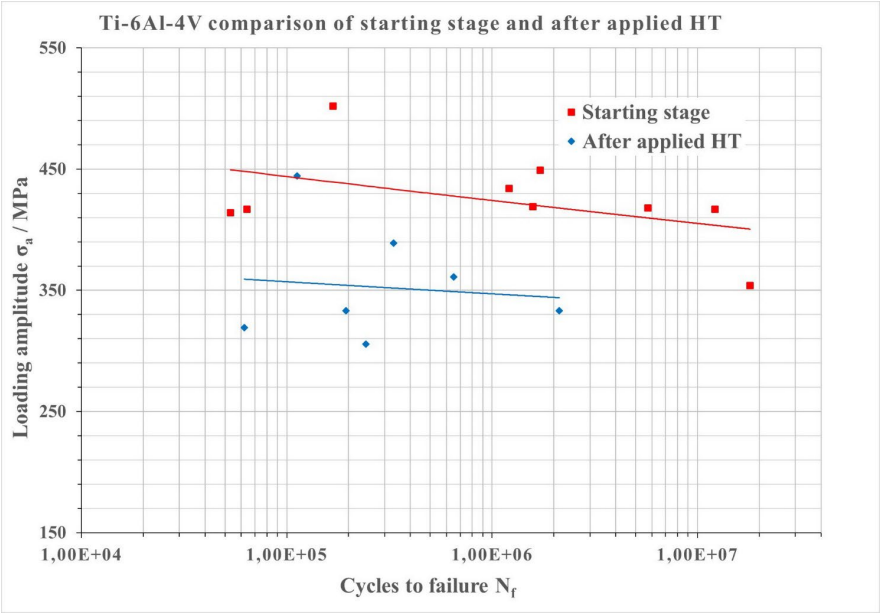

Fig. 4. S-N curves after three-point bending fatigue test of Ti-6Al-4V alloy.

From the curves shown, it is possible to characterize the dependence of the number of cycles to failure N_f on the load amplitude σ_a using Eq. 2 and Eq. 3.

For the initial state: $\sigma_a = 557.71 \times N_f^{-0.2}$ (2)

After HT (OA) application: $\sigma_a = 411.35 \times N_f^{-0.012}$ (3)

The significant decrease in fatigue life and fracture loading amplitude σ_a is caused by the elimination of the α-case layer and the presence of significant surface cracks, given that the process of fatigue crack initiation is surface-sensitive. This fact is also confirmed by the fractography analysis of the fracture surfaces of the samples after the fatigue test, Fig. 5.

From a fractography point of view, the initiation of fatigue cracks in the alloy in its initial state occurred on the surface and is characterized by a combination of intercrystalline cleavage with pronounced cleavage facets oriented at approximately 45° to the direction of loading and transcrystalline ductile failure, Fig. 5a. The propagation of the fatigue crack was subsequently a combination of intercrystalline and transcrystalline mechanisms with the occurrence of pronounced fatigue striations.

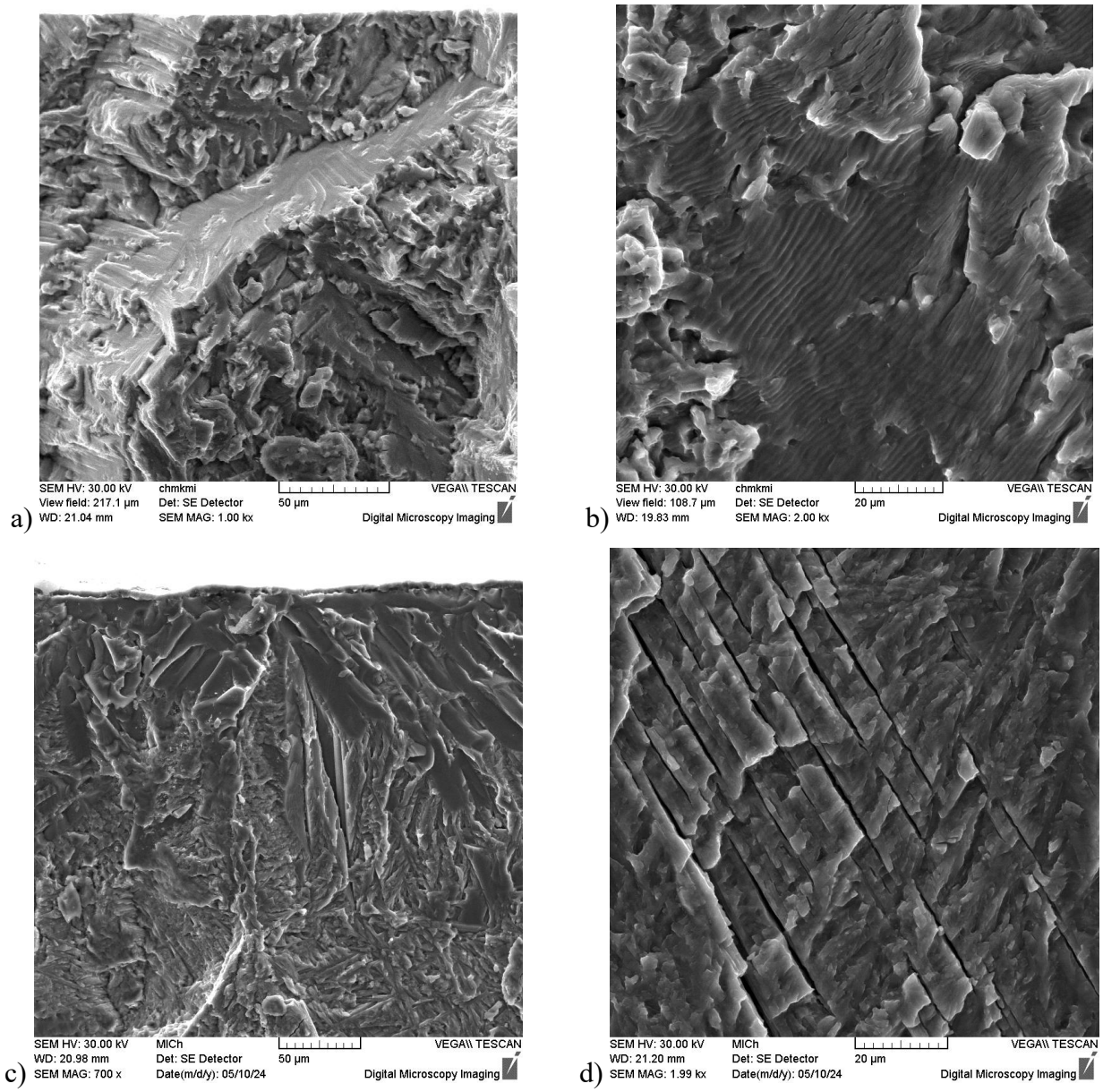

Fig. 5. Ti-6Al-4V micrographs after fatigue testing; a) fatigue crack initiation site, starting stage, b) fatigue crack propagation with a significant fatigue striations, starting stage, c) fatigue crack initiation site, HT (OA) alloy, d) fatigue crack propagation with secondary crack presence, no striation observed, HT (OA) alloy, SEM.

On the other hand, the initiation of the fatigue crack after the applied HT (OA) was different. Although the crack initiated on the surface of the sample, the mechanism was only intercrystalline, significantly influenced by the formation of the thin TiO_2 oxide layer on the top and, especially, the formation of the α-case layer and the presence of surface cracks, Fig. 5c. The crack in the first stage of propagation copied the hard needles of the α′-phase (or α-case). The subsequent propagation of the fatigue crack, its mechanism, is also predominantly intercrystalline cleavage, with significant secondary cracks, oriented at an angle of approximately 45° to the main direction of fatigue crack propagation, Fig. 5d.

Summary

The aim of the article was to provide metallography and fractography analyze and consider the influence of the formation of the α-case layer on the initiation and propagation of a fatigue crack and the influence of the change in the microstructure on the fatigue life itself. Based on the experiments performed, the following conclusions can be formulated:

i) Quasi-polyhedral grains and lamellae of the α-phase form the microstructure in the starting stage. After the applied HT (OA), the α-case layer was formed on the surface and the core microstructure changed to polyhedral with various grain sizes and the α-phase was transformed into α′-martensite.
ii) The formation of the α-case layer significantly affected the overall fatigue life, the value of the load amplitude σ_a decreased.
iii) From a fractography point of view, the formation of the α-case layer had an impact on the initiation mechanism and the propagation of the fatigue crack, with the formation of significant secondary fatigue cracks.

Acknowledgement

The authors acknowledge the KEGA projects No. 004ŽU-4/2023 and No. 009ŽU-4/2023 for the financial support of this work.

References

[1] C. Leyens, M. Peters, Titanium and Titanium Alloys: Fundamentals and Applications, first ed., Wiley-VCH GmbH & Co. KGaA, Weinheim, 2003.

[2] G. Lütjering, J.C. Williams, Titanium, second ed., Springer Berlin Heidelberg New York, 2007.

[3] W. Sha, S. Malinov, Titanium alloys: modelling of microstructure, properties and applications, first ed., Woodhead Publishing Limited and CRC Press LLC, New Delhi and Boca Raton, 2009.

[4] R. Gaddam, B. Safer, R. Pederson, M.-L. Antti, Oxidation and alpha-case formation in Ti-6Al-2Sn-4Zr-2Mo alloy, Mat. Charact., 99 (2015) 166-174.

[5] R. Gaddam, M.-L. Antti, R. Pederson, Influence of alpha-case layer on low cycle fatigue properties of Ti-6Al-2Sn-4Zr-2Mo alloy, Mat. Science and Eng. A, 500 (2014) 51-56.

[6] ASM Handbook, Alloy Phase Diagrams, Vol 3, Okamoto, H., Schlesinger, M.E., Mueller, E.M., Eds.; ASM International, 2016, p 1714, https://doi.org/10.31399/asm.hb.v03.a0006247.

[7] H.L. Du, P.K. Datta, D.B. Lewis, J.S. Burnell-Gray, Air oxidation behaviour of Ti-6Al-4V alloy between 650°C and 850°C, Corrosion Science, 36, 4 (1994) 631-642.

[8] H. Guleryuz, H. Cimenoglu, Oxidation of Ti–6Al–4V alloy. Journal of Alloys and Compounds, 472, 1-2 (2009) 241-246.

[9] G. Lindwall, K.W. Moon, Z. Chen, et al., Diffusion in the Ti-Al-V System, J. Phase Equilib. Diffus., 39 (2018) 731-746.

[10] D. Poquillon, C. Armand, J. Huez, Oxidation and Oxygen Diffusion in Ti–6Al–4V Alloy: Improving Measurements During Sims Analysis by Rotating the Sample, Oxid Met, 79 (2013) 249-259.

[11] E. Dong, W. Yu, Q. Cai, et al., High-Temperature Oxidation Kinetics and Behavior of Ti–6Al–4V Alloy, Oxidation of Metals, 88 (2017) 719-732.

[12] J. Belan, M. Uhríčik, L. Kuchariková, E. Tillová, & L. Pastierovičová, Formation of Alpha-Case Layer during Oxidation of Ti6Al4V Surface by Annealing at 1050 °C and Change of Microstructure after Different Cooling Rates, Materials Science Forum, 1081 (2023) 161-166.

[13] K.S. Chan, M. Koike, B.W. Johnson, T. Okabe, Modeling of Alpha-Case Formation and Its Effects on the Mechanical Properties of Titanium Alloy Castings, Metal. and Mater. Trans. A, 39A (2008) 171-180.

[14] X. Yan, H.C. Kou, F.B. Han, B. Tang, L.J. Zhang, J.S. Li, Effect of Alpha Phase Characteristics on the High Cycle Fatigue Properties of Ti-6Al-4V Alloy, Materials Science Forum, 849 (2016) 259-265.

Published in: Key Engineering Materials
ISSN: 1662-9795, Vol. 1043, pp 107-112
doi:10.4028/p-Ss3pTt

Submitted: 2025-05-30
Revised: 2025-12-05
Accepted: 2025-12-19
Online: 2026-02-27

Influence of High-Pressure Hydrogen on Tensile Properties of Pipeline Steels Evaluated by Autoclave In-Situ SSRT

Jan Kander[1,2,a*] and Gabriela Rožnovská[2,b]

[1]Material and Metallurgical Research, Ltd. Pohraniční 693/31, 703 00 Ostrava, Czechia

[2]VŠB – Technical University of Ostrava, Faculty of Materials Science and Technology, 17. listopadu 2172/15, 708 00 Ostrava, Czechia

[a*]jan.kander@mmvyzkum.cz, [b]gabriela.roznovska@mmvyzkum.cz

Keywords: High-Pressure Hydrogen, SSRT, Pipeline Steel, X-52, X-60, X-70.

Abstract. With search for clean and sustainable energy sources European union is determined to fully substitute natural gas with hydrogen in 2050. With these requirements it is really important to study materials used in existing gas infrastructure and evaluate their resistance to hydrogen embrittlement, which is common phenomena in material degradation. In this article, a comparative study was conducted using slow strain rate testing (SSRT) in situ at 10 MPa hydrogen pressure and tensile testing in air on X-52, X-60, and X-70 pipeline steels commonly used in Czech gas infrastructure. The results revealed reduction in elongation and a significant reduction in contraction in SSRT samples exposed to hydrogen compared to those tested in air, while yield and tensile strengths remained nearly unchanged. Furthermore, fracture morphology transitioned from ductile dimple to cleavage/quasi-cleavage. These findings suggest that hydrogen primarily affects the plastic properties of the materials, leading to a shift towards a lower energy fracture mechanism.

Introduction

With regard to the socially relevant topic of decarbonization and achieving so-called carbon neutrality related to the Green Deal agreement, but also to the REPowerEU project, which seeks to ensure sustainable energy sources for Europe [1]. The gas industry is also becoming an area of current interest, where the carbon footprint should be reduced by adding hydrogen (over time to full replacement) to natural gas. As part of the Green Deal agreement and the European Hydrogen Backbone (EHB) initiative, a backbone hydrogen distribution network for the whole of Europe should be built by 2050, where the use and modification of the existing gas infrastructure is expected, which should lead to significant material savings, because the costs of operating the existing network are about 20 % compared to building a new network [2, 3].

In recent years, hydrogen is discussed more and more as a source of ecological fuel and energy. The foundation of this energy transformation lies in the first phase in the addition of hydrogen to natural gas and thus reduce the CO_2 emissions. The next phase is to gradually increase the hydrogen content in the gas infrastructure, while medium to long-term scenarios include a transition from natural gas to pure hydrogen only. The basic problem of this transitional phase is the minimum information on the current state of the gas infrastructure and the degrading effect of hydrogen on the steel pipes currently used in the gas network. Historically, it is known that that the degrading effect of hydrogen is certainly not negligible [4–6] and is influenced by many external factors [7–9].

Most local pipeline distribution systems contain a polyethylene liner (or are completely plastic), which should be much more resistant to the effects of hydrogen, together with the much lower operating parameters of local networks compared to backbone networks, so they do not pose a serious safety risk. However, the problem becomes backbone networks, where there are steel pipelines operating at significantly higher pressures and flows; according to available information, backbone routes in the Czech Republic constitute approximately 40–45 % of the entire gas infrastructure [10]. The aim of the article is therefore to verify the behavior of the above-mentioned materials in an environment of high-pressure hydrogen gas.

Material and Methods

The main of the experimental work was to compare tensile tests in air and high-pressure hydrogen environments. Experimental material were three operated pipelines from X-52, X-60 and X-70 steels, which are commonly used materials in Czech gas infrastructure. Chemical composition of studied steels analyzed by WD-XRF and combustion analysis is in Table 1.

Table 1 Chemical composition of studied steels [wt. %].

Pipeline	C	S	Mn	Si	P	Cu	Ni
X-52	0.16	0.040	1.26	0.29	0.026	0.22	0.29
X-60	0.084	0.004	1.59	0.43	0.015	0.065	0.025
X-70	0.10	0.005	1.60	0.37	0.018	0.040	0.030

Continuation of Table 1.

Pipeline	Cr	Mo	V	Ti	Nb	W	Co
X-52	0.11	0.045	< 0.003	< 0.005	< 0.003	0.006	0.011
X-60	0.028	0.008	0.087	< 0.005	0.058	< 0.005	0.005
X-70	0.072	0.023	0.030	0.005	0.040	< 0.005	0.010

From abovementioned pipelines round bar tensile test specimens were prepared (M10, Ø6 mm). After installing the autoclave in the MTS 100 kN servo-hydraulic testing machine and clamping the sample in the machine jaws, the autoclave was closed, flushed with nitrogen and then evacuated. It was then gradually pressurized with hydrogen up to a working pressure of 10 MPa, while compensating the hydrogen pressure hydraulically to avoid sudden failure of the sample. The test specimens were broken in-situ in hydrogen at a pressure of 10 MPa at a slow strain rate (SSRT), Fig. 2. The shape of the stress-strain curves, the achieved stress-strain characteristics, as well as the macro and micromorphology of the fracture surfaces were evaluated. The obtained parameters were then compared again with a conventional tensile test in air at normal speed. SEM fractography was performed on broken samples.

Fig. 1 Test specimen prepared for in-situ high-pressure hydrogen SSRT.

Results and Discussion

The results of the tensile tests comparison are given in Table 2. For the X-60 steel, two SSRTs were intentionally performed at different crossbar speeds (0.01 and 0.08 mm min^{-1}) to assess the effect of the strain rate on the achieved mechanical properties. The stress-strain curves for hydrogen and air were also compared in Fig. 2. While the $R_{p0.2}$ and R_m stayed almost the same the ductility A and reduction of area Z decreased significantly, which corresponds to [11]. Lower crossbar speed showed lower values of A and Z, which confirms other findings [12, 13].

Table 2 Comparison of the stress-strain properties.

Sample	Environment	Crossbar speed [mm·min^{-1}]	$R_{p0,2}$ [MPa]	R_m [MPa]	A [%]	Z [%]
X-52	air	-	331	531	36.0	68.4
X-60	air	-	555	659	28.9	72.2
X-70	air	-	523	659	23.7	71.6
X-52	H_2, 10 MPa	0.017	323	519	29.0	20.8
X-60-1	H_2, 10 MPa	0.080	557	663	24.3	25.1
X-60-2	H_2, 10 MPa	0.010	549	655	22.0	23.0
X-70	H_2, 10 MPa	0.025	517	660	14.7	13.5

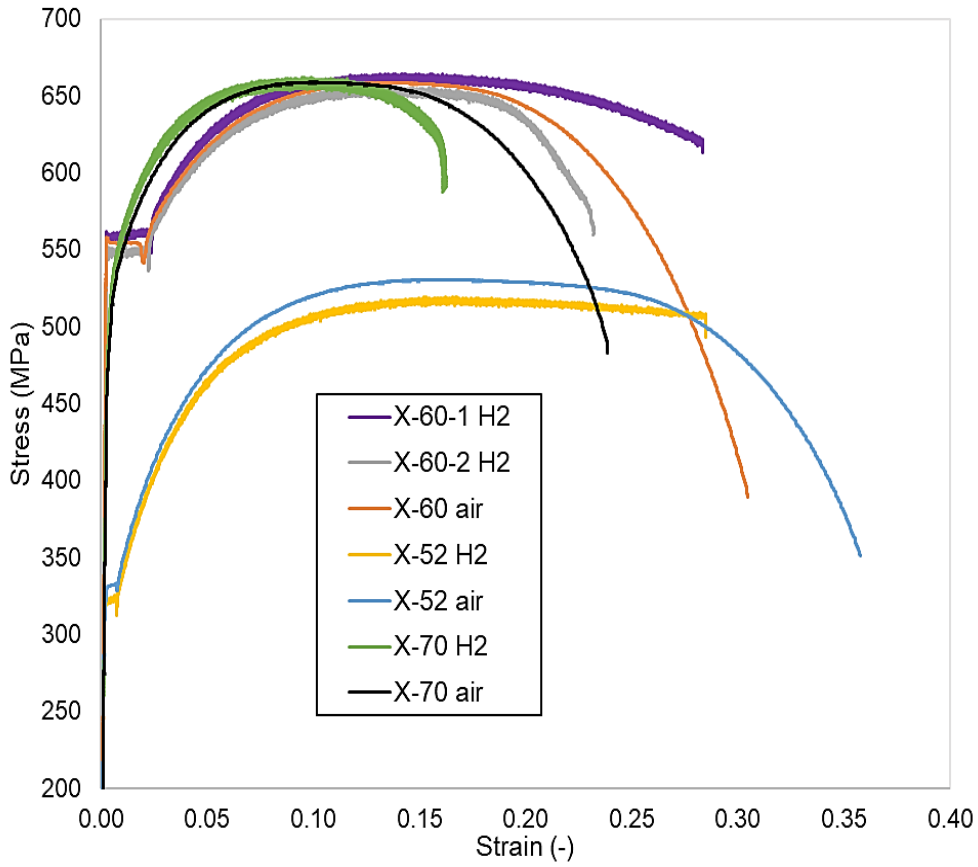

Fig. 2 Comparison of the stress-strain curves.

From a visual point of view, all fracture surfaces of specimens tested in air appeared dim with minor shear lip. The micromorphology of the fracture surfaces of all samples was formed by the mechanism of transcrystalline ductile fracture with dimple morphology, Fig. 3a–c.

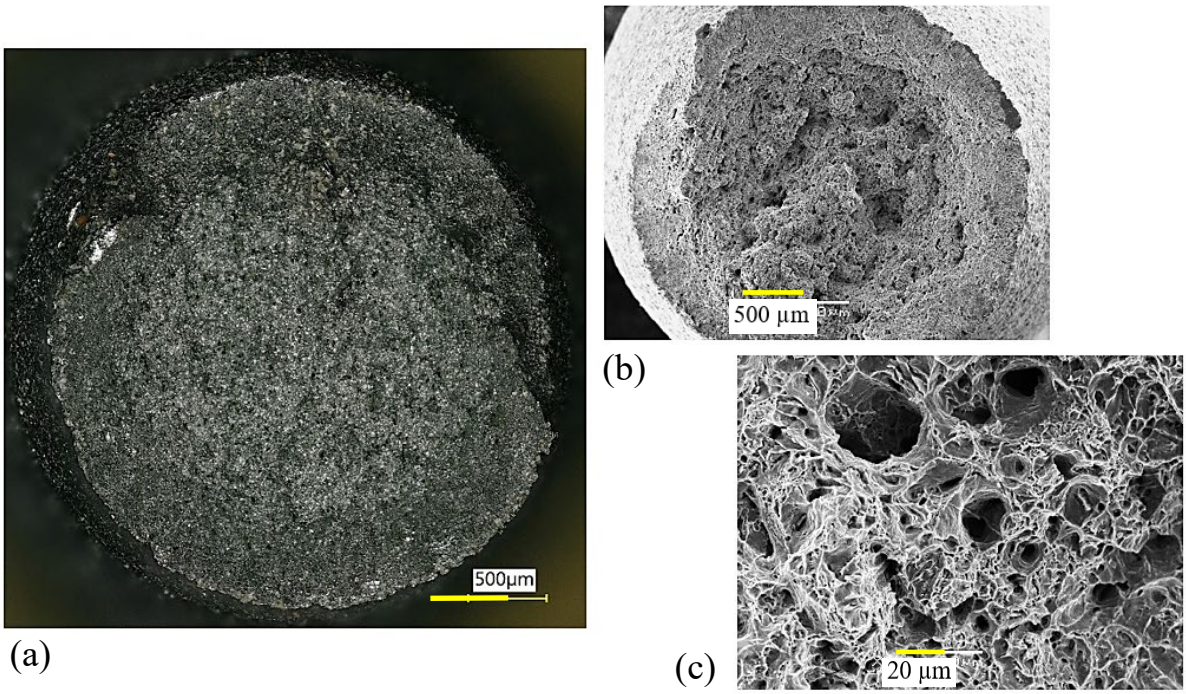

Fig. 3 Specimen X-52 tested in air: (a) whole fracture surface, (b) visible shear lip, (c) trancrystalline ductile dimple fracture.

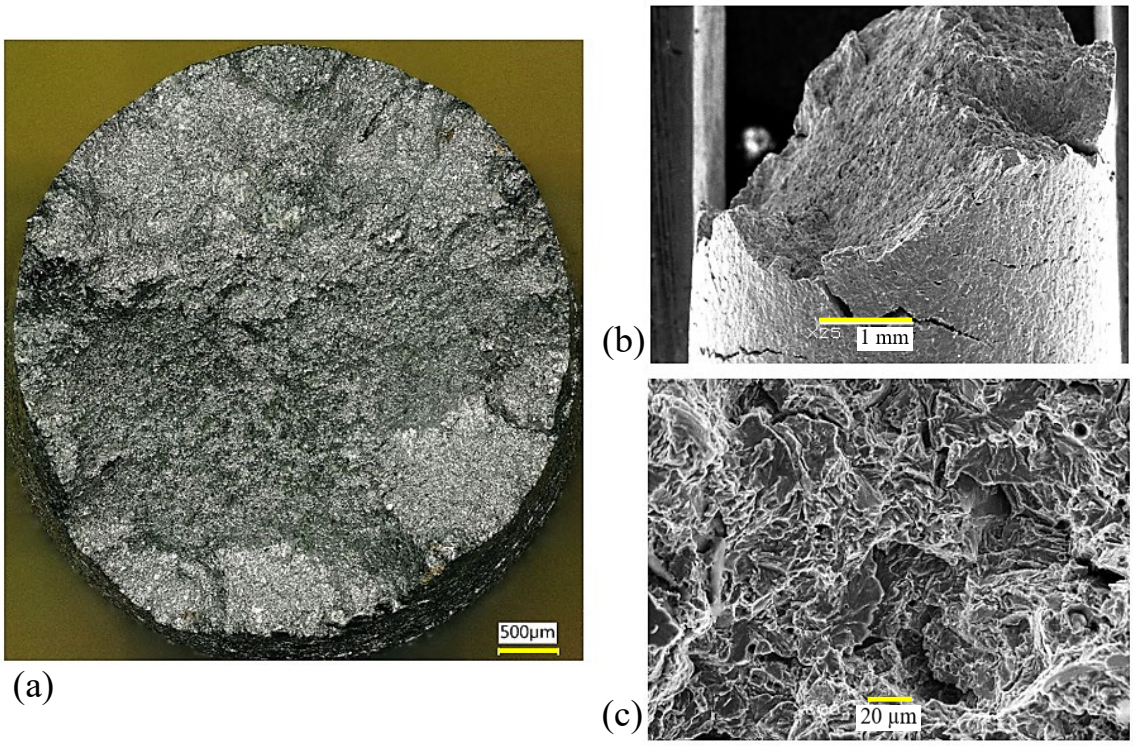

Fig. 4 Specimen X-52 tested in high-pressure hydrogen: (a) whole fracture surface, (b) 45° slope of the fracture surface, (c) transcrystalline quasi-cleavage/cleavage fracture.

In all hydrogen-tested specimens, a much smaller reduction of area was instantly visible, Fig. 4a. The fracture surfaces were often sloped at an angle of approximately 45°, Fig. 4b. The micromorphology of the fracture surfaces was predominantly formed by transcrystalline quasi-cleavage/cleavage fracture, Fig. 4c. This change of fracture morphology in hydrogen is also common, regardless the hydrogen charging method [14, 15].

Conclusion

Tensile tests in air and slow tensile tests (SSRT) in hydrogen showed practically the same yield strength and ultimate tensile strength, but there was a decrease in ductility and a significant decrease in reduction of area. SSRTs tested in-situ in a hydrogen autoclave showed earlier fracture than in the corresponding specimens tested in air.

It seems that the additional deformation of the material and its rate during exposure play a crucial role. From the graphical comparison of the stress-strain curves, it is evident that the X-60-2 specimen (lower deformation rate) fractured earlier than the X-60-1 specimen (higher deformation rate), so it can be stated that longer hydrogen diffusion times negatively affect mainly the ductility and reduction of area of the sample. From the fractographic analysis, a change in the fracture mechanism was observed practically in all specimens. While specimens tested in air show almost exclusively transcrystalline ductile fracture, the hydrogen tested specimens show transcrystalline quasi-cleavage/cleavage mechanism, and the fracture surfaces were also sloped at an angle of approximately 45°. The change in fracture mechanism reflects the change in fracture energy caused by hydrogen degradation.

Acknowledgements

This work was created as part of the TA CR project SS06020165 “Mapping the impacts of efforts to reduce greenhouse gas emissions using hydrogen additions on the lifetime of the existing infrastructure of gas power infrastructure plant” and project SP2025/076 “Material and technological properties of construction materials in relation to their production method, processing and the effect of degradation mechanisms” and institutional support for the long-term and conceptual development of the research organization in 2025, which was provided by the Ministry of Industry and Trade of the Czech Republic.

References

[1] REPowerEU. Affordable, secure and sustainable energy for Europe. European Commision. https://commission.europa.eu/strategy-and-policy/priorities-2019-2024/european-green-deal/repow ereu-affordable-secure-and-sustainable-energy-europe_en.

[2] EHB Implementation Roadmap: Public support as catalyst for hydrogen infrastructure. European Hydrogen Backbone. https://ehb.eu/page/publications.

[3] J.B. Cristello, J. Yang, R. Hugo, Y. Lee, S.S. Park, Feasibility analysis of blending hydrogen into natural gas networks, International Journal of Hydrogen Energy, 48, 46 (2023) 17605-17629. https://doi.org/10.1016/j.ijhydene.2023.01.156.

[4] J. Sojka. Odolnost ocelí vůči vodíkové křehkosti. Ostrava: Vysoká škola báňská-technická univerzita, 2007. ISBN 978-80-248-1648.

[5] A.J. Lee, S. Woods. Hydrogen Embrittlement. NASA/TM-2016-218602. 2016. https://ntrs. nasa.gov/citations/20160005654.

[6] Y.-S. Chen, et al., Hydrogen trapping and embrittlement in metals – A review. International Journal of Hydrogen Energy (2024), ISSN 0360-3199. https://doi.org/10.1016/j.ijhydene. 2024.04.076.

[7] S. Dwivedi, M. Vishwakarma. Hydrogen embrittlement in different materials: A review. International Journal of Hydrogen Energy, 43 (2018), https://doi.org/10.1016/j.ijhydene. 2018.09.201.

[8] H. Zhang, et al., Research progress on corrosion and hydrogen embrittlement in hydrogen–natural gas pipeline transportation. Natural Gas Industry B, 10, 6 (2023) 570-582. ISSN 2352-8540. https://doi.org/10.1016/j.ngib.2023.11.001.

[9] Y. Zhang, Q. Ye, Y. Yan, Processing, microstructure, mechanical properties, and hydrogen embrittlement of medium-Mn steels: A review, Journal of Materials Science & Technology, (2024), ISSN 1005-0302, https://doi.org/10.1016/j.jmst.2024.03.014.

[10] GasNet je připraven zvedat podíl biometanu a vodíku ve své síti. GasNet, s.r.o., https://www.gasnet.cz/o-spolecnosti/novinky/2022/05/GasNet-je-pripraven-zvedat-podil-biometanu-a-vodiku.

[11] R. Walallawita, M.C. Hinchliff, D. Sediako, J. Quinn, V. Chou, Evaluating the Effect of Blended and Pure Hydrogen in X60 Pipeline Steel for Low-Pressure Transmission Using Hollow-Specimen Slow-Strain-Rate Tensile Testing, Metals, 14, 10 (2024), ISSN 2075-4701, https://doi.org/ 10.3390/met14101132.

[12] S.S. Shishvan, G. Csányi, V.S. Deshpande, Strain rate sensitivity of the hydrogen embrittlement of ferritic steels, Acta Materialia, 257 (2023) 119173, ISSN 1359-6454, https://doi.org/ 10.1016/j.actamat.2023.119173.

[13] W. Dietzel, M. Pfuff, The Effect of Deformation Rates on Hydrogen Embrittlement. In: Hydrogen Effects in Materials. 1994, pp. 301-312. ISBN 9781118803363, https://doi.org/ 10.1002/9781118803363.ch28.

[14] S. Rahimi, K. Verbeken, T. Depover, E. Proverbio, Hydrogen embrittlement of pipeline steels under gaseous and electrochemical charging: A comparative review on tensile properties: A comparative review on tensile properties, Engineering Failure Analysis, 167 (2025) 108956, ISSN 1350-6307, https://doi.org/10.1016/j.engfailanal.2024.108956.

[15] D.-S. Bae, C.-E. Sung, H.-J. Bang, S.-P. Lee, J.-K. Lee, Effect of highly pressurized hydrogen gas charging on the hydrogen embrittlement of API X70 steel, Metals and Materials International, 20, 4 (2014) 653-658, ISSN 2005-4149, https://doi.org/10.1007/s12540-014-4010-5.

Published in: Key Engineering Materials
ISSN: 1662-9795, Vol. 1043, pp 113-118
doi:10.4028/p-FPgy1T

Submitted: 2025-05-31
Revised: 2025-12-10
Accepted: 2025-12-19
Online: 2026-02-27

Fracture Mechanisms of Aluminum Alloy Caused by Fatigue Tests

Milan Uhríčik[1,a*], Peter Palček[1,b], Juraj Belan[1,c], Veronika Chvalníková[1,d], Martin Slezák[1,e] and Lukáš Šikyňa[1,f]

[1]University of Žilina, Faculty of Mechanical Engineering, Department of Material Engineering, Univerzitná 8215/1, 010 26 Žilina, Slovakia

[a*]milan.uhricik@fstroj.uniza.sk, [b]peter.palcek@fstroj.uniza.sk, [c]juraj.belan@fstroj.uniza.sk, [d]veronika.chvalnikova@fstroj.uniza.sk, [e]martin.slezak@fstroj.uniza.sk, [f]lukas.sikyna@fstroj.uniza.sk

Keywords: Aluminum Alloy, Structure, Fatigue, Fracture, SEM.

Abstract. Fatigue damage is one of the key degradation mechanisms affecting the service life and reliability of aluminum alloys in a wide range of technical applications. The present study focuses on the fracture mechanisms of aluminum alloys under cyclic loading, with a view to the initiation and analysis of fatigue crack propagation in the context of the microstructural characteristics of the material. Special attention was paid to the influence of grain morphology, distribution and type of intermetallic phases, as well as the presence of casting defects on the initiation and development of cracks. Fatigue experiments were performed on a selected Al-Mg alloy of the EN AC 51200 type for the use of three-point bending loading. The results show that the key factors affecting the fatigue behavior are the size and distribution of precipitates, the nature of the interfaces between the phases and the occurrence of microcracks initiated mainly in areas of stress concentration. The knowledge gained contributes to a deeper understanding of fatigue mechanisms in aluminum alloys and provides a basis for their optimization in terms of composition and technological processing in order to increase their resistance to fatigue failures.

Introduction

Aluminum alloys represent an important group of structural materials that have wide application in the automotive, aerospace and mechanical engineering industries, due to their favorable combination of low density, good machinability and excellent casting properties. One of them is EN AC 51200 (AlMg9), which belongs to the group of Al-Mg alloys doped with silicon. This alloy exhibits favorable properties of strength, toughness and corrosion resistance, while its mechanical properties can be further modified by heat treatment, especially hardening [1–3].

Fatigue failure represents a serious engineering problem in the design and operation of metallic structures. It occurs as a result of repeated cyclic loading, with fatigue crack initiation occurring at a microscopic level, often due to local defects, stress concentrators, or microstructural inhomogeneities. The initial crack then grows steadily over a large number of loading cycles until it reaches a critical size leading to a sudden and usually brittle failure in the last cycle of the fatigue life [4, 5].

A deeper understanding of fatigue mechanisms is crucial for taking into account technical and operational factors affecting the fatigue behavior of a material. These factors include, for example, the quality of the surface treatment, the presence of residual stresses after technological operations, or the influence of the operating environment (e.g. corrosive media). This knowledge is essential for reliable analysis of the fatigue life of structural components and for the design of optimized solutions with higher resistance to cyclic damage [6].

Experimental Material

The commercially available type of aluminum alloy EN AC 51200 was used as the experimental material, which was supplied by the respective manufacturer in a cast state (through the continuous casting method) without heat treatment in the form of an ingot. The actual chemical composition of

this alloy was determined using a SPECTROMAXx spark emission spectrometer and the result is shown in Table 1.

Table 1 The chemical composition of EN AC 51200, in wt.%.

Element	Si	Mg	Mn	Fe	Cu	Ni	Cr	Pb	Al
Content	1.322	10.352	0.437	0.144	0.004	0.004	0.007	0.029	balance

Experimental Procedures

The experimental material was subjected to a comprehensive metallographic analysis. The microstructural characteristics were examined using a Neophot 32 optical microscope and a TESCAN Vega II LMU scanning electron microscope equipped with a Bruker-Quantax energy-dispersive analyzer, after the application of deep etching. The analysis also included a quantitative evaluation of the microstructure, which included the percentage determination of the volume fractions of individual phases, the calculation of the secondary dendritic arm spacing (SDAS) and the average grain size. These parameters were quantified on a Neophot 32 optical microscope equipped with a NIKON Coolpix 4500 camera, while the NIS Elements software was used for image processing and analysis. The microstructure of the alloy was analyzed in its initial state.

For experimental purposes, test specimens prepared in the form of simple block samples with dimensions of 18 mm x 10 mm x 40 mm (width x height x length) were used. Fatigue tests were performed on these samples in the three-point bending mode. Fatigue tests were performed on a high-frequency fatigue device ZWICK/ROELL Amsler 150 HFP 5100 at a laboratory temperature of 21 °C ±5 °C. The test was performed under conditions of static pre-stressing force F_{static} = –5.6 kN and dynamic load $F_{dynamic}$ in the interval 4.7 to 5.4 kN. The value of $2x10^7$ cycles was set as a reference criterion, where samples that exceeded this limit without failure (so-called run-out) were considered to have reached the ultimate fatigue life. The cycling frequency during the tests was approximately f = 90 Hz. Based on the experimental data, an S-N curve (Wöhler curve) was constructed, showing the relationship between the stress amplitude σ_a and the number of cycles to failure N_f.

Fractographic analysis of the failed samples was performed using a TESCAN Vega II LMU scanning electron microscope. The aim of this analysis was to identify the micromechanisms of fatigue crack initiation, its propagation and to characterize the morphology of the final fracture area.

Results and Discussion

The microstructure of the EN AC 51200 aluminum alloy (Fig. 1a) showed a distinct dendritic character, formed by a matrix of the α phase (solid solution of alloying elements in aluminum). Secondary intermetallic phases were identified in the interdendritic regions, mainly Mg_2Si, the β phase (Al_3Mg_2), as well as phases formed by the reaction of additive elements with aluminum (for example, the iron phase $Al_6(FeMn)$) [7]. For identification and confirmation of structural components was used square analysis (Fig. 1b and Fig. 1c).

Quantitative phase analysis (Fig. 2a to Fig. 2c) was performed at 1000x magnification on a sample etched with a 0.5 % hydrofluoric acid (HF) solution. The results were obtained based on fifteen measurements, with the dominant intermetallic phase being the β phase with an average proportion of 8.4 %. The Mg_2Si phase was present in an amount of 7.1 %, while the $Al_6(FeMn)$ phase occurred in a minimum amount of 0.92 %. The secondary dendritic arm spacing factor (SDAS) was determined by the line method on the matrix area at 100x magnification. The measurement consisted of counting the number of secondary dendritic arms intersected by a reference line of 12 cm length. The average SDAS value, calculated from fifteen measurements, reached 39 μm. The grain size was evaluated on the sample after electrolytic etching using polarized light and 100x magnification (Fig. 2d). The calculation was based on the areal content of individual grains, with the resulting average grain size value being 57361 μm^2, also determined as the average of fifteen measurements.

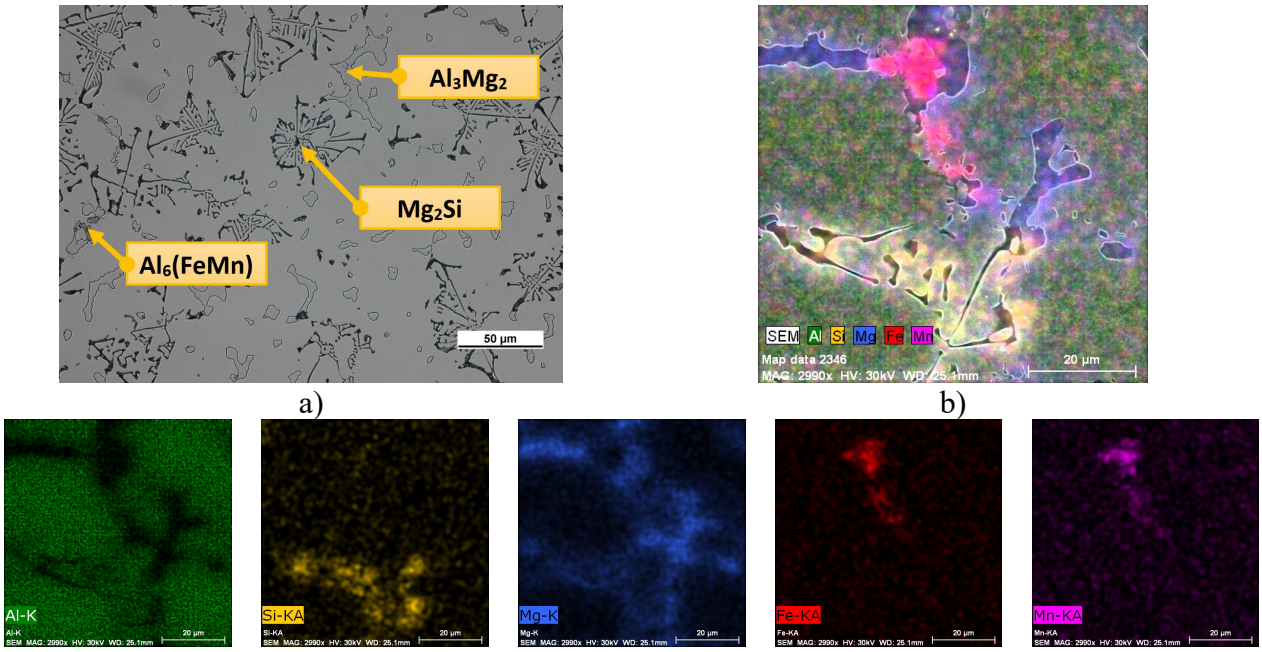

a) b) c)

Fig. 1 Microstructure of aluminum alloy EN AC 51200; a) phases in the microstructure, LM; b) identification of structural components (a square analysis), SEM; c) identification of individual elements (Al, Si, Mg, Fe, Mn), SEM.

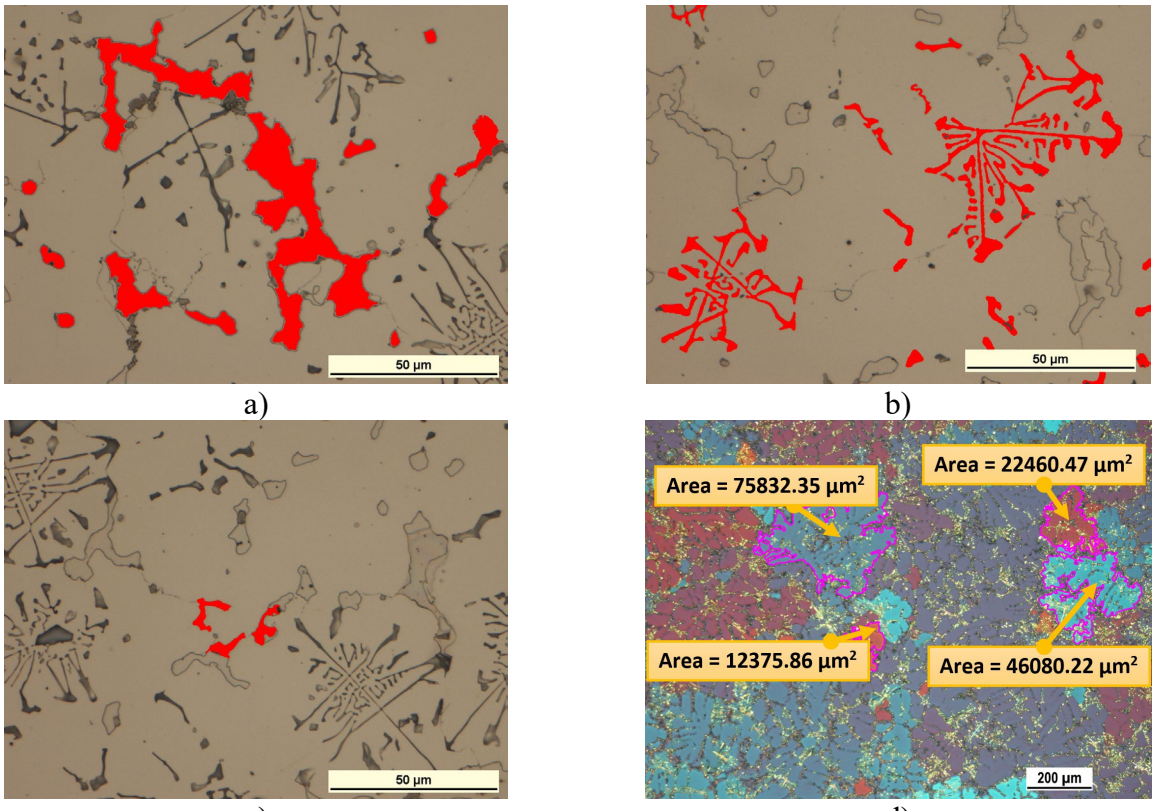

a) b) c) d)

Fig. 2 Quantitative phase analysis and a grain size evaluation of aluminum alloy EN AC 51200, LM; a) share of Al_3Mg_2; b) a share of Mg_2Si; c) a share of $Al_6(FeMn)$; d) a grain size measuring of aluminum alloy EN AC 51200.

Fifteen test specimens with block geometry without stress concentrators (notches) were used for cyclic fatigue tests in three-point bending. Based on the measurement results, a Wöhler (S–N) curve (Fig. 3) in semilogarithmic coordinates was constructed, which describes the relationship between

the stress amplitude σ_a and the number of cycles N_f to failure. The experimental data were then mathematically approximated using the Basquin formula (Equation 1), which is used to describe the high-cycle fatigue region of metallic materials. This dependence has the form [8, 9]:

$$\sigma_a = \sigma_f' \times \left(2 \times N_f\right)^b \quad (1)$$

where σ_f' is fatigue strength coefficient and b is fatigue strength exponent. The parameters σ_f' and b were determined by the method of least squares (least squares method) based on linear regression in log coordinate space, which obtained an approximation of the S–N curve with sufficient accuracy for predicting the service life.

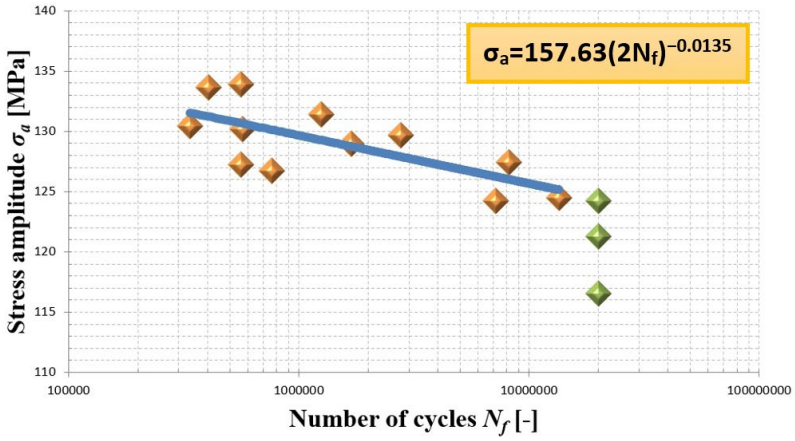

Fig. 3 Results of fatigue tests for aluminum alloy EN AC 51200.

Experimental results show that the fatigue life of the material increases with decreasing stress amplitude. The constructed S–N curve shows a typical decreasing trend (yellow points), while with an extended life, its smooth decrease occurs. Samples that did not reach failure within the maximum number of cycles ($N_f = 2\text{x}10^7$) are marked as run-out (green points) and serve as an indication of the ultimate fatigue life of the material. The longest achieved fatigue life was shown by the sample loaded with the maximum bending stress $\sigma_{o,max} = 124$ MPa, at which failure occurred only after 20000072 cycles.

To investigate the failure mechanism in detail, fracture surfaces of samples with different loading stresses and different fatigue lives were analyzed. Macrofractographic analysis allowed to identify the initiation sites of fatigue cracks (Fig. 4 and Fig. 5), as well as to distinguish the areas of stable fatigue propagation from the area of final (static) fracture. In all cases, crack initiation occurred on the surface of the samples, which is typical for high-cycle fatigue.

At higher stress amplitudes, two initiation sites were observed on opposite sides of the fracture surface, while at lower amplitudes, there was mainly one dominant initiation site. The extent of the area of stable fatigue propagation of the crack correlates with the stress amplitude – higher amplitudes led to a smaller fatigue area and a large area of final static rupture. Conversely, at lower amplitudes, the fatigue zone was significantly extended. In cast materials, it is possible to observe the presence of microstructural inhomogeneities (e.g. pores, segregations, inclusions), which can serve as initiation points of fatigue cracks. However, in this case, it was not possible to clearly determine a specific initiation defect from the macrofractographic analysis.

Microfractographic analysis revealed that fatigue failure of the α-phase matrix occurred by a transcrystalline mechanism, which is evidenced by the presence of striations – characteristic features of stable fatigue propagation. Intermetallic phases located at grain boundaries or in interdendritic regions were preferentially fractured by interfacial (intergranular) fracture. In the region of final static failure, transcrystalline ductile fracture with pitting morphology and plastically deformed protrusions, typical of ductile matrix failure, dominated. Intermetallic phases in this region also showed signs of interfacial failure, which indicates their lower cohesion with respect to the matrix.

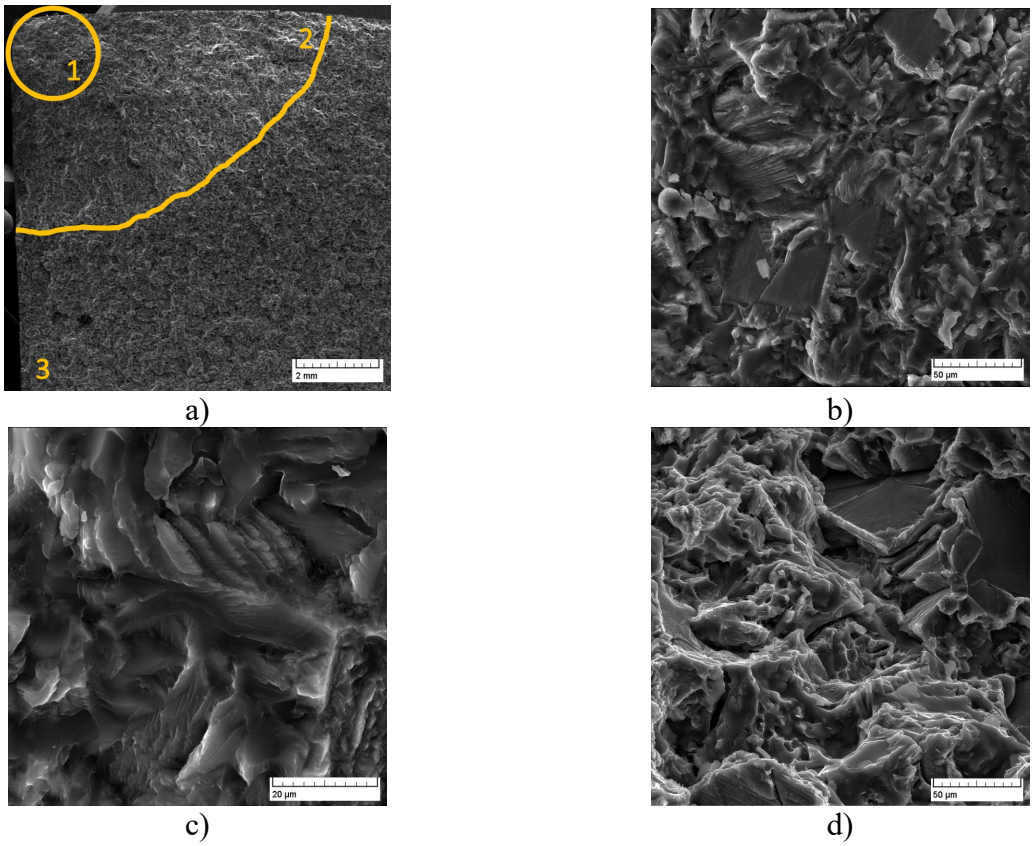

a) b)

c) d)

Fig. 4 Fractography surface of aluminum alloy EN EC 51200 after fatigue test at lower cyclic loading, SEM; a) a macroscopic view (1 – initiation site, 2 – fatigue area, 3 – area of static final failure); b) a fatigue area; c) a detail of the fatigue area; d) an area of static final failure.

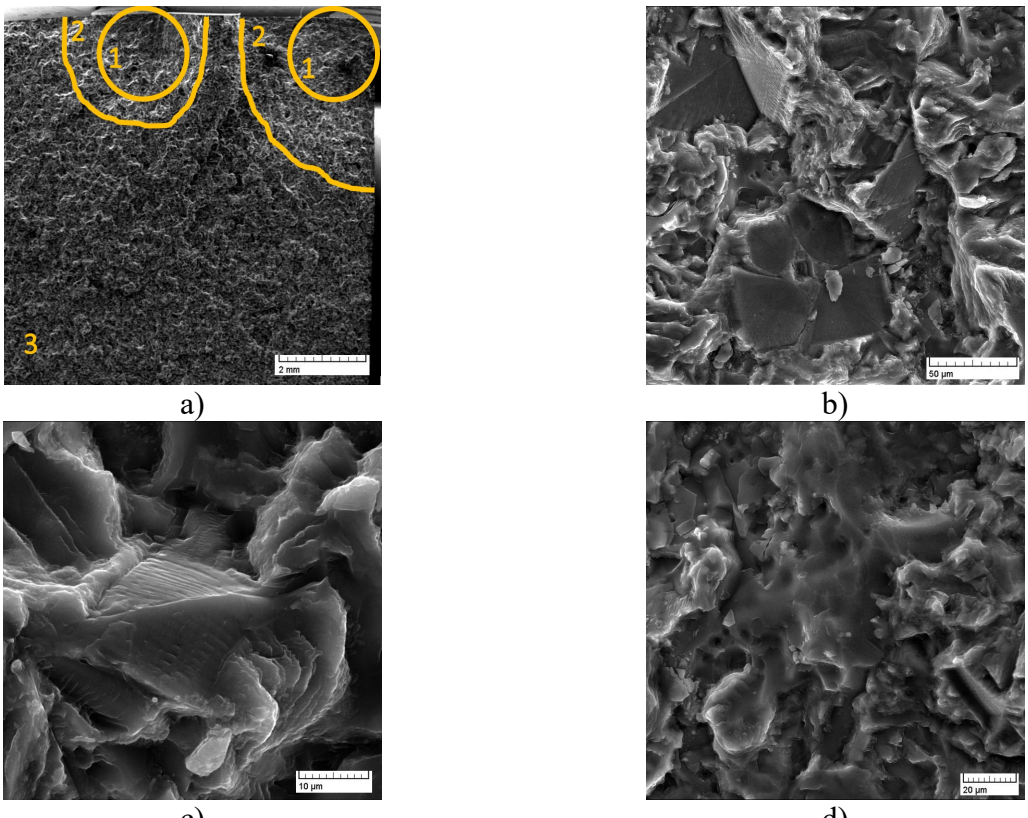

a) b)

c) d)

Fig. 5 Fractography surface of aluminum alloy EN EC 51200 after fatigue test at higher cyclic loading, SEM; a) a macroscopic view (1 – initiation site, 2 – fatigue area, 3 – area of static final failure); b) a fatigue area; c) a detail of the fatigue area; d) an area of static final failure.

Conclusions

Fatigue tests performed on the EN AC 51200 (Al-Mg) aluminum alloy revealed several key mechanisms influencing its behavior under cyclic loading. Microstructural analysis showed that the dominant phase in the structure was the β phase (Al_3Mg_2), followed by the intermetallic phase Mg_2Si and a smaller proportion of the ferrous phase $Al_6(FeMn)$. These phases, together with the grain size and distribution (average 57361 μm^2) and the secondary dendrite arm spacing (SDAS ≈ 39 μm), can play a significant role in the initiation and propagation of fatigue cracks.

Basquin's analysis of the experimental data showed that the fatigue behavior of the alloy can be approximated with sufficient accuracy by the Equation 2:

$$\sigma_a = 157.63 \times \left(2 \times N_f\right)^{-0.0135} \quad (2)$$

where the coefficient of determination $R^2 \approx 0.493$ (moderately strong correlation – data dispersion is more pronounced, which is common in cast aluminum alloys with the presence of inhomogeneities) reflects the influence of microstructural inhomogeneities and variability in the failure mechanism. Fractographic analysis showed that fatigue cracks preferentially initiate on the surface of the samples, probably often in areas of microdefects or at the interface between the matrix and intermetallic phases. Crack propagation is mostly transcrystalline through the α-matrix with observed striations, while areas of static fracture showed ductile pitting failure.

The obtained results indicate the sensitivity of the EN AC 51200 alloy to microstructural parameters and support the need to optimize the composition, casting technology and subsequent processing in order to improve its fatigue resistance. Identification of the dominant failure mechanisms represents an important step in the design of components from this alloy for dynamically loaded applications.

Acknowledgment

The research was supported by the Scientific Grant Agency of the Ministry of Education of Slovak Republic and Slovak Academy of Sciences, No. 1/0461/24, No. 004ŽU-4/2023, No. 016ŽU-4/2023, APVV-20-0427 and project to support young researchers at UNIZA, the ID of project 20422.

References

[1] W. Yan, Y. Li, Y. Wu, Trans Tech Publications, 331 (2022) 85-89.

[2] M.C. Shaji, K.K. Ravikumar, M. Ravi, K. Sukumaran, Trans Tech Publications, 765 (2013) 54-58.

[3] S.W. Choi, Y.C. Kim, C.S. Kang, J.M. Jung, S.K. Hong, Trans Tech Publications, 813 (2013) 427-430.

[4] G.F. Eggeler, Creep and creep-fatigue of metal-matrix composites, Encyclopedia of Materials: Science and Technology (Second Edition). 2001. 1757-1759.

[5] S.-T. Tu, X.-C. Zhang. Fatigue crack initiation mechanisms, Reference Module in Materials Science and Materials Engineering. 2016.

[6] A. la Monaca, J.W. Murray, Z. Liao, A. Speidel, J.A. Robles-Linares, D.A. Axinte, M.C. Hardy, A.T. Clare, International Journal of Machine Tools and Manufacture, 164 (2021) 103718.

[7] G. Mrówka-Nowotnik, J. Sieniawski. Solid State Phenomena, 197 (2013) 238-243.

[8] Y. Murakami, T. Takagi, K. Wada, H. Matsunaga, International Journal of Fatigue, 146 (2021) 106138.

[9] Y.B. Liu, Y.D. Li, S.X. Li, Z.G. Yang, S.M. Chen, W.J. Hui, Y.Q. Weng, International Journal of Fatigue, 32 (2010) 1351-1357.

Keyword Index

Author Index